Springer Proceedings in Earth and Environmental Sciences

V. I. Karev *Editor*

Physical and Mathematical Modeling of Earth and Environment Processes

Proceedings of 7th International Conference, Moscow, 2021

Springer

Springer Proceedings in Earth and Environmental Sciences

Series Editors

Natalia S. Bezaeva, The Moscow Area, Russia

Heloisa Helena Gomes Coe, Niterói RJ Brazil, Brazil

Muhammad Farrakh Nawaz, Department of Forestry and Range Management, University of Agriculture, Faisalabad, Pakistan

The series Springer Proceedings in Earth and Environmental Sciences publishes proceedings from scholarly meetings and workshops on all topics related to Environmental and Earth Sciences and related sciences. This series constitutes a comprehensive up-to-date source of reference on a field or subfield of relevance in Earth and Environmental Sciences. In addition to an overall evaluation of the interest, scientific quality, and timeliness of each proposal at the hands of the publisher, individual contributions are all refereed to the high quality standards of leading journals in the field. Thus, this series provides the research community with well-edited, authoritative reports on developments in the most exciting areas of environmental sciences, earth sciences and related fields.

More information about this series at https://link.springer.com/bookseries/16067

V. I. Karev
Editor

Physical and Mathematical Modeling of Earth and Environment Processes

Proceedings of 7th International Conference, Moscow, 2021

Springer

Editor
V. I. Karev
Institute for Problems in Mechanics
Russian Academy of Sciences
Moscow, Russia

ISSN 2524-342X ISSN 2524-3438 (electronic)
Springer Proceedings in Earth and Environmental Sciences
ISBN 978-3-030-99503-4 ISBN 978-3-030-99504-1 (eBook)
https://doi.org/10.1007/978-3-030-99504-1

© The Editor(s) (if applicable) and The Author(s), under exclusive license to Springer Nature Switzerland AG 2022
This work is subject to copyright. All rights are solely and exclusively licensed by the Publisher, whether the whole or part of the material is concerned, specifically the rights of translation, reprinting, reuse of illustrations, recitation, broadcasting, reproduction on microfilms or in any other physical way, and transmission or information storage and retrieval, electronic adaptation, computer software, or by similar or dissimilar methodology now known or hereafter developed.
The use of general descriptive names, registered names, trademarks, service marks, etc. in this publication does not imply, even in the absence of a specific statement, that such names are exempt from the relevant protective laws and regulations and therefore free for general use.
The publisher, the authors and the editors are safe to assume that the advice and information in this book are believed to be true and accurate at the date of publication. Neither the publisher nor the authors or the editors give a warranty, expressed or implied, with respect to the material contained herein or for any errors or omissions that may have been made. The publisher remains neutral with regard to jurisdictional claims in published maps and institutional affiliations.

This Springer imprint is published by the registered company Springer Nature Switzerland AG
The registered company address is: Gewerbestrasse 11, 6330 Cham, Switzerland

Preface

The seventh International Scientific Conference-School for Young Scientists "Physical and mathematical modeling of processes in geomedia" is held at the Ishlinskii Institute for Problems in Mechanics of the Russian Academy of Sciences for the seventh time and is of great interest in the scientific community. For the seventh year in a row more than one hundred scientists have taken part in it, two-thirds of whom are young scientists.

At the previous six schools, the reports of the participants were traditionally accompanied by an active discussion, which continued after the end of the program sessions. Based on the results of the School's work, it was decided to hold the 8th Scientific Conference-School of Young Scientists "Physical and Mathematical Modeling of Processes in Geomedia" in 2022. The scientific program of the 7th Conference-School includes theoretical and experimental studies of processes in the atmosphere, oceans, the lithosphere and their interaction; environmental issues; study of the anthropogenic contribution to the dynamics of natural systems; and methods of geophysical research. The focus of the Conference-School was the following areas of research: the development of geomechanical approach to solving the problems of oil and gas production, physical and mathematical modeling of deformation and fracture of solid materials, both natural and artificial, study of interaction of these processes in porous media on the seepage, creation effective mathematical models, and experimental base for research of flows in complex heterogeneous liquids.

The 7th Youth Forum, as well as the previous six, has to contribute to the solution of fundamental scientific problems arising in the study of natural processes in different geomedia, the impact of anthropogenic activities to the environment. One of the central topics for the Conference-School is associated with the elaboration of scientific bases, the creation of new breakthrough approaches to the development of hydrocarbon deposits, including non-traditional sources.

Research of the dynamics of natural systems—the geosphere, the hydrosphere, the atmosphere—and their interactions, the human contribution to naturally occurring processes are among the most urgent and practically important scientific problems. Intensive development of research in these areas is due to several factors. The widespread introduction of computer technology has allowed beginning calculation

of complex phenomena, previously unavailable for analysis. Creation and improvement of a new generation of geophysical instruments, remote observing systems based on the ship, aircraft, and satellite allowed us to obtain a large amount of data to objectively reflect the picture of the processes.

An alternative to the use of hydrocarbons as a main source of energy on the planet in the coming decades is unlikely to be found. At the same time, the resource base of hydrocarbons is quickly depleted, new non-traditional sources are required. Among them, shale oil and gas, hydrocarbons of the Arctic region, gas hydrates, deep and ultra-deep oil, and gas deposits. The development of low permeability deposits may become the main source of expanding the resource base of hydrocarbons according to many experts. The creation of new breakthrough approaches to the development of hydrocarbon fields is very important in today's geopolitical conditions and requires the involvement of young minds and strength. International activities, including the youth scientific schools, can become an effective tool for exchange of information and the organization of interdisciplinary research of processes in geomedia.

Scientists of all specialties are invited to participate in the Conference-School: experimenters, analysts, and computer specialists. The lectures of prominent experts will be given in key sections of geomechanics and geophysics. Reports of young scientists who have made a deep original research were heard. Program Committee, which includes the leading scientists on the scientific directions of the Conference-School, has conducted peer review of the reports submitted to the Conference-School and produced a competitive selection. In the form of short papers, the most interesting results presented at the Conference-School are published by Springer in this book in the Geosciences Conferences Proceedings Series. The Conference-School is organized by Ishlinsky Institute for Problems in Mechanics of RAS, Physics Faculty of Lomonosov Moscow State University, Branch in Sevastopol of Lomonosov Moscow State University. The conference organizers are deeply grateful recognized scientists who have given consent to take part in its work and presented their works; young professionals and post-graduate students who have responded to the invitation; and, of course, the institutions which have provided organizational support to the Conference-School.

Moscow, Russia

V. I. Karev
Chairman of the Organizing Committee

Contents

Role of Nonlinear Processes in Infragravity Waves Evolution

Ya. V. Saprykina

Abstract Laboratory and numerical experimental studies carried out reveal that difference nonlinear interactions form bound IGW propagating with group velocity and in phase with the envelope of GW. It is shown that, due to nonlinear interactions, the IGW height can depend on the GW in a fairly wide range of values, having a quadratic dependence on average. For breaking waves and waves after breaking, this dependence is stronger.

Keywords Infragravity waves · Nonlinear wave transformation · Wave breaking · Wave height

1 Introduction

Infragravity waves (hereinafter referred to as IGW) are long waves with periods of 20–300 s, formed as a result of the propagation of shorter gravitational (hereinafter GW) sea waves (periods 2–20 s).

IGW and their impact on dynamical processes are most clearly manifested in the coastal zone of the seas. Since IGW are less dissipating during wave breaking, their energy near the coast can exceed the energy of wind waves [1, 2]. From a practical point of view, IGW are important because of their impact on the sediment transport in the coastal zone [3] and also because they are the main cause of the formation of long waves movements in ports and harbors [4]. However, despite the intensive study of IGW in various dynamic processes of the coastal zone, there is still no complete physical picture of their origin and evolution. This is due to different mechanisms of their generation, complex manifestations of their dynamics associated with the interaction of IGW with both wind waves and IGW reflected from the underwater slope, as well as the lack of detailed field experiments.

According to modern concepts, the infragravity waves observed in the coastal zone can be form by different processes. The main source of IGW is the group structure of

Ya. V. Saprykina (✉)
Shirshov Institute of Oceanology RAS, Moscow, Russia
e-mail: saprykina@ocean.ru

© The Author(s), under exclusive license to Springer Nature Switzerland AG 2022

V. I. Karev (ed.), *Physical and Mathematical Modeling of Earth and Environment Processes*,
Springer Proceedings in Earth and Environmental Sciences,
https://doi.org/10.1007/978-3-030-99504-1_1

gravitational waves. It has been theoretically shown that changes in radiation stress due to wave group structure cause infragravity waves [5]. These IGW propagate with wave group velocity.

Another mechanism for the formation of IGW is a spatio-temporal shift of the wave breaking point (for example, [6]. It is assumed that these infragravity waves are free and propagate with phase velocity according to the dispersion relation.

On the other hand, infragravityl waves can be the result of difference nonlinear interactions between pairs of incoming shorter GW [7], Longuet-Higgins and Stewart [5]. Theoretically, IGW formed in the coastal zone due to difference near-resonance nonlinear three-wave interactions, by analogy with high-frequency waves arising due to sum nonlinear three-wave interactions, should propagate with phase velocity different from the dispersion relation [8].

The possible existence of such IGW according to the data of a field experiment was observed in [9, 10]. However, according to theoretical estimates, their energy should be significantly less than the observed energy of IGW of experimental waves. The analysis of the IGW of this experiment also showed that in the field data the fraction of free IGW significantly exceeds the fraction of the bound IGW associated with wave group structure of GW.

It was previously shown that in the coastal zone, nonlinearity is the main reason for the change the wave group structure, and the group structure itself exists throughout the coastal zone and does not disappear even after the waves break [11]. From this point of view, it seems important to study the evolution of IGW associated with the group structure and its nonlinear changes. Therefore, the purpose of this work is, on the basis of numerical and laboratory experiments, to find out the influence of nonlinear difference interactions on the formation of infragravity waves during the transformation of waves with group structure.

2 Experiment and Methods

For the study, we used the data of a laboratory experiment carried out in the hydrodynamic flume of the Institute of Water Construction of the Polish Academy of Sciences (Gdansk) in 2005. The depth of the flume is 1.4 m, the length is 64 m. Different initially bichromatic waves with a simple wave group structure - the sum of two cosine signals propagated over a flat bottom at a depth of 0.3 m and above a trapezoidal bar at a depth of 60 cm. Recording length—2 min, sampling frequency 200 Hz. To register waves, 7 resistance and 8 capacitive string wave gauges were used. The positions of wave gauges and the bottom reliefs of the experiment are shown in Fig. 1.

The phase velocity of infragravity waves was determined from the shift of the maximum of the cross-correlation function between wave chronograms at nearest measurement points [12]:

$$cf_l = l/\Delta t \tag{1}$$

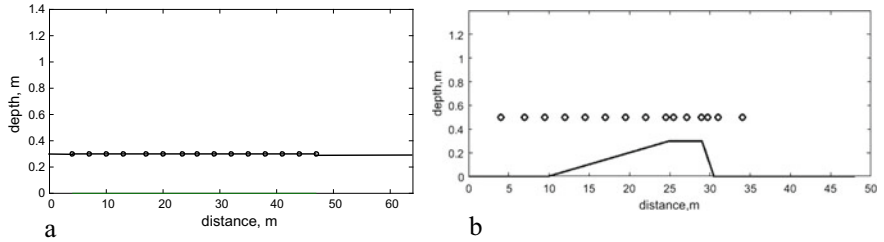

Fig. 1 Experiment setups: constant depth (**a**) and bar bottom profile (**b**)

where l is the distance between measurement points, Δt is the shift of the maximum of the mutual correlation function of waves between these measurement points. The value of the phase velocity obtained in this way was referred to the midpoint of the interval l.

The wave group velocity was determined as the phase velocity of propagation of wave envelope, which was also calculated by the formula (1).

Preliminary, linear filtering of the wave chronogram was carried out into the frequency ranges of IGW (frequencies less than 0.05 Hz) and gravitational waves (frequencies more than 0.05 Hz, but less than 2 Hz), as well as into the ranges of the first and second nonlinear harmonics to assess the contribution of high frequencies to the formation of IGW. The wave envelopes were calculated by the formula

$$\zeta_e = \sqrt{\{L[\zeta(t)]\}^2 + [X\{L[\zeta(t)]\}]^2} \tag{2}$$

where X is the Hilbert transform, L is the linear filtration operator, $\zeta(t)$ are the elevations of the free surface.

3 Discussion of Results

3.1 Waves on Constant Depth

Bichromatic waves with frequencies of 0.5 and 0.52 Hz and amplitudes of 3 cm propagated on constant depth of 0.3 m were investigated in flume and in model.

According to the experimental conditions and modelling, the waves propagated without wave breaking and energy dissipation caused only by friction. The wave reflection was small at experiment and absent in modelling. Therefore, the main physical mechanisms of the evolution of model IGW are nonlinear interactions and radiation stresses generated by the wave group structure.

Figure 2 shows the changes in the correlation coefficient between the IGW and the group structure of waves, i.e., between the envelopes of GW and the frequency range of the first and second nonlinear harmonics within the wave chronogram in all measured points. It is seen that at all distances infragravity waves have a large correlation coefficient with the wave group structure. At the initial time, the correlation coefficient is negative, IGW are in antiphase with the group structure of waves that corresponds to the theory of IGW associated with radiation stresses [5]. As the contribution of nonlinear interactions to IGW increases, the correlation coefficient becomes positive, i.e. infragravity waves propagate in phase with a wave envelope. It can also be noted that IGW can have a large correlation coefficient both with the envelope of the waves of the first harmonics, and with the envelope of the waves of high-frequency second harmonics. This, apparently, depends on the contribution of which frequency range prevails in the transfer of energy to the IGW. Such a positive correlation of IGW with the envelope of the wave group structure is often observed in field experiments, and in the absence of reflected IGW, this was previously explained by experimental errors or incorrect analysis. Thus, we can say that difference nonlinear interactions form IGWs that propagate with the group velocity and in phase with the wave envelope.

The velocity of propagation of IGW, both in laboratory and in model data, at the beginning of wave transformation exceeds the velocity of propagation of the envelope (group velocity) and the phase velocity of IGW (Fig. 2). In this case, the values of the phase velocity do not correspond to the phase velocity of the linear theory of waves for IGW. This can be related both to the influence of the discreteness of the given initial conditions, when the amplitudes and, accordingly, the spectrum energy are initially set for only two frequencies. It can also be caused by the fact that the set on the boundary the wave group structure and the creation of radiation stresses does not in itself mean the creation an infragravitational wave, since the main feature of waves is their propagation (Fig. 3).

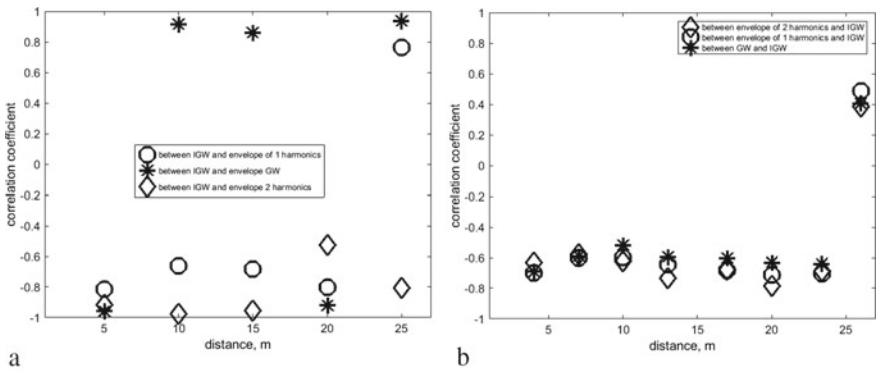

Fig. 2 Correlation coefficient between wave envelope and infragravity waves as bichromatic waves propagate over constant depth in **a** numerical and **b** laboratory experiments

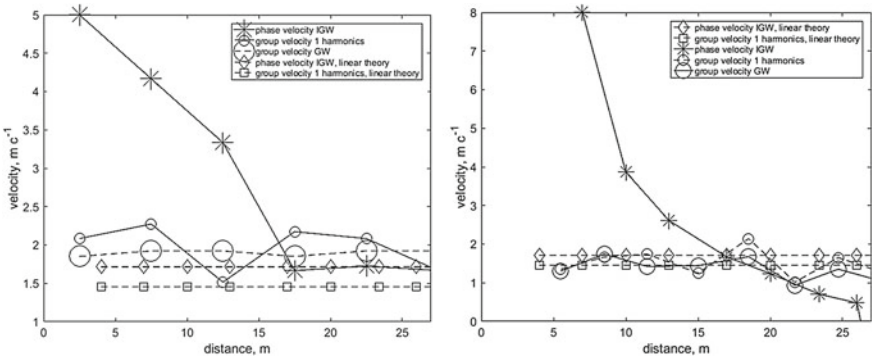

Fig. 3 The phase velocities of the IGW and the envelope of the wave group structure in the numerical (**a**) and laboratory (**b**) experiments, constant depth

When the phase velocity is calculated on the shift of the maximum of the mutual correlation function, large phase velocities are obtained when there is a small time shift between the wave crests on two gauges. It means that the waves practically do not propagate or that this IGW chronogram is not a real "wave". This happens when the energy of the first harmonics is transferred to the second nonlinear harmonics (sum three-wave interactions) and to the IGW (difference three-wave interactions). A nonlinear addition to the phase velocity of IGW decreases their initial phase velocity. Starting from the moment when the second harmonics were formed and the reverse transfer of energy from the second harmonics to the first (a distance of about 17 m) began, the phase velocity of IGW propagation became close to the group velocity of the first harmonics and to the group velocity of waves in the range of the first and second harmonics. The group velocity of the first harmonics changes periodically in accordance with the exchange of energy between the first and second harmonics, on average slightly exceeding the group velocity calculated by the formula of the linear wave theory. At waves propagation the difference between the phase velocity of the IGW and the group velocity of the first harmonics and the group velocity of all GW decreases. That is, nonlinear interactions giving a constant contribution to the energy of IGW generate forced or bound IGW, which propagate with the velocity of the envelope or with the group velocity of waves. In laboratory data, the IGWs phase velocity decreases, which is associated with the interaction with counterpropagating IGW waves and the formation of a standing wave [13].

3.2 Waves Above Underwater bar

Let consider waves propagating above underwater bar. Wave breaking occurs at the top of the bar. Evolution of bichromatic waves with different frequencies and amplitudes propagated above underwater bar in the flume were analyzed.

As in the case of wave propagation over a constant depth, initially bichromatic waves immediately form forced IGW as a result of changes in radiation stresses caused by the wave group structure. These waves are bound with GW that is confirmed by a large negative correlation coefficient between them and the envelope of wind waves. It is consistent with the theory [5]. Their spectral composition also confirms that these waves are bound. It is similar to the spectral composition of the envelope of the first harmonics and these waves are always coherent to the envelope. At the initial transformation the IGWs height decreases, as well as the height of the gravitational waves. This is due to the processes of dissipation of wave energy due to influence of bottom friction. Simultaneous similar decreasing IGW and GW also confirm that they are bound.

The spectrum frequency of these waves corresponds to the difference frequency of the initial bichromatic waves. At the beginning of the wave transformation, it is only one main peak frequency in the IGWs range. Further, as the groups of waves are transformed, the second harmonics grow. While the second harmonics are small, the process of backward transfer of energy from them to the frequencies of the first harmonics and to the IGW frequency exists, but the fraction of the transferred energy is very small. It can be conclude that at this moment the processes of energy dissipation in the frequency range of the first harmonics and in IGW prevail over the energy input due to difference nonlinear interactions. This is confirmed by a steady decreasing in the height of significant waves of GW and IGW (Fig. 4).

In the spectrum, the energy of the spectrum maximum frequency decreases. Because of this the frequency of the spectrum maximum changes sometimes. That reflects both the IGW spectrum and the spectrum of envelope of the waves of the first harmonics. But, as soon as the second harmonics have sufficient large amplitude, the transport of energy due to difference interactions from the second to the first harmonics and due to the first into IGW increases. The height of the IGW is growing. At this moment, the IGW become free (the correlation coefficient with the envelope has a positive sign) and this happens before the waves breaking.

When waves break and after breaking, the correlation coefficient also has a positive sign. The IGW spectrum is similar to the GW envelope spectrum. The peak frequency corresponds to the difference frequency. Free IGW can further increase in amplitude (due to shoaling), and can decrease due to wave breaking (Figs. 5a and 6a, breaking corresponds to 0.35). That is, they behave in corresponding to the group structure. This process is similar for bichromatic waves with different initial width of spectrum and for different initial frequencies.

However, it should be noted that with an increase in the frequency difference, the second harmonics increase faster, since with a larger difference the bi-chromatic harmonics interact less with each other. If the difference is smaller, then there is an interaction between the fundamental harmonics, which weakens the transfer of energy to high and low frequencies.

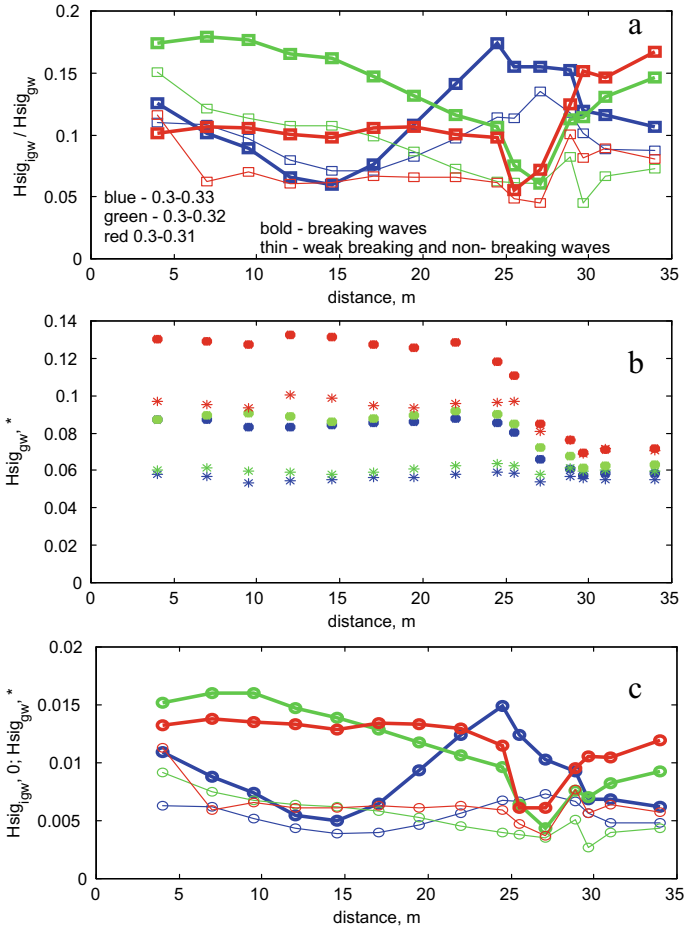

Fig. 4 Change in the height of IGW (**c**), the height of GW (**b**) and their ratio (**a**) during the transformation of bichromatic waves of spectra of different widths above the underwater bar

As for the general dependence of the IGW height on the GW in breaking waves and not in breaking waves, on average it is quadratic and there will be fewer deviations for breaking waves (Figs. 5b and 6b).

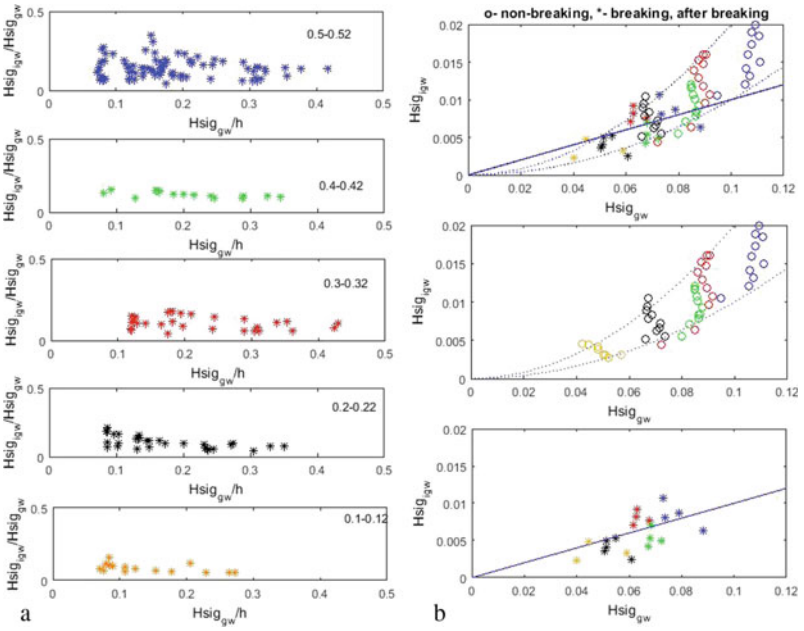

Fig. 5 Dependence of the ratio of the heights of IGW and GW on the relative depth of water (**a**) and heights of IGW on GW (**b**) the transformation of initially bichromatic waves of spectrum with width of 0.02 Hz

4 Conclusions

Experimental studies carried out reveal that difference nonlinear interactions form bound IGW propagating with group velocity and in phase with the envelope of GW. However, the observed IGW height largely depends on the interaction with reflected free IGW. At the initial stage of wave transformation, the calculated phase velocity of the IGW, the wave group velocity and the phase velocity of the linear wave theory are not coincide. It is shown that, due to nonlinear interactions, the IGW height can depend on the GW in a fairly wide range of values, having a quadratic dependence on average. For breaking waves and waves after breaking, this dependence is stronger.

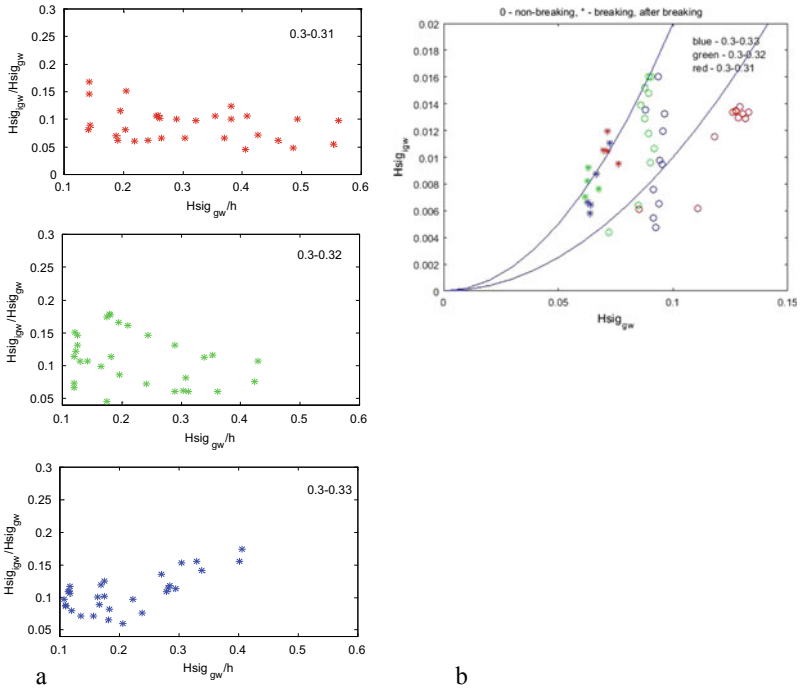

Fig. 6 Dependence of the ratio of the heights of IGW and GW on the relative depth of water (**a**) and heights of IGW on GW (**b**), the transformation of initially bichromatic waves of different spectrum width

Acknowledgements This work was supported by the RFBR project 20-55-46005.

References

1. Thornton E.B., Guza R.T. 1983. Transformation of wave height distribution. Journal Geophysical Research, vol.88, No C10. pp.5925-5938.
2. Masselink G., 1995. Group bound long waves as a source of infragravity energy in the surf zone. Continental Shelf Research, 15 (3), pp. 1525-1547.
3. Hanes D.M., 1991. Suspension of sand due to wave groups. J. of Geoph. Res., 96 (C5), pp. 8911-8915.
4. Miles, J., W. Munk, 1961. Harbour paradox. J. Waterways and Harbors Div,WW3, pp.111–130.
5. Longuet-Higgins, M. S., Stewart R. W., 1962. Radiation stress and mass transport in surface gravity waves with application to ‘surf beats.‘ J. Fluid Mech.75: 481-504.
6. Symonds G., D.A. Huntley, A.J. Bowen, 1982. Two dimensional surf beat: long wave generation by a time-varying breakpoint. J. of Geoph. Res., 87(C), pp.492–498.
7. Hasselmann, K., 1962: On the non-linear energy transfer in a gravity-wave spectrum, Part 1. General theory. J. Fluid Mech., 12,481-500.
8. Madsen P.A., Sorensen O.R., 1993. Bound wave and triad interactions in shallow water. J. Ocean Eng. 20(4): 359-388.

9. Herbers, T. H. C., Steve Elgar, and R. T. Guza, 1994, Infragravity-frequency (0.005-0.05 Hz) motions on the shelf, Part I: Local nonlinear forcing by surface waves, J. Physical Oceanography, 24, 917—927.
10. Herbers, T. H. C., S. Elgar, R. T. Guza, and W. C. O.Reilly, 1995, Infragravity-frequency (0.005-0.05 Hz) motions on the shelf, II, Free waves, J. Phys. Oceanogr., 25, 1063-1079.
11. Kuznetsov S.Yu., Saprykina Ya.V. An experimental study of near shore evolution of wave groups. Oceanology. 2002. T. 42. № 3. C. 336–343.
12. Wen-Song Ciang et al. 2005. Experiments on the front of continuous wave traines in a large wave tank. Proceeding of 29th International Conference on Coastal Engineering, 19–24 September, Lisbon, Portugal, edited by Jane McKee Smith, World Scientific, 2005, pp. 145–156.
13. Saprykina, Y.V., Kuznetsov, S.Y., Kovalenko, A.N., 2015.Experimental studies of the local reflection of long waves from an underwater slope. Oceanology, 55 (2), pp. 171-181.

On the Boundaries of Paleostructures of the Ashamba River in the Blue Bay Near Gelendzhik According to Broadband Continuous Seismic and Acoustic Profiling and GPS Positioning

M. S. Klyuev, A. A. Schreider, A. S. Zverev, A. L. Brekhovskikh, I. Ya Rakitin, and A. E. Sazhneva

Abstract The boundaries of paleostructures of the Ashamba River in the Blue Bay and adjacent areas near Gelendzhik have been determined. The method of broadband continuous seismoacoustic profiling and GPS positioning was used. Maps of the location of the identified structures and objects, the acoustic permeability of precipitation at a frequency of 20 kHz and the average height of the roughness of the bottom surface are presented.

Keywords Geomorphology · River paleostructures of the seabed · Broadband continuous seismoacoustic profiling · GPS positioning

One of the unique features of the geomorphology and structure of the bottom of the Blue Bay near Gelendzhik are the paleostructures of the Ashamba River flowing into the bay. These structures were discovered and investigated in 2018–2021 by employees of the P.P.Shirshov Institute of Oceanology of the Russian Academy of Sciences together with specialists of the V.I. Vernadsky Institute of Geochemistry and Analytical Chemistry of the Russian Academy of Sciences [1–10].

At the same time, the technology of continuous broadband seismoacoustic profiling was used [1, 3–5], the essence of which is vertical seismoacoustic sounding of the bottom of the coastal water area over an area in a wide frequency range f (200 kHz–200 Hz) using various directional patterns θ (narrow from 4° and wide to 180°), while providing high-precision GPS navigation.

M. S. Klyuev (✉) · A. A. Schreider · A. L. Brekhovskikh · I. Y. Rakitin · A. E. Sazhneva
Shirshov Institute of Oceanology RAS, 36 Nakhimov Ave, Moscow 117997, Russia

A. S. Zverev
Vernadsky Institute of Geochemistry and Analytical Chemistry RAS, 19/1 Kosygina St, Moscow 119991, Russia

© The Author(s), under exclusive license to Springer Nature Switzerland AG 2022

V. I. Karev (ed.), *Physical and Mathematical Modeling of Earth and Environment Processes*,
Springer Proceedings in Earth and Environmental Sciences,
https://doi.org/10.1007/978-3-030-99504-1_2

The wide frequency range of the seismoacoustic means used is due to the fact that paleostructures can be located not only on the surface of the bottom, but also at a depth of units to tens of meters below its surface, and the depth of penetration into the bottom of the probing signal depends on the frequency. The lower the frequency, the greater the penetration, but the lower the spatial resolution, and, accordingly, the higher the frequency, the less penetration, but the higher the spatial resolution [1–5].

The classification features developed in [1–12] were used as criteria for the detection and recognition of bottom river paleostructures in the coastal marine zone. These criteria are based on the fact that the paleostructures under consideration are characterized by the so-called "box-like" transverse profile, which repeats smoothly and translationally in space. Under the "box" profile here is meant a transverse profile in the form of a bowl with pronounced coastal slopes and a flattened bottom, and the degree of flattening can vary widely from flat to U- and V-shaped. In this case, the coastal slopes of the paleochannel can either rise above the sedimentary filling, or be completely buried in the sedimentary stratum, without giving any manifestation on the bathymetry of the seabed. In addition, paleochannels can be associated with coastal river structures, have a branching structure in the form of paleotributaries and paleodeltas, and be accompanied by gas flares.

For the practical implementation of the technology under consideration, a complex of hydroacoustic profiling of the bottom surface and the upper layer of sediments developed by the IO RAS (high-frequency narrow-beam echo sounder $f = 200$ kHz, $\theta = 4°$ and parametric profiler $f = 20$ kHz, $\theta = 4.5°$) [13–21] and seismoacoustic complex "Geont-shelf" manufactured by "Spektr-geofizika" LLC (non-directional emitters of the "boomer" type $f = 1$–2 kHz and "sparker" $f = 300$–800 Hz) [22, 23].

Continuous seismoacoustic profiling of the Blue Bay water area [1–5] was carried out on board small research vessels (MNIS) of the "Ashamba" type (length 15 m, width 4 m, draft 1.5 m, displacement 27t.), Professor Longinov (boat MaryFisher 625, length 6.4 m, width 2.5 m) and "Cayman" (inflatable boat, length 3 m, width 1.6 m). The SeaKing DST transceiver head was mounted on a rod overboard of the MRIS, and the boomer, sparker, and Geon-shelf receivers were towed behind the ship. When profiling by the IO RAS complex, a rectangular grid of lines was located in the west–east and north–south directions with a spatial step of about 40 and 30 m, respectively.

Let us dwell briefly on the main results of research and their illustrations [1–10].

Figure 1 shows one of the typical transverse "box-shaped" profiles of the Ashamba River paleo riverbed in the Blue Bay near Gelendzhik (area C in Fig. 3) according to the profiler $f = 20$ kHz, $\theta = 4°$ (a) and according to the "boomer" $f = 1$–2 kHz (b). From the figure it can be seen that the paleo riverbed forms a channel about 250 m wide in marl rocks rising 7 m (according to sampling), which is filled with layers of silty-sandy sediments (according to sampling data) to a depth of about 3 m. At the same time, the profiler displays the relief and structure of the upper sediment layer in sufficient detail, and the "boomer" gives information about the structure of the sedimentary filling of the paleo riverbed bowl, but with less detail.

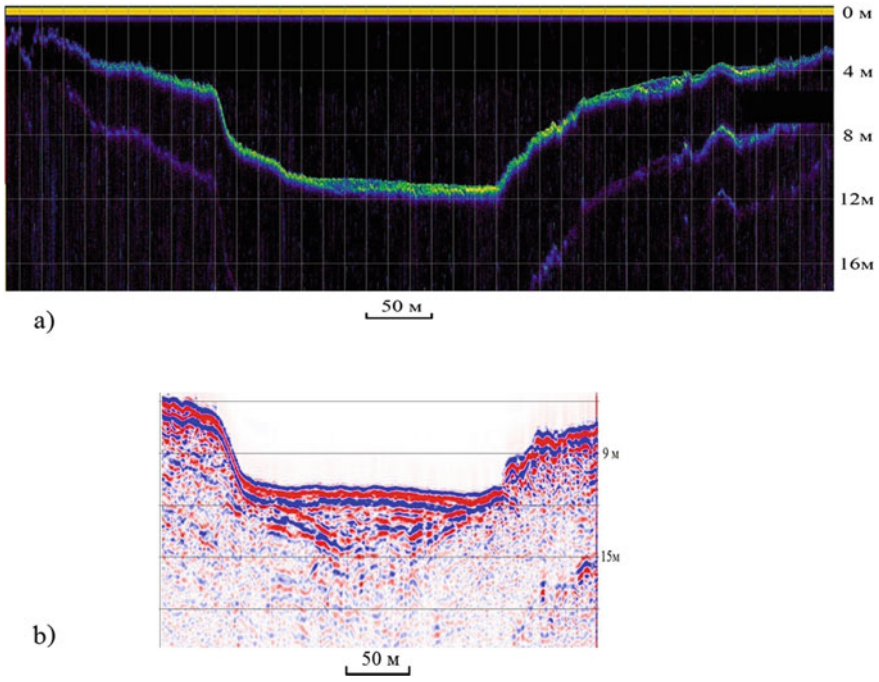

Fig. 1 "Box-shaped" transverse profile of the Ashamba River paleo riverbed in the Blue Bay near Gelendzhik (area C in Fig. 3): **a** profiler (f = 20 kHz, θ = 4°), **b** "boomer" (f = 1–2 kHz)

Figure 2 shows one of the typical transverse "box-shaped" profiles of the Ashamba River paleo riverbed on the traverse of the Blue Bay near Gelendzhik (area D in Fig. 3), completely buried in marine sediments according to the profiler f = 20 kHz, θ = 4° (a) and according to the "boomer" f = 1–2 kHz (b). From the figure it can be seen that the paleo riverbed forms a channel with a pronounced "bottom", completely buried in bottom sediments, with a width of about 400 m and a depth of about 7 m. At the same time, the profiler does not recognize the paleo riverbed channel, since the bottom relief is aligned, and the signal penetration into the bottom is insufficient, while the "boomer" well detects the paleo riverbed bowl in the surrounding sediments and provides information about its sedimentary filling.

As a result of processing the entire array of seismoacoustic data, a number of "box-shaped" transverse profiles of the bottom surface and the internal structure of the bottom were found with smooth translational repetition in space, which was identified as a paleochannel or paleotributary, respectively. This made it possible to determine the boundaries of the paleostructures of the Ashamba River and their accompanying formations, which were mapped in flat geographical coordinates, constructed using the Global Mapper computer program in the universal transverse Mercator projection UTM zone 37 (36 °E–42 °E of the northern geosphere, meters north/south - meters west/east) in the WGS84 coordinate system (Fig. 3) [4].

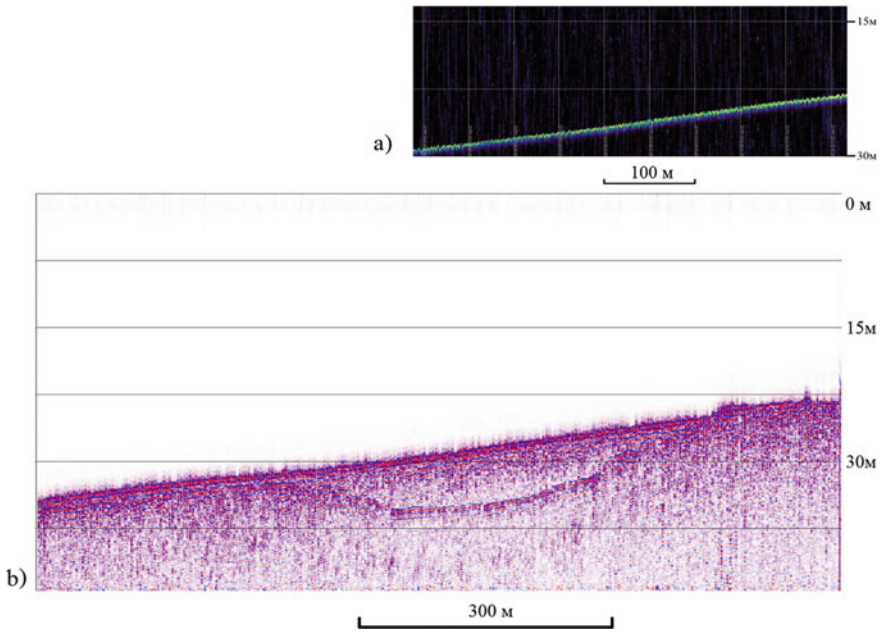

Fig. 2 "Box-shaped" transverse profile of the Ashamba River paleo riverbed on the traverse of the Blue Bay near Gelendzhik, completely buried in marine sediments (area D in Fig. 3): **a** profiler (f = 20 kHz, θ = 4°), **b** "boomer" (f = 1–2 kHz)

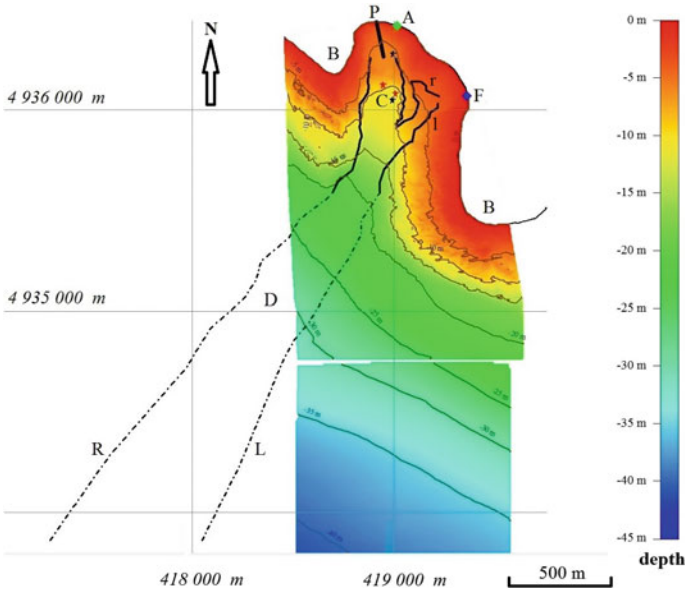

Fig. 3 Borders of paleostructures of the Ashamba River in the Blue Bay near the city of Gelendzhik [1, modified]

Here B is the coastline, P is the pier, A is the modern mouth of the Ashamba River, R is the right bank of the Ashamba paleo riverbed (solid line—20 kHz profiler, dotted line—1–2 kHz "boomer", dashed line—300–800 Hz "sparker"), L is the left bank of the Ashamba paleo riverbed (solid line – 20 kHz profiler, dashed line—1–2 kHz "boomer" and 300–800 Hz "sparker"), F—the modern mouth of the stream, r—the right bank of the paleo tributary, l—the left bank of the paleo tributary, asterisks—some gas flares, C—the position of the profiles of the echo sounder, profiler and "boomer" (Fig. 1a and b), D—the position of the profile of "sparker" and "boomer" (Fig. 2a and b). Dashed dotted lines (data of "sparker" and "boomer") show the position of the paleo riverbed section completely buried in bottom sediments, while solid lines (data of the profiler)—towering above the bottom.

The bathymetric map of the bottom of the Blue Bay with paleostructures of the Ashamba River (Fig. 3) shows that the paleo riverbed begins at the modern mouth of the Ashamba River, where its width is about 100 m at a bottom depth of about 5 m, and extends in a southwesterly direction for a distance of about 3000 m, where its width reaches 500 m at a bottom depth of about 45 m, ending with a confluence with the vast southwestern dump of the seabed. In addition, the paleo riverbed flows into the paleo riverbed, which begins at the modern mouth of the stream flowing into the Blue Bay. Along with this, the positions of gas flares in the paleo riverbed bed are shown.

Along with this, a map of the conditional (visible on the sonogram) depth of sound penetration into the thickness of bottom sediments was built at a profiler frequency f = 20 kHz with superimposed paleostructures of the Ashamba River (Fig. 4). It shows that in the upper (coastal) section of the paleochannel of the Ashamba River, its bed is filled with sediments with good acoustic permeability. This indicates their relatively weak densification and consolidation, as well as possible mobility. In addition, it can be seen that the seabed of the western and eastern parts of the bay are characterized by rocky relief (pink areas).

The obtained data also made it possible to compile a detailed map of the average height of the roughness of the Blue Bay bottom surface (Fig. 5). It can be seen from the map that the local difference in the heights of roughness (top-bottom) in some places of the bottom can reach several meters, while in other areas the bottom is almost even. It also follows from the figure that in ancient times the paleochannel of the Ashamba River made its way among the roughness of the surrounding relief (preserved at the bottom to the present day), smoothing them and punching a channel of its movement through them.

In conclusion, we note that the study of paleostructures of the Ashamba River in Blue Bay made it possible to develop the fundamentals of technology for broadband seismoacoustic detection and detailed study of riverine paleostructures in the coastal marine zone. This technology is of a general nature and can be used to determine the boundaries and characteristics of coastal river paleostructures along the entire coastline of the World Ocean. Similar coastal river paleostructures discovered through it can be very useful and significant both in terms of mining various minerals, and in numerous engineering and environmental applications in the development of the coastal zone. In addition, the presence of riverine paleostructures in Blue Bay

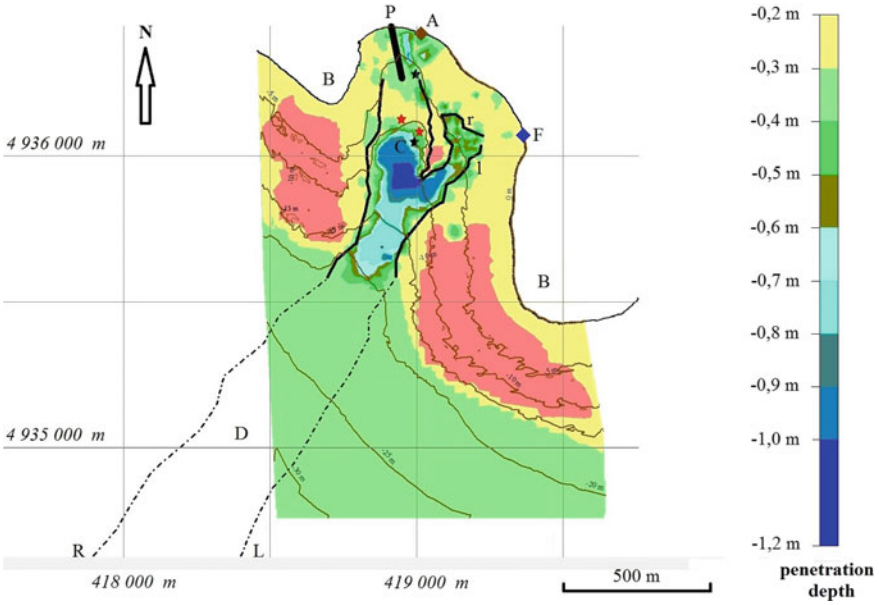

Fig. 4 The map of the conditional (visible on the sonogram) depth of sound penetration into the thickness of bottom sediments at a frequency of 20 kHz with paleostructures of the Ashamba River. Areas of rocky relief are shown in pink. The designations are the same as in Fig. 3

significantly increases its role as a coastal marine testing ground of the Institute of Oceanology of the Russian Academy of Sciences for developing advanced modern technologies, methods and equipment for marine geological research. In this regard, the study of paleostructures of the Ashamba River in Blue Bay should certainly be continued.

We express our great gratitude and appreciation for the great help in carrying out this work to Academician of the Russian Academy of Sciences Lobkovsky L.I., Director of the Southern Branch of the IO RAS Kuklev S.B., Professor D.G. Kosyan R.D., scientific director of the Black Sea Experimental Range, Ph.D. Zatsepin A.G., Deputy Director for Scientific Work of the Geological direction of the IO RAS Shevchenko V.P., as well as many other employees and colleagues.

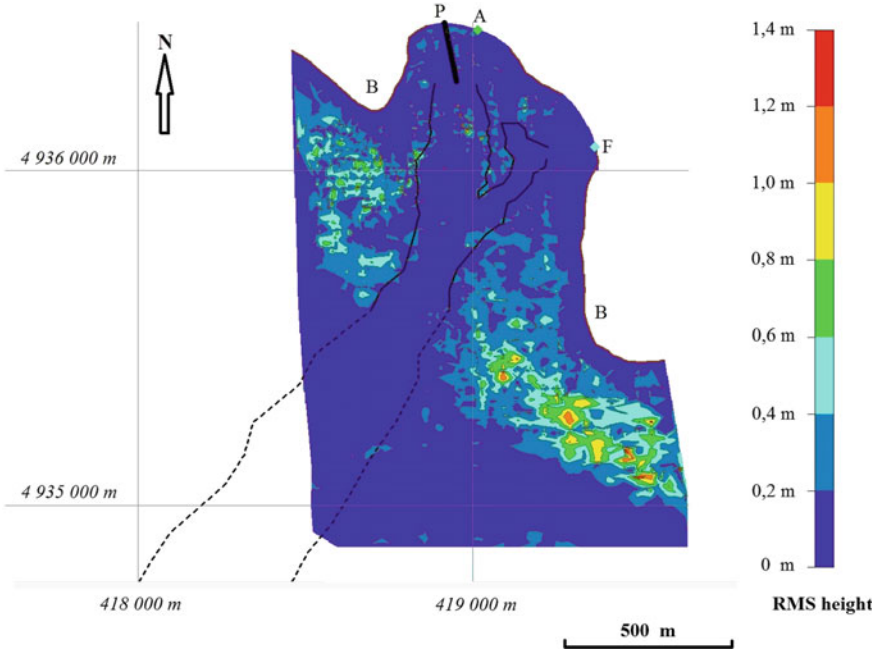

Fig. 5 The map of the average height of the roughness of the bottom surface of the Blue Bay

Acknowledgements This work was carried out within the framework of the topic of State Assignment No. 0128-2021-0004 of the P.P.Shirshov Institute of Oceanology of the Russian Academy of Sciences, and in its preparation some methods developed under the RFBR grant No. 20-05-00089 A were used.

References

1. Klyuev M.S., Schreider A.A., Brekhovskikh A.L., Sazhneva A.E., Zverev A.S. On some aspects of the detection and study of river paleostructures of the coastal zone of the seabed by broadband seismic acoustic profiling and GPS positioning // Geophysics. 2021. No. 3. pp.56–65. (In Russian).
2. 3. Klyuev M.S., Schreider A.A., Brekhovskikh A.L., Zverev A.S. On paleo riverbed of the Ashamba River in the Blue Bay according to broadband seismic acoustic profiling // Oceanological research. 2020. Volume 48. No. 4. pp. 127-140. DOI: https://doi.org/10.29006/1564-2291.JPG-20.48(4).5 (In Russian).
3. Brekhovskikh A. L., Klyuev M. S., Sazhneva A. E., Schreider A. A., and Zverev A. S. Technology of Seismic Acoustic Detection and Research of River Paleostructures of the Sea Bottom of the Coastal Zone and Its Approbation in Blue Bay / /In: Chaplina T. (eds) Processes in GeoMedia. Springer Geology. Springer, Cham. 2021. Volume IV. P.345–356. https://doi.org/10.1007/978-3-030-76328-2_36.

4. Brekhovskikh A.L., Zverev A.S., Klyuev M.S., Sazhneva A.E., Schreider A.A. On the principles of seismoacoustic study of the paleostructures of the seabed of the coastal zone (on the example of the Blue Bay) // Processes in geomedia. 2020. No. 3 (25). pp.755–763. (In Russian).
5. Brekhovskikh A.L., Volter E.R., Zverev A.S., Klyuev M.S., Rakitin I.Ya., Sazhneva A.E., Schreider A.A. On the features of seismoacoustic studies of the paleostructures of the seabed in the coastal zone. // Works of GOIN. Research of oceans and seas. Issue 221, Moscow: 2020. - pp.236–255. (In Russian).
6. Brekhovskikh A.L., Volter E.R., Grinberg O.V., Evsenko E.I., Zakharov E.V., Zverev A.S., Klyuev M.S., Kosyan R.D., Kuklev S.B., Mazurkevich A.N., Olkhovsky S.V., Rakitin I.Ya., Sazhneva A.E., Schreider A.A. On paleostructures of the Ashamba River in the geomorphology of the bottom of the Blue Bay according to parametric profilograph with satellite navigation // Geology of the Seas and Oceans: Proceedings of the XXIII International Scientific Conference (School) on Marine Geology. Volume V. M.: IO RAS, 2019. pp.72–76. (In Russian).
7. Klyuev M.S., Schreider A.A., Brekhovskikh A.L., Rakitin I.Ya., Zverev A.S., Volter E.R., Olkhovsky S.V., Grinberg O.V., Evsenko E.I., Sazhneva A.E. Paleodoline of the Ashamba River in the geomorphology of the bottom of the Blue Bay near Gelendzhik according to parametric profilograph with satellite navigation // Physical and mathematical modeling of processes in geomedia: The Fifth International School of Young Scientists, Moscow: Conference materials. – M.: IPMeh RAS, 2019. pp. 81–83. (In Russian).
8. Brekhovskikh A.L., Volter E.R., Grinberg O.V., Evsenko E.I., Zakharov E.V., Klyuev M.S., Kosyan R.D., Kuklev S.B., Sazhneva A.E., Mazurkevich A.N., Olkhovsky S.V., Schreider A.A. Paleostructures of the Ashamba River in the geomorphology of the bottom of the Blue Bay according to parametric profilograph with satellite navigation // Materials of the XVI All-Russian Scientific and Technical Conference “MSOI-2019”: Modern methods and means Oceanological research. - M.: Publishing House of the Zhukovsky Academy, 2019, Vol.1, pp.144–147. (In Russian).
9. Klyuev M.S., Schreider A.A., Zverev A.S., Brekhovskikh A.L., Rakitin I.Ya., Sazhneva A.E. On mapping paleostructures of the Ashamba River in the Blue Bay near Gelendzhik according to continuous broadband seismic acoustic profiling and GPS positioning // Geology of the Seas and oceans: Proceedings of the XXIV International Scientific Conference (school) on Marine Geology. Volume V. M.: IO RAS, 2021. pp.250–254. (In Russian).
10. Klyuev M.S., Schreider A.A., Zverev A.S., Brekhovskikh A.L., Rakitin I.Ya., Sazhneva A.E. On the boundaries of paleostructures of the Ashamba River in the Blue Bay near Gelendzhik according to broadband continuous seismoacoustic profiling and GPS positioning // Physical and mathematical modeling of processes in geomedia: Seventh International School of Young Scientists, Moscow: Conference Proceedings. - M.: IPMeh RAS, 2021. pp. 144–148. (In Russian).
11. Brekhovskikh A.L., Volter E.R., Grinberg O.V., Evsenko E.I., Zakharov E.V., Zverev A.S., Klyuyev M.S., Kosyan R.D., Kuklev S.B., Mazurkevich A.N., Olkhovsky S.V., Rakitin I.Ya., Sazhneva A.E., Schreider A.A. About gas flares of the Blue Bay near Gelendzhik according to parametric profilograph data using satellite navigation // Geology of the Seas and Oceans: Proceedings of the XXIII International Scientific Conference (School) on Marine Geology. Volume V. M.: IO RAS, 2019. pp.77–81. (In Russian).
12. Klyuev M.S., Schreider A.A., Brekhovskikh A.L., Rakitin I.Ya., Zverev A.S., Volter E.R., Olkhovsky S.V., Grinberg O.V., Evsenko E.I., Sazhneva A.E. Methane torches of the Blue Bay near Gelendzhik according to parametric profilograph data with satellite navigation // Physical and mathematical modeling of processes in geomedia: The Fifth International School of Young Scientists, Moscow: Conference Proceedings. – M.: IPMeh RAS, 2019. pp. 83–84. (In Russian).
13. Klyuev M.S., Olkhovsky S.V., Fazlullin S.M., Sazhneva A.E., Evseenko E.I., Schreider Al.A. On the capabilities of the parametric profilograph system, echo sounder and GLONASS/GPS receiver for complex studies of bottom Anthropocene sedimentary deposits // Geology of the Seas and Oceans: Proceedings of the XXI International Scientific Conference (school) on Marine Geology. Volume V. M.: GEOS. 2015. pp.132–136. (In Russian).

14. Brekhovskikh A.L., Grinberg O.V., Evsenko E.I., Klyuev M.S., Olkhovsky S.V., Rakitin I.Ya., Sazhneva A.E., Schreider A.A., Schreider Al.A. Development of the fundamentals of technology for the study of cultural heritage objects buried in bottom unconsolidated sediments by parametric profilograph using satellite navigation data // Oceanological research. 2018. № 2. Volume 46. pp. 5–14. (In Russian).
15. Schreider Al. A., Schreider A. A., Klyuev M.S. Sazhneva A.E., Brekhovskikh A.L., Olkhovsky S.V., Zakharov E.V., Chizhikov V.V., Evsenko E.I., Rakitin I.Ya., Grinberg O.V. Features of the technology of using parametric hydroacoustic means for searching, identifying and monitoring objects in the bottom layer // Processes in geomedia. 2018. No. 2(15). pp. 920- 927. (In Russian).
16. Schreider Al.A., Schreider.A., Klyuev M.S., Sazhneva A.E., Brekhovskikh A.L., Olkhovsky S.V., Zakharov E.V., Chizhikov V.V., Evsenko E.I., Rakitin I.Ya., Grinberg O.V. Technological features of the use of parametric profilograph for the study of the bottom layer // Processes in geomedia. 2018. No. 4 (18). pp.1249–1252. (In Russian).
17. Schreider Al. A., Schreider A. A., Galindo-Zaldivar Zh., Klyuev M.S., Evsenko E.I., Olkhovsky S.V., Sazhneva A.E., Zakharov E.V., Chizhikov V.V., Brekhovskikh A.L., Rakitin I.Ya., Grinberg O.V. The first data of the geological and archaeological study of the Patreian shelf of the Taman Gulf of the Black Sea // Processes in geomedia. 2017. No. 2. pp. 557- 562. (In Russian).
18. Schreider Al.A., Schreider A.A., Klyuev M.S., Evseenko E.I. High-resolution acoustic system for geological and archaeological study of the bottom // Processes in geomedia. 2016. No. 2. pp. 156–161. (In Russian).
19. Brekhovskikh A.L., Grinberg O.V., Evsenko E.I., Klyuev M.S., Olkhovsky S.V., Rakitin I.Ya., Sazhneva A.E., Zakharov E.V., Chizhikov V.V., Schreider A.A., Schreider Al.A. On the structure of the collapse of stones in the flooded part of the settlement of Patrey according to hydroacoustic parametric profilography and its geochronology // Physical and mathematical modeling of processes in geomedia: The Third International School of Young Scientists, Moscow: collection of school materials. – Moscow: IPMeh RAS, 2017, pp.58–61. (In Russian).
20. Brekhovskikh A.L., Grinberg O.V., Evsenko E.I., Klyuev M.S., Olkhovsky S.V., Sazhneva A.E., Schreider A.A., Schreider Al.A. On structures and objects of the bottom anthropocene in the GIAMZ “Phanagoria” // Materials of the XV All-Russian Scientific and Technical Conference “MSOI-2017”: Modern methods and means of oceanological research. M., APR, 2017, Vol.1, pp.251–254. (In Russian).
21. Brekhovskikh A.L., Grinberg O.V., Evsenko E.I., Klyuev M.S., Olkhovsky S.V., Rakitin I.Ya., Sazhneva A.E., Schreider A.A., Schreider Al.A. On increasing the areal productivity of hydroacoustic parametric profilographs // Proceedings of the XV All-Russian Scientific and Technical Conference “MSOI-2017”: Modern methods and means of oceanological research. M., APR, 2017, Vol.1, pp.268–271. (In Russian).
22. Mayev E.G., Myslivets V.I., Zverev A.S. The structure of the upper sediment layer and the relief of the bottom of the Taganrog Bay of the Sea of Azov // Bulletin of the Moscow University. Series 5: Geography. 2009. No. 5. pp. 78–82. (In Russian).
23. Gainanov V.G., Polyak L.V., Gataullin V.N., Zverev A.S. Seismoacoustic studies of traces of cover glaciations in the Kara Sea // Bulletin of the Moscow University. Series 4: Geology. 2005. No. 1. pp. 38–44. (In Russian).

Selection of the Distribution of Sea Surface Elevations for Modeling the Reflected Pulse of the Radio Altimeter

A. S. Zapevalov

Abstract The influence of the choice of the probability density function (PDF) of sea surface elevations on the shape of the altimeter pulse reflected from the sea surface is analyzed. Currently, the main PDF model in problems of interaction of radio waves with the sea surface is a model based on the truncated Gram-Charlier series. This model allows us to describe changes in elevations only in a limited range, beyond which strong distortions occur, up to the appearance of negative values. The relatively small number of members of the Gram-Charlier series is due to the fact that in field experiments it is possible to determine the cumulants of elevations no older than the fourth order. Distortion at the tails of the distribution when calculating the reflected pulse of the altimeter leads to distortion of its shape, as a result, an error occurs in determining the level of the sea surface. For application of reflection of radio waves from the sea surface, it is proposed to use PDF in the form of a Gaussian mixture, free from the limitation of the truncated Gram-Charlier series. The parameters of the Gaussian mixture, as well as the parameters of the truncated Gram-Charlier series, are calculated based on the first four cumulants.

Keywords Remote sensing · Altimetry · Sea surface · Brown model · Distribution of surface elevations

1 Introduction

Improving the accuracy of altimetric measurements from spacecraft remains one of the main tasks of modern satellite oceanography [1, 2]. The main physical factor that affects the error of determining the sea level is the variability of the state of its surface [3, 4]. This factor is called sea state bias (SSB). There are three components of SSB. The first component SSB is due to the difference in the reflections of microwave radio waves from the crests and troughs of sea wave (electromagnetic bias) [5]. The second component is related to signal processing on board the spacecraft [6].

A. S. Zapevalov (✉)
Marine Hydrophysical Institute RAS, Sevastopol, Russia
e-mail: sevzepter@mail.ru

© The Author(s), under exclusive license to Springer Nature Switzerland AG 2022

V. I. Karev (ed.), *Physical and Mathematical Modeling of Earth and Environment Processes*,
Springer Proceedings in Earth and Environmental Sciences,
https://doi.org/10.1007/978-3-030-99504-1_3

The third component is caused by the deviation of the distribution of sea surface elevations from the Gaussian distribution (skewness bias) [7–9]. Deviations from the Gaussian distribution lead to the fact that the median of the distribution does not coincide with the average surface level, which leads to an error in determining it when radio sounding the sea surface from a spacecraft. In this paper, the skewness bias is analyzed.

Sea surface disturbance is a weakly nonlinear process [10, 11]. Currently, the main model describing the probability density function of elevations in application of the interaction of radio waves with the sea surface is the model built on the basis of the truncated Gram-Charlier series [12–14]. Modeling a distribution using truncated series has a significant limitation. Truncated series lead to distortions on the distribution tails [15]. Also, the question of how many members of the series should be left remains unresolved.

An alternative is to use the distributions of sea heights in the form of a Gaussian mixture [16]. Earlier this approach was proposed for modeling the slopes of the sea surface [17, 18]. Let's analyze how the shape of the reflected pulse depends on the choice of a model for the distribution of elevations of the sea surface.

2 Modeling the Shape of the Reflected Pulse of the Altimeter

At small angles of incidence, the pulse reflected from the sea surface is formed as a result of quasi-mirror reflection [19]. The shape of the reflected pulse of the altimeter is described by the Brown model [20]

$$V(t) = \chi(t) * s(t) * q(t), \tag{1}$$

where t is the time, $\chi(t)$ is the shape of the pulse reflected from a flat surface, $s(t)$ is the shape of the sounding pulse, $q(t)$ is the function associated with the probability density of the heights of the mirror reflection points; the symbol * means convolution. Initially, model (1) was constructed for the Gaussian distribution of sea surface elevations. Later, the scope of its use was expanded to the case when the distribution is quasi-Gaussian and can be described using truncated Gram-Charlier series [7].

Functions $\chi(t)$ and $s(t)$ set in the form [12]

$$\chi(t) = a \exp\left[-\frac{4c}{\gamma h}\cos(2\xi)t\right] I_0\left(2\sqrt{\frac{4c}{\gamma^2 h}\sin^2(2\xi)t}\right) H(t), \tag{2}$$

$$s(t) = \frac{1}{\sqrt{2\pi D_r}} \exp\left(-\frac{t^2}{2D_r}\right), \tag{3}$$

where a is the amplitude, c is the speed of light, γ is the width of the antenna beam, h is the height of the spacecraft orbit, ξ is the absolute value of the incidence angle, I_0 is the modified Bessel function of the first kind, $H(t)$ is the Heaviside unit step function, parameter D_r determines the width of the radio pulse.

The function $q(t)$ is calculated by replacing the variable probability density function (PDF) of the sea surface elevations $P(\eta)$ using the relationship between the spatial and temporal coordinates $t = \eta/(c/2)$. We get

$$P(\eta) = q[t(\eta)]\frac{d\,t(\eta)}{d\eta} \tag{4}$$

The relation $t = \eta/(c/2)$ is linear, respectively, the skewness A_η and kurtosis E_η of the sea surface elevations η and the coefficients A_q and E_q calculated for the function $q(t)$ are numerically equal to each other. Lowering the level of the sea surface leads to an increase in the time of passage of the radio pulse of the altimeter. Therefore, the asymmetry A_q should have a sign opposite to the sign of the skewness A_η.

3 Gram-Charlier Distribution

Gram-Charlier series are based on the well-known decomposition into a series of derivatives of the function [15]

$$PN(x) = \frac{1}{\sqrt{2\pi}}\exp\left(-\frac{1}{2}x^2\right) \tag{5}$$

Derived functions are defined by the expression

$$\frac{d^n}{dx^n}PN(x) = (-1)^n H_n(x)\cdot PN(x) \tag{6}$$

where $H_n(x)$ is Hermite polynomial of order n.

The coefficients of the Gram-Charlier series are expressed in terms of the cumulants of a random variable x. If the average value of a random variable is zero and its variance is one, then the first seven cumulants are described by expressions

$$\begin{cases} \lambda_1 = 0 \\ \lambda_2 = 1 \\ \lambda_3 = \mu_3 \\ \lambda_4 = \mu_4 - 3 \\ \lambda_5 = \mu_5 - 10\,\mu_3 \\ \lambda_6 = \mu_6 - 15\,\mu_4 - 10\,\mu_3^2 + 30 \\ \lambda_7 = \mu_7 - 21\,\mu_5 - 35\,\mu_4\mu_3 + 210\mu_3 \end{cases} \tag{7}$$

where

$$\mu_n = \int\limits_{-\infty}^{\infty} x^n P(x)\,dx \tag{8}$$

is the statistical moment of the distribution random variable x. Usually, when modeling the PDF of sea surface elevations, the Edgeworth form of type A of Gram-Charlier series is used [10]

$$P_{GC}(x) = \frac{\exp\left(-\frac{x^2}{2}\right)}{\sqrt{2\pi}}\left[1 + \frac{\lambda_3}{6}H_3(x) + \frac{\lambda_4}{24}H_4(x) + \frac{\lambda_5}{120}H_5(x) + \right.$$
$$\left. + \frac{\lambda_6 + 10\,\lambda_3^2}{720}H_6(x) + \frac{\lambda_7 + 35\,\lambda_4\lambda_3}{5040}H_7(x) + \cdots\right] \tag{9}$$

In field experiments, cumulants not older than the fourth order are determined for elevations of the sea surface. Therefore, when constructing a PDF, it is usually assumed that $\lambda_n = 0$ if $n > 4$. According to (7), cumulants of the third and fourth order are, respectively, skewness and kurtosis.

When simulating the reflected pulse of a radio altimeter, two forms of PDF of sea surface elevations are used

$$P_{GC}^{(1)}(\tilde{\eta}) = \frac{\exp\left(-\frac{\tilde{\eta}^2}{2}\right)}{\sqrt{2\,\pi}}\left[1 + \frac{\lambda_3}{6}H_3(\tilde{\eta}) + \frac{\lambda_4}{24}H_4(\tilde{\eta})\right] \tag{10}$$

$$P_{GC}^{(2)}(\tilde{\eta}) = \frac{\exp\left(-\frac{\tilde{\eta}^2}{2}\right)}{\sqrt{2\,\pi}}\left[1 + \frac{\lambda_3}{6}H_3(\tilde{\eta}) + \frac{\lambda_4}{24}H_4(\tilde{\eta}) + \frac{\lambda_3^2}{72}H_6(\tilde{\eta})\right] \tag{11}$$

where $\tilde{\eta} = \eta/\sqrt{\mu_2}$,

$$\frac{\exp\left(-\frac{\tilde{\eta}^2}{2}\right)}{\sqrt{2\,\pi}} = P_G(\tilde{\eta}) \tag{12}$$

is PDF for the Gaussian distribution.

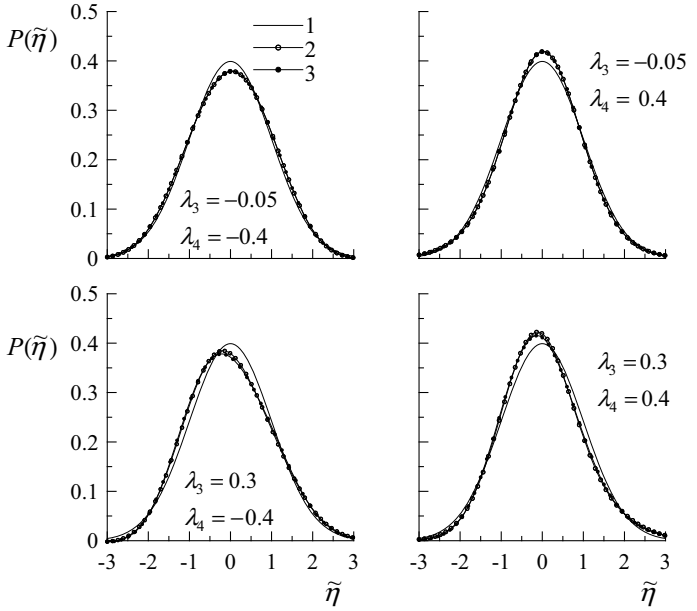

Fig. 1 PDF of sea surface elevations, curve 1 is $P_G(\tilde{\eta})$, curve 2 is $P_{GC}^{(1)}(\tilde{\eta})$, curve 3 is $P_{GC}^{(2)}(\tilde{\eta})$

According to the data of wave measurements carried out on a stationary oceanographic platform of the Marine Hydrophysical Institute of the Russian Academy of Sciences located on the Black Sea, the values of skewness and kurtosis mainly lie within range $-0.05 < \lambda_3 < 0.3$ and $-0.4 < \lambda_4 < 0.4$ [21]. The correlation between λ_3 and λ_4 is weak. PDF $P_{GC}^{(1)}(\tilde{\eta})$ and $P_{GC}^{(2)}(\tilde{\eta})$, calculated for the limit values of cumulants λ_3 and λ_4, are shown in Fig. 1.

The features of PDF behavior in the region of large values $|\tilde{\eta}|$ are shown in Fig. 2. It can be seen that with some combinations λ_3 and λ_4, negative PDF values are observed. Negative PDFs are observed both in the area of negative values $\tilde{\eta}$ and in the area of positive values $\tilde{\eta}$. An earlier analysis of the possibility of using the Gram–Charlier distribution to describe the distributions of sea surface slopes showed that this distribution can be used if the value of the normalized random variable does not exceed in absolute value 2.5 [22]. Since the values of cumulants λ_3 and λ_4 elevations and slopes of the sea surface are close, it can be assumed that for surface elevations, a possible area of use of the Gram–Charlier distribution. This assumption is consistent with the results of [23], in which the Gram–Charlier model distribution was compared with the data of direct wave measurements.

PDF $P_{GC}^{(1)}(\tilde{\eta})$ and $P_{GC}^{(2)}(\tilde{\eta})$ turned out to be very close to each other. This allows us to further consider only one PDF when calculating the reflected pulse of the radio altimeter. We will use PDF in the form (10).

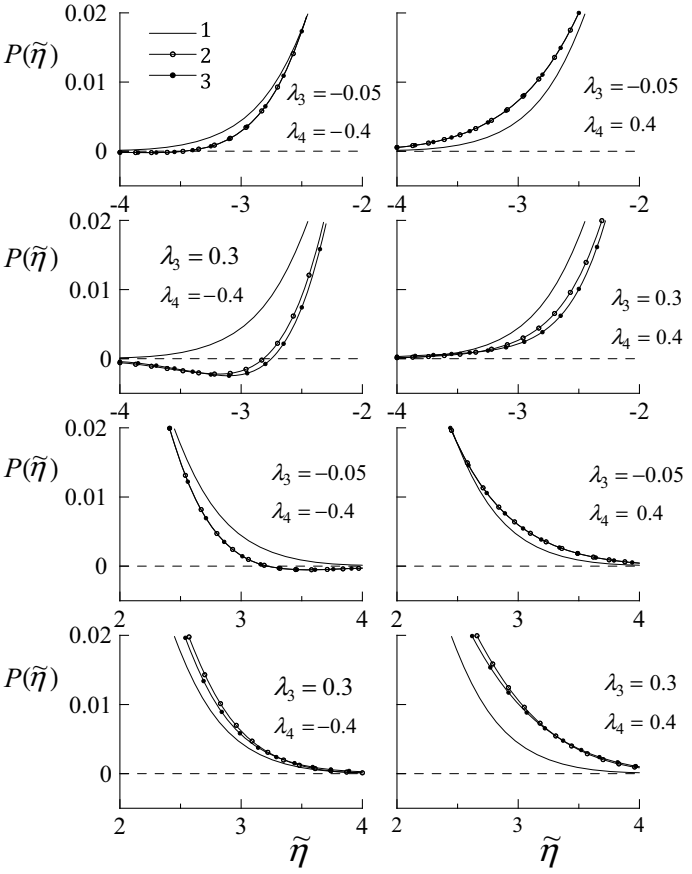

Fig. 2 PDF fragments of sea surface elevations at high values $|\tilde{\eta}|$, curve 1 is $P_G(\tilde{\eta})$, curve 2 is $P_{GC}^{(1)}(\tilde{\eta})$, curve 3 is $P_{GC}^{(2)}(\tilde{\eta})$

4 Two-Component Gaussian Mixture

The PDF approximation in the form of a two-component Gaussian mixture has the form [24]

$$P_S(\tilde{\eta}) = \frac{\alpha_1}{\sqrt{2\pi}\sigma_1} \exp\left(-\frac{(\tilde{\eta} - m_1)^2}{2\,\sigma_1^2}\right) + \frac{\alpha_2}{\sqrt{2\pi}\sigma_2} \exp\left(-\frac{(\tilde{\eta} - m_2)^2}{2\,\sigma_2^2}\right) \qquad (13)$$

where α_i is the weight of the i-th component, $(i = 1,\ 2)$, $\alpha_i \in (0, 1)$, m_i is the mathematical expectation, σ_i^2 is variance. The following conditions are met for the weight coefficients

$$\alpha_i > 0 \text{ and } \alpha_1 + \alpha_2 = 1 \tag{14}$$

The statistical moments of a Gaussian mixture are related to the statistical moments of its components by the equation

$$\mu_j = \alpha_1 \mu_{j,1} + \alpha_2 \mu_{j,2} \tag{15}$$

where $\mu_{j,i}$ is the statistical moment of the i-th component ($i = 1,\ 2$).

When develop a PDF $P_S(\tilde{\eta})$, taking into account the condition for the weighting coefficients, it is necessary to determine five parameters m_1, m_2, σ_1^2, σ_2^2 and α_1. To calculate the parameters m_1, m_2, σ_1^2, and σ_2^2 the first four statistical moments of sea surface elevation can be used. The parameter α_1 is selected from the unimodal condition of the distribution [18].

The PDF $P_s(\tilde{\eta})$ approximation parameters are calculated by solving a system of four equations for statistical moments [16, 18]

$$\begin{cases} \mu_1 = 0 \\ \mu_2 = 1 \\ \mu_3 = \lambda_3 \\ \mu_4 = \lambda_4 + 3 \end{cases} \tag{16}$$

Cumulants λ_3 and λ_4 are set according to measurement data [21] or as a result of mathematical modeling obtained within the framework of various nonlinear wave modeling models [25, 26].

PDF $P_s(\tilde{\eta})$ constructed with the same values of cumulants λ_3 and λ_4 that were used in the construction $P_{GC}^{(1)}(\tilde{\eta})$ are shown in Fig. 3.

Unlike the distribution constructed on the basis of truncated Gram-Charlier series, the Gaussian mixture has no negative values.

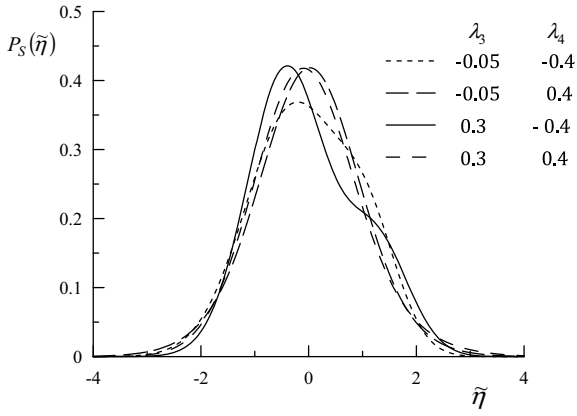

Fig. 3 PDF approximation in the form of a Gaussian mixture

Any PDF approximation of sea surface elevations must meet several requirements. It should be single-mode, and not have more than two inflection points. It turned out that these requirements may not be met for all values of cumulants λ_3 and λ_4. No solution for the system of Eq. (16) has been found in which the condition for the number of inflection points at $\lambda_3 = 0.3$ and $\lambda_4 = -0.4$ is satisfied. The approximation PDF described by third curve in Fig. 3 is not completely correct.

The main problem when develop PDF approximation in the form of a Gaussian mixture is that the procedure for calculating its parameters is very complex. It can be assumed that it is this circumstance that so far prevents the widespread use of this approximation for describing the statistical characteristics of the sea surface.

5 Numerical Simulation of the Reflected Pulse of a Altimeter

For numerical calculations, the values of the parameters included in Eqs. (2) and (3) are assumed to be equal to the corresponding parameters of the altimeter located on SEASAT-1: $\gamma = 1.6\,^\circ$, $\sqrt{D_r} = 1.327$ ns and $h = 8 \times 10^5$ m [12].

A shift of the leading edge by 0.1 ns corresponds to a change in the calculated surface level by 1.5 cm.

The shape of the leading edge of the reflected altimeter pulse calculated for the PDF $P_{GC}^{(1)}(\tilde{\eta})$ of sea surface elevations in form (2) is shown in Fig. 4. For clarity, when constructing Fig. 4, anormalization is introduced, according to which the amplitude of the reflected pulse is equal to unity. Significant wave height is taken equal to 3 m. Calculations were carried out for the same values λ_3 and λ_4 for which PDF approximations are constructed in Figs. 1 and 2.

Note that with some combinations of values λ_3 and λ_4, a non-physical effect is observed. It manifests itself as the occurrence of a negative intensity of the reflected signal. It can be assumed that negative values of the PDF approximation $P_{GC}^{(1)}(\tilde{\eta})$ also distort the shape of the pulse in the vicinity of its maximum.

The main factors that determine the accuracy of the representation of the shape of the reflected radio pulse is the correct approximation of the PDF of the sea surface elevations. The use of PDF in the form (10) or (11) in the problems of radio altimetric measurements can lead to the appearance of negative values in the models describing the shape of the reflected radio pulse. Negative values $V(t)$ are small in comparison with the amplitude of the reflected pulse, but their appearance indicates the need to construct an PDF approximation that allows to correctly describe the distribution of sea surface elevations.

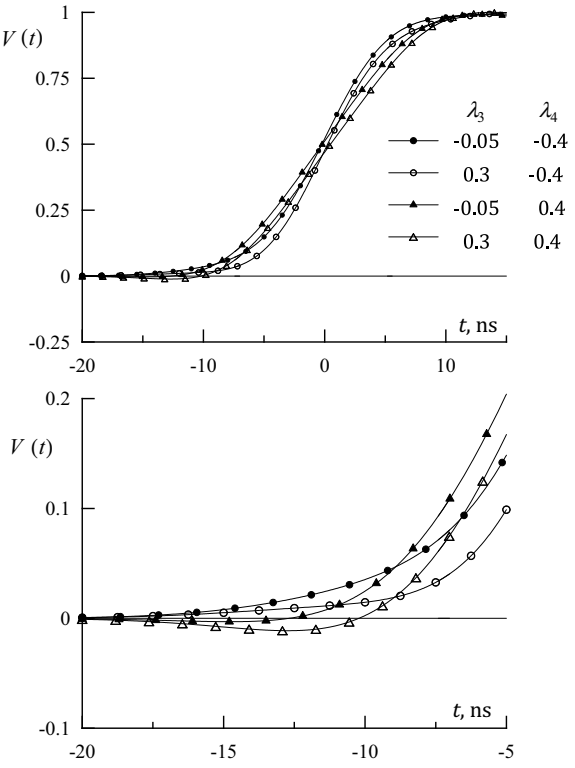

Fig. 4 The leading edge of the altimeter pulse reflected from the sea surface, built in accordance with the PDF approximation of the sea surface elevations in the form (9)

6 Conclusion

Sea disturbance is a random quasi-Gaussian process. Uncertainty of the state of the sea surface is the main source of error in determining the mean surface level from the data of measurements with a radio altimeter installed on the spacecraft. The mean level is calculated from the transit time of a radio pulse from the spacecraft to the sea surface and back. This parameter depends on the PDF elevation of the surface, which is not known a priori.

Currently, the main PDF model of the sea surface in problems of interaction of radio waves with the sea surface is a model based on the truncated Gram-Charlier series. This model allows us to describe the distribution of elevations only in a limited range, beyond which strong distortions occur, up to the appearance of negative values. The limitation of the number of members of the Gram-Charlier series is caused by the fact that in field experiments it is possible to determine the cumulants of elevations no older than the fourth order. Cumulants of the fifth and higher orders are assumed to be equal to zero. Distortion at the tails of the elevation distribution when calculating the reflected pulse of the altimeter leads to distortion of its shape, as a result, an error occurs in determining the level of the sea surface. Currently, two approximations in

the form (10) and (11) are used to simulate the reflected pulse of the altimeter using Gram–Charlier series. Numerical modeling has shown that both approximations lead to similar results. Both approximations have the same disadvantages.

As an alternative to approximations (10) and (11), it is proposed to use the PDF of sea surface elevations in the form of a Gaussian mixture. To calculate the parameters of the Gaussian mixture, as well as for the truncated Gram-Charlier series, the first four cumulants of the surface elevations are used. Unlike the truncated Gram-Charlier series, the Gaussian mixture does not have negative values.

Acknowledgements This work was carried out as part of a state assignment on the topic No. 0555-2021-0003 "Development of operational oceanology methods based on interdisciplinary research of processes of the marine environment formation and evolution and on mathematical modeling using data of remote and contact measurements".

References

1. Ablain, M., Legeais, J.F., Prandi, P., Marcos, M., Fenoglio-Marc, L., Dieng, H.B., Benveniste, J., Cazenave, A.: Satellite altimetry-based sea level at global and regional scales. Surv. Geophys. 38, 7–31 (2017). https://doi.org/10.1007/978-3-319-56490-6_7.
2. Lebedev, S.A., Gusev, I.V.: International experience in calibration of satellite altimetry data on the stationary and temporary calibration sites. Sovremennye problemy distantsionnogo zondirovaniya Zemli iz kosmosa. 18(2), 18-35. (2021). https://doi.org/10.21046/2070-7401-2021-18-2-18-35.
3. Cheng, Y., Xu, Q., Gao, L., Li, X., Zou, B., Liu, T.: Sea State Bias Variability in Satellite Altimetry Data. Remote Sensing, 11(10), 1176 (2019). https://doi.org/10.3390/rs11101176.
4. Badulin, S.I., Grigorieva, V.G., Shabanov, P.A., Sharmar V.D., Karpov, I.O.: Sea state bias in altimetry measurements within the theory of similarity for wind-driven seas. Advances in Space Research. 68(2), 978-988 (2021). https://doi.org/10.1016/j.asr.2019.11.040.
5. Ghavidel, A., Schiavulli, D., Camps, A.: Numerical Computation of the Electromagnetic Bias in GNSS-R Altimetry. IEEE Transactions on Geoscience and Remote Sensing, 54(1), 489–498 (2016). https://doi.org/10.1109/tgrs.2015.2460212.
6. Gómez-Enri, J., Gommenginger, C.P., Challenor, P.G., Srokosz, M.A., Drinkwater, M.R.: ENVISAT radar altimeter tracker bias // Marine Geodesy. 29, 19–38 (2006). https://doi.org/10.1080/01490410600582296.
7. Zapevalov, A.S. Effect of skewness and kurtosis of sea-surface elevations on the accuracy of altimetry surface level measurements // Izvestiya, Atmospheric and Oceanic Physics. 48(2), 200–206 (2012). https://doi.org/10.1134/S0001433812020120.
8. Pires, N., Fernandes, M., Gommenginger, C., Scharroo, R.A.: Conceptually simple modeling approach for Jason-1 sea state bias correction based on 3 parameters exclusively derived from altimetric information. Remote Sensing. 8(7), 576 (2016). https://doi.org/10.3390/rs8070576.
9. Wang, X., Miao, H.L., Wang, G.Z., Wang, Y.Q., Zhang, J.: Direct-estimation of sea state bias in Hy-2 based on a merged dataset. International Conference on Computer Information Systems and Industrial Applications (CISIA 2015). 762–766. (2015). https://doi.org/10.2991/cisia-15.2015.207.
10. Longuet-Higgins, M.S.: The effect of non-linearities on statistical distribution in the theory of sea waves // J. Fluid Mech. 17(3), 459–480 (1963).
11. Taklo, T.M.A., Trulsen, K., Gramstad, O., Krogstad, H.E., Jensen, A.: Measurement of the dispersion relation for random surface gravity waves. J. Fluid Mech., 766, 326-336. (2015). https://doi.org/10.1017/jfm.2015.25.

12. Hayne, G.S.: Radar altimeter mean return waveforms from near-normal-incidence ocean surface scattering. IEEE Transactions on Antennas and Propagation. AP-28, 687–692 (1980).
13. Callahan, P.S., Rodriguez, E.: Retracking of Jason-1 data: Marine Geodesy. 27, 391–407 (2004). https://doi.org/10.1080/01490410490902098.
14. 15. Pokazeev, K.V., Zapevalov, A.S., Pustovoytenko, V.V.: The simulation of a radar altimeter return waveform. Moscow University Physics Bulletin, September. 68(5), 420-425 (2013). https://doi.org/10.3103/S0027134913050135.
15. Kendall, M.J., Stewart, A.: The Advanced Theory of Statistics. Vol. I. Distribution theory. London: Butler & Tanner Ltd. 675 p. (1958).
16. 17. Gao, Z., Sun, Z., & Liang, S. Probability density function for wave elevation based on Gaussian mixture models. Ocean Engineering, 213, 107815 (2020). https://doi.org/10.1016/j.oceaneng.2020.107815.
17. 18. Tatarskii,V.I.: Multi-Gaussian representation of the Cox–Munk distribution for slopes of wind-driven waves. J. of Atmospheric and Oceanic Technology. 20, 1697–1705 (2003).
18. 19. Zapevalov, A.S., Ratner, Yu.B.: Analytic model of the probability density of slopes of the sea surface. Physical Oceanography. 13(1), 1–13 (2003). https://doi.org/10.1023/A:1022444703787.
19. Bass, F.G., Fuks, I.M.: Wave scattering by statistically rough surface. Pergamon, 540 p. (1979).
20. Brown, G.S.: The average impulse response of a rough surface and its applications IEEE Trans. Antennas Propagat. AP-25, 67–74 (1977).
21. Zapevalov, A.S. Garmashov, A.V.: Skewness and kurtosis of the surface wave in the coastal zone of the Black Sea. Physical Oceanography. 28(4), 414–425 (2021). https://doi.org/10.22449/1573-160X-2021-4-414-425.
22. Cox C., Munk W.: Measurements of the roughness of the sea surface from photographs of the sun glitter. J. Optical. Soc. America. 44(11), 838–850 (1954).
23. Zapevalov, A.S., Bol'shakov, A.N., Smolov, V.E.: Simulating of the probability density of sea surface elevations using the Gram–Charlier series. Oceanology. 51(3), 406–413 (2011). https://doi.org/10.1134/S0001437011030222.
24. Aprausheva N.N., Sorokin S.V. Exact equation of the boundary of unimodal and bimodal domains of a two-component Gaussian mixture. Pattern Recognition and Image Analysis. 23(3), 341–347 (2013). https://doi.org/10.1134/S1054661813030024.
25. Tayfun, M.A., Alkhalidi, M.A. Distribution of surface elevations in nonlinear seas. In: Offshore Technology Conference Asia. Offshore Technology Conference (2016). https://doi.org/10.4043/26436-MS.
26. Annenkov, S. Y., Shrira, V. I.: Evaluation of skewness and kurtosis of wind waves parameterized by JONSWAP spectra. Journal Physical Oceanography, 44(6), 1582–1594. (2014). https://doi.org/10.1175/jpo-d-13-0218.1.

Adapting the Method of Directional Unloading of the Formation for Low Permeable Deposits

V. I. Karev and S. O. Barkov

Abstract The paper is devoted to considering the possibility and manners of applying the method of directional unloading of the formation (DUF) served for increasing well productivity for low permeable deposits. An analysis of stress state in the vicinity of a well for various geometry of borehole bottom is presented. The methodic of experimental study of deformation and fracture processes near the well for conditions of certain field is developed on the base of this analysis. According this methodic, the tests of specimens cut from reservoir rock under study have been carried out by using the unique setup of IPMech RAS Triaxial Independent Load Test System. The results of experiments allowed the practically important conclusions about the possibility of applying DUF metod for low permeable deposits and the manners of its applicability.

Keywords Low-permeability reservoirs · Directed unloading of formation method · Triaxial independent load test system · Strains · Stresses · Permeability

1 Introduction

The relevance of the work is due to the reduction of the resource base of hydrocarbon raw materials and the need to develop and adapt new efficient environmentally friendly production technologies for the conditions of fields with hard-to-recover reserves, primarily with low-permeability reservoirs [1–3]. These technologies include: multistage hydraulic fracturing [4, 5], wave action [6], the method of directional unloading of the formation (DUF) [7–9]. DUF was developed at the IPMech RAS and passed successful pilot field tests in the fields of Western Siberia and the Urals. The method is based on a geomechanical approach and involves the creation of stresses in the near-wellbore zone, leading to rock cracking and an increase in permeability.

V. I. Karev (✉) · S. O. Barkov
Ishlinsky Institute for Problems in Mechanics RAS, Moscow, Russia
e-mail: wikarev@ipmnet.ru

© The Author(s), under exclusive license to Springer Nature Switzerland AG 2022

V. I. Karev (ed.), *Physical and Mathematical Modeling of Earth and Environment Processes*,
Springer Proceedings in Earth and Environmental Sciences,
https://doi.org/10.1007/978-3-030-99504-1_4

2 The Problem

The main questions that need to be answered when using the DUF method are what stresses should be created in the formation to cause multiple rock cracking, and what technological operations are necessary for this. The type and level of required stresses depend on the design and deformation properties of the rock, the depth of the formation bedding, reservoir fluid pressure. There are two ways to change the stresses in the vicinity of the well: reduce the pressure in the well and change the bottomhole geometry (remove the casing, make perforations, cut slots). The use of DUF in fields with low-permeability reservoirs, due to the increased strength of the rocks, may require preliminary creating of stress concentrators into the formation—perforation of a certain type and density, including in uncased wells. It is possible to determine the parameters of the method (the magnitude of the pressure drawdown, technological operations for the formation of the required bottomhole geometry) on the basis of laboratory tests that simulate on specimens of reservoir rocks of the field real stresses arising at implementing method. To do this, it is necessary to carry out a theoretical analysis of the stress state in the vicinity of the well for various bottomhole designs, on its basis to develop a laboratory test procedure.

The work carried out the adaptation of the DUF method for the conditions of one of the gas condensate field, which has a low-permeability reservoir and is located in the north of Eastern Siberia. Calculations of stresses acting in the vicinity of perforations in cased and uncased wells have been carried out. On the Triaxial Independent Loading Test System (TILTS) of IPMech RAS [9], a series of tests of rock samples from the reservoir of this field was carried out using special loading programs.

3 Stress State in the Vicinity of a Well for Various Constructions of the Bottom Hole

3.1 Stress State in the Vicinity of a Perforation Hole for a Cased Wellbore

The stress state in the vicinity of a perforation hole for a cased well is determined by the external stress from the rock pressure in the depth of the formation q ($q < 0$, since compressive stresses are considered negative), the back pressure on the formation from the side of the cement stone and the fluid pressure inside the perforation hole for a cased well, equal to the pressure in well p_w. It is generally accepted that on the cased hole contour, after the cement slurry has hardened, the pressure is restored completely to the rock pressure value $|q|$.

Then from the solution of the Lamé problem [10] for the effective stresses acting in the soil skeleton in the vicinity of the perforation hole for the cased well, we have in every point of the perforation hole wall

$$s_{r'} = -(q + p_w)\left(R_h/r'\right)^2 + q + p(r'),\ \ s_{z'} = q + p(r')$$

$$s_{\varphi'} = (q + p_w)\left(R_h/r'\right)^2 + q + p(r') \tag{1}$$

R_h is the perforation radius, r' is a distance from the well wall. Thus, stresses along the surface of the perforation in a cased hole are constant and equal (assuming in [1] $r' = R_h, p(r') = p_w$)

$$s_{r'} = 0,\ \ s_{z'} = q + p_w$$

$$s_{\varphi'} = 2(q + p_w) \tag{2}$$

3.2 Stress Condition in the Vicinity of a Perforation in an Open Hole

In this case, the perforation hole will not be in an external stress field from rock pressure in the depth of the formation q, but in an uneven stress field from an open hole, in which the perforation hole is shot through. In turn, the stress field around the open hole is determined by the rock pressure in the depth of the formation q and the pressure in the well p_w.

Then, at the upper point N of the vertical section of the perforation hole, to change the effective stresses depending on the distance from the well axis, we have [11].

3.3 Stress State in the Vicinity of a Perforation in an Open Hole

In this case, the perforation hole will not be in an external stress field from rock pressure in the depth of the formation q, but in an uneven stress field from an open borehole. In turn, the stress field around the open hole is determined by the rock pressure in the depth of the formation q and the pressure in the well p_w.

Then, at the upper point N of the vertical section of the perforation hole, to change the effective stresses depending on the distance from the well axis, we have

$$s_{r'}(r) = 0,\ \ s_{z'}(r) = -(q + p_w)(R/r)^2 + q + p_w$$

$$s_{\varphi'}(r) = 3(q + p_w)(R/r)^2 + 2(q + p_w) \tag{3}$$

It can be seen from [3] that stresses along the surface of the perforation hole vary depending on the distance from the well.

$$r = R,\ s_{r'} = s_{z'} = 0,\ s_{\varphi'} = 5(q + p_w) \tag{4}$$

$$r = 2R,\ s_{r'} = 0,\ s_{z'} = 3/4(q + p_w),\ s_{\varphi'} = 11/4(q + p_w) \tag{5}$$

Relations [2], [3]–[5] show that the concentration of the maximum effective stress $\alpha = s_{\varphi'}/q$ on the surface of the perforation hole for the case of an open hole is much higher than for the case of a cased hole. So, $\alpha = 2$ on the entire surface of the perforation in a cased well in the case complete drainage of the well ($p_w = 0$), a the same time he value α exceeds 2 on the entire surface of the perforation in an uncased well. On the wall of the well at $r = R$, the concentration is maximum ($\alpha = 5$) and decreases gradually with increasing a distance from the well wall.

On the basis of relations [2] and [3], for the conditions of the studied field, loading programs simulating the change in stresses on the surface of perforations in cased and uncased wells with a decrease in pressure at their bottom p_w were compiled. In the experiment with an open hole, the stress change was simulated at a point on the surface of the perforation hole, which was by a distance $r = 1,25R$ from the well axis.

During the experiments, the strains of the specimens were measured in three directions and the change in their permeability in the bedding plane was recorded.

4 Specimens Test Results

Ten specimens from the studied field were tested at the TILTS setup according to the above programs. During tests according to a program that simulates a change in stresses in the vicinity of a perforation hole in a cased borehole, the specimens were deformed elastically without increasing the permeability even when reaching the maximum stresses corresponding to complete drainage of the well are reached.

A different picture was observed when testing the specimens using the “open hole perforation” program, which simulates the stress change at a point on the surface of the perforation hole at a distance $r = 1,25R$ from the well axis. Figure 1 shows the strain curves of one of the specimens obtained in the experiment and the change in its permeability.

Figure 1a shows that when simulating on the TILTS the conditions that occur in the vicinity of an open wellbore with a decrease in pressure in it, the specimen was deformed elastically up to stress $s_2 = 120$ MPa, and then its inelastic deformation began, and the sample collapsed at $s_2 = 126$ MPa. Since the stress s_2 applied to the specimen in the loading unit of the TILTS corresponds to the absolute value of the circumferential stress $|s_{\varphi'}|$ in the vicinity of the perforation hole, we have $p_w =$

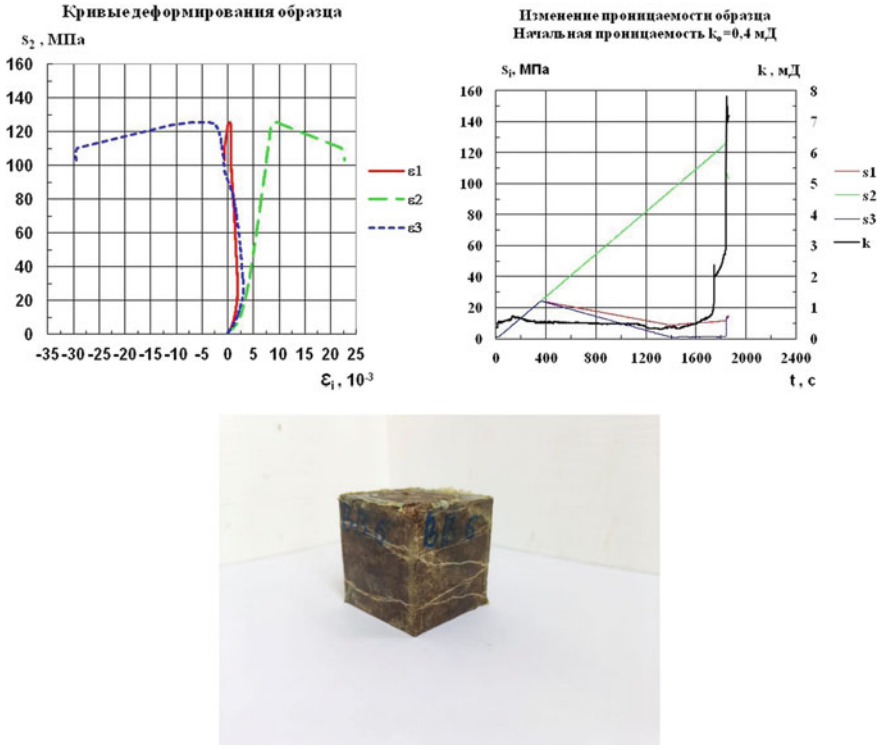

Fig. 1 Specimen test results using the "open hole perforation" program; a—strain curves, b—change in the permeability of the specimen during the experiment, c—a picture of the specimen after testing

$|q| - (25/98)s_2$ from expression [3]. Accordingly, the start of inelastic deformation of the specimen corresponds to a pressure at the bottom of the well of $p_w = 9.6$ MPa, and the destruction of the specimen corresponds to a pressure of $p_w = 8.1$ MPa.

The initial permeability of the specimen was 0.4 mD, and it increased to 7.8 mD in the result of its destruction in the process of the loading the specimen, Fig. 1b.

Figure 1c shows a photograph of the sample after testing. It clearly shows the system of cracks formed in the sample, which led to an increase in its permeability.

5 Conclusions

A number of practically important conclusions follow from the results obtained.

1. From practice, it is known that lowering the pressure at the bottom of cased wells with a perforated bottom to minimum possible value does not lead to an increase

in well production, especially in fields with low-permeability reservoirs,. A similar pattern is often observed for open wellbores.

2. A preliminary perforation of the open hole can help for such conditions, since in this case, as follows from [3]–[5], compressive stresses arise in the vicinity of the perforation hole, which significantly exceed the stresses at other bottomhole designs.

   This conclusion is confirmed by the results of the experiments presented in the work.

   It follows from [3]–[5] that large concentrations of stresses on the surface of a perforation hole in an open hole occurs no more than at a distance of 2–3 radii of the well from its axis. From the above, an important conclusion follows regarding the optimal shape of the perforations in an open hole for the implementation of the DUF method—they should be rather short, but wide. In this case, the effect of their use will be maximum.

3. Summarizing the results of experiments and mathematical calculations, we can conclude that the geomechanical approach using physical modeling of deformation, destruction and filtration processes in productive formations can serve as a basis for the development of new efficient and environmentally friendly technologies for increasing the productivity of oil and gas wells and increasing oil recovery in low-permeable formations.

Acknowledgements The work was carried out with the financial support of the grant of the Russian Federation represented by the Ministry of Science and Higher Education of the Russian Federation No. 13.1902.21.0018 (agreement 075-15-2020-802).

References

1. Alekseev A.D., Zhukov V.V., Strizhnev K.V., Cherevko S.A. Study of hard-to-recover and unconventional objects according to the principle of “reservoir factory in the formation” // Zapiski Gornogo instituta. 2017.T.228. S. 695–704. DOI: 10.25515 / PMI.2017.6.695. in Russian.
2. 3. Song Y., Li Z., Jiang L., Hong F. The concept and the accumulation characteristics of unconventional hydrocarbon resource // Petroleum Science. 2015. V12. P. 563–572. DOI: https://doi.org/10.1007/s12182-015-0060-7.
3. Karev V.I., Kovalenko Yu.F., Ustinov K.B. Modeling of geomechanical processes in the vicinity of oil and gas wells M .: IPMech RAS, 2018. 528 p. in Russian.
4. Galeev R.R., Zorin A.M., Kolonskikh A.V. et al. Choice of the optimal system for the development of low-permeability reservoirs using horizontal wells with multiple hydraulic fractures // Oil industry. 2013. No. 10. S.62–65. in Russian.
5. Govzich A.N., Bilinchuk A.V., Faizullin I.G. Experience of multistage hydraulic fracturing in horizontal wells of JSC Gazprom Neft // Oil Industry. 2012. No. 12. P. 59–61. in Russian.
6. Ganiev R.F., Ukrainsky L.E. Nonlinear wave mechanics and technologies. Wave and oscillatory phenomena on the Basis of High Technologies. USA: Begell Hause. Inc. Publishers. 2012. 527 p.

7. Karev V., Kovalenko Y., Ustinov K. Directional unloading method is new approach to enhancing oil and gas well productivity. Advances in Oil and Gas Exploration and Production. Switzerland: Springer International Publishing. 2020. P. 155–166. DOI: https://doi.org/10.1007/978-3-030-26608-0_10.
8. Karev V.I., Kovalenko Yu.F. Triaxial loading system as a tool for solving geotechnical problems of oil and gas production. In book: True Triaxial Testing of Rock. Leiden: Balkema. P. 301–310.
9. Karev V.I., Kovalenko Yu.F. Simulation of directional unloading of a formation on a true triaxial loading unit for conditions of low-permeability reservoirs. Conference proceedings of 7th International Scientific Conference-School of Young Scientists "Physical and mathematical modeling of processes in geo-environments". October 20–22, 2021 M: IPMech RAS. 2021 p. 132–137. in Russian.
10. Lyav A. Mathematical theory of elasticity. M.-L: ONTI NGKiP USSR. 1935. 674 p. in Russian.
11. Timoshenko S.P., Goodyer J. Theory of elasticity. M .: Science. 1979.560 p. in Russian.
12. Khristianovich S.A., Kovalenko Yu.F., Kulinich Yu.V., Karev V.I. Increasing the productivity of oil wells using the method of geoloosening // Oil and Gas Eurasia. 2000. No. 2. P. 90–94.

Simulation of Filtration into a Well Taking into Account of Elastoplastic Deformation Near Borehole

V. I. Karev

Abstract The paper presents the results of the modeling of filtration into a well taking into account of elastoplastic deformation near borehole. The Drucker-Prager model was chosen to describe the transition to inelastic deformation. The parameters of the model, and the dependence of the permeability of rocks on stresses have been found experimentally for the conditions of one of the offshore gas condensate fields with a low-permeability reservoir. The experiments were carried out on a unique experimental setup—the Triaxial Independent Load Test System of IPMech RAS. It have been shown the model makes it possible to determine the optimal manner of well stimulation to increase the well production rate by varying the pressure drawdown value and the bottomhole design.

Keywords Modeling · Low-permeability reservoirs · Directed unloading of formation method · True triaxial test apparatus · Strains · Stresses · Elasticity · Drucker-prager model

1 Introduction

A model of oil filtration into a well has been developed in the laboratory of geomechanics of IPMech RAS taking into account the influence of the stress-strain state on the permeability of rocks and the formation of a zone of a disturbed structure near the well. The model makes it possible to determine the optimal parameters of well stimulation to increase the well production rate by varying the pressure drawdown value and the bottomhole design. The proposed approach consists in combined experimental and mathematical modeling of deformation and filtration processes in the reservoir. The Drucker-Prager model was chosen to describe the transition to inelastic deformation. The parameters of the model, as well as the dependence of the permeability of rocks on stresses, are determined by testing reservoir rocks on

V. I. Karev (✉)
Ishlinsky Institute, Problems in Mechanics RAS, Moscow, Russia
e-mail: wikarev@ipmnet.ru

© The Author(s), under exclusive license to Springer Nature Switzerland AG 2022

V. I. Karev (ed.), *Physical and Mathematical Modeling of Earth and Environment Processes*,
Springer Proceedings in Earth and Environmental Sciences,
https://doi.org/10.1007/978-3-030-99504-1_5

a true triaxial loading unit. The proposed approach is implemented for a specific gas-condensate field with a low-permeability reservoir.

2 Directed Unloading of Formation—A Method for Increasing the Permeability of Rocks of Formation

A development of fields with low-permeability reservoirs and unconventional sources is becoming an urgent problem in connection with the depletion of large and accessible hydrocarbon deposits [1, 2]. In this regard, it is required to create new efficient production technologies and adapt existing well-tested technologies [3–6] to the conditions of developing hard-to-recover reserves. In the case of low-permeability reservoirs, it becomes necessary to ensure an increase in the natural permeability of the reservoir rocks for the successful development of such reservoirs. According to numerous studies, the permeability of rocks can strongly depend on the stresses, strains and their changes arising in rocks during technological operations on wells. Stresses can cause both the closure of filtration channels and, as a consequence, a decrease in permeability, and the growth of fracture systems, leading to an increase in permeability [7, 8]. The formation and growth of fractures occurs under the action of stresses and pressure of the reservoir fluid. The required stresses can be created by directional unloading of the formation from rock pressure. Directional unloading can be carried out by changing the pressure in the well in combination with special operations for preliminary formation of the bottomhole geometry [9].

3 A Model

A determination of the parameters of the required impact on the formation is based on a combined experimental and mathematical modeling of deformation and filtration processes occurring in the formation in the vicinity of a well.

3.1 Elastoplastic Model of Rock Deformation

The Drucker-Prager model [11] was chosen to describe the transition to the state of inelastic deformation taking into account the action of the average pressure [10], which makes it possible to describe not only the transition, but also the process of further deformation with hardening. The plasticity function for this model can be written as

$$F = \sigma_i + \alpha \cdot \sigma_m - \tau_s = 0 \tag{1}$$

$$\sigma_m = \frac{1}{3}(\sigma_1 + \sigma_2 + \sigma_3), \quad \sigma_i = \sqrt{3I_2}, \quad I_2 = \frac{1}{2}s_{jk}s_{jk}, \quad s_{jk} = \sigma_{jk} - \frac{1}{3}\sigma_{ii}\delta_{jk} \quad (2)$$

σ_i is stress intensity; I_2 is the second invariant of the stress deviator s_{jk}; σ_m is average pressure; α and τ_s are material constants.

When the criterion (1) is fulfilled, a further increase in stresses is accompanied by an increase in inelastic deformation which is described by the flow law. An essential feature of the used flow law is its non-associativity, i.e. the representation in the form

$$d\varepsilon_{ij}^P = \lambda \frac{\partial Q}{\partial \sigma_{ij}} \quad (3)$$

$d\varepsilon_{ij}^p$ is a plastic deformation increment; λ is Lagrange multiplier; Q is plastic potential, which differs from the plasticity function F by the coefficient at σ_m:

$$Q = \sigma_i + \alpha' \cdot \sigma_m - \tau_s = 0$$

The use of unassociated plastic potential (4) in combination with the plasticity function (1) makes it possible to describe both the effect of hydrostatic compression on the deformation process and the behavior of the rock beyond the transition to plasticity (in particular, its non-dilatant nature).

3.2 Experimental Determination of Model Parameters

Deformation characteristics (elastic moduli, parameters of the Drucker-Prager model, hardening parameters), filtration characteristics and the dependence of permeability on the stress-strain state were determined using the experimental setup of IPMech RAS Triaxial Independent Loading Test System [9] on specimens made from the rocks of the productive formation of the field under study.

The experimental data were used for mathematical modeling of deformation and filtration processes occurring in the reservoir during various technological operations: creating a pressure drawdown of a certain level, perforation of a particular type and density, cutting slits with different orientations.

4 Math Modeling

A finite element mesh was generated for zone of the reservoir near the wellbore for the bottom hole geometry of interest. The stress and strain fields were calculated for the given boundary and initial conditions. The filtration properties of mesh elements were calculated on the basis of the experimentally obtained dependence of permeability

on the stress-strain state for the elastic zone and the zone of plastic deformation (Drucker-Prager model). Then the filtration flow was calculated and the well flow rate was determined.

4.1 A Solution of the Problem on the Example of One of the Offshore Gas Condensate Fields with a Low-Permeability Productive Formation

The problem of fluid filtration into a production well for one of the offshore gas condensate fields with a low-permeability productive formation located at a depth of 4 km is considered. The results of the test of one rock specimen from the field under study are presented at the Figs. 1 and 2. Modeling deformation and filtration processes in the vicinity of an open borehole at the decrease the pressure in a well was being carried out. Figure 1 shows the dependence of rock permeability on shear stress. The strain curves along each specimen axis during the test are presented at the Fig. 2.Tests of the reservoir rock showed that the permeability decreases initially with an increase in shear stresses, then, upon reaching a certain level of stresses, the rock cracks and a sharp increase in permeability is observed (Fig. 1) [9]. In Fig. 2 shows the curves of deformation of rocks near a well, obtained as a result of testing at the TILTS when simulating an decrease of the pressure in the well. The

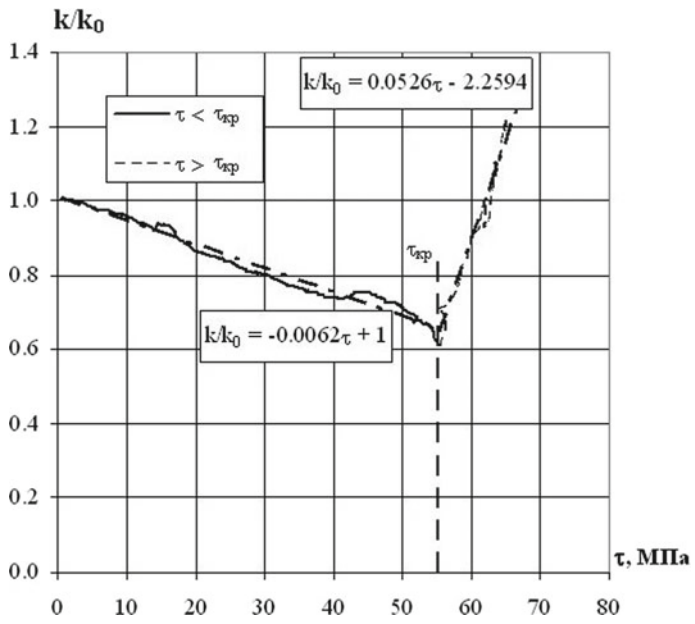

Fig. 1 Dependence of permeability on shear stress when simulating stress state near the well

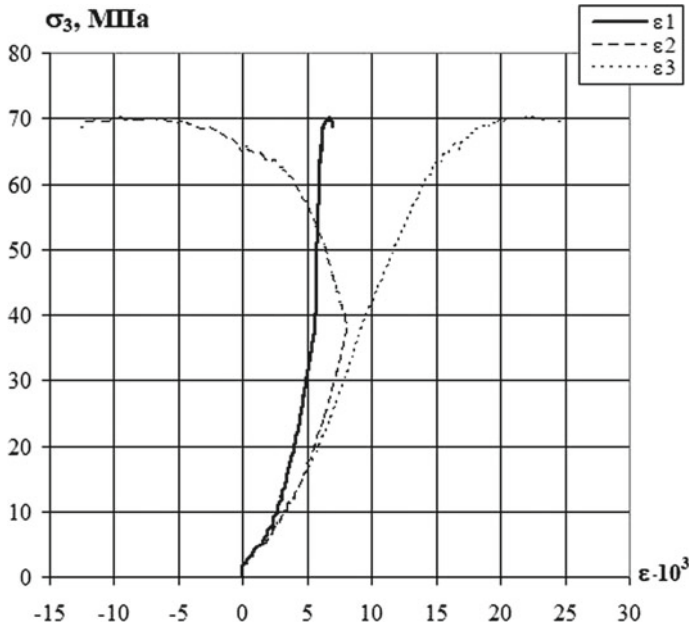

Fig. 2 Strain curves

Table 1 xxx

Bottom hole geometry	No dependence on stresses	Elastic setting	Elastoplastic setting
Open bottom hole	1	0.94	0.92
Open bottom hole with two vertical slots	1.5	1.43	1.38

ordinate represents the loading parameter—a monotonically increasing component of the stress tensor corresponding to the absolute value of the circumferential stress.

The following variants of the well bottom were considered: an open hole and an open hole with two vertical slots with a depth of two well radii. Table 1 shows the values of the calculated well flow rates related to the flow rate of an ideal well, in which the permeability in the vicinity of the well is constant, homogeneous and equal to the natural permeability of the formation.

5 Conclusions

The performed mathematical modeling for the cases of the considered bottomhole designs showed that taking into account the experimentally obtained dependence of permeability on the stress-strain state has a noticeable effect on the values of well

flow rates obtained in the calculations. For the investigated rocks, characterized by the dependences obtained as a result of physical modeling on the TILTS (one of which is shown in Fig. 1), taking into account elastic deformation influence reduces the calculated flow rates for both bottomhole geometries. Taking into account the effect of elastoplastic deformation on permeability reduces the flow rates caculated to an even greater extent.

The described approach can form the basis for the creation of new technologies for the development of deposits with low-permeability reservoirs, including the Bazhenov formation, oil and gas shales, and gas-saturated coals.

Acknowledgements The work was carried out with the financial support of the grant of the Russian Federation represented by the Ministry of Science and Higher Education of the Russian Federation No. 13.1902.21.0018 (agreement 075-15-2020-802).

References

1. Alekseev A.D., Zhukov V.V., Strizhnev K.V., Cherevko S.A. Study of hard-to-recover and unconventional objects according to the principle of "reservoir factory in the formation" // Zapiski Gornogo instituta. 2017.T.228. S. 695–704. https://doi.org/10.25515/PMI.2017.6.695. in Russian.
2. Song Y., Li Z., Jiang L., Hong F. The concept and the accumulation characteristics of unconventional hydrocarbon resource // Petroleum Science. 2015. V12. P. 563–572. https://doi.org/10.1007/s12182-015-0060-7.
3. Galeev R.R., Zorin A.M., Kolonskikh A.V. et al. Choice of the optimal system for the development of low-permeability reservoirs using horizontal wells with multiple hydraulic fractures // Oil industry. 2013. No. 10. S.62–65. in Russian.
4. Govzich A.N., Bilinchuk A.V., Faizullin I.G. Experience of multistage hydraulic fracturing in horizontal wells of JSC Gazprom Neft // Oil Industry. 2012. No. 12. P. 59–61. in Russian.
5. Ganiev R.F., Ukrainsky L.E. Nonlinear wave mechanics and technologies. Wave and oscillatory phenomena on the Basis of High Technologies. USA: Begell Hause. Inc. Publishers. 2012. 527 p.
6. Khristianovich S.A., Kovalenko Yu.F., Kulinich Yu.V., Karev V.I. Increasing the productivity of oil wells using the method of geoloosening // Oil and Gas Eurasia. 2000. No. 2. P. 90–94.
7. Klimov D.M., Karev V.I., Kovalenko Yu F. Experimental study of the influence of a triaxial stress state with unequal components on rock permeability // Mech. Sol. 2015.50 (6). P. 633–640.
8. Zhuravlev A.B., Karev V.I., Kovalenko Yu.F., Ustinov K.B. The effect of seepage on the stress – strain state of rock near a borehole // J. Appl. Math. Mech. 2014.78 (1). P.56–64.
9. Karev Vladimir, Kovalenko Yuri, Ustinov Konstantin. Geomechanics of Oil and Gas Wells. Springer Nature Switzerland AG 2020.166 p. https://doi.org/10.1007/978-3-030-26608-0. ISBN 978–3–030–26607–3.
10. Karev V. I. Coupled problem of elastoplastic deformation of reservoir rocks and filtration into the well. Conference proceedings of 7th International Scientific Conference-School of Young Scientists "Physical and Mathematical Modeling of Processes in Geomedia" October 20–22, 2021 M: IPMech RAS. 2021 P. 128–132. in Russian.
11. Drucker, D.C., Prager, W. Soil Mechanics and Plastic Analysis for Limit Structure. Quarterly of Appl. Math. 10 (2). 1952. P. 157–165.

Far Internal Gravity Waves Fields from Radially Symmetric Perturbation

V. V. Bulatov

Abstract The paper solves the problem of constructing uniform asymptotics of the distant fields of internal gravitational waves from the initial perturbation of lines of equal density of radial symmetry. A constant model distribution of the buoyancy frequency is considered and an analytical solution of the problem in the form of a sum of wave modes is obtained using the Fourier-Hankel transform. Uniform asymptotics of solutions describing the spatio-temporal characteristics of the elevation of isopicns (lines of equal density), vertical and horizontal (radial) velocity components are obtained. The asymptotics of a separate wave mode of the main components of the wave field are expressed in terms of the square of the Airy function and its derivatives. The exact and asymptotic results are compared, and it is shown that at times of the order of ten or more periods of buoyancy, equal-dimensional asymptotics make it possible to efficiently calculate long-range wave fields.

Keywords Internal gravity waves · Stratified media · Far fields · Uniform asymptotics · Wave fronts

In experimental and field observations of internal gravitational waves in natural stratified environments (ocean, atmosphere), as well as when considering a large number of specific tasks, a lot of factual material has been accumulated that needs theoretical understanding [1–5]. Wave motions in these media can occur both due to natural causes and generated by artificial sources of disturbances [6–12]. The main results of the solutions to the problems of the generation of (GW are presented in the most general integral form, and in this case the obtained integral solutions require the development of asymptotic methods of their analysis, allowing qualitative analysis and express evaluations of the solutions obtained [6, 7, 12–16]. Solutions in the linear formulation by means of the Fourier transform make it possible to calculate wave fields by numerical integration [2, 3, 17–19]. However, as the time and distance

V. V. Bulatov (✉)
Ishlinsky Institute for Problems in Mechanics RAS, Vernadskogo ave. 101-1, 119526 Moscow, Russia
e-mail: internalwave@mail.ru

© The Author(s), under exclusive license to Springer Nature Switzerland AG 2022

V. I. Karev (ed.), *Physical and Mathematical Modeling of Earth and Environment Processes*,
Springer Proceedings in Earth and Environmental Sciences,
https://doi.org/10.1007/978-3-030-99504-1_6

from the sources of disturbances increase, it is necessary to calculate integrals from more and more oscillating functions, and numerical calculations become laborious. In addition, it is practically impossible to obtain from numerical calculations a qualitative description of the (GW departing from the source, their evolution in time and space, dependence on the characteristics of the source, or it requires large calculations. At the same time, asymptotic expressions for wave fields are explicit formulas expressed in terms of known special functions, and their qualitative analysis, as a rule, does not cause difficulties. In addition, the asymptotics found make it possible to move to a more realistic situation of media whose parameters slowly change horizontally and over time, since the presence of explicit analytical constructions allows us to take into account the change in the parameters of the medium along the path of the propagation of (GW by means of a corresponding change in the arguments describing the field of special functions, as well as amplitude phase multipliers [6, 7]. One of the main generation models used can be considered the assumption of the occurrence of (GW packets by pulsed action of various physical nature [1, 2, 4, 5]. To carry out predictive calculations of the VGV, the parameters of the wave generation models are selected in such a way as to bring the simulated wave system closer to the actually observed wave patterns, which makes it possible to verify these mathematical models.

The aim of this work is to construct uniform asymptotics of the distant IGW fields excited by a non-local source of radial symmetry disturbances that erupted at the initial moment in a layer of a stratified medium of finite thickness. A source of radial symmetry that erupted at the initial moment of time in a layer of an inviscid incompressible stratified medium of finite thickness H is considered. The elevation field of isopicns (lines of equal density) $\eta(r, z, t)$ in cylindrical coordinates (r, z) (there is no dependence on the angle, the z axis is directed upwards) in the Boussinesq approximation is determined from the problem [2, 6, 7]

$$\frac{\partial^2}{\partial t^2}(\Delta + \frac{\partial^2}{\partial z^2})\eta(r, z, t) + N^2(z)\Delta\eta(r, z, t) = 0, \quad \Delta = \frac{\partial^2}{\partial r^2} + \frac{1}{r}\frac{\partial}{\partial r}$$
$$\eta(r, z, 0) = \Phi(r)\Pi(z), \quad \eta(r, z, t) = 0 \quad \text{when} \quad z = 0, -H$$

where here and further the Brent-Väsälä frequency (buoyancy frequency) assumed to be constant:$N^2(z) = N^2 = \text{const}$. It is assumed that the initial perturbation of isopicns (lines of equal density) has radial symmetry and some depth distribution with a single maximum, which corresponds to the qualitative nature of non-local sources observed in real natural environments (ocean, atmosphere) [3, 9, 10, 15]. The solution of the resulting initial boundary value problem is constructed using the Fourier-Hankel transform, and in dimensionless variables $r^* = r\pi/H$, $z^* = z\pi/H$, $k^* = k\pi/H$, $t^* = Nt$ (the index "*" is further excluded) has the form

$$\eta(r,z,t)=\sum_{n=1}^{\infty}\eta_n=\sum_{n=1}^{\infty}a_n\sin(nz)g_n(r,t)$$
$$g_n(r,t)=\int_0^{\infty}A(k)kJ_0(kr)\cos(\omega_n(k)t)dk$$
$$A(k)=\int_0^{\infty}rJ_0(kr)\Phi(r)dr,\ a_n=\frac{2}{\pi}\int_{-\pi}^{0}\Pi(z)\sin(nz)dz,\ \omega_n(k)=k/\sqrt{k^2+n^2} \tag{1}$$

where J_0 is zero-order Bessel functions [20]. Using these solutions, it is possible to obtain expressions for the vertical $W(r,z,t)=\frac{\partial\eta(r,z,t)}{\partial t}$ and horizontal (radial) $U(r,z,t)$ velocity components of IGW, which have the forms

$$W(r,z,t)=\sum_{n=1}^{\infty}W_n=\sum_{n=1}^{\infty}a_n\sin(nz)p_n(r,t),$$
$$U(r,z,t)=\sum_{n=1}^{\infty}U_n=\sum_{n=1}^{\infty}na_n\cos(nz)q_n(r,t)$$
$$p_n(r,t)=-\int_0^{\infty}kA(k)J_0(kr)\omega_n(k)\sin(\omega_n(k)t)dk$$
$$q_n(r,t)=\int_0^{\infty}A(k)J_1(kr)\omega_n(k)\sin(\omega_n(k)t)dk,$$

where J_1 is the Bessel function of the first order [20]. The functions $g_n(r,t),\ \ p_n(r,t),\ \ q_n(r,t)$ determine the space-time structure of the main components of the fields of IGW. In this paper, we consider the problem of constructing uniform asymptotics that allow us to describe wave fields when $r,\ t>>1$ both near and far from wave fronts. To this end, it is necessary to replace the Bessel function with its asymptotics: $J_0(kr)\approx\sqrt{2/\pi kr}\cos(kr-\pi/4)$ [20]. The resulting integral can be represented as

$$g_n(r,t)=I_n^{+}(r,t)+I_n^{-}(r,t),\ \ I_n^{\pm}(r,t)=\frac{1}{2}\int_0^{\infty}\frac{F(k)}{\sqrt{k}}\exp(it\gamma_{\pm n}(k)-i\pi/4)dk$$
$$F(k)=\frac{kA(k)}{\sqrt{2\pi r}},\ \gamma_{\pm n}(k)=kV\pm\omega_n(k),$$

where $V = r/t$ and $\sqrt{k} = i\sqrt{|k|}$ when $k < 0$. Because $\omega_n(k)$ is monotonically increasing function of a variable k, then the phase function $\gamma_{+n}(k)$ of integral I_n^+ has no stationary points on the real axis, so for large values $r,\ t$ the integral I_n^+ is exponentially small. Let's evaluate the integral I_n^-. Denote $c_n = \omega'_n(0) = 1/n$ is the maximum group speed of a single mode of IGW [1, 2, 6, 7]. Then when $0 < V < c_n$ the phase function $\gamma_{-n}(k) = kV - \omega_n(k)$ has two stationary points on the real axis:$k_n(V) = \pm n\sqrt{(Vn)^{-2/3} - 1}$. Near the wavefront of each mode, that is, when $V \to c_n$, these two stationary points merge with each other, as well as with the branching point when $k = 0$. When $V > c_n$ two stationary points $\pm k_n(V)$ they are located on an imaginary axis. Then the main term of the uniform (by parameter $V = r/t$) asymptotics a separate wave mode when $r,\ t \to \infty$ has the form [21, 22]

$$
\begin{aligned}
g_n(r,t) \approx & G_n(r,t)Ai(\theta)Ai'(\theta),\\
G_n(r,t) = & -2\pi^{3/2}\sqrt{\frac{2}{tk_n(V)\gamma'_{-n}{}'(k_n(V))}}F(k_n(V))\\
\theta = & -\sigma(t/2)^{2/3}, \sigma = (-3\gamma_{-n}(k_n(V))/2)^{2/3},\\
Ai(\theta) = & \frac{1}{2\pi}\int\limits_{-\infty}^{\infty}\exp(i(-\theta s + s^3/3))ds
\end{aligned}
$$

Uniform asymptotics of functions $p_n(r,t)$ and $q_n(r,t)$ when $r,\ t \to \infty$ are calculated similarly, and have the form

$$p_n(r,t) \approx P_n(r,t)((Ai'(\theta))^2 + \theta(Ai(\theta))^2)$$

$$P_n(r,t) = -2^{1/3}\pi^{3/2}t^{-5/6}\sqrt{\frac{2}{\sigma k_n(V)\gamma'_{-n}{}'(k_n(V))}}F(k_n(V))\omega_n(k_n(V))$$

$$q_n(r,t) \approx Q_n(r,t)Ai(\theta)Ai'(\theta)$$

$$Q_n(r,t) = -2\pi^{3/2}\sqrt{\frac{2}{tk_n(V)\gamma'_{-n}{}'(k_n(V))}}F(k_n(V))\frac{\omega_n(k_n(V))}{k_n(V)}$$

For numerical calculations in the initial distribution of the elevation of isopicns (lines of equal density), it is assumed that the functions $\Phi(r),\ \Pi(z)$ are normalized to their maximum modulo values. As a model, we can consider the following radial distribution of the initial isopicn perturbation: $\Phi(r) = \exp(-r^2/4)/2$ and function representation $\Pi(z) = z^\alpha(1 - z^\beta)$, $\alpha = 33,\ \beta = 57$. The spatial scales used and the variability of the initial isopicn disturbance correspond to the typical horizontal and vertical scales of non-local sources of IGW excitation in the ocean [4, 5, 8–10]. Figures 1, 2 and 3 shows the results of calculations of functions $g_1(r,t)$, $p_1(r,t)$,

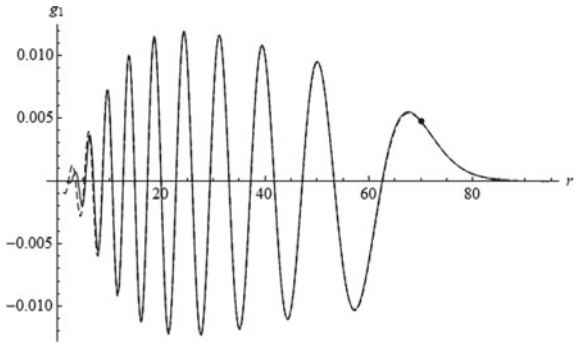

Fig. 1 First mode of elevation: exact solutions and asymptotics

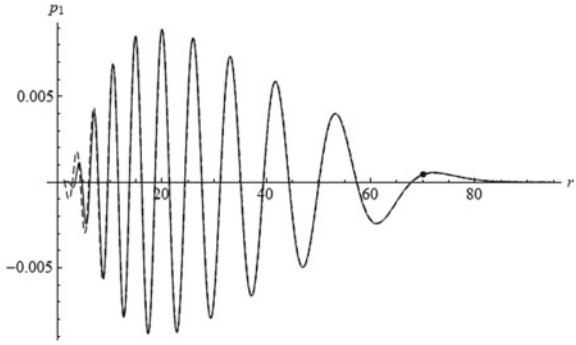

Fig. 2 First mode of vertical velocity: exact solutions and asymptotics

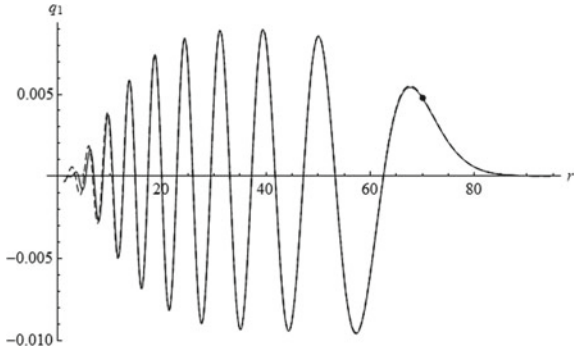

Fig. 3 First mode of horizontal (radial) velocity: exact solutions and asymptotics

$q_1(r, t)$ for the value $t = 70$, the solid line in the figures is the results of exact numerical calculations, the straight line is calculations based on asymptotic formulas. A dot in the figures marks the position of the wavefront. The presented results show a good coincidence of exact and asymptotic formulas for large values $r,\ t$. As numerical calculations show, at times of the order of ten or more periods of the buoyancy frequency, the constructed uniform asymptotics of wave modes allows us to calculate the far IGW fields both near and far from the wave fronts with a good degree.

Thus, we obtain the following qualitative picture of the propagation of the fields of the distant IGW fields excited by the initial perturbation of the isopicn at sufficiently large r, t. First, when $t < c_1^{-1}r$, full fields $\eta(r,z,t)$, $W(r,z,t)$, $U(r,z,t)$ are exponentially small. When $t \approx c_n^{-1}r$ the first wave mode is turned on, and when $c_1^{-1}r < t < c_2^{-1}r$ the field consists of this mode, the amplitudes of the other modes are exponentially small. When $t \approx c_2^{-1}r$ the second wave mode is connected and in the interval $c_2^{-1}r < t < c_3^{-1}r$ the field consists of the sum of the first and second modes, then the third wave mode is "turned on" and so on.

In this paper, uniform asymptotic solutions describing the dynamics of IGW packets over long times and distances are constructed for a given initial perturbation of isopicns (lines of equal density) with radial symmetry and vertical distribution with one maximum. The uniform asymptotics of a separate wave mode of the wave field components are expressed in terms of the square of the Airy function and its derivatives and allow us to calculate the spatiotemporal characteristics of the elevation of the iso-picn, vertical and horizontal (radial) velocity components both near and far from the wavefronts. The model elevation distribution used as an initial one can adequately describe various physically based mechanisms of generation of IGW packets in natural stratified environments. The obtained results allow us to analytically represent both the elevation of the isopicns and all the velocity components of the excited IGWs. The obtained uniform asymptotics of distant IGW fields make it possible to efficiently calculate the main characteristics of wave fields, and, in addition, to qualitatively analyze the solutions obtained, which is important for the correct formulation of mathematical models of wave dynamics of natural stratified media. The obtained asymptotic results with different values of the physical parameters included in them allow us to evaluate the characteristics of the initial disturbances observed in real conditions.

Asymptotic methods for studying the dynamics and generation of GW combine the comparative simplicity and computational power of analytical results, as well as the possibility of their qualitative analysis. These mathematical modeling methods can be used to study any other wave processes (acoustic and seismic waves, SHF radiation, tsunami waves, etc.) in real environments with a complex structure. The significance of such methods of wave field analysis is determined not only by their visibility, universality and efficiency in solving various problems, but also by the fact that they can be some semiempirical basis of other approximate methods in the mathematical modeling of wave packets of a different physical nature.

The universal character of the used asymptotic methods of mathematical modeling of IGW packages can be supplemented by universal heuristic conditions of applicability of these methods. These criteria provide internal control of the applicability of the used asymptotic methods, and in some cases, based on the formulated criteria, it is possible to evaluate wave fields where other methods are not applicable. This opens up wide possibilities for analyzing wave patterns in general, which is important both for the correct formulation of theoretical studies and for carrying out evaluation and express calculations for full-scale measurements of IGW packets, including using remote satellite radar methods. The special role of these methods is due to the fact that the parameters of natural stratified media, as a rule, are known approximately,

and attempts to accurately solve the initial equations using such parameters can lead to a loss of accuracy. Therefore, the results obtained in the work can be used by specialists in the field of numerical and mathematical modeling of complex environments, geophysical hydrodynamics, oceanology, marine hydraulic engineering, in the construction of complex marine hydraulic structures, as well as in solving other physical and applied problems.

Acknowledgements The work is carried out with financial support from the Russian Foundation for Basic Research, project 20-01-00111A.

References

1. Lightill J (1978) Waves in fluids. Cambridge University Press, Cambridge.
2. Miropol'skii YuZ, Shishkina OV (2001) Dynamics of internal gravity waves in the ocean. Kluwer Academic Publishers, Boston.
3. Vlasenko V, Stashchuk N, Hutter K (2005) Baroclinic tides. N.Y.: Cambridge University Press.
4. Mei CC, Stiassnie M, Yue DK-P (2017) Theory and applications of ocean surface waves. Advanced series of ocean engineering. V. 42. World Scientific Publishing.
5. Morozov TG (2018) Oceanic internal tides. Observations, analysis and modeling. Springer, Berlin.
6. Bulatov VV, Vladimirov YuV (2012) Wave dynamics of stratified mediums. Nauka, Moscow.
7. Bulatov VV, Vladimirov YuV (2019) A general approach to ocean wave dynamics research: modelling, asymptotics, measurements. OntoPrint Publishers, Moscow.
8. Morozov EG, Tarakanov RYu, Frey DI, Demidova TA, Makarenko NI (2018) Bottom water flows in the tropical fractures of the Northern Mid-Atlantic Ridge // J Oceanography 74(2): 147–167.
9. Khimchenko EE, Frey DI, Morozov EG (2020) Tidal internal waves in the Bransfield Strait, Antarctica // Russ J Earth Science20: ES2006.
10. Haney S, Young WR (2017) Radiation of internal waves from groups of surface gravity waves // J Fluid Mech 829:280-303.
11. Broutman D, Rottman J (2004) A simplified Fourier method for computing the internal wave field generated by an oscillating source in a horizontally moving, depth-dependent background // Phys Fluids 16: 3682–3689.
12. Bulatov VV, Vladimirov YuV, Vladimirov IYu (2019) Far fields of internal gravity waves from a source moving in the ocean with an arbitrary buoyancy frequency distribution // Russian J Earth Sci 19: ES5003.
13. Bulatov V, Vladimirov Yu (2020) Generation of internal gravity waves far from moving non-local source // Symmetry 12(11): 1899.
14. Lecoanet D, Le Bars M, Burns K J, Vasil G M, Brown B P, Quataert E, Oishi J S (2015) Numerical simulations of internal wave generation by convection in water // Phys Rev E – Statistical, Nonlinear, and Soft Matter Physics 9: 1–10.
15. Voelker GS, Myers P, Walter M, Sutherland B R (2019) Generation of oceanic internal gravity waves by a cyclonic surface stress disturbance // Dyn Atm Oceans 86: 16–133.
16. Meunier P, Dizиs S, Redekopp L, Spedding G (2018) Internal waves generated by a stratified wake: experiment and theory // J Fluid Mech 846: 752-788.
17. Wang H, Chen K, You Y (2017) An investigation on internal waves generated by towed models under a strong halocline // Phys Fluids 29: 065104.
18. Svirkunov PN, Kalashnik MV (2014) Phase patterns of dispersive waves from moving localized sources //Phys.-Usp. 57 (1): 80–91.

19. Broutman D, Brandt L, Rottman J, Taylor C (2021) A WKB derivation for internal waves generated by a horizontally moving body in a thermocline// Wave Motion 105: 102759.
20. Watson GN (1995) A treatise on the theory of Bessel functions (Reprint of the 2nd ed.). Cambridge: Cambridge University Press.
21. Borovikov VA (1994) Uniform stationary phase method. IEE electromagnetic waves. Series 40. London: Institution of Electrical Engineers.
22. Kravtsov Yu, Orlov Yu (1999) Caustics, catastrophes and wave fields. Berlin: Springer.

Four Methods for Estimating the Concentration of Ions in Electrolyte Solutions

N. B. Kosykh, S. A. Varzin, P. V. Glavnov, S. A. Guzev, and A. M. Yafyasov

Abstract The results of measuring the volt-ampere characteristics of a 1% aqueous solution of KCl at room temperature are presented. The question of the parameters determined from the dependence I(U) is discussed. A hypothesis about the electrical shielding of the electrode potential by ions is proposed. Based on the information about electrochemical functions, a method for determining the concentration of ions from the experimental curve is developed and shown.

Keywords KCl solution · Volt-Ampere characteristic · Electric field · Ion Mobility · Solubility · Modelling

1 Introduction

Many applied problems concerning the physicochemical properties of electrolyte solutions require the determination of electrolyte parameters, such as solubility, density, electrical conductivity, concentration of charged particles, and the like. In this paper, an overview of the main methods for measuring the concentration of ions is carried out and an attempt is made to determine this concentration by electrical measurements of the volt-ampere characteristic in the interelectrode space of 1% KCl solution.

N. B. Kosykh (✉)
Branch of Lomonosov Moscow State University in Sevastopol, Sevastopol, Russia
e-mail: ipnk5419@mail.ru

S. A. Varzin · P. V. Glavnov · S. A. Guzev · A. M. Yafyasov
Faculty of Physics, Saint Petersburg State University, Saint Petersburg, Russia

© The Author(s), under exclusive license to Springer Nature Switzerland AG 2022

V. I. Karev (ed.), *Physical and Mathematical Modeling of Earth and Environment Processes*,
Springer Proceedings in Earth and Environmental Sciences,
https://doi.org/10.1007/978-3-030-99504-1_7

1.1 The First Method

The substance is weighed and dissolved in an electrolyte solution. In the case when the solution is far from saturation, it is believed that the substance completely dissociates into ions. Otherwise, salt solubility tables are used.

1.2 The Second Method

In it, the concentration of ions in solution is determined by the method of appendages [1]. The volt-ampere characteristic (VAC, I(U)) of the electrolyte is measured, then the corresponding substance is dissolved in it and the VAC is measured again. From the proportion, the initial concentration is found by increasing the electric current. It is assumed that the concentration of ions and, respectively, I(U) are linearly related.

1.3 The Third Method

Allows us to determine the ion density from the experimental dependence I(U). To measure the VAC, an electrolytic cell with a size of 0.05 × 0.05 m2 was made, the electric current through which was measured using operational amplifiers [5]. To prepare the electrolyte, 6.6 × 10–5 kg of potassium bromide was weighed, which was dissolved in 0.1 kg of distilled water. Niobium plates with areas of 5.6×10^{-5} and 5.27×10^{-4} m^2, respectively, were used as electrodes. Figures 1 and 2 show the dependencies I(U) and E(U). Here we give the dependence I(U) with the opposite sign, as is customary in probe diagnostics. In this case, it becomes obvious that the curve I(U) is a hyperbolic sine [8]. As can be seen from Fig. 1, the low current region is in the range of ± 0.2 V. Outside of this segment, the electric current increases sharply. The electric field repeats the dependence I(U) in a similar way (see Fig. 2).

The method of determining the concentration from the VAC graph is borrowed from the theory of plasma. A pulse is passed through the conductive medium. In this case, the electric current in the circuit and the electric field are measured. In our case, taking into account the diffusion motion of charged particles and the ion distribution function in the electrolyte solution, the current to the electrode is described by the formula

$$I(U) = C \cdot qnbES \cdot sh(f[qU_0/kT]) \tag{1}$$

where q is the electric charge of the ion, n is concentration of ions in solution, b is mobility of ions in a liquid medium, E is electric field, U0 is the potential that is applied to the electrode, kT is thermal energy of the particle, f is a number of electrochemical functions, C is some constant associated with the ion energy distribution

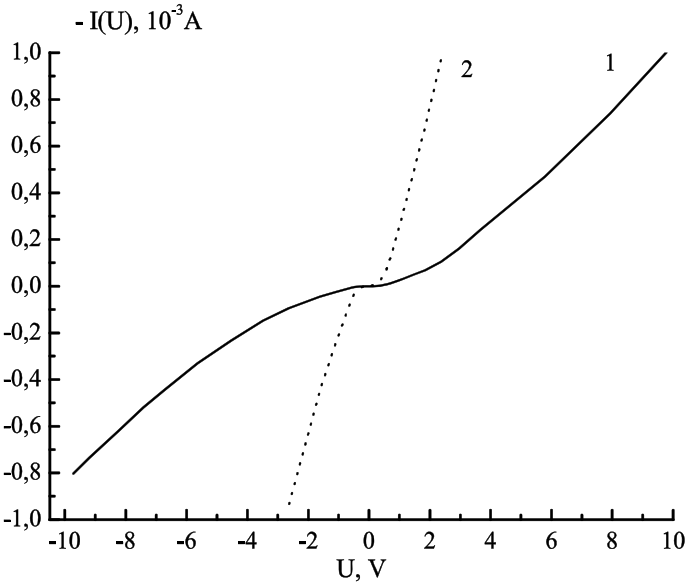

Fig. 1 VAC in KBr solution: 1—on the usual scale, 2—the dependence of I(U) is increased by 10 times

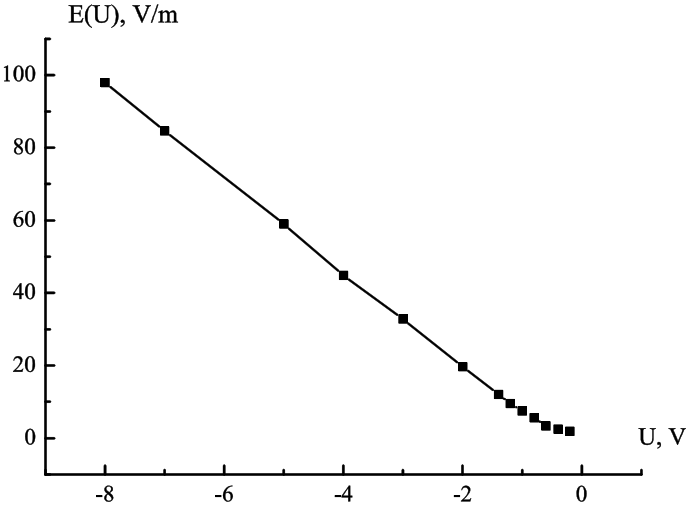

Fig. 2 Dependence of E(U) in KBr solution

function. In the case of electrolytic VAC, the ion density can be determined from the expression

$$n = \frac{I(U)}{q \cdot b \cdot S \cdot E} \tag{2}$$

Here we assume that sh[f(qU/kT))] = 1. The ion concentration value calculated by Eq. (2) is.

$$n = \frac{7.8 \times 10^{-6}}{1.6 \times 10^{-19} \times 6.8 \times 10^{-8} \times 0.56 \times 10^{-4} \times 3.8 \times 1} = 3.37 \times 10^{24} \mathrm{m}^{-3}$$

The ion concentration calculated by weight KBr is 3,765·1024 m^{-3}. As can be seen from the calculations, the error of the method is no more than 10–12%. In our model, we assume that C = 0.5. In fact, behind this coefficient there is a very complex series of hypotheses about the distribution of ions by energy, the discussion of which we would like to postpone for some time. This issue is not a matter of principle, but requires a large volume of in-depth discussions.

The fourth method is also related to the measurement of VAC. An algorithm for determining the ion concentration was proposed in [7]. Let's look at it in more detail. The charge that accumulates in the POPS from the beginning of the experiment to time t is equal to.

$$Q = \int_0^t I(U(t))dt$$

We transform the integrand as follows

$$Q = \int_0^t I(U(t))\frac{dU}{dU}dt = \int_0^t I(U(t))\frac{dt}{dU}dU = \int_0^t I(U(t))\frac{1}{V_p}dU \tag{3}$$

where Vp is the scanning speed when measuring VAC, and the integral (3) itself is the hysteresis area I(U(t))dU. In our experiment, the scanning speed is a strictly linear function, since an integrator based on an operational amplifier serves as a linearly varying signal generator. However, we are not interested in the charge itself, but in the density of ions in close proximity to the smaller electrode. Then

$$n(r,t) = \frac{Q}{q \cdot S \cdot h(U)} \tag{4}$$

therefore, the left and right sides of Eq. (4) must be divided by the volume surrounding the electrode. Then

$$n(r.t) = \frac{1}{q \cdot S \cdot h(U)} \int_0^t I(U(t)) \frac{1}{V_p} dU = \frac{1}{q \cdot S \cdot h(U)} \cdot \frac{S_{I(U(T))}}{V_p} \quad (5)$$

As can be seen, to determine the ion concentration in this technique, it is necessary to know the thickness of the bulk charge layer, the area of the electrodes, the magnitude of the hysteresis of the VAC and the scanning speed I(U). Since we have the opportunity to determine the concentration of charged particles by method 1 and 3, we will solve the inverse problem: using Eq. (5), we estimate the thickness of the POPS.

In an electrolytic cell with a size of 5 × 5 sm, the VAC of a KCl solution was measured (KCl is chemically pure, the molar concentration was 0.01). The ions of this substance have mobility close in absolute value and, accordingly, drift velocity. This circumstance makes it possible to obtain an almost symmetrical VAC. This is important for modeling the kinetic processes accompanying the passage of electric current through the solution. Niobium plates with areas of $1.34 \cdot 10^{-4}$ and $5.27 \cdot 10^{-4}$, respectively, were used as electrodes. The measurement of the I(U) curves was carried out in a pulsed mode, since this method minimizes the influence of electrochemical processes [5]. In the center of the cell, at a distance of 0.01 m from each other, two auxiliary niobium electrodes with an area of $0.4\ 10^{-4}$ were located. The difference of their potentials was recorded on a digital oscilloscope.

In the course of the research, a series of VAC was measured. The experimental curves I(U) are shown in Fig. 3. We present an image of the dependencies I(U) with the inverse sign. Before registering the curves, the electrodes were treated with an

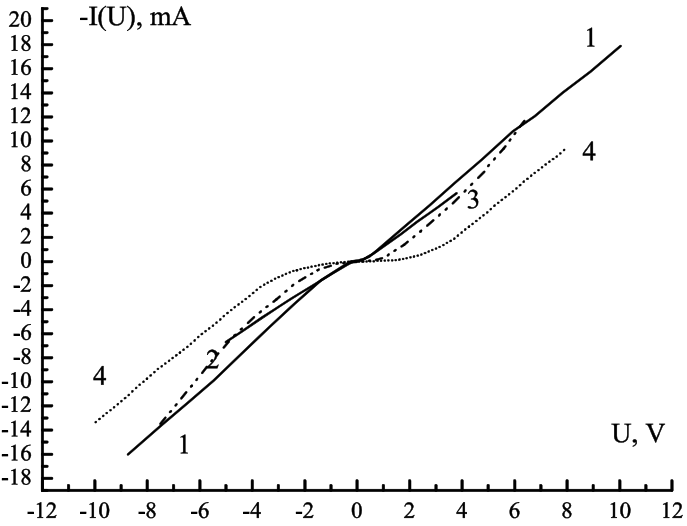

Fig. 3 VAC in 1% KCl solution: 1—first measurement I(U): 2,3, 4—VAC curves obtained after 10, 20 and 90 min of measurements

abrasive that removed the oxide layer of the electrode. Further measurements were carried out without processing the electrodes and mixing the electrolyte. The first curve I(U) was obtained immediately after processing the electrodes, the second and third—after 10 and 20 min of measurements, respectively. When registering the fourth curve, the electrolyte was replaced without processing the electrodes. The total time of the electrodes spent in the electrolyte solution during the experiment, we estimate about 90 min. To one degree or another, all VAC have hysteresis; with repeated scanning of the VAC, its manifestation becomes especially noticeable. For example, curves 2 and 3 in Fig. 3.

Figure 4 shows the first derivatives of the VAC according to the potential of the previous figure. As for the graphs, the "fast cosine" i.e. I'(U) is located on the interval of the slowly growing VAC, and the flat part is in the remaining part. This means that the cosine argument is a complex function. In other words, there is a screening effect in solutions: while the field in the solution and in the layer is small, we observe a "fast cosine", but as soon as the shielding takes effect, the cosine becomes "flat". Note that with a small electric field and the shielding is small in the entire volume: i.e. the sine argument is close to qU/kT ~ 1. The shielding of ions in this VAC interval is carried out by water molecules. With an increase in the field, its effect is weakened due to additional shielding by ions of opposite signs that are in POPS.

Figure 5 shows the dependence of the electric field (in absolute magnitude) on the voltage applied to the electrodes. The numbering of the curves corresponds to the notation in Fig. 3.

The evolution of curves over time, presented in Figs. 3, 4, 5, reveals several experimental facts. As a result of the experiment, symmetric curves I(U), I'(U),

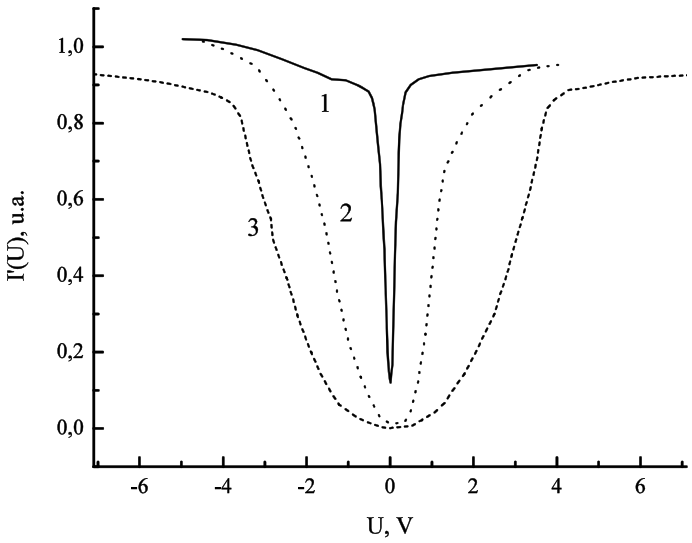

Fig. 4 I'(U) in 1% KCl solution:—first measurement I(U): 2—VAC curves obtained after 20 and 90 min of measurements

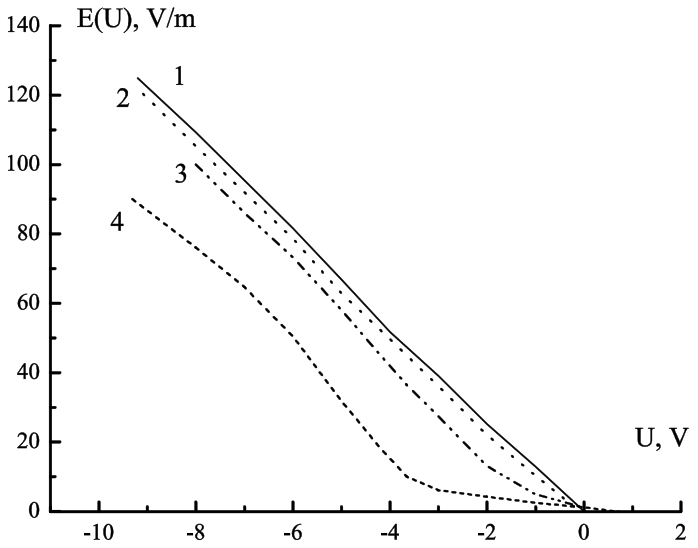

Fig. 5 Shows the dependences of the electric field in the middle of the cell: 1—the first measurement I(U): 2,3, 4—the VAC curves obtained after 10, 20 and 90 min of measurements

E(U) were indeed obtained. Further, the measured graphs show an expansion of the low current region. The third fact is that the shape of the VAC, its derivative and the corresponding dependence E(U) change. So, the non-current interval for curve 1 in Fig. 3 is several tenths of a volt, and for curve 4 this area expands to ± 3V. According to curve 4, shown in Fig. 1, at the inflection point of the graph, we take a current of 1.47 mA. This current value corresponds to a field of 13 V/m. Then, taking into account the mobility of potassium ions 6,8 10^{-8} $m^2/(V * s)$ and the area of the smaller electrode 1,34 * 10^{-4} m^2 for ion density, we obtain

$$n = \frac{I(U)}{qbS\Delta E \cdot sh(\varepsilon(U) \cdot qU_0/kT)} = \frac{0.00147}{1.6 \times 10^{-19} \times 6.8 \times 10^{-8} \times 1.34 \times 10^{-4} \times 13 \times 1} = 7.8 \times 10^{25} m^{-3}$$

The real density (1% KCl solution) is 8*1025 m^{-3}. The application of this technique to curve 3 in Fig. 1 at a current of 0.512 mA, an electric field of 81 V/m makes it possible to obtain an ion concentration of 8.1 1025 m^{-3}. Thus, we get a quantitative agreement with an error of 5%. Now we can estimate the thickness of the layer by the formula (5). We find the hysteresis area of curves 1 and 3 in Fig. 3 and determine the scanning speed of the potential (0.25 V/s). Then the value of the layer thickness is 2.67·10^{-6} m.

It is usually assumed that the thickness of the bulk charge layer in a solution with ions having similar mobility values is 5–6 Debye radii From Fig. 3 it follows that changing the electrolyte portion does not change its resistance, since the slope of

curve 4 remains the same as for the 1st curve. On the other hand, if we continued the measurement without changing the solution, we would get curves with increasing hysteresis. Then it should be recognized that the thickness of the layer at the electrodes increases significantly, since the other parameters included in formula (5) do not change. This is possible only under the assumption that the thickness of the layer depends on the concentration of hydrogen ions, the presence of which dramatically increases the thickness of POPS [8]. An increase in the thickness of POPS leads to a greater polarization of charged particles in the layer. As for curve 4 in Fig. 3, it is obvious the emission of hydrogen ions from the surface of the electrodes. Or in other words, during the passage of an electric current, the metal surface sorbs hydrogen atoms from water.

These methods may be of interest to specialists in physico-chemical, chemical-biological, geological-ecological and other related areas, where different approaches are required to determine the parameters of electrolyte solutions.

References

1. Chen F. Electrical probes. In the collection Diagnostics of plasma edited by R. Huddlestone and S. Leonard. M., 1967.
2. Mechkovsky S.A. Analytical chemistry. //Minsk. BSU Publishing House. 1975. (in Russian).
3. Bohinc K., Kralj-Iglic V., Iglic A. Thickness of electrical double layer. Effect of ion size. Electrochimica Acta. 2001. V. 46. pp. 3033–3040.
4. Varzin S.A., Gusev S.A. Calculation of the thickness of the bulk charge layer taking into account the dipole moment of water molecules in KCl and NaCl solutions. Engineering and Physics journal. 2018. Volume 91, No. 6. pp.1637-1644. (in Russian).
5. Varzin S.A., Guzev S.A., Kotsyubko V.M. Comparison of volt-ampere characteristics in solutions of NaCl and KCl electrolytes measured using stationary and pulse circuits. Bulletin of St. Petersburg State University. Ser.4. Vol. 4 (62). 2017. Issue 2. pp.131–137. (in Russian).
6. P. Debye, E. Huckel Zur Theorie der Elektrolyte. Physikalische Zeitschrift. 1923. N 9. S. 185–206.
7. Handbook of Electrochemistry. Edited by A.M. Sukhotin. L.: Chemistry. 1981. 488c. (in Russian).
8. Guzev S. A. Measuring the temperature of ions from VAC electrolytes.//Engineering and Physics journal. 2017 Vol. 90. No. 5. C.1267–1274. (in Russian).

Mathematical Modelling of Anomalous Dynamic Processes in Geomedia

V. K. Kazankov, S. E. Kholodova, and S. I. Peregudin

Abstract The problem of the possibility of the existence of a special nonlinear effect arising in the marine environment, called "rouge waves", is considered. Rouge waves are a phenomenon that cannot be described by means of the apparatus of linear wave theory, the existence of which is beyond doubt. There are various hypotheses explaining the occurrence of rouge waves, but there is no generally accepted point of view about the nature of their occurrence. The paper presents a formal apparatus that generalizes the concept of a dynamic system, in which it is possible to formulate the necessary conditions imposed on the system that determine the occurrence of a rouge wave.

Keywords Mathematical modelling · Dynamic processes in Geo-environments · Dynamic systems · Rouge waves · Time series

1 Introduction

It is known that abnormally large waves occur in the oceans, which have different shapes and profiles, but there are also characteristic features, such as sudden occurrence, a relatively short time span of life and a huge destructive potential. This phenomenon was called rouge waves [1, 2]. A few decades ago, rouge waves were perceived as a myth. Only the existence of "extreme waves" was allowed, as a phenomenon similar at first glance to a phenomenon whose occurrence does not go beyond the statistical distribution of random wind waves. The precedent for the independent study of rouge waves was the "New Year's Wave", registered on January 1, 1995 on the Drapner oil platform [1, 2], the appearance of which was an unexpected event, and the statistical data from the instruments did not agree with the theory of "extreme waves".

V. K. Kazankov (✉) · S. E. Kholodova
ITMO University, Saint Petersburg, Russia

S. I. Peregudin
Saint Petersburg State University, Saint Petersburg, Russia

© The Author(s), under exclusive license to Springer Nature Switzerland AG 2022

V. I. Karev (ed.), *Physical and Mathematical Modeling of Earth and Environment Processes*,
Springer Proceedings in Earth and Environmental Sciences,
https://doi.org/10.1007/978-3-030-99504-1_8

Subsequently, several different scenarios were developed to explain the causes of rouge waves, namely, experimental studies were conducted that allowed for the first time to generate a rouge wave in the pool by colliding waves at a certain angle [3]. The classical method of describing the dynamics of waves is the use of the apparatus of partial differential equations, the system of which, as a rule, is a special case of the Cauchy-Kovalevskaya system, and, at first glance, does not contain a rouge wave, however, in [5–7], as a result of a computational experiment, it was possible to register the appearance of a rouge wave.

From the point of view of random processes, there is nothing surprising in the occurrence of abnormally large waves, even if their statistical indicators go beyond the framework of linear theory [4], especially with an unlimited time impact on the system. There is a need to build a formal apparatus that combines different scenarios of the occurrence of rouge waves, without losing sight of the very nature of the phenomenon, and each scenario of the occurrence of rouge waves requires taking into account the energy exchange between waves, which served as the basis for the creation of the corresponding axiomatic, which is a more general structure compared to dynamic systems, which allowed to prove the existence of rouge waves.

2 Problem Statement

2.1 Static

Consider a continuous medium V. Lets divide it into disjoint volumes v_i and fix them. We define for any v_i evaluation functionality $J_t : V \to K \subset \mathbb{R}$, where the parameter $t \in T \subset \mathbb{R}^+$ describes continuous time. Denote $w_i(t)$ energy assessment of each v_i at three time t, defined by the formula

$$J_t(v_i) = w_i(t),$$

where each number $w_i(t)$ displays the number of units of energy in the volume. Symbol W denotes the set of all estimates $w_i(t)$. And for anyone t the inequality is fulfilled

$$\sum_{v_i \in V} J_t(v_i) \leq \sup K < \infty.$$

Let's introduce the notation $H = (V, J_t)$ and we will call H as energy space. Finite sequences u off the form $u = (v_j, ..., v_i) = ji$

let's call the trajectory of energy from the volume v_i into volume v_j. Next, we assume that

$$ij = \begin{cases} ij, i \neq j, \\ e_{ii}, i = j. \end{cases}$$

Consider the set U of all finite sequences $u,$, by defining an equivalence relation on it $\sim$. We investigate the quantitative change of energy in the sequence at a fixed time moment t regardless of the intermediate volumes.

Definition 1.1 Finite sequences $a = (v_j, ..., v_i)$ и $b = (v_l, ..., v_k)$ belong to the same equivalence class $[u] \subset U$, if $v_j = v_l$ and $v_i = v_k$. Remark: In this case, we will consider that a and b indistinguishable from each other $a \sim b$.

Let's introduce the gluing operation «∘», such that for any $jk = (v_j, ..., v_k), ki = (v_k, ..., v_i), ji = (v_j, ..., v_i), ij = (v_i, ..., v_j) \in U$ the relations are valid

$$jk \circ ki = ji,$$

$$ij \circ ji = e_{ii},$$

$$ij \circ e_{jj} = ij.$$

As a representative of any class $[u]$ we will consider the sequence u, consisting of two elements. By means G denote the set of all sequences consisting of two elements $\left(v_i, v_j\right)$. Note that the statement is true.

Statement If for any i and $c \neq e_{ii}$ there are $a \neq e_{ii}$ and $b \neq e_{ii}$, such that

$$c = a \circ b,$$

where $a, b, c \in G$, then $\langle V, G\rangle-$ the complete graph.

It follows from the presented statement that the system considered above is closed and described by a complete graph.

Definition 1.2 Sequence $u = (v_i, v_j)$ it is called connected at a time moment t, if between the elements v_i and v_j there is an exchange of energy at a time t.

3 Dynamics

Let in a closed dynamical system for any element $w_i(t) \in W$ there is a two—parameter family of closed operators $D = \left\{D_t^u : W \to W\right\}_{u \epsilon \mathrm{G}}$, such that when $t = 0$ $D_0^u = I$, and $D \subset (T)$. The result of the operator's action D_t^u characterizes the dynamics of energy in the energy space.

Definition 2.1 Let $\left(v_i, v_j\right)-$ a related sequence at a point in time τ. If at $u = ji = (v_j, v_i)$ the equality is fulfilled.

$D_t^{ij} J_\tau(v_i) = J_i(v_j)$,

then v_j is called the valence point of the operator D_t^{ji} at the time moment t when $\tau \leq t$.

If for the operator $D_t^{ji} \epsilon \mathrm{D}$ there is a valence point v_i lets define a norm for it in the energy space H according to the formula

$$\|D_t^{ji}\|_H = \left| \int_\tau^t F\left(D_t^{ji}\right) d J_\tau(v_i) \right| = \left| J_t(v_i) - J_\tau(v_j) \right|,$$

where integration occurs by Lebesgue, the function F has the form

$$F\left(D_t^u\right) = \begin{cases} D_t^u, \frac{dD_t^u}{dt} \geq 0, \\ -D_t^u, \frac{dD_t^u}{dt} < 0. \end{cases}$$

Lemma For any sequence consisting of two elements v_i and v_j there is an operator D_t^u, and the only one with accuracy up to the choice of the valence point.

Proof Since the linked sequence consists of elements v_i and v_j, then there are two operators D_t^{ji} and D_t^{ij}, where $ji = (v_j, v_i)$ and $ij = (v_i, v_j)$.

Consider the norm of the difference of these operators in space H

$$\|D_t^{ji} - D_t^{ij}\|_H = \left| \int_\tau^t F\left(D_t^{ji}\right) d J_\tau(v_i) - \int_\tau^t F\left(D_t^{ij}\right) d J_\tau\left(v_j\right) \right| =$$

$$= \left| \left(J_t\left(v_j\right) - J_t(v_i)\right) - \left(J_\tau\left(v_j\right) - J_\tau(v_i)\right) \right| = \left| w_i - w_j \right| = \overline{w}$$

So $\overline{w}$ belongs to the set W, then there is an element $w^* \epsilon W$, to which the operator corresponds D_t^u such that the equality holds

$$D_t^u\left(w^*\right) = \overline{w}.$$

From existence $\overline{w}$ and the existence of a valence point $\overline{v}$, such that

$$J_t(\overline{v}) = \overline{w}.$$

According to the lemma, taking into account the statement about the completeness of the graph, it becomes a correct record of the energy exchange process in the space H for the volume v_i in the following form

$$D_t(w) = J_t(v_i),$$

in this case, the operator D_t describes energy exchange.

Definition 2.2 Let's call a class of operators a cycle $S \subset D$ such that under any $u \in \mathrm{G}, v \in V$ and $D_t^u \epsilon \mathrm{S}$ the equality is fulfilled

$$\|D_t^u\|_H = 0,$$

where $\tau \leq t$.

Let's split the set $\mathfrak{D} = \mathfrak{S} \cup \mathfrak{L}$, where $\mathfrak{S}-$ circles, and $\mathfrak{L}-$ other operators.

Definition 2.3 . Let's call a moment in time τ the end of the epoch, if for the operator $\overline{D_\tau} \epsilon \mathrm{L}$ equality is valid

$$\|\overline{D_\tau}\|_H = \sup_{\mathrm{t}\epsilon\mathrm{T}} \|D_t\|_H = \sup K,$$

where $D_t \epsilon \mathrm{D}$.

Example Let $V = \{A, B, C\}$, then $G = \{AA, BB, CC, AB, BA, CB, BC, AC, CA\}$.. The amount of energy in the system $supK = 15$, and $J_\tau(A) = 5, J_\tau(B) = 8, J_\tau(C) = 2, J_t(A) = 7, J_t(B) = 3, J_t(C) = 5-$ energy estimates of volumes at time points τ and t correspondingly.

Then $\|D_t^{BA}\|_H = \|D_t^{BC}\|_H = \|D_t^{BB}\|_H = 5$, $\|D_t^{AB}\|_H = \|D_t^{AC}\|_H = \|D_t^{AA}\|_H = 2$,

$$\|D_t^{CC}\|_H = \|D_t^{CB}\|_H = \|D_t^{CA}\|_H = 3.$$

For any $\widehat{D}_t^a, \overline{D}_\tau^b \epsilon \mathfrak{D}$ let 's define the composition of operators as

$$\widehat{D}_t^a \overline{D}_\tau^b = \tilde{D}_{t+\tau}^{a \circ b},$$

when $\tau \leq t$ and $a \circ b = c \sim u \epsilon \mathrm{G}$.

Let $\Delta\tau-$ the time interval taken as a conditional unit, then the following entry describes a dynamic process

$$(D_{n\Delta\tau}(w))^n = J_t(v_i),$$

where $n \in N$ the number of time intervals. The value $\Delta\tau$ can also be interpreted as a time sampling parameter t, therefore, if, then and $n \to \infty$. Among the operators $D_t \in \mathfrak{L}$ an ordered hierarchy of operator classes arises $[D_t] = \mathfrak{L}_i$ regarding the growth rate of energy estimates. Let $2w \neq 0-$ is the conventional unit of energy measurement that can be registered is then the exact upper edge of the class $\mathfrak{S}$ there will be a representative of the operator class $\mathfrak{L}_1$ such that if $D_t \in \mathfrak{L}_1$, then

$$D_t \in \mathfrak{L}_1,$$

Since for each conditional period of time the amount of energy increases by a constant value $2w$, then

$$\sup S = O(t).$$

Consider $sup\mathfrak{L}_1$. Assuming that at a time moment t the amount of energy change is equal to $2w$, for any $D_t \in \mathfrak{L}_1$ the assessment will be valid

$$\|D_t\|_H \leq 2w + 2 \cdot 2w + \cdots + t \cdot 2w = (2w + w(t-1))t = w(t+1)t = O\left(t^2\right),$$

and for any operator $D_t \in \mathfrak{L}_2$, such that at each moment of time, the change in the amount of energy will be in $2w$ times more than at the previous time t the assessment will be valid

$$\|D_t\|_H \leq 2w + (2w)^2 + \cdots + (2w)^t = \frac{2w\left(1-(2w)^t\right)}{1-2w} \leq Ae^{\alpha t} = O\left(e^{\alpha t}\right),$$

where $A = \frac{2w}{2w-1}$ and $\alpha = \ln(2w)$. For an arbitrary operator D_t of the class $\mathfrak{L}_n$, when $n \geq 2$ the assessment will be valid

$$\|D_t\|_H \leq \sum_{k=1}^{t} 2w \uparrow^{n-1} k,$$

where $\uparrow^{n-1}$ is the hyperoperator designation in Knuth's annotation [8].

Note that the class of operators $\mathfrak{L}_2$ contains a set of semigroups of operators D_t, describing the evolutionary process, that is $D_t(w) = \partial w(t)/\partial t$, and the record is valid

$$\frac{\partial w(t)}{\partial t} = J_t(v_i).$$

Let the following be the behavior of the operator D_t, at the time moment t depends only on the moment $t - \Delta\tau$. Then the operator D_t can be interpreted as a Markov process.

4 Rouge Waves

The height of the waves in hydrodynamics correlates with the amount of energy, so the most important thing is to distinguish these physical indicators. Wave height v we will find by the formula

$$h_t(v) = x_{mx} - (x_{mf} - x_{ms})/2,$$

where $x_{mx}-$ is wave crest height, and x_{mf} and x_{ms} the nearest soles surrounding the crest.

To determine the rouge wave, it is necessary to introduce the concept of an amplitude criterion μ. Amplitude criterion μ for the wave v it is calculated as the ratio of the height of the wave itself to the average value among the third of the highest waves [9].

Definition 3 A rogue wave is the wave v, for which the amplitude criterion is $\mu(v) \geq 2.1$ [10].

Amplitude criterion $\mu(v)$ it can be represented in the following form

$$\mu(v) = \frac{h_t(v)}{s_t} = \frac{\|D_t\|_H}{\frac{1}{|M|}\sum_{\tau\epsilon \mathrm{M}} \|D_\tau\|_H}$$

where $\|D_t\|_H-$ displays the height of the wave at the time moment t, $M-$ a set consisting of a third of the highest waves up to the moment t. Let the operator $D_t \notin \mathfrak{S}$. Then the following inequality is true.

$$\frac{1}{|M|}\sum_{\tau\epsilon \mathrm{M}} \|D_\tau\|_H \leq \frac{\|D_{t-1}\|_H + \|D_{t-2}\|_H}{2}$$

taking into account the registration of at least two waves until t.

Then for the value of the amplitude criterion μ the assessment is valid

$$\mu \geq \frac{2\|D_t\|_H}{\|D_{t-1}\|_H + \|D_{t-2}\|_H}. \tag{1}$$

Let operator $D_t \epsilon \mathfrak{L}_2$, and let's make an upper estimate of the right side of the inequality (1). Considering that up to the moment t there were at least two waves, so $t \geq 3$, and assuming $w = 1$, will get

$$\frac{2\|D_t\|_H}{\|D_{t-1}\|_H + \|D_{t-2}\|_H} \leq \frac{2\|D_t\|_H}{2\min(\|D_{t-1}\|_H, \|D_{t-2}\|_H)} \leq \frac{\|D_t\|_H}{\|D_{t-2}\|_H} \leq$$

$$\leq \frac{2e^{t\ln 2w}}{(2w-1)(t-1)(t-2)}\bigg|_{t=3} = \frac{2e^{3\ln 2}}{2} = 8.$$

Next, we will make a lower estimate of the amplitude criterion μ :

$$\frac{2\|D_t\|_H}{\|D_{t-1}\|_H + \|D_{t-2}\|_H} \geq \frac{2\|D_t\|_H}{2\max(\|D_{t-1}\|_H, \|D_{t-2}\|_H)} \geq \frac{\|D_t\|_H}{\|D_{t-1}\|_H} \geq$$

$$\geq \frac{(2w-1)(t+1)t}{2e^{(t-1)\ln 2w}}\bigg|_{t=3} = \frac{4 \cdot 3}{2e^{2\ln 2}} = 1.5.$$

Hence, there is an operator $D_t \epsilon \mathfrak{L}_2$, describing the dynamic process in which rogue waves arise.

So, the analysis allows us to formulate a hypothesis: "The dynamic process is represented by repeating epochs, each of which is a combination of a cycle and a trend, which corresponds to a part of the epoch that arises as a result of filtering it from cycles, while rogue waves are born before the end of the epoch," for confirmation of which we turn to computational experiments.

5 Processing of Computational Experiments

Computational experiments were carried out in [6, 7]. The resulting waveform is shown in Fig. 1. We will interpret it as a time series X_t. We introduce an estimate of the height of each wave according to the following formula

$$J_t = x_{mx} - \left(x_{mf} + x_{ms}\right)/2.$$

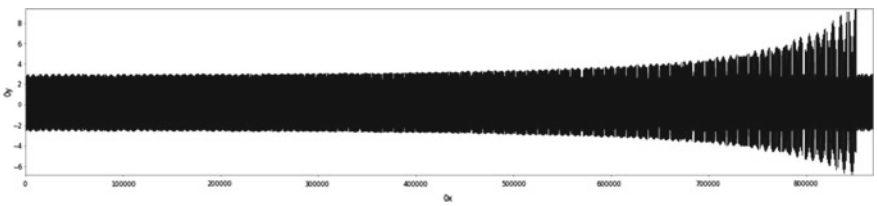

Fig. 1 Visualization of a computational experiment

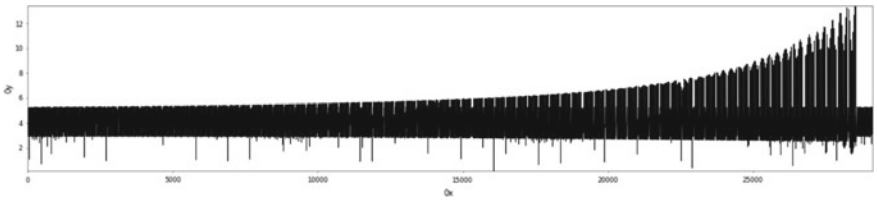

Fig. 2 Wave height

Figure 2 shows the result of the time series transformation X_t into Y_t, which displays the change in wave height over time.

According to the amplitude criterion, in the time series Y_t 25 rouge waves have been recorded. For a time series Y_t we define an estimate of local uniformity $\mu(U_n)$, as the standard deviation calculated for the set $U_n \subset Y_t$, where $n-$ the number of elements in the set U_n.

5.1 Frequency Response

Time series Y_t consist of 29,103 elements, rouger waves occurred only at moments in time

$$t = [26925; 27164; 27198; 27232; 27403; ...; 28429; 28463; 28497; 28531].$$

Denote T_r the set of all the moments of the occurrence of rouge waves. Lets introduce the set P, consisting of time intervals during which rogue waves occur in the next control.

$$p_i = t_{i+1} - t_i$$

where $t_i, t_i + 1 \in T_r$. We assume that the dynamic process contains cycles, which means that the occurrence of a rouge wave must be systematic. Moreover, it is more important that there is only one rouge wave in each cycle, or there are none. There are several possible options for choosing the value of the number n. First, let's assume that $n = 67$, since the averaging of all elements of the set P up to three digits is equal to 66.917, where $n \in N$. The number 34 is often found in the set P, therefore, it may be $n = 34$. Note that the average value of the elements of the set P close to twice the value of the most encountered element, decomposing it into prime numbers, we get 17 and 2, therefore $n = 17$.

The graphs are shown below in Figs. 3, 4, 5 for $\mu(U_n)$ when $n = 67, 34, 17$. The blue color shows the change in the value $\mu(U_n)$, denoted as «Origin». Bya «Trend» the result of exponential smoothing of «Origin» is indicated for $\alpha = 0.02$. The red

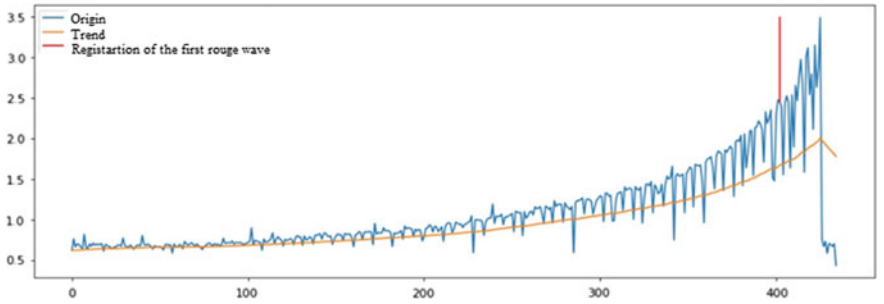

Fig. 3 The variation of $\mu(U_n)$ over time, when $n = 67$

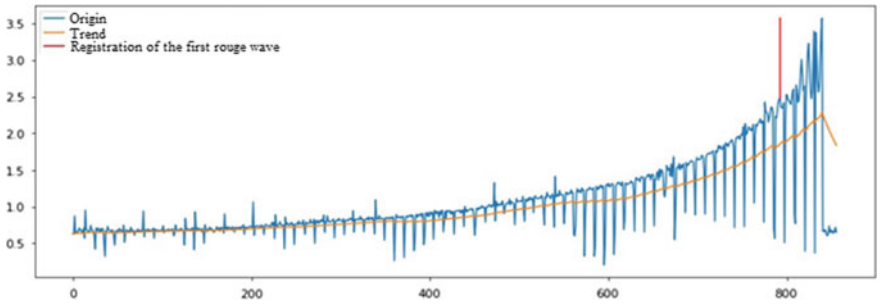

Fig. 4 The variation of $\mu(U_n)$ over time, when $n = 34$

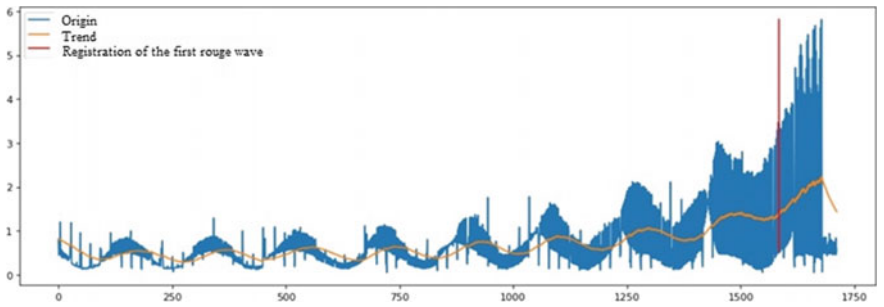

Fig. 5 The variation of $\mu(U_n)$ over time, when $n = 17$

line marks the moment of registration of the first rouge wave, while it begins with the value of the indicator $\mu(U_n)$ and ends at the maximum possible value $\mu(U_n)$.

Figure 5 shows an epoch consisting explicitly of a cyclic component in the form of a sine wave and a trend in the form of an exponent.

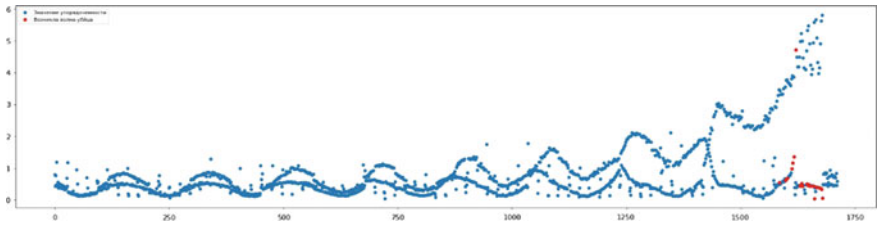

Fig. 6 Point-by-point graph $\mu(U_n)$

5.2 Minimization of Functionality

According to the hypothesis, the occurrence of a rouge wave should be a systematic phenomenon. And if this is the case, then you can choose one in which the value $\mu(U_n)$ it will be minimal at all points in the time of the occurrence of the rouge wave. The solution to this problem is reduced to the construction of the objective function $\rho(n)$ and its minimization. Let the objective function have the form

$$\rho(n) = \frac{1}{25} \sum_{t \epsilon \mathrm{T}} (\mu_t(U_n))^2 \rightarrow min.$$

Before starting optimization, it is necessary to determine the range of acceptable values. Let $n \in [3, 500]$. By a particle we will understand the implementation of the annealing simulation method for the objective function $\rho(n)$. The smallest value of the objective function $\rho(n)$ achieved when $n = 17$. This value was found most often and had the smallest value of all those obtained as a result of launching a swarm of 60 particles. Figure 6 shows the function $\mu_t(U_n)$ when $n = 17$.

So, the analysis of the presented computational experiment allows us to conclude about the validity of the hypothesis formulated above.

6 Conclusions

The presented method of mathematical modeling of anomalous dynamic processes in continuous media, being more general in comparison with the methods of the theory of dynamical systems, but more specialized than the methods of the theory of random processes, whose elements can be introduced and used without any difficulties, allowed us to prove the existence for some differential operators of a special nonlinear effect arising in a continuous medium, called “rouge waves”.

References

1. Kurkin, A.A. Rouge waves: facts, theory and modeling / A.A. Kurkin, E.N. Pelinovsky. - 2nd ed. - Moscow; Berlin :Direct-Media, 2016. - 178 p.ISBN978–5–4475–5883- 3.
2. Stephane Brule, Stefan Enoch, Sebastien Guenneau.: On the possibility of seismic rogue waves in very soft soils. Geophysics (physics.geo-ph); Pattern Formation and Solitons (nlin.PS); Computational Physics (physics.comp-ph); Fluid Dynamics (physics.flu-dyn).
3. McAllister M. L., Draycott S., Adcock T. A. A.,Taylor P. H., van den Bremer T. S.: Laboratory recreation of the Draupner wave and therole of breaking incrossingseas. J.Fluid Mech.(2019),vol. 860, pp.767–786. c CambridgeUniversityPress 2018.
4. V.E.Zakharov,R.V.Shamin: On the probability of occurrence of rouge waves // Letters to the JETF, 91:2 (2010), 68–71; Letters to the JETF, 91:2(2010), 62–65 (in Russian).
5. V. E. Zakharov, R. V. Shamin.: Statistics of rouge waves in computational experiments // Letters in JETF. 96:1 (2012). 68–71; JETPLetters. 96:1 (2012).66–69 (in Russian).
6. R.V. Shamin, A.V. Yudin.: Modeling of spatio-temporal propagation of rouge waves//Reports of the Academy of Sciences.2013.T.448.N5.C.592–594 (in Russian).
7. R.V.Shamin, A.V.Gorlenko, A.I.Smirnova.: Questions of stability of rouge waves //Computing technologies. 2013. vol.18. No. 1. pp.96–105 (in Russian).
8. Knuth, Donald E.: Mathematics and Computer Science: Coping with Finiteness // Science. 194 (4271). (1976), 1235–1242.
9. R. V. Shamin, A.V. Yudin.: Processes of energy concentration in the formation of rouge waves // Nonlinear dynamics.,10:1(2014),49–58 (in Russian).
10. Kharif C., Pelinovsky E., Slunyaev A.: Rogue waves in the ocean. Berlin: Springer, 2009.216 pp.

Construction of a Mathematical Model of a Wave System in the Ocean Using Observations from Space

S. A. Kumakshev

Abstract Earth's space satellites make it possible to observe the surface of the World Ocean. The incoming information is mainly undergoing statistical processing. However, it is interesting to conduct visual observations in order to identify natural phenomena that pose a potential danger to people. To record such phenomena, the space experiment "Uragan" (Hurricane) is conducted, consisting in photographing the processes in the atmosphere and on the surface of the World Ocean by astronauts from the International Space Station (ISS). It is also necessary to predict the development of such phenomena. To do this, it is necessary to create such mathematical models, the results of calculations for which correspond to observations. This paper analyzes one of the photos taken from the ISS, which depicts a system of ring waves near Darwin Island in the Pacific Ocean. Based on the photo, physical assumptions were made and a mathematical model was proposed. The exact solution of such a model is obtained. As a result of the calculations, such parameters of the model were selected that made it possible to approximate the result of calculations performed in accordance with the model with the image on the photograph. This makes it possible to forecast the development of such a ring wave system and assess the potential danger to people.

Keywords Ring waves · Wave system in the ocean · Modeling of natural phenomena · Space experiment "Uragan" (Hurricane)

1 Introduction

Observation of the Earth's surface (in particular, the surface of the world's oceans) is an important task. Such observation allows you to track the occurrence and development of potentially dangerous natural or man-made phenomena that can lead to destruction and even victims. Basically, automatic monitoring of natural phenomena from artificial Earth satellites is carried out, which gives a continuously incoming

S. A. Kumakshev (✉)
Ishlinsky Institute for Problems in Mechanics RAS, Moscow, Russia
e-mail: kumak@ipmnet.ru

© The Author(s), under exclusive license to Springer Nature Switzerland AG 2022

V. I. Karev (ed.), *Physical and Mathematical Modeling of Earth and Environment Processes*,
Springer Proceedings in Earth and Environmental Sciences,
https://doi.org/10.1007/978-3-030-99504-1_9

stream of measurements. The created mathematical software performs statistical processing. However, for a better understanding of such phenomena, it is also interesting to conduct visual observations. To do this, the space experiment (SE) "Hurricane" is being conducted on the Russian segment of the International Space Station (ISS). It consists in the fact that astronauts from the ISS observe the processes taking place in the atmosphere or in the ocean, and photograph those phenomena that interest them. Next, these photographs need to be analyzed. The analysis consists in creating first a physical, and then a mathematical model of the recorded phenomenon. Further, according to the mathematical model, calculations should be carried out in order to build a forecast of the development of events. The forecast must be executed quickly, and this implies the availability of a ready-made mathematical model. This demands the simplicity of such a model and a relatively small number of parameters included in the model. This is necessary so that calculations can be carried out on a regular personal computer.

An important task in the Uragan space Station is to observe the surface of the World Ocean and record various systems of ocean waves. Previously, the analysis and construction of models for other identified wave systems have already been carried out. Examples of modeling a non-periodic system of waves in the Atlantic Ocean within the framework of the SE can be found in [1, 2]. In these works, the conducted physical analysis allowed us to conclude about the pulsed nature of the wave source (explosion). Mathematical analysis within the framework of the created model allowed us to assess the parameters of such an impulse effect.

This article analyzes one of the photographs that recorded an unusual ring wave system in the Pacific Ocean near Darwin Island. This system consists of ring waves of the same length, which implies the presence of a harmonic source of these waves. A physical model of such a phenomenon is proposed. A mathematical model with a small number of parameters is based on it. The derived formulas allow you to perform calculations on a personal computer. Thus, the modeling of the surface system of ring waves is carried out. The analysis of the image made it possible to determine the characteristics of the waves: the areas near the source where the waves are just forming and the area in which the wave system is most clearly visible. The wavelength was also determined. These observations suggested that the source of the waves was most likely not a point, but had some extent. Most likely, the source has a seismic nature (possibly a pulsating geyser). These physical assumptions made it possible to construct a mathematical model of the elevation of the free surface of the ocean. The exact solution for this model is obtained. It turned out that the solution consists of two terms. The first term is responsible for creating ring-shaped waves, and the second one distorts them. The calculation and comparison of the amplitudes of these terms allowed us to refine the source parameters. In the area where the waves are formed, the first term should be smaller than the second, and in the area where the wave system is clearly visible, the amplitude of the second term should be greater. This observation allowed us to determine the size of the source. As a result of numerous calculations, it was possible to select such parameters of the model in which the solution coincides with the wave system depicted in the photo taken from

the ISS. The result of this work is a forecast of the development of wave propagation from such a source.

An alternative way to solve the problem is to construct the shape of the liquid surface as a solution to the boundary value problem [3–5].

2 Geometric Parameters of the Analyzed System

The analyzed image shows an area of the Pacific Ocean 1000 km west of Ecuador. There is the Galapagos Archipelago. From the ISS in 2006, a picture was taken of an area in the ocean, including Darwin Island, which is part of the archipelago. The image shows the island itself and the area of the ocean near it with a system of ring waves (Fig. 1) [6]. The linear dimensions of the island allowed the introduction of a scale. In the center of the wave system, where the source of the waves is located, we place one of the ends of the segment (point A). The other end (point B) will be placed at a distance of 1 km. It can be seen that the source is localized, but is not a point and has some linear dimensions.

The introduction of a scale made it possible to make geometric estimates of the observed wave system from the photograph. It is possible to determine the size of the area where the wave system originates and the waves are not clearly visible. Next comes an area with clearly distinguishable wave crests. It can be seen that the

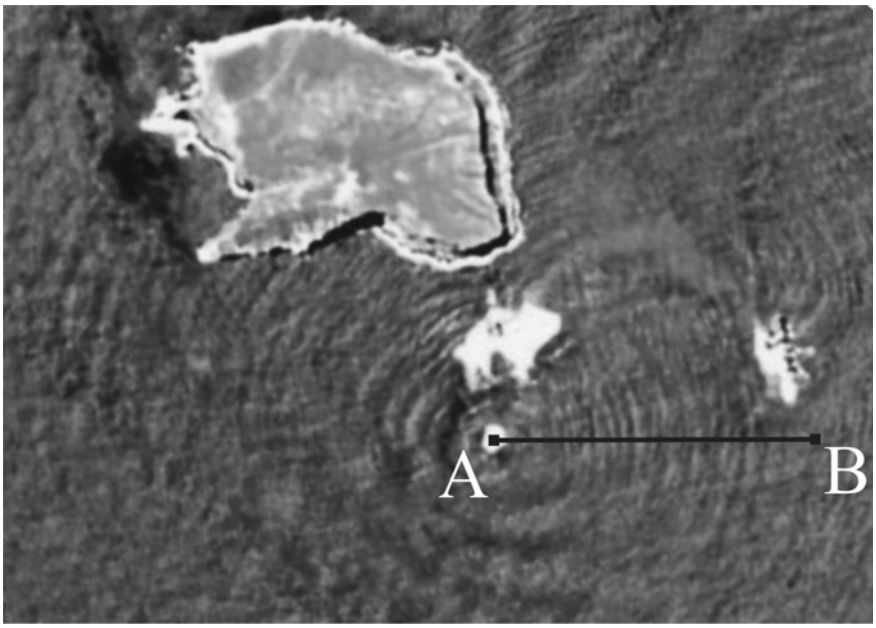

Fig. 1 Analyzed photograph of the ocean near Darwin Island with a ring wave system

wavelengths are equal to each other with good accuracy. You can count the wave crests that fit on the segment and determine their length.

On the other hand, it is known that the Galapagos Archipelago was formed under the influence of seismic activity. The same wavelengths give reason to assert that the source is harmonic with a constant frequency. This indicates that the source may have a seismic nature—for example, it may be a pulsating geyser.

Let's determine the geometric dimensions of the area adjacent to the source, where the waves are formed and are not clearly visible. There are two zones in it: a zone where there are no waves and a zone where the waves are not clearly expressed. It is possible to estimate the radius d_0 of the zone closest to the source at 90 m. The estimate of the radius of the second zone d_w, where waves are just forming, can be taken to be 180 m. And finally, in the far (relative to the source) zone, where the wave crests are clearly visible, about 15 ring waves can be counted. Using the entered scale, we will determine the radius of this zone. It is calculated as follows: $860 - 180 = 680$ m. Based on the geometric estimates made, we calculate an important parameter—the wavelength. To do this, divide the resulting radius of the far zone by the number of wave crests. We get that the wavelength is equal to $\lambda = 680/15 \sim 45$ m.

Another important parameter is to estimate the depth of the ocean in the area of Darwin Island. Measurements show that the characteristic depth varies in the interval $5m \leq H_0 \leq 10m$.

3 Physical Estimates and Mathematical Model

The observations made during the analysis of the photograph about the equal wavelength allow, as indicated above, to assume the harmonic nature of the wave source. To create a physical model, we assume that this harmonic source is located at the bottom of a liquid layer with a constant depth H_0 (the liquid layer is unlimited horizontally). Based on the photo of the wave system, we assume the presence of some non-zero source sizes, which we will determine further. As it was established above, the source excites waves with a length of $\lambda = 680/15 \sim 45$ m and a constant frequency σ.

Let us formalize our geometric observations. To do this, we introduce a Cartesian rectangular coordinate system Ox_1x_2z, the center of which (a point O), we place in the source of the wave system, using the fact that the source is localized. We will direct the axis Oz vertically upwards. We will direct the axis Ox_1 parallel to the ocean surface along the segment AB. Thus, the horizontal plane Ox_1x_2 will coincide with the undisturbed surface of the ocean (the free surface of the liquid). In this case, the bottom equation will be as follows $z = -H_0$.

The operation of the source at the bottom leads to the appearance of a vertical velocity $W(x, t)$ of the liquid particles. Thus, waves appear on the free surface of the layer with the coordinate $x = (x_1, x_2)$ at a moment in time t. Considering that $|x| = \sqrt{x_1^2 + x_2^2}$ and taking into account the frequency of the source, we can write

the equation for the velocity

$$W(x,t) = W(x)\ cos\sigma t, \tag{1}$$

where the value $W(x)$ is determined by such a physical parameter of the source as the maximum intensity W_0. Also assume that the characteristic horizontal size of the source is l. The relationship between the entered source parameters and the velocity of the liquid particle at the point x will be as follows

$$W(x) = \frac{W_0 l^3}{[|x|^2 + l^2]^{3/2}}. \tag{2}$$

In accordance with the previously determined depth of the ocean in the area of Darwin Island, we assume the depth H_0 of the liquid layer in the model to be constant. Comparing the estimates made of the wavelength and depth of the ocean, you can see that $\lambda \gg H_0$. This is the justification for the use of long wave approximation in modeling.

So, the construction of a mathematical model will be based on the use of linear theory. Within the framework of this theory, we assume that the pressure on the ocean surface (at the undisturbed level of the free surface of the liquid) is zero. Thus $p = 0$, when $z = 0$.

For the mathematical description of the physical assumptions made, we use the linear theory of long waves [7–9]. The analyzed photo shows a wave system on the ocean surface. Therefore, it will be justified to accept the elevation of the free surface of the liquid $\eta(x,t)$ as an unknown quantity to be determined. Within the framework of the coordinate system introduced earlier, we will introduce the components of the fluid velocity vector: $v_1(x,t)$ along the axis Ox_1 and $v_2(x,t)$ along the axis Ox_2. Now it is possible to write out a system of equations for the connection of an unknown function with the velocity components v_1, v_2

$$\frac{\partial v_1}{\partial t} = -g\frac{\partial \eta}{\partial x_1}, \qquad \frac{\partial v_2}{\partial t} = -g\frac{\partial \eta}{\partial x_2}, \qquad \frac{\partial \eta}{\partial t} = -H_0\left(\frac{\partial v_1}{\partial x_1} + \frac{\partial v_2}{\partial x_2}\right) + W(x,t). \tag{3}$$

Here g is the acceleration of gravity.

From this system it is possible to derive an equation for an unknown function η

$$\frac{\partial^2 \eta}{\partial t^2} = C_0^2\left(\frac{\partial^2 \eta}{\partial x_1^2} + \frac{\partial^2 \eta}{\partial x_2^2}\right) + \frac{\partial W(x,t)}{\partial t}, \tag{4}$$

where $C_0 = \sqrt{gH_0}$.

Using Eq. (1) linking the source parameters and the vertical velocity of the liquid particles, based on (4) we obtain

$$\frac{\partial^2\eta}{\partial x_1^2}+\frac{\partial^2\eta}{\partial x_2^2}-\frac{1}{C_0^2}\frac{\partial^2\eta}{\partial t^2}=Re\left[-i\frac{\sigma}{C_0^2}\,W(x)\right], \tag{5}$$

It is obvious that as a solution we can consider only those waves whose amplitude decreases when moving away from the source horizontally. This consideration helps to cut off unnecessary solutions and highlight the right solution $\eta(x,t)$. We are looking for this solution in the form of

$$\eta(x,t)=Re[\eta(x)\,e^{i\sigma t}]. \tag{6}$$

Now we obtain an equation that is a mathematical model of the wave system under study. To do this, we need to substitute (6) into (5) and, thus, together with the condition at infinity, we get the equation for the unknown function $\eta(x)$

$$\frac{\partial^2\eta(x)}{\partial x_1^2}+\frac{\partial^2\eta(x)}{\partial x_2^2}+\frac{\sigma^2}{C_0^2}\eta(x)=-i\,\frac{\sigma}{C_0^2}\,W(x),\qquad -\infty<x_1,x_2<\infty. \tag{7}$$

4 Finding the Solution of the Mathematical Model

To find a solution to the mathematical model (7), we use the following approach. We will look for the unknown elevation function of the free surface that interests us in a special form. To do this, we use the two-dimensional forward Fourier transform F_k and the inverse Fourier transform F_x^{-1} by $x=(x_1,x_2)$

$$\eta(x)=F_k[F_x^{-1}[\eta(x)]]. \tag{8}$$

$$F_k[f(k)](x)=\frac{1}{2\pi}\int\limits_{R^2} f(\xi)e^{i(x,k)}dk. \tag{9}$$

$$F_x^{-1}[W(x)](k)=\frac{1}{2\pi}\int\limits_{R^2} W(x)e^{-i(k,x)}dx,\qquad (k,x)=k_1x_1+k_2x_2, \tag{10}$$

We will perform integration in the range from $-\infty$ to ∞ by two variables x_1 and x_2.

Thus, the left part of our mathematical model (7), which includes an unknown function $\eta(x,t)$ of the form (8), is transformed to the form

$$\frac{\partial^2\eta(x)}{\partial x_1^2}+\frac{\partial^2\eta(x)}{\partial x_2^2}=F_k[-|k|^2F_x^{-1}[\eta(x)]]. \tag{11}$$

Now we transform the right part of the mathematical model (7). By analogy, we represent the velocity function of liquid particles $W(x)$ in the form

$$W(x) = F_k[F_x^{-1}[W(x)]], \tag{12}$$

Now, by virtue of model (7) and taking into account Eqs. (8), (11) and (12), we equate the transformed left and right parts. We obtain

$$\left(-|k|^2 + \frac{\sigma^2}{C_0^2}\right) F_x^{-1}[\eta(x)] = -i\frac{\sigma}{C_0^2} F_x^{-1}[W(x)]. \tag{13}$$

Using Eqs. (2) and (10), we can find the inverse Fourier transform of the velocity function of liquid particles $F_x^{-1}[W(x)]$

$$F_x^{-1}[W(x)](k) = \frac{W_0\, l^3}{2\pi} \int\limits_{R^2} \frac{e^{-i(k,x)}}{(x^2 + l^2)^{3/2}} dx, \tag{14}$$

Here it is convenient to use the transition to the polar coordinates $x_1 = |x|cos\psi$, $x_2 = |x|sin\psi$ and $k_1 = |k|cos\varphi$, $k_2 = |k|sin\varphi$. Then, using the zero-order Bessel function $J_0(.)$, Eq. (14) will have the form [8]

$$F_x^{-1}[W(x)](|k|, \psi) = \frac{W_0 l^3}{2\pi} \int\limits_0^{\infty} \frac{|x|d|x|}{(|x|^2 + l^2)^{3/2}} \int\limits_0^{2\pi} e^{-i|k|\,|x|cos(\psi-\varphi)} d\psi =$$
$$\frac{W_0 l^3}{2\pi} \int\limits_0^{\infty} \frac{|x| J_0(|k||x|) d|x|}{(|x|^2 + l^2)^{3/2}},$$

Calculate the integral from the resulting expression and get:

$$F_x^{-1}[W(x)](|k|) = W_0 l^2 e^{-|x||k|}. \tag{15}$$

Now, taking into account (15), the mathematical model (7) has the following form

$$F_x^{-1}[\eta(x)] = i\frac{\sigma}{C_0^2} \frac{W_0 l^2}{|k|^2 - \frac{\sigma^2}{C_0^2}} e^{-l|k|}. \tag{16}$$

We obtain an integral representation for an unknown function $\eta(x)$. To do this, substitute the resulting Eq. (16) in (8):

$$\eta(x) = i\frac{\sigma}{2\pi C_0^2} \frac{W_0 l^2}{|k|^2 - \frac{\sigma^2}{C_0^2}} \int\limits_{R^2} e^{-l|k|} e^{i(x,k)} dk. \tag{17}$$

The final form for the integral representation of the unknown elevation function of the free surface can be obtained by introducing a dimensionless integration variable $\kappa = (\kappa_1, \kappa_2)$. It is introduced as follows: $k_1 = \kappa_1/l$, $k_1 = \kappa_2/l$. Formula (17) will take the form

$$\eta(x) = i\frac{\sigma\ W_0 l^2}{2\pi C_0^2}\int\limits_{R^2}\frac{e^{-|\kappa|}}{|\kappa|^2 - s^2}e^{i\left(\frac{x}{l},\kappa\right)}d\kappa,$$

where

$$s = \frac{l\sigma}{C_0}, \tag{18}$$

It is also convenient to go to the polar coordinates using the formulas

$$x_1 = |x|cos\psi,\ x_2 = |x|sin\psi, \qquad \kappa_1 = \rho cos\varphi,\ \kappa_2 = \rho sin\varphi.$$

Then the function $\eta(x)$ will take the form

$$\eta(x) = i\frac{\sigma W_0 l^2}{2\pi C_0^2}\int\limits_0^\infty\frac{e^{-\rho}}{\rho^2 - s^2}\rho d\rho\int\limits_0^{2\pi}e^{i\frac{|x|}{l}\rho cos(\varphi-\psi)}d\varphi.$$

The integral by φ in this expression is to be calculated. This allows us to obtain an integral representation for an unknown function $\eta(x)$

$$\eta(x) = i\frac{\sigma W_0 l^2}{C_0^2}\int\limits_0^\infty\frac{e^{-\rho}J_0\left(\frac{|x|}{l}\rho\right)}{\rho^2 - s^2}\ \rho\ d\rho.$$

Unfortunately, in the integral representation of the elevation function of the free surface, a non-integrable feature turned out. However, the application of the theory of functions of a complex variable allows us to overcome this. To do this, you need to specify a path L on the complex plane along which integration from zero to infinity takes place. We will bypass the non-integrable feature as follows: on the real axis, we connect the segment from zero to a singular point and the segment from a singular point to infinity with a semicircle centered at a singular point and bypassing it from above. Thus, the segment $0 \le \rho \le s - \varepsilon$ and the segment $s + \varepsilon \le \rho < +\infty$ will be connected by a semicircle with a radius ε such that $0 < \varepsilon << s$.

Finally we have

$$\eta(x) = i\frac{\sigma W_0 l^2}{C_0^2}\int\limits_{(L)} \frac{e^{-\rho} J_0\left(\frac{|x|}{l}\rho\right)}{\rho^2 - s^2}\ \rho\ d\rho. \tag{19}$$

This formula is not very convenient for calculations due to the Bessel function, which experiences rapid oscillations. We will bring this formula to a more convenient form for calculations.

To do this, we rewrite the Bessel function through the half-sum of the Hankel functions. We use Hankel functions of the first and second kind of zero order

$$J_0\left(\frac{|x|}{l}\rho\right) = \frac{1}{2}\left[H_0^{(1)}\left(\frac{|x|}{l}\rho\right) + H_0^{(2)}\left(\frac{|x|}{l}\rho\right)\right].$$

Hence the formula follows

$$\eta(x) = i\frac{\sigma W_0 l^2}{2C_0^2}\left[\int\limits_{(L)} \frac{e^{-\rho} H_0^{(1)}\left(\frac{|x|}{l}\rho\right)}{\rho^2 - s^2}\rho d\rho + \int\limits_{(L)} \frac{e^{-\rho} H_0^{(2)}\left(\frac{|x|}{l}\rho\right)}{\rho^2 - s^2}\rho d\rho\right].$$

In this formula, it is possible to replace the integration path on the complex plane: by the positive part of the imaginary axis in the first integral and by the negative part in the second. To do this, we use the theory of residues in the second integral and apply the asymptotic representations of the Hankel function [10]

$$H_0^{(1)}\left(\frac{|x|}{l}\rho\right) \sim \sqrt{\frac{2l}{\pi|x|\rho}} e^{i\left(\frac{|x|}{l}\rho - \frac{\pi}{4}\right)}, \quad H_0^{(2)}\left(\frac{|x|}{l}\rho\right) \sim \sqrt{\frac{2l}{\pi|x|\rho}} e^{-i\left(\frac{|x|}{l}\rho - \frac{\pi}{4}\right)}, \tag{20}$$

We get

$$\eta(x) = \frac{i\sigma W_0 l^2}{2C_0^2}\left[\int\limits_0^\infty \frac{e^{-i\kappa} H_0^{(1)}\left(\frac{i|x|}{l}\kappa\right)}{\kappa^2 + s^2}\kappa d\kappa + \int\limits_0^\infty \frac{e^{i\kappa} H_0^{(2)}\left(-i\frac{|x|}{l}\kappa\right)}{\kappa^2 + s^2}\kappa d\kappa - \right.$$

$$\left. - i\pi e^{-s} H_0^{(2)}\left(\frac{|x|}{l}s\right)\right]$$

We introduce a modified Bessel function of the second kind of zero order $K_0(.)$ [11]

$$H_0^{(2)}\left(-i\frac{|x|}{l}\kappa\right) = -H_0^{(1)}\left(i\frac{|x|}{l}\kappa\right), \qquad H_0^{(1)}\left(\frac{|x|}{l}\kappa\right) = -\frac{2i}{\pi}K_0\left(\frac{|x|}{l}\kappa\right),$$

Then we get

$$\eta(x) = \frac{\pi\sigma W_0 l^2}{2C_0^2} e^{-s} H_0^{(2)}\left(\frac{|x|}{l}s\right) - i\frac{2\sigma W_0 l^2}{\pi C_0^2}\int_0^\infty \frac{sin(\kappa) K_0\left(\frac{|x|}{l}\kappa\right)}{\kappa^2 + s^2}\kappa d\kappa. \quad (21)$$

The resulting formula is more convenient for numerical calculations. The function $K_0(.)$ included in Eq. (21) decreases rapidly as the argument increases.

In accordance with formula (6), to calculate the unknown function $\eta(x, t)$, it is necessary to take the real part of the integral representation (21).

It can be noted that the elevation of the free surface depends on two terms

$$\eta(x, t) = \eta_1(x, t) + \eta_2(x, t), \quad (22)$$

where

$$\eta_1(x, t) = \frac{\pi\sigma W_0\, l^2}{2\, C_0^2} e^{-s} Re\left[e^{i\sigma t}\; H_0^{(2)}\left(\frac{|x|}{l}s\right)\right] \quad (23)$$

and

$$\eta_2(x, t) = \frac{2\sigma W_0 l^2}{\pi\; C_0^2}\int_0^\infty \frac{sin(\kappa)\; K_0\left(\frac{|x|}{l}\kappa\right)}{\kappa^2 + s^2}\;\kappa\; d\kappa\; Re\left[e^{i\left(\sigma t - \frac{\pi}{2}\right)}\right]. \quad (24)$$

It can be seen that standard procedures can be used to calculate the integral in the second term. This allows you to fulfill the requirement to use a personal computer for calculation.

5 Calculation of the Wave Profile

The task is to select such parameters of the model during calculations that allow us to approximate the result of calculations to the observed wave system. As a result of numerous calculations, it was possible to do this.

Let us present the final results of the calculations in Fig. 2. It shows the dependence of the wave system profile $\eta(|x|, t*)$ on $|x|$ for a depth $H_0 = 10$ m.

For the convenience of comparing the calculation results with the photo in Fig. 1, we present a view of the wave system from above. This is done in Fig. 3. It shows the crests of the calculated wave system on the ocean surface. The comparison shows that the result of the calculation is similar to the original photo. This indicates that the model parameters are selected correctly.

Let's describe the algorithm for selecting parameters.

First, the ocean depth H_0 was set in the model. In the area of Darwin Island, this depth is 10 m.

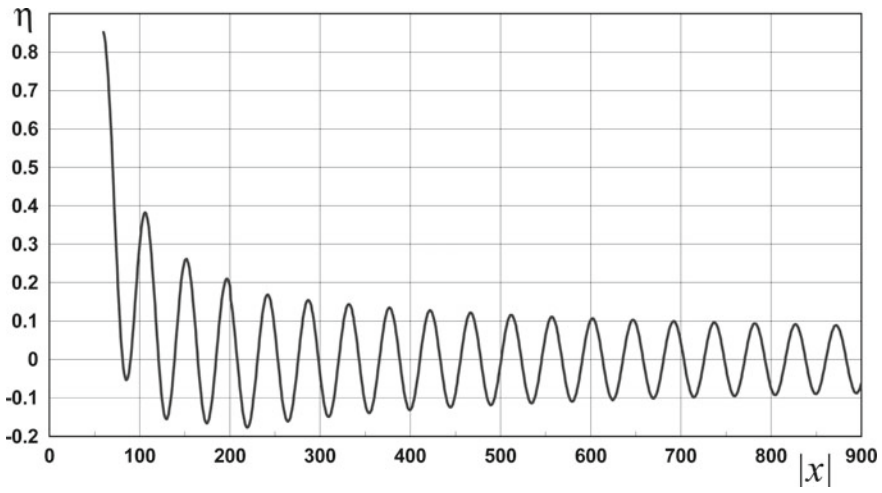

Fig. 2 The wave system profile for $H_0 = 10$ m, $l = 35$ m

Fig. 3 Tops of the wave system on the ocean surface

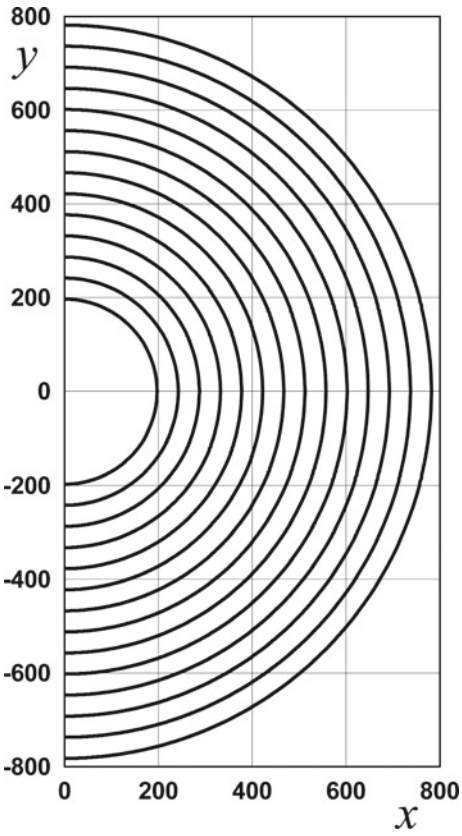

The harmonic frequency of the source can be obtained from the wavelength λ estimates made earlier. Calculations show that the amplitude of the waves in the system under study decreases with distance from the source according to the law $1/\sqrt{|x|}$, and the wavelength is included in the equation $s\lambda/l = 2\pi$. Here s we take from Eq. (18). Then we get the equation for the frequency of the source $\sigma = 2\pi C_0/\lambda$, where $C_0 = \sqrt{gH_0}$. This equation includes only known quantities defined earlier. As a result of the calculation, we get $\sigma = 1.41$ rad/s.

Now let's explain how the choice of a fixed point in time $t = t^*$ at which calculations were performed took place.

The photo shows that the wave system is clearly visible starting from some distance from the source. The analysis of Eq. (22) shows that the wave profile consists of two terms. The first term is responsible for ring waves. Another term introduces a distortion. Based on the analysis carried out earlier on the allocation of areas with a clear and blurred image of the wave system, the following conclusion can be drawn. In the area closest to the source, the maximum value of the second term should be greater than the first. In this case, the wave system will be blurred. In the area farthest from the source, the wave system is clearly visible. This suggests that there is a maximum of the first term greater than the second. The maximum of the second term will be at $t^* = \pi/2\,\sigma$. This determines the time of the calculations made.

Let 's estimate the possible sizes of the source of the wave system l. This can also be done from the ratios of the terms of the components of the elevation of the free surface. To do this, you need to temporarily set the intensity of the source, for example, take $W_0 = 1$ m/s. Now it is possible to calculate both terms in the near and far regions. After that, it is necessary to compare the amplitudes of the terms. The calculations have shown that the desired ratio of the amplitude maxima is achieved at $l = 35$ m.

Now let 's estimate the estimated intensity of the source W_0. This parameter is a coefficient in the formula by which the elevation of the free surface is calculated. In order for a structure that has a large size on the surface of the Earth to be noticeable in a photograph from space, it should not rise much above the surface. In our case, it is quite enough that the height of the waves is around 10 cm. This leads us to the following value of the source intensity $W_0 = 6$ m/s.

6 Conclusions

In accordance with the objectives of the space experiment Hurricane, a photo was taken of an unusual ring wave system in the Pacific Ocean. In this paper, this photograph has been analyzed. As a result, it was possible to construct physical and mathematical models of the observed phenomenon. It was possible to select such parameters of the model in which the results of calculations of ring waves coincided with the wave system shown in the photo. The selected parameters show that the source of the waves has a seismic nature. The constructed mathematical model has simplicity,

and calculations based on it can be performed on a personal computer. This makes it possible to make operational forecasts of the development of such phenomena and assess their potential danger to people.

Acknowledgements The study was supported by the Government program (contract AAAA-A20-120011690138-6).

References

1. Belyaev M.Yu., Desinov L.V., Kumakshev S.A., Sekerzh-Zen'kovich S.Ya., Krikalev S.K. (2009) Identification of a system of oceanic waves based on space imagery J Comput Syst Sci Int 48(1):110–120.
2. Kumakshev S.A. (2022) Modeling of the Ocean Wave System Based on Image from Satellite. In: Chaplina T. (eds) Processes in GeoMedia—Volume IV. Springer Geology. Springer, Cham. https://doi.org/10.1007/978-3-030-76328-2_35
3. Akulenko L.D., Korovina L.I., Kumakshev S.A. and Nesterov S.V. (2002) Radial Oscillations of a Circulating Cylindrical Fluid Mass // Fluid Dynamics 37, 171–178. https://doi.org/https://doi.org/10.1023/A:1015809212769
4. Akulenko L.D., Kumakshev S.A. and Nesterov S.V. (2001) Natural Oscillations of a Heavy Fluid in an Elliptic Vessel // Fluid Dynamics 36, 640–651. https://doi.org/https://doi.org/10.1023/A:1012354016355
5. Kumakshev S.A. (2019) Natural oscillation shapes for a heavy fluid in an elliptic vessel // J. Phys.: Conf. Ser. 1301(1) 012002 DOI:https://doi.org/10.1088/1742-6596/1301/1/012002
6. Belyaev M.Y., Vinogradov P.V., Desinov L.V., Kumakshev S.A., Sekerzh-Zen'Kovich S.Y. (2011) Identification of a source of oceanic ring waves near Darwin's Island based on space photos J Comput Syst Sci Int 50(1):67-80.
7. Kochin N.K., Kibel I.A. and Roze N.V. (1964) Theoretical Hydromechanics. Wiley Interscience
8. Lighthill M.J. (1978) Waves in fluids. Cambridge University Press
9. Sretenskii L.N. (1977) Theory of wave motions in a fluid. Moscow Nauka. Pp. 816.
10. Copson E.T. (1965) Asymptotic Expansions. Cambridge University Press
11. Handbook of Mathematical Functions (Abramowitz M. and Stegun I.A. (ed.)). Moscow: National Bureau of Standards, 1979.

Remote Measurement of Vibration in the Marine Environment

I. P. Shumeyko and A. Yu. Abramovich

Abstract The analysis of the possibility of using an acoustic method for determining the vibration characteristics of objects located in the marine environment is carried out. The article discusses the limitations of using a mathematical apparatus created for radar methods for measuring vibration in acoustic sounding. The main factor affecting the accuracy of acoustic measurements of vibration is the dependence of the speed of sound on the state of the environment in which it propagates. The speed of sound is affected by changes in temperature, salinity and pressure, as well as changes in flow velocity. The maximum relative error in determining the amplitude resulting from uncontrolled changes in temperature and salinity of the marine environment does not exceed 5%. The relative error resulting from the presence of strong currents is less than 0.2%. It is noted that acoustic measurements near the sea surface have a number of features associated with wave breaking, as a result of which air bubbles enter the aquatic environment. Large differences in the density and compressibility of air and seawater, as well as resonant phenomena in bubbles, significantly affect the scattering and attenuation of sound.

Keywords Hydroacoustics · Vibration · Doppler spectrum · Coherent location · Marine environment

1 Introduction

In recent years, methods of remote determination of vibration parameters by remote sensing in different ranges of electromagnetic waves (in the optical and microwave ranges) have been actively developed [1–4]. The remote determination of the vibration amplitude is based on the analysis of the nonlinear transformation of the signal spectrum reflected from the oscillating surface [5].

The use of optical equipment requires special surface preparation, so it is usually used in laboratory conditions. Microwave radio waves fade very quickly in the marine

I. P. Shumeyko (✉) · A. Yu. Abramovich
Sevastopol State University, Sevastopol, Russian Federation
e-mail: shumeyko-irina-74@yandex.ru

© The Author(s), under exclusive license to Springer Nature Switzerland AG 2022

V. I. Karev (ed.), *Physical and Mathematical Modeling of Earth and Environment Processes*,
Springer Proceedings in Earth and Environmental Sciences,
https://doi.org/10.1007/978-3-030-99504-1_10

environment. An alternative would be acoustic sounding. In a marine environment, pressure pulsations can propagate over long distances without noticeable attenuation [6].

There is a fundamental difference between determining the vibration amplitude by radar sounding in the air and by acoustic sounding in the marine environment. It lies in the fact that the speed of propagation of electromagnetic waves is practically independent of the state of the atmosphere, while for acoustic waves propagating in the marine environment, such a dependence is essential [7]. A change in the speed of sound is caused by a dynamic factor, which are variations in the speed of a water flow [8], as well as a change in the physical and chemical state, i.e. change in the fields of temperature, salinity, pressure and flow rate [9, 10].

Another factor affecting the accuracy of vibration measurements in a marine environment is natural hydro acoustical noise. Noise occurs as a result of breaking of surface waves [11, 12]. The intensity of wave breaking is related to wind speed and near-surface currents [13, 14]. The nonlinear wave-wave interaction also leads to the appearance of noise [15, 16].

The purpose of this work is to analyze the possibility and limitations of determining the acoustic method of vibration of an object placed in the marine environment.

2 Vibration Measurement by Acoustic Sensing

Methodological substantiation of remote vibration detection in a marine environment does not differ from a similar problem of vibration detection using a coherent microwave radar station [3]. Here are its main provisions and solutions.

We will consider the situation when the surface of a vibrating object moves according to the law

$$\xi(t) = \xi_0 \sin(\Omega t), \tag{1}$$

where ξ_0 and Ω there are an amplitude and a circular frequency of vibration. The sensing acoustic wave is given as

$$S_S(t) = A_S \sin(\omega_0 t), \tag{2}$$

where A_S is the amplitude of the acoustic wave, ω_0 is the circular frequency of the acoustic wave. The relationship between the length λ and frequency ω of a wave is determined by its phase velocity

$$C = \lambda\,\omega/(2\,\pi). \tag{3}$$

In the described formulation of the problem, the reflected signal has the form

$$S_R(t) = A_R \cos\left(\omega_0 t - \frac{4\pi\xi_0}{\lambda}\ \sin(\Omega t) - \frac{4\,\pi\ L}{\lambda} + \varphi_0\right), \tag{4}$$

where A_R is reflected wave amplitude, L is the average distance from the sonar to the vibrating surface, φ_0 is a change in the phase of the wave during reflection. It follows from (4) that information about the vibration amplitude is carried by the Doppler change in the frequency of the reflected wave. Let's isolate it by phase detection

$$S_F(t) = A_F \cos[m\ \ \sin(\Omega t) + \varphi\,], \tag{5}$$

where A_F is signal amplitude after phase detection; m is phase deviation, $\varphi = -4\,\pi\ L/\lambda + \varphi_0$. Phase deviation depends on vibration amplitude and sounding wave length

$$m = 4\pi\xi_0/\lambda. \tag{6}$$

The function $S_F(t)$ depends on three parameters. It is necessary to exclude dependence on unknown parameters A_F and φ. For this, we expand the function $S_F(t)$ in a Fourier series

$$\begin{aligned} S_F(t) = \tilde{A}\Bigg[J_0(m) + 2\cos\varphi \sum_{n=1}^{\infty} J_{2n}(m)\cos(2n\,\Omega\,t) - \\ -2\sin\varphi \sum_{n=1}^{\infty} J_{2n-1}(m)\cos((2n-1)\,\Omega\,t)\Bigg], \end{aligned} \tag{7}$$

where

$$J_n(z) = \frac{1}{\pi}\int_0^{\pi} \cos(n\tau - z\sin\tau)\,d\tau \tag{8}$$

is Bessel functions of the first kind of order n. Expression (7) shows that the reflected signal is a superposition of harmonics with frequencies multiples of the fundamental vibration frequency.

Thus, with a change in the parameter m, there is a change in the amplitudes of the signal harmonics. The amplitudes of the odd and even harmonics are, respectively, equal

$$A_{2n-1} = A_F|2\ \sin\varphi\ J_{2n-1}(m)|, \tag{9}$$

$$A_{2n} = A_F|2\ \cos\varphi\ J_{2n}(m)|. \tag{10}$$

To exclude dependence on unknown parameters you can use the relations A_3/A_1 and A_4/A_2 [3]. These relations are determined only by the relations of the Bessel functions, which depend on a single parameter m.

3 Limitation of the Calculation of the Vibration Amplitude by the First Four Harmonics

The limitations of the method of calculating the vibration amplitude considered in the previous section are as follows. Bessel functions of the first kind are alternating. Therefore, the ratio of harmonic amplitudes has a number of maxima, and, as a consequence, several values of the phase deviation correspond to the same ratio of harmonic amplitudes (see Fig. 1).

Depending on the magnitude of the phase shift φ, both ratio A_3/A_1 and ratio A_4/A_2 or both can be used. Accordingly, an unambiguous calculation of the phase deviation is possible if the conditions $m < m_1$ or $m < m_2$ are met. The parameters m_1 and m_2 correspond to the first zero values of the Bessel functions J_1 and J_2.

The limitations caused by the presence of noise in acoustic measurements are illustrated in Fig. 2. When constructing this figure, it was assumed that it is possible to determine the ratio of the amplitudes of the harmonics only in a situation where

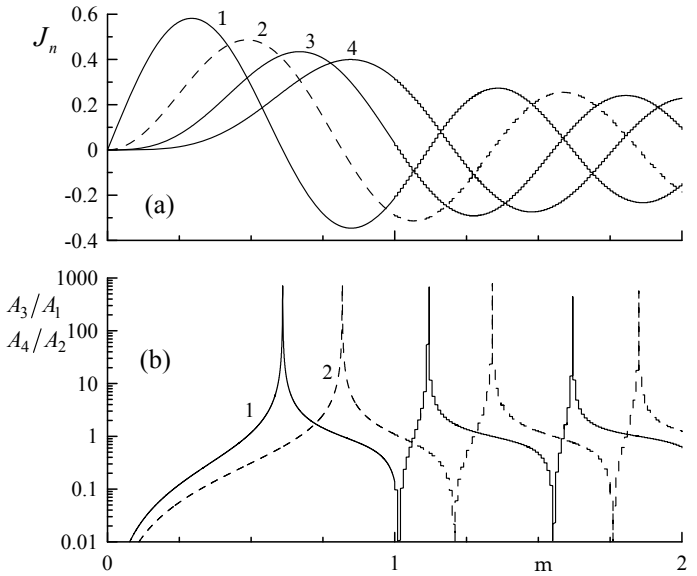

Fig. 1 Characteristics of the signal reflected from the vibrating surface: **a** — curves 1–4 correspond to the amplitudes of the first four harmonics; **b** — curve 1 corresponds A_3/A_1, curve 2 corresponds A_4/A_2

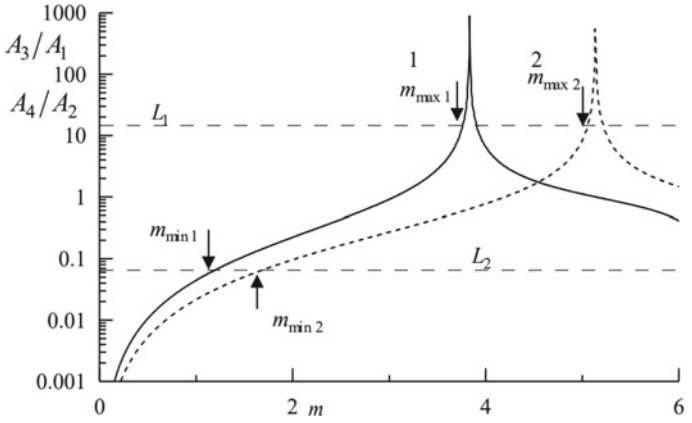

Fig. 2 Influence of acoustic noise on the range of measured phase modulation indices: curve 1 corresponds A_3/A_1, curve corresponds A_4/A_2, dashed lines are the values of parameters L_1 and L_2

the indicated ratio does not go beyond some critical values, which are designated as L_1 and L_2. The critical values are related to each other by the relation $L_2 = L_1^{-1}$. It was assumed that the critical values correspond to a ratio of 1:15.

The maximum and minimum values of the phase deviation shown in Fig. 2 correspond to the values of the vibration amplitude in the ranges $0.10 \leq \xi_0/\lambda \leq 0.30$ if the calculations are carried out with respect to A_3/A_1, and $0.14 \leq \xi_0/\lambda \leq 0.40$ if the calculations are carried out with respect to A_4/A_2. The values of the phase deviation shown by the arrows are the smallest roots of the equations

$$\left.\begin{aligned} J_3(m_{\min 1})/J_1(m_{\min 1}) &= L_2 \\ J_3(m_{\max 1})/J_1(m_{\max 1}) &= L_1 \\ J_4(m_{\min 1})/J_2(m_{\min 1}) &= L_2 \\ J_4(m_{\max 1})/J_2(m_{\max 1}) &= L_1 \end{aligned}\right\} \tag{11}$$

4 Noise Source During Acoustic Vibration Measurement

The main factor determining the error in calculating the vibration amplitude is how accurately the phase velocity of the acoustic wave is known. The calculation procedure includes the transition from temporal to spatial coordinates based on Eq. (3).

The acoustic wave belongs to the class of longitudinal waves. Its rate of propagation in the marine environment is determined by the equation

$$C = \sqrt{K/\rho}, \tag{12}$$

where K is the modulus of volumetric elasticity, ρ is a density of sea water. Both parameters depend on temperature T, salinity S and pressure P (depth H). An increase in any of these parameters leads to an increase in the speed of sound.

With observed changes in temperature and salinity in the World Ocean, the speed of sound in the vicinity of the sea surface varies from 1430 to 1540 m/s. The average value of the speed of sound can be assumed to be equal to 1500 m/s [17].

The speed of sound is associated with a change in the basic physical and chemical characteristics of seawater as follows [18]. If an acoustic wave propagates in conditionally cold water when the temperature is below 10 °C, then at $S = const$ and $P = const$, a change in water temperature by 1 °C leads to a change in the speed of sound by about 4 m/s. If sea water is conditionally warm (25 °C < T < 30 °C), then a change in its temperature by 1 °C changes the speed of sound by about 2.5 m/s. With a change in salinity by 1 ‰, the value of the speed of sound changes by about 1 m/s. A pressure change corresponding to a depth change of 1 m leads to an increase in the speed of sound in the upper hundred-meter layer of the ocean by 0.0165 m/s, at a great depth (about 5,000 m) the increase is 0.0183 m/s.

The effects associated with changes in temperature and salinity are most pronounced in water areas where water masses of different origins are present. A good example is the Sea of Marmara, where the upper layer is formed by the Black Sea water, the lower layer is formed by the Mediterranean. The salinity of different water masses differs almost twofold [19].

If $C = 1500$ m/s is taken when measuring the vibration amplitude near the sea surface, then the error resulting from unaccounted changes in temperature and salinity will not exceed 5%.

We will briefly indicate additional possible sources of vibration measurement error. The speed of sound propagation in the marine environment is influenced by currents [8]. The most intense current of the World Ocean is the Somali Current [20]. The indicated value of the flow velocity is much less than the speed of sound in still seawater. If the flow velocity is not controlled, the error in determining the amplitude in the presence of a strong current is less than 0.2%.

When measuring near the sea surface in strong winds, noise occurs caused by the collapse of wind waves, the noise level increases with increasing wind speed [21, 22]. It has been shown that noise is associated with the formation of cavitating gas–vapor bubbles and resonant stable bubbles distributed in the water column near the surface [23, 24]. The air bubbles entering the marine environment by their total volume make up a very small part of it. However, large differences in the density and compressibility of air and sea water, as well as resonant phenomena in bubbles, significantly affect the scattering and attenuation of sound. The sound scattering cross-section on bubbles significantly exceeds the scattering cross-section on other

types of marine inhomogeneities, such as solid particles, suspensions, zooplankton and phytoplankton [25, 26]. Another factor that must be taken into account when making measurements near the sea surface is the scattering of acoustic waves on it [27].

5 Two-Frequency Sensing

Expand the range in which the vibration amplitude is uniquely determined by sensing a vibrating surface with acoustical waves of different lengths. Consider a situation where the sensing is carried out at wavelengths λ_0 and $\nu\lambda_0$. Here ν is a dimensionless multiplier, which for certainty we will assume to satisfy the inequality $\nu > 1$. A change in the length of the sensing acoustical wave in times ν corresponds to a change in the phase deviation $m \to m/\nu$.

First, let's consider the case when the calculation of the vibration amplitude is carried out using odd harmonics. In order for the range of measured vibration amplitudes to be continuous, it is necessary, as shown in Fig. 3, that the condition is met

$$J_3(m_{\min 1}/\nu)/J_1(m_{\min 1}/\nu) = L_2. \tag{13}$$

Thus, when condition (13) is met, the value of the upper limit of the ξ_0 range has changed from $\xi_0 = 0.30\ \lambda_0$ with single-frequency sensing to $\xi_0 = 0.91\ \lambda_0$ with two-frequency sensing.

When calculating the vibration amplitude by even harmonics, the condition must be met

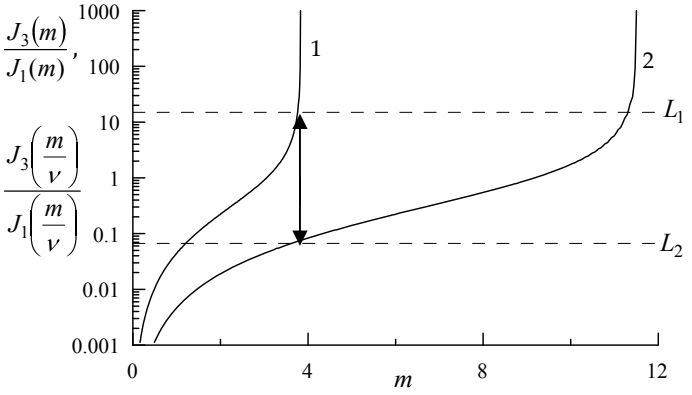

Fig. 3 Expansion of the measurement range of the phase *deviation* with two-frequency sensing. Calculation of odd harmonics, curve 1 is $J_3(m)/J_1(m)$, curve 2 is $J_3(m/\nu)/J_1(m/\nu)$

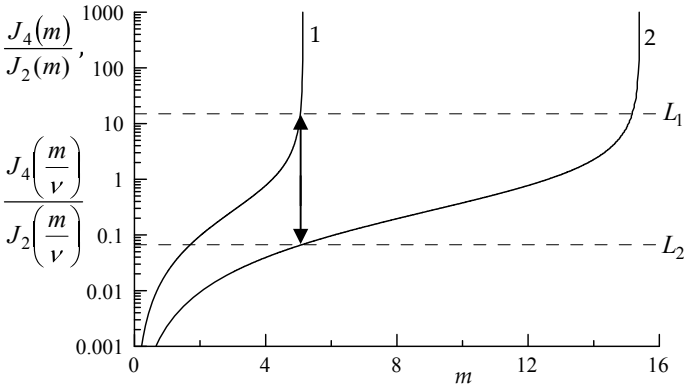

Fig. 4 Expansion of the measurement range of the phase deviation with two-frequency sensing. Calculation of even harmonics, curve 1 is $J_4(m)/J_2(m)$, curve 2 is $J_4(m/\nu)/J_2(m/\nu)$

$$J_4(m_{\min 2}/\nu)/J_2(m_{\min 2}/\nu) = L_2. \tag{14}$$

The position of the upper limit of the range for ξ_0 varies from 0.40 λ_0 with single-frequency *s*ensing to 1.22 λ_0 with two-frequency sensing. When comparing the graphs shown in Figs. 3 and 4, it can be seen that the use of the ratio of the fourth and second harmonics to determine the phase deviation makes it possible to estimate its values in a wider range than when using the ratio of the third and first harmonics.

6 Conclusion

The analysis of the possibility of using the acoustic method to determine the vibration characteristics of an object located in a marine environment is carried out. When making measurements, it is proposed to use a mathematical apparatus created for radar vibration measurement methods. Within the framework of this method, the vibration amplitude is measured in sensing wave lengths, the transition from temporal to spatial characteristics is carried out on the basis of the dispersion equation for the sensing wave. For acoustic measurements, it is necessary to know the speed of sound.

The main factor affecting the accuracy of acoustic vibration measurements is the dependence of the speed of sound on the state of the medium in which it propagates. The speed of sound is affected by changes in physical and chemical characteristics, such as temperature, salinity and pressure, as well as changes in flow velocity. The maximum relative error in determining the vibration amplitude resulting from uncontrolled changes in temperature and salinity of the marine environment does not exceed 5%. The value of the relative error is obtained taking into account the fact that the depth of the vibrating object is known and the correction taking into account the

pressure is made. The speed of the current in the ocean is much less than the speed of sound, so its influence on the results of vibration measurement can be neglected.

Acoustic vibration measurements near the sea surface have a number of features associated with wave breaking. As a result of the wave breaking, air bubbles fall into the aquatic environment. Large differences in the density and compressibility of air and sea water, as well as resonant phenomena in bubbles, significantly affect the scattering and attenuation of sound.

References

1. Vikram, C.S., McDevitt, T.E.: Simple spectrum analysis in laser Doppler studies of sinusoidal vibrations. Opt. Eng. 28, 922-925 (1989).
2. Du, S., Hu, J., Zhu, Yu., Hu C.: Analysis and compensation of synchronous measurement error for multi-channel laser interferometer. Measurement Science and Technology. 28(5) 55201 (2017). doi: https://doi.org/10.1088/1361-6501/aa5f0c.
3. Burdyugov, V.M., Shumeiko, I.P., Ozhiganova, M.I. Measurement of vibration of sea surface objects by radio sounding. J. Radio Electronics. (1), (2019). doi: https://doi.org/10.30898/1684-1719.2019.1.10.
4. Scalise, L., Yu,Y., Giuliani, G., Plantier, G., Bosch, T.: Self-mixing laser diode velocimetry: application to vibration and velocity measurement. IEEE Transactions on Instrumentation and Measurement. 53(1), 223-232 (2004). doi: https://doi.org/10.1109/TIM.2003.822194.
5. Zapevalov, A.S., Burdyugov, V.M.: Transformation of the frequency–phase response of a signal reflected from a vibrating surface. J. Commun. Technol. Electron. 65, 640–644 (2020). doi:https://doi.org/10.1134/S1064226920050149.
6. Vadov, R.A.: Long-range sound propagation in the Mediterranean Sea. Acoustical Physics. 50(3) 255-264 (2004).
7. Grigor'ev, V.A., Katsnel'son, B.G., Lynch, J.F.: Energy fluctuations of high-frequency sound signals in a shallow water in the presence of nonlinear internal waves. Acoustical Physics. 59(4), 431-438 (2013).
8. Serebryany, A.N., Khimchenko, E.E.: Strong variability of sound velocity in the Black Sea shelf zone caused by inertial waves. Acoustical Physics. 64(5), 580–590 (2018).
9. Wilson, W.D.: Extrapolation of the equation for the speed of sound in sea water. J. Acoust. Soc. Am. 34(6), 866 (1962).
10. Leroy, C.C., Robinson, S.P., Goldsmith, M.J.: A new equation for the accurate calculation of sound speed in all oceans. J. Acoust. Soc. Am. 124(5), 2774-2782 (2008). doi: https://doi.org/10.1121/1.2988296.
11. Knudsen, V.O., Alford, R.S., Emling, J.W.: Underwater ambient noise. J. Mar. Res. 7, 410-429 (1948).
12. Kerman, B.R., Evans, D.L., Watts, D.R., Halpern, D.: Wind dependence of underwater ambient noise. Boundary-Layer Meteorology. 26, 105-113 (1983).
13. Schwendeman, M.; Thomson, J.: Observations of whitecap coverage and the relation to wind stress, wave slope, and turbulent dissipation. J. Geophys. Res. (Oceans) 120, 8346–8363 (2015). doi:https://doi.org/10.1002/2015JC011196.
14. Kubryakov, A.A., Kudryavtsev, V.N., Stanichny, S.V.: Application of Landsat imagery for the investigation of wave breaking. Remote Sensing of Environment. 253, 112144. (2020). doi:https://doi.org/10.1016/j.rse.2020.112144.
15. Longuet–Higgins, M.S. : A theory of the origin of microseisms // Phil. Trans., Ser. A. 243, P. 1-35 (1950).
16. Zapevalov, A.S., Pokazeev, K.V.: Modeling the spectrum of infrasonic hydroacoustic radiation generated by the sea surface under storm conditions. Acoustical Physics 62(5), 554-558 (2016). doi https://doi.org/10.1134/S1063771016050195.

17. Bezrukov, Yu.F.: Oceanology. Part I. Physical phenomena and processes in the ocean. Simferopol: V. I. Vernadsky Tauride National University. 159 p. (2006). (in Russion).
18. Andreeva, I.B.: Physical bases of sound propagation in the ocean. Leningrad: Hydrometeoizdat. 189 p. (1975). (in Russion).
19. Zapevalov, A.S., Dovgaya, S.V.: Transformation of black-sea waters in the Sea of Marmara. Physical Oceanography. 17(2), 106-112 (2007). doi: https://doi.org/10.1007/s11110-007-0009-5.
20. Eremeev, V.N., Zhukov, A.N., Zapevalov, A.S. Lebedev N.E., Sizov A.A. Seasonal variations of the Arabian Sea level anomaly fields and circulation. Oceanology 54, 289–297 (2014). doi: https://doi.org/10.1134/S0001437014020076.
21. Furduev, A.V.: Underwater noises of dynamic origin. Review. Acoustical Physics. 9(3), 265-274 (1963). (in Russion).
22. Vijayabaskar, V., Rajendran, V.: Analysis and modeling of wind dependence of ambient noise in shallow water of Arabian Sea. European J. Scientific Research. 50(1), 28-34 (2011).
23. Chapman, N.R., Cornish, J.W.: Wind dependence of deep ocean ambient noise at low frequencies. J. Acoust. Soc. Am. 93(2), 782-789 (1993).
24. Prosperetti, A.: Bubble elated ambient noise in the ocean. J. Acoust. Soc. Am. 84, 1042-1054 (1988).
25. Medwin, H., Clay, C.S.: Fundamentals of Acoustical Oceanography. N.Y.: Academic Press. 712 p. (1997).
26. Galimzyanov, M.N.: Propagation of compression waves in bubble zones of finite dimensions. Bulletin of the Udmurt University. Mechanics. (2), 57-66 (2010). (in Russion).
27. Zapevalov, A.S.: Evaluation of the scattering coefficient for high-frequency sound scattered from the sea surface. Acoustical Physics. 53(5), 603–610 (2007). doi:https://doi.org/10.1134/s1063771007050119.

The Study of Pollutants' Pathways in the Caspian Sea by Modeling Lagrangian Trajectories

O. S. Klyagina, S. N. Zatsepa, K. V. Pokazeev, and V. V. Solbakov

Abstract A numerical simulation of 3-D passive tracer trajectories is used to study pollutants pathways in the Caspian Sea. We used the INMOM reanalysis data set representing the state of the Caspian Sea Hydrology to simulate trajectories. We found that upwelling featured to the eastern coast of the Middle Caspian is characterized by vertical particle movement with the order of hundredths mm/s. The vertical motion is modulated with a frequency close to the inertial one. As a result of the passive tracers' trajectories analysis, the features of water exchange in the Middle and Southern Caspian Sea were found. Lagrangian particles move from the western part of the Middle Caspian along the bottom of the Apsheron sill towards the Southern Caspian, rise in the water column and cross the Apsheron sill, and then descend to the deeper layer.

Keywords Lagrangian particle 3-D trajectory modelling · Computational experiment · Inertial waves · Upwelling · The Caspian Sea water exchange

O. S. Klyagina (✉) · K. V. Pokazeev
Faculty of Physics, Lomonosov Moscow State University, Moscow, Russia
e-mail: klyagina@oceanography.ru

K. V. Pokazeev
e-mail: sea@phys.msu.ru

S. N. Zatsepa
N.N. Zubov's State Oceanographic Institute, Rosgydromet, Moscow, Russia
e-mail: zatsepa@oceanography.ru

V. V. Solbakov
Federal Research Center "Computer Science and Control" of the RAS, Moscow, Russia
e-mail: solbakov@oceanography.ru

© The Author(s), under exclusive license to Springer Nature Switzerland AG 2022

V. I. Karev (ed.), *Physical and Mathematical Modeling of Earth and Environment Processes*,
Springer Proceedings in Earth and Environmental Sciences,
https://doi.org/10.1007/978-3-030-99504-1_11

1 Introduction

The spread of pollutants in the marine environment is an integral part of water exchange processes. Water exchange is a set of physical processes, including advection and mixing of water masses. It leads to the renewal of water masses in an arbitrary sea area. A change in the state of the marine environment in one area of the sea can impact remote areas due to currents influence. This may lead to the transboundary transfer of various pollutants. How the different sea regions are connected and when and along what paths the disturbances propagate are essential questions for many applications. This problem is interdisciplinary and extremely important for water bodies where transboundary impacts are possible.

The chemical composition of the pollutants determines their lifetime in the marine environment. Simultaneously with the spread of the impurity, its physicochemical transformation and biodegradation occur. However, one can consider most marine pollutants as passive impurities. For this reason, the routes of their distribution in the sea are virtually independent of the type of pollutant. One should analyze the possible stable ways of pollutants transport, "rivers" inside the sea, so stable connections between separate sea areas could be specified.

One of the tools for analyzing the transport routes of pollutants in the Caspian Sea on a considerable time scale is the study of Lagrangian trajectories. They were calculated based on reanalysis data of hydrological conditions. In recent decades, modeling of Lagrangian trajectories was used not only at the regional level [6] but also made it possible to determine the connectedness of circulation processes between individual regions of the World Ocean (global conveyor) [7] and even the oceans [8, 9]. The Lagrangian approach makes it possible to trace the "origin" of the water mass, the parameters of which are recorded as a result of observations. A systematized ensemble of the trajectories of tracer particles, plotted on the map, makes it possible to identify the pathways for the transfer of water masses and water exchange between separate areas of the sea.

2 Initial Data and Research Method

We conducted a series of computational experiments to figure out the pathways of pollutants. The initial data for modeling the trajectories of Lagrangian particles were the results of a reanalysis of hydrological fields in the Caspian Sea for 2020, conducted at GOIN with the INMOM model [6]. The CFSR v2 reanalysis data were used for the atmospheric forcing setting [10]. The spatial resolution of the model is 1.5 km, time discreteness of the output array 1 h. The climatic fields of temperature and salinity were used for the model initializing [5]. The experiment consisted in modeling the Lagrangian trajectory of floats of neutral buoyancy, starting their movement at various points of the Caspian Sea. We calculated the trajectories of the floats for two months between May 1 to October 30. For the Lagrangian trajectories

calculation, we used the open-source software OpenDrift, created by the independent research organization SINTEF [7]. The software is designed to calculate Lagrangian trajectories based on hydrological fields and has an advanced visualization system for the resulting data. The authors adapted OpenDrift to use the data fields obtained in the Russian INMOM model. The velocities of Lagrangian particles were found by trilinear interpolation of velocity components from the INMOM model grid to the particle position. We used the implicit Runge–Kutta scheme of the 4th order to integrate the kinematic equation of motion of the tracer particle. The scheme of the experiment involved the calculation of 3-D trajectories of tracer particles, initially located at the nodes of a virtual lattice with dimensions of 5 * 5 * 5 elements, "immersed" in each of the traditionally distinguished parts of the sea. Figure 1 shows the position of the particles in the projections on the horizontal (a) and vertical (b) projections.

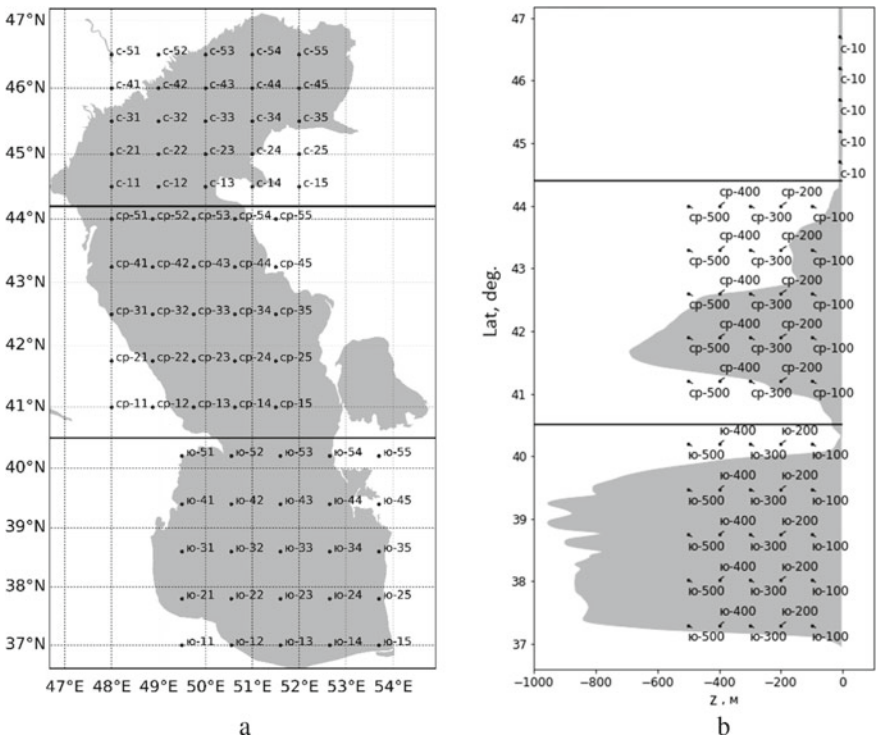

Fig. 1 Diagram of the initial position of particles

3 Results and Discussion

During the implementation of the computational experiment, more than 1000 trajectories of tracer particles were calculated, located in various regions of the Caspian Sea, including deep-water ones in the waters of the Middle and South Caspian. The results obtained in our computational experiments, in general, correspond to the published results of field measurements of deep-water contour currents in the Middle Caspian [1] and calculations using the model of the Hydrometeorological Center of Russia [4] and the results of studying water exchange across the Apsheron threshold [3]. We obtained new results and confirmed the known facts about the circulation in certain parts of the Caspian Sea.

The calculation of the particles' trajectories in the eastern part of the Middle Caspian (Fig. 2) showed that in May–June, deep waters rise from a horizon of 50 m to a horizon of 20 m, which corresponds to the traditional concepts of seasonal upwelling in the eastern part of this sea area. The results of trajectory modeling show that the rise of deep waters occurs at a speed of the order of hundredths of mm/s.

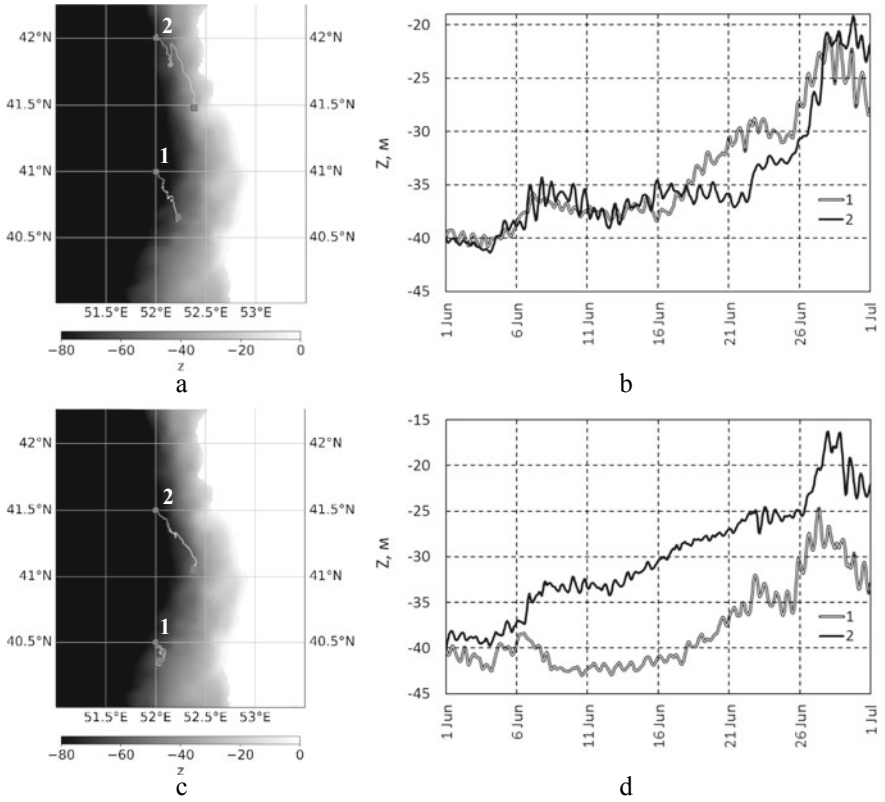

Fig. 2 Trajectories of particles (**a**, **c**) and changes in their depth (**b**, **d**)

Figure 2b, d shows oscillations of the vertical position of a particle with an amplitude of about 50 cm, the period of which corresponds to the inertial period. Inertial vibrations were noted in the trajectories of tracers released at various depths. The inertial fluctuations, manifested in the change in the value of the vertical coordinate of tracers originating at different depths, were practically in phase, and the value of the correlation coefficient was 0.8.

Another result of our computational experiments is the study of water exchange between the Middle and South Caspian through the Apsheron sill. The book [2] noted the existence of an overflow of the Middle Caspian waters into the South Caspian. The authors associate this phenomenon with the density runoff of cold waters from the northern regions of the sea and the eastern shelf. These waters descend into the bottom layers of the Middle Caspian depression, overflow through the Apsheron sill, and enter the South Caspian depression. As a result of computational experiments, it was found that the transport of tracer particles, starting their movement in the southwestern part of the Middle Caspian at depths of more than 200 m (Fig. 3a), has a direction of propagation in almost all studied periods of the year towards the South Caspian (Fig. 3a, b), with maximal intensity in autumn. As shown in Fig. 3b—the graph of the change in the vertical coordinate versus time—the particles rise as they approach the Apsheron threshold and descend as they move away from it.

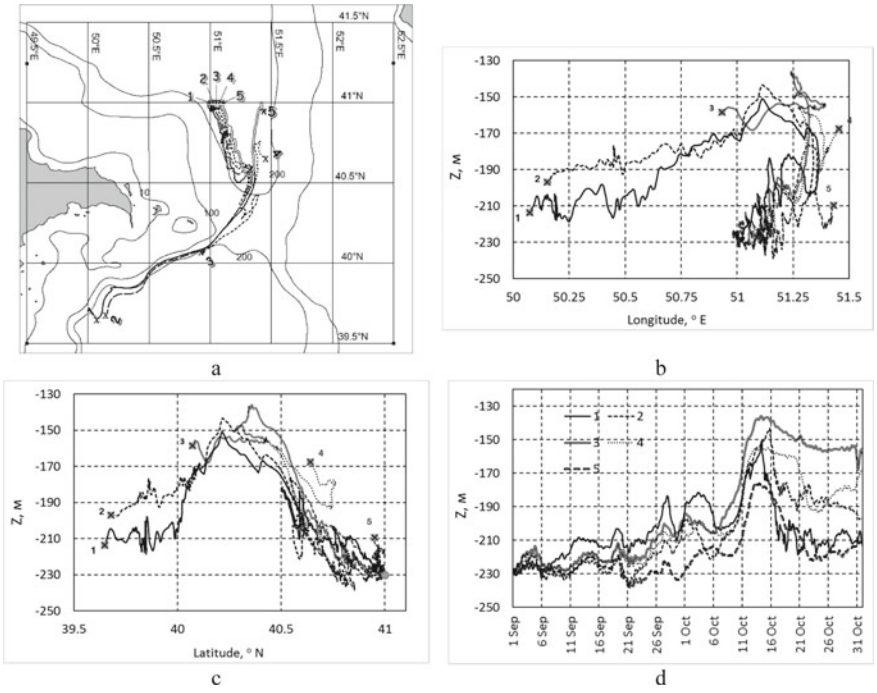

Fig. 3 Trajectories of tracer (**a**) and time dependence of their coordinates and depth (**b**, **c**, **d**)

The maximum rise of tracers in depth is happening in the area of the Apsheron sill (Fig. 3c, d).

4 Conclusion

Modeling Lagrangian trajectories based on reanalysis of hydrological fields for 2020 made it possible to.

1. estimate the rate of water rise in the upwelling area near the eastern coast of the Middle Caspian,
2. estimate the amplitude of periodic vertical oscillations caused by inertial oscillations,
3. analyze the features of the penetration of deep-water masses of the Middle Caspian into the deep-water part of the South Caspian.

Computational experiments on modeling Lagrangian trajectories were based on calculating the currents of the Caspian Sea with the INMOM model. Any model is a simplified representation of the modeling object. Therefore, the obtained results should be confirmed independently.

The experiments are a part of a planned large-scale project to study the statistical patterns of the distribution of pollutants in the Caspian Sea. We conducted the current study based on a reanalysis of the hydrological fields of the Caspian Sea for a relatively short period, related to a specific 2020 year. In other years, the intensity of hydrometeorological processes may be different, affecting the intensity of transport of deep-water masses. For assessing the interannual variability of the ways of transport of water masses and pollutants, it is necessary to conduct similar studies with preliminary preparation of reanalysis fields of hydrological fields for a representative time interval.

References

1. Ambrosimov A. K. Seasonal variability and anomalies of the cyclonic cycle flow in the north-eastern sector of the Middle Caspian Sea. Water Resources, 2019, 46(5), 485-495 (In Russian).
2. Baydin S. S., Kosarev A. N. (eds.). Kaspiyskoe more: Gidrologiya i gidrokhimiya [The Caspian Sea: Hydrology and Hydrochemistry]. Institute of Water Problems of the USSR Academy of Sciences, Moscow: Nauka Publ., 1986, 261 p. (In Russian).
3. Dyakonov G. S., Ibraev R. A., Dynamics of the waters of the Caspian Sea over the Apsheron threshold in 2003. Marine Hydrophysical Journal, vol. 35, No. 6, 2019. (In Russian).
4. Popov S. K. Modeling of climatic thermohaline circulation in the Caspian Sea. Meteorology and Hydrology, 2004, (5), 76−84. (In Russian).
5. Tuzhilkin V. S., Kosarev A. N. Long-Term Variations in the Vertical Thermohaline Structure in Deep-Water Zones of the Caspian Sea. Water Resources, 2004, 31(4), 376−383 (In Russian).
6. Fomin, V. V., Diansky, N. A. Korshenko, E. A., Vyruchalkina. System of operational diagnosis and forecast of hydrometeorological characteristics of the Caspian Sea and assessment of

forecast accuracy based on field measurements. Meteorology and Hydrology, 2020. (9), 49–64. (In Russian).
7. Dagestad, K.-F., Röhrs, J., Breivik, Ø., and Ådlandsvik, B., OpenDrift v1.0: a generic framework for trajectory modelling, Geoscientific Model Development, 11, 1405–1420, https://doi.org/10.5194/gmd-11-1405-2018., 2018.
8. Kelly, S., Popova, E., Aksenov, Y., Marsh, R., Yool, A. Lagrangian modeling of Arctic Ocean circulation pathways: Impact of advection on spread of pollutants. Journal of Geophysical Research: Oceans, 2018, 123(4), 2882−2902.
9. Kelly, S. J., Popova, E., Aksenov, Y., Marsh, R., Yool, A. They came from the Pacific: How changing Arctic currents could contribute to an ecological regime shift in the Atlantic Ocean. Earth's Future, 2020, 8(4), e2019EF001394.
10. Saha, S., Moorthi, S., Wu, X., Wang, J., Nadiga, S., Tripp, P., & Becker, E. (2014). The NCEP climate forecast system version 2. Journal of climate, 27(6), 2185−2208.

The Analysis of Organic Matter Content in the Sea Bottom Sediments of Sevastopol Region (Black Sea)

O. V. Soloveva, E. A. Tikhonova, and O. A. Mironov

Abstract The assessment of the level of bottom sediments organic matter pollution in the period 2009–2015 in various water areas of the coast of Sevastopol (Kamyshovaya, Streletskaya and Kazachya bays) was made. Nowadays there are no precise criteria for assessment the pollution levels. So, various approaches to assess pollution were analyzed and compared to determine the most appropriate one. The results showed that statistical methods did not verify differences that were revealed by the analysis of the benthic community reaction on the content of chloroform-extractable substances in the bottom sediments. Spoken about the pollution dynamics, a scientific assessment showed that the average level of organic pollution in Streletskaya bay decreased, while in Kamyshovaya and Kazachya it corresponded to relatively clean water areas.

Keywords Sea bottom sediments · Chloroform-extractable substances · Mann–Whitney U-criteria · Comparison of mean ranks · Harbor waters · Black sea

1 Introduction

A particular feature of the Sevastopol coast is the presence of numerous bays. Within the region there are more than 30 of them. Sevastopol Bay is the most studied of the listed areas [1]. In addition, it is characterized by consistently high organic pollution of bottom sediments [2], in other bays such levels are not so elevated [2]. At the same time, due to historical factors, the intensity of exploitation of individual water areas had multidirectional trends. On the other hand, the shores of such bays as the Kazachya and Streletskaya were being intensively built up with residential houses. For example, it is planned to build up the eastern 82 hectares massif of Kazachya bay by multi-storey buildings (the total coastal area is 181.3 hectares) [3]. It could lead to an increase of organic matter content in the coastal waters. As a result of massive, often chaotic development, the physicochemical characteristics of bottom sediments

O. V. Soloveva · E. A. Tikhonova · O. A. Mironov (✉)
A. O. Kovalevsky Institute of Biology of the Southern Seas of RAS (IBSS), Sevastopol, Russia
e-mail: mironov87@gmail.com

© The Author(s), under exclusive license to Springer Nature Switzerland AG 2022

V. I. Karev (ed.), *Physical and Mathematical Modeling of Earth and Environment Processes*,
Springer Proceedings in Earth and Environmental Sciences,
https://doi.org/10.1007/978-3-030-99504-1_12

in places of input of organic substances change, due to the content of chloroform-extractable substances (CES) in some areas increases [4–6]. The purpose of this work was to assess the current dynamics (2009–2015) of organic matter content in bottom sediments, as well as a comparison of trends in their state in different harbors of the Sevastopol coast in face of changes in anthropogenic load using the different approaches.

2 Material and Methods

The analysis of the organic pollution long-term dynamics for port water areas was based on the data on the content of CES and OH in the sea bottom sediments. The samples of the last were collected in the framework of the long-term monitoring of the Department of Marine Sanitary Hydrobiology IBSS in the summer of 2009, 2012, 2015 (Fig. 1). The concentration of CES was determined by the gravimetric method, OH—by the method of IR-spectrometry [7] on the FSM-1201 spectrophotometer.

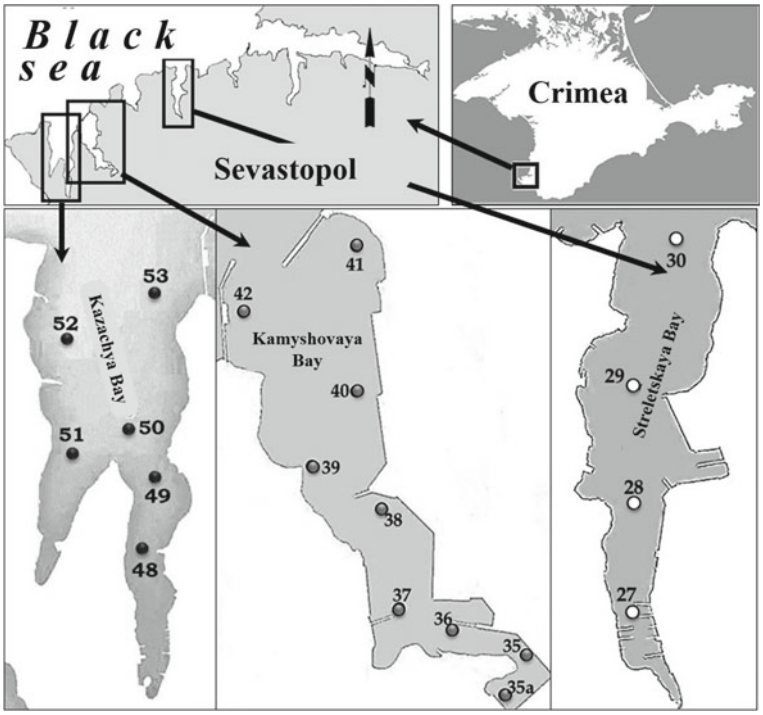

Fig. 1 Location of the sea bottom sediments sampling stations in the framework of monitoring surveys 2009, 2012, 2015

To assess the ecological state of the water area, the division of bottom sediments according to pollution levels from I to V was used, adopted in accordance to the response of the benthic community to the content of CES in the bottom sediments. The I-th level correspond to natural clean sea soils with high biodiversity. Level V is practically lifeless bottom sediments [8]. Along with estimates based on environmental indicators, an attempt to use statistical data analysis methods was made. The use of parametric statistics in this study is excluded due to the small sample group size. In this case, applicable non-parametric methods of statistical analysis. The Mann–Whitney U-criteria ($p = 0.05$) was used as a statistical tool for comparing the temporal dynamics of the pollutants content in the bottom sediments of individual water areas, which makes it possible to reveal the reliability of the difference between a pair of independent samples. The assessment of the reliability of the difference in the content of pollutants in the bottom sediments of different water areas was carried out by comparing the average ranks of the studied samples ($p = 0.05$). The calculations were performed using the software package Statistica 6.0.

3 Results and Discussion

The main part of Kamyshovaya bay bottom was covered by gray mud with admixture of sand, with the exception of shell rock on st. 39. The indicators of natural moisture in different periods ranged from 37% (in the shells) to 71% (in the muds). pH was from 7.2 to 8.1. The Eh values varied from positive figures (+332 mV) in shells to negative amounts in silts (–94 mV) [4]. The bottom sediments in the apex and central part of Streletskaya bay, as well as in Kamyshovaya bay, were presented by black or dark-gray silts mixed with sand with a large amount of decaying organic matter (st. 29), the smell of hydrogen sulfide (st. 27a–30). The natural humidity in different years ranged from 48.7% in silts with sand admixture to 68.2% in silts, the pH was 7.6–7.8. In silts, highly reducing conditions were formed (negative values of the redox potential) [5]. Sediments composition of Kazachya bay changed over the time. Earlier [9] it was represented by black silts with a large amount of decaying organic matter and the smell of hydrogen sulfide, and silts with admixture of sand. In 2015, the authors of [6] noted the following changes: An uncharacteristic odor and an increase in the share of rotted organic matter. Physical and chemical parameters, such as natural humidity, pH and Eh of bottom sediments of the bay water area in the studied time interval remained on average unchanged, and corresponded to the nature of precipitation [6].

During 2009–2015 the highest CES content among the studied areas was in the sea bottom sediments of Streletskaya bay. The average value in this water area fluctuated in the range of 975–1493 mg/100 g air-dry. sub., which referred to IV-V levels of pollution. Their concentrations in the bottom sediments of the Kazachya and Kamyshovaya bays were quite low (168–179 mg/100 g and 167–187 mg/100 g, respectively), on the average they were characterized as pure water areas.

The average content of OH in the bottom sediments of the studied areas was also significantly different for the bays under study. In Streletskaya bay it ranged from 560 mg/100 g to 360 mg/100 g, which in the period of 2009 and 2012 exceeded the conditional standards proposed by the so-called "Dutch lists" [10]. OH concentration in bottom sediments Kamyshovaya and Kazachya bays in the study period did not exceed 100 mg/100 g, which corresponded to the natural level of the content of this class of substances. The decrease of OH content in the study period was the greatest at st. 28 and 29 (48%, and 57% respectively), at st. 27 it decreased less noticeably (21%). A 3 times increase in the concentration of OH was almost noted at the most prosperous st. 30, but, nevertheless, the level of pollution there remained low. Thus, along with a decrease in the average indicators for the water area, there was a redistribution of pollutants within the water bodies; some areas purified, others more intensively accumulated pollution.

In the Southern part of the coast Kamishovaya bay is located. There at 4 of 9 sampling stations (st.35, 37, 38, 39), a decrease in the concentration of CES was noted. This reduction ranged from 15% (which can be attributed to the error of the method) to 360%. The last figure characterized the change in the content of CES in bottom sediments definitely. At 3 of the stations, an increase in the content of organic substances was noted (35a, 36, 40), which also ranged from 21 to 470%.

A decrease in the content of OH was noted at the st. 35, 38, 39. In all the listed areas the fall down was significant and ranged from 3 to 6 times. A significant increase in the OH content was noted at st. 40, where in recent years this figure had increased almost 6 times. All the fluctuations in the content of organic substances described, none of the recorded values exceed the permissible norms [10] or relative levels characterizing the sanitary and biological well-being of the water area [8].

In 2015 in Kazachya bay relatively high (up to 700 mg/100 g) CES values were noted in the southern (apical) part (st. 48). The content of OH for the entire period of research decreased. On the close st. 49, the content of CES remained almost unchanged. The growth of organic matter content was noted at the st. 51 and 52 (9 and 4 times respectively), which were relatively pure. The growth of OH content was noted at the following stations: non-essential st. 48, 1.5 times at the st. 49. The most pronounced this phenomenon was at the st. 51 (11 times) and 52 (5 times), which were practically clean in previous years. In Kazachya bay the growth of OH content was noted almost throughout the entire water area, and it was the most intensive in its pure areas.

The described change and difference in parameters have not statistical evaluation; they were determined only by the expert opinion of the authors. This practice takes place in research articles devoted to this topic [11–14]. In the present work, an attempt to carry out a statistical analysis of the material and to assess the applicability of some statistical methods in the framework of this kind of research had been done. Due to the small amount of data in the sample, the use of parametric statistics was impossible. The Mann–Whitney U-test was used to compare the temporal dynamics of the organic matter content in the sea bottom sediments of some harbors ($p = 0.05$). It allowed to analyze the reliability of differences between a pair of independent samples. This

analysis did not show the presence of significant differences in contamination levels of CES and OH of the studied water areas in the period from 2009 to 2015.

The assessment of the reliability of the difference in the pollution levels in the sea bottom sediments of different water areas was carried out by means of comparing the average ranks of the studied samples ($p = 0.05$). In 2009, there were no significant differences in the concentrations of CES and OH in the bottom sediments of the bays under study. At the same time, the studied water areas, basing on the concepts available in hydrobiology [8], had different levels of organic pollution: Kamishovaya and Kazachya bays—III-rd, Streletskaya—V-th. Subsequently, the situation changed. So, in 2012, there was a statistically significant difference in the content of CES in the bottom sediments Streletskaya and Kazachya bays. The level of water areas pollution during this period could be generally classified, as in the previous one. There were no significant differences in the content of OH. As a result of the last survey (2015) in terms of the content of CES, significant differences were between sediments Streletskaya and Kazachya bays. Significant differences in the content of CES in marine soils of Kamishovaya and Kazachya bays did not identified. There were no significant differences for Kamyshovaya and Streletskaya bays also. According to the content of OH, the difference was significant for Streletskaya and Kazachya bays. OH concentration in the bottom sediments of Kamyshovaya bay had no significant differences with other studied areas of the Sevastopol coast. Pollution level in Streletskaya bay during this period could be characterized as IV-th. The remaining bays—III-rd. Thus, during the period of this study (2009−2015), changes were noted that contradict the trend of changes in average indicators. They were due to changes within individual stations. In some, previously practically pure areas, an increase in the levels of pollutants was observing currently.

The data presented on Fig. 2 demonstrates the difference in sea bottom sediments pollution of the studied bays, based on statistical and expert estimates. It shows that the greatest difference exists for b. Kazachya and Streletskaya and over time it increased. In 2009, this distinction reveals only up to the division of bottom sediments

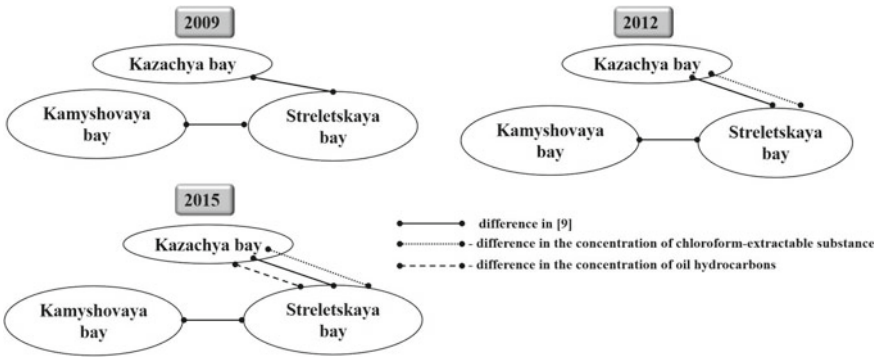

Fig. 2 The difference in the content of organic matter in the sea bottom sediments of some Sevastopol harbors in the period 2009, 2012, 2015

according to the level of pollution. In 2012, the content of CES in bottom sediments was statistically distinguishable. According to the results of 2015 survey, not only the content of CES, but OH was statistically distinguishable also. The state of sea bottom sediments of Kazachya and Kamyshovaya bays during the research period according to of the criteria under consideration did not differ significantly. The bottom sediments of Kamishovaya and Streletskaya bays over the years of research had different levels of pollution, based on the response of bottom biota to the content of pollutants in bottom sediments [8], but this difference was not confirmed statistically. Based on the comparison of statistical data obtained using the Mann—Whitney U-test to estimate the inter annual variability of the parameters studied and comparing the average ranks to assess the significance of differences in the state of bottom sediments of the studied objects within one-year, statistical estimates were obtained contradicting the expert ones. The difference in the content of CES in bottom sediments, which significantly affects the state of the bottom community, was not defined as significant using the specified statistical criterion. In this case, we can talk about the inapplicability of these non-parametric methods for the evaluation of the studied indices.

4 Conclusion

The application of some statistical tools (Mann—Whitney U-test and comparison of average ranks) showed insufficient sensitivity of these criteria for use in such studies. Statistical evaluation did not allow to identify differences that existed in accordance with expert estimates based on the response of the bottom community to the presence of CES in the sea bottom sediments. During the study period (2009−2015) in Streletskaya bay marked (on average over the water area) a decrease in the level of organic pollution. In the remaining bays (Kazachya and Kamyshovaya), the level corresponding to the conditionally clean water areas was maintained.

Acknowledgements Present work has carried out within framework of the State assignment of the IBSS on the theme "Molismological and biogeochemical foundations of the marine ecosystems homeostasis" (№ AAAA-A18-118020890090-2).

References

1. Sanitary-biological investigation in coastal area of Sevastopol region, Ed. O. G. Mironov, ECOSY-Hydrophysics, Sevastopol, 2009, 192 p.
2. Mironov O. G., Kiryukhina L. N., Alyomov S. V., Sanitary-biological aspects of the Sevastopol bays ecology in XX century, ECOSY-Hydrophysics, Sevastopol, 2003, 185 p.
3. Draft Strategy for Social and Economic Development of the City of Sevastopol until 2030, Resolution of the Government of Sevastopol from 17.04.2017, no 315, 2017, 133 p.

4. Polisovaya A. I., Tikhonova E. A., Ecological condition of sea bottom sediments of the port water area (on the example of Kamyshova Bay, the Black Sea). Proceedings of theX All-Russian Scientific and Practical Conference «Pontus Euxinus 2017», 2017, pp. 169−171.
5. Tikhonova E. A., Kotelyanets E. A., Volkov N. V., Characteristic of pollution of the bottom deposits in the coastal area of Sevastopol on the example on the Streletskaya bay (the Black Sea), Ecological safety of coastal and shelf zones of sea, vol. 1, iss. 74, 2018, pp. 74−80.
6. Kotelyanets E. A., Gurov K. I., Tikhonova E .A., Soloveva O. V., Some geochemical indicators of sea bottom sediments in coastal waters under the influence of anthropogenous factor (using Kazachya bay, Sevastopol, as an example), Bulletin of Udmurt University Series Biology. Earth Sciences, vol. 27, iss. 1, 2017, pp. 5−13.
7. Manual by methods of chemical analysis of sea water, Ed. S. G. Oradovsky, Gidrometeoizdat, Leningrad, 1977, 208 p.
8. Mironov O. G., Milovidova N. Yu., Kiryukhina L. N., About the maximum permissible concentrations of oil products in bottom sediments of the coastal zone of the Black Sea, Hydrobiological journal, vol. 22, no 6, 1986, pp. 76−78.
9. Alyomov S. V., Tikhonova E. A., The characteristics of sea bottom sediments and macrozoobenthos Kazachya bay of the first decade 21st century, Ecological safety of coastal and shelf zones and comprehensive use of shelf resources, vol. 1, iss. 26, (2012), pp. 38−50.
10. NeueNiederlandischeListe, Altlasten Spektrum, 3/1995.
11. Ignateva O. G., Orekhova N. A., Romanov A. S., Kotelyanec E. A., Physical and chemical characteristics of sea bottom sediments of Kazachya Bay (Black Sea), as indicators of its environmental condition, Scientific Notes of V. I. Vernadsky Crimean Federal University, vol. 18 (58), no 2, 2005, pp. 43−48.
12. Tikhonova E. A., The long-term dynamics of the sea bottom sediments pollution of the Kruglaya bay (Black sea), Marine Biological Journal, vol. 1, no 1, 2016, pp. 70−75.
13. Stuart G., Wakeham and Roy Carpenter Aliphatic hydrocarbons in sediments of Lake Washington, Limnology and oceanography, Vol. 21 (5), 1976, pp. 711−723.
14. Charles R. Phillips, James R. Payne, James L. Lambach, Garry H. Farmer, Robert R. Sims, Georges bank monitoring program: hydrocarbons in bottom sediments and hydrocarbons and trace metals in tissues, Marine Environmental Research, Vol. 22, iss. 1, 1987, pp. 33−74.

Analysis of Fields of Currents and Energy Characteristics of Water Circulation in the Northern Part of the Black Sea on the Basis of Assimilation of Hydrological Observational Data in the Autumn Season of 2016

S. G. Demyshev, N. A. Evstigneeva, and O. A. Dymova

Abstract Fields of currents and arrays of energy budget components were investigated with the help of the numerical model of dynamics using hydrological data from 89th cruise of the R/V Professor Vodyanitsky. To implement the procedure of data assimilation, we used a four-dimensional analysis procedure, based on a Kalman filtering, taking into account the heterogeneity and non-isotropy of error estimates of thermohaline characteristics. Wind action and vertical friction made a significant contribution in the change of kinetic energy, vertical turbulent diffusion and advection of potential energy—in the change of potential energy. The following features of circulation were obtained in the numerical experiment for the autumn season of 2016: anticyclonic eddies near Sevastopol, cyclonic and anticyclonic eddies at the south-eastern coasts of Crimea and other parts of area under consideration, a flow of the Rim Current along the Crimean coast. High values of work of the wind force and vertical dissipation were observed in the zones of formation of mesoscale eddies. Negative values of the buoyancy work were noticed to the west of the region and along the eastern coast of Crimea.

Keywords Black sea · Numerical modeling · Assimilation of observational data · Energy analysis · Mesoscale and submesoscale eddies

1 Introduction

Modern hydrodynamic models with a block for assimilating data of contact observations are widely used for calculating hydrophysical fields close to the observed ones and for studying the patterns of evolution of eddies and currents at various scales. A problem of using the data measurements of hydrological parameters and current

S. G. Demyshev · N. A. Evstigneeva (✉) · O. A. Dymova
Marine Hydrophysical Institute RAS, Sevastopol, Russian Federation

© The Author(s), under exclusive license to Springer Nature Switzerland AG 2022

V. I. Karev (ed.), *Physical and Mathematical Modeling of Earth and Environment Processes*,
Springer Proceedings in Earth and Environmental Sciences,
https://doi.org/10.1007/978-3-030-99504-1_13

velocity during their assimilation into the model, using the Kalman filter, in the equatorial region of the western Atlantic in the region of the Lomonosov countercurrent formation, was discussed in [1]. The data of sea surface temperature was assimilated in the Black Sea dynamics model in order to reconstruct surface fluxes in [2]. A recurrent neural network and Kalman filtering was used in [3] for modeling dynamic processes on the Earth's surface. The main hydrophysical fields of the World Ocean for the period 2005–2015 were calculated using the ocean data assimilation system of Hydrometeorological Center of Russia, described in [4]. The quality of simulation of model fields was analyzed in [5], depending on the assimilation of various types of data using the PDAF software product assimilating synthetic data into the NEMO global-ocean model. Strongly coupled data assimilation and weakly coupled data assimilation by analyzing the assimilation effect on the estimation of the ocean and the atmosphere variables was compared in [6].

Hydrothermodynamic fields for small areas of the Black Sea (near the coast of western Crimea and in the Sevastopol region) were reconstructed in [7] on the basis of the hydrodynamic model, using data from scientific cruises in 2007 and 2009.

Regular expeditionary studies of the Black Sea area, carried out by the Marine Hydrophysical Institute (MHI) RAS, allow to expand knowledge about the structure of hydrophysical fields and identify a number of features of seasonal and synoptic variability of water dynamics (for example, [8]). We used an assimilation procedure, developed in [9, 10], to process and analyze in detail the hydrological survey, conducted in September–October of 2016.The scheme of stations, in which the hydrological data were obtained during the 89th cruise in the Black Sea region, was presented in Fig. 1

The purpose of the research was to study the circulation features on the basis of the analysis of calculated energy characteristics and fields of currents in the northern part of the Black Sea using a numerical model and contact data of temperature and salinity, obtained in the autumn season of 2016 at the R/V "Professor Vodyanitsky". Unlike the work [7], a numerical calculation had been carried out for the entire Black Sea and a more vast set of data in time and space was used.

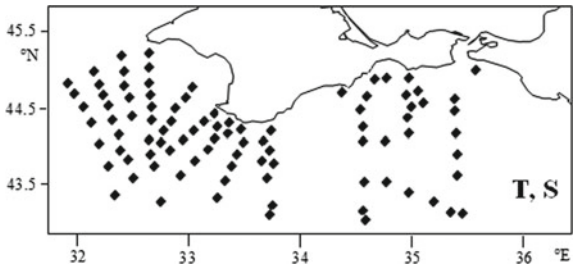

Fig. 1 Location of stations of the 89th cruise of R/V "Professor Vodyanitsky" in the autumn season of 2016

2 Statement of the Problem and Parameters of the Numerical Experiment

The system of equations of the used numerical model of the Black Sea dynamics was developed at MHI [11]. The finite-difference discretization of the model equations, initial and boundary conditions was carried out on the C grid. Kalman filtering [9, 10] was used in the data assimilation procedure. The prognosis of the characteristics of temperature, salinity, current velocity and variances of error estimates of the thermohaline fields was carried out according to a numerical model until the moment of data arrival of the hydrological measurements, taking into account the boundary and initial conditions. Further, the covariance matrix of estimates of errors of the thermohaline fields was calculated, for which a simplified parametrization of their covariance functions was used, obtained in earlier works [9, 10]. After inverting the matrix, the weighting coefficients were calculated, with the help of which the temperature and salinity fields and their covariance functions were corrected. The resulting fields were taken as initial and then the whole procedure was repeated. The advective terms of the transport-diffusion equations for the variances of the error prediction D_T, D_S were approximated using *TVD* schemes. At all boundaries, the conditions $\partial D_T^2/\partial n = 0$, $\partial D_S^2/\partial n = 0$ were set, and at the initial moment of time, the covariance functions were taken to be equal to the covariance functions of the field itself.

To calculate the energy characteristics of the circulation, the dynamics model was supplemented with a block for calculating the terms in the equations for changing the kinetic and potential energy [12].

The numerical calculation was carried out with a spatial resolution ~1.64 km and 27 vertical layers. The time step was 96 s. Mellor–Yamada 2.5 parameterization [13] was used when specifying vertical viscosity and diffusion coefficients. The calculation time—21 days (from 29th of September to 20th of October).

We used the hydrophysical fields, calculated in experiment with a coarser resolution for 29th of September, 2016, for the initial conditions. The data of the Greek center for atmospheric forecasts SKIRON (1/10°) [14] were set on the sea surface.

The data of the hydrological survey of the 89th cruise of the R/V "Professor Vodyanitsky", carried out in the northern part of the Black Sea in the autumn season of 2016, was used in the work. The *CTD SBE 911plus complex* was used to measure hydrological characteristics. The maximum depth to which the soundings were carried out varied from 30 to 1,000 m. The covariance functions of the fields T, S were approximated by an exponential-type function with parameters selected on the basis of an analysis of the statistical structure of the measured temperature and salinity fields and from the results of numerical experiments. Data from 128 stations were grouped by 14 days and assimilation was carried out once a day. The region of the Black Sea, located between the meridians of 31 and 37° E and parallels 43 and 45.5° N, in which the hydrological data were obtained, will be analyzed in details below.

3 Characteristics of the Fields of Currents and the Terms of the Energy Budget Equations in the Autumn Season of 2016 According to the Results of Numerical Calculation

Two anticyclonic eddy formations near Sevastopol and an anticyclonic eddy formation in the west of the area under consideration (noted to a depth of 300 m, with radii of about 30 km, with a maximum velocity in the upper layer up to 46 cm/s), anticyclonic eddies with a radius of about 20 km in the upper water layer near the south-eastern coast of Crimea, one anticyclonic and two cyclonic eddies with radii of about 35 km in the central part of the region (noted to a depth of 100 m) were noticed in the field of currents for 29th of September. Anticyclonic eddies near Sevastopol and large eddies in the western and central parts of the region were clearly reconstructed during the whole estimated period. With an increase of the wind forcing they were less noticeable in the upper layer. An intense flow of RC was fixed along the Crimean coast, directed to the west and southwest. Its maximum velocity at the upper horizon was 55 cm/s. Anticyclonic eddy formations with a radius of about 25 km generated and developed between the coastline and the RC.

We also analyzed the formation of meso- and submesoscale circulation features, associated with flowing around bottom topography inhomogeneities and coastline. The fields of currents at different horizons for 4th of October were presented at the Fig. 2a, b, c.

An anticyclonic eddy was generated along the eastern coast at the depth of 3 m (Fig. 2a). The maximum value of RC decreased with depth from 42 to 20 cm/s. Eddy formations in the deep-water part of the region were observed to the depth of 300 m (Fig. 2c). With an increase in the wind forcing from 16th of October (the wind speed was more than 15 m/s) we noticed that eddy formations in the upper layer were less pronounced, an intensification of the RC was observed.

The fields of currents at different horizons for 17th of October were presented at Fig. 2d, e, f. Some of the previously observed eddies were absent or were less pronounced in the upper layer (Fig. 2d). The maximum value of the RC flow along the coast decreased with depth from 55 to 28 cm/s.

According to the results of the calculation of the energy characteristics of the circulation, it was found that from 29th of September to 20th of October, 2016, the main contribution to the kinetic energy was made by the work of the wind force. The loss of energy occurred due to dissipation due to vertical and horizontal internal friction, as well as the work of the buoyancy force. Terms of vertical turbulent diffusion and advection of potential energy determined the change in potential energy.

Spatial distributions of the term $\tau \rightarrow E = u_0\tau^x + v_0\tau^y$ that determined the contribution to the kinetic energy from the wind, and fields of instantaneous values of the terms of the kinetic energy budget equations were analyzed t in detail. Figure 3 illustrated the fields of energy characteristics on the upper horizon for 4th and 17th of October, 2016.

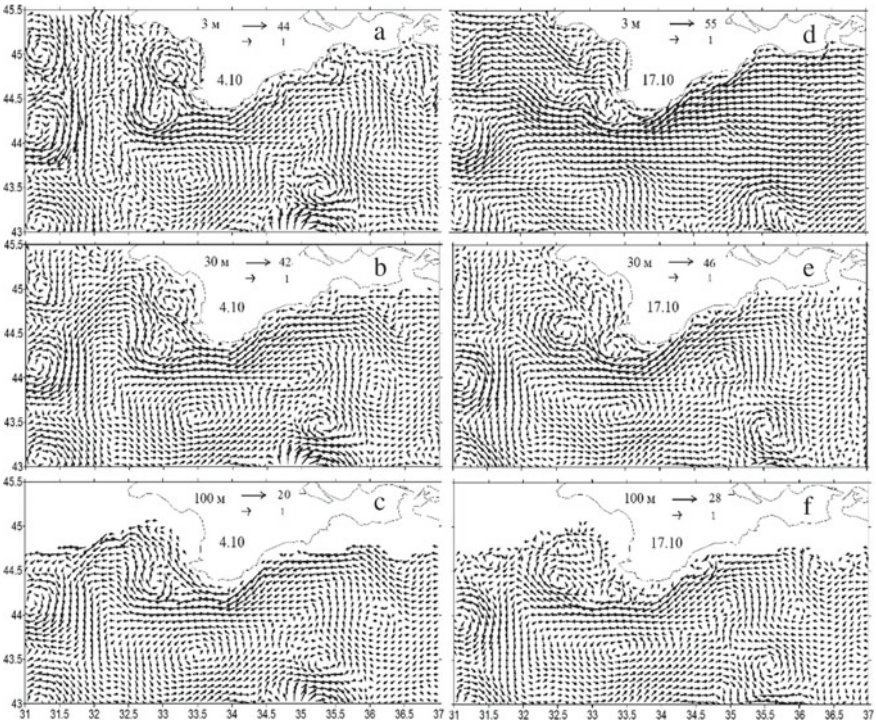

Fig. 2 Fields of currents (cm/s) at the depth of 3, 30 and 100 m on 4th and 17th of October, 2016

The areas, where mesoscale eddies were formed, were characterized by positive values of term $\tau \rightarrow E$ for 4th of October (Fig. 3a), i.e. the process of increasing kinetic energy due to the work of the wind force was observed. A negative value of the term $\tau \rightarrow E$ meant that the wind and currents on the sea surface were directed in opposite directions. The shaded areas corresponded to negative values of $\tau \rightarrow E$.

The inflow of energy from the wind prevailed in almost the whole area, except for the central deep-water part for 17th of October (Fig. 3d). The coastal part of the region was characterized by an intense work of vertical dissipation. We found that the maximum values of $Diss_{Ver}\ (E)$ (energy dissipation due to vertical internal friction), were obtained in the areas, where anticyclonic eddies were formed, in the west and along the coast. The maximum value of $Diss_{Ver}(E)$ was $7 \cdot 10^{-3}$erg/(s·cm^3) for 4th of October (Fig. 3b).

According to our calculation, the inflow of energy from the wind was compensated by vertical friction, the modulus values reached $2 \cdot 10^{-2}$ erg/(s·cm^3) due to a sharp increase in wind on 17th of October (Fig. 3e). It increased by an order of magnitude compared to the values for 4th of October.

The fields of $\Pi \leftrightarrow E$ (work of the buoyancy force) had a complex time-variable spatial structure. We observed in the fields both areas with positive values and areas with negative values were (Fig. 3c, f). Zones of negative values of $\Pi \leftrightarrow E$ were

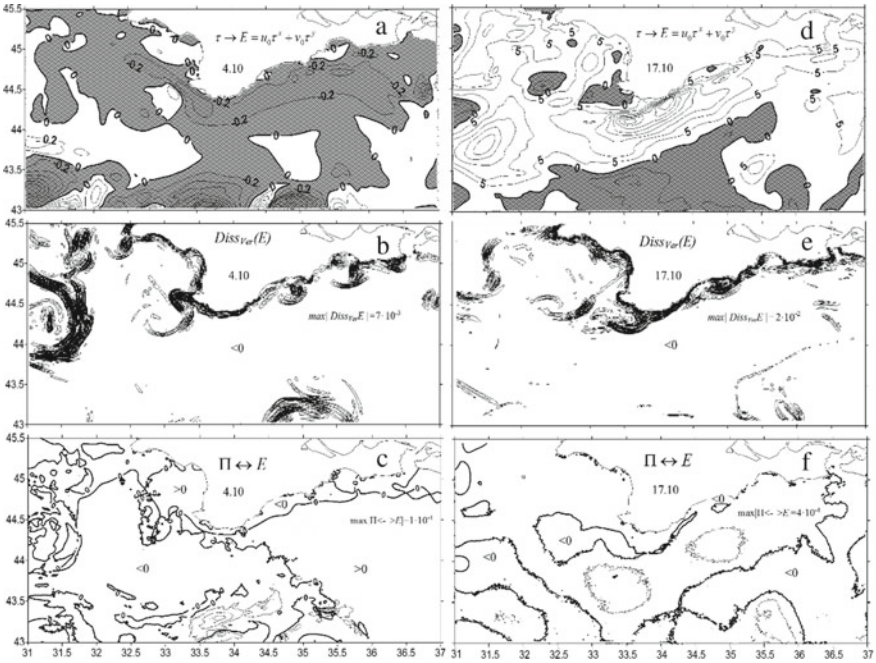

Fig. 3 Fields of $\tau \rightarrow E = u_0\tau^x + v_0\tau^y$ (erg/(s cm^2)), $Diss_{Ver}(E)$ (erg/(s·cm^3)) and $\Pi \leftrightarrow E$ (erg/(s·cm^3)) at the depth of 3 m on 4th and 17th of October, 2016

located along the eastern Crimean coast and in the western part. As was known, the areas in which the buoyancy force was negative and, as a consequence, a transition from kinetic to potential energy occurred, could be zones of baroclinic instability.

To summarize the conclusions: the dynamic and energy characteristics of the Black Sea were obtained on the basis of a four-dimensional analysis of data from hydrological survey in 2016 (89th cruise of the R/V "Professor Vodyanitsky"). Integral energy terms in the kinetic and potential energy budget equations were estimated for the period under consideration. The areas of generation of meso- and submesoscale features of hydrophysical fields were determined and possible physical mechanisms of their formation were considered (shear instability, flow around the irregularities of the coastline, baroclinic instability).

The following circulation features were obtained in the fields of currents in the autumn season of 2016: anticyclonic eddies near the city of Sevastopol and eddies of different signs of vorticity to the west of the region under consideration, in the central and eastern parts of the region. A flow of RC along the Crimean coast, directed to the west and south-west, with the maximum value of velocity 55 cm/s on the upper horizon. Anticyclonic eddy formations with a radius of about 25 km were quasi-periodically formed and developed between the coastline and the Rim Current as a result of shear instability of the flow. Small-scale anticyclonic and cyclonic eddies generated in the upper layer along the coast when the Rim Current flowed around

coastline and bottom topography inhomogeneities under the action of weak winds. All the eddy formations were less pronounced with an increase of the wind forcing. Positive values of the work of the wind force, the maximal in absolute values of vertical dissipation and negative values of the work of the buoyancy force were noted in the areas, characterized by intense mesoscale variability,

Acknowledgements The analysis of hydrophysical fields, reconstructed taking into account the data of hydrological survey of 2016, was carried out within the framework of the state assignment on topic No. 0555-2021-0003 (code "Operational Oceanology"). The study of possible physical mechanisms for the generation of meso- and submesoscale circulation features on the basis of the analysis of energy fields was carried out within the framework of the state assignment on topic No. 0555-2021-0004 (code "Oceanological processes").

References

1. Knysh VV, Korotaev GK, Mizyuk AI, Sarkisyan AS (2012) Assimilation of hydrological observation data for calculating currents in seas and oceans. Izv. Atmos. Ocean. Phys. V. 48: 57–73. doi: https://doi.org/10.1134/S0001433812010057.
2. Agoshkov V.I., Parmuzin E.I., Shutyaev V.P. (2013) Observational data assimilation in the problem of Black Sea circulation and sensitivity analysis of its solution // Izv. Atmos. Ocean. Phys. V. 49: 592–602. doi:https://doi.org/10.1134/S0001433813060029.
3. Feoktistov AS, Nezhevenko ES (2015) Operational forecasting of spatially distributed dynamic processes on the Earth's surface on the basis of data assimilation // Bulletin of the Novosibirsk State University. Series: Information Technologies. V. 13 (2): 103–115. (in Russian).
4. Zelenko AA, Vil'fand RM, Resnyanskii YuD et al. (2016) An ocean data assimilation system and reanalysis of the world ocean hydrophysical fields. Izvestiya. Atmospheric and Oceanic Physics. V. 52(4): 443–454. doi: https://doi.org/10.1134/S0001433816040149.
5. Stepanov V, Resnyanskii YuD, Strukov BS, Zelen'ko AA (2021) Evaluating effects of observational data assimilation in general ocean circulation model by ensemble kalman filtering: numerical experiments with synthetic observations. Russian Meteorology and Hydrology. V. 46(2):94–105. doi: https://doi.org/10.3103/S1068373921020047
6. Tang Qi, Longjiang Mu, Goessling HF et al. (2021) Strongly Coupled Data Assimilation of Ocean Observations Into an Ocean-Atmosphere Model. Geophysical Research Letters, 48(24). doi: https://doi.org/10.1029/2021GL094941
7. Demyshev SG, Evstigneeva NA (2020) Analysis of dynamic and energy characteristics of water circulation near the coast of the western Crimea on the basis of assimilation of observational data from hydrological surveys of 2007-2009 in a numerical dynamics model. Processes in geomedia. V. 4 (26): 892–901. (in Russian).
8. Artamonov YuV., Skripaleva EA, Alekseev DV et al. (2018) Hydrological Research in the Northern Part of the Black Sea in 2016 (87th, 89th and 91st Cruises of R/V Professor Vodyanitsky). Physical Oceanography, V. 25(3): 229–234. doi: https://doi.org/10.22449/1573-160X-2018-3-229-234.
9. Knysh VV, Moiseenko VA, Chernov VV (1988) Some results of four-dimensional analysis of hydrophysical fields in the Tropical Atlantic. Izv. Academy of Sciences of the USSR. Physics of the atmosphere and ocean. V. 24 (7): 744–752. (in Russian).
10. Demyshev SG, Korotaev GK (1992) Numerical experiments on four-dimensional assimilation of observational data in the Black Sea in June 1984 based on a numerical energy-balanced model. Marine Hydrophysical Journal. 2: 21–33. (in Russian).

11. Demyshev SG (2012) A numerical model of online forecasting Black Sea currents. Izv. Atmos. Ocean. Phys. 48: 120–132. doi: https://doi.org/10.1134/S000143381201002.
12. Demyshev SG (2004) Energy of the Black Sea climatic circulation. Part I. Discrete equations for the rate of change of kinetic and potential energies. Meteorology and Hydrology. 9: 65–80. (in Russian).
13. Mellor GL, Yamada T. (1982) Development of a turbulence closure model for geophysical fluid problems. Rev.Geophys. Space Phys. V. 20 (4): 851–875.
14. NonHydrostatic SKIRON/Eta Modelling System. URL: http://forecast.uoa.gr/forecastnew.php.

The Black Sea Undercurrents: Observations and Numerical Simulation Results

N. V. Markova and O. A. Dymova

Abstract The aim of the presented study is to investigate one remarkable feature of the Black Sea deep-water circulation. These are unsteady narrow anticyclonic currents that propagate under the main pycnocline in the direction opposite to the surface circulation and are called undercurrents. According to observation data, undercurrents were discovered in several field expeditions, and were also revealed in some results of the Black Sea dynamic modeling. However, due to the lack of regular observations, it was not entirely clear whether they were a real feature of the Black Sea current field or an artifact of the experiments carried out. In this work, to assess the spatial variability of the Black Sea current field and identify undercurrents, the results of modeling the Black Sea circulation for several periods were analyzed. Simulations were carried out using the MHI model, and the results were validated based on deep-water field observation data on temperature and salinity. As well, in the northeastern part of the sea the simulated currents were compared with the data of ADCP deep-water velocity measurements (with Aqualog profiler). It is shown that undercurrents are more often formed in the spring–summer period and their lifetime is from one to several weeks. And although the length of undercurrents along the continental slope can reach several hundred kilometers, their width is only 8–12 km. Such characteristics of undercurrents explain the difficulty of their detection and identification in previous works.

Keywords Black Sea · Deep-water circulation · Undercurrents · Observations · Numerical experiment · Simulation

1 Introduction

In contrast to the current structure of the Black Sea upper 200–300-m layer, circulation below the permanent pycnocline has been studied rather poorly. In the upper layer the circulation scheme was drawn up in the middle of the 20th century according to the

N. V. Markova (✉) · O. A. Dymova
Marine Hydrophysical Institute of RAS, Sevastopol, Russia
e-mail: n.v.markova@mail.ru

© The Author(s), under exclusive license to Springer Nature Switzerland AG 2022

V. I. Karev (ed.), *Physical and Mathematical Modeling of Earth and Environment Processes*,
Springer Proceedings in Earth and Environmental Sciences,
https://doi.org/10.1007/978-3-030-99504-1_14

data of field observations, and later it was only refined. Its general pattern is presented in [1, 2] and continues to be detailed. In the dynamics of the upper Black Sea layer, it is well-known some basic elements, such as the cyclonic Main Black Sea Current (the Rim Current), periodically forming sub-basin cyclonic gyres in the western and eastern parts of the sea, the Batumi and Sevastopol anticyclones, and the series of mesoscale and submesoscale eddies between the Rim Current and the coast. At the same time, there is still no current scheme of the seawater layer below the permanent pycnocline. Moreover, before the beginning of some large-scale expeditions in the Black Sea at the end of 20th century [3], deep-water currents were considered negligible. The results of the research vessel expeditions carried out showed that there are specific current systems with interannual variability at great depths, as well. At the end of the 20th and the beginning of 21st centuries, ARGO floats were started to deploy. ARGO floats drifting on deep horizons could be used as Lagrangian tracers to estimate the current velocity at the float parking depths [4]. Thus, it was confirmed that basin-wide circulation is generally cyclonic and deep currents have seasonal variability, as well. The few data of velocity measurements, indicating the presence of deep-water anticyclonic dynamic structures (eddies, currents) [5–7], have not found a convincing explanation yet. The main reason for the lack of detailed studies is the persistent deficit of field data at depths of more than 300 m. The greatest shortage is evident in the observational velocity data collected over the entire history of observations in the Black Sea. So, the anticyclonic circulation elements observed in deep seawater layers can be interpreted as undercurrents (opposite to the cyclonic currents on the sea surface), or as short parts of deep-water eddies, the evolution of which has not yet been studied.

Nowadays, it is know that in deep layers the average velocities are an order of magnitude lower than on the surface, and a single basin-scale gyre, similar to the Rim Current in the upper layer, is not observed. As already mentioned, a more detailed study of the structure of currents using only observational data is difficult due to the lack of the required amount of data, and a solution to this problem is not expected in the near future. Therefore, in this work, numerical modeling is used as the most effective and least resource-intensive method for reconstructing the three-dimensional structure of the velocity field and studying deep-water currents. But since the results of any modeling still need to be compared with observation data, additional processing of the available data is also carried out. Based on the processing of observation data and comparison with the simulation results, some features of deep-water circulation in the Black Sea, including anticyclonic undercurrents, have been discovered.

2 Simulation and Numerical Analysis

To calculate the seawater circulation in the basin, the Black Sea dynamics numerical model developed at the Marine Hydrophysical Institute (MHI) [8] is used. The complete system of equations of ocean thermo-hydrodynamics in the Boussinesq and

hydrostatic approximations is integrated in numerical experiments. The MHI-model includes the momentum, continuity, hydrostatics, heat and salt advection–diffusion equations, and the state equation [8, 9]. Horizontal resolution of the MHI-model is 1.6 km for the entire basin, with a time step of 1.5 min. The assimilation of observation data is not used in that version of the model, so the simulations are prognostic. The MHI-model takes into account the rivers runoff and exchange through the straits. The boundary conditions are: free slip for solid boundaries, the Dirichlet condition for liquid ones, and the linear kinematic condition at the sea surface. The full model formulation and numerical implementation are presented in [9]. The model is driven by wind and thermohaline forcing of the atmospheric models ALADIN (for 2006), ERA-Interim (for 2010 and 2013), and SKIRON (for 2011).

The structure of the calculated current fields at different horizons is analyzed in detail. Numerical analysis of three-dimensional daily fields of the Black Sea currents for several periods (2006, 2011, autumn–winter 2010, summer 2013) is carried out. Validation of the simulation results is performed on the basis of data from drifter observations [10], ARGO temperature and salinity profiling [11], and research vessel observations [12]. It is shown that all well-known features of the upper layer circulation are reconstructed in numerical experiments. The Rim Current, the seasonal evolution of the Cold Intermediate Layer, and the salinity field features (more saline seawater in the Bosporus region and in the centers of cyclonic eddies, and less saline waters in anticyclones) are reproduced. A similar structure of hydrophysical fields persists down to depth of about 300 m (lower boundary of permanent pycnocline). Some traces of the upper circulation are still found at depths of 300–500 m, such as the lower parts of the western branch of the Rim Current and largest mesoscale eddies.

The velocity field at depths of more than 500 m is characterized by the presence of numerous mesoscale eddies and currents. Mean current velocities are 2–5 cm/s, and background velocities do not exceed 1–2 cm/s. Maximum velocities of 15–20 cm/s are reached in eddy structures. Despite the great depth, a seasonal increase of currents is observed in winter and autumn, as well as in the upper layers. In the abyssal part of the sea some deep-water eddies are revealed. They are not clearly distinguished near the surface, but their structure is clearly traced below a depth of 150–300 m. In the central abyssal part of the sea that eddies retain their structure down to the bottom. The relief of the continental slope bottom can lead to deformation of deep-water eddies and their transformation into eddies of a smaller scale and dissipation.

The presence of deep-water undercurrents is found out. These are relatively narrow, irregular currents propagating in an anticyclonic direction along separate parts of the continental slope, opposite to the direction of currents at the surface. They are found according to the data of all the presented numerical experiments at horizons of 1,000 m and deeper. Undercurrent's wide is up to 10–12 km and it can propagate along the continental slope with mean velocity of 3–5 cm/s and maximum one up to 15–20 cm/s. Their generation is observed in all seasons but more often in the spring–summer period. The lifetime of undercurrents is from one to several weeks. Undercurrents are most often formed at the northeastern part of continental slope in the spring–summer period at horizons of 1,000 m and more (Fig. 1). Note

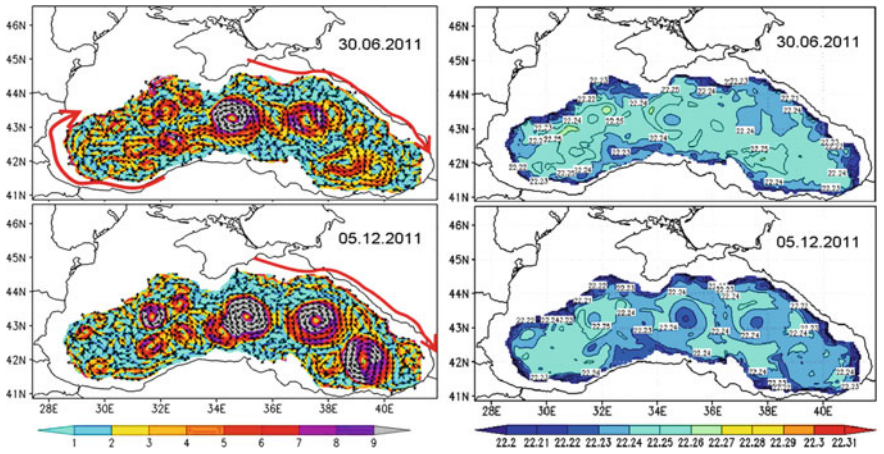

Fig. 1 Modeled fields of currents, cm/s (left panel) and salinity, ‰ (right panel) at 1,100 m horizon according to the simulation results for 2011

also the presence of mesoscale deep-water eddies of different vorticity signs (Fig. 1a) and the corresponding anomalies in salinity fields (Fig. 1b).

The generation of deep-water anticyclonic currents in the western part of the Black Sea occurs less frequently than in the northeastern region. For example, the formation of undercurrents at horizons of more than 1,000 m is found near the Bulgarian coast, as well as along the northwestern part of the continental slope (Fig. 2). Here, the

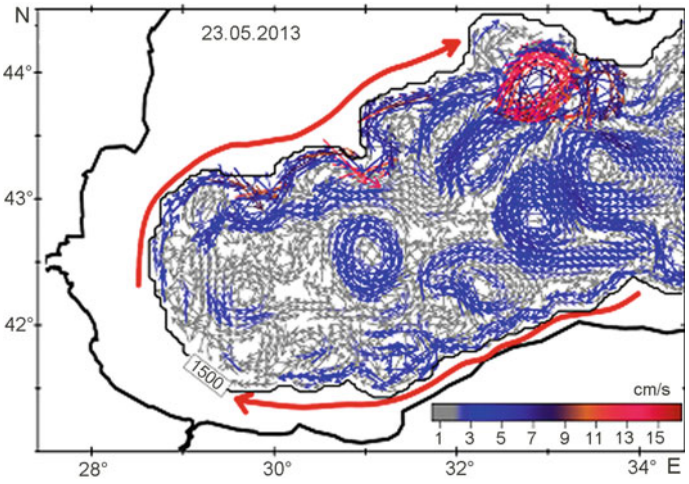

Fig. 2 Modeled currents in the western part of the Black Sea on May 23, 2013 at 1,500 m horizon. Anticyclonic currents are duplicated by additional red arrows

currents are also rather narrow (up to 8–12 km) and it is characterized by lifetime from several days to several weeks. Their mean velocities are 3–5 cm/s, while maximum velocities can reach 9–13 cm/s.

3 Comparison with Observations

The model results are consistent with the data obtained in other works. Thus, the values of the velocities of deep-water currents can be confirmed by information from 16 autonomous profiling ARGO floats with parking depth of more than 350 m. These velocities were calculated over a 10-year period in [13]. In that study it was also showed that the cyclonic direction prevails in the deep-water circulation, and the strongest currents were located above the continental slope. The range of calculated velocities of deep-water currents was from 1 to 20 cm/s, but no undercurrents were identified there. According to ARGO float ID6901833 data, undercurrents were discovered some later—in 2016–2017. The float was moved at a depth of 200 m along the northeastern part of the Black Sea continental slope (Fig. 3). Its trajectory was tracked using satellite positioning. Coordinates of the float were obtained when it ascended to the surface to transmit the data collected (every 120 h). The movement of the float to the southeast along the North Caucasus coast in September 2016 (for 40 days) and in February 2017 (10 days) indicates the presence of anticyclonic currents. The mean velocity of the float motion between stations #20 and #28 in the autumn of 2016 was 2.4 cm/s, and between stations #50 and #52 in the winter of 2017—8 cm/s. The characteristics of the undercurrents are generally consistent with our results of modeling the current velocities in this region and in other years.

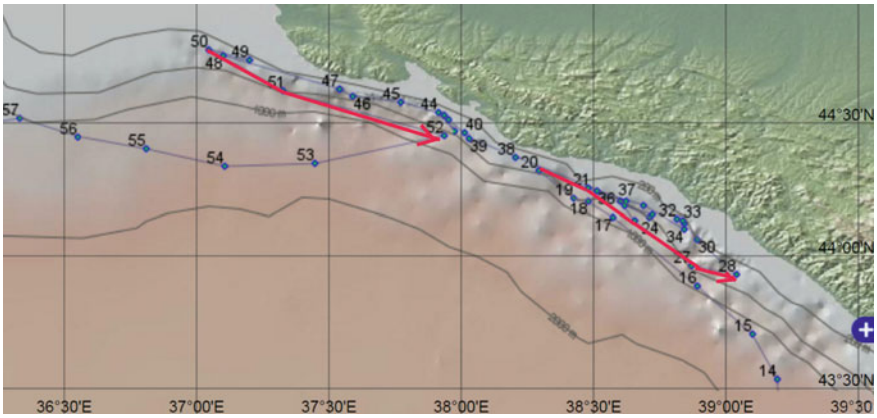

Fig. 3 Satellite positioning of ARGO float ID6901833 offshore North Caucasus coast in 07.08.2016–10.03.2017 (numbered blue dots indicate float stations, red arrows mark undercurrents). Drawn using service http://www.ifremer.fr/co-argoFloats/float?ptfCode=6901833

The presence of undercurrents along the northeastern part of the continental slope (Fig. 1) is also consistent with the results of current velocity profiling by the Aqualalog moored station. These measurements were carried out on June 17–19, 2011 at the test site of the Institute of Oceanology of the Russian Academy of Sciences in Gelendzhik [14]. According to the data of deep-water (to a depth of more than 1,000 m) profiling of the velocity, the anticyclonic current during this period was recorded at depths of 500–950 m. Its core with a velocity of about 3 cm/s was located in a layer of 700–850 m. At the nearest node of the model grid, the presence of undercurrent was also revealed (Fig. 4). Analysis of the results of simulations shows that it is quasi-periodically revealed at that region at the lower horizons throughout the year.

In the western part of the Black Sea, the presence of anticyclonic currents with characteristics similar to those calculated using the MHI model is consistent with the published results of long-term (more than a year) deep-water velocity observations using ADCP at a horizon of 1,700 m southwest of Cape Chersonesos [15], as well as with the results of a number of experiments using other numerical models, for example, simulations based on the Institute of Numerical Mathematics model [16] or recent experiments based on the modified ROMS model [17].

4 Discussion

It should be noted that the features of undercurrents established in this work correspond to the hypotheses of their formation available in the scientific literature. Thus, a number of authors point to the possibility of generating currents propagating along the continental slope in the anticyclonic direction as a result of low-frequency wave processes under the main Black Sea pycnocline. The formation of such currents at horizons over 300 m is indicated, for example, in [5–7]. The periodicity in the intensity of undercurrents found from the results of modeling on scales from several days to several weeks can be an argument for the wave hypothesis.

The formation of undercurrents can also be associated with the passage of mesoscale anticyclonic eddies over the continental slope (as in the situation in Fig. 2). The behavior of coastal mesoscale eddies was studied, for example, in [18, 19]. Eddies act as generators of jet flow between the periphery of the eddy and the bottom, and also change the slope of isopycnic surfaces, as a result of which internal waves and gradient flows can also form. Currents associated with the passage of mesoscale anticyclonic eddies near the shelf zone boundary were also noted in other regions of the World Ocean, for example, near the western coast of the Bay of Bengal [20].

In the Black Sea, the formation of mesoscale anticyclonic eddies is mainly caused by seasonal, spring–summer weakening and meandering of the Rim Current, in turn, caused by seasonal changes in wind vorticity over the sea. Features of stratification and bottom topography are also of great importance for deep-water processes. At present, given the current level of observation data availability, it is difficult to discuss about any specific reason for the formation of under currents in the Black Sea. In

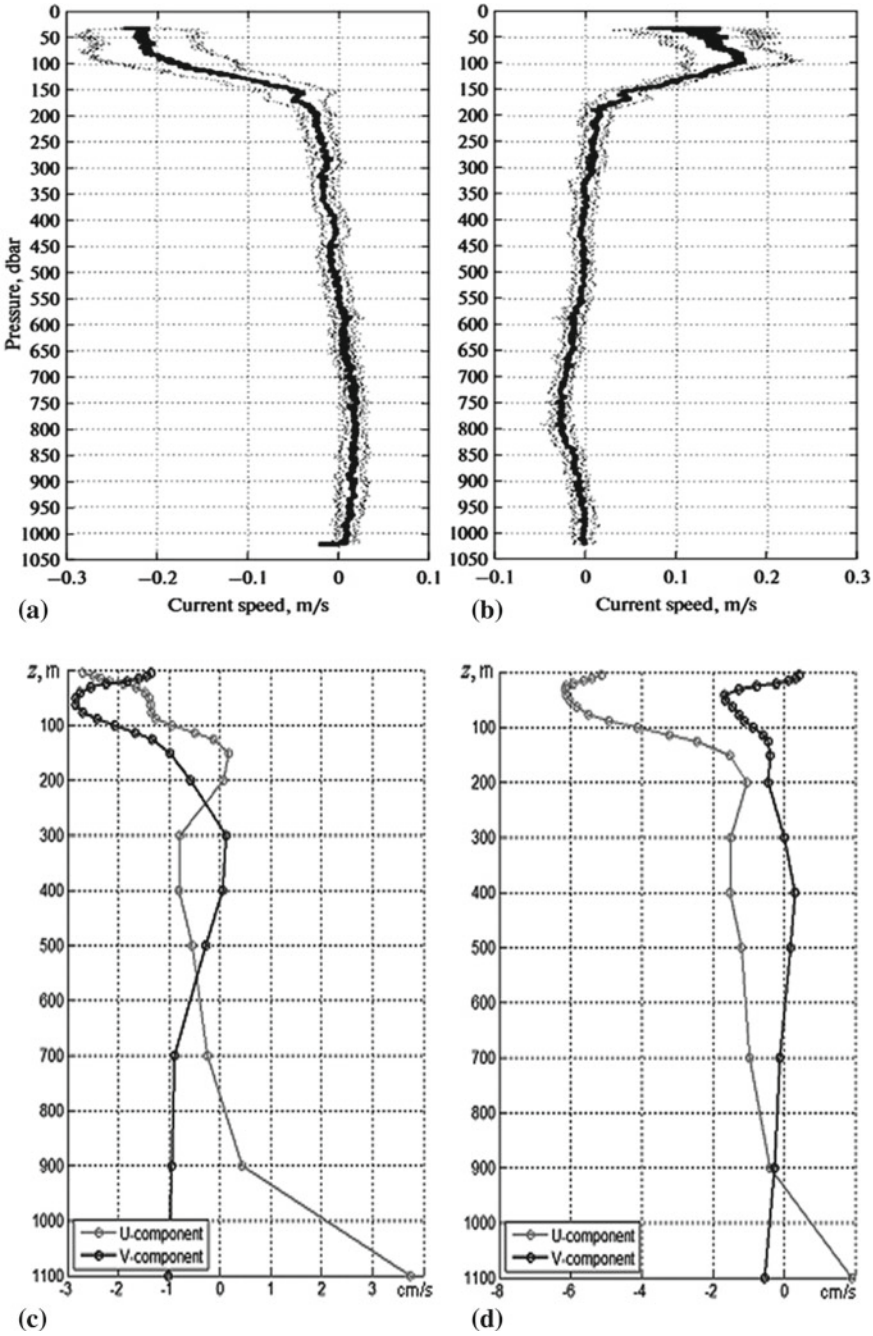

Fig. 4 Profiles of velocity components (u—zonal, v—meridional) at Gelendzhik region in June, 2011: **a**, **b**—u, v velocity components measured by Aqualog profiler at point (44°23′24″ N, 37°51′36″ E) [14], and modeled velocity components at nearest model grid node: **c**—on June 16, 2011, **d**—on June 20, 2011

a complicated system of interactions between the atmosphere and the ocean, much larger observation data and further research are required to clarify the prerequisites for the occurrence of undercurrents and to determine the dominant forcing factor.

Thus, the formation of anticyclonic currents in the deep layers of the Black Sea can be caused by various reasons: the movement of mesoscale eddies, wave processes, changes in density gradients, the combined effect of baroclinicity and bottom topography, and others. The final solution to the question of the mechanisms of the occurrence of undercurrents is the subject of further research.

Acknowledgements The study was carried out within the frame of the State task theme № 0555-2021-0003 "Development of operational oceanology methods based on interdisciplinary research of processes of the marine environment formation and evolution and on mathematical modeling using data of remote and contact measurements" ("Operational oceanology" code).

References

1. Oguz T., Latun V.S., Latif M.A., Vladimirov V.V., Sur H.I., Markov A.A., Özsoy E., Kotovshchikov B.B., Eremeev V.V., Ünlüata Ü. Circulation in the Surface and Intermediate Layers of the Black Sea // Deep-Sea Res. 1993. 40, № 8. pp. 1597–1612. DOI: https://doi.org/10.1016/0967-0637(93)90018-X.
2. Kosyan, R.D., Podymov, I.S., Pykhov, N.V. Dynamical Processes in the Sea Nearshore Zone–Moskow: "Nauchnjj mir", 2008. 255 p. (in Russian).
3. Murray, J.W., Izdar, E. The 1988 Black Sea Oceanographic Expedition: Overview and New Discoveries // Oceanography. 1989. V. 2(1). pp. 15–21. DOI: https://doi.org/10.5670/oceanog.1989.25.
4. Korotaev, G.; Oguz, T.; Riser, S. Intermediate and Deep Currents of the Black Sea Obtained from Autonomous Profiling Floats // Deep-Sea Res. II 2006, 53, pp. 1901–1910. DOI: https://doi.org/10.1016/j.dsr2.2006.04.017.
5. Bulgakov N.P., Golubev Yu.N. On the Question of the Existence of Deep Anticyclonic Circulation in the Black Sea // Complex oceanographic studies of the Black Sea (Hydrology, Hydrophysics, Hydrochemistry). Sevastopol: MHI, 1990. pp. 23–29. (in Russian).
6. Latun V.S. On the Motions of the Deep Layers of the Black Sea // Complex oceanographic studies of the Black Sea (Hydrology, Hydrophysics, Hydrochemistry). Sevastopol: MHI, 1989. pp. 9–16. (in Russian).
7. Lemeshko E., Morozov A., Stanichny S., Mee L.D., Shapiro G.I. Vertical Structure of the Current Velocity Field in North-Western Part of the Black sea by the LADCP Data Measurements, May, 2004 // Physical Oceanography. 2008. № 18. pp. 319–331.DOI: https://doi.org/10.1007/s11110-009-9029-7.
8. Demyshev, S.G., Korotaev, G.K. Numerical Energy-Balanced Model of the Baroclinic Currents in Ocean with Uneven Bottom on a C-grid // Numerical models and results of calibration calculations of currents in the Atlantic Ocean: Atmosphere – Ocean – Space. The program "Sections". Moscow: Institute of Numerical Mathematics RAS, 1992. pp. 163–231. (in Russian).
9. Demyshev, S.G. A Numerical Model of Online Forecasting Black Sea Currents // Izvestiya, Atmospheric and Oceanic Physics 2012, 48, pp. 120–132. DOI: https://doi.org/10.1134/S0001433812010021.
10. Demyshev, S.G., Dymova, O.A. Numerical analysis of the Black Sea currents and mesoscale eddies in 2006 and 2011 // Ocean Dynamics, 2018, V.68 (10), pp. 1335–1352. DOI: https://doi.org/10.1007/s10236-018-1200-6.

11. Markova, N.V., Dymova, O.A., Demyshev, S.G. Numerical Simulations of the Black Sea Hydrophysical Fields Below the Main Pycnocline: Validation by ARGO Data // Springer Proceedings in Earth and Environmental Sciences. Physical and Mathematical Modeling of Earth and Environment Processes (2018). Springer, 2019. pp. 15–21. DOI: https://doi.org/10.1007/978-3-030-11533-3_2.
12. Dymova, O.A., Miklashevskaya, N.A., Markova, N.V. Modeling the Black Sea Deep Circulation with ERA-Interim Forcing in Summer 2013 // Springer Proceedings in Earth and Environmental Sciences. Physical and Mathematical Modeling of Earth and Environment Processes (2018). Springer, 2019. pp. 33–40. DOI: https://doi.org/10.1007/978-3-030-11533-3_4
13. Markova, N.V.; Bagaev, A.V. The Black Sea Deep Current Velocities Estimated from the Data of ARGO Profiling Floats // *Physical Oceanography* 2016, № 3, pp. 23–35. DOI: https://doi.org/10.22449/1573-160X-2016-3-23-35.
14. Ostrovskii, A.G., Zatsepin, A.G., Soloviev, V.A. et al. Autonomous System for Vertical Profiling of the Marine Environment at a Moored Station // Oceanology. 2013. V. 53. № 2. pp. 233–242. DOI: https://doi.org/10.1134/S0001437013020124.
15. Klyuvitkin, A.A.; Ostrovskii, A.G.; Lisitzin, A.P.; Konovalov, S.K. The Energy Spectrum of the Current Velocity in the Deep Part of the Black Sea // Dokl. Earth Sc. 2019, 488, pp. 1222–1226. DOI: https://doi.org/10.1134/S1028334X1910012X.
16. Lukyanova, A.N.; Bagaev, A.V.; Plastun, T.V.; Markova, N.V.; Zalesny, V.B.; Ivanov, V.A. The Black Sea Deep-Water Circulation Research by Results of Numerical Modelling and In-Situ Data: INM RAS Model Numerical Experiment (in Russian) // Ecological Safety of Coastal and Shelf Zones of Sea 2016, pp. 9–14.
17. Bouzaiene M., Menna M., Elhmaidi D., et al., 2021. Spreading of Lagrangian Particles in the Black Sea: A Comparison between Drifters and a High-Resolution Ocean Model // Remote Sens. 13, 2603. DOI: https://doi.org/10.3390/rs13132603.
18. Krivosheya V.G., Moskalenko L.V., Titov V.B. On the Current Regime over the Shelf near the North Caucasian Coast of the Black Sea // Oceanology. 2004. Vol. 44. № 3. pp. 331–336.
19. Zatsepin A.G., Elkin D.N., Korzh A.O., Kuklev S.B., Podymov O.I., Ostrovskii A.G., Soloviev D.M. On Influence of Current Variability in the Deep Black Sea upon Water Dynamics of Narrow North Caucasian Continental Shelf // *Physical Oceanography* 2016, № 3, pp. 14–22.DOI: https://doi.org/10.22449/1573-160X-2016-3-14-22.
20. Francis, P.A.; Jithin, A.K.; Chatterjee, A.; Mukherjee, A.; Shankar, D.; Vinayachandran, P.N.; Ramakrishna, S.S. Structure and dynamics of undercurrents in the western boundary current of the Bay of Bengal // Ocean Dynamics 2020, 70, pp. 387–404. DOI: https://doi.org/10.1007/s10236-019-01340-9.

The Northern Caspian Levels and Its Ice Regime Changing During Current Climate Warming

A. V. Kholoptsev and Zh. K. Naurozbayeva

Abstract The sea level and ice conditions changing in any shallow freezing water body (FWB) strongly affect to the safety of navigation, fishing, and environmental conditions. Therefore, these processes with modern climate warming should be considered when modeling and forecasting. The features of the influence of changes in the level of water bodies on the ice regime during climate warming have not been sufficiently studied. Current sea level changes are of great interest. The shallow freezing water bodies include seas of the Arctic Ocean, the Azov Sea, and many lakes. They also include the northern part of the Caspian Sea. Purpose of the research: revealing, using the example of the North Caspian, the peculiarities of the influence of changes in the level of freezing water bodies on the ice regime during modern climate warming. The article uses the data of sea level, maximum ice thickness and characteristic periods of ice regime at representative hydrometeorological stations of the North Caspian. The research was carried out using traditional methods of mathematical statistics. The current trends in the dynamics of all the characteristics of the Northern Caspian are revealed. The significance of the influence of fluctuations in the level of the North Caspian on the indicators of ice conditions is estimated. A qualitative forecast of further changes in ice conditions in the North Caspian is proposed for the scenario in which the decrease in the level of the Caspian Sea will continue.

Keywords North Caspian · Sea level · Maximum ice thickness · Characteristic dates · Ice period · Trends · Connections

A. V. Kholoptsev (✉)
Sevastopol State University, Sevastopol, Russian Federation
e-mail: kholoptsev@mail.ru

Sevastopol department of the State Oceanographic Institute named N.N. Zubov, Sevastopol, Russian Federation

Zh. K. Naurozbayeva
Department of Hydrometeorological Research of the Caspian Sea, Scientific Research Center RSE Kazhydromet, Almaty, Kazakhstan

© The Author(s), under exclusive license to Springer Nature Switzerland AG 2022

V. I. Karev (ed.), *Physical and Mathematical Modeling of Earth and Environment Processes*,
Springer Proceedings in Earth and Environmental Sciences,
https://doi.org/10.1007/978-3-030-99504-1_15

1 Introduction

Ice conditions in any shallow freezing water body significantly affect to the safety of the population of its coasts, as well as the fishing and shipping carried out in it. Therefore, improving the methods of modeling and forecast their changes is an actual problem of oceanography, limnology, as well as the operation of water transport.

The main indicators of ice conditions include the maximum ice thickness, the duration of the ice period and the characteristic periods of the ice regime. The most important dates are the formation of the first ice, the appearance of a stable ice cover, the date of maximum thickness and the date of complete clearing of ice. According to the existing factors of variability of ice conditions in a freezing water body [30], the main ones are variations in the thermal balance of the surface layer [27].

The incoming part of the thermal balance is formed by the absorption of solar and thermal radiation, as well as the arrival of heat because of heat exchange with the lower atmosphere, other layers of the surrounding water environment and during the formation of ice. Its consumable part forms a loss of heat during evaporation, heat exchange of the layer under consideration with the atmosphere and other layers of water and during ice melting.

The interrelation between the various components of the thermal balance of surface waters depends on the geographic location, hydrological features, bottom topography, and local climate. The heat fluxes received and lost by surface waters depends on the characteristics of its water exchange with other water bodies (or other parts of the reservoir).

The most significant is the discharge of currents that bring warm or cold water into the sea. Their changes depend on sea level fluctuations. But also, a significant effect on the thermal balance of surface waters is exerted by heat exchange with the atmosphere [11, 27, 29, 33]. However, it has not previously been verified. As you know, the level of the Caspian Sea varies greatly. Observations of changes in the level of the Caspian Sea have been going on for more than two centuries [14, 16, 24, 33].

For the period from the beginning of the 20th century to the present, three characteristic time intervals can be distinguished: an abnormally level decrease (1930–1977), an abnormally increase (1978–1995), and a slow decline (2005–up to the present time) [3–5, 13, 33]. In the interval from 1930 to 1977 sea level decreased by almost 3 m and in 1978–1995 it increased by 2.5 m [1, 14, 31, 32].

Changes in the level of the North Caspian Sea significantly changed the area of its water surface. When the sea level increased, the coast was flooded. The coastline was displaced by 25–50 km [20, 21].

Since 2006 the level of the Caspian Sea has been decreasing. In 2020 its mark was –28.24 m (according to the Baltic system), and in December 2020 the level was –28.36 m [10]. During this period, the area of the sea's water surface decreased by 23 thousand km^2. The Kazakhstan part of the Northern Caspian has greatly decreased. A decrease in sea level leads to a radical restructuring of the coast, desertification of coastal areas. This greatly complicates economic activities in coastal and shallow

water areas. Business entities associated with the operation of port facilities and maritime transport are especially vulnerable.

Since the North Caspian is shallow, sea level changing significantly influenced to the characteristics of water exchange with the deep-water part of the Caspian Sea. And this could have affected to the ice conditions.

The ongoing changes in the level of the North Caspian Sea are associated with climate changes in the Caspian Sea basin and neotectonic processes (transgressions and regressions) [33]. Anthropogenic factors also had some influence on them. The main ones are the consumption of part of the river runoff during irrigation and the creation of reservoirs on the Volga [25].

With further warming of the regional climate and activation of anthropogenic impacts, one of the likely scenarios for further changes in the level of the North Caspian is its decrease.

The question of what the changes in ice conditions in the North Caspian will be requires additional study. The answer to it largely depends on the results of testing the validity of the hypothesis put forward. As a result, such a check is of considerable theoretical and practical interest.

2 Methods and Materials

The aim of this work: the North Caspian's level changing and influence on ice regime with a modern warming of the climate.

To achieve this goal, the following tasks have been solved:

1. Identification of current trends in climate change in the North Caspian region and assessment of their sustainability.
2. Analysis of dynamics trends of the North Caspian level and characteristics of ice conditions for the period of continuous observations.
3. Assessment of the statistical relationship significance between changes in the processes at different intervals of this period.

To solve these objectives was used next information:

- the background level of the Caspian Sea for the period from 1900 to 2020 for all representative points of the sea, in meters of the Baltic system (BS) [10].
- mean monthly sea level values for Kazakhstan sea stations and posts, in m BS, for the period from 1960 to 2020;
- characteristic dates of the ice regime for the period from 1980 to 2020;
- maximum ice thickness from 1973 to 2020;
- the duration of the ice period in days from 1980 to 2020;
- monthly sum of atmospheric precipitation from 1960 to 2020;
- mean monthly air temperature from 1900 to 2020.

The method of observation, processing and transmission of data, the timing of observation is made in accordance with the manual and guidelines.

Atyrau and Peshnoy stations belong to the Kazakhstani coast of the Northern Caspian. Station Atyrau (Guryev) was founded in 1878, located 25 km from the sea on the right cost of the Ural River. The station was moved several times, since 1969 it is in the northeast of Atyrau, 4 km from the Ural River. The Peshnoy station was founded in 1939. It was also moved several times, the last time in 1964. Now it is located 4 km from the outfall of the Ural River, there were no interruptions in observations [12].

In accordance with the WMO recommendations, when solving the first objective, the value of the difference in its climatic norm, calculated for a particular time interval of 30 years, in relation to its value for the period 1961–1990, was considered as an indicator of the trend in the dynamics of a particular climate characteristic [26, 36].

The difference in climatic norms for the periods 1991–2020 and 1961–1990 was considered as a modern trend.

The stability of the trend in the dynamics of the indicator for the modern period was assessed by comparing with the trend for the period 1981–2010.

The technique for solving the second objective consists in assessing the average rates of interannual variability of the mean monthly levels of the North Caspian and the characteristic dates of the ice regime from November to March. The average rate of such a process was considered as the value of the slope of the linear trend of the corresponding time series, which was calculated in a "sliding window" with a length of 30 years. The dependences of the average speed of each indicator on the year of the beginning of the "sliding window" for which it was calculated were compared.

When solving the third objective the method of correlation analysis and Student's criterion [17, 28, 37] were used. The significance of the relationship between changes in the characteristics of the ice regime of the North Caspian and variations in the mean values of the level for the winter season was assessed in various "sliding windows" lasting 30 years. Linear trends have been calculated in time series. If the reliability of the statistical inference exceeded 0.9, it is considered significant. And if it exceeds the level of 0.95, the connection is strong. The values of the threshold levels of the correlation coefficient were calculated considering the number of degrees of freedom of the compared time series. They are for the reliability of the conclusion 0.9–0.32, and for the reliability of the conclusion 0.95–0.37 [17, 28, 37].

3 Results

In accordance with the described methodology, the tendencies of interdecadal changes in the characteristics of the climate of the North Caspian were studied.

Figure 1 shows the dependences on the beginning year of the 30-year time interval (the so-called "sliding window") of the difference between the average air temperatures calculated for it at Peshnoy and Atyrau stations for the period from November to March in relation to the period 1961–1990.

Figure 1 shows that in the "sliding windows" with a duration of 30 years, which begin from 1900 to 1928, the values of the difference in the average for the period

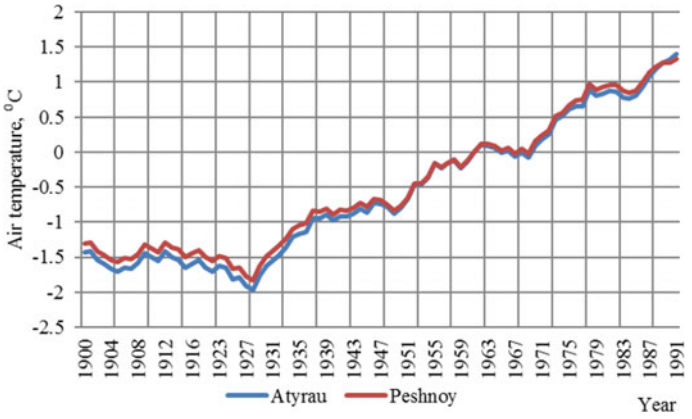

Fig. 1 Dependence of air temperatures of the beginning year "sliding window" in relation to climatic norms for the period November–March at Peshnoy and Atyrau

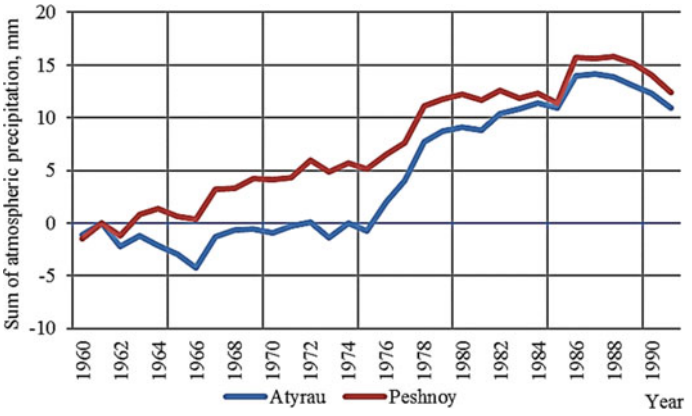

Fig. 2 Dependences on the year of the beginning of the "sliding window" of the difference in the average amounts of atmospheric precipitation from November to March in Peshnoy and Atyrau in relation to the climatic norms of the indicator

November–March air temperatures in Peshnoy and Atyrau in relation to their basic climatic norms (1961–1990) change at an almost unchanged level.

In "sliding windows starting from 1929, the values of the indicators as the year of the beginning of these windows increases at an average rate of 0.056 per year. Moreover, their climatic norms for the period 1991–2020 significantly exceed their levels for the period 1961–1990 and 1981–2010, which confirms the presence of a stable warming of the regional climate and corresponds to the conclusions [6, 26].

An essential feature of the considered dependences is the presence in the spectrum of variability of indicators of a component with a period close to 20 years.

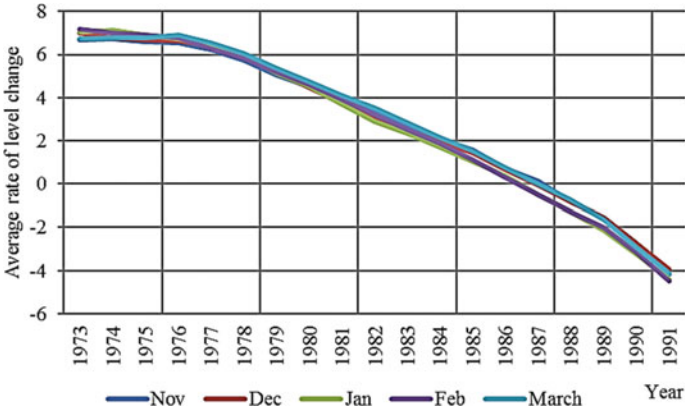

Fig. 3 Dependences on the beginning year of the angular coefficient of the linear trend of the monthly average values of the level of the North Caspian

Figure 2 shows the dependence on the year of the beginning of the "sliding window" with a duration of 30 years, the difference in the average values of the sums of atmospheric precipitation from November to March in Peshnoy and Atyrau, in relation to the climatic norm of this indicator corresponding to the period 1961–1990.

Figure 2 shows the dependences are increasing at both stations. At the same time, the values of the climatic norms of this indicator for the periods 1981–2010 and 1991–2020 practically coincide. Therefore, the revealed trend towards an increase in its climatic norms is not sustainable.

When solving the second objective, changes in the average rates of interannual changes in the level of the North Caspian and characteristics of ice conditions were studied. Figure 3 shows the dependences on the beginning year of the angular coefficient of the linear trend of the monthly average values of the level of the North Caspian.

It follows from Fig. 3 that over time intervals of 30 years, beginning from 1973 to 1987, the average monthly values of the North Caspian Sea level for November–March increased, but the average rates of these processes decreased. In "sliding windows" beginning after 1987, the monthly average values of the same indicators are decreasing.

As follows from Fig. 1 and from [26], one of the reasons for this may be climate warming in the North Caspian region, which contributes to an increase in the intensity of water evaporation from the water surface. It should be noted that the reason of North Caspian level decreasing is not the main one. This is evidenced by Fig. 4, which shows the changes in the differences between the Northern Caspian average levels and the entire Caspian Sea for the period November–March in relation to the base values of these indicators [36].

Evaporation in the water balance of the North Caspian is more significant than in the water balance for the entire Caspian Sea. The maximum dependence of the Caspian Sea average level is observed in 1985–2014, while for the North Caspian

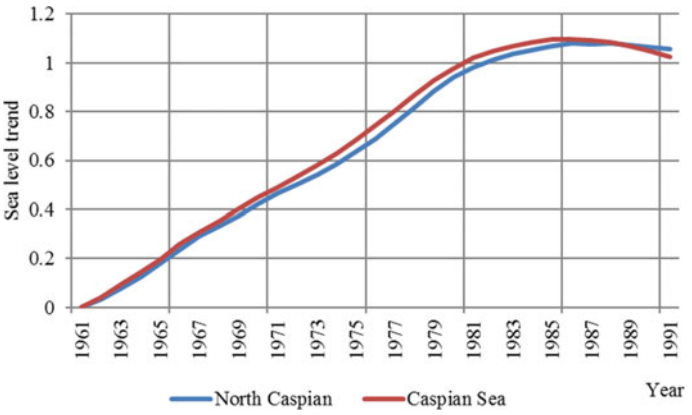

Fig. 4 Dependences between the North Caspian averages levels for the period from November to March and the entire Caspian Sea

the maximum is in 1986–2015. Consequently, the main reason for the change in the North Caspian average level is the change in the level of the entire Caspian Sea, which depends on its water balance and the basin climate.

Figure 5 shows the year dependences of the coefficient of the linear trend of interannual changes in the ice thickness of the North Caspian.

Figure 5 shows the indicators are increasing at both stations. At Peshnoy station, the average rate of change in ice thickness for the period 1973–2020 decreased. And it should be assumed that in the coming years these values may start to increase. At Atyrau station, the sign of the mean rate of increase in ice thickness has already changed. And since 1981, the values of this indicator have been increasing rapidly, despite the warming of the climate in the North Caspian region. It follows from this

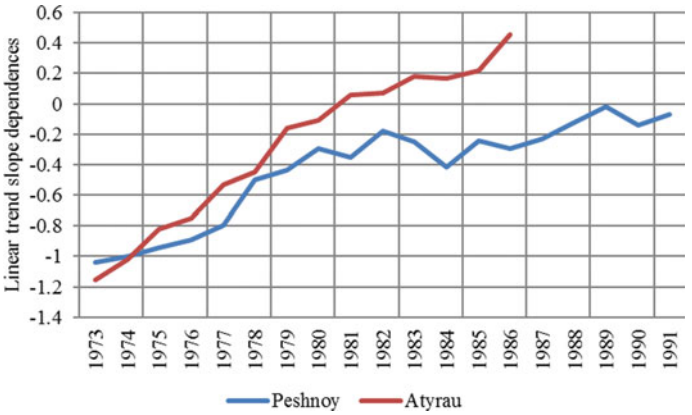

Fig. 5 Dependences of the coefficient of the linear trend of interannual changes in the ice thickness of the North Caspian

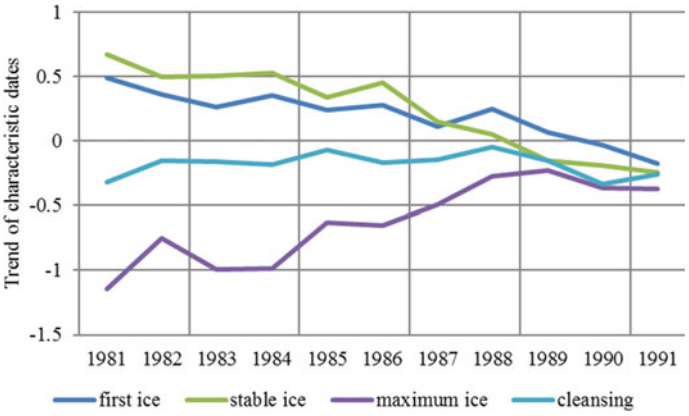

Fig. 6 Dependences of the characteristic dates of the ice regime for Peshnoy station

that the warming of the regional climate does not significantly affect the interannual changes in the ice thickness of the North Caspian.

Figure 6 shows the dependences of the characteristic dates of the ice regime for Peshnoy station.

From Fig. 6 the dependences of the linear trend coefficient of the first dates of ice formation and dates of stable ice decrease. The dates of the appearance of the first ice from 1981 to 1990 are increasing, which corresponds to the warming of the regional climate. At the same time, the average rate of this process decreased, but in the modern period 1991–2020, the dates of the appearance of ice are increasing, despite the warming of the regional climate. The dates of stable ice also increased, but at a slower rate. In the modern period, stable ice at Peshnoy station also forms earlier.

The ice is cleared from the sea earlier, as it should have been during the warming of the regional climate. In this case, the value of the linear trend coefficient approaches zero.

Ice of maximum thickness in the Northern Caspian is observed from January to March. The maximum ice formed earlier, and its maximum thickness became smaller, as it should have happened with a decrease in the clearing date. In the period 1991–2020, the value of the linear trend coefficient of the maximum ice thickness date in absolute value increased.

Figure 7 shows the dependence on the year of the beginning of the "sliding window" of the corresponding value of the coefficient of the linear trend of interannual changes in the duration of the ice period in the North Caspian.

It is clear from Fig. 7 that in the period 1981–2020, the values of interannual changes in the duration of the ice period in the North Caspian were negative. Nevertheless, the average rate of decrease in the duration of the ice period decreased even though, as can be seen from Fig. 1, the rate of warming of the local climate did not decrease.

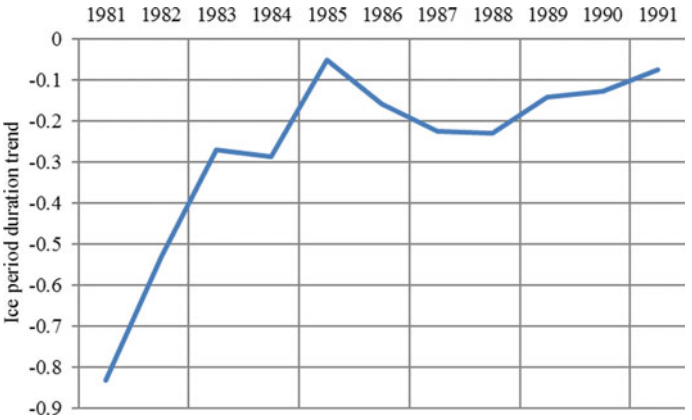

Fig. 7 Dependence on the year of the beginning of the "sliding window" of the corresponding value of the coefficient of the linear trend of interannual changes in the duration of the ice period in the North Caspian

Thus, it was established that the tendencies of changes in the characteristics of ice conditions in the North Caspian in the modern period were opposite to those that would have been possible with a warming of the regional climate [6, 26].

The revealed feature indicates that the interdecadal variability of these indicators is caused not by changes in the characteristics of thermal exchange between surface waters and atmosphere, but by another factor. Such a factor may be a level change, which affects the currents and water exchange of the North Caspian with other regions of the Caspian Sea.

This factor can lead to a decrease in the values of the thermal balance of the surface waters of the Northern Caspian. From Figs. 3, 4, 5, 6 and 7, such currents really affect the interdecadal variability of all indicators of the North Caspian. With a decrease in the level of the Northern Caspian, the flow rates of these currents decrease, therefore, the values of the heat balance decrease, and ice conditions change as if the climate was cooling in its region.

When solving the third problem, the statistical relationships of interannual changes in the mean monthly level values at the Peshnoy post were studied. The dependences on the year of the beginning of 30-year "sliding windows" of the corresponding values of the correlation coefficient between the time series segments of the ice thickness and the monthly average values of the level for November–March are shown in Fig. 8.

Figure 8 shows statistical relationships between changes in the Northern Caspian level and variations in ice thickness at any time intervals of 30 years, except for the modern period, were not significant. At the same time, for the period 1991–2020, the conclusion about the significance of such a relationship for March is characterized by a reliability of at least 0.95. For November, January and on average for the months under consideration, the reliability of such a conclusion exceeds 0.9. Significant correlation of the considered processes is positive.

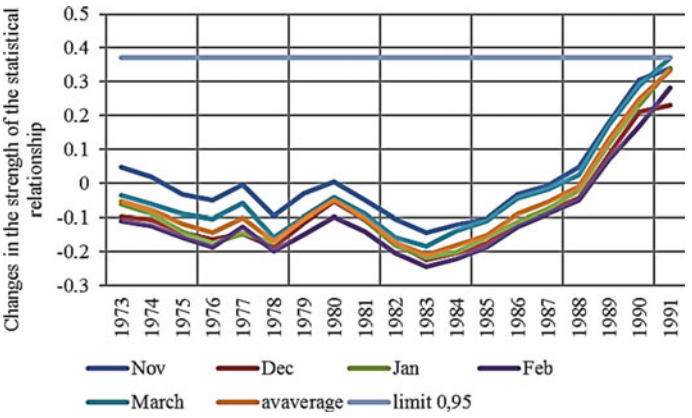

Fig. 8 Dependences of the values of the correlation coefficient of interannual changes in the level and ice thickness calculated for it on the year of the beginning of the 30-year "sliding window" for Peshnoy station

As mentioned above, some currents of the Caspian Sea deliver water to the North Caspian, which in November–March has a lower temperature. Such waters are formed at the estuary of the Volga River. Because the river basin is located farther north, the temperature of its waters is lower than the temperature of its surface waters. In addition, the water in the river is insipid and has a lower density than sea water. And this reduces the thermal balance. The less they enter the North Caspian, the less ice is thick in it. Therefore, the correlation of the considered processes is positive.

Figure 9 as an example, shows the dependences on the year of the beginning of a 30-year "sliding window" of the corresponding value of the correlation coefficient

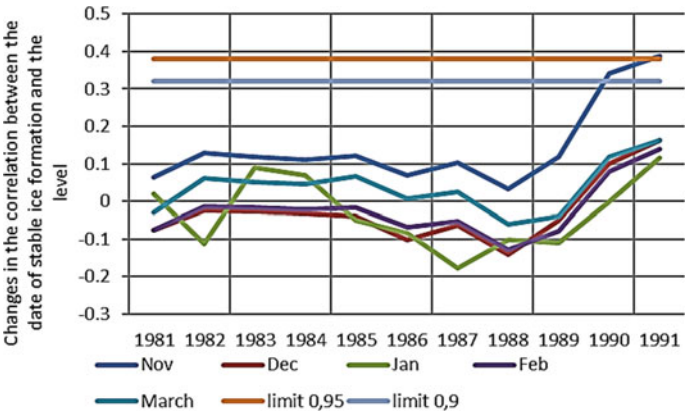

Fig. 9 Dependences on the year of the beginning of a 30-year "sliding window" of the corresponding value of the correlation coefficient of interannual changes in the Caspian Sea level in November–March, with variations in the date of stable ice

of interannual changes in the Caspian Sea level in November–March, with variations in the date of stable ice.

Figure 9 shows that the correlation is positive for the November of modern period and exceeds 0.9. In a similar way, it was found that the correlation of interannual changes in the duration of the ice period and the monthly average values of the North Caspian level in November–March 1981–2020 was not significant. At the same time, there are increasing trends in the changes. In the modern period its values are positive.

Thus, the results were obtained that the interannual variability of the North Caspian level is influenced by the flow rates of currents that carry cold waters into it. They strongly influence the ice thickness and ice regime dates. Therefore, the hypothesis put forward is valid.

4 Discussion

The analysis of the results shows that on the interdecadal variability of ice conditions in the North Caspian, the prevailing influence is exerted by variations in current flow rates. In the interval of their interannual variability, currents that bring colder water to the North Caspian have a stronger effect. It follows from this that with a further decrease in the Northern Caspian level tendencies towards more complicated ice conditions will prevail in it. The values of the ice thickness and the duration of the ice period and possibly the dates of the maximum ice thickness and the date when the sea was cleared of ice, will increase, while the values of the dates of the first and stable ice will decrease.

Such a forecast contradicts the conclusions [7–9, 22, 23], according to which, in the second half of the XX–beginning of the XXI century, the values of the maximum ice thickness for the Northern Caspian decreased.

Indeed, in 1940–1950 the maximum ice thickness was often more than 1 m and at the beginning of the XXI century they were not 50 cm. During this time the duration of the ice period in the Northern Caspian decreased by 18 days, because ice appears 13 days later and melts 6 days earlier. The appearance of the first ice at Peshnoy station occurs 4 days later and the maximum ice thickness reaches 13 days closer to the beginning of the year [18].

As follows from the results, the thermal exchange of the Northern Caspian waters with the waters of other Caspian Sea regions it has a greater effect on ice conditions than thermal exchange with the atmosphere.

The main reason for the change in North Caspian ice conditions is level fluctuations. Changes in the average monthly volumes of water brought by the Volga River affect the sea level. This, in turn, depends on climate change and water consumption in agriculture [26].

With a further warming of the climate, the intensity of evaporation from the Volga River will increase as well as the volume of its water withdrawal for the needs of agriculture. As a result, the volume of its waters entering the Caspian Sea will decrease, leading to a decrease in the values of its water balance.

Consequently, the scenario in which a further decrease in the Caspian Sea level will occur in the future can indeed be regarded as the most realistic.

The results obtained indicate that for other freezing water bodies, changes in their level in the winter season can be a significant factor in variations in ice conditions.

The shallow freezing water bodies include the Arctic seas through which the routes of the Northern Sea Route run. In the modern period, year-round navigation is carried out only in the Kara Sea [2, 34, 35], into which, like the Caspian Sea, full-flowing rivers flow. In contrast to the Northern Caspian, the level of the Kara Sea in the modern period is increasing, although the ice conditions characteristic in winter and spring are also becoming more complicated here [15, 16]. The higher the sea level, the more difficult ice conditions are in winter.

5 Conclusion

Thus, using the example of the North Caspian Sea, it has been established that sea level variations are a significant factor in changes in ice conditions. The lower the sea level, the lower the flow rates of the currents.

The interdecadal variability of North Caspian ice conditions are most significantly affected by changes in the flow rates of currents bring warm water into it. Their interannual variability is influenced by the change in the flow rates of currents bringing colder water.

With a further decrease in the North Caspian level ice conditions in its water area will become more complicated, regardless of the ongoing warming of the regional climate.

The practical significance of the research is to substantiate the feasibility of considering, when planning shipping and fishing in the North Caspian, the factor of climate change in the Volga River area. This factor in the future can cause a significant complication of ice conditions in the North Caspian and affect the life safety of the population of the coastal territories of Russia and Kazakhstan.

Prospects for further research in this direction are due to the need to consider the results obtained when clarifying plans for the development of the marine economic complex of the North Caspian, as well as planning measures aimed at preventing emergencies in this region.

References

1. Abuzyarov Z.K., Nesterov E.S. (2011) Some features of spatial temporal changes in the level of the Caspian Sea // Proceedings of the Hydrometeorological Research Center of the Russian Federation. No. 345. p. 5–22.
2. Aksenov Ye. (2017) On the Future Navigability of Arctic Sea Routes: High-resolution Projections of the Arctic Ocean and Sea Ice. Ye. Aksenov, E. E. Popova, A. Yool. A. J. G. Nurser et al. Marine Policy. V. 75: 300–317.

3. Bolgov M.V., Krasnozhon G.F., Lyubushin A.A. (2007) Caspian Sea extreme hydrological events. - M.: Nauka, 381 p.
4. Bukharitsin P.I. (2019) Studies of the Caspian ice. - Palmarium Academic Publishing.122 p.
5. Bukharitsin P.I., Boldyrev B.Yu., Novikov V.I. (2014) Integrated system of hydrometeorological support for the safety of navigation, ports, and transport complexes in the Caspian Sea. Astrakhan, 319 p.
6. Climate Change: The Physical Science Basis. (2013) https://www.ipcc.ch/report/ar5/wg1/lncs, last accessed 2016/11/21.
7. Dumanskaya I.O. (2014) Ice conditions of the seas of the European part of Russia. Moscow: Hydrometeorological Center of Russia. 608 p.
8. Elguindi, N. & Giorgi, F. (2006) Projected changes in the Caspian Sea level for the 21st century based on the latest AOGCM simulations. Geophys. Res. Lett. 33, L08706.
9. Ivkina N.I., Terekhov A.G., Naurozbaeva Zh.K. (2015) Fluctuations in the level of the Caspian Sea and diagnostics of modern changes in the position of the coastline according to satellite data from lands at the period 2005–2015 // Hydrometeorology and ecology. No 2.- p. 89–99.
10. General catalog of the level of the Caspian Sea. Official site of CASPCOM. - [Electronic resource], 2020, http://www.caspcom.com/index.php?razd=sess&lang=1&sess=17&podsess=61.
11. Girs A.A. (1971) Long-term fluctuations in atmospheric circulation and long-term hydrometeorological forecasts. - L.: Hydrometeoizdat. p. 7–31.
12. History and physical-geographical description of meteorological stations and posts. (1968) KazSSR, Alma-ata. 545 p.
13. Hydrometeorology and hydrochemistry of the seas. (1992) volume VI. Caspian Sea. Hydrometeorological conditions. SPb.: Hydrometeoizdat, Issue. 1. -359 p.
14. Kholoptsev A.V., Podporin S.A. (2020) Changes in the 21st century in the average levels of the Caspian Sea. // Astrakhan Bulletin of Environmental Education. No. 3 (57). p. 11–21.
15. Kholoptsev A.V., Podporin S.A. (2020) Analysis of changes in ice conditions on the Northern Sea Route at the end of the XX - beginning of the XXI century. Bulletin of the S.O. Makarov.T.12. No. 1: p.71–84.
16. Kholoptsev A.V., Podporin S.A., Shubkin R.G. (2021) Variations in the Norwegian sea levels and the ice conditions of the Kara sea in winter-spring months // Book of abstract proceedings International Conference Arctic: Marine Transportation Challenges, Saint-Petersburg.
17. Lobanov V.A., Smirnov I.A., Shadurskiy A.E. (2011) Workshop on climatology. Part 1. (tutorial). St. Petersburg.144 p.
18. Naurozbaeva Zh.K., Lobanov V.A. (2020) Changes in the wind regime of the northern and middle Caspian in the cold half of the year. // Quarterly scientific and technical journal "Hydrometeorology and Ecology" No. 4. p. 36–45.
19. Nesterov E.S. (2013) The North Atlantic Oscillation: Atmosphere and Ocean. M.: TRIADA LDT.144 p.
20. Nikonova R.E. (2008) On the causes and consequences of long-term fluctuations in the level of the Caspian Sea in the XX-XXI centuries // Proceedings of GOIN. Issue. 211.p. 127–151.
21. Nikonova R.E. (2011) On fluctuations in the level of the Caspian Sea and the current state of the observation network // Caspian Bulletin. No. 2. p. 72-81.
22. Ogorodov S.A., Arkhipov V.V., Zemlyanov I.V., Tsvetsinsky A.S. (2014) The impact of ice cover on the bottom of the northern Caspian in conditions of level fluctuations and ice coverage // Proceedings of the State Oceanographic Institute. No. 215. p. 170–182.
23. Panin G.N., Vyruchalkina T.Yu., Solomonova I.V. (2015) Climatic changes in the Arctic, North Atlantic, the Caspian region and their relationship. // Fundamental and Applied Climatology.Vol. 1. p. 183–210.
24. Prange M., Wilke T., Wesselingh F.P. (2020) The other side of sea level change. // Communications Earth & Environment. No. 69. https://doi.org/10.1038/s43247-020-00075-6.
25. Reference and analytical review of the hydrological regime of the mouth areas of the Volga, Terek, Sulak rivers. (2016) Moscow: FGBU "GOIN".74 p.

26. Roshydromet (2014) The second assessment report of Roshydromet on climate changes and their consequences on the territory of the Russian Federation. Moscow: 1009 p.
27. Shuleikin V.V. (1968) Physics of the sea. M.: Science. 1083 p.
28. Statistical methods in hydrology. (1970) Ed. Alekseeva G.A. L.: Hydrometeorological publishing house. 271 p.
29. Tuzhilkin V.S., Kosarev A.N., Arkhipkin V.S., Nikonova R.E. (2011) Long-term variability of the hydrological regime of the Caspian Sea due to climate variations. // Bulletin of Moscow University. Series 5: Geography No. 2. p. 62–71.
30. Frolov I.E. (2011) Oceanography and Sea Ice. Paulsen: 432 p.
31. Frolov A.V. (2019) Features of the mechanism of long-term fluctuations in the level of the Caspian Sea. // Scientific notes of the Russian State Hydrometeorological University. No. 55. p. 120-128.
32. Yagotintsev V.N., Postavik P.V. (2013) The level of the Caspian Sea in the past and present. // Proceedings of the Geographical Society of the Republic of Dagestan. No. 41. p. 26–40.
33. Water balance and fluctuations in the level of the Caspian Sea. Modeling and forecasting. (2016) Ed. Nesterova E.S. M.: Triada LTD. 378 p.
34. Wine, M. L. & Davison, J. H. (2019) Untangling global change impacts on hydrological processes: resisting climatization. Hydrol. Processes 33. p. 2148–2155.
35. Woolway, R. I. et al. (2020) Global Lake response to climate change. Nat. Rev. Earth Environ. 1. p.388–403.
36. WMO Guidelines for the Calculation of Climate Norms. (2017) WMO No. 1203. 32p.
37. Zachs L. (1976) Statistical estimation. Moscow: Statistics.598 p.

Analytical Solution of the Equation for the Stream Function in the Model of Ekman-Type Flows with Variable Wind Stress in Space

V. S. Kochergin, S. V. Kochergin, and S. N. Sklyar

Abstract In this paper, we consider a mathematical model of wind currents in a rectangular reservoir of constant depth. The analysis was carried out on the basis of the dimensionalization procedure and the subsequent exclusion of terms describing advection and horizontal diffusion from the system of equations. Additional limitations are that the components of the tangential wind friction stress are set according to a special law that allows describing complex wind situations. Within the framework of the above limitations, we manage to find analytical solutions for the integral components of the horizontal flow velocity. Note that the accepted restrictions are quite soft and allow you to save the most important properties of the simulated objects in the model. This makes it possible, when choosing the main parameters in the model that reflect the specifics of the reservoir, to obtain some properties of currents in this reservoir "in the first approximation".

Keywords Dimensionless problem · Wind currents · Test problem · Analytical solution · Current function · Integral velocity

1 Introduction

Numerical modeling of ocean dynamics is an important and urgent task [1] in solving which it is necessary to use methods and algorithms that allow obtaining solutions corresponding to objective reality. But the models themselves and especially the modeling object are quite complex, so most often the comparison of the results obtained from different models are compared with each other. This approach is subjective and strongly depends on the preferences of the researcher, the traditions of the scientific school, etc. Another approach can be proposed. Simplify the model

V. S. Kochergin (✉) · S. V. Kochergin
Marine Hydrophysical Institute RAS, Russian Federation, 299029 Sevastopol, Russia

S. N. Sklyar
American University of Central Asia, Bishkek, Kyrgyzstan

© The Author(s), under exclusive license to Springer Nature Switzerland AG 2022

V. I. Karev (ed.), *Physical and Mathematical Modeling of Earth and Environment Processes*,
Springer Proceedings in Earth and Environmental Sciences,
https://doi.org/10.1007/978-3-030-99504-1_16

itself and the object of study to such an extent that we were able to build an analytical solution to the problem and, using this example, tested the schemes and methods used in the numerical implementation of hydrodynamic models. The use of adequate schemes and methods does not exclude the use of high discretization. However, the development of the models themselves and the methods of their numerical implementation allows us to obtain similar results using less computing resources. Analytical solutions exist for the simplest statements, for example, the Stommel model [2–4]. In [5, 6], such a task is implemented using the dynamic operator inversion method to test the special-type difference schemes used to calculate velocity fields. In [7–9], a model is investigated that takes into account the variability of velocity in all three directions, which allows analyzing the accuracy of calculating not only its horizontal components, but also the vertical component. The solution was obtained by specifying the simplest wind action. As a result of numerical experiments, the advantage of the run-through algorithm in calculating the vertical velocity is shown. In this paper, the components of the shear stress of wind friction are set according to a special law that allows describing complex wind situations.

2 the Problem in Dimensionless Form

We assume that the surface of some reservoir in the xOy plane has the shape of a rectangle:

$$\Omega_0 = [0, r] \times [0, q],$$

its depth $H > 0$ is constant. The axes of the Cartesian coordinate system are directed as follows: Ox—to the east, Oy—to the north, Oz—vertically down. In the three-dimensional domain:

$$\Omega = \{(x, y, z) | (x, y) \in \Omega_0, 0 \le z \le H\}.$$

consider the following model of Ekman-type wind currents:

$$\begin{cases} -lv = -\frac{\partial P^s}{\partial x} + \frac{\partial}{\partial z}\left(k\frac{\partial u}{\partial z}\right) \\ lu = -\frac{\partial P^s}{\partial y} + \frac{\partial}{\partial z}\left(k\frac{\partial u}{\partial z}\right), t > 0, (x, y, z) \in \Omega^0, \\ \frac{\partial U}{\partial x} + \frac{\partial V}{\partial y} + \frac{\partial W}{\partial z} = 0 \end{cases} \quad (1)$$

with boundary conditions:

$$\begin{gathered}\left\{z=0,(x,y)\in\Omega_{0,}^{0}\right\}:k\frac{\partial u}{\partial z}=-\tau_x,k\frac{\partial V}{\partial z}=-\tau_y,w=0;\\ \left\{z=H,(x,y)\in\Omega_{0,}^{0}\right\}:k\frac{\partial u}{\partial z}=-\tau_x^b,k\frac{\partial V}{\partial z}=-t_y^b,w=0;\\ \{0\geq z\geq H,(x,y)\in\partial\Omega_0\}:U\cdot n_x+V\cdot n_y=0,\end{gathered}\tag{2}$$

where Ω^0—interior domain. Integral velocities are defined as:

$$U(x,y)=\int_0^H u(x,y,z)dz,\ V(x,y)=\int_0^H v(x,y,z)dz,\tag{3}$$

and in (2) the following variant of parametrization of bottom friction is accepted:

$$\tau_x^b=\mu\cdot U,\tau_y^b=\mu\cdot V,\mu\equiv const>0.\tag{4}$$

According to the Stommel model [2–4], assume that:

$$l=l_0+\beta\cdot y,\ k=const;\tag{5}$$

the components of the wind stress friction will be given by the following formulas:

$$\begin{cases}\tau_x=[F_1\cdot cos(r_l x)+F_2\cdot sin(r_l x)]\cdot cos(q_m y)\\ \tau_y=[G_1\cdot cos(r_s x)+G_2\cdot sin(r_s x)]\cdot sin\left(q_p y\right)\end{cases}\tag{6}$$

in which the designations are accepted:

$$r_l=\frac{\pi l}{r};\ r_s=\frac{\pi s}{r};\ q_m=\frac{\pi m}{q};\ q_p=\frac{\pi p}{q};\tag{7}$$

$$l,s=0,1,2,\ldots;\ m,p=1,2\ldots.$$

Thus, the wind model contains four real: F_1, F_2, G_1, G_2 and four integer: l, s, m, p numerical parameters, the choice of which makes it possible to describe a fairly general wind situation. For example, if $F_1=\frac{F\cdot q}{\pi}$, $F_2=G_1=G_2=0$; $l=0$; $m=1$ we have

$$\tau_x=\frac{F\cdot q}{\pi}\cos\left(\frac{\pi y}{q}\right),\tau_y=0,\tag{8}$$

and when

$$F_1=\frac{F\cdot q}{\pi},\ F_2=0;G_1=-\frac{F\cdot q}{\pi};\ G_2=0\ l=0;\ m=1\tag{9}$$

we have a cyclone over the water area.

3 Analytical Solution

In (1) we integrate each equation vertically in the range from 0 to H, taking into account the boundary conditions, we obtain a problem for integral velocities:

$$\begin{cases} \mu U - lv = -H\frac{\partial P^s}{\partial x} + \tau_x, \\ lU + \mu V = -H\frac{\partial P^s}{\partial y} + \tau_y, \\ \frac{\partial U}{\partial x} + \frac{\partial V}{\partial y} = 0, (x, y) \in \Omega^0, U \cdot n_x + V \cdot n_y = 0, (x, y) \in \partial\Omega_0. \end{cases} \tag{10}$$

From the first two equations in (10), we exclude pressure gradients using cross-differentiation:

$$\begin{cases} \mu\left(\frac{\partial U}{\partial y} - \frac{\partial V}{\partial x}\right) - \beta V = \frac{\partial \tau_x}{\partial y} - \frac{\partial \tau_y}{\partial x}, \\ \frac{\partial U}{\partial x} - \frac{\partial V}{\partial y} = 0, (x, y) \in \Omega_0^0; \\ U \cdot n_x + V \cdot n_y = 0, (x, y) \in \partial\Omega_0. \end{cases} \tag{11}$$

To solve problem (11), we introduce the stream function by the formulas:

$$U = \frac{\partial \Psi}{\partial y}, V = -\frac{\partial \Psi}{\partial x}.$$

For the stream function, we get the following problem:

$$\begin{cases} \mu\left(\frac{\partial^2 \Psi}{\partial x^2} + \frac{\partial^2 \Psi}{\partial y^2}\right) + \beta\frac{\partial \Psi}{\partial x} = \frac{\partial \tau_x}{\partial y} - \frac{\partial \tau_y}{\partial x}, (x, y) \in \partial\Omega_{0,}^0 \\ \Psi = 0, (x, y) \in \partial\Omega_0 \end{cases} \tag{12}$$

The solution of problem (12) is represented as the sum of two functions:

$$\Psi(x, y) = \Psi_1(x, y) + \Psi_2(x, y),$$

which satisfy the following tasks:

$$\begin{cases} \mu\left(\frac{\partial^2 \Psi_1}{\partial x^2} + \frac{\partial^2 \Psi_1}{\partial y^2}\right) + \beta\frac{\partial \Psi_1}{\partial x} = \frac{\partial \tau_x}{\partial y}, (x, y) \in \partial\Omega_{0,}^0 \\ \Psi_2 = 0, (x, y) \in \partial\Omega_0; \end{cases} \tag{13}$$

$$\begin{cases} \mu\left(\frac{\partial^2 \Psi_2}{\partial x^2} + \frac{\partial^2 \Psi_2}{\partial y^2}\right) + \beta\frac{\partial \Psi_2}{\partial x} = -\frac{\partial \tau_y}{\partial x}, (x, y) \in \partial\Omega_0^0, \\ \Psi_2 = 0, (x, y) \in \partial\Omega_0. \end{cases} \tag{14}$$

We are looking for a solution to each of the problems (13), (14) within the framework of the traditional approach: first we find a partial solution of the equations from (13), (14), then a general solution of the corresponding homogeneous equations (this is the same equation for both cases), consider their sum, and finally satisfy the boundary conditions of these problems using the arbitrariness contained in the general solution of the homogeneous equation.

In [5], analytical expressions for the barotropic velocity component, additional components and the vertical velocity component for the task were obtained. The obtained analytical solutions for velocities were used for calculation in various ways, including according to the formula obtained in [5].

4 Partial Solutions

Let $\overline{\Psi}_1(x, y)$ be a partial solution of the equation from (13), then, taking into account the formula (8):

$$\mu\left(\frac{\partial^2\overline{\Psi}_1}{\partial x^2}+\frac{\partial^2\overline{\Psi}_1}{\partial y^2}\right)+\beta\frac{\partial\overline{\Psi}_1}{\partial x}=-q[F_1\cdot\cos(r_l x)+F_2\cdot\sin(r_l x)]\cdot\sin(q_m y),$$

$$(x, y)\in\partial\Omega_{0.}^{0} \tag{15}$$

We will look for a partial solution of Eq. (15) in the form:

$$\Psi_1(x, y)=[D_1\cdot\cos(r_l x)+D_2\cdot\sin(r_l x)]\cdot\sin(q_m y). \tag{16}$$

After substituting the function $\overline{\Psi}_1(x, y)$ into Eq. (15), we can find

$$D_1=\frac{\mu\left({r_l}^2+{q_m}^2\right)F_1+\beta r_l F_1}{\mu^2\left({r_l}^2+{q_m}^2\right)^2+\beta^2{r_l}^2}\cdot q_m,\quad D_2=\frac{\mu\left({r_l}^2+{q_m}^2\right)F_2-\beta r_l F_1}{\mu^2\left({r_l}^2+{q_m}^2\right)^2+\beta^2{r_l}^2}\cdot q_m. \tag{17}$$

Similarly, to determine $\overline{\Psi}_2(x, y)$ the partial solution of the equation from (14), using (8), we obtain:

$$\mu\left(\frac{\partial^2\overline{\Psi}_2}{\partial x^2}+\frac{\partial^2\overline{\Psi}_2}{\partial y^2}\right)+\beta\frac{\partial\overline{\Psi}_2}{\partial x}=r_s[G_1\cdot\sin(r_s x)-G_2\cdot\cos(r_s x)]\cdot\sin\left(q_p y\right),$$

$$(x, y)\in\partial\Omega_{0.}^{0} \tag{18}$$

We present the solution of Eq. (18) as:

$$\overline{\Psi}_2(x, y)=\left[\overline{D}_1\cdot\cos(r_s x)+\overline{D}_2\cdot\sin(r_s x)\right]\cdot\sin\left(q_p y\right), \tag{19}$$

where:

$$\overline{D}_1 = -\frac{\beta r_s G_1 - \mu\left(r_s{}^2 + q_p{}^2\right)G_2}{\mu^2\left(r_s{}^2 + q_p{}^2\right)^2 + \beta^2 r_s{}^2} \cdot r_s,\ \overline{D}_2 = -\frac{\mu\left(r_s{}^2 + q_p{}^2\right)G_1 + \beta r_s G_2}{\mu^2\left(r_s{}^2 + q_p{}^2\right)^2 + \beta^2 r_s{}^2} \cdot r_s.$$

5 General Solution

Let ‘s write down the required homogeneous equation:

$$\mu\left(\frac{\partial^2\overline{\Psi}_0}{\partial x^2} + \frac{\partial^2\overline{\Psi}_0}{\partial y^2}\right) + \beta\frac{\partial\overline{\Psi}_0}{\partial x} = 0,\ (x, y) \in \partial\Omega_0^0. \tag{20}$$

Since the area Ω_0^0, is a rectangle, we will look for the solution of Eq. (20) in the form:

$$\overline{\Psi}_0(x, y) = X(x) \cdot Y(y). \tag{21}$$

Substitute function (21) into Eq. (20) and, following the method of separation of variables, we obtain:

$$\frac{\mu X^{''} + \beta X^{'}}{X} = -\frac{\mu Y^{''}}{Y} \equiv W \equiv const.$$

We will rewrite the last relations in the form of the following equations:

$$\mu Y'' + \omega Y' = 0,\ y \in (0, q), \tag{22}$$

$$\mu X'' + \beta X' - \omega X = 0,\ x \in (0, r). \tag{23}$$

Solve Eq. (22), counting $\omega > 0$, we get:

$$Y(y) = K_1 \cdot \cos\left(\sqrt{\frac{\omega}{\mu}} \cdot y\right) + K_2 \cdot \sin\left(\sqrt{\frac{\omega}{\mu}} \cdot y\right), \tag{24}$$

where K_1 and K_2 are arbitrary real constants. To solve Eq. (23), consider the “characteristic equation”:

$$\mu A^2 + \beta A - \omega = 0$$

and we will find its roots:

$$A = -\frac{\beta}{2\mu} + \sqrt{\left(\frac{\beta}{2\mu}\right)^2 + \frac{\omega}{\mu}}, B = -\frac{\beta}{2\mu} - \sqrt{\left(\frac{\beta}{2\mu}\right)^2 + \frac{\omega}{\mu}}. \quad (25)$$

Now, the general solution of Eq. (23) is written as:

$$X(x) = C_1 e^{Ax} + C_2 e^{Bx}. \quad (26)$$

Finally, we will write the solution of the equation from (13) found by us in the form:

$$\Psi_1(x, y) = \Psi_0(x, y) + \overline{\Psi}_1(x, y) = X(x)Y(y) + \overline{\Psi}_1(x, y). \quad (27)$$

Satisfying the boundary conditions, one can obtain:

$$\Psi_1(x, y) = \left[C_1 e^{Ax} + C_2 e^{Bx} + D_1 \cdot \cos(r_l x) + D_2 \cdot \sin(r_l x)\right] \cdot \sin(q_m y), \quad (28)$$

where

$$C_1 = D_1 \cdot \frac{e^{Br} - (-1)^l}{e^{Ar} - e^{Br}}, \; C_2 = D_1 \cdot \frac{(-1)^l - e^{Ar}}{e^{Ar} - e^{Br}}. \quad (29)$$

These arguments can be used to construct a solution $\Psi_2(x, y)$ to the problem (14).

6 Basic Formulas for the Stationary Model

Let's put together all the formulas necessary for programming. First we write out the formulas for the stream function. Solving the problem (12):

$$\Psi(x, y) = \Psi_1(x, y) + \Psi_2(x, y);$$

according to the formula (28):

$$\Psi_1(x, y) = \left[C_1 e^{Ax} + C_2 e^{Bx} + D_1 \cdot \cos(r_l x) + D_2 \cdot \sin(r_l x)\right] \cdot \sin(q_m y),$$

where:

$$D_1 = \frac{\mu\left({r_l}^2 + {q_m}^2\right)F_1 + \beta r_l F_2}{\mu^2\left({r_l}^2 + {q_m}^2\right)^2 + \beta^2 {r_l}^2} \cdot q_m, \; D_2 = \frac{\mu\left({r_l}^2 + {q_m}^2\right)F_2 - \beta r_l F_1}{\mu^2\left({r_l}^2 + {q_m}^2\right)^2 + \beta^2 {r_l}^2} \cdot q_m,$$

and, in accordance with (29), (25):

$$C_1 = D_1 \cdot \frac{e^{Br} - (-1)^l}{e^{Ar} - e^{Br}},\ C_2 = D_1 \cdot \frac{(-1)^l - e^{Ar}}{e^{Ar} - e^{Br}};$$

$$A = -\frac{\beta}{2\mu} + \sqrt{\left(\frac{\beta}{2\mu}\right)^2 + (q_m)^2},\ B = -\frac{\beta}{2\mu} - \sqrt{\left(\frac{\beta}{2\mu}\right)^2 + (q_m)^2}.$$

Similar formulas for the second component of the solution:

$$\Psi_2(x, y) = \left[\overline{C}_1 e^{\overline{A}x} + \overline{C}_2 e^{\overline{B}x} + \overline{D}_1 \cdot \cos(r_s x) + \overline{D}_2 \cdot \sin(r_s x)\right] \cdot \sin\left(q_p y\right),$$

where

$$\overline{D}_1 = -\frac{\beta r_s G_1 - \mu\left({r_s}^2 + {q_p}^2\right)G_2}{\mu^2\left({r_s}^2 + {q_p}^2\right)^2 + \beta^2 {r_s}^2} \cdot r_s,\ \overline{D}_2 = -\frac{\mu\left({r_s}^2 + {q_p}^2\right)G_1 + \beta r_s G_2}{\mu^2\left({r_s}^2 + {q_p}^2\right)^2 + \beta^2 {r_s}^2} \cdot r_s$$

and, in accordance with (29), (25):

$$\overline{C}_1 = \overline{D}_1 \cdot \frac{e^{\overline{B}r} - (-1)^s}{e^{\overline{A}r} - e^{\overline{B}r}},\ \overline{C}_2 = \overline{D}_1 \cdot \frac{(-1)^s - e^{\overline{A}r}}{e^{\overline{A}r} - e^{\overline{B}r}};$$

$$\overline{A} = -\frac{\beta}{2\mu} + \sqrt{\left(\frac{\beta}{2\mu}\right)^2 + (q_m)^2},\ \overline{B} = -\frac{\beta}{2\mu} - \sqrt{\left(\frac{\beta}{2\mu}\right)^2 + (q_m)^2}.$$

The integral components of the horizontal velocity vector are obtained by differentiation, in accordance with the formulas:

$$U = \frac{\partial \Psi}{\partial y},\ V = \frac{\partial \Psi}{\partial x}$$

$$\begin{aligned} U(x, y) =& \frac{\partial}{\partial y}[\Psi_1(x, y) + \Psi_2(x, y)] \\ =& q_m \cdot \left[C_1 e^{Ax} + C_2 e^{Bx} + D_1 \cdot \cos(r_l x) + D_2 \cdot \sin(r_l x)\right] \cdot \cos(q_m y) \\ &+ q_p \cdot \left[\overline{C}_1 e^{\overline{A}x} + \overline{C}_2 e^{\overline{B}x} + \overline{D}_1 \cdot \cos(r_s x) + \overline{D}_2 \cdot \sin(r_s x)\right] \cdot \cos\left(q_p y\right), \end{aligned}$$

$$\begin{aligned} V(x, y) =& -\frac{\partial}{\partial x}[\Psi_1(x, y) + \Psi_2(x, y)] \\ =& -\left[AC_1 e^{Ax} + BC_2 e^{Bx} - r_l D_1 \cdot \sin(r_l x) + r_l D_2 \cdot \cos(r_l x)\right] \cdot \sin(q_m y) \\ &- \left[\overline{AC}_1 e^{\overline{A}x} + \overline{BC}_2 e^{\overline{B}x} - r_s \overline{D}_1 \cdot \sin(r_s x) + r_s \overline{D}_2 \cdot \sin(r_s x)\right] \cdot \sin\left(q_p y\right). \end{aligned}$$

7 Results of Numerical Experiments

To illustrate, consider as a model object a rectangular pond with a flat bottom with the characteristic dimensions of the Black Sea:

$$a = 11 \cdot 10^7(sm) = 1100(km),\ R = 0.046\left(\frac{sm}{s}\right),\ b = 5 \cdot 10^7(sm) \approx 500(km),$$

$$D = 2 \cdot 10^5(sm) = 2000(m),\ G = 1\left(\frac{dyn}{sm^2}\right),\ E = 1\left(\frac{sm^2}{s}\right),\ \rho_0 = \frac{1kg}{sm^3},$$

$$f_0 = 10^{-4}(1/s),\ f_1 = 2 \cdot 10^{-13}\left(\frac{1}{sm} \cdot s\right).$$

Let's choose the characteristic scales:

$$L = 10^7(sm),\ \ h = 2 \cdot 10^5(sm),\ \ u_0 = 10(sm/s).$$

Then we have:

$$r = 11,\ \ q = 5,\ \ H = 1,\ \ k = 0.05;$$

$$l_0 = 1,\ \ \beta = 0.0017;$$

$$\beta = 0.(\text{without } \beta - \text{effect})$$

$$F = \frac{\pi}{2} \cdot 10^{-3},\ \mu = 0.0023;\ \ w_0 = 0.2.$$

Figure 1. shows the wind obtained by the formula (8). Such a wind was set in works [5–9] when analyzing the accuracy of calculating the vertical velocity. Figure 2. shows the values of the current function for a given wind action. The circulation is cyclical.

Using (6), it is possible to describe a rather complex wind situation. For example, Fig. 3. shows a cyclonic wind obtained by formula (6) with parameters (9) using the first decomposition modes. Note that due to the linearity of problem (12), each subsequent mode can be considered separately.

The current function corresponding to such a wind effect is shown in Fig. 4, which also has a cyclonic character.

Figures 2 and 4 show the exact, analytical values for the current function obtained under various wind effects. It is clear that problem (12) can be solved numerically by one of the known methods using various difference discretization. Comparing the obtained solutions with the exact one, it is possible to evaluate the quality of a particular numerical scheme.

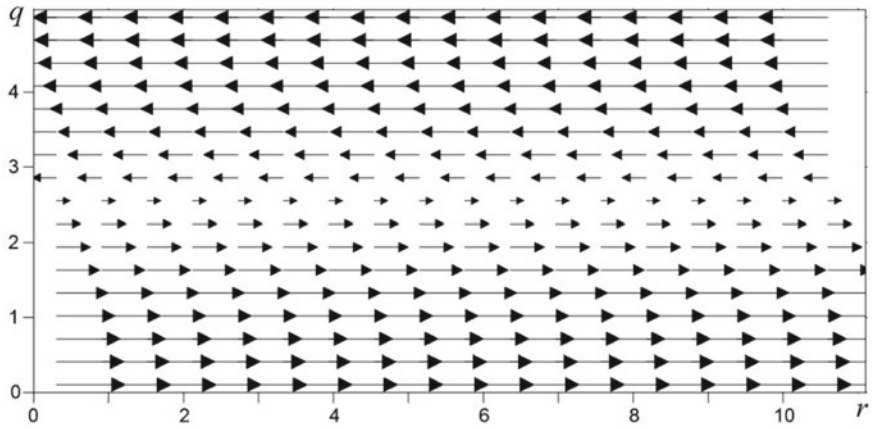

Fig. 1 The wind is given by the formula (8)

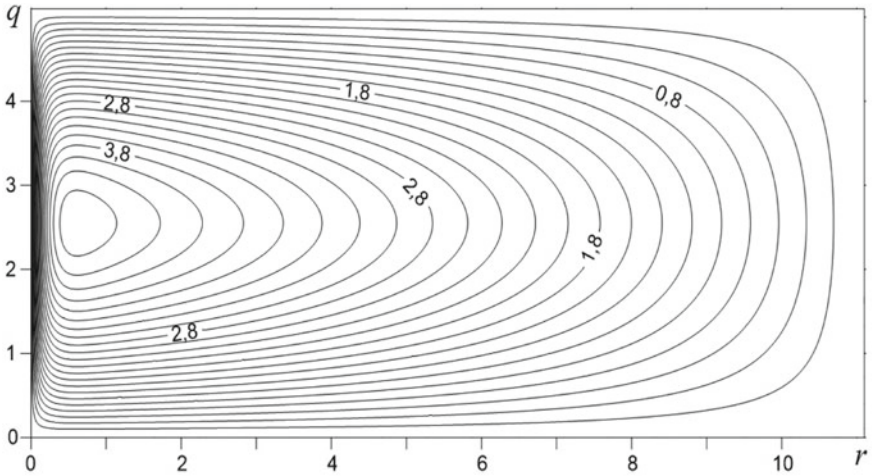

Fig. 2 The function of the current at the wind given by the formula (8)

8 Conclusions

For the problem of Ekman-type wind circulation, an analytical solution is obtained for a space-variable wind effect. The obtained solutions can be used as reference for testing various difference schemes. The results can be used to construct numerical models of the dynamics of the ocean and various reservoirs.

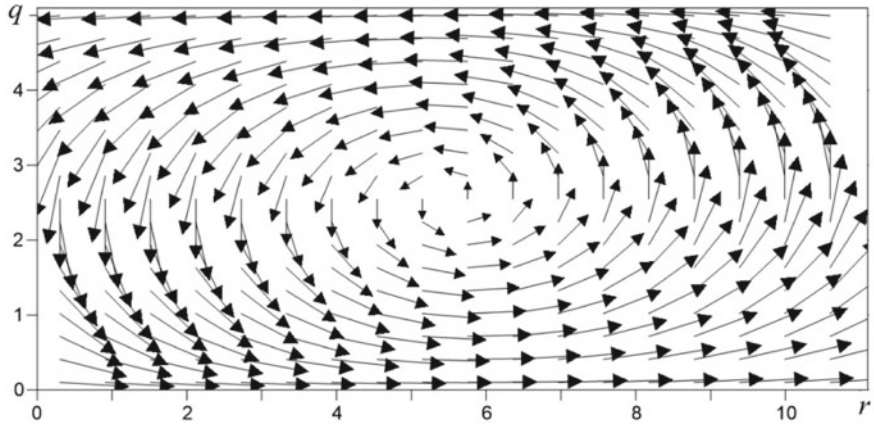

Fig. 3 Cyclonic wind with parameters (9)

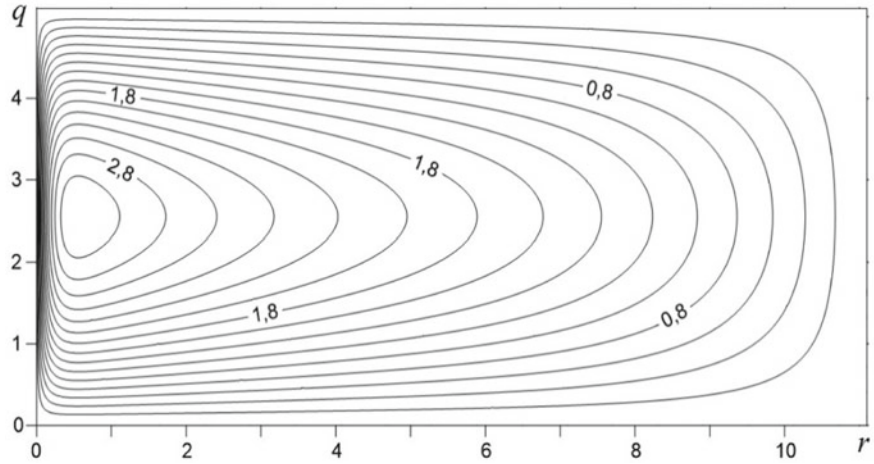

Fig. 4 Wind current function with parameters (9)

Acknowledgements The work was carried out within the framework of the state task on the topic 0555-2021-0005 "Complex interdisciplinary studies of oceanological processes that determine the functioning and evolution of ecosystems of the coastal zones of the Black and Azov Seas" (code "Coastal research").

References

1. Marchuk G.I., Sarkisyan A.S. Mathematical modeling of ocean circulation, Moskva: Nauka, 302 p. (1988).
2. Stommel H. The westward intensification of wind-driven ocean currents.- Trans. Amer. Geoph. Un., 1948, 29, p. 202–206.
3. Stommel, H. Gulf stream., Moscow: IL, 227p. (1965).
4. Stommel, H. The GULF STREAM. A Physical and Dynamical Description, University of California Press, 227p. (1965).
5. Eremeev V. N.,Kochergin V. P., Kochergin S. V., Sklyar S. N. Mathematical modeling of hydrodynamics of deep-water basins. ECOSI-Gidrophisika, Sevastopol, 238p. (2002).
6. Kochergin V.P., Dunets T.V. Computational algorithm of the evaluations of inclinations of the level in the problems of the dynamics of basins, Physical oceanography, №3, Vol. 11,p. p. 221−232 (2001).
7. Kochergin V.S., Kochergin S.V., Sklyar S.N. Analytical Test Problem of Wind Currents. In: Olegovna C. (eds) Processes in GeoMedia—Volume I. Springer Geology. Springer, Cham., p.p. 17–25, (2020).
8. Kochergin V.S., Kochergin S.V., Sklyar S.N. Analytical solution of the test three-dimensional problem of wind flows In: Chaplina, Tatiana (eds) Processes in GeoMedia, Vol. II Springer Geology, Springer, pp. 65–71 (2021).
9. Kochergin V.S., Kochergin S.V., Sklyar S.N. Analytical test problem of wind currents, Processes in geomedia, Moskva, No 2(20),p.p. 193−198.

Variational Identification of the Initial Cs^{137} Concentration Field in the Black Sea After the Chernobyl Accident

V. S. Kochergin and S. V. Kochergin

Abstract The paper implements a variational algorithm for assimilation of measurement data in a passive admixture transport model for the Black Sea. The identification for the initial concentration field is carried out iteratively by minimizing the prediction cost function. Information on the concentration of Cs137 in the Black Sea after the Chernobyl accident was used as measurement data. The results obtained are in good agreement with the data on the intensity of radioactive precipitation over the sea area.

Keywords Variational algorithm · Assimilation · Adjoint problem · Chernobyl accident · Black sea

1 Introduction

In this work, the initial field of Cs137 concentration in the Black Sea is determined according to measurements [1] that were made after more than a month after the Chernobyl accident. The information used is distributed across space and time. The paper considers a variational algorithm [2–6] for assimilation of measurements of Cs137 concentration on the sea surface by identifying the initial data. The flow fields necessary for the implementation of the assimilation algorithm were obtained using the MGI model for calculating the circulation of Black Sea waters [8, 9] with a spatial resolution of 1.6 km with real wind impact according to SKIRON data [10]. These velocities were previously used in the assimilation of similar data based on the estimation method [11]. Calculations based on this model were used in [12] when constructing influence functions based on solving adjoint problems. A variational assimilation algorithm is used to determine the initial isotope concentration field. The data of the National Centers for Environmental Prediction (NCEP) on wind and precipitation are analyzed together with information from the IRSN (Institute of

V. S. Kochergin (✉) · S. V. Kochergin
Marine Hydrophysical Institute RAS, Russian federation, 299029 Sevastopol, Russia

© The Author(s), under exclusive license to Springer Nature Switzerland AG 2022

V. I. Karev (ed.), *Physical and Mathematical Modeling of Earth and Environment Processes*,
Springer Proceedings in Earth and Environmental Sciences,
https://doi.org/10.1007/978-3-030-99504-1_17

Nuclear and Radiation Safety of France) on the processes of transfer of radioactive contamination from the Chernobyl nuclear power plant towards the Black Sea.

2 Transport Model

The equation of the isotope transport model has the following form:

$$\frac{\partial C}{\partial t} + \frac{\partial (uC)}{\partial x} + \frac{\partial (vC)}{\partial y} + \frac{\partial (wC)}{\partial z} = A_H \Delta^2 C + \frac{\partial}{\partial z} A_V \frac{\partial C}{\partial z}, \tag{1}$$

where C is the isotope concentration; A_H is the coefficient of horizontal turbulent diffusion; A_V is the coefficient of vertical turbulent diffusion.

On the surface ($z = 0$), the absence of a flow is set:

$$A_V \frac{\partial C}{\partial z} = 0. \tag{2}$$

Conditions for the absence of a substance flow are set on solid boundaries, bottom and in the area of river mouths. In the area of the Bosphorus and the Kerch Strait, the Dirichlet condition of the first kind is used (zero in this calculation). At the initial moment of time, the concentration field $C^0(x, y, z)$ is set.

For finite-difference approximation over the space of Eq. (1), a grid C [13] is used. The TVD scheme is used for discretization of advective terms [14]. The horizontal coefficient of turbulent diffusion $A_H = 10^7$ cm^2/s, and the vertical coefficient of turbulent diffusion is set in the range of 2.5—0.03 cm^2/s [15]. Problem (1)—(2) is solved in the domain $M_t = M \times [0, T]$.

3 Variational Identification Algorithm

The task of assimilation of measurement data is realized by searching for the initial concentration field based on minimizing the prediction cost function:

$$I_0 = \frac{1}{2}[P(RC - C_m), P(RC - C_m)]_{M_t}, \tag{3}$$

where P —operator of filling in the field of forecast residuals with zeros in the absence of measurement data, R—operator of projecting to the observation points. Adding the model (1)—(2) as limitations in Lagrange method, we write down the variation of the

general functional and integrate it in parts, taking into account the boundary conditions and the continuity equation. Choosing the solution of the following problem as Lagrange multipliers:

$$-\frac{\partial C^*}{\partial t} - \frac{\partial (uC^*)}{\partial x} - \frac{\partial (vC^*)}{\partial y} - \frac{\partial (wC^*)}{\partial z} = A_H \Delta^2 C^* + \frac{\partial}{\partial z} A_V \frac{\partial C^*}{\partial z} - P(RC - C_m), \tag{4}$$

$$z = 0 : A_V \frac{\partial C^*}{\partial z} - wC^* = 0, z = H : A_V \frac{\partial C^*}{\partial z} = 0, \Gamma : A_H \frac{\partial C^*}{\partial n} = 0, C_T^* = 0,$$

when identifying the initial field, we have:

$$\nabla_{C_0} I = -C^*\big|_{t=0}. \tag{11}$$

Iteratively, the following approximation is sought by the formula:

$$C_0^{n+1} = C_0^n + \tau \bullet \nabla_{C_0} I \tag{12}$$

where τ—iterative parameter.

4 Results of Numerical Experiments

The first measurements of Cs^{137} concentration in the Black Sea were taken from June 15, 1986 to July 4. The next series of measurements was carried out from November 26 to November 30 [32]. In this work, 11 measurements from the first survey are assimilated, which included data with values of the order of 300—400 Bq/m^3 or more. At point 11, the measurements showed a maximum value of about 720 ^{Bq}/m^3. No measurements were carried out earlier on June 15, and the background values of Cs^{137} in the Black Sea were insignificant. Figure 1. shows the coordinates of the measurement points.

The flow velocities for the period from 01.05.1986 to 04.07.1986 were obtained on the basis of the MGI model [26] with a step in latitude and longitude of 1.6 km, taking into account the real atmospheric impact (according to ERA-5 data with a spatial resolution of 0.25°) [7]. The reanalysis data [16, 17] interpolated onto the model grid were used as the initial fields. The analysis of the model dynamic flow fields used in this work was carried out in [11]. These flow fields are used in the integration of the main and associated tasks as input information. Note that the circulation in the sea area (Fig. 2.) was quite typical for this season.

In the period from 01.05.1986 to 05.05.1986, according to NCEP data on precipitation intensity (https://psl.noaa.gov/data/gridded/data.ncep.html), in the Black Sea area there were heavy rains with values from 10 to 22 kg/m^2. During this period,

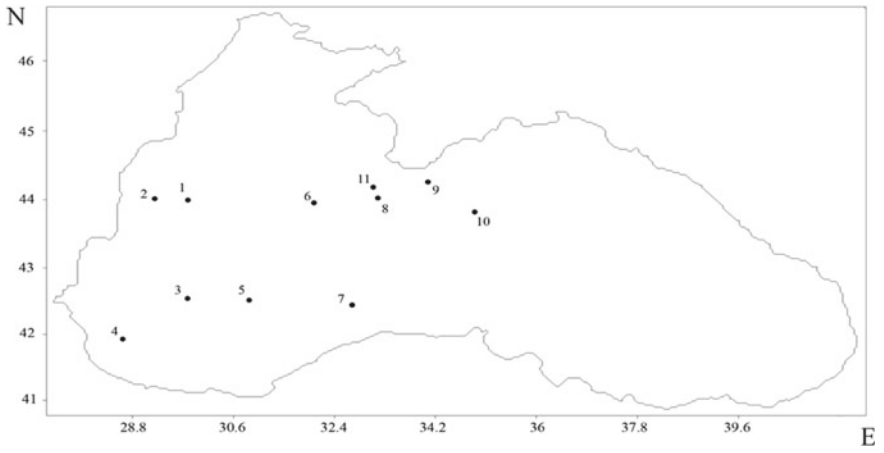

Fig. 1 Measurement points

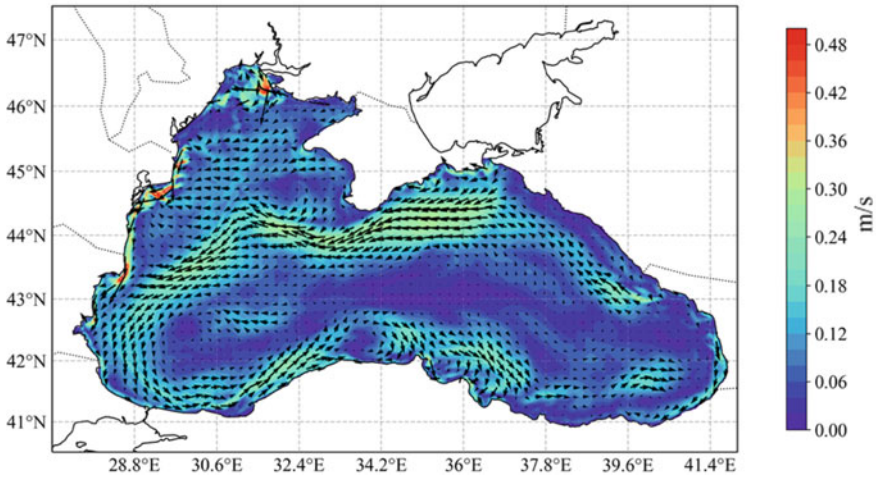

Fig. 2 The current velocity field on the horizon of 2.5 m on May 2, 1986

the radioactive cloud reached the northeastern part of the sea. The average values of precipitation intensity on May 2 for the entire Black Sea area are about 20 kg/m^2. The maximum values (up to 22 kg/m^2) are concentrated in the southeastern part of the sea near the Caucasian coast. Average values of precipitation intensity on May 3–4 decrease to 10–15 kg/m^2.

Radioactive isotopes with intense precipitation entered the surface layer of the sea. According to the Institute of Nuclear and Radiation Safety of France (https://www.irsn.fr/EN/global_partner/Radiation_protection) the radiation trace (with a concentration of up to 100 Bq/m^3) from the Chernobyl NPP reached the northeastern part

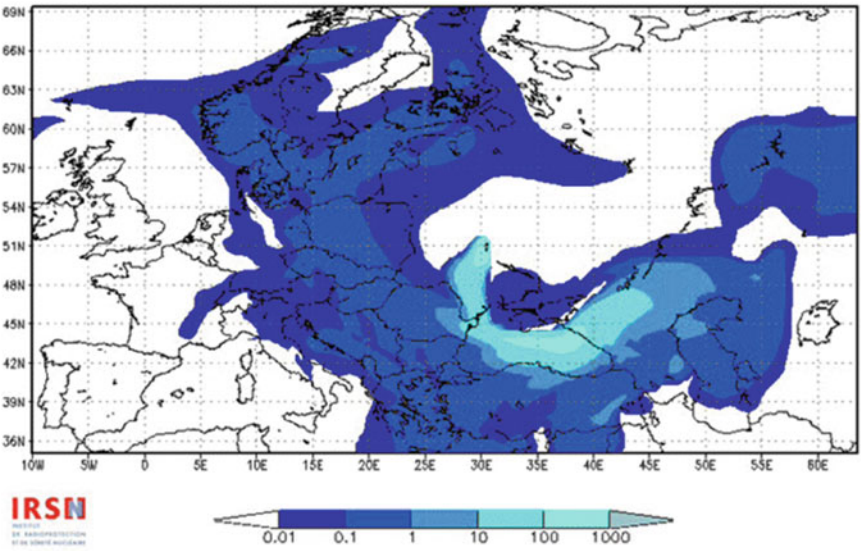

Fig. 3 Distribution of Cs^{137} on May 4, 1986 (Bq/m^3)

of the sea on May 2. A more intense plume with values up to 1000 Bq/m^3 reached the northeastern part of the sea on May 3, and the central and northwestern parts of the sea on May 4 (Fig. 3).

In the future, the radioactive cloud left the Black Sea in the direction of the Anatolian coast and the Balkans. That is, for three days with intense precipitation in the designated areas of the Black Sea, the initial Cs137 concentration field was formed in its upper layer. The task is to find an initial concentration field based on the variational assimilation method so that the model estimates of the isotope concentration are close to the measurement data.

As a result of numerical experiments, the initial isotope field was obtained (Fig. 4), which allowed us to obtain model concentration estimates consistent with the measurement data due to the minimization of the cost function characterizing the deviations of model estimates from measurements.

The found field correlates well with information about the processes of formation of isotope pollution in the Black Sea. Thus, based on the iterative algorithm of assimilation of the available information, the initial distribution of the isotope is found. Further integration of the model makes it possible to obtain a solution (Fig. 5) consistent with the model and with the measurement data due to the minimization of functionality.

Figure 6 characterizes the decline in the normalized functional of the forecast quality. As can be seen from the presented graph, the variational algorithm used under the given conditions and parameters of the problem has a fairly good convergence of the iterative process.

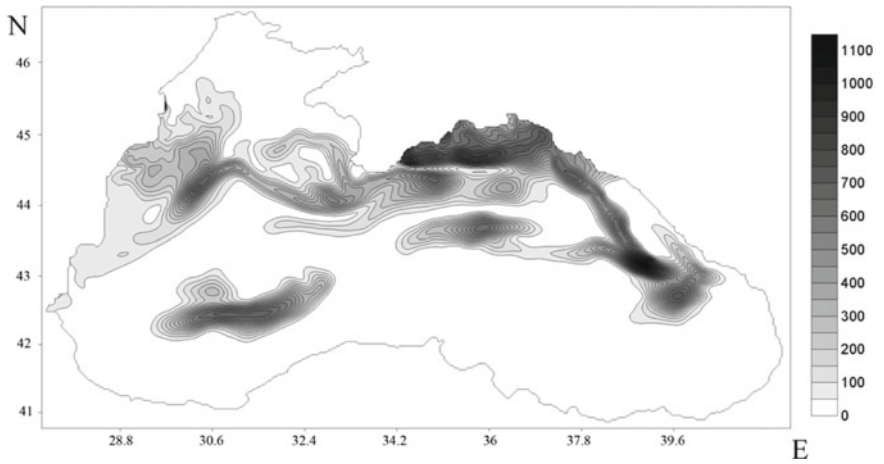

Fig. 4 The initial concentration field of Cs^{137} on May 4, 1986 (Bq/m^3)

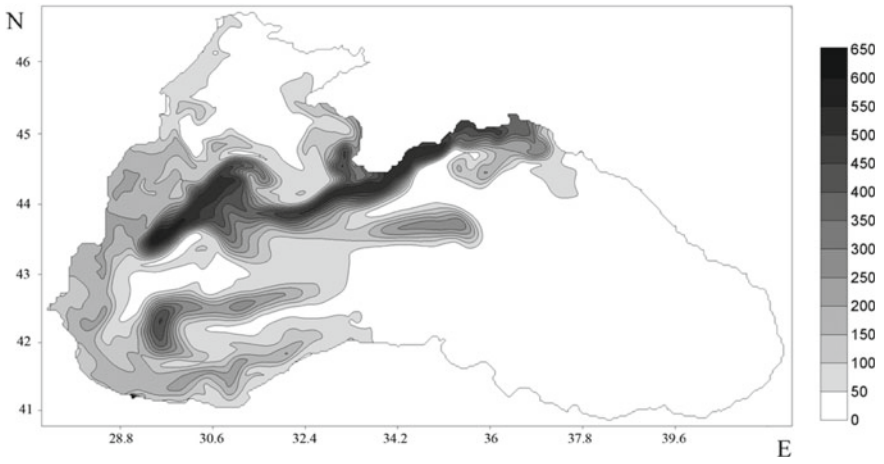

Fig. 5 Cs^{137} concentration field on July 4, 1986 (Bq/m^3)

5 Conclusions

As a result of the variational procedure of the available data assimilation, a good coincidence of the initial concentration field of Cs137 with the IRSN data on it concentration in the atmosphere over the Black Sea region in late April—early May 1986 was obtained. The values in the initial field reach 1100 Bq/m3, which are mainly concentrated in the northeastern part of the sea, where the most intense precipitation and isotope deposition occurred. The initial isotope field found as a result of iterations makes it possible to obtain model estimates of the concentration consistent with the

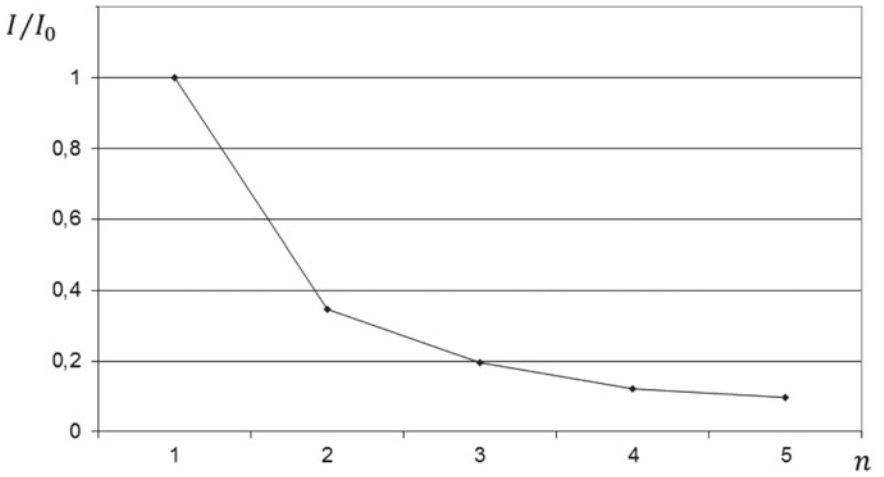

Fig. 6 The fall of the normalized cost function

measurement data due to the minimization of the cost function. These fields are agreed to the model transport, because they are found with its help. These given results correlates with information about the processes of isotope pollution formation in the Black Sea. Thus, based on the assimilation of measurement data, the task of identifying the initial concentration field for further modeling of the transfer of radioactive isotope into the sea is realized.

Acknowledgements The work was carried out within the framework of the state task on the topic 0555-2021-0005 "Complex interdisciplinary studies of oceanological processes that determine the functioning and evolution of ecosystems of the coastal zones of the Black and Azov Seas" (code "Coastal research").

References

1. Bayankina T.M., Godin E.A., Zhuk E.V., Ingerov A.V., Isaeva E.A., and Vetsalo M.P. Information resources of marine hydrophysical institute, RAS: current state and development prospects, Processes in GeoMedia - Volume II Hardcover, pp. 187−197 (2021).
2. Marchuk G.I., Penenko V.V. Application of optimization methods to the problem of mathematical simulation of atmospheric processes and environment. In: Modelling and Optimization of Complex Systems, IFIP-TC7 Working conf. – NewYork: Springer, pp. 240−252 (1978).
3. Sutyaev V.P. Adjoint equations in variational data assimilation problem, Russian Journal of Numerical Analysis and Mathematical Modelling, T. 33, no. 2. pp. 137−147 (2018).
4. Kochergin V.S., Kochergin S.V. Identifying the parameters of the instantaneous point pollution source in the Azov Sea based on the adjoint equation method, Physical Oceanography, Iss.1, pp. 62−67 (2017).
5. Kochergin V.S., Kochergin S.V. Identification of the initial Cs^{137} concentration field in the Black Sea after the Chernobyl accident based on solving a related problem. In: Ecological

safety of coastal and shelf zones and comprehensive use of shelf resources, MGI, Sevastopol, Iss. 22, pp. 240−244 (2010).
6. Kochergin S.V., Kochergin V.S. Variational data assimilation in a transport model Rapport du 38e Congress de la SIESM, Istanbul (Turquie). p.162. (2007).
7. Demyshev S.G. A numerical model of online forecasting Black Sea currents, Izv. Atmos. Ocean. Phys., Vol. 48, Iss.1. pp. 120−132 (2012).
8. Demyshev, S.G., Dymova, O.A. Numerical analysis of the mesoscale features of circulation in the Black Sea coastal zone, Izv. Atmos. Ocean. Phys. Vol. 49 pp. 603−610. (2013).
9. Demyshev S.G., Dymova O.A. Computing complex for modeling of the Black Sea, IOP Conf. Series: Earth and Environmental Science, p. 211. (2018).
10. Kallos G et. al. The regional weather forecasting system SKIRON: An overview, Proc. of the Int. Symp. on Regional Weather Prediction on Parallel Computer Environments (Athens, Greece), pp. 109−122 (1997).
11. Demyshev S.G., Dymova O.A., Kochergin V.S., Kochergin S.V. Determination of the initial Cs137 concentration field in the Black Sea after the Chernobyl accident on the basis of solving adjoint problems “Processes in geomedia” No. 3 (29) 2021, pp. 1202–1211.
12. Demyshev S.G., Dymova O.A., Kochergin V.S. and Kochergin, S.V. Determination of Location of the Concentration Initial Field of a Possible Contamination Source in the Black Sea Water Area near the Gerakleisky Peninsula Based on the Adjoint Equations, Method.Physical Oceanography, [e-journal] 27(2), pp. 210−221 (2020).
13. Arakawa A., Lamb V. R. A Potential Enstrophy and Energy Conserving Scheme for the Shallow Water Equations, Monthly Weather Review, Vol.109, №1. pp. 18−36. (1981).
14. Harten A. High resolution schemes for hyperbolic conservation laws. J Comput Phys, Vol.49, pp. 357−393 (1983).
15. Demyshev S.G., Zapevalov A.S., Kubryakov A.I., Chudinovskikh T.V. Evolution of the 137Cs concentration field in the Black Sea after the passage of the Chernobyl cloud // Meteorology and hydrology. - 2001. - No. 10. - pp. 49–61.
16. Climate Data Store https://cds.climate.copernicus.eu/cdsapp#!/dataset/reanalysis-era5-single-levels?tab=overview.
17. Korotaev G.K., Ratner Y.B., Ivanchik M.V., Kholod A.L., Ivanchik A.M. Operational system for diagnosis and forecast of hydrophysical characteristics of the Black Sea, Izv. Atmos. Ocean. Phys., Vol.52, Iss.5, pp.542−549 (2016).

Numerical Calculation of Vertical Wave Momentum Fluxes on a Shear Flow

A. A. Slepyshev and D. I. Vorotnikov

Abstract In the Boussinesq approximation, inertia-gravity internal waves on a two-dimensional vertically non-uniform stratified flow are considered. The boundary value problem for the vertical velocity amplitude has complex coefficients and is solved both numerically and by perturbation method. Comparison of the results shows that the dispersion curves practically do not change, but the imaginary part of the frequency in the perturbation method increases by two or three orders of magnitude. The vertical wave fluxes of momentum are different from zero and may be comparable with turbulent fluxes or exceed them. Wave fluxes obtained by numerical calculations are almost an order of magnitude smaller than those obtained by the perturbation method used earlier.

Keywords Internal waves · Wave fluxes of momentum · Complex wave frequency

1 Introduction

Vertical exchange in the ocean is important for the functioning of marine ecosystems. According to current ideas, vertical exchange is caused by small-scale turbulence, which is strongly suppressed in the stratified sea column. At the same time, due to stratification, internal waves are possible. Internal waves are generated by atmospheric disturbances, the interaction of flows and tides with seabed landforms irregularities, and internal quasi-inertial waves are present due to the rotation of the Earth. Small-scale turbulence in the stratified sea column has an intermittent character and one can speak of an effective turbulent exchange coefficient. Internal waves are damped when turbulent viscosity and diffusion are taken into account [1–3]. In this case, the vertical wave momentum fluxes are different from zero [4]. However,

A. A. Slepyshev (✉)
FSBSI FRC Marine Hydrophysical Institute, Russian Academy of Sciences, Sevastopol 299011, Russia

D. I. Vorotnikov
Physics Department, Lomonosov Moscow State University, Moscow 119991, Russia

© The Author(s), under exclusive license to Springer Nature Switzerland AG 2022

V. I. Karev (ed.), *Physical and Mathematical Modeling of Earth and Environment Processes*,
Springer Proceedings in Earth and Environmental Sciences,
https://doi.org/10.1007/978-3-030-99504-1_18

on two-dimensional shear flow at accounting of the Earth rotation, when the flow velocity component perpendicular to the direction of wave propagation depends on the vertical coordinate, the vertical wave momentum flux is different from zero even without taking into account turbulent viscosity and diffusion [5]. The point is that in this case the equation for the vertical velocity amplitude has complex coefficients, the eigenfunction and the wave frequency are complex, the phase shift between the vertical w and horizontal u components of the wave disturbances of the flow velocity is different from $\pi/2$ and the vertical wave momentum flux $\overline{uw}$ is different from zero [5]. The boundary value problem for the vertical velocity amplitude having complex coefficients in the equation was solved in [5] by perturbation method, by decomposing the solution and the wave frequency into a series using a small parameter $\varepsilon = V_0^*/(H\omega_*)$, where V_0^* is the characteristic value of the flow velocity, ω_* is the characteristic wave frequency, H is the sea depth. However, this parameter is not always small, and the applicability of the method is limited. Therefore, we applied an implicit Adamsscheme of the third order of accuracy in the numerical solution of this boundary value problem for the real Brunt-Vaisala frequency and flow profiles. The boundary value problem for the amplitude of the vertical velocity of internal waves was solved analytically in [6] for a plane-parallel shear flow at a constant Brunt-Väisälä frequency. It was obtained that the eigenfunction—the solution of this boundary value problem is complex and the wave frequency is real. The case was considered when the wave propagates perpendicularly to the flow. In the present paper, numerical calculations show that in the two-dimensional flow, the wave frequency is complex. The vertical wave momentum fluxes in this case are different from zero. We compare the momentum fluxes obtained by the perturbation method and the numerical method. The imaginary part of the wave frequency is nonzero. Both weak amplification and weak attenuation of the wave is possible. We compare the dependence of the real and imaginary parts of the frequency on the wave number, obtained by the numerical method and the perturbation method.

2 Linear Approximation

The solution of the system of hydrodynamic equations [5] for wave disturbances on a two-dimensional flow with flow velocity components U_0, V_0 in the linear approximation will be sought in the form:

$$\begin{aligned} &u = u_{10}(z)A\mathrm{e}^{i\,\theta} + \text{c.c.}, \quad v = v_{10}(z)A\mathrm{e}^{i\,\theta} + \text{c.c.}, \quad w = w_{10}(z)A\mathrm{e}^{i\,\theta} + \text{c.c.} \\ &P = P_{10}(z)A\mathrm{e}^{i\,\theta} + \text{c.c.}, \quad \rho = \rho_{10}(z)A\mathrm{e}^{i\,\theta} + \text{c.c} \end{aligned} \tag{1}$$

where c.c. are complex conjugate terms; A is the amplitude multiplier; θ—wave phase ($\partial\theta/\partial x = k$, $\partial\theta/\partial t = -\omega$, k is the horizontal wave number, ω is the frequency of the wave). It is assumed that the wave propagates along the x axsis.

After substitution of (1) into system of hydrodynamic equations [5], there follows a connection between the amplitude functions $u_{10},\ v_{10},\ \rho_{10},\ P_{10}$ with w_{10}:

$$u_{10} = \frac{i}{k}\frac{dw_{10}}{dz},\ \ \Omega = \omega - k \cdot U_0 \tag{2}$$

$$\frac{P_{10}}{\rho_0(0)} = \frac{i}{k}\left[\frac{\Omega}{k}\frac{dw_{10}}{dz} + \frac{dU_0}{dz}w_{10} + \frac{f}{\Omega}(i\frac{dV_0}{dz}w_{10} - \frac{f}{k}\frac{dw_{10}}{dz})\right] \tag{3}$$

$$\rho_{10} = -\frac{i}{\Omega}w_{10}\frac{d\rho_0}{dz},\ \ v_{10} = \frac{1}{\Omega}\left(\frac{f}{k}\frac{dw_{10}}{dz} - iw_{10}\frac{dV_0}{dz}\right). \tag{4}$$

The function w_{10} satisfies the boundary value problem [5]:

$$\begin{aligned}&\frac{d^2w_{10}}{dz^2} + k\left[\frac{if\frac{dV_0}{dz}}{\Omega^2 - f^2} - \frac{f^2\frac{dU_0}{dz}}{\Omega(\Omega^2 - f^2)}\right]\frac{dw_{10}}{dz} + \\ &+kw_{10}\left[\frac{\Omega\frac{d^2U_0}{dz^2} - k(\frac{g}{\rho_0(0)}\frac{d\rho_0}{dz} + \Omega^2) + if\frac{d^2V_0}{dz^2}}{\Omega^2 - f^2} + \frac{ifk\frac{dU_0}{dz}\frac{dV_0}{dz}}{\Omega(\Omega^2 - f^2)}\right] = 0,\end{aligned} \tag{5}$$

$$w_{10}(0) = w_{10}(-H) = 0. \tag{6}$$

Equation (5) has complex coefficients, so the eigenfunctions of the boundary value problem (5) and (6) are complex. The numerical calculations below show that the frequency of the wave is also complex for a fixed wavenumber and mode number. Therefore, the vertical wave fluxes of momentum are nonzero.

3 Wave Momentum Fluxes

Vertical wave momentum fluxes are determined by the formulas [5]:

$$\overline{uw} = |A_1^2|\frac{i}{k}\left(w_{10}^*\frac{dw_{10}}{dz} - w_{10}\frac{dw_{10}^*}{dz}\right) \tag{7}$$

$$\overline{vw} = |A_1^2|\frac{iw_{10}w_{10}^*}{\Omega\Omega^*}(\Omega - \Omega^*)\frac{dV_0}{dz} + |A_1^2|\frac{f}{\Omega\Omega^*k}\left(\Omega^*w_{10}^*\frac{dw_{10}}{dz} + \Omega w_{10}\frac{dw_{10}^*}{dz}\right) \tag{8}$$

where $A_1 = A\exp(\delta\omega \cdot t)$, $\delta\omega = \mathrm{Im}(\omega)$ is the imaginary part of the frequency. The line at the top means averaging over the wave period.

Vertical wave fluxes of momentum are nonzero if the derivative of the flow velocity component V_0 with respect to the vertical coordinate is nonzero. If the vertical

gradient of the current velocity component V_0 is zero, then the momentum flux $\overline{uw}$ is zero and the flux $\overline{vw}$ is nonzero.

4 Calculation Results

Let us calculate the vertical wave momentum fluxes for internal waves on the northwestern continental slope of the Black Sea. The vertical profiles of the two components of the flow velocity and the Brent-Väisälä frequency are shown in Fig. 1 [7, 8].

The boundary value problem (5) and (6) is solved numerically using the implicit Adams scheme of the 3rd order of accuracy [9]. The complex frequency of the wave is found by shooting from the need to satisfy the boundary conditions (6) for a fixed wavenumber and mode number.

The dependence of the real part of the wave frequency on the wave number for the first two modes is shown in Fig. 2a for positive wave numbers both in the numerical solution of the boundary value problem (5) and (6) and by the perturbation method [5], in Fig. 2b—the same for negative wavenumbers. Both the numerical method and the perturbation method give almost identical results for the dispersion curves.

The dependence of the imaginary part of the wave frequency on positive wavenumbers for the first two modes is shown in Fig. 3a when solving the boundary value problem (5) and (6) by the perturbation method and by the numerical method in Fig. 3b.

Similar dependences for negative wavenumbers are shown in Fig. 4a and b. The perturbation method gives the values of the modulus of the imaginary part of the wave frequency overestimated by 2–3 orders of magnitude.

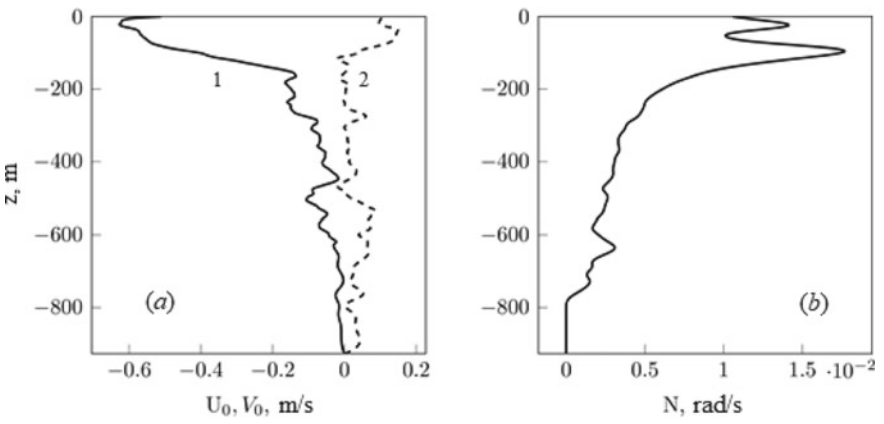

Fig. 1 Vertical profiles of the flow velocity components $U_0(1)$, $V_0(2)$—(**a**); Brunt–Väisälä frequency—(**b**)

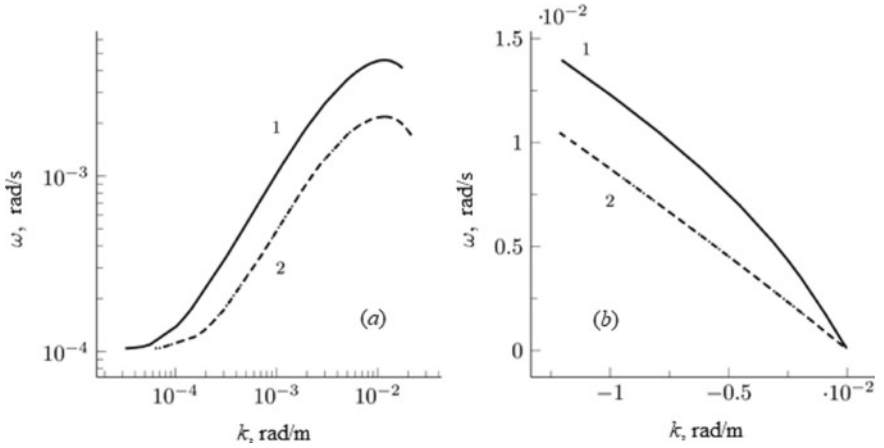

Fig. 2 Dispersion curves of the first (1) and second (2) modes at positive wavenumbers (a) and negative wavenumbers (b)

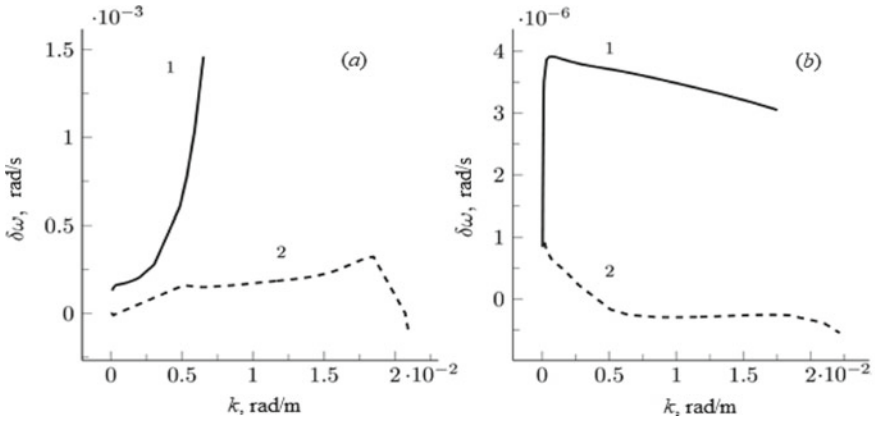

Fig. 3 Dependence of the imaginary part of the wave frequency on the wave number for the first (1) and second (2) modes: **a** method of perturbations; **b** numerical method

The numerical solution of the boundary value problem (5) and (6) allows us to conclude that for positive wavenumbers the imaginary part of the wave frequency for the first mode is positive—there is a weak amplification of the wave. In the second mode, the imaginary part of the wave frequency is positive in the long-wavelength region, when $k < 0.37 \cdot 10^{-2}$ rad/m, there is a weak amplification of the wave; at large wave numbers, the imaginary part of the frequency is negative (Fig. 3b); weak attenuation of the wave occurs. In the region of negative wavenumbers, numerical calculation gives a negative imaginary part of the wave frequency for the first mode (Fig. 4b). For the second mode, the imaginary part of the frequency is positive for low modulus wave numbers, if $k < -0.6 \cdot 10^{-2}$ rad/m the imaginary part of the frequency

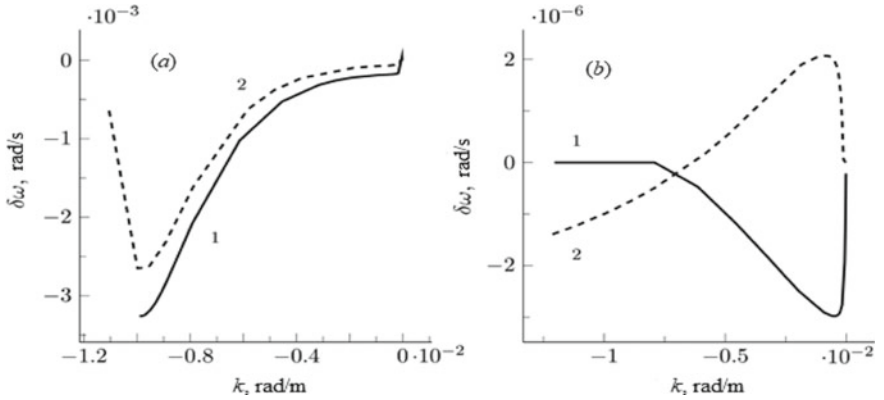

Fig. 4 Dependence of the imaginary part of the wave frequency on negative wavenumbers for the first (1) and second (2) modes: **a** the method of perturbations; **b** numerical method

is negative, i.e. weak amplification at low in absolute value negative wavenumbers is replaced by weak damping at large ones (Fig. 4b). The perturbation method gives a negative imaginary part for the first and second modes at negative wavenumbers (Fig. 4a). According to the results of numerical calculations, for 15 min internal waves, the wavenumber for the first mode is negative and is equal to −0.0045 rad/m, for the second mode it is $k = -0.0079$ rad/m. The imaginary part of the wave frequency is also negative: $\delta\omega = -1.2 \cdot 10^{-6}$ rad/s—for the first mode, $\delta\omega = -0.49 \cdot 10^{-6}$ rad/s—for the second mode.

The normalizing factor is found from the known amplitude of vertical displacements. Indeed, vertical speed is related to vertical displacement ζ ratio $\frac{d\zeta}{dt} = w$. From here comes ζ and expression for $|A_1|$:

$$\zeta = \frac{iw_{10}}{\Omega} A_1 \exp(ikx - i\omega_0 t) + c.c., \tag{9}$$

$$|A_1| = \frac{\max \zeta}{2 \max|w_{10}/\Omega|}. \tag{10}$$

The vertical profiles of the wave momentum flux $\overline{uw}$ are shown in Fig. 5a for 15 min internal waves of the first mode at a maximum wave amplitude of 0.5 m. The solid line corresponds to the numerical solution of the boundary value problem (5) and (6), the dashed line corresponds to the perturbation method. The perturbation method gives overestimated values of the wave momentum flux. In Fig. 5b shows the same fluxes for the second mode of internal waves.

It is of interest to compare the turbulent and wave momentum fluxes. The turbulent momentum flux is determined by the formula $\overline{u'w'} = -K_z \frac{dU_0}{dz}$, for the vertical exchange coefficient in the upper 200 m highly stratified layer, the $K_z = 8.4N_c^{-1} \cdot 10^{-4}$ m^2/s estimate is valid, N_c corresponds to the Brunt-Väisälä

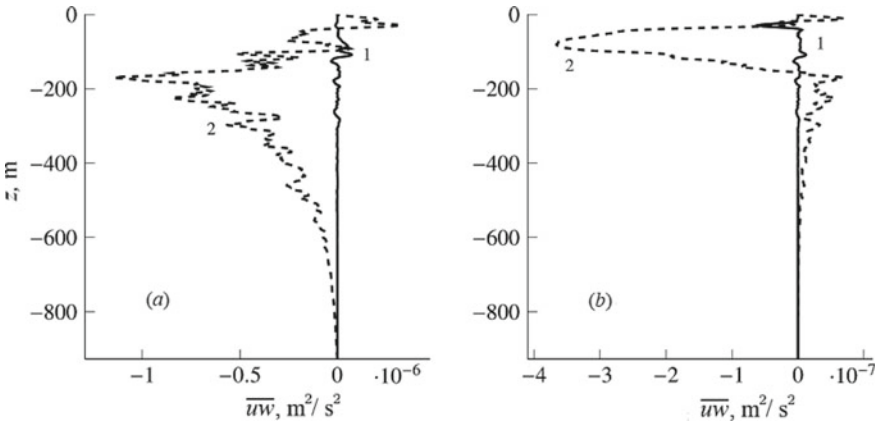

Fig. 5 Vertical profiles of the wave momentum flux $\overline{uw}$ for the first (**a**) and second (**b**) modes: 1—numerical method; 2—perturbation method

frequency per cph [10]. In deeper weakly stratified layers, the coefficient of turbulent exchange is proportional N_c [11]. Figure 6 shows the profiles of wave (solid line) and turbulent (dotted line) momentum fluxes for the first two modes in the numerical solution of the boundary value problem (5) and (6). The turbulent flux dominates, especially over the flux of the second mode. For the first mode, the wave flux is comparable to the turbulent flux only in the pycnocline in the depth range of 80–120 m.

The vertical profiles of the wave momentum flux $\overline{vw}$ are shown in Fig. 7a for 15 min internal waves of the first mode with a maximum wave amplitude of 0.5 m. The solid curve corresponds to the numerical solution of the boundary value problem

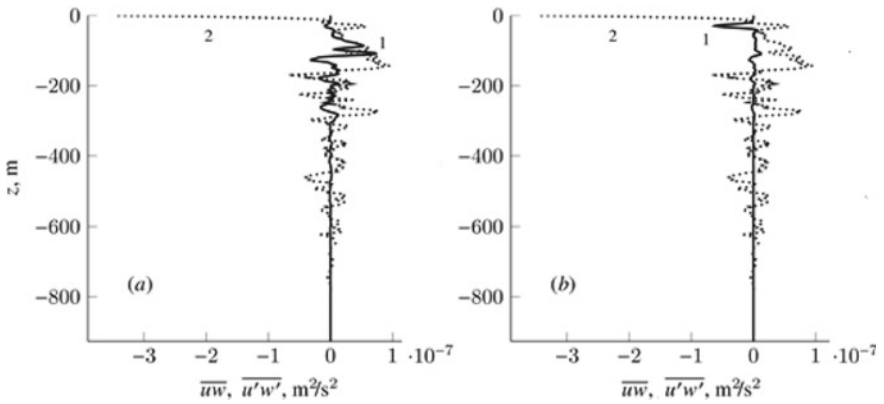

Fig. 6 Vertical profiles of wave and turbulent momentum fluxes for the first (**a**) and second (**b**) modes: 1—wave momentum flux; 2—turbulent flux

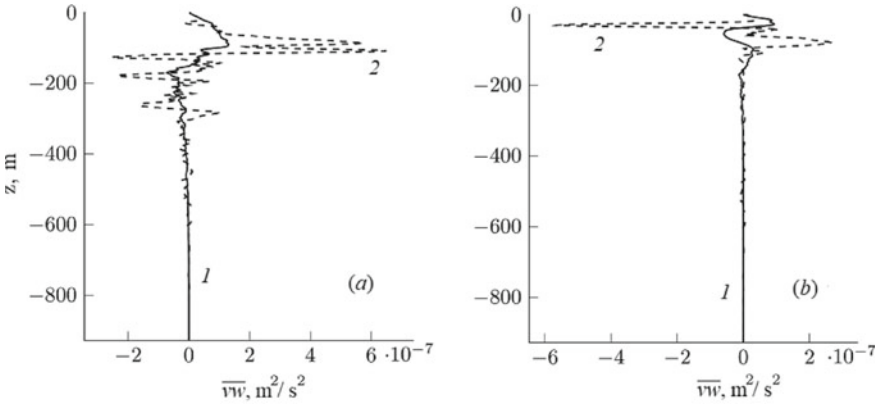

Fig. 7 Vertical profiles of the wave momentum flux $\overline{vw}$ for the first (**a**) and second (**b**) modes: 1—numerical method; 2—perturbation method

(5) and (6), the dashed curve corresponds to the perturbation method. Figure 7b shows the same fluxes for the second mode of internal waves.

The wave fluxes $\overline{vw}$ of the first mode obtained by the numerical method and the perturbation method do not differ as much as the fluxes $\overline{uw}$. In general, the perturbation method gives inflated values for flows. It is of interest to compare the turbulent and wave momentum fluxes. The turbulent momentum flux is determined by the formula $\overline{v'w'} = -K_z \frac{dV_0}{dz}$. Figure 8 shows the profiles of the wave $\overline{vw}$ and turbulent $\overline{v'w'}$ momentum fluxes for the first two modes.

The turbulent flux $\overline{v'w'}$ is inferior to the wave flux in the first mode only in the upper highly stratified 120 m layer. In the second mode in this layer, the turbulent

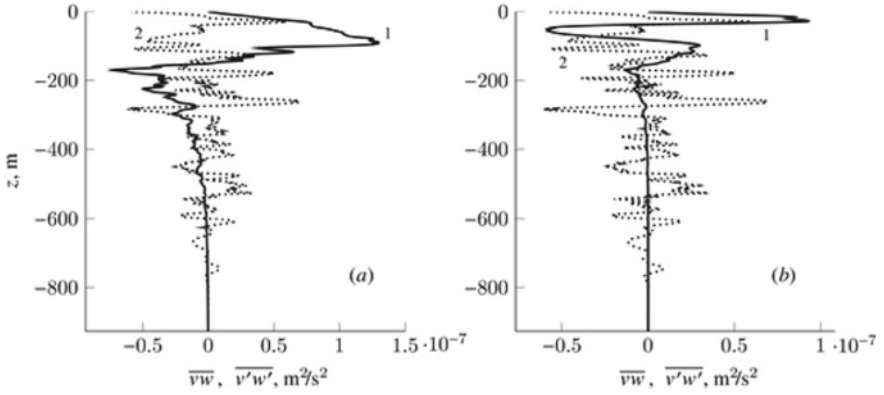

Fig. 8 Vertical profiles of wave $\overline{vw}$ and turbulent momentum fluxes for the first (**a**) and second (**b**) modes: 1—wave momentum flux; 2—turbulent flux

and wave fluxes are comparable in magnitude. In deeper layers, the turbulent flux dominates the wave one's.

5 Conclusions

Internal waves, taking into account the rotation of the Earth on a two-dimensional stratified flow, when the component of the flow velocity perpendicular to the direction of the wave propagation depends on the vertical coordinate, have an imaginary correction to the frequency. The solution of the boundary value problem (5) and (6) by the perturbation method gives an overestimated modulo value of this correction in comparison with the numerical solution of this problem.

The vertical wave fluxes of the momentum $\overline{uw}$, $\overline{vw}$ are different from zero and the perturbation method gives inflated values compared to the numerical method for solving the boundary value problem (5) and (6).

The wave momentum flux $\overline{vw}$ in the first mode may exceed the corresponding turbulent flux in the pycnocline, while in the second mode these fluxes are comparable in magnitude. Outside the pycnocline, the turbulent flux dominates the wave one's.

The wave flux of the momentum $\overline{uw}$ is inferior to the corresponding turbulent flux.

Acknowledgements The authors are grateful to Morozov A. N. for the presented experimental material on the deep-sea part. The work was carried out as part of the state assignment on the subject › 0555-2021-0004, Fundamental studies of oceanological processes determining the state and evolution of the marine environment under the influence of natural and anthropogenic factors based on observation and modeling methods (code "Oceanological processes").

References

1. LeBlond, P. H. and Misek, L. A.: Waves in the Ocean. Amsterdam: Elsevier Scientific Publishing Company, 2, 365 (1978).
2. LeBlond, P. H.: On damping of internal gravity waves in a continuously stratified ocean, Journal of Fluid Mechanics, 25(1), 121–142 (1966). doi:https://doi.org/10.1017/S0022112066000089.
3. Ostrovskii, L. A. and Soustova, I. A.: The upper mixing layer as a sink of internal waves energy, Okeanologiya, 19 (6), 973–981 (1979).
4. Slepyshev, A. A.: Vertical Momentum Transfer by Internal Waves when Eddy Viscosity and Diffusion are Taken into Account, Izvestiya, Atmospheric and Oceanic Physics, 52(3), 301–308 (2016). doi: https://doi.org/10.1134/S0001433816030117.
5. Vorotnikov, D. I., Slepyshev, A. A.: Vertical Momentum Fluxes Induced by Weakly Nonlinear Internal Waves on the Shelf, Fluid Dynamics, 53(1), 21–33. (2018). https://doi.org/https://doi.org/10.1134/S0015462818010160.
6. Slepyshev, A. A., Laktionova, N. V.: Vertical Transport of Momentum by Internal Waves in a Shear Current, Izvestiya, Atmospheric and Oceanic Physics, 55(6), 662–668 (2019). doi: https://doi.org/10.1134/S0001433819060148

7. Lemeshko, E. M., Morozov, A. N., Stanichnyi, S. V., Mee, L. D., Shapiro, G. I.: Vertical structure of the field of current velocities in the northwest part of the Black Sea based on the LADCP data for May 2004, Physical Oceanography, 18(6), 319–331. (2008).
8. *Slepyshev, A. A., Vorotnikov D. I.:* Generation of vertical fine structure by internal waves in a shear flow, *Open Journal of Fluid Dynamics,* 9(2), 140-157. (2019). doi: https://doi.org/10.4236/ojfd.2019.92010
9. Ankudinov, N.O., Slepyshev, A.A.: Vertical Momentum Transfer Induced by Internal Waves in a Two-Dimensional Flow, Fluid Dynamics, 56(3), 343-352 (2021). doi: https://doi.org/10.1134/S0015462821030022
10. Ivanov, V. A., Samodurov, A. S., Chukharev A. M., and Nosova A. V.: Intensification of vertical turbulent Exchange in areas of pairing of the shelf and the continental slope in the Black Sea, Dop. Nats. Akad. Nauk Ukr. 6, 108—112. (2008).
11. Samodurov, A. S.: Complimentarity of Different Approaches for Assessing Vertical Turbulent Exchange Intensity in Natural Stratified Basins, Physical Oceanography, 6, 32–42 (2016). doi: https://doi.org/10.22449/1573-160X-2016-6-32-42.

Weather Conditions of Summer Months and Fires in the Forest Zone of Siberia

A. V. Kholoptsev, R. G. Shubkin, S. V. Babenyshev, and A. Yu. Perelygin

Abstract It is generally accepted, that the significant factors of Siberian forest fires in the summer months can be changes in the average intensities of atmospheric precipitation and evaporation. The statistical significance of the relationship between these processes has been repeatedly confirmed empirically. Therefore, taking into account changes in the local meteorological conditions makes it possible to successfully predict the risk of fires with lead times of one to ten days. At the same time, attempts at long-term forecasting, based on the same factors, are usually less effective. Since forest fires is a multifactorial phenomenon, it was suggested that the reason for the latter problems is the significantly lower influence on the fire hazard of variations in local meteorological conditions over the year-to-year period. The aim of this work is to test the validity of this assumption. To achieve this, we contrast some results of the ERA-5 reanalysis with the satellite information on the forest fires actually occurring in these areas. The chosen parameters are changes in the hourly sums of atmospheric precipitation and the hourly mean values of the meridional and zonal components of the wind speed at an altitude of 1000 hPa over various parts of the territory of Siberia. For months of increased fire hazard in Siberia, we identify those when interannual variations in the frequency of forest fires were statistically significantly associated with changes in the specified characteristics of local meteorological conditions. We have established that in some of the areas, the current trends in the frequency of forest fires correspond to the trends in the considered characteristics of meteorological conditions. Therefore, long-term forecasting of fire hazard on them, based on variations in local meteorological conditions, is possible. Moreover, there are very few such sites with respect to the total amount of areas where forest fires were detected. This confirms the validity of the suggested hypothesis and testifies to the advisability of taking into account other more significant factors for the long-term forecasting of the fire hazard in the forests of Siberia.

A. V. Kholoptsev (✉)
Sevastopol Branch of Government Oceanography Institute, Sevastopol, Russia
e-mail: kholoptsev@mail.ru

A. V. Kholoptsev · R. G. Shubkin · S. V. Babenyshev · A. Yu. Perelygin
FSBEE HE Siberian Fire and Rescue Academy, EMERCOM of Russia, Zheleznogorsk, Krasnoyarsk Krai, Russia

© The Author(s), under exclusive license to Springer Nature Switzerland AG 2022

V. I. Karev (ed.), *Physical and Mathematical Modeling of Earth and Environment Processes*,
Springer Proceedings in Earth and Environmental Sciences,
https://doi.org/10.1007/978-3-030-99504-1_19

Keywords Siberia · Forest fires · Frequency · Wind speed components · Precipitation · Statistical relationship · Trend · Forecast

1 Introduction

Forest fires that occur over a particular territory has a huge impact on safety and quality of life of its population, the conditions of natural landscapes and the intensity of emissions into the atmosphere of greenhouse gases and aerosols. Therefore, the improvement of forest fires forecasting is an urgent problem of meteorology and important aspect of the population safety in the emergencies.

The solution of this problem is of special interest for the regions of our planet, in which a significant part of Earth forest resources is concentrated. As of 2020, the Russian Federation has 20% of all forested areas in the world (815 million hectares) [1], of which 65% are located in Siberia. The territory of Siberia stretches from the Ural Mountains to the watershed ridges on the western border of the Pacific Ocean basin and from the southern border of Russia to the coast of the Arctic seas. It includes the territories of all constituent entities of the Russian Federation that belong to the Siberian Federal District, as well as the territory of the Republic of Sakha (Yakutia), the northern regions of the Amur region (Far Eastern Federal District), the Tyumen region, the Kurgan region, as well as the eastern parts of the Sverdlovsk and Chelyabinsk regions (Ural Federal District).

Numerous forest fires occur in Siberia every year. In the modern period, the total area of territories that were affected by forest fires is most rapidly increasing in the Republics of Sakha and Buryatia, Krasnoyarsk and Transbaikal Territories, as well as Irkutsk Oblast [2, 3].

According to current models about the patterns of occurrence and development of forest fires [4–11], the processes under study are due to the joint action of many factors. The level of influence of particular factors depends on the location of the respective territories, as well as a time factor. It also depends on the successes in early forecasts of forest fires.

For forecasts of forest fires with a lead time of 1–12 days, meteorological factors (variations in daily precipitation, average daily surface wind speed, and relative air humidity) are among the most significant. This is used in the method for assessing forest fire hazards, proposed by Nesterov [12], as well as its modifications [13]. The divisions of the Forest Guard and the State Fire Service of the Ministry of Emergency Situations of Russia commonly use these methods in the short-term planning of their activities.

When planning the long-term activities of such units, fire hazard forecasts are needed with a lead time of a few months or years. To develop such forecasts in the regions of the Far East, a method based on local meteorological conditions, information on forest fires, and atmospheric circulation in the Northern hemisphere, was proposed in [10, 14]. As the analysis of the results of the mentioned method on the territory of Siberia has shown, the accuracy of the forecasts obtained is,

as a rule, unsatisfactory. Consequently, the problem of developing a more suitable methodology for such forecasting remains relevant.

A useful step for solving this problem would be to identify the reasons for the low efficiency of the aforementioned method [10, 14] for Siberia. One of possible reasons may be the assumption that for interannual and intra-annual variability of fire hazard in the forests of Siberia meteorological factors are significant. The validity of this assumption is far from obvious. Forest fires in Siberia most often occur in the period from April to October, and atmospheric precipitation that falls at this time in Siberia is often convective. Such precipitation is produced in cumulonimbus clouds (Cb), which form at the cold atmospheric fronts of the II type (cyclones) and usually are thunderstorms. At such fronts, as a rule, the wind also intensifies [15]. Therefore, an increase in the intensity of atmospheric precipitation in the summer months can not only moisten the vegetation and dead wood, but also increase the frequency of "cloud-earth" lightnings, which directly cause fires. It is also obvious that a necessary condition for the occurrence of a forest fire in a certain area is the presence of combustible material, which accumulates at a rate that depends on the characteristics of its landscape and climate. In populated areas, the anthropogenic factor can also have a significant impact.

Fire hazard for a particular forested area characterizes the idea of the risk of a forest fire in it, which reflects not only objectively occurring natural processes, but also existing human opinions about them. Of no less theoretical and practical interest is the long-term forecasting of a completely objective indicator (further referred to as FFF)—the frequency of forest fires, with characteristics exceeding certain threshold levels.

2 Materials and Methods

The purpose of this work is to verify the validity of the hypothesis that meteorological factors are significant for interannual and intra-annual variability of fire hazard in the forests of Siberia. Secondly, we will determine the areas of Siberia for which the interannual changes in the monthly sums of atmospheric precipitation (hereinafter MSP), as well as the meridional and zonal components of the mean monthly wind speeds in the lower tropospheric layer (hereinafter, MWS_m and MWS_z) in months from April to October are significant factors in FFF variations. To achieve this, it is necessary to identify areas of the territory of Siberia for which interannual changes in FFF, in the months from April to October, are closely associated with variations in MSP, MWS_m, or MWS_z. By the latter we mean that in such areas:

– There is high enough significance of the statistical link between the processes in question.
– We observe the required correspondence between the modern tendencies of their interannual variability.

Therefore, for various parts of the territory of Siberia, three tasks were undertaken in this paper:

1. Analysis of the peculiarities of distribution of FFF over the territory of Siberia in different months of the increased wildfire hazard.
2. Assessment of the significance of statistical relationships of interannual changes in FFF in areas where time variations in MSP, MWS_m and MWS_z coincide.
3. Revealing the correspondence between modern tendencies of interannual variability of the studied processes.

For solving these problems, we studied the time series describing the interannual changes in FFF, MSP, MWS_m and MWS_z in areas of Siberia for a particular month related to the period of increased wildfire hazard. The mentioned time series were formed using information obtained from various sources.

The database [16] provided us with factual material about wildfires that took place on a given day in Siberia. The database contains information on the dates of detection, geographical coordinates and the type of all thermal anomalies—areas of the Earth's surface with a generalized characteristic of a possible fire (for instance the average temperature is 70 °C higher than the background temperature [17]). The thermal anomalies are registered by satellite instruments, like radiometers MODIS or VIIRS, which provide radiometric surveys of the entire Earth's surface in the infrared and visible ranges. On the ground, an operator processes the received information to weed out the false-positives and determine types of the remained cases. The type of a thermal anomaly corresponds to its cause: forest fire, natural fire, technological process, waste incineration, etc. After subsequent confirmation at the regional level, information about the coordinates of detected "forest fire"-type thermal anomaly is sent to the Rosleskhoz Information System, which provides them to users. Such information is available for the period 2012–2021 years.

For the formation of the FFF time series, the entire territory of Eurasia, bounded by the parallels of 50° N and 70°N and meridians 65°E and 160°E was divided into cells (further can be also referred to as areas or sites) measuring 15 × 15 arc minutes (total 84 × 404 = 33,936 cells). Each cell is a trapezoid, with a node of the ERA-5 reanalysis grid in its geometric center (with latitude—φ and longitude—λ). The number of "forest fire"-type thermal anomalies registered within a cell in a given month was taken as a characteristic of the FFF at this cell. The FFF value is determined for a particular month from April to October of a certain year t from the period 2012–2020 years for each of the 33,936 considered cells of the territory of Siberia. From the identified FFF values at (φ, λ, t) for each site and each month, the corresponding time series was formed.

When analyzing the specified factual material about the FFF, for each cell we estimate the number of years during which at least one thermal anomaly occurred in a given month of the period of increased wildfire hazard.

For study the variability of MWS and MSP, relevant data presented by the ERA-5 reanalysis [18, 19] for a chosen month and each cell in of Siberia was used. The ERA-5 reanalysis provides the results of mathematical modeling of changes in the hourly amounts of atmospheric precipitation, as well as the meridional and zonal

components of the hourly average wind speed at an altitude of 1000 hPa, for the period from 01/01/1979 to the present, for all grid nodes with a step of 0.25 angular degrees. For verifying mathematical IMERG models [20] used to generate ERA5, the results of both ground and satellite observations [2, 21] are used, which are accumulated and processed using cycle 41r2 of the Integrated Forecasting System (IFS) [19, 22]. The ERA-5 reanalysis is produced by the Copernicus Climate Change Service and supplied by the European Center for Medium-Range Forecasts. The validity of the ERA-5 information has been also confirmed by comparing it with the results of ground-based observations at some points in the world [23].

Based on the ERA-5 information, for each studied area of the territory of Siberia and each month from April to October, we consider time series MSP(φ, λ, t), $MWS_m(\varphi, \lambda, t)$ and MWS_z (φ, λ, t).

Analysis of the data on the characteristics of precipitation and wind showed that in the period 1979–2020 years the duration of time intervals between years with increased (or decreased) values of these indicators for various months and parts of the territory of Siberia lies within 2–4 years.

When solving the first stated task, for each cell of the territory of Siberia, we also computed the number of years during which at least one thermal anomaly occurred in a given month of the period of increased fire hazard.

The method for solving the second task assumed the implementation of a correlation analysis of the relationships between the FFF time series and the MSP, MWS_m, MWS_z series for each area and each month from April to October. We compensated the linear trend for each time series before performing this analysis.

The relationship was deemed significant if the reliability of such a statistical connection, assessed by the Student's test, exceeded 0.9. The connection was recognized as strong if the reliability of the statistical conclusion about its significance, according to the Student's criterion, exceeded 0.95. The thresholds for the correlation coefficient corresponding to the indicated levels of reliability were determined based on the number of degrees of freedom of the series under consideration and constituted 0.64 and 0.74, correspondingly.

The methodology for solving the third stated task consists in assessing for each area and each month in 2012–2020 years period the tendencies of temporal variability of FFF, MSP, MWS_m and MWS_z. At the same time, we took the differences between their average values for the periods of 2012–2016 and 2017–2020 years as a measure of the tendency of interannual variability of the studied indicators. For such processes as interannual changes in the MSP, MWS_m and MWS_z, we also considered the slope of a linear trend of the respective time series (hereinafter SLT) as the characteristic of the trend.

To assess the sustainability of the current trend for MSP, MWS_m and MWS_z in a particular area of the territory of Siberia, we took the value of the difference in the climatic norms of these indicators, calculated for 1991–2020 years as well as 1981–2010 years (the latter characterizes the tendency of interdecadal variability).

The modern tendency of interannual variability of a certain indicator was considered as stable in time, if its direction coincided with the direction of its interdecadal variability tendency. Such coincidence suggests that the current trend of this indicator

will not change in the near future. The latter is a prerequisite for the expediency for using it in forecasting.

It is easy to see that the major factor of uncertainty in the implementation of the proposed methodology is the short duration of the period of time during which the satellite monitoring of the FFF has taken place. The deviations of the reanalysis results of the studied indicators from their actual values can also have a significant impact on the reliability of the conclusions. As shown by their testing with the use of ground weather stations information, such deviations for some points of the territory of Siberia are very large. In this case, the information that is averaged over a certain territory is more accurate, the larger the area of this territory. Consequently, the conclusions obtained using this technique are quite adequate only in relation to certain, preferably large parts of the territory of Siberia.

3 Results

In accordance with the earlier described methodology, for solving the first task, we need to see how often wildfires actually occurred over the territory of Siberia in a given month throughout the period 2012–2020 years. We found that almost all thermal anomalies found in a particular cell were registered during one year. In rare cases, they refer to two years spaced by 4–5 years apart. The number of cells, where thermal anomalies were detected during one or two years (usually non-consecutive) of the period 2012–2020 years is presented in Table 1.

As can be seen from Table 1, the number of cells, where forest fires were detected over the period 2012–2020 years exactly during one year for a fixed month, is significantly less than their total number. Furthermore, there are even more significantly fewer areas where wildfires were detected in different years during the same period. The largest number of cells, where the thermal anomalies of the "forest fire"-type occurred, were in July, and the smallest number were in October.

For the majority of the cells, the number of thermal anomalies detected in them (which we take as an indicator of FFF) varied from several cases up to tens of cases during the respective month range. In such cases, the duration of a continuous interval of dates during which thermal anomalies took place in the same cell can range from

Table 1 Information on the total number of cells over the territory of Siberia, where, for a particular month of the period of increased fire hazard throughout the period of 2012–2020 years thermal anomalies were detected in one or two years

Month	1 year	2 years	Month	1 year	2 years
April	112	0	August	526	1
May	270	0	September	287	0
June	540	3	October	96	0
July	803	12	Total	2634	16

one to 115 days. The coordinates of these thermal anomalies usually change during this time interval. Such long durations of the mentioned time intervals correspond to areas, where fires can run continuously for several months and stop only with the arrival of autumn rains and cold weather. On the date corresponding to the beginning of each such interval, one thermal anomaly is usually found in the cell. On subsequent dates, the hot spots may become larger, and their coordinates may change, including moving to neighboring areas.

As an example, Fig. 1 shows the location of areas of Siberia, on which for the period 2012–2020 years in the months from April to July, the "forest fire"-type thermal anomalies were registered. As can be seen from Fig. 1, such areas constitute only a small part of their total number. Some of them are surrounded by areas where no thermal anomalies were found during the same period, but many of them form clusters. Clusters containing two or more sites may occur in any month, but their number is increased from June to July. In areas belonging to the same cluster, thermal anomalies can be detected as in the same year, as well as (rarely) in different years, but, as a rule, only once during the period 2012–2020 years. The locations of many clusters of sites, during consecutive months, coincide, which indicates that the forest continues to burn in these months. The number of sites that form a particular cluster may vary from month to month, but its general location remains unchanged. These features indicate the existence of latitudinal zones on the territory of Siberia, where wildfires mainly occur, as well as vast territories for which FFF is zero.

Data also show that, for the absolute majority of areas of the territory of Siberia, the time intervals between the maxima (minima) in the FFF time series are much larger than between the respective extrema of the MSP, MWS_m and MWS_z series. At some sites, an extremum in the time series MSP, MWS_m and MWS_z occurs in a year when FFF is zero. This supports a conclusion that there are other significant factors affecting fire hazard circumstances in a particular area under similar meteorological conditions.

When solving the second stated problem, we assessed the significance of statistical relationships between the time series of FFF and MSP, MWS_m and MWS_z for all cells in the territory of Siberia and each month of the period of increased fire hazard. For each month, the location of the areas was determined for which the reliability of the conclusion about the significance of the relationships between interannual changes in FFF with variations of one or another of their factors exceeds 0.9. We also calculated the number of areas for which the correlation of the considered processes is positive or negative, whenever the reliability of such correlation exceeds 0.9 and 0.95. The results of these calculations we present in Table 2.

Table 2 shows that the areas of the territory of Siberia, for which interannual changes in FFF in any months are significantly and even strongly statistically associated with the considered factors, exist. At the same time, a comparison of Tables 1 and 2 indicates that the number of such sites in the months under consideration is only tenths-units of a percent of the total number of sites, where in 2012–2020 years "forest fire"-type thermal anomalies were registered. Their maximum share is 10.83% (for such factor as MWS_m and for July). Such areas in the autumn months occur significantly less frequently than in the summer months.

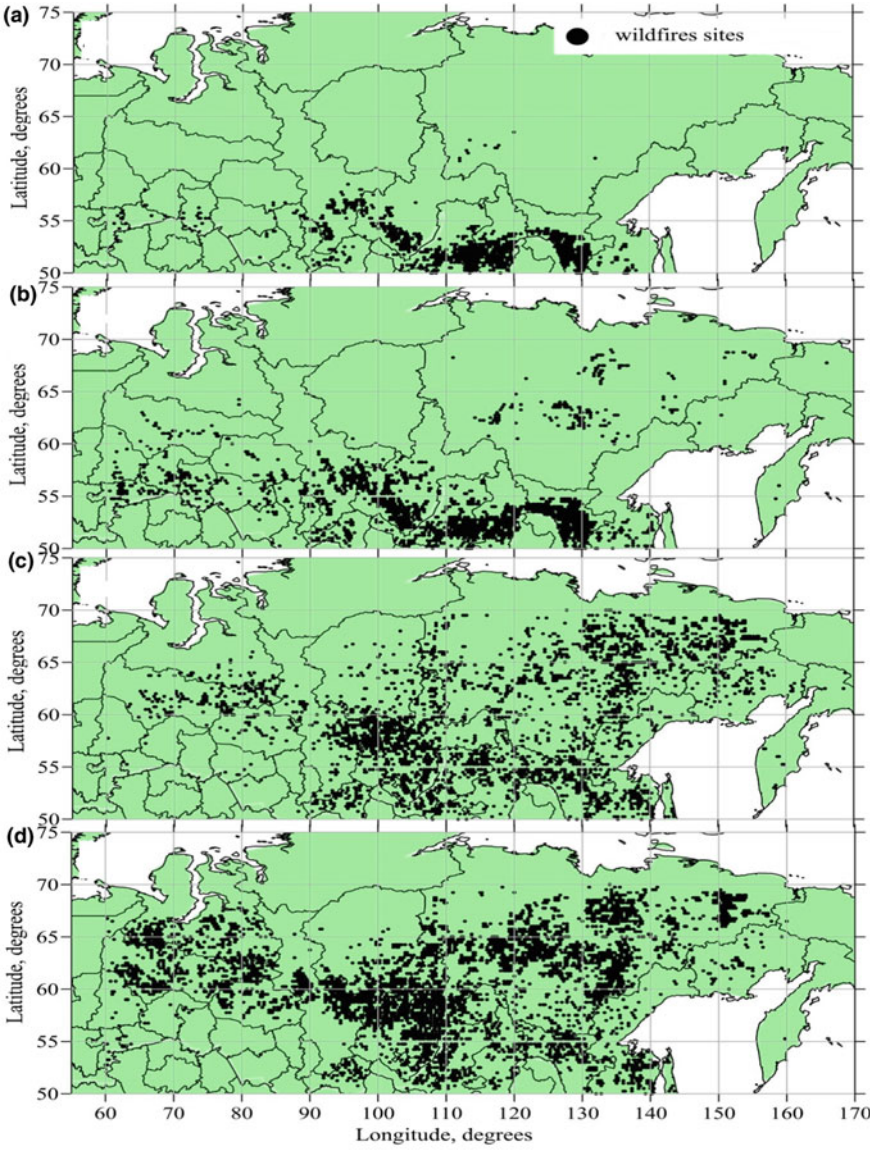

Fig. 1 Location of cells on the territory of Siberia, with thermal anomalies of the "forest fire"-type for the period 2012–2020 years. **a** April; **b** May; **c** June; **d** July

Table 2 The number (N) of cells on the territory of Siberia, for which the reliability of the conclusion about the significance of the relationship of interannual changes in FFF with variations in the respective factor exceeds 0.9 and 0.95, as well as their percentage (M) of the total number of cells where thermal anomalies were detected

MSP								
Reliability of conclusion	0,9				0,95			
Significance threshold	0,64		−0,64		0,74		−0,74	
Indicator	N	M (%)	N	M (%)	N	M (%)	N	M (%)
April	3	2,68	3	2,68	2	1,79	2	1,79
May	16	5,93	1	0,37	8	2,96	0	0
June	36	6,67	31	5,74	21	3,89	17	3,15
July	59	7,35	15	1,88	33	4,11	0	0
August	23	4,37	10	1,90	17	3,23	1	0,19
September	9	3,14	4	1,39	6	2,09	0	0
October	2	2,08	1	1,04	1	1,04	0	0
MWS_m								
Reliability of conclusion	0,9				0,95			
Significance threshold	0,64		−0,64		0,64		−0,64	
Indicator	N	M (%)	N	M (%)	N	M (%)	N	M (%)
April	10	8,93	8	7,14	3	2,68	6	5,36
May	14	5,19	6	2,22	8	2,96	4	1,48
June	24	4,44	23	4,26	11	2,04	13	2,41
July	25	3,11	87	10,83	13	1,62	45	5,60
August	21	3,99	29	5,51	7	1,33	1	0,19
September	9	3,14	7	2,44	3	1,05	1	0,35
October	3	3,13	2	2,08	1	1,04	0	0
MWS_z								
Reliability of conclusion	0,9				0,95			
Significance threshold	0,64		−0,64		0,64		−0,64	
Indicator	N	M (%)	N	M (%)	N	M (%)	N	M (%)
April	2	1,79	1	0,89	0	0	0	0
May	3	1,11	2	0,74	0	0	1	0,37
June	4	0,74	2	0,37	2	0,37	1	0,19
July	5	0,62	4	0,50	1	0,12	2	0,25
August	2	0,38	3	0,57	0	0	1	0,19
September	1	0,35	1	0,35	0	0	0	0
October	0	0	0	0	0	0	0	0

All other things being equal, the number of sites, where interannual changes in FFF are statistically significantly associated with variations in MWS_m, is noticeably greater than the number of sites in which MWS_z variations are a significant factor of these changes. Also among the areas, there are those where significant correlation of the studied processes is positive, as well as areas where it is negative. For such a factor as the interannual changes in the MSP, the areas where it is positive are of noticeably higher number. Furthermore, the number of areas, where the correlation of interannual FFF changes with MWS_m variations is significant and negative, is bigger than the number where it is positive. For such a factor as interannual changes in MWS_z, the number of sites where it is positive is approximately the same as the number of sites where it is negative.

As an example, Fig. 2 shows the location of areas of the territory of Siberia, on which in a given month of increased fire hazard throughout 2012–2020 years "forest fire"-type thermal points were found, and the conclusion about the significance of the relationship between interannual changes in FFF and MSP was characterized by a reliability of at least 0.9. We can conclude that in April (Fig. 2a) such occurrences took place mainly in the southern part of Siberia, in areas where the forests not only got rid of snow, but also had time to dry out. In May (Fig. 2b), the number of detected fires increases, especially in the south of the Krasnoyarsk, Trans-Baikal Territories, Irkutsk, Amur Oblasts and the Republic of Buryatia. In addition to the southern regions of Siberia, there are many northern territories of such type in May. We can infer from Fig. 2b, that in June the number of areas of Siberia where forest fires occurred in the zone of deciduous forests decreases, but in the taiga zone it increases significantly. The maximum number of such sites in the taiga zone occurs in July (Fig. 2d). In many taiga areas, fires that started in June continue to develop. The coordinates of the corresponding thermal anomalies vary within the same areas. August (Fig. 2d) shows a noticeable decrease in the total number of detected fires, which continue to be registered throughout Siberia, but most often in the Republic of Sakha (Yakutia). In general, Fig. 2 shows that in the summer months, the number of areas where interannual changes in FFF are significantly associated with variations in MSP, and the correlation of these processes is negative, is noticeably less than their number, where it is positive. A similar conclusion is fully valid for the autumn months, but the total number of identified areas is sharply less. Some areas where FFF significantly correlates with MSP form clusters, but not usually for more than one month.

The observed results can be explained by the fact that the direct cause of many naturally started forest fires is cloud-to-earth lightnings, which are formed in Cb clouds, which form the most intense and heavy atmospheric precipitation. When a lightning strikes a dry tree, the latter lights up. When it hits a living tree, the discharge passes into the ground along the trunk (along the path of least electrical resistance). This phenomenon leads to the formation of characteristic "tears" and "scars" on the tree trunk and accompanied by the release of a large amount of heat. When the electric discharge exits the trunk into the root system of the tree, the heat generated by it can ignite the dead wood and cause a ground fire. Consequently, the more often thunderstorm clouds pass over a certain area in summer, the higher MSP, and the

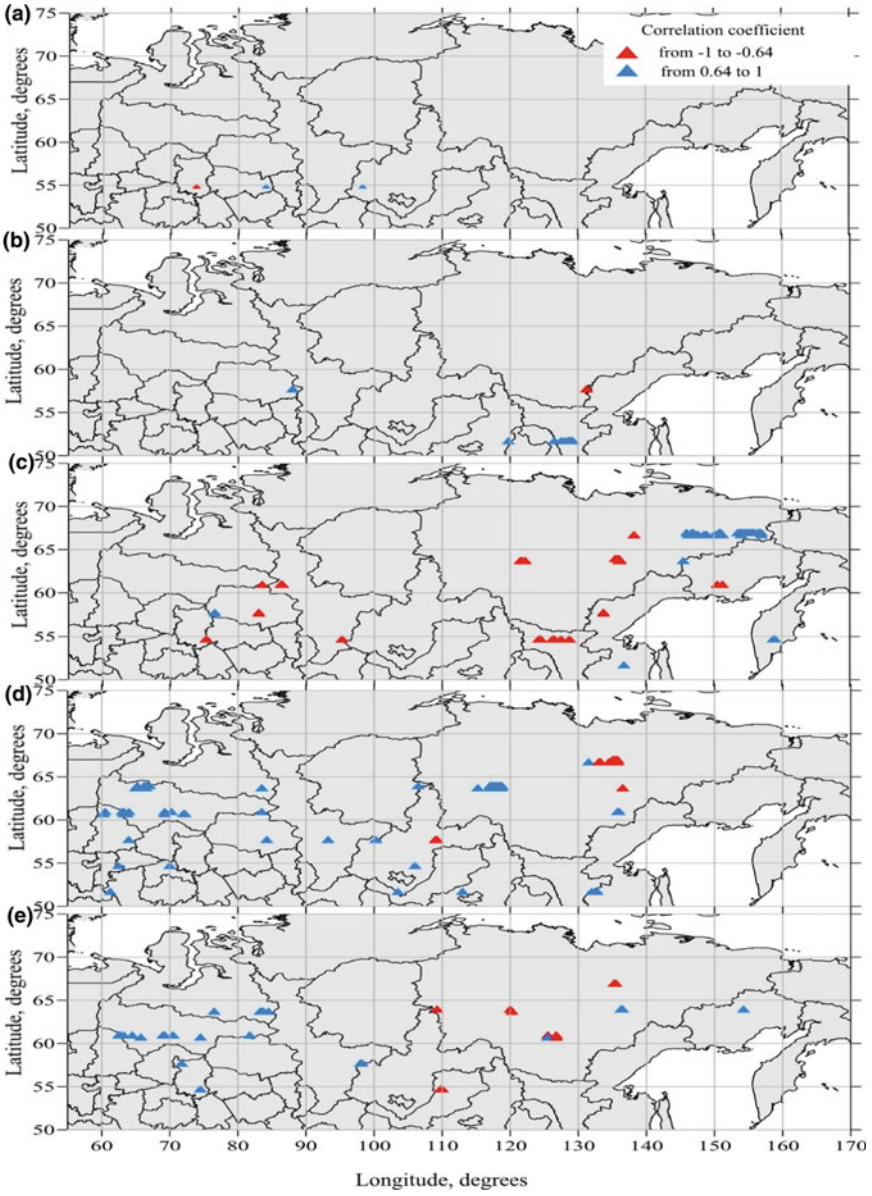

Fig. 2 Location of areas of the territory of Siberia, where in 2012–2020 years the "forest fire"-type thermal points were found, for which the reliability of the conclusion about the significance of the relationships between the time series of FFF and MSP was not lower than 0.9. **a** April; **b** May; **c** June; **d** July; **e** August

more often forest fires occur. Since heavy rainfall distributes over the land in spots, this leads to extinguishing fires only within these spots. Since the areas of such spots, as a rule, are much smaller than the total area, an increase in the MSP can lead to a decrease in the FFF, but not always.

Thus, Fig. 2. indicates that the number of areas of the territory of Siberia, where an increase in MSP leads to a decrease in FFF in any months is small.

Figure 3. shows areas of the territory of Siberia, on which in a given month of the period of increased fire hazard in 2012–2020 years the relationships between the interannual changes in FFF and MWS_m variations were significant with a confidence level of at least 0.9. It follows that the general nature of the distribution of the considered areas over the territory of Siberia is similar to that shown in Fig. 2. At the same time, the areas in which interannual changes in FFF significantly negatively correlate with variations in MWS_m are much larger in the summer months. Their number reaches maximum in July. Some of these areas coincide with those where the correlation of the FFF and MSP series is significant and negative. The latter can be explained by the fact that the MWS_m sign is determined by the direction of the meridional component of the mean monthly wind speed.

With the prevalence of northern winds, bringing drier air formed at high latitudes, the MWS_m sign is negative, and otherwise it is positive. If the frequency and average speed of north winds over the respective area increase, the monthly average values of the relative air humidity above it decrease. Consequently, a decrease in the MWS_m has the same effect on the FFF dynamics as a decrease in MSP.

Among the considered areas, there are also those, with positively correlated variations of FFF and MWS_m. Some of them coincide with areas where there is a positive correlation between FFF and MSP, since thunderstorms are more likely during periods of predominance of southern winds, bringing warmer and, as a rule, more humid air.

A similar study carried out in relation to the relationship of interannual changes in FFF with variations in MWS_z showed that this factor is considerably less significant. Thus, it shows that among the three considered meteorological factors of FFF, the most significant are MWS_m and MSP. Among the corresponding physical processes, those that lead to a decrease in the relative humidity of the air, a decrease in the intensity of atmospheric precipitation and the intensification of thunderstorms (which confirms the conclusions [2, 4–14]) are the most conducive to an increase in the fire hazard in the forests of Siberia.

For solving the third stated problem, we studied the distributions of tendencies of FFF, MSP, MWS_m and MWS_z interannual changes over the territory of Siberia for different months of the period of increased fire hazard for 2012–2020 years.

Figure 4 obtained from [24], shows the corresponding distributions over the territory of Siberia of the current trends of interannual changes in FFF.

Figure 4a shows that for April, the increase in the number of detected forest fires in 2012–2020 years took place in many regions of all constituent entities of the Russian Federation located in Siberia, with the exception of the Yamalo-Nenets and Khanty-Mansiysk Autonomous Districts. The average rate of these processes was maximum (more than one fire per year per site) in the Amur and Tyumen regions.

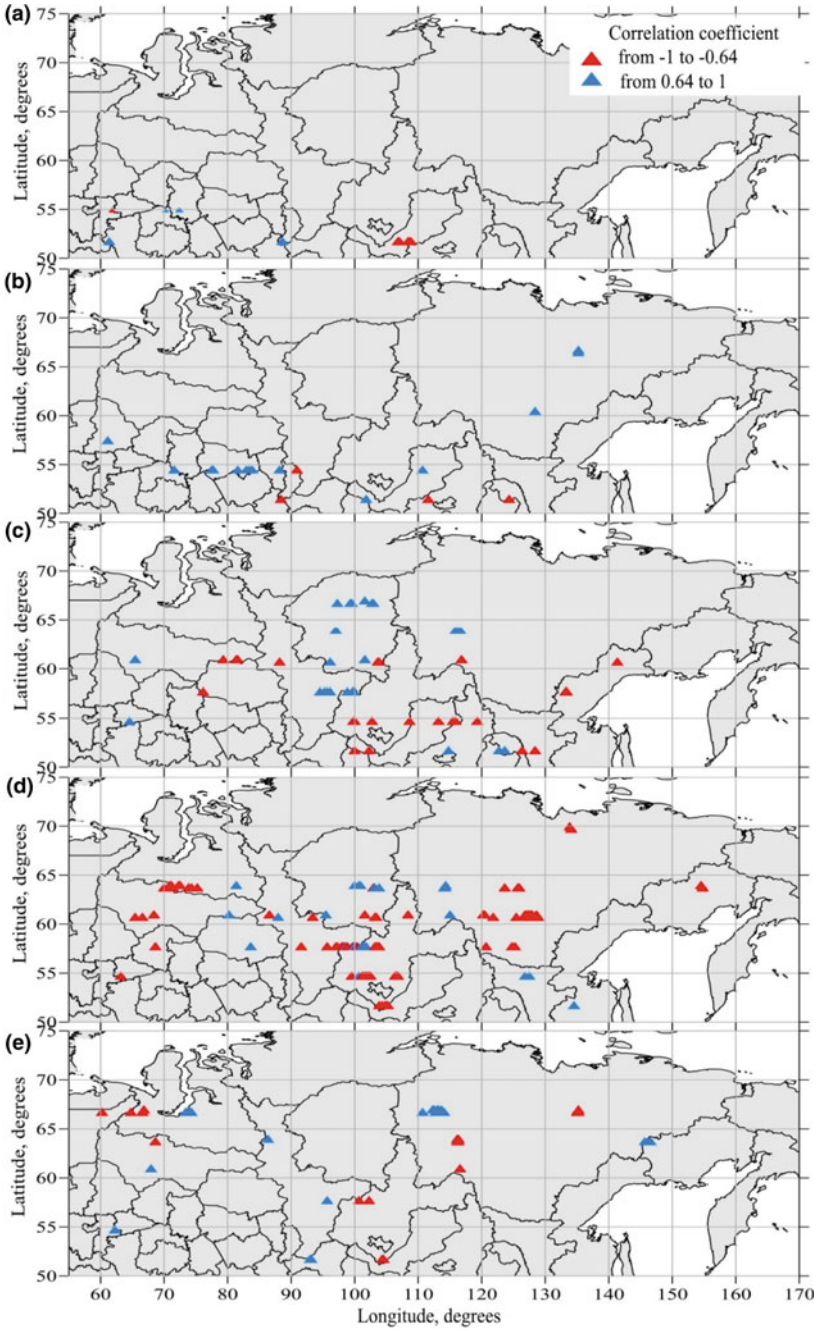

Fig. 3 Location of cells on the territory of Siberia, for which, with a confidence level of at least 0.9, the relationship of interannual FFF changes and MWS_m variations in 2012–2020 years were significant for months: **a** April; **b** May; **c** June; **d** July; **e** August

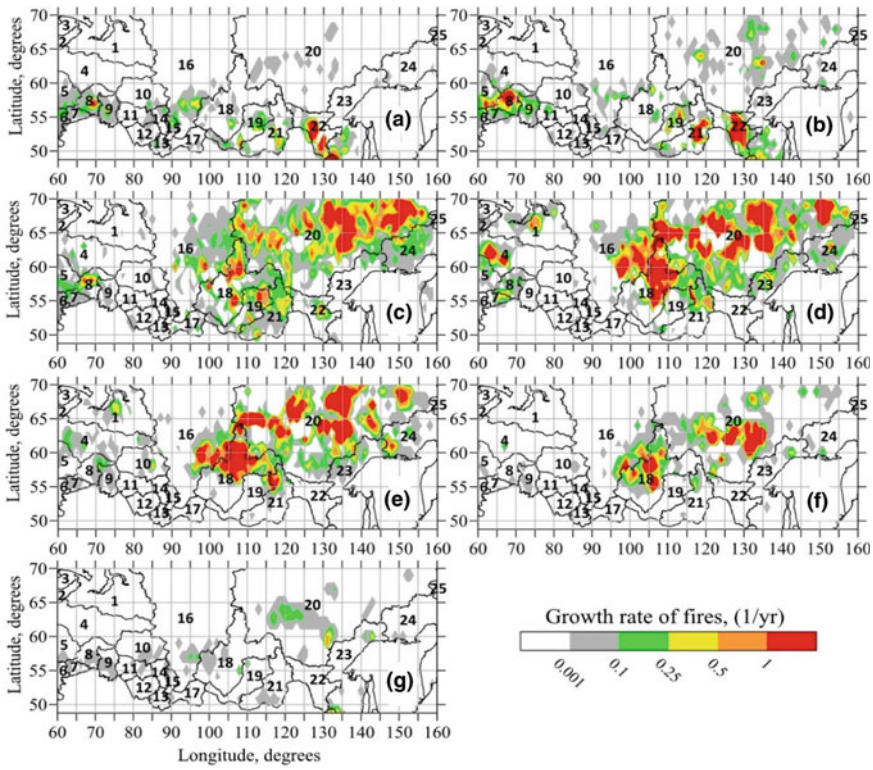

Fig. 4 Sites of the territory of Siberia, where in 2012–2020 years tendencies towards an increase in FFF prevailed. **a** April; **b** May; **c** June; **d** July; **e** August; **f** September; **g** October. The figure shows the territories: (1) Yamalo-Nenets Autonomous Okrug; (2) Republic of Komi; (3) Nenets Autonomous Okrug; (4) Khanty-Mansiysk Autonomous Okrug; (5) Sverdlovsk region; (6) Chelyabinsk region; (7) Kurgan region; (8) Tyumen region; (9) Omsk region; (10) Tomsk region; (11) Novosibirsk region; (12) Altai Territory; (13) Republic of Altai; (14) Kemerovo region; (15) Republic of Khakassia; (16) Krasnoyarsk Territory; (17) Republic of Tuva; (18) Irkutsk region; (19) Republic of Buryatia; (20) Republic of Sakha (Yakutia); (21) Trans-Baikal Territory; (22) Amur Region; (23) Khabarovsk Territory; (24) Magadan region; (25) Chukotka Autonomous District

Figure 4b shows that for May, an increase in the number of large forest fires over the same period occurred in practically the same territories as in April, except for the Kemerovo Region and the Republic of Khakassia. The same tendency holds in the southwest of the Khanty-Mansiysk Autonomous Okrug. The average rate of increase in the number of large forest fires in one area exceeded one per year for some territories of the Republics of Sakha (Yakutia), Buryatia, Trans-Baikal Territory, Amur Tyumen and Sverdlovsk regions. It follows from Fig. 4b that for June, an increase in the number of large forest fires over the considered period occurred mainly in Eastern Siberia. The largest increase in the total area of sites where the average rate of increase in the number of large forest fires exceeded one per year corresponded to the territory of the Republic of Sakha (Yakutia). At the same time,

in the territories of the Amur and Novosibirsk regions, the area of the sites where they occurred has significantly decreased. Figure 4d, e testify to the validity of this conclusion also for July and August. It should be noted that, typical for these months, a significant increase in the number of forest fires that were detected in the north of the Irkutsk Region, Krasnoyarsk Territory, as well as the appearance of such areas in the Yamalo-Nenets Autonomous Okrug.

September (Fig. 4f) shows a noticeable increase over the period 2012–2020 years of the number of registered forest fires mainly in the Republic of Sakha (Yakutia), the northern part of the Irkutsk region, as well as in the north of the Trans-Baikal Territory.

As follows from Fig. 4g, for October, the increase in the number of large forest fires in 2012–2020 years occurred mainly in the southern part of the territory of the Republic of Sakha (Yakutia), in the south of Western Siberia, as well as in the Irkutsk region, Krasnoyarsk and Trans-Baikal Territories.

To facilitate the perception of the distributions of the tendencies of interannual changes in MWS_m for different months over the territory of Siberia, Fig. 5. shows the corresponding distributions of the average values of these indicators.

From Fig. 5a, it is clear that in the northern part of the territories of Western Siberia and the Urals, located to the west of the 90° meridian, as well as over the Khabarovsk and Primorsky Territories for April in 2012–2021 years south winds predominated. For the rest of Siberia, this conclusion does not hold, since in many of its parts the north winds dominate, bringing in relatively dry Arctic air.

Figure 5b–e show that for the months from May to August over most parts of Siberia, located to the west of the meridian 120° E north winds dominate (the average value of MWS_m values is negative). This is also true for the areas of the territory of Siberia located to the north of the parallel of 65°N and to the west of the meridian 140°E.

For many parts of the Far Eastern Federal District (and located to the east of the indicated boundaries), the average MWS_m values are positive. Consequently, they had experienced the predominately south winds. Over the territories where the MWS_m were negative, the manifestation of a decreasing trend in MWS_m means that there the frequency and average speed of the north winds increase. Considering this, let us analyze the distribution over the territory of Siberia of the SLT of the MWS_m time series, which is shown in Fig. 6.

Figure 6a shows that for April, positive values of SLT MWS_m were typical for almost the entire territory of the subjects of the Russian Federation belonging to the Siberian and Ural Federal Districts (which are located to the west of the 120°E). To the east of this meridian, the opposite tendencies prevailed in the changes in MWS_m. Keeping in mind Fig. 5a, this shows that over the northern part of the territories of Western Siberia and the Urals, located to the west of the meridian of 70°E, a tendency towards increased north winds prevailed. Over the Transbaikal, Khabarovsk and Primorsky Territories, as well as the southern uluses of the Republic of Sakha (Yakutia), there was a tendency towards weakening of the south winds. For the rest of the territory of Western Siberia, tendencies towards strengthening of the south winds took place, and over Eastern Siberia, there was a weakening of the north winds.

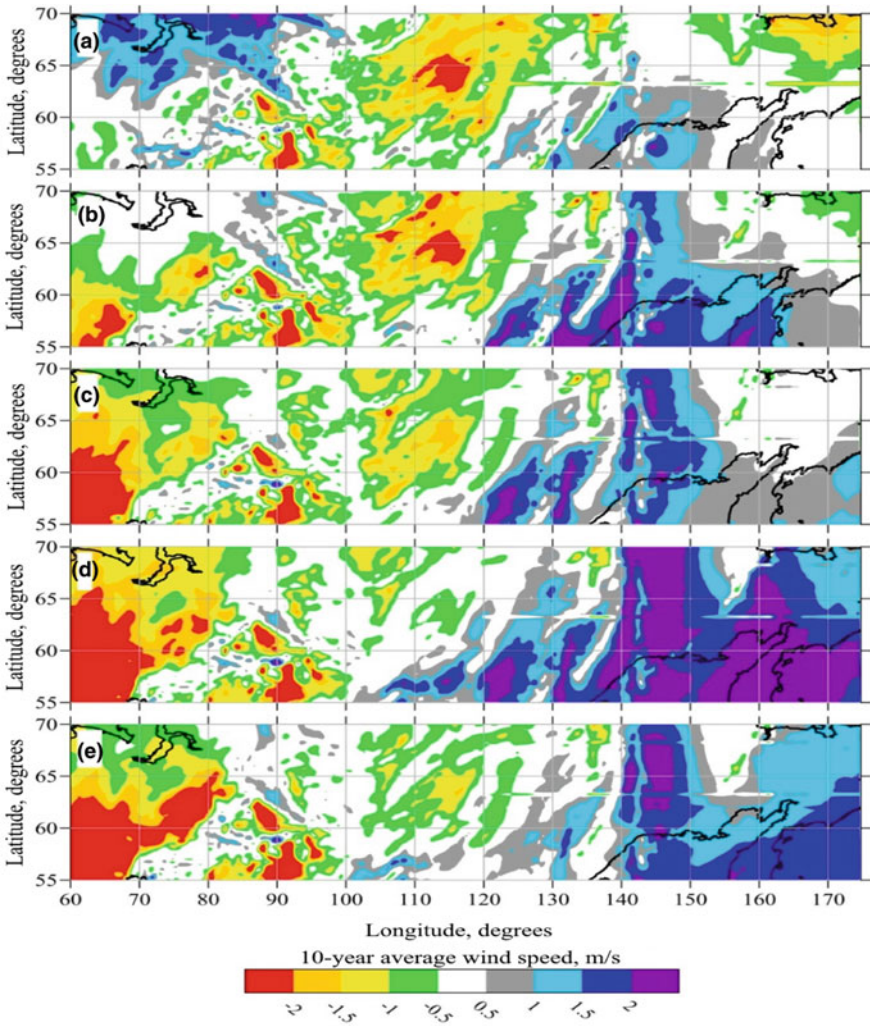

Fig. 5 Distribution of the average MWS_m values for 2012–2021 years over the territory of Siberia for months: **a** April; **b** May; **c** June; **d** July; **e** August

As can be seen from Fig. 6b–e, negative values of SLT MWS_m for the months from May to August were typical for the territories of Eastern Siberia located in the strip between the meridians of 120 and 140°E. For May and August, specifically, a similar trend prevailed over the northern territories of Western Siberia, limited by the meridians of 75 and 90°E. For other parts of the territory of Siberia, this conclusion does not hold.

Considering Fig. 5b–e, it is clear from Fig. 6b–e that for the months from May to August, north winds strengthened during 2012–2020 years period for the territory

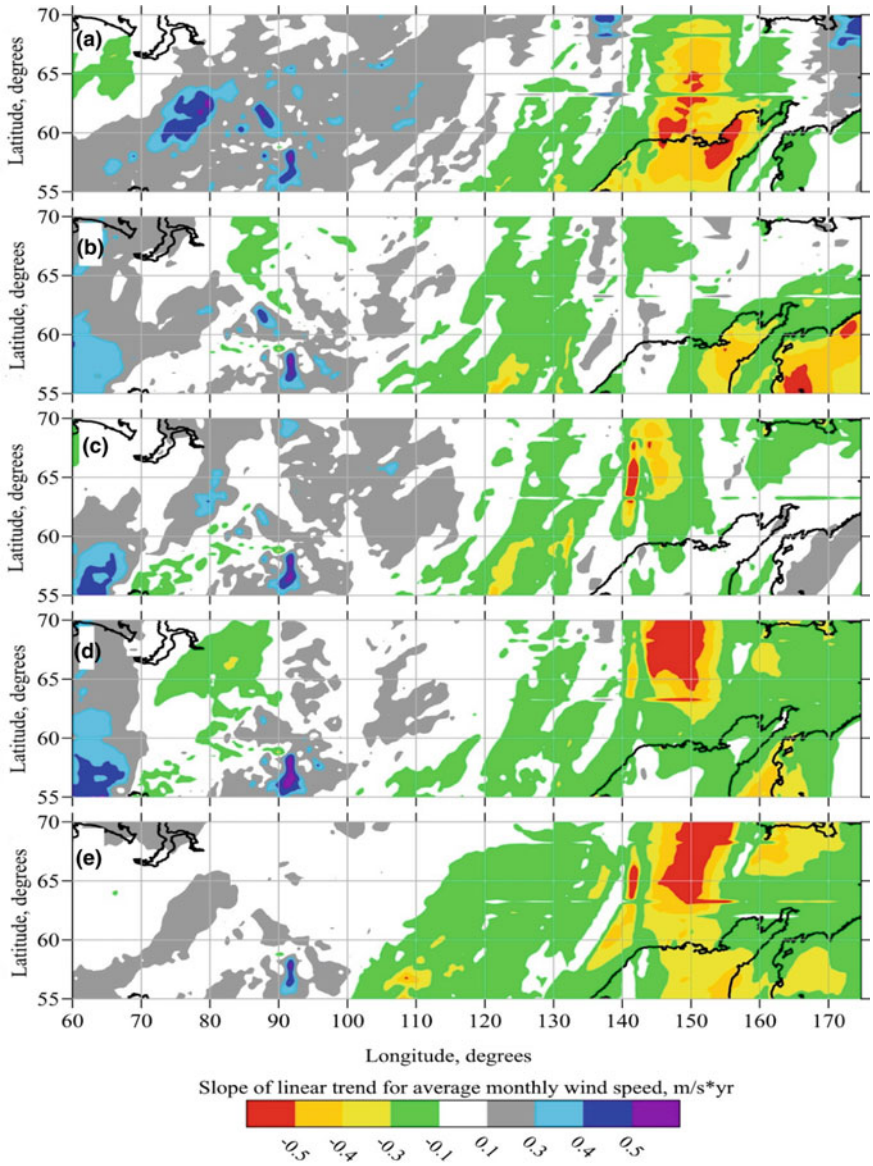

Fig. 6 Distribution over the territory of Siberia of SLT values of MWS_m time series for the months April-August 2012–2020 (negative values correspond to north winds). **a** April; **b** May; **c** June; **d** July; **e** August

of Eastern Siberia, located between the meridians of 120 and 140°E, as well as to the north of the parallel of 65°N (territory of the Republic of Sakha (Yakutia). By comparing with Fig. 4b–e, it is easy to see that the locations of such areas coincide with areas where increasing trends for FFF prevailed in the corresponding months.

Figure 7 shows the distribution over the territory of Siberia of the difference in the climatic norms of MWS_m for chosen months over the periods 1991–2020 and 1981–2010 years We can see that for April the tendency to an increase in the frequency and strength of north winds in the interdecadal interval was typical for the part of the territory of the Republic of Sakha (Yakutia) located within the meridians of 120 and 150° E, as well as to the north of the parallel of 65°N. As it is easy to see from Fig. 5a, to the south of the indicated parallel in the interval of interdecadal variability, a tendency towards weakening of the south winds prevailed.

Over the northern regions of Western Siberia, tendencies towards a weakening of the north winds dominated, and over its southern regions—to an increase in the south winds.

Similar distributions over the territory of Siberia of trends in the dynamics of climatic norms of MWS_m are also typical for June (Fig. 7c). For May, July and August, no significant changes in the climatic norms of MWS_m were revealed in the indicated area, but to the south of it in July and August, decreasing tendencies in MWS_m prevail.

It follows from Fig. 7. that the distribution over the territory of Siberia of the difference in climatic norms of MWS_m for April and June, calculated for the periods 1991–2020 and 1981–2010 years are in many respects similar to distributions of tendencies of interannual changes in MWS_m, which confirms the stability of the revealed regularities.

Figure 8 shows the distribution over the territory of Siberia of the values of the SLT of MSP, calculated for the period 2012–2021 years.

It follows from Fig. 8 that for all considered months, the tendency for an increase in MSP in 2012–2020 years prevails closer to the Urals Mountains in Western Siberia, as well as in the south and in the Baikal region of Eastern Siberia. Figure 8a shows that for April, opposite trends in the same years dominated in the east of the Republic of Sakha (Yakutia), as well as in the Far East of Russia. For May (Fig. 8b), the downward trends in MSP in 2012–2020 years showed in the north of the Krasnoyarsk Territory and throughout the Republic of Sakha (Yakutia). Figure 8c, d show that for June and July, the tendencies for a decrease in MSP in 2012–2020 years took place in the western part of the Republic of Sakha (Yakutia), as well as in the Trans-Baikal Territory and the Amur Region. As follows from Fig. 8e, for August, the tendencies towards a decrease in MSP during that period were typical for the northern part of the territory of Siberia (in the area to the east of the 80°E).

We can see from the comparison of Fig. 8 with Fig. 4 that in many parts of Siberia, with increasing tendencies of FFF in April, MSP also increases. Since thunderstorms in April are very rare, anthropogenic factor may be one of the probable causes of this phenomenon. The warming of the local climate may also be a significant factor, because of which the intensity of evaporation has increased. Its increase could compensate for the increase in MSP.

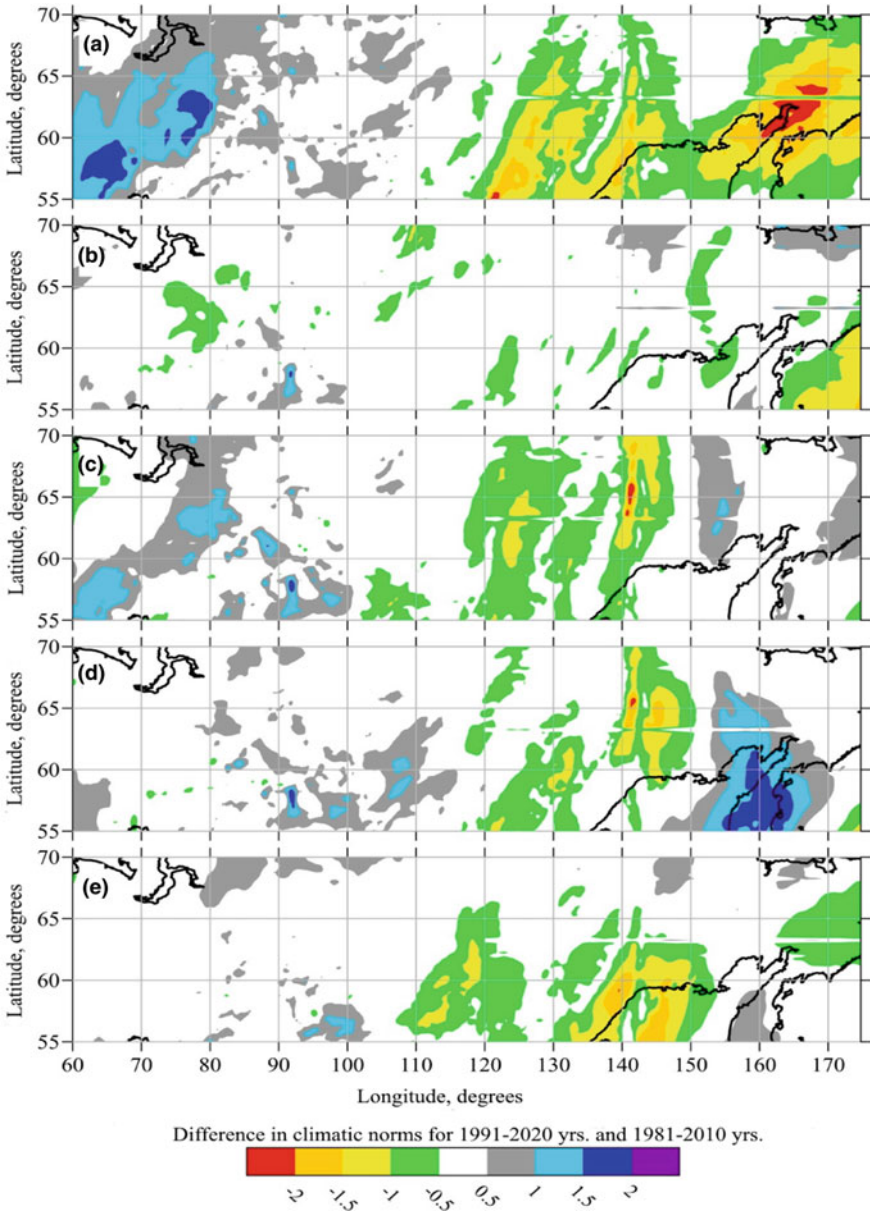

Fig. 7 Distribution over the territory of Siberia of the difference in climatic norms MWS_m, calculated for the periods 1991–2020, 1981–2010 years. **a** April; **b** May; **c** June; **d** July; **e** August

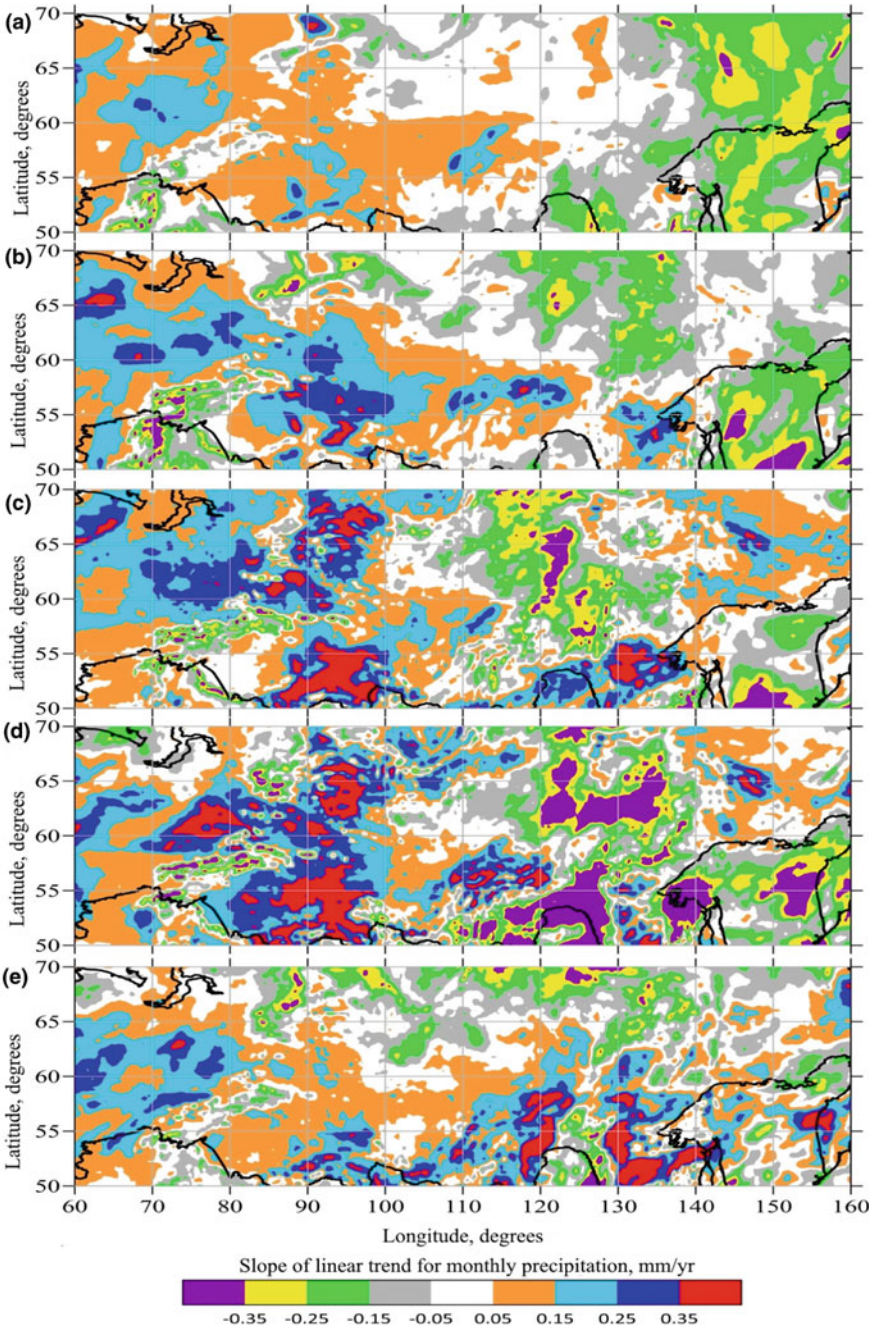

Fig. 8 Distribution over the territory of Siberia of SLT of MSP values, estimated for the period 2012–2021 years. **a** April; **b** May; **c** June; **d** July; **e** August

In many parts of the Republic of Sakha (Yakutia), where an increase in FFF occurred in May, trends towards a decrease in MSP prevailed. At the same time, on the territory of the Baikal region, the FFF values increased, despite the increase in MSP. In the southern part of the territory of Western and Eastern Siberia, no similar correspondence manifested (both FFF and MSP increase). In June and July, the considered correspondence between the trends of interannual changes in FFF and MSP shows up for the territories of the Republic of Sakha (Yakutia), the northern regions of the Irkutsk region, as well as the Trans-Baikal Territory. For August, a similar correspondence takes place for the northern parts of the territories of the Krasnoyarsk Territory and the Republic of Sakha (Yakutia). Similarly, for the autumn months, the tendencies towards a decrease in MSP prevail in the same areas of the southern uluses of the territory of Sakha (Yakutia), where in 2012–2020 years tendencies towards an increase in FFF prevailed. Consequently, the considered correspondence between the tendencies of interannual changes in the FFF, as well as the MSP for the months of the period of increased fire hazard takes place for many parts of the territory of Siberia.

As can be seen from the comparison of Figs. 6 and 8 and, the location of many parts of the territory of Siberia, where FFF in 2012–2020 years increased with a similar increase in MWS_m, coincide with the locations of the cells, where MSP also decreased (both factors acted unidirectionally, which enhances the response of FFF to them). At the same time, for many parts of Siberia, the tendency towards an increase in FFF was combined with an increasing tendency for MSP, which could be a consequence of not only the intensification of the anthropogenic factor and an increase in evaporation, but also the more frequent occurrence of thunderstorms in May–August.

Comparing Fig. 8 with the distribution of tendencies of the interdecadal variability of the MSP over the territory of Siberia, the areas where the direction of these tendencies coincide are very few. Therefore, we can hardly expect the stability of the tendencies of interannual changes in the MSP in the past, as well as in the future.

Summarizing the above observations, we can conclude that our assumption is correct, and interannual changes of local meteorological conditions can be considered as significant factors of FFF on the territory of Siberia only in rather rare cases. At the same time, the current trends in the interannual dynamics of the MSP, as a rule, are not stable.

4 Discussion

As follows from the obtained results, among the three considered meteorological factors, the most promising for use in forecasting are the interannual changes in the MWS_m. The current trends in the interannual variability of this indicator for many parts of the territory of Siberia coincide with the trends in their interdecadal variability, as well as trends in the interannual variability of the FFF.

The revealed specifics of the statistical relationship for interannual variations in MWS_m with FFF indicate the possibility of the existence of causal relationships between them.

According to the current understanding about the reasons for interannual changes in MWS_m, one of the main factors is the variation in the difference in mean atmospheric pressures over the waters of the Arctic seas and over the inner territories of Siberia [15]. This phenomenon can contribute both to intensification of the Arctic monsoons over Siberia in the summer months, as well as to an increase in the frequency of Arctic air incursions into Siberia.

With the modern warming of the Siberian climate, the average atmospheric pressure over its inner territories tend to decrease (this phenomenon is most pronounced in the summer months). The reason for this may be the changes in the average atmospheric pressure over the water areas of the Arctic seas due to the variations in the average temperatures of their surface. In the months when the surfaces of these seas are partially covered with ice, their average temperatures are the lower, the greater is the concentration of their ice cover (ice extent). Therefore, the reason for the increase in MWS_m over the territories of Eastern Siberia that happened in the period 2012–2020 years may be due to an increase in the ice coverage of the waters of the Laptev and East Siberian Seas. This phenomenon was revealed and described in [25]. A likely reason for the increase in the ice cover of the Arctic seas is, paradoxically, the warming of the Siberian climate [26]. The latter now causes the earlier formation of floods in the estuarine areas of the Siberian rivers flowing into the Arctic seas, with the subsequent formation of polynyas on their pre-estuarine seashore. On some rivers, in recent years, this phenomenon has already occurred at the end of May.

As is known [27], the average daily intensity of insolation of the underlying surface depends on the average height of the Sun above the horizon during daylight hours, as well as on day duration. Therefore, the average amount of direct solar radiation absorbed by a unit area of the polynyas free water surface at the date of the beginning of its formation (t_0) is the less, the longer the time interval separating this date from the beginning of the Polar day. The water surface of the formed polynya not only absorbs solar radiation, but also loses heat due to evaporation, as well through heat exchange with the atmosphere and underlying water layers.

The difference between heat absorbed by the surface waters and lost by them is spent on melting the ice surrounding it. The longer the time interval separating the date t_0 from the beginning of the Polar Day, the smaller the value of this difference. If the duration of this interval is so long that the difference in the indicated characteristics becomes negative, the previously formed polynya begins cover with ice again [28].

Starting from the year in which this phenomenon first occurred, further warming of the Siberian climate will cause it more and more often, and the total area of the polynyas will become less and less by the time the Polar Day begins [26]. Judging by the results of [25], this year was 2012. Consequently, with further warming of the Siberian climate, polynyas on the pre-estuarine coastal areas of the Siberian rivers flowing into the Laptev and East Siberian seas will appear earlier, and the total average monthly area and volume of the ice cover of these seas in May–August will

increase. The latter will lead to an increase in the absolute value of MWS_m over the territory of Eastern Siberia.

Thus, the current trends of interannual changes in MWS_m can be expected to be stable in the future as long as the climate in Siberia continues to warm. Considering this, it seems likely that among the significant factors of interannual changes in FFF in Siberia we can count not only variations in MWS_m, but also in the average ice extent of the waters of the Laptev and East Siberian Seas.

As can be seen from the results of this paper, the FFF values in the months of increased fire hazard rise in many populated territories. In the same territories, where MSP is also increasing. The latter occurs, including April and October, during the months in which thunderstorms are an extremely rare phenomenon, which indicates the possible involvement of the human factor in the intensification of forest fires. The only but singularly effective way to counteract this factor is to improve the preventive and supervisory activities of the Forest Guard units and the State Fire Service of the Ministry of Emergency Situations of Russia.

5 Conclusion

In contrast to the day-to-day variability of the FFF, the interannual variability of FFF much weaker depends on the variations of the considered meteorological conditions. The percentage of area of the territory of Siberia for which this dependence is statistically significant is substantially less than the total number of areas with detected forest fires.

For the absolute majority of the cells in the territory of Siberia, where thermal anomalies associated with forest fires were detected, their occurrence took place within one year. Over the period 2017–2020, such years become more frequent than over the period 2012–2016 years.

Many of the areas where thermal anomalies were found are located in clusters. The FFF values in the areas belonging to such clusters are significantly higher than outside them. The reasons for this phenomenon require additional study.

The time interval between the years with extreme (increased or decreased) values of MSP, MWS_m or MWS_z in the territory of Siberia is 3–4 years.

The number and location of areas in the territory of Siberia, with significantly strong statistical connection of interannual changes in FFF with variations in either MSP, MWS_m or MWS_z, depend on the month and the considered factor. For any of the three considered factors, this number reaches maximum in July and minimum in April and October. The largest number of such sites corresponds to MWS_m, and the smallest—to MWS_z. Some of the so identified areas are located within areas in which interannual variations in FFF increase, and interannual variations in MSP and MWS_m decrease (meanwhile, the average speed and frequency of northern winds increase). At the same time, in many of these areas, the tendencies of interannual and interdecadal changes in MWS_m coincide in direction, which indicates their stability

in time. There are significantly fewer areas where a similar property holds for MSP tendencies.

A probable reason for the stability of the tendencies of interannual changes in MWS_m is the influence of the ongoing warming of the Siberian climate for the spring months on the interannual changes in the summer months of the ice concentration of the Laptev and East Siberian Seas. If the warming of the Siberian climate continues, the current trends of interannual changes in MWS_m may continue into the future (which indicates their usefulness in forecasting).

The practical significance of this study lies in the fact that it identifies areas of the territory of Siberia where the influence of the considered meteorological factors on interannual changes in the FFF for months of increased fire hazard is significant, as well as an assessment of the stability of the identified trends. The obtained results create the prerequisites for the successful development of a methodology for long-term forecasting of FFF, which is necessary to improve the adequacy of the plans developed by the Forest Guard and State Fire Service of the Ministry of Emergency Situations of Russia. Prospects for further research in the stated direction are due to the need to develop such a methodology, as well as to identify areas of the territory of Siberia, where the most effective way to reduce damage from the forest fires is to improve preventive, control and supervisory activities.

References

1. Global Forest Resources Assessment 2020 (OLR-2020). [Electronic resource]. Access mode: https://www.fao.org/forest-resources-assessment/2020/ru.
2. Bondur V. G., Mokhov I. I., Voronova O. S., Sitnov S. A. Satellite Monitoring of Siberian Wildfires and Their Effects: Features of 2019 Anomalies and Trends of 20-Year Changes //Doklady Earth Sciences. – 2020. Vol. 492. Issue 1. – pp. 370–375. ISSN 1531-8354 1028-334X, 1531–8354, https://doi.org/10.1134/S1028334X20050049.
3. Information System for Remote Monitoring of the Federal Forestry Agency: official site: https://pushkino.aviales.ru/main_pages/index.shtml.
4. Vorobyov Yu. L. Forest fires on the territory of Russia: State and problems // Yu. L. Vorobiev, V.A. Akimov, Yu. I. Sokolov. Ed. Yu. L. Vorobyov. MChS of Russia. – Moscow, DEX-PRESS. – 2004. – 312 c. ISBN 5-9517-0008-6. (In Russian).
5. Drozdova T. I., Sorokovikova E. V. Analysis of forest fires in the Irkutsk region in 2010–2019 // XXI Century. Technosphere safety. – 2021. – 6 (1), pp. 29–41. (In Russian).
6. Timofeeva S. S., Garmyshev V. V. Valuation of fire hazards of subjects of the Russian Federation of the Siberian federal district based on integrated indicators of fire risk // Fundamental'nye issledovaniya. – 2015. № 2 (14), pp. 3059–3064. (In Russian).
7. Chuykov A. M., Smetankina G. I., Dorokhova O. V. The problem of reducing the level of fire risk areas at risk of forest fires // Sovremennye tekhnologii obespecheniya grazhdanskoi oborony i likvidatsii posledstvii chrezvychainykh situatsii. 2019. № 1 (10), pp. 465–468. (In Russian).
8. Mozyrev N. K., Kornishin V. A., Koshkarov V. S. Fire safety of forests. Vestnik sovremennykh issledovanii. 2019. № 2 (1), pp. 60–63. (In Russian).
9. Sheshukov M. A., Kovalev A. P., Orlov A. M., Pozdnyakova V. V. Problems and prospects of forest protection from fires // Sibirskii lesnoi zhurnal. – 2020. № 2, pp. 14–20. doi: https://doi.org/10.15372/SJFS20200202. (In Russian).

10. Sverlova L. I. A method for assessing fire hazard in forests by weather conditions, taking into account the zones of atmospheric aridity and seasons. Khabarovsk. – 2000. – 46 p. (In Russian).
11. Calculation of a complex indicator of fire hazard in forests [Electronic resource]. Access mode: http://method.meteorf.ru/danger/fire/calculate/calculate.html.
12. Nesterov V. G. Burningness of the forest and methods of its determination. – Moscow: Goslesbumizdat. – 1949. – 76 p. (In Russian).
13. Sokolova G. V., Teteryatnikova E. P. Problems of long-term forecasting of fire hazard in the forests of the Khabarovsk Territory and the Jewish Autonomous Region based on meteorological conditions. Khabarovsk: Publishing house of the Far Eastern Branch of the Russian Academy of Sciences. – 2008. – 150 p. (In Russian).
14. Sokolova G. V. The method of long-term forecasting of fire hazard indicators in the forests of the Amur region based on the account of atmospheric circulation parameters // IVUZ "Forest Journal". – 2014. № 5. (In Russian).
15. Khromov S. P., Petrosyants M. A. Meteorology and climatology, 7. (Classic university textbook). – Moscow: Moscow State University. – 2006. pp. 18–19. – 582 p. ISBN 5-211-05207-2. (In Russian).
16. Database Coordinates of thermal points. [Electronic resource]. Access mode: https://www.mchs.gov.ru/ministerstvo/otkrytoe-ministerstvo/otkrytye-dannye/7707034952-ThermoPoints.
17. Coal and Peat Fires: A Global Perspective, *Eds: G.B. Stracher, A. Prakash, E.V. Sokol,* Elsevier, 2015, Vol. 3, pp 57–93.
18. Hersbach H., Bell B., Berrisford P., Hirahara S., András Horányi., et al. July 2020 Part A. Vol. 146. Issue 730. P. 1999–2049. The ERA5 global reanalysis. Quarterly Journal of the Royal Meteorological Society. https://doi.org/10.1002/qj.3803.
19. Hersbach H., Dee D. ERA5 reanalysis is in production // *ECMWF Newsletter*. 2016. Vol. 147. P. 7.
20. IMERG: Integrated Multi-satellitE Retrievals for GPM | NASA [Electronic resource]. Access mode: https://gpm.nasa.gov/data/imerg.
21. Timofeev Yu. M. Global system for monitoring atmospheric and surface parameters. – Saint Petersburg: Saint Petersburg State University. – 2010. – 129 p. (In Russian).
22. Hoffmann L., Günther G., Li D., Stein O. et al. From ERA-Interim to ERA5: the considerable impact of ECMWF's next-generation reanalysis on Lagrangian transport simulations // Atm. Chem. Phys. 2019. Vol. 19. –pp. 3097–3124.
23. Fedorov V. M. Insolation of the Earth and modern climate change. – Moscow: Fizmatlit. – 2017. 192 p.
24. Bridging the Gap: Connecting Ecologists to Earth Data [Electronic resource]. Access mode: https://gpm.nasa.gov/applications/bridging-gap-connecting-ecologists-earth-data.
25. Kholoptcev A. V., Shubkin R. G., Babenyshev S. V. Water exchange of areas of the Earth surface with the atmosphere and forest fires, on the example of Siberia//2021. (In print).
26. Kholoptsev A.V., Podporin S.A. (2021). Meridional components of atmospheric circulation and ice cover of the Arctic in summer seasons. *Meteorology and Hydrology*. – 2021. № 6. – pp. 34–42.
27. Kholoptsev A. V., Shubkin R. G., Baturo A. N., Babenyshev S. V. The Climate change in the Arctic zone of Russia and climate warming in Siberia // *Processes in GeoMedia.* – Vol. 2. Springer Geology. Ed. Tatiana Chaplina. – 2021. (In print).
28. Kholoptsev A.V., Shubkin R.G., Podporin S.A. Climate change in Siberia, forest fires and ice coverage of the Northern Sea Route in the summer months // IOP Conference Series: Earth and Environmental Science. Energy & Environmental Science.

New Opportunities for the Development of Renewable Sources of Hydrosphere Energy

K. V. Pokazeev, D. A. Solovyev, and L. V. Nefedova

Abstract The assessment of the future role of various types of renewable energy sources (RES) in the world electricity consumption, including hydropower based on intelligent forecasting methods, is made., Artificial neural networks were used for modelling. That makes it possible to implement some principles of artificial intelligence based on a neural network algorithm with the extension to use several input functions. A comparison of our estimates of the various types of hydrosphere energy potentials, which can be used in renewable energy installations, is undertaken. Prospects for the development of renewable energy in the hydrosphere across multiple world regions are considered. Some creative directions for the use of energy resources of the hydrosphere are discussed.

Keywords Hydrosphere resources · Renewable energy · Forecasting · Electricity consumption · Energy Efficiency

1 Introduction

Due to global warming, considerable attention is paid to the development of renewable energy as an alternative to traditional types of energy generation. Extensive political and economic measures to limit carbon-bearing power are planned in Europe [1]. The widespread use of renewable energy is interpreted as the primary tool that can significantly reduce greenhouse gas emissions of carbon fuels [2]. At the same time,

K. V. Pokazeev (✉)
Faculty of Physics of Lomonosov, Moscow State University, Leninskie gory, 1, Moscow 119991, Russia
e-mail: sea@phys.msu.ru

D. A. Solovyev
Shirshov Institute of Oceanology, Russian Academy of Sciences, Nahimovskiy prospect, 36, Moscow 117997, Russia

L. V. Nefedova
Faculty of Geography of Lomonosov, Moscow State University, Leninskie gory, 1, Moscow 119991, Russia

© The Author(s), under exclusive license to Springer Nature Switzerland AG 2022

V. I. Karev (ed.), *Physical and Mathematical Modeling of Earth and Environment Processes*,
Springer Proceedings in Earth and Environmental Sciences,
https://doi.org/10.1007/978-3-030-99504-1_20

direct attention is paid to some successful renewable energy projects implemented in certain regions in a short period. In this case, as a rule, the possibility of implementing similar projects in other areas, the general potential of the corresponding type of energy, and the ability of renewable energy to partially or entirely replace the traditional carbon fuels on a planetary scale are not considered.

2 Research Methods

To assess the current and future role of various types of RES in world electricity consumption, including traditional hydropower, we made a model forecast based on the BP Statistical Review of World Energy 2021, available from 1985 to 2021 [3].

For modelling, artificial neural networks were used to implement some of the principles of artificial intelligence. We have implemented a neural network algorithm in the STATISTICA software environment (Automated Neural Networks) based on a multilayer neural network architecture with backpropagation of an error discussed in detail in [4, 5]. The algorithm included the «mixing» option for input functions in this case. Thus, after training, at the stage of predicting the inputs, the same number remains, but the values of the admixed functions are not taken into account in the result. Still, they are used only to feed the neural network input when calculating subsequent values. Retrospective time series characterizing global macroeconomic indicators and natural processes, including World Gross domestic product dynamics, hydrocarbon prices, and various climatic indicators, which were used as «mixing» functions. Data are available based on the open statistical archive Our World in Data (OWID) were used. It is an online scientific publication that focuses on major global issues such as poverty, disease, hunger, climate change, war, existential risks and inequality.

3 Discussion of the Results

The obtained results are presented in Fig. 1. The graphs show retrospective and forecast data of the various types of alternative energy sources role in world electricity energy consumption (EEC), including traditional hydropower and nuclear power, up to 2035. It can be seen that the overall increase in the share of renewable energy sources brings it closer to conventional types of generation. At the same time, traditional hydropower will continue to dominate over other kinds of RES in global electricity consumption. This indicates its high potential, despite certain environmental restrictions. However, it should be noted that this figure did not include graphs of renewable energy sources that have significant energy potential but are not currently widely used. The prospect for using such energy sources, which include other individual types of renewable energy sources in the atmosphere and hydrosphere of the

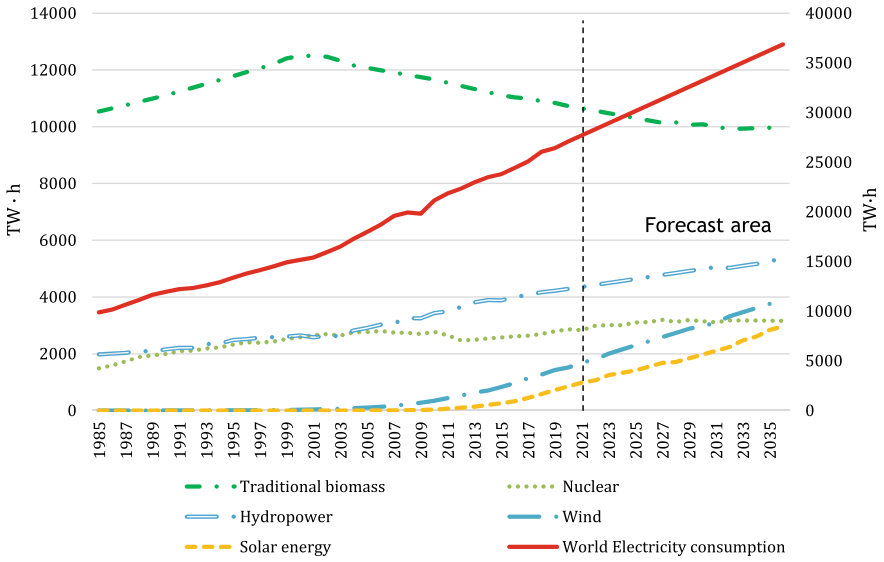

Fig. 1 Retrospective and forecast data (with a step of 10 years from 1985 to 2035) of the role of various types of alternative energy sources, including traditional hydropower and nuclear power in world electricity consumption (EEC) on the additional right axis, [3]

Earth, requires detailed consideration. The study of this subject is the goal of our work.

The hydrosphere has significant energy potential, which can be used in renewable energy, along with the atmosphere [6]. According to the evaluations in publications of a number of authors [7–11], the energy potential of the hydrosphere is approximate twice as significant as the current energy consumption by humanity.

Some types of hydrosphere energy have been used in the energy sector for a long time. Therefore, considerable experience has already been accumulated in their use, while the others have just begun to be used. In recent years, many technical solutions have been developed that made it possible to use various types of hydrosphere energy: thermal, dynamic, the power of the biota of the hydrosphere, salinity, chemical, energy of mineral resources of the hydrosphere [10]. The first group includes hydropower, the second - thermal energy converters of the hydrosphere.

Before the start of the large-scale implementation of specific technical solutions for renewable energy in the hydrosphere, it is necessary to obtain estimates of the energy potential of the corresponding type of hydrosphere energy that can be used in renewable energy, assess the prospects for its use on a global and regional scale, and assess possible environmental consequences.

The available part of the World Ocean energy (or “energy potential of the hydrosphere”) is usually called the only part of it that can be practically used at the current level of conversion technology.

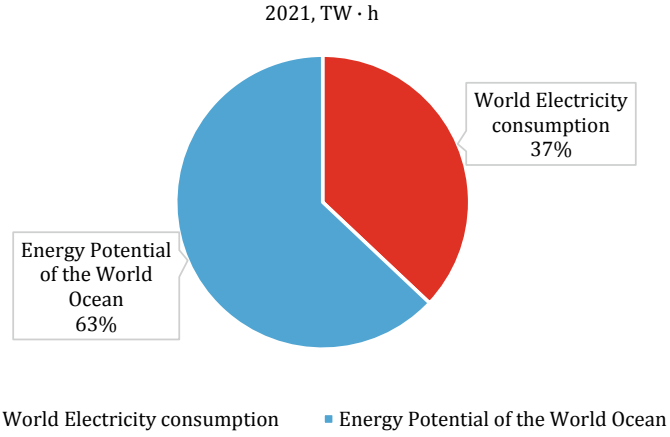

Fig. 2 The Comparison of the current level of energy consumption in the world (2021) and the energy potential of the World Ocean [12]

If we compare (Fig. 2) the current level of energy consumption in the world and the energy potential of the World Ocean, it turns out that the latter exceeds the current consumption by about 1.7–2.0 times [12, 13].

Most of the energy is concentrated in the ocean [6]. This is predominantly ocean thermal energy since the ocean is a giant heat accumulator of the Sun's energy. The internal thermal energy corresponding to the overheating of the ocean's surface waters in Comparison with the bottom waters, for example, by 20 °C, has a value of about 10 to the power of 10^{26} J. The kinetic energy of ocean currents is estimated to be about 10 to the power of 10^{18} J. Thus, the total power of the world ocean exceeds the value of 10 to the power of 10^{44} J.

However, at present, only fractions of this energy are used because such power has been considered unpromising until now. At the same time, the ongoing rapid depletion of fossil fuels, the use of which is associated with significant environmental pollution (including thermal pollution, threatening global climatic consequences), and the limited reserves of nuclear power, force us to pay attention to the search for opportunities to use the energy of the hydrosphere.

As a quantitative assessment of the energy potential of various types of energy in the hydrosphere, an off-system unit is used—a meter of a water column. This unit of measurement allows you to compare the potentials of different types of energy with high clarity. One meter of the water column is equal to the hydrostatic pressure of a column of water 1 m high at the highest water density at a temperature of about 4 °C and gravitational acceleration $g = 9.81$ m/s^2. This value is called the density of the potential pressure energy flux and characterizes the degree of concentration of this type of energy.

Other types of ocean energy have significantly lower flux density values. For example, for a temperature difference between the warm and cold layers of 20 °C, the potential pressure energy flux density is 570 m. Such a head could exist in a reservoir with a dam more than half a kilometre high. And for the temperature difference of 12 °C, the flux density is 210 m. Only the salinity gradient (osmosis) energy has a similar flux density in the ocean—240 m. Therefore, for wind waves, it is 1.5 m, and for ocean currents—only 0.05 m.

The main known methods for transforming the energy of the Earth's hydrosphere can be divided into two types: the using of various technical (mechanical, electrical, etc.) devices for converting thermal, kinetic and chemical energy, and the second type includes transformation methods that are characterized by the predominant use of natural processes and materials that are potentially available as a primary resource for energy production. Such methods are associated with the use of biological and raw energy sources. The most relevant problems and trends in using hydrosphere resources include hydrosphere biotechnology and their combined technologies options, hydrogen energy accumulation technologies [8].

Prospects for the development of renewable energy in the hydrosphere in various regions of the world and in Russia can be roughly estimated based on knowledge of water resources. Figure 3 shows the world ranking of 13 countries of the world according to water resources with reserves over 1,000 km^3: Brazil (8,233 km^3), Russia (4,508 km^3), USA (3,051 km^3), Canada (2 902 km^3), Indonesia (2 838 km^3), China (2 830 km^3), Colombia (2 132 km^3), Peru (1 913 km^3), India (1 880 km^3), Congo (1,283 km^3), Venezuela (1,233 km^3), Bangladesh (1,211 km^3), Burma (1,046 km^3).

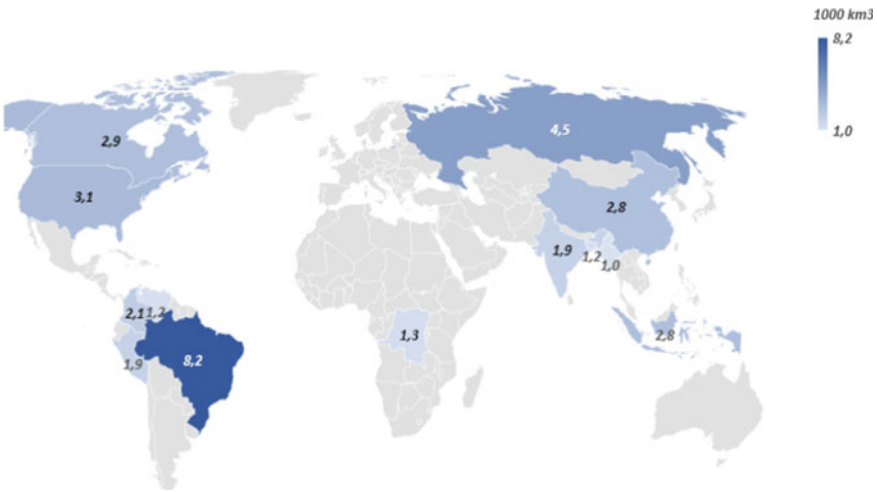

Fig. 3 World ranking of 13 countries according to water resources availability, [14]

4 Conclusions

The future development of the entire energy industry directly depends not only on the possibility of realizing the energy potential of the world ocean but also on the availability of water as a valuable independent resource. There is reason to believe that the available water resources may be depleted shortly, as the population and the world economy continue to grow against the backdrop of impending negative climate changes. And this will undoubtedly affect the reliability and efficiency of the entire world energy sector. The water demand for traditional thermal power plants—the most significant water consumers in the energy sector—can be significantly reduced by using advanced alternative cooling systems. The growth of energy efficiency and the use of traditional and new types of renewable resources of the hydrosphere will contribute to the future development of "low-carbon" energy. The efficiency in using hydrosphere resources will become a standard and, at the same time, a criterion for assessing the technological, economic and environmental viability of energy projects.

Acknowledgements The work was carried out with the support of the grant of the Ministry of Science and Higher Education of the Russian Federation, the project 14.W03.31.0006.

References

1. Uğurlu E. Renewable energy strategies for sustainable development in the European Union // Renewable Energy Spring, 2019, pp. 63–87.
2. Yan J. The impact of climate policy on fossil fuel consumption: Evidence from the Regional Greenhouse Gas Initiative (RGGI) // Energy Economics. 2021. (100). S. 105333. https://doi.org/10.1016/j.eneco.2021.105333.
3. BP Statistical Review of World Energy 2021. London, 2021.
4. Haykin S. Neural Networks and Learning Machines. New York: Pearson, 2009.
5. Kamenev A.S., KorolevS.Yu. Neuromodeling as an ideology and a tool for the intellectualization of energy-information networks. Moscow: EC "Energia", 2012.
6. Karev V.I., Pokazeev K.V., Chaplina T.O. Some topical issues in the physics of hydrosphere // Processes in geomedia. 2019. No. 4. P. 519–527.
7. Bushuev V.V., Soloviev D.A. Hydrosphere resources: energy, ecology, climate. Moscow: Publishing House "Energia," 2019.
8. Nigmatulin R.I. Energy capabilities of the Earth's hydrosphere // Environment and Energy Science. 2020. No. 1. P. 48–59.
9. Khan N., Kalair A.,Abas N., Haider A. Review of ocean tidal, wave and thermal energy technologies. (72) 2017.
10. Pelc R., Fujita RM Renewable energy from the ocean // Marine Policy. 2002. No. 6 (26). S. 471–479.
11. Soerensen HC, Weinstein A. Ocean energy: position paper for IPCC // Hohmeyer and Trittin. 2008. S. 93–102.
12. Soloviev A.A., Nigmatulin R.I. Potential and ways of transforming the energy of the hydrosphere // Collected "Physical problems of ecology" No. 17. Ed. IN AND. Trukhina, Yu.A. Pirogova, K.V. Pokazeeva. Moscow: MAKS PRESS, 2011, pp. 430–438.

13. Degtyarev K. Key Trends of World Energy Consumption in XXI Century // Energy Policy. 2021. No. 5. P. 54–63. https://doi.org/10.46920/2409-5516_2021_5159_54.
14. Huang Z., Yuan X., Liu X. The key drivers for the changes in global water scarcity: Water withdrawal versus water availability // Journal of Hydrology. 2021. (601). S. 126658. https://doi.org/10.1016/j.jhydrol.2021.126658.

Forecasting the Mutual Effect of Power Industry and Climate

D. A. Solovyev, L. V. Nefedova, and O. A. Razorenova

Abstract The paper examines the anthropogenic contribution to global climatic processes, using the methods of intelligent forecasting and correlation analysis of statistics of anomalous natural and climatic phenomena. Estimates of the correlation between the main interacting elements that determine modern climatic and economic cycles and rhythms: global consumption of primary energy, the level of carbon dioxide emissions and the dynamics of natural and climatic anomalies in the first half of the 21st century were completed. The interrelation of these events in the past and the future has been investigated. It is shown that the cyclicality of energy and climatic phenomena associated with the development of energy can be considered as one of the essential indicators in predicting climatic changes and their consequences. Based on a specially developed neural model, the cyclical manifestation of the climatic changes is indicated for the period up to 2036.

Keywords Power industry · Climate change · Forecasting · Primary energy consumption · Greenhouse gases · Natural anomalies

1 Introduction

The beginning of the 21st century was marked by several major natural, climatic, technologic, social, financial, economic and virological disasters [1–3]. Due to the global pandemic in 2020, the growth in energy consumption in the world decreased by 4% [4]. Energy consumption has declined in most countries except China—the largest energy consumer globally. However, energy consumption in China increased by 2.2%, which is much less than in previous years. Due to anti-epidemic lockdowns,

D. A. Solovyev (✉) · O. A. Razorenova
Shirshov Institute of Oceanology, Russian Academy of Sciences, Nahimovskiy prospect, 36, Moscow 117997, Russia
e-mail: solovev@ocean.ru

L. V. Nefedova
Faculty of Geography of Lomonosov, Moscow State University, Leninskie gory, 1, Moscow 119991, Russia

© The Author(s), under exclusive license to Springer Nature Switzerland AG 2022

V. I. Karev (ed.), *Physical and Mathematical Modeling of Earth and Environment Processes*,
Springer Proceedings in Earth and Environmental Sciences,
https://doi.org/10.1007/978-3-030-99504-1_21

economic activity in the world has significantly decreased. This has had a significant impact on the energy consumption of most countries. For example, in the US, energy consumption fell by 7.6%; in the EU, it was also reduced by about 7%. The most noticeable downturns occurred in developed market economies such as Spain, France, Italy, Germany, Japan, and Canada. Also, in Russia, energy consumption fell by 4.8%.

Primary energy consumption determines the amount of carbon dioxide emissions into the atmosphere. The five countries with the highest gross emissions (megatons of CO_2) include China (6283.56), the US (6006.71), Russia (1672.62), India (1400.71). The contribution of carbon dioxide (CO_2) to global warming is about 76%, and methane (CH_4) is about 16% [5].

The oil and gas sector, often blamed for poisoning the planet, produces approximately 12% of anthropogenic greenhouse gas emissions. These emissions include direct production and indirect emissions associated with the energy supply of companies. The rest of the emissions are provided by agriculture, energetics, transport and industry.

Four National Oceanic and Atmospheric Administration (NOAA) weather stations around the world in 2020 recorded an extremely high level of carbon dioxide (CO_2) equal to 412.5 ppm, setting a new record level, despite the slowdown in economic growth due to the COVID-19 pandemic [6]. Since 2000, the carbon dioxide content in the atmosphere has increased by 12%.

It is believed that the main driver of climate change is human activity. To prevent the worst possible consequences, we need to reduce emissions from burning fossil fuels to near zero. However, according to the International Energy Agency (IEA), global greenhouse gas emissions in 2021 will grow by 5% compared to 2020 and remain at 33 billion tons. This may be the most significant one-time increase in the last ten years. Developing countries already account for two-thirds of the world's emissions. Fossil fuels (gas, oil and coal) burning to generate energy are significant greenhouse gases.

According to the World Resources Institute, the power industry accounts for 76% of carbon dioxide emissions from human activities [7]. Includes both direct production of electricity for industrial and domestic needs (30.4% of global emissions), and fuel combustion in transport (15.9%), industrial production (12.4%), construction and maintenance of buildings (5.5%) and other areas.

We need to appreciate the anthropogenic contribution to the global climate. It is necessary to study the relationship between the main interacting elements of this system: the world consumption of primary energy, carbon dioxide emissions and the dynamics of natural and climatic anomalies. The use of methods of intelligent forecasting, spectral and correlation analysis allows solving this problem successfully. This paper presents one of the options for implementing these methods in forecasting and analyzing complex interactions in the "economy-energy-climate" system.

2 Forecasting Method

The calculations were carried out using the STATISTICA Neural Networks software package. This package implements the entire set of neural network data analysis methods. The program uses a neural network—a multilayer perceptron (MLP) with training by backpropagation of an error [8]. Due to many interrelated economic statistics and anomalous natural and climatic phenomena, these software products can "mix" other parallel inputs. This makes it possible to take into account the influence of correlated processes. To analyze the spectral characteristics of various curves of natural and economic dynamics, spectral analysis methods were applied. That allows us to identify the main statistic patterns of these phenomena. In particular, a study of the curves of the temporal relationship between the main dominant global natural factors has been carried out. The set of these factors contains the following time series of data: global surface temperature (T) and Arctic region (TA) anomalies, the international number of natural anomalies (NA), and the average annual rate of change in global primary energy consumption (PEC). The curves are plotted over the twenty years (1991–2021) time interval, with a further expansion until 2036 due to the inclusion in the actual data series of the forecast data obtained using the neural model of the Institute of Energy Strategy [9–11]. It is important to note that due to many interrelated factors in the used neural model, there is a possibility of "mixing" other parallel inputs, thereby considering the influence of correlated processes.

3 Discussion of the Results Obtained

The yearly change in PEC was measured in terawatt-hours (TW·h) in one year compared to the previous year [12]. The number of natural disasters recorded in the world was measured in terms of the number of events in any given year. This data includes droughts, floods, extreme weather events, landslides, mudflows, forest fires, volcanic eruptions and earthquakes. The data are contained in the open archive of the Center for Research on the Epidemiology of Disasters (CRED) [13]. The obtained results of the neural forecast of the comparative dynamics of the PEC and NA curves are shown in Fig. 1.

Figures 2 and 3 show the neural forecast of changes in temperature anomalies (base period: 1979–2000) on a global scale T, in the Arctic region TA (60° N-90°N, 0° E-360°E) and the growth rate of the global concentration of CO_2 in the atmosphere for the period 1986 -2036. Actual data for predicting changes in temperature anomalies included actual monthly data on temperature anomalies (°C) until June 1, 2021, were obtained from the NCEP/NCAR Reanalysis VI archive [14].

In recent years, along with the observed increase in global surface air temperature anomalies, measurements carried out by specialists in different countries show the same rapid growth in the content of carbon dioxide (CO_2) in the atmosphere)-the longest remaining in the air gases, compared to others greenhouse gases (Fig. 3.). In

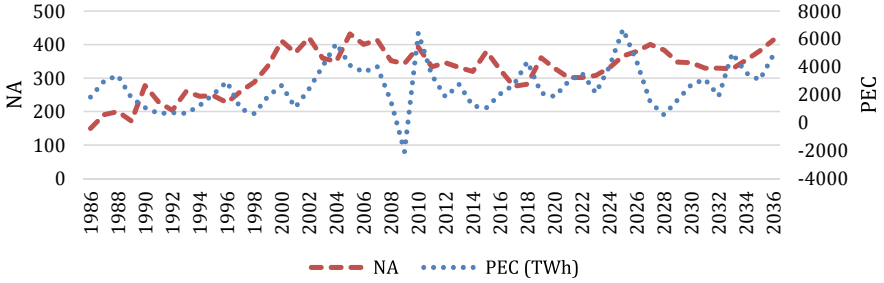

Fig. 1 Neural forecast of the average annual global rate of change in primary energy consumption and the number of natural anomalies from 1986 to 2036, based on statistical data source [12, 13]

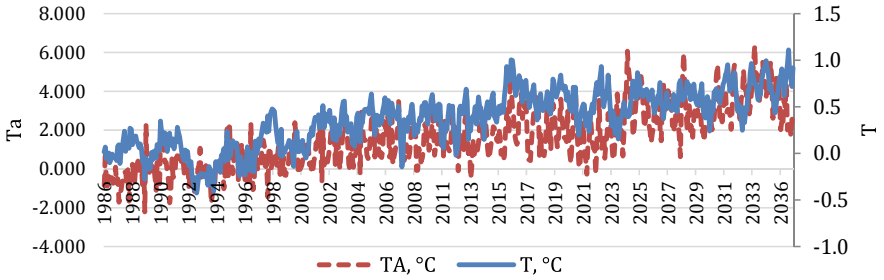

Fig. 2 Forecast of changes in global temperature anomalies in the world and the Arctic for 1986–2036, based on statistical data source [14]

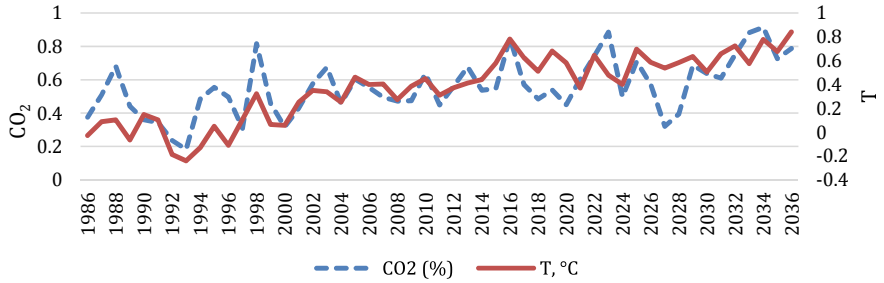

Fig. 3 Forecast of changes in the global carbon dioxide content in the atmosphere and smoothed global surface temperature anomalies for 1986–2036, based on statistical data source [14]

our time, carbon concentration in the atmosphere increases. The increase is undergoing carbon, which used to be part of the composition of combustible minerals. Carbon is added to the air not only due to natural processes, but also to fuel combustion in the process of anthropogenic activity. The graphs of changes in the concentration of CO_2 and temperature anomalies T almost follow each other. This correlation alone

is not evidence that the increase in atmospheric carbon dioxide is the cause of the warming. This can be explained by the fact that there are natural factors for changes in the concentration of carbon dioxide in the atmosphere. The said factors include CO_2 release by oceans and soils during heating and absorption during cooling, ejection by volcanoes, absorption in photosynthesis by plants and some bacteria, release in respiration of living organisms, during forest fires, droughts, floods, etc. The World Ocean makes the most significant contribution of natural causes. Warm water cannot contain as much carbon dioxide in dissolved form as cold water; therefore, it releases CO_2 into the atmosphere when heated. In pre-industrial times, carbon dioxide concentrations in the atmosphere were similar to today. About 450 million years ago, the concentration of carbon dioxide in the atmosphere was more than an order of magnitude higher than it is now. However, there were signs of some glaciation.

Currently, the increase in CO_2 content in the air is about 0.5% per year and fluctuates according to economic activity. For example, the years of crisis (2008 and 2020) are displayed quite well in Fig. 3 as a slowdown in the increase in carbon dioxide content. As noted above, approximately 76% of the total anthropogenic increase in carbon dioxide in the air is due to the burning of fossil hydrocarbons. Most of the rest of the growth of CO_2 is due to a variety of natural processes, global warming and the destruction of vegetation due to natural disasters (fires, floods, droughts). About half of human activity released CO_2 remains in the atmosphere and is absorbed by plants and oceans. Anthropogenic CO_2 emissions account for approximately 5% of all its emissions from the land and ocean surfaces. Long-term analysis of the retrospective and forecast up to 2036 show that anthropogenic emissions from fuel combustion will account for only 8–10% of the total emissions.

Knowledge of processes and feedbacks in the Earth's climatic system is still incomplete. Therefore, there is no definite answer to whether the warming can be warmed due to anthropogenic greenhouse gas emissions being compensated by changes in the distribution of water vapour, clouds, the functioning of the biosphere, or the influence of other climatic conditions. It is also possible that an increase in carbon dioxide concentration, on the contrary, can restrain the heating of surface air, introducing a cooling effect by increasing vertical circulation in the atmosphere and faster dissipation of energy in space.

Spectral analysis of performed neuronal prediction of CO_2 concentration in the atmosphere growth rates and abnormalities of global growth temperature T and temperature anomalies in TA Arctic shows that they are poorly correlated with the vibrations of the primary energy consumption PEC. In this case, the correlation coefficient between the curves of CO_2 concentration, T, and PEC was 0.3 and 0.2, respectively. At the same time, there is a good correlation between the curves of CO_2 concentration, the number of natural anomalies (NA) and temperature anomalies, the coefficient of which is 0.65 and 0.75, respectively. Therefore, it can be assumed that global warming may be associated, among other things, with an increase in the concentration of CO_2 in the Earth's atmosphere and a cyclical rise in the number of NA. Thus, global warming of the climate is also determined by other factors (more

likely not anthropogenic factors), such as the frequency of occurrence of natural disasters (fires, floods and droughts) and other natural and space processes.

The results of neural predictions of individual indicators of climatic processes, such as CO_2 level and T anomalies, suggest that the main trends in climate change for the considered period from 1986 to 2036 boil down to the following: there are periods of warming, alternating with stages of stabilization and cooling. The warming period observed lasts from 2010 to 2011 for about ten years and will continue for about 1–3 years more. According to the neural forecast (Fig. 3), the warming peak will be in 2024–2025, and after some stabilization—in 2036.

4 Conclusions

The obtained results of spectral analysis and neural forecasting allow concluding that an inevitable cyclicality is associated with the dynamics of climate change and anthropogenic activity, determined by the development of the world energy industry. From the neural forecast presented in Fig. 1, it can be seen that the PEC curve has relatively high volatility with recent crises in 2009, 2020 and projected economic downturns in 2028, 2032 and 2035. The crisis periods of 2028 and 2035 correspond to the upward trend of the NA curve. This determines the possibility of a synergistic effect from the interaction of these two factors. It is important to note that the combined impact of these factors significantly exceeds the simple sum of the actions of each of these factors, which can increase the depth of crisis phenomena in the "economy-energy-climate" system.

It was found that the correlation level of the forecast of the rate of increase in the concentration of CO_2 in the atmosphere, as well as the growth of global T anomalies, shows that they are weakly correlated with fluctuations in the consumption of primary energy. Therefore, global warming can be associated directly with an increase in the concentration of CO_2 in the Earth's atmosphere and with other non-anthropogenic factors, including an increase in the global number of natural anomalies (NA). The forecast of the main trends in climate change for the period under consideration from 1986 to 2036 revealed cyclical periods of warming with a frequency of about 12 years, alternating with stages of stabilization and cooling.

Some studies show that an increase in temperature anomalies can lead to a long-term negative impact on economic growth [15, 16], which in turn determines the importance of taking into account both direct and feedback "energy-climate".

Acknowledgements The work was carried out within the framework of state assignments No. 0128-2021-0003; 121051400082-4.

References

1. Malova T.A. What the paradoxes of the global economy signalize // Bulletin of MGIMO University. 2020. No. 3 (72).
2. Dynkin A.A., Telegina E.A. Pandemic shock and post-crisis world // World Economy and International Relations. 2020. No. 8 (64). S. 5–16.
3. Dynkin A., Burrows M., Mikheev V.V., Arbatov A.G., Ivanova N.I., Voitolovsky F.G., Kuznetsov A.V., Machavariani G.I., Arbatova N.K ., Afontsev S.A., others. The global system at a turning point: paths to a new normality // World Economy and International Relations. 2016. No. 8 (60). S. 5–25.
4. Wang Q., Lu M., Bai Z., Wang K. Coronavirus pandemic reduced China's CO_2 emissions in short-term, while stimulus packages may lead to emissions growth in medium- and long-term // Applied Energy. 2020. (278). S. 115735. https://doi.org/10.1016/j.apenergy.2020.115735.
5. Montzka SA, Dlugokencky EJ, Butler JH Non-CO_2 greenhouse gases and climate change // Nature. 2011. No. 7358 (476). S. 43–50. https://doi.org/10.1038/nature10322.
6. Lindsey R. Climate Change: Atmospheric Carbon Dioxide [Electronic resource]. ... 2021. https://www.climate.gov/news-features/understanding-climate/climate-change-atmospheric-carbon-dioxide.
7. Friedrich J., Damassa T. The history of carbon dioxide emissions [Electronic resource]. ... 2014. https://www.wri.org/insights/history-carbon-dioxide-emissions.
8. Kubat M. Neural networks: a comprehensive foundation by Simon Haykin, Macmillan, 1994, ISBN 0-02-352781-7. // The Knowledge Engineering Review. 1999. No. 4 (13). S. 409–412.
9. Bushuev V.V., Klepach A.N., Soloviev D.A., Sokotushchenko N.V. Analysis and forecast of the cyclical nature of socio-natural phenomena in the first half of the 21st century // Environment and energy science. 2020. No. 4 (8). S. 36–44. https://doi.org/10.5281/zenodo.4428379.
10. Sokotushchenko N.V. Influence of solar activity on socio-political phenomena // Energy policy. 2013. (1). S. 60–66.
11. Bushuev V.V., Sokotushchenko V.N. Intelligent forecasting. Moscow: Energy, 2015.
12. bp Statistical Review of World Energy 2021. London: 2021.
13. Database Center for Research on the Epidemiology of Disasters [Electronic resource]. ... 2021. https://www.emdat.be/database (date accessed: 8.12.2021).
14. Climate Reanalyzer [Electronic resource]. 2021. https://climatereanalyzer.org/reanalysis/monthly_tseries/ (date accessed: 8.12.2021).
15. Rudebusch GD, others. Climate change and the Federal Reserve // FRBSF Economic Letter. 2019. (9).
16. Nefedova L.V., Solovyev, D.A. Assessment of the global climate change impact on Fuel and Energy Complex infrastructure and adaptation opportunities in the Russian Arctic // IOP Conference Series. 2020. No. 606. S. 1040. https://doi.org/10.1088/1755-1315/606/1/012040.

Turbulent Mass Exchange in a Stratified Fluid and the Conditions of Its Fine Structure Layering

A. G. Zatsepin and V. V. Gerasimov

Abstract The basic aim of the investigation is to study the regularities of fine structure layering of the stratified fluid (i.e., the oceanic pycnocline) under vertically homogeneous turbulent stirring. By means of physical (laboratory) modeling turbulent exchange through the density (salinity) interface, as well as the structure of this interface between two quasi-homogeneous layers of different salinity is investigated. The layers are continuously stirred by a system of horizontally oscillating vertical rods, passing through both layers. The rods produce vertically homogeneous turbulent stirring of a two-layered fluid media. During every experimental run the salinity in the upper layer is measured with the four electrode conductometer. In a part of experiments vertical profiles of salinity are periodically measured using a single-electrode conductivity microsensor. These measurements are used to calculate the turbulent flux of salt (mass) between layers and to relate these measurements with the structure of the density interface, as well as to determine the dependences of the mass flux and thickness of the interface on the defining dimensionless parameter—the Richardson number. It is shown that the interface with a decrease in the Richardson number first sharpens and then expands (diffuses). In this case, the mass flux between the layers reaches a maximum at a sharpened interface between the layers just before the interface begin to sharpen.

Keywords Density stratification · Turbulent mixing · Fine scale layering

1 Introduction

It is well known that the stratification of oceans and seas is almost never "smooth" and is characterized by the presence of a fine structure (FS), which is expressed in the alternation of layers and interlayers with different values of vertical gradient of characteristics (temperature, salinity, density, etc.). Konstantin N. Fedorov—the

A. G. Zatsepin (✉) · V. V. Gerasimov
P. P. Shirshov Institute of Oceanology, Russian Academy of Sciences, Nakhimovsky ave., 36, 117997 Moscow, Russia
e-mail: zatsepin@ocean.ru

© The Author(s), under exclusive license to Springer Nature Switzerland AG 2022

V. I. Karev (ed.), *Physical and Mathematical Modeling of Earth and Environment Processes*,
Springer Proceedings in Earth and Environmental Sciences,
https://doi.org/10.1007/978-3-030-99504-1_22

famous researcher of the FS in the ocean, presented it as a kind of "handwriting" of water mixing processes, both vertical and horizontal [4, 5]. It should be noted that sometimes this handwriting is "calligraphic": in these cases, a regular FS is formed, consisting of a system of quasi-uniform layers separated by sharp density interfaces. Examples of such structures are contained in the above mentioned monographs by Fedorov.

From general considerations, it follows that the type of mixing (convection, double-diffusive convection, velocity shear, or shear-free turbulence, etc.) should not have a decisive effect on the final result—the transformation of an initially smooth vertical density gradient into a step-like structure profile. Indeed, theoretical and laboratory modeling data show, that vertically homogeneous turbulent mixing under certain conditions transforms a continuous density stratification to a step-like form. The basic mechanism of thin layering of the stratified fluid under an impact of turbulent stirring was proposed by Phillips and Posmentier and described in [11, 12]. It consists in the instability of vertical turbulent exchange in a strongly stratified fluid. It was shown that at values of the Richardson number greater than the critical one, any local increase in the vertical density gradient tends to further increase. This is due to the decrease of the vertical turbulent mass flux in the region of increased gradient. Below and above it where the gradient decreases, the mass flux increases. Over time, in the areas of turbulent mass flux decrease, sharp density interfaces are formed (similar to that how traffic jams occur in places of narrowing of the road). They suppress turbulence, and in the vicinity of them, in the areas of turbulent mass flux increase, quasi-uniform layers are formed.

The possibility of fine structure layering of initially linearly density-stratified fluid exposed to vertically homogeneous stirring was confirmed in laboratory experiments [2, 9, 13, 15], as well as by means of mathematical and numerical modeling [1, 3] (see Fig. 1.).

In the present work, which can be considered as a development of the studies described in [3, 15], the method of physical (laboratory) modeling is used to investigate quantitatively turbulent exchange between two quasi-homogeneous layers of equal thickness but different salinity, as well as the structure of the density transition zone between the layers The layers are continuously stirred by a system of horizontally oscillating vertical rods, passing through both layers. They produce vertically homogeneous turbulent stirring of a two-layered fluid media. The experiment is different in its implication from the essentially similar experiment of Linden [8], who studied turbulent mass transfer through the density interface between the layers forced by a vertically falling grid with square rods.

2 Experimental Setup and Technique

The experimental runs were carried out on a laboratory setup, the schematic diagram of which is shown in Fig. 2. Here (1) a tank with an internal size of 36 * 13.5 * 25 cm^3, made of organic glass. Horizontally oscillating metallic rod (3) directed along

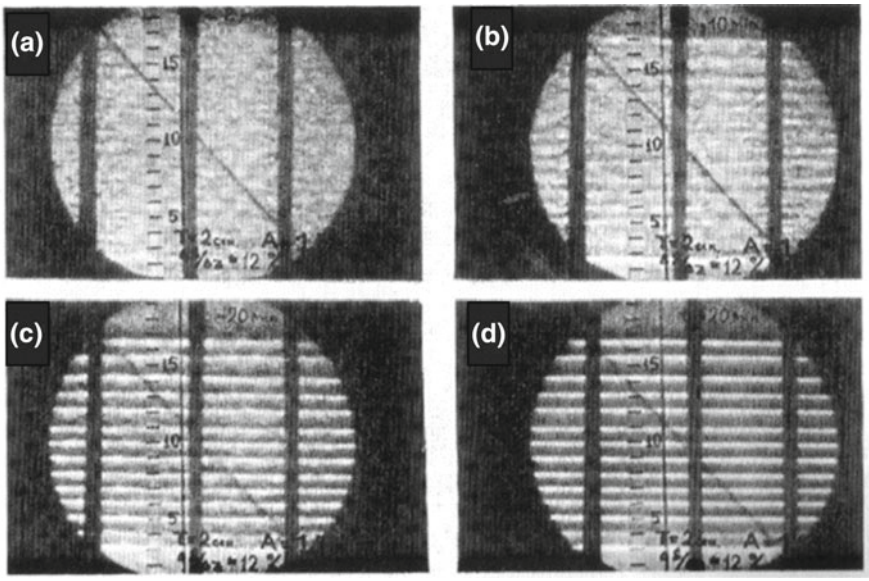

Fig. 1 Consecutive shadowgraphs illustrate the formation of step-like fine structure during the long-term stirring of linearly stratified water column by horizontally oscillating vertical rods [3, 15]. **A**—10 min, **B**—30 min. **C**—240 min. **D**—630 min. ($A = 0.75$ cm; $T = 2$ s; $N^2 = (d\rho/dz)g/\rho = 8.4$ c^{-2}. Here A—amplitude, T—period of rod oscillation, N—Brunt-Vaisala frequency, $d\rho/dz$—density gradient, ρ—water density, g—gravity acceleration)

the longer side of the tank is situated above the tank. A system of 6 grids (2) is fixed evenly at this rod with a 5.5 cm distance between the adjacent grids. Each grid consists of six vertical glass rods (0.65 cm in diameter) with a distance 2.8 cm between each other. The glass rods are submerged in water from the surface and almost to the bottom of the tank. The metallic rod, on which the grids with the glass rods are fixed, is connected to a DC electric motor with an eccentric (4), which provides horizontal oscillation of the rod and the grids. By changing the supply voltage to the motor, the oscillation period T of the grids can be varied in the range from 1.3 to 6.7 s. By changing the attachment point of the metallic rod to the eccentric it is possible to vary the amplitude A of oscillations in the range from 0.5 to 1.8 cm.

Before each experimental run, the tank was half filled with fresh distilled water, below which an aqueous solution of NaCl of a given concentration was poured at a slow speed to prevent mixing. As a result, a two-layered aqueous medium with layers of different salinity, but equal thickness ($H_1 = H_2$, where H_1 is the thickness of the upper layer, and H_2 is the lower one) was formed with a narrow density gradient zone $h << H_1, H_2$ (5) between the layers. The temperature of the layers was the same with the accuracy of ± 0.2 °C and close to the room temperature.

Two series of experiments were carried out. In the experiments of the first series, stirring with oscillating rods was switched on almost immediately after the completion of filling the tank with two-layered water medium. In the second series, this

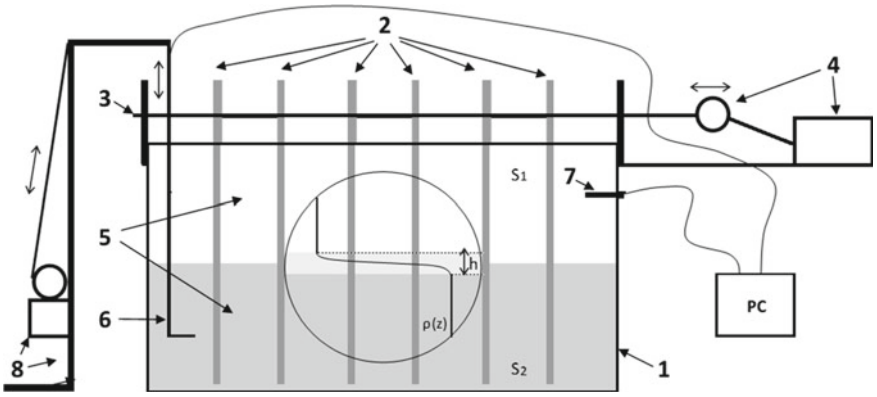

Fig. 2 Experimental setup: 1—an organic glass tank with an internal size of 36 * 13.5 * 25 cm^3; 2—a grid system with vertical glass rods; 3—a metallic rod on which 6 grids with the glass rods are fixed; 4—an electric motor with an eccentric providing horizontal oscillation of the metallic rod; 5—two-layered fluid with an intermediate layer of a high density (salinity) gradient; 6—single-electrode conductivity microsensor for measuring the salinity profile; 7—four-electrode conductivity sensor for measuring salinity in the upper quasi-uniform layer; PC—personal computer for registration and processing of measured data; S_1 and S_2—salinity of the upper and lower quasi-uniform layers. 8—an elevator, which provides vertical displacement of the conductivity microsensor. The circle in the center of the tank corresponds to the outline of the plane-parallel beam of light produced by the shadowgraph device

two-layered aquatic medium was in rest for more than half a day. During this time the density transition zone between the layers expanded to some extent due to the molecular diffusion of salt. To prevent water evaporation and the development of thermal convection the tank was covered from above with a special cover.

A moment of switching on the electric motor was taken as the start of each experimental run. An eccentric driven by the motor was providing a sinusoidal oscillation of the metallic rod with the grids of glass rods for a given amplitude and period. During each experimental run, the current salinity S_1 in the upper water layer was measured using a laboratory conductivity meter "Expert 002" (https://magazinlab.ru/konduktometr-jekspert-002.html). A value of S_1 gradually increased with time due to the influx of salt from the lower layer across the density transition layer. Throughout each experiment the thickness of the upper and lower layers remained practically unchanged. The four-electrode sensor of the "Expert 002" conductivity meter (7) was placed horizontally in the upper layer at a distance of 1.5 cm from the water surface in the tank. The measurement of the electrical conductivity with this sensor was carried out from the beginning to the end of the experimental run with a period of 1 s. The measured data was registered by a personal computer (PC) and recorded in the corresponding file.

In the second series of experiments, along with the measurements of the salinity in the upper layer with the "Expert 002" conductivity meter, vertical profiles of salinity (6) were measured using a single-electrode conductivity microsensor. It was attached

to a mechanical device—an elevator (6), providing vertical displacement of the sensor (sounding) at a speed of about 0.06 cm/s. Since the diameter of the electrode was only 0.01 cm, its vertical resolution was on the order of 0.1 cm. This made it possible to measure an almost non-smoothed vertical structure of the salinity distribution in the layers and across the density transition layer. Sounding data were also recorded on a PC used for collection and processing of all measured experimental data.

It should be noted that before each series of experiments, the conductivity sensors were calibrated by immersing them together in plastic glasses filled with water of a given salinity. Initially, the salinity of the water in the glasses was set by the gravimetric method, and then it was determined with an accuracy of 0.01 ppm using the Australian laboratory salinometer "Autolab". The error of salinity measurements using the "Expert 002" conductivity meter did not exceed 2% of the measured value. The data of salinity measurements by a single-electrode microsensor in the upper layer were absolutely referenced to the simultaneous readings of the "Expert 002" conductivity meter. The stability of salinity measurements with a single electrode microsensor was quite high: its drift did not exceed 0.1 ppm per day.

In addition to the quantitative measurements described above, the visual picture of a density structure and fluctuations in the stratified fluid was reproduced at the screen behind the tank using the Schlieren shadowgraph device (Fig. 2). Due to the use of a shadowgraph method, it was possible to monitor the density interface position even in the absence of measurements of the vertical salinity profiles by a single-electrode conductivity microsensor.

3 Results

Throughout of each experimental run, the process of stirring a two-layer aqueous medium with oscillating vertical rods was carried out from a certain initial state up to the complete mixing of the layers and achieving the homogeneity of water column. The buoyancy flux F_b between the layers was calculated using the data on time changes in the salinity of the upper layer measured by the "Expert 002" conductivity meter:

$$F_b = g\beta(dS_1/dt)H_1, \tag{1}$$

Here S_1 is the current salinity of the upper layer, t—the time, dS_1/dt—the rate of salinity change in the upper layer between two successive measurements, g—the acceleration of gravity, β—the coefficient of salinity compression. Neglecting the thickness h of the density transition zone, we represent the buoyancy flux between the upper and lower quasi-homogeneous layers in the form:

$$F_b = g\beta U_e DS, \tag{2}$$

where U_e is the rate of turbulent entrainment of salt water from the lower layer to the upper layer, and $DS = S_2 - S_1$ is the salinity difference across the density interface between the layers, and $S_2 = S_{20}–S_1$. Therefore, $DS = S_{20}–2S_1$, where S_{20} is the initial salinity value of the lower layer. Equating the right-hand sides of (1) and (2), we obtain an expression for calculating U_e:

$$U_e = (dS_1/dt)H_1/DS = (dS_1/dt)H_1/(S_{20}--2S_1) \tag{3}$$

Following [3, 9, 15] the experimental data were presented in dimensionless form and analyzed on the base of dimensionless parameters—Richardson and Reynolds numbers. The non-dimensional form of U_e was obtained by dividing it by the maximum speed of sinusoidal oscillation of the rods $U = 2\pi A/T$, where A is the amplitude, and T is the period of rod oscillations, the Reynolds number, $Re = UH_1/\nu$, where ν is the kinematic viscosity of water, the Richardson number, $Ri = g\beta DSH_1/U^2$. The selection of the maximum oscillation speed as the defining velocity dimensional parameter was motivated by the consideration that the quadratic law of turbulent resistance of water to an oscillating rod makes the maximum value of the velocity dominant in the transfer of kinetic energy from the rod to an aqueous medium. In turn, the selection of the thickness H_1 of the upper layer as the determining dimensional length-scale, was motivated by the consideration that the diameter of energy-containing eddies should have a scale proportional to the thickness quasi-uniform layers.

The representation in logarithmic coordinates of the dependence of U_e/U on the Ri number made it possible to confirm the concept of the power-law dependence of the dimensionless entrainment rate on the Richardson number in a two-layered turbulent aqueous medium [8]:

$$U_e/U = C * Ri^{-n} \tag{4}$$

In all experimental runs, the same behavior of the experimental points was observed: an existence of two pronounced quasi-linear sections on the graph (see Fig. 3).

At the point of intersection of straight lines at Fig. 3 there is a transition from one turbulent mass transfer mode to another. It should be noted that both values of the exponent n and the coefficient C in (3), as well as the value of Ri*, are the functions of the Reynolds number Re as well as Ri* is a growing function of Re. However in this short paper the results of the study of the dependences of the internal parameters of the experiment on Re are not presented.

In the course of the experiments, a pronounced picture of the evolution of salinity profiles was obtained. Since each experimental run began with a certain maximum value of Ri (with the greatest difference in salinity (density) between the layers), and ended when $Ri = 0$ (no density difference between the layers), it was possible to obtain the dependence of the density transition zone thickness on the Richardson number. In a wide range of this number variation, the density interface thickness first narrows reach a minimum value at $Ri \approx Ri^*$, and then it expands. These observations

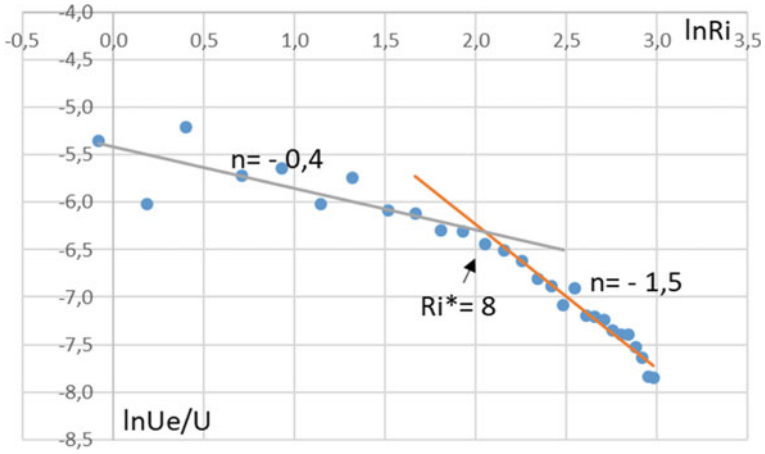

Fig. 3 Dependence of $\ln U_e/U$ on lnRi for the experimental run with the initial value of Ri = 80 and Re = 4300. The straight lines indicate the existence of two different dependences. Their intersection point at Ri = Ri* refers to the transition from one dependence to another

are in qualitative agreement with the result of the experiment in which the density transition zone was formed under the impact of turbulence generated by vertically oscillating horizontal grids in the upper and lower water layers of different salinity and temperature [6].

A more detailed examination of the salinity profile shows that the entire water column actually consists of 5 zones (Fig. 4). As shown in this figure, h_1 and h_5 are quasi-homogeneous layers, h_3 is a layer with a maximum salinity gradient (density interface), h_2 and h_4 are transitional layers, from the density interface to quasi-homogeneous layers. In total, h_2, h_3, h_4 constitute the thickness h of the transition zone between quasi-homogeneous layers.

The next figure (Fig. 5) shows the dependence of the density interface thickness h_3 on Ri.

The point at which the derivative of the $h_3/H_1(\mathrm{Ri})$ function change the sign characterizes the transition from the mode of the density interface "sharpening" to the mode of its "erosion" (turbulent diffusion). In Fig. 5 this transition corresponds to the number Ri = Ri* = 17. This result allows us to conclude that the formation of a fine-structure layering (step-like structure of the density profile) under a vertically homogeneous turbulent stirring in the initially continuously stratified fluid is possible only at Ri ≥ Ri*.

It is important to analyze the dependence of the Richardson flux number Rf as a function of Ri. In its physical meaning, Rf is the fraction of the kinetic energy of turbulence spent on mixing, i.e., on increasing the potential energy of a stratified fluid system [8]. Here,

$$\mathrm{Rf} = (U_e/U) * \mathrm{Ri} \tag{5}$$

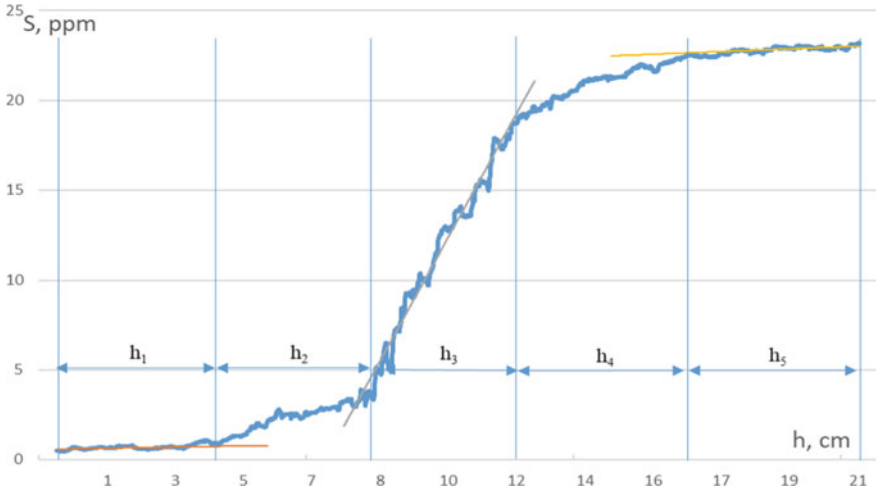

Fig. 4 Vertical distribution of salinity in a two-layer fluid with an initial DS = 24 ppm, Ri = 80 and Re = 2400. The start of the salinity profile measurement coincides with the beginning of turbulent stirring of the fluid

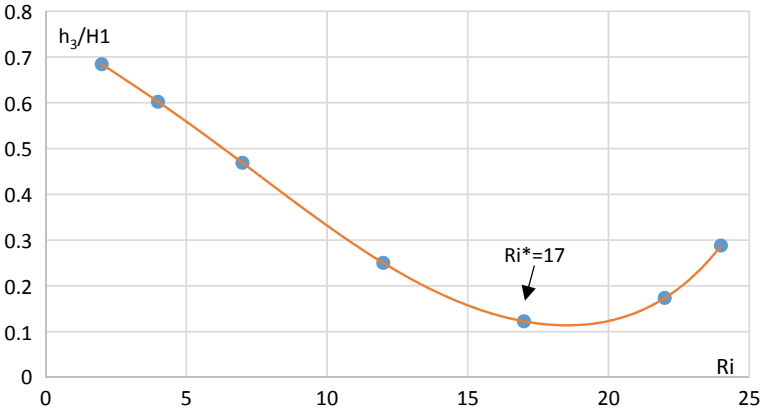

Fig. 5 Dependence of h_3/H_1 on Ri for the experimental run with DS = 88 ppm and Re = 6700

The dependence of Rf on Ri (Fig. 6), reach a maximum value of 0.2–0.3 at Ri = Ri* ≈ 17. The maximum corresponds well to the point where the derivation of h_3/H_1(Ri) change sign (Fig. 5). Thus, it characterizes the transition from the "sharpening" interface mode to an "eroding" one.

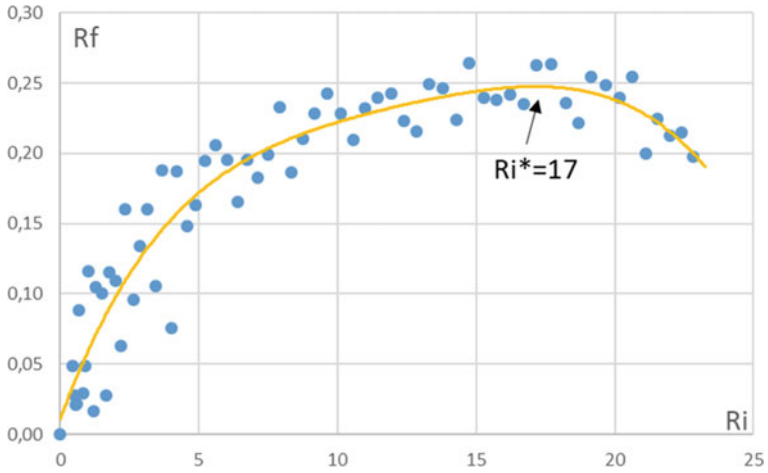

Fig. 6 Dependence of Rf on Ri for the experimental run with Re = 6700

4 Discussion and Preliminary Conclusions

The results of the experiments described in the paper confirmed that the sharpening of the density interface between the turbulent layers of different salinity occurs in accordance with the Phillips-Posmentier mechanism [11, 12].

The formulation of this mechanism is as follows. In a turbulent stratified shear flow, the vertical mass flux can be represented as:

$$F = K(d\rho/dz) \tag{6}$$

where K is the coefficient of turbulent exchange, dρ/dz—the vertical density gradient. It should be noted that vertical exchange in a stratified fluid is dependent on the Richardson number—$Ri = g(d\rho/dz)/\rho(dU/dz)^2$, where dU/dz is the velocity shear. Let us assume that K is represented by a decreasing power function of this parameter:

$$K \sim CRi^{-n} \tag{7}$$

If n > 1, it follows from (6 and (7) that the mass flux F is a decreasing function of the density gradient dρ/dz. This means that if somewhere in the flow the density gradient has increased locally, then the mass flux through this region has decreased, as a result of which the gradient has grown even more.

This situation is dynamically unstable, since a small deviation from equilibrium leads to a further increase in the deviation. Stratification tends to break up into turbulent layers of uniform density, separated by narrow interfaces with a large density gradient. For $n \leq 1$, such instability is absent, since the local inhomogeneities of the density gradient degenerate under the impact of the vertical mass flux.

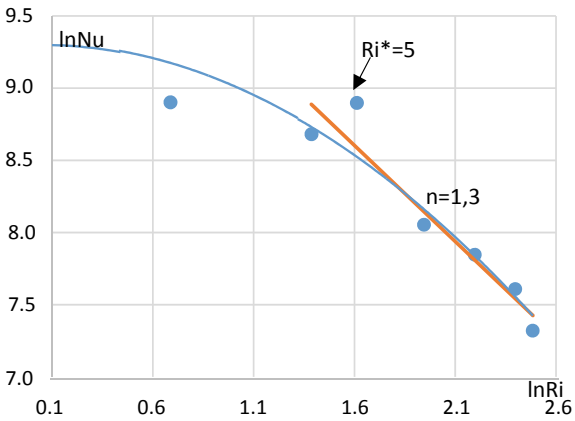

Fig. 7 Dependence of Nu on Ri in logarithmic coordinates in the experimental run with DS = 24 ppm and Re = 2400

Dealing with the obtained experimental data, we can move from the describing turbulent mass transfer through the density transition zone using the entrainment velocity U_e to the turbulent exchange coefficient K. In our case, $K = U_e*h$, where $h = h_2 + h_3 + h_4$. Since both U_e and h were measured in the second series of experiments, it is possible to construct the dependence K(Ri), or Nu(Ri), where $Nu = K/k = (C/k)*Ri^{-n}$ is the Nusselt number for salt and $k = 1.3*10^{-5}$ cm^2/s is the salt molecular diffusion coefficient.

A plot of Nu versus Ri in logarithmic coordinates is shown in Fig. 7. It follows from the figure that in the mode of the density interface sharpening ($Ri \geq 5$), the value of exponent $n = 1.3$ (>1) well corresponds with the Phillips-Posmentier mechanism.

As was shown in the previous section of the paper, in the mode of density interface sharpening, the efficiency of the transition of the kinetic energy of turbulence into the potential energy of stratification reaches a maximum value, which is about 20–30%. Linden [7] analyzed the results of his experiments, as well as those carried out by other authors, and obtained the result quite close to that. This means that we have chosen an integral scale of the turbulent velocity close to real. At the same time, it is necessary to investigate further how the integral scale of turbulence and the root-mean-square velocity of turbulent pulsations are related to the parameters of vertical rods oscillation. After that, it will be possible to use regularities established in laboratory experiment in relation to natural conditions.

Of course, it can be argued that shear-free grid turbulence has nothing to do with natural conditions, where turbulent mixing is occurs in the regions of flow velocity shear which is often observed at the density interfaces. Based on that, in the original work of Peligri and Sandra [10], an alternative to Phillips-Posmentier mechanism of mixing in stratified shear flow was proposed. According to them, the maximum vertical mass flux occurs in the area of the maximum vertical density gradient, and not in the area of low density gradient. As a result, a mixed layer is formed in the region of the initial density interface, and new density interfaces are formed above and below this mixed layer. For an experimental confirmation of this mechanism,

Peligri and Sandra refer to the experiment of Thorpe [14] in an inclined sealed pipe filled with a two-layer stratified miscible fluid. As a result of the formation of a chain of turbulent Kelvin-Helmholtz billows along the length of the pipe and the mixing caused by them, the interface really "split" and two new density interfaces are formed above and below the initial one.

For all the attractiveness of this mechanism, its implementation in natural conditions requires the fulfillment of at least two conditions. First, the region of development of the Kelvin-Helmholtz instability should have a large horizontal extension in order not to be collapsed. Secondly, turbulence should be maintained for a long time to form a well-mixed region bounded above and below by sharp density interfaces. How often such conditions are realized in nature is unclear.

On the other hand, let us assume that intrusive type of fine structure layering is observed in the frontal zone. Then, even weak and sporadic turbulence can maintain the density boundaries of intrusions in a sharpened state due to the implementation of the Phillips-Posmentier mechanism if $Ri \geq Ri^*$. The presence of strong turbulence ($Ri < Ri^*$), on the contrary, will destroy the density interfaces and mix the intrusions with the surrounding fluid. Additional research (laboratory, numerical, field) is needed to check this assumption.

In the final of the paper, we would like to make two preliminary conclusions related to the regularities of step-like FS formation in a initially continuously stratified fluid under the action of vertically homogeneous turbulent stirring.

1. The formation of a fine-structure layering (step-like density structure) under a vertically homogeneous turbulent stirring in the initially continuously stratified fluid is possible only at $Ri \geq Ri^*$.
2. The maximum mixing efficiency of a stratified fluid, is achieved at $Ri \approx Ri^*$, when the thickness of the density interfaces between the quasi-homogeneous layers reaches a minimum. Thus, the transformation of a continuously density-stratified aqueous medium into a step-like density structure increases the efficiency of vertical turbulent exchange.

Acknowledgements The work was carried out within the framework of the state assignment №-FMWE-2021-0002 and with the support of the RFBR grant № 20-05-0496.

References

1. Balmforth, N.J., Llewellyn Smith, S.G., Young, W.R. Dynamics of interfaces and layers in a stratified turbulent fluid // J. Fluid Mech. 1997. 355, 329–358.
2. Barenblatt, G.I., Bertsch, M., Dal Passo, R., Prostokishin, V.M., Ughi, K. A mathematical model of turbulent heat and mass transfer in stably stratified shear flow // J. Fluid Mech. 1993. 253, 341–358.
3. Dmitrenko I., Golovin P., Dehn J., Kassens H., Zatsepin A. Influence of sea ice on under-ice mixing under stratified conditions: potential impacts on particle distribution //Estuarine, Coastal and Shelf Science. 1998. V. 46. No. 4. p. 523–529.

4. Fedorov K. N. The thermohaline finestructure of the ocean – Pergamon press. 1978.
5. Fedorov K. N. The Physical Nature and Structure of Oceanic Fronts - Springer-Verlag, New York, 1986, 333pp.
6. Krylov A.D., Zatsepin A.G. Frazil ice formation due to difference in heat and salt exchange across a density interface // Journal of Marine Systems. 1992. V. 3. No. 6. p. 497–506.
7. Linden, P.F. Mixing in stratifled fluids // Geophys. Astrophys. Fluid Dyn. 1979. 13, 3(23).
8. Linden, P.F. Mixing across a density interface produced by grid turbulence// J. Fluid Mech. 1980. 100, 691–703.
9. Park, Y.-G., Whitehead, J.A., Gnanadesikan, A. Turbulent mixing in stratified fluids: layer formation and energetics // J. Fluid Mech. 1994. 279, 279–311.
10. Pelegri J. L., Sangra P. A mechanism for layer formation in stratified geophysical flows // Journal of Geophysical Research. 1998. V. 103, №. C13. P. 30,679–30,693.
11. Phillips, O. M. Turbulence in a strongly stratified fluid: Is it unstable? // Deep Sea Res. Oceanogr. Abstr. 1972. 19. 7–81.
12. Posmentier, E. S. The generation of salinity fine structure by vertical diffusion // J. Phys. Oceanogr. 1977. 7. 298–300.
13. Ruddick, B.R., McDougall, T.J., Turner, J. S. The formation of layers in a uniformly stirred density gradient // Deep-Sea Res. 1989. 36, 597–609.
14. Thorpe, S. A. Experiments on the instability of stratified shear flow: miscible fluids // J. Fluid Mech., V.46. No. 2. p. 299–319, 1971.
15. Zatsepin A.G. On peculiarities and similarities of the coherent structure formation in stratified and rotating fluid // In: Turbulent mixing in geophysical flows (P.F. Linden and J.M. Redondo – Eds.). 2001. p. 211–299. CIMNE, Barcelona.

The Assessment of Arctic Sea Ice Area Changes

M. S. Teider, S. A. Oskotskaia, N. S. Frolova, and N. A. Podrezova

Abstract The article shows the results of a research on the interannual changes in the Arctic sea ice area. Descriptive statistics as well as linear and nonlinear trends are used as methods of statistical research. The classification according to the severity of winter seasons for the White, Kara, Laptev and East Siberian Seas is also described in the paper.

Keywords Ice cover · Arctic seas · Ice area · Severity of winter · Cumulative freezing-degree days (CFDD)

In recent decades, there has been a significant reduction in the area of old ice and size of drift ice in the seas of the northern polar region [1]. The observation of ice conditions in the polar region is crucial in the current difficult situation because of climate changes.

Much of the Arctic Ocean is covered in ice all year round, except for the Norwegian Sea and the western part of the Barents Sea influenced by the warm North Cape Current (Fig. 1). The ice accumulating around the North Pole forms meridional tongues in some places, the edges of which extend far to the south in winter and significantly shorten in summer. The position of the ice boundary changes throughout the year under the influence of atmospheric processes. Due to such movement some ice-free spaces and thin ice appear along the Siberian shores in summer [2]. The duration of the ice season is associated with the Arctic ice melt and freeze onset. The total ice area in the Arctic in summer is about two times less than in winter.

The Arctic and Antarctic Scientific Research Institute data were used in this work. These data represent the average monthly values of the Arctic sea ice area since 1978, obtained from visible and infrared satellite observations with spatial resolution from 250 m to 1 km [3, 4].

M. S. Teider (✉) · S. A. Oskotskaia · N. S. Frolova · N. A. Podrezova
Russian State Hydrometeorological University, St. Petersburg, Russia
e-mail: Nadinapod@mail.ru

© The Author(s), under exclusive license to Springer Nature Switzerland AG 2022

V. I. Karev (ed.), *Physical and Mathematical Modeling of Earth and Environment Processes*,
Springer Proceedings in Earth and Environmental Sciences,
https://doi.org/10.1007/978-3-030-99504-1_23

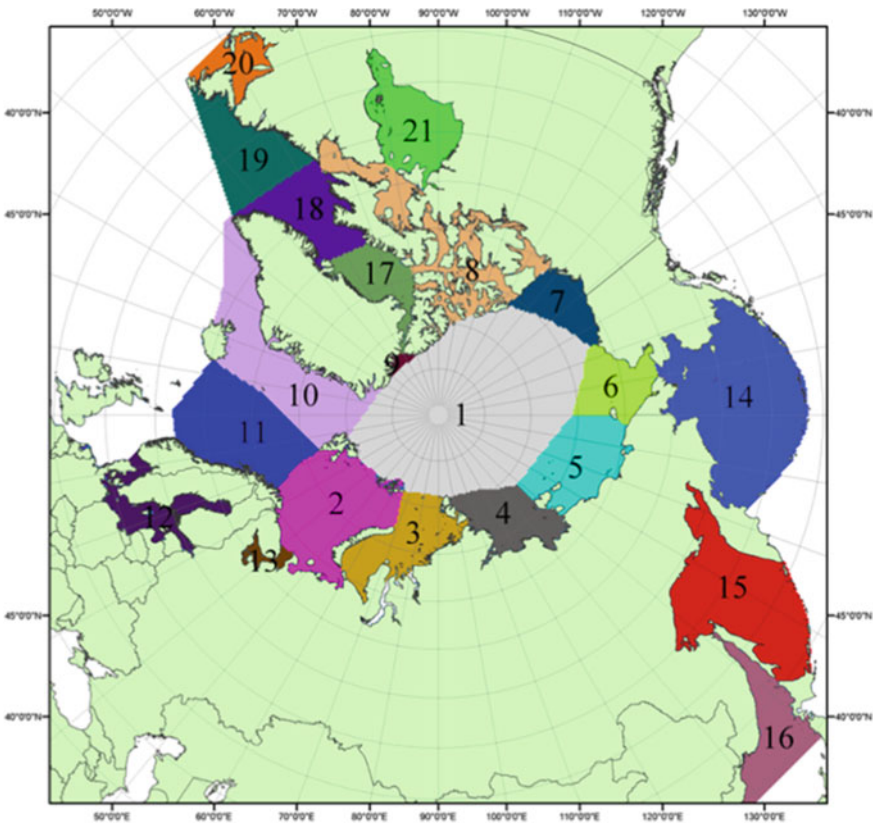

Fig. 1 Seas of the northern polar region. The numbers on the map indicate the following areas: (1) Arctic Basin; (2) Barents Sea; (3) Kara Sea; (4) Laptev Sea; (5) East Siberian Sea; (6) Chukchi Sea; (7) Beaufort Sea; (8) Canadian Arctic Archipelago; (9) Lincoln Sea; (10) Greenland Sea; (11) Norwegian Sea; (12) Baltic Sea; (13) White Sea; (14) Bering Sea; (15) Okhotsk Sea; (16) Japan Sea; (17) Baffin Bay; (18) Davis Strait; (19) Labrador Sea; (20) Saint Lawrence Bay; (21) Hudson Bay

The data from aisori.meteo.ru and rp.5.ru, which represent the daily values of atmospheric temperature in the Arctic seas, were also used for calculating the cumulative freezing-degree days (CFDD) and the classification of winters by severity [5, 6]. A similar approach for winters typing in the Arctic seas was used by Dumanskaia [7].

Descriptive statistics, linear and nonlinear trends have been used as methods of statistical analysis. The first one includes mean, variance, standard deviation, range of variation, coefficient of variation, coefficient of kurtosis and coefficient of asymmetry [8]. To identify the direction of the ice area changes, a linear trend has been calculated. It characterizes the presence of a long-period fluctuation in the temporal variability of the ice cover with a period significantly exceeding the sample length.

Primary descriptive statistics calculated for the Arctic seas are presented in Table 1.

Arctic basin (AB) makes the greatest contribution to ocean ice cover (49%), as it is the northernmost region of Earth which has the largest area. Each of its seas is covered with solid ice for a significant part of the year. The graph of the central part of the basin is characterized by the maximum standard deviation among all the considered areas ($\sigma = 145$ thousand km^2). The maximum ice area (4216 thousand km^2) was observed at the beginning of the research period, namely in 1978. By 2019, this value had decreased by 9% and amounted to 3828 thousand km^2.

The East Siberian Sea holds the record for the ice coverage on the Siberian shelf, which is explained by the drift of ice from the central part of the AB in winter. At the same time, the development of fast ice occurs in the western shallow water. Beyond the fast ice edge, there is a zone of open drift ice and first-year ice. The change in the course of the sea ice area is characterized by a significant deviation of the empirical curve from the standard normal curve ($|Ex| = 1$ and $|As| = 0.01$).

The Lincoln Sea demonstrates a rise in ice coverage for 2–3 years and a decline of the same duration with small-scale fluctuations (R = 1.63 thousand km^2). The standard deviation is equal to $\sigma = 0.4$ thousand km^2. The relatively stable ice situation is typical for Hudson Bay after 1998 and Baffin Bay after 2002. The Canada Basin contributes about 9% to the total ice area.

The North European Basin (NEB) of the ocean is more heavily covered with ice in its central part (the Barents and Greenland Seas). The Norwegian Sea has the lowest ice cover among all the Arctic seas, which is due to its location—warm North Atlantic waters affect this sea, so most of the year the water surface is free of sea ice. Ice in the Norwegian Sea, as a rule, is not of local origin—it is brought from neighboring seas under the influence of circulation.

Atlantic waters also prevent the formation of ice in the south-west part of the Barents Sea, as a result of which a quarter of its area always remains free from ice. Basically, first-year ice forms here, while the old ones are found only in the far north. The sea ice has the largest range of variation (461 thousand km^2) among all Arctic seas. The maximum area was in 1982 (548 thousand km^2), and the minimum in 2016 (87 thousand km^2). By 2019, the situation had slightly stabilized with the ice area of 215 thousand km^2.

In the Labrador Sea ice occupies about two-thirds of its water area. Drift and first-year ice is mainly widespread. The first one comes from the north of the sea through the Davis Strait.

The water area of the Canadian archipelago is covered with ice in the north and northeast. The average ice area is 845 thousand km^2—it is the second largest ice center after the Arctic basin.

Due to its southern location, the Gulf of St. Lawrence doesn't have a large ice cover (the average value is 31.83 thousand km^2).

The Arctic sea ice is shrinking, and as it loses mass, it becomes more at risk from warming waters and atmosphere. In this work, we examine this ongoing loss of Arctic sea ice using satellite data. Since continuous satellite-based measurement began in November 1978, data have shown a trend of more ice melting away during summers

Table 1 Primary descriptive statistics of the Arctic seas' ice cover

Sea		$\bar{x}$, thousand km^2	σ, thousand km^2	D = σ^2	Ex	As	X_{min}, thousand km^2	X_{max}, thousand km^2	R, thousand km^2	C, %
AB	East Siberian Sea	718,6	71,87	5164,7	−1,0	0,01	583,6	866,1	282,5	10,00
	Kara Sea	551,7	86,22	7433,3	0,03	−0,3	340,8	757,8	417,0	15,63
	Beaufort Sea	362,4	40,63	1650,9	−0,4	−0,3	278,8	447,3	168,5	11,21
	Laptev Sea	511,4	49,74	2474,1	−0,1	0,14	423,2	644,1	220,9	9,73
	Chukchi Sea	376,3	49,10	2410,4	−0,5	0,04	274,3	471,4	197,1	13,04
	Arctic Basin Center	4030	145,4	21,146	0,26	−1,0	3632	4216	583,6	3,61
CB	Hudson Bay	433,09	40,48	1638,8	4,73	1,23	360,0	591,8	231,8	9,35
	Baffin Bay	312,7	33,38	1114,5	1,78	0,86	258,4	425,3	166,9	10,67
	Lincoln Sea	37,54	0,40	0,16	−0,6	−0,5	36,67	38,30	1,63	1,07
NEB	Barents Sea	325,6	127,1	16,153	−1,0	0,09	87,23	548,9	461,6	39,03
	White Sea	22,09	5,76	33,12	−0,7	0,15	11,67	33,74	22,08	26,05
	Greenland Sea	429,7	60,73	3688,6	−0,5	0,28	304,6	552,8	248,3	14,13
	Norwegian Sea	3,17	3,21	10,31	0,43	1,16	0,01	11,27	11,26	101,4
Other sectors	Bering Sea	180,3	49,89	2489,3	0,27	−0,5	53,53	290,1	236,6	27,68
	Davis Strait	202,65	39,48	1558,3	0,79	0,86	138,4	314,6	176,2	19,48
	Saint Lawrence Bay	31,83	11,76	138,31	−1,0	0,21	12,48	53,90	41,42	36,95
	Canadian Arctic Archipelago	845,3	56,21	3159,3	2,71	0,88	741,5	1045	304,3	6,65
	Labrador Sea	68,32	27,40	750,50	0,83	0,94	18,79	140,6	121,8	40,10

and less new ice forming during winters. However, satellite observations have been lasting for only 40 years, so it is difficult to say what certain sea ice changes were in the Arctic region before these records. Some scientists suggest that changes in the sea-ice coverage are not only driven by anthropogenic influence. Without any doubt, now we can say that the long-term trend is towards lower ice cover in the Arctic Ocean.

Ice and snow have a high albedo (solar shortwave radiation is reflected back to the atmosphere). The decrease in the sea ice area reduces the albedo, which, in turn, leads to more melting of ice. It means that solar heat contributes to better warming of the dark water surface because of its absorption. In other words, the current reduction in sea ice cover started in 1978 century became very pronounced over the last three decades, and some Arctic seas are expected to be ice-free in the relatively near future.

It is worth noting that the long-term melting of ice in the Arctic seas occurs at different rates, which is explained by seasonality and certain features of air and water circulation in a particular area. These changes can be expressed as a linear trend.

As it has already been noted, the Arctic Basin is the largest area in terms of water area. A great amount of the pack ice of the entire Arctic is concentrated here. According to the obtained linear trend, there is a rapid reduction in the ice cover of the central part of the AB—the ice cover decreases by 102.9 thousand km^2 per a decade. From our point of view, it is very important to consider each Arctic sea separately because each of them has its own features. The sea ice area reduction in the Kara and East Siberian Seas slightly falls behind in comparison to the AB. The ice area in the Kara and East Siberian Seas decreases by 56.1 thousand km^2/decade and 45.1 thousand km^2/decade, respectively. In the Laptev Sea the ice area loss is about 29.5 thousand km^2/decade, in the Beaufort and Chukchi Seas it is 21.5 thousand km^2/ decade and 33.0 thousand km^2/decade, respectively.

As for the trends in the variability of the Canada Basin ice area, the situation is ambiguous. The ice area of the Hudson Bay and Baffin Bay (Sea) declines at approximately the same rate (19.5 and 19.6 thousand km^2/decade). However, the Hudson Bay ice area has been increasing slowly for the last 15 years. The Lincoln Sea has hardly changed at all during the period—the ice area decadal rate of change is about 0.008 thousand km^2/decade. As a result, it can be concluded that the variability of ice conditions in the Canada Basin in terms of reducing the area is the most insignificant relative to other basins of the Arctic Ocean.

Having investigated the North European Basin, we discovered that ice melts most quickly in the Barents Sea. Due to income of warm Atlantic waters brought by the North-Atlantic current, the Barents Sea (even in the most severe winters) is never covered completely with ice. The decrease in the sea ice area is 86.5 thousand km^2/decade, which is the absolute maximum of the ice cover reduction among all Arctic seas. The Greenland Sea ice cover is shrinking 2 times slower—38.3 thousand km^2/ decade, because of the cold East Greenland. The influence of water circulation also explains the low indicators of ice cover in the ice-free Norwegian and White Seas, where the decadal reduction of the ice area is 2.1 and 3.3 thousand km^2/ decade, respectively. It is important to notice that the Norwegian Sea is characterized by an

almost complete absence of ice for the last 10 years, and in the White Sea an ice-free regime could occur under these conditions in the next 15–20 years.

In other Arctic regions, the tendency of sea ice area decline is much weaker than in the Arctic and Canada Basins of the Arctic Ocean, but stronger than ice melting in the White and Norwegian Seas of the North European Basin. The reduction of the ice area in the Davis Strait, Bering and Labrador Seas is approximately equal to 16.4 thousand km^2/decade, 7.5 thousand km^2/decade and 8.7 thousand km^2/decade, respectively. In the Gulf of St. Lawrence, the ice cover reduces at the rate of 4.5 thousand km^2/decade. The ice of the Canadian archipelago is melting at a much faster rate—the reduction in the area is 32.4 thousand km^2/decade.

The statistical analysis has shown the significance of regression coefficients for all water areas with the exception of the Lincoln Sea and Davis Strait.

Thus, the coefficient of determination demonstrates the most significant linear trends in sea ice area changes in the central part of the Arctic Basin and in the Barents, Kara, East Siberian and Greenland Seas. Numerical values of the trends for each ten-year period are 102.9; 86.5; 56.1; 45.1 and 38.3 thousand km^2, respectively. It is also worth mentioning that the linear trend of the interannual evolution of ice cover is significant for the Norwegian Sea. The reduction of the ice area in this sea is equal to 2.1 thousand km^2/decade. The Lincoln Sea is characterized by minimum variability of sea-ice coverage from 1978 to 2019.

A nonlinear trend has also been calculated for the Arctic seas. However, test of significance for the nonlinear trend has shown that it describes the ice cover changes worse because of its insignificance for all Arctic seas.

We also classify winter seasons of the Russian Arctic seas by their severity using cluster analysis.

1 The White Sea

In this research, we summarized negative air temperatures of winter seasons from Arkhangelsk in the period from 1885 to 2005. As a result, the following classification was obtained according to the severity of winter [9]: mild winter—up to 1052 CFDD, moderate winter—1053–1578 CFDD, severe winter—more than 1579 CFDD. The annual values of CFDD, as well as the severity of winter are presented in Table 2. The minimum value recorded in the winter of 1936/37 is 760 CFDD. The maximum value recorded in the winter of 1901/02 is 2288 CFDD.

Table 2 The cumulative freezing-degree days in Arkhangelsk (The White Sea)

Year	Severity	Year	Severity	Year	Severity
1885–86	Severe	1925–26	Severe	1965–66	Severe
1886–87	Moderate	1926–27	Moderate	1966–67	Moderate
1887–88	Severe	1927–28	Moderate	1967–68	Severe
1888–89	Severe	1928–29	Severe	1968–69	Severe
1889–90	Moderate	1929–30	Mild	1969–70	Moderate
1890–91	Moderate	1930–31	Severe	1970–71	Moderate
1891–92	Severe	1931–32	Moderate	1971–72	Moderate
1892–93	Severe	1932–33	Moderate	1972–73	Moderate
1893–94	Moderate	1933–34	Moderate	1973–74	Moderate
1894–95	Severe	1934–35	Mild	1974–75	Mild
1895–96	Moderate	1935–36	Moderate	1975–76	Moderate
1896–97	Severe	1936–37	Mild	1976–77	Moderate
1897–98	Moderate	1937–38	Moderate	1977–78	Moderate
1898–99	Severe	1938–39	Moderate	1978–79	Severe
1899–00	Severe	1939–40	Severe	1979–80	Moderate
1900–01	Moderate	1940–41	Severe	1980–81	Moderate
1901–02	Severe	1941–42	Severe	1981–82	Moderate
1902–03	Severe	1942–43	Moderate	1982–83	Mild
1903–04	Moderate	1943–44	Mild	1983–84	Moderate
1904–05	Moderate	1944–45	Moderate	1984–85	Severe
1905–06	Moderate	1945–46	Severe	1985–86	Severe
1906–07	Moderate	1946–47	Moderate	1986–87	Severe
1907–08	Severe	1947–48	Moderate	1987–88	Severe
1908–09	Moderate	1948–49	Mild	1988–89	Moderate
1909–10	Mild	1949–50	Moderate	1989–90	Moderate
1910–11	Moderate	1950–51	Moderate	1990–91	Moderate
1911–12	Severe	1951–52	Moderate	1991–92	Moderate
1912–13	Moderate	1952–53	Moderate	1992–93	Moderate
1913–14	Severe	1953–54	Mild	1993–94	Moderate
1914–15	Moderate	1954–55	Moderate	1994–95	Mild
1915–16	Severe	1955–56	Severe	1995–96	Moderate
1916–17	Severe	1956–57	Moderate	1996–97	Moderate
1917–18	Severe	1957–58	Moderate	1997–98	Severe

(continued)

Table 2 (continued)

Year	Severity	Year	Severity	Year	Severity
1918–19	Severe	1958–59	Moderate	1998–99	Severe
1919–20	Moderate	1959–60	Severe	1999–00	Moderate
1920–21	Mild	1960–61	Moderate	2000–01	Moderate
1921–22	Severe	1961–62	Moderate	2001–02	Moderate
1922–23	Moderate	1962–63	Severe	2002–03	Severe
1923–24	Moderate	1963–64	Moderate	2003–04	Moderate
1924–25	Mild	1964–65	Moderate	2004–05	Moderate

2 The Kara Sea

To classify the severity of winters in the Kara Sea, meteorological data from 1978 to 2017 from the port Dickson were used. As a result, the following classification of winters was obtained [10]: mild winter—up to 3300 CFDD, moderate winter—3301–4500 CFDD, severe winter—more than 4501 CFDD. The annual values of CFDD, as well as the severity of winter are presented in Table 3. It should be noted that in the period from 2004 to 2016, there was no severe winter, while a mild winter with a minimum value of 2058 CFDD was recorded in the winter of 2013/14. The maximum value recorded in the winter of 1978/79 was 5426 CFDD.

Table 3 The cumulative freezing-degree days in the port Dickson (The Kara Sea)

Year	Severity	Year	Severity	Year	Severity
1978–79	Severe	1991–92	Severe	2004–05	Moderate
1979–80	Moderate	1992–93	Moderate	2005–06	Moderate
1980–81	Moderate	1993–94	Mild	2006–07	Moderate
1981–82	Severe	1994–95	Moderate	2007–08	Moderate
1982–83	Moderate	1995–96	Moderate	2008–09	Moderate
1983–84	Moderate	1996–97	Mild	2009–10	Moderate
1984–85	Moderate	1997–98	Severe	2010–11	Mild
1985–86	Severe	1998–99	Moderate	2011–12	Mild
1986–87	Severe	1999–00	Moderate	2012–13	Moderate
1987–88	Severe	2000–01	Severe	2013–14	Mild
1988–89	Severe	2001–02	Severe	2014–15	Moderate
1989–90	Severe	2002–03	Severe	2015–16	Mild
1990–91	Severe	2003–04	Severe	2016–17	Moderate

3 The Laptev Sea

To classify the severity of winters in the Laptev Sea, weather data from meteorological station Tiksi in the period from 1936 to 2018 were used. As a result, the following classification of winters was obtained: mild winter—up to 4900 CFDD, moderate winter—4901–5650 CFDD, severe winter—more than 5651 CFDD. The annual values of CFDD, as well as the severity of winter are presented in Table 4. The minimum value—4454 CFDD was recorded in the winter of 1942/43. The maximum value—6210 CFDD was recorded in the winter of 1940/41. It should be noted that

Table 4 The cumulative freezing-degree days in the port Tiksi (The Laptev Sea)

Year	Severity	Year	Severity	Year	Severity
1936–37	Moderate	1964–65	Severe	1991–92	Moderate
1937–38	Moderate	1965–66	Severe	1992–93	Moderate
1938–39	Moderate	1966–67	Moderate	1993–94	Moderate
1939–40	Mild	1967–68	Moderate	1994–95	Moderate
1940–41	Severe	1968–69	Moderate	1995–96	Moderate
1941–42	Severe	1969–70	Moderate	1996–97	Moderate
1942–43	Mild	1970–71	Moderate	1997–98	Moderate
1943–44	Moderate	1971–72	Moderate	1998–99	Severe
1944–45	Moderate	1972–73	Moderate	1999–00	Moderate
1945–46	Moderate	1973–74	Moderate	2000–01	Severe
1946–47	Moderate	1974–75	Moderate	2001–02	Moderate
1947–48	Mild	1975–76	Moderate	2002–03	Mild
1948–49	Mild	1976–77	Moderate	2003–04	Severe
1949–50	Moderate	1977–78	Severe	2004–05	Moderate
1950–51	Severe	1978–79	Severe	2005–06	Moderate
1951–52	Moderate	1979–80	Severe	2006–07	Mild
1952–53	Moderate	1980–81	Moderate	2007–08	Moderate
1953–54	Moderate	1981–82	Moderate	2008–09	Moderate
1954–55	Moderate	1982–83	Severe	2009–10	Moderate
1955–56	Moderate	1983–84	Moderate	2010–11	Mild
1956–57	Moderate	1984–85	Severe	2011–12	Moderate
1957–58	Severe	1985–86	Moderate	2012–13	Moderate
1958–59	Moderate	1986–87	Severe	2013–14	Mild
1959–60	Moderate	1987–88	Moderate	2014–15	Mild
1960–61	Severe	1988–89	Mild	2015–16	Mild
1961–62	Moderate	1989–90	Mild	2016–17	Mild
1962–63	Moderate	1990–91	Moderate	2017–18	Moderate
1963–64	Moderate				

in the period from 2004 to 2017 there was no severe winter, and in the period from 2013 to 2016 there were only mild winters.

4 The East Siberian Sea

To classify the severity of winters in the East Siberian Sea, meteorological data from the weather achieve on Wrangel Island were used in the period from 1960 to 2017. As a result, the following classification of winters was obtained: mild winter—up to 3850 CFDD, moderate winter—3851–4500 CFDD, severe winter—more than 4501 CFDD. The annual values of CFDD, as well as the severity of winter are presented in Table 5. The minimum value 2649 CFDD was recorded in the winter of 2017/18. The maximum value 4957 CFDD was recorded in the winter of 1975/76. It should be noted that in the period from 1984 to 2017 no severe winters were recorded, and from 2001 to 2017 only mild winters were recorded.

Based on the average annual sea ice area data for the period under review, the analysis of the interannual variability of the Arctic ice cover was carried out. It was

Table 5 The cumulative freezing-degree days on Wrangel Island (The East Siberian Sea)

Year	Severity	Year	Severity	Year	Severity
1960–61	Moderate	1980–81	Moderate	2000–01	Moderate
1961–62	Moderate	1981–82	Moderate	2001–02	Mild
1962–63	Moderate	1982–83	Moderate	2002–03	Mild
1963–64	Severe	1983–84	Severe	2003–04	Mild
1964–65	Severe	1984–85	Moderate	2004–05	Mild
1965–66	Severe	1985–86	Moderate	2005–06	Mild
1966–67	Moderate	1986–87	Moderate	2006–07	Mild
1967–68	Moderate	1987–88	Moderate	2007–08	Mild
1968–69	Moderate	1988–89	Moderate	2008–09	Mild
1969–70	Moderate	1989–90	Moderate	2009–10	Mild
1970–71	Moderate	1990–91	Moderate	2010–11	Mild
1971–72	Moderate	1991–92	Moderate	2011–12	Mild
1972–73	Moderate	1992–93	Moderate	2012–13	Mild
1973–74	Moderate	1993–94	Moderate	2013–14	Mild
1974–75	Moderate	1994–95	Moderate	2014–15	Mild
1975–76	Severe	1995–96	Mild	2015–16	Mild
1976–77	Severe	1996–97	Mild	2016–17	Mild
1977–78	Moderate	1997–98	Moderate	2017–18	Mild
1978–79	Moderate	1998–99	Moderate		
1979–80	Moderate	1999–00	Moderate		

found that there is a linear negative trend of ice cover almost in all Arctic seas. This means that there is a decrease in the amount of ice, except for the Lincoln Sea where the situation is stable. The classification according to the severity of winter seasons for the White, Kara, Laptev and East Siberian Seas indicates that mild winters have mainly been recorded over the past ten years. The rapid decline of the total ice area significantly affects the climatic conditions not only in the Arctic region, but throughout the whole world.

References

1. Shalina E.V., Bobylev L.P. Sea ice transformations in the Arctic from satellite observations. Sovremennye problemy distantsionnogo zondirovaniia Zemli iz kosmosa [Modern problems of remote sensing of the Earth from space], 2017, vol.14, pp. 28–41. (In Russian).
2. Zakharov V.F. Sea ice in the climatic system. Problemy Arktiki i Antarktiki [Problems of the Arctic and Antarctic]. Issue 69. St. Petersburg: Gidrometeoizdat, 1995, pp. 15–26. (In Russian).
3. AARI WDC Sea Ice file server. Available at: http://wdc.aari.ru/datasets/ssmi/data/ (Accessed 30.05.2020).
4. Sputnikovye metody opredeleniia kharakteristik ledianogo pokrova morei. Satellite methods for determination of sea ice cover characteristics. Ed by V.G. Smirnov. St. Petersburg, AARI Edition, 2011, 239 p. (In Russian).
5. Specialized arrays for climate research. Available at: http://aisori-m.meteo.ru/waisori/ (Accessed 15.04.2020).
6. Weather in the world. Available at: https://rp5.ru/ (Accessed 17.04.2020).
7. Dumanskaia I.O. Ledovye usloviia morei evropeiskoi chasti Rossii. [Ice conditions of the seas of the European part of Russia]. Moscow: IG SOTSIN, 2014. 608 p. (In Russian).
8. Gordeeva S.M. Statisticheskie metody obrabotki i analisa gidrometeorologicheskoi informatsii [Statistical methods of processing and analysis of hydrometeorological information]. Saint-Petersburg, RSHU, 2010. 74p. (In Russian).
9. Sergeev D.I., Podrezova N.A. Calculation of ice growing in the White Sea in conditions of mild, moderate and severe winter. Meteorologicheskii Vestnik [The Meteorological Bulletin], 2017, vol. 9, no. 2, pp.187–190 (In Russian).
10. Petruchenko A.I., Kruglova E.E., Mechova O.S., Podrezova N.A. Assessment of sea ice changes in the Kara Sea depending on the severity of winter. Trudy IX Mezhdunarodnoi nauchno-prakticheskoi konferentsii "Morskie issledovaniia i obrazovanie" [Proc. of the IX International Scientific and Practical Conference "Marine Research and Education"]. Tver, 2020, pp. 273–274. (In Russian).

Theoretical and Experimental Modeling of Olein Spreading Over the Surface of a Liquid with Various Thermodynamic Characteristics

A. V. Kistovich, T. O. Chaplina, and V. P. Pachnenko

Abstract A theoretical model of olein spot spreading based on the laws of conservation of mass and total energy of the system is presented. Experiments on spreading a compact spot of reference engine oil under various physical conditions have been carried out. It is shown that the increase in the oil spill spot area over time is greater in fresh water than in salt water, and also depends on the volume of oil and its properties. The dependence of the size of the distribution area on the salinity of water is revealed.

Keywords Modeling · Spreading · Olein · Engine oil

1 Introduction

Solving the problem of environmental protection of the environment from anthropogenic pollution requires forecasting the spread of oil. The availability of these well-conditioned forecasts allows us to obtain reasonable estimates of the spill area, the thickness of the contamination layer, the possibility of the formation of a thin oily film on the water surface, etc. By itself, the process of oil spreading over the surface of the sea or other water area is a complex physical phenomenon, the nature of which depends on many factors. These factors include the temperatures of water, oil and air, the salinity of the near-surface layer of water, the presence or absence of surfactants on the surface. In addition, the physico-chemical properties of various grades of oil can vary significantly (at times) depending on its composition Sørheim [1]. In addition, after entering the environment, the composition of oil due to evaporation, oxidation, precipitation, etc. of its individual components often undergoes such changes that this leads to irreversible changes in the physical and chemical parameters of the spill spot.

A. V. Kistovich · T. O. Chaplina (✉) · V. P. Pachnenko
A. Ishlinsky Institute for Problems in Mechanics of the Russian Academy of Sciences, Moscow, Russia
e-mail: tanya75.06@mail.ru

© The Author(s), under exclusive license to Springer Nature Switzerland AG 2022

V. I. Karev (ed.), *Physical and Mathematical Modeling of Earth and Environment Processes*,
Springer Proceedings in Earth and Environmental Sciences,
https://doi.org/10.1007/978-3-030-99504-1_24

In addition, after entering the environment, the composition of oil due to evaporation, oxidation, precipitation, etc. of its individual components often undergoes such changes that this leads to irreversible changes in the physical and chemical parameters of the spill spot.

All these processes occur on different time scales. So the spill and evaporation of oil belong to the category of the smallest-scale times Stiver et al. [2]. Mixing with water, reaching the state of emulsion or even dispersion, is a process with average time scales Fingas [3]. Oil deposition and biodegradation are processes with a large time scale.

This paper presents the necessary theoretical estimates of the characteristics of oil spills based on the laws of conservation of a number of physical quantities, as well as experimental results of measurements of the dynamics of expansion of mineral oil (selected as a model object) spots on the surface of fresh and salt water.

2 Theoretical Foundations of the Spreading of Olein Spots on the Surface of Water

Let a spot of olein placed on the surface of water and spreading over it be considered axisymmetric and described by the equations of its upper and lower surfaces (in accordance with the designations of the scheme on the Fig. 1).

$$z - U(r,t) = 0, \quad z - B(r,t) = 0 \tag{1}$$

At the initial moment of time, the shape of the drop surfaces is given by the functions

$$z - U_0(r) = 0, \quad z - B_0(r) = 0; \quad U_0(r) = U(r,t)|_{t=0}, \quad B_0(r) = B(r,t)|_{t=0} \tag{2}$$

The radius of the drop is defined as the radius of the circle on which the points of the triple contact (olein–water–air) are located, and is indicated by the symbols

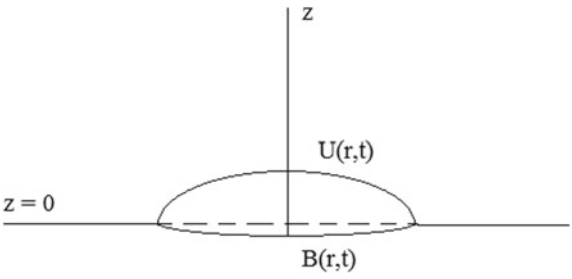

Fig. 1 Model of a drop on water

$$R(t), \quad R_0 = R(t)|_{t=0} \tag{3}$$

Similarly to the relations (1, 2), we can define an axially symmetric velocity field inside the spot

$$\begin{aligned}
&\mathbf{v}(r, z, t) = \mathrm{v}(r, z, t)\mathbf{e}_r + \mathrm{w}(r, z, t)\mathbf{e}_z, \\
&z \in [B(r, t),\ U(r, t)], \quad r \in [0,\ R(t)] \\
&\mathbf{v}_0(r, z) = \mathrm{v}_0(r, z)\mathbf{e}_r + \mathrm{w}_0(r, z)\mathbf{e}_z \\
&\mathrm{v}_0(r, z) = \mathrm{v}(r, z, t)|_{t=0}, \\
&\mathrm{w}_0(r, z) = \mathrm{w}(r, z, t)|_{t=0}, \\
&z \in [B_0(r),\ U_0(r)], \quad r \in [0,\ R_0]
\end{aligned} \tag{4}$$

and in the water

$$\begin{aligned}
&\mathbf{u}(r,z,t) = \mathrm{u}_r(r,z,t)\mathbf{e}_r + \mathrm{u}_z(r,z,t)\mathbf{e}_z,\ [z]\otimes[r] = \left(-\infty, B(r,t)\right]\otimes\left[0, R(t)\right]\cup\left(-\infty, 0\right]\otimes\left[R(t), \infty\right) \\
&\mathbf{u}_0(r,z) = \mathrm{u}_{r0}(r,z)\mathbf{e}_r + \mathrm{u}_{z0}(r,z)\mathbf{e}_z \\
&\mathrm{u}_{r0}(r,z) = \mathrm{u}_r(r,z,t)\big|_{t=0}, \quad \mathrm{u}_{z0}(r,z) = \mathrm{u}_z(r,z,t)\big|_{t=0},\ [z]\otimes[r] = \left(-\infty, B_0\right]\otimes\left[0, R_0\right]\cup\left(-\infty, 0\right]\otimes\left[R_0, \infty\right)
\end{aligned} \tag{5}$$

where $\mathbf{e}_r$, $\mathbf{e}_z$ are the unit orts of the cylindrical coordinate system shown in Fig. 1. The upper parts of expressions (4, 5) describe the velocity field in time, and the lower ones describe the initial conditions for these fields.

And finally, the designations of the surface tension coefficients at the boundaries of the media are introduced: σ_{wa}—at the water–air boundary; σ_{oa}—at the olein–air boundary; σ_{wo}—at the water-olein boundary.

In the considered physical system, the law of conservation of olein mass is obviously fulfilled, the mathematical expression of which has the form

$$\int_0^{R(t)} h(r, t) r\, dr = \text{const}, \quad h(r, t) = U(r, t) - B(r, t) \tag{6}$$

Differentiation (6) in time leads to the expression

$$R(t)R_t'(t)h(R(t), t)) + \int_0^{R(t)} h_t'(r, t) r\, dr = 0 \tag{7}$$

Since in the center of the drop the radial velocity of the liquid elements of olein is zero, and at the boundary of the drop coincides with the velocity of the boundary, then boundary conditions take place

$$\mathrm{v}(r,z,t)|_{z=0,\ r=R(t)} = R_t'(t), \quad \mathrm{v}(r,z,t)|_{r=0} = 0 \tag{8}$$

Using (8) allows you to present (7) in the form

$$\int_0^{R(t)} \left(h_t'(r,t)r + \frac{\partial}{\partial r}(r\,\mathrm{v}(r,0,t)h(r,t)) \right) dr = 0 \tag{9}$$

Type (9) can be used to solve the spreading problem, but it is almost impossible to get any qualitative conclusions based on it. Let's turn to the law of conservation of energy. At the initial moment of time $t = 0$, the total energy of the olein–water drop system is

$$E_0 = 2\pi g \int_0^{R_0} \left(\rho_o \int_{B_0(r)}^{U_0(r)} z\,dz - \rho_w \int_0^{B_0(r)} z\,dz \right) r\,dr + 2\pi \int_0^{R_0} \left(\sigma_{oa}\sqrt{1+U_{or}'^2} + \sigma_{wo}\sqrt{1+B_{or}'^2} - \sigma_{wa} \right) r\,dr + \\ + \pi \left[\rho_o \int_0^{R_0} \left(\int_{B_0(r)}^{U_0(r)} \mathbf{v}_0^2\,dz \right) r\,dr + \rho_w \left(\int_0^{R_0} \left(\int_{-\infty}^{B_0(r)} \mathbf{u}_0^2\,dz \right) r\,dr + \int_{R_0}^{\infty} \left(\int_{-\infty}^{0} \mathbf{u}_0^2\,dz \right) r\,dr \right) \right] \tag{10}$$

where the first term describes the potential energy in the gravity field, the second—the sum of surface energies stored at the boundaries of olein—air and water—olein, respectively, and the third—kinetic energy. Here ρ_o, ρ_w are the densities of olein and water, g is the gravitational acceleration.

In the approximation of the absence of significant viscous losses, the energy of the system in time is described by a similar relation

$$E(t) \approx 2\pi g \int_0^{R(t)} \left(\rho_o \int_{B(r,t)}^{U(r,t)} z\,dz - \rho_w \int_0^{B(r,t)} z\,dz \right) r\,dr + 2\pi \int_0^{R(t)} \left(\sigma_{oa}\sqrt{1+U_r'^2} + \sigma_{wo}\sqrt{1+B_r'^2} - \sigma_{wa} \right) r\,dr + \\ + \pi \left[\rho_o \int_0^{R(t)} \left(\int_{B(r,t)}^{U(r,t)} \mathbf{v}^2\,dz \right) r\,dr + \rho_w \left(\int_0^{R(t)} \left(\int_{-\infty}^{B(r,t)} \mathbf{u}^2\,dz \right) r\,dr + \int_{R(t)}^{\infty} \left(\int_{-\infty}^{0} \mathbf{u}^2\,dz \right) r\,dr \right) \right] \tag{11}$$

Since the model of approximate fulfillment of the law of conservation of the total energy of the system under consideration is adopted, the expressions (10) and (11) must be equal to each other, that is, (11) does not depend on the moment of time t.

The density of olein ρ_o is unchanged, and the change in the density of water ρ_w due to salinity can be neglected, since for the limit values of salinity (about 40 ppm), the deviation in density does not exceed 4%.

The value of the surface tension coefficient σ_{oa} at the olein-air interface is invariable, the surface tension coefficient σ_{wa} at the water–air interface is extremely weakly dependent on salinity in the widest temperature range (Fig. 2).

The only value left is the surface tension coefficient σ_{wo} at the water-olein boundary. But all the reference data state that this value decreases significantly with an increase in water salinity. Then, for the immutability of the value of $E(t)$ at the same value of $R(t)$ at some point in time, it is necessary to dramatically increase the kinetic energy reserve in the system, which should lead to the following result—in salt water, the drop will spread out faster than in fresh water.

3 Laboratory Investigation of the Distribution of Hydrocarbons on the Water Surface

Figure 3 shows photographs of the final stationary state of the spots of Volga M8B-SAE 20 API engine oil spilled over the surface of salt water (salinity $S = 15\,^{\circ}/_{\circ\circ}$, Fig. 3a) and fresh water (salinity $S = 0\,^{\circ}/_{\circ\circ}$, Fig. 3b). The oil volumes in both photos are the same. It can be seen that in Fig. 3b, the thickness of the spot is greater than in Fig. 3a, which is due to the surface tension coefficient at the "salt water—engine oil" boundary is more than 2 times less than at the "fresh water—engine oil" boundary.

In the article of Kistovich and Chaplina [5], differential equations defining the shape of an "oil body" and its solutions for the quasi-stationary shape of a hydrocarbon spot on the surface of the water were obtained. The thickness of the spill

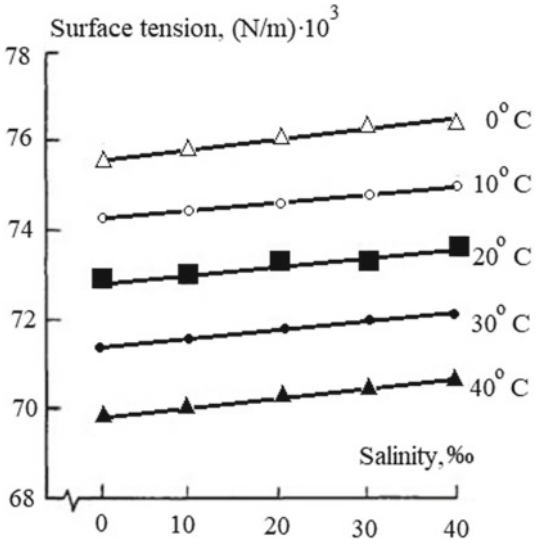

Fig. 2 Graph of the dependence of the surface tension coefficient σ_{wa} on salinity [4]

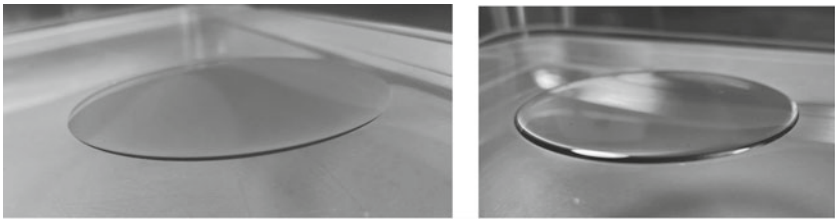

(a) (b)

Fig. 3 Photos of machine oil spots on salt **a** and fresh, **b** water

spot in the center increases with an increase in the surface tension at the water-olein boundary, but changes slightly with an increase in the radius of the spill and, consequently, with an increase in the volume of the spilled olein.

At the same time, not only the final stage of the hydrocarbone spill is of great interest, but also the dynamics of such spills. This requires obtaining the dependence of the spill area on time, which is what the experiments were aimed at.

Laboratory studies of the process of spilling machine oil over the surface of stationary water in a cuvette in the form of a rectangular parallelepiped 50 cm long, 40 cm wide and 5 cm deep. To eliminate light glare that may occur when the light stream is reflected from water or engine oil, the experimental area was illuminated from different sides by specially positioned light sources spaced in space.

The working substance of the experiments carried out is Volga M8B-SAE 20 API engine oil, reference in viscometry, the characteristics of which are presented in Table 1.

During the experiments, various volumes of engine oil were placed on the free surface of the water. The spill process was recorded using a video camera for several hours with a high frame rate (more than 350 frames per minute). The use of photometry methods and batch processing of the results of fixing the observed oil spill pattern made it possible to obtain not only qualitative, but also quantitative experimental results.

In addition to varying the volume of the experimental oil, the temperature and salinity of the water also changed independently in the laboratory studies. The temperature of the oil poured on the water surface always corresponded to the reference value $T = 21$ °C. The output data of the experiments are the temporary realizations of the oil spot area.

Table 1 Characteristics of engine oil

Oil density at temperature $T = 20$ °C	Viscosity index	The dependence of kinematic viscosity on temperature	Solidification temperature
$\rho_o =$ 883.7 kg/m^3	$VI = 100$	$\nu_o =$ $8.03 \times 10^{-6} \cdot \exp(-0.0466 \cdot (T - 100))$ m^2/s	$T_p = -32$ °C

The time realizations of the oil spot area (the oil volume is $V = 10$ ml) for three different values of the temperature of fresh (a) and salt (b) water are shown in Fig. 4. Both in Figure (a) and Figure (b), there is an increase in the area of the oil stain with an increase in water temperature. A similar relationship occurs with an increase in the concentration of salt dissolved in water. These experimental results are in full accordance with the known property of reducing the surface tension coefficient with an increase in the above-mentioned thermodynamic characteristics. This indicates that the experimental oil belongs to the class of so-called normal media in terms of its surface characteristics.

It is also necessary to emphasize the experimental fact that follows from the comparison of the dynamics of the spill area presented in Fig. 4a, b for fresh and salt water, respectively. These experimental curves show that the spill area increases much faster on the surface of salt water than on fresh water. In the case of fresh water, curve 3 (this corresponds to the temperature $T = 28\,^{o}$C). In Fig. 4a, it does not have time to reach its limit value during the observation, unlike the similar curve shown in Fig. 4b. The reason for this phenomenon lies in the different values of the surface tension coefficients at the oil–water boundary at different water salinities. In turn, this confirms the efficiency of the Hoult classification [6], where it is indicated that the gravitational-inertial and viscous-gravitational stages are quickly completed after the start of the spill and are replaced by the viscous-capillary stage.

The change in the area of the spilled spot for different values of the volume of engine oil, but at a constant water temperature, regardless of its salinity, is shown in Fig. 5. As in the experiments already described, the qualitative characteristics of the spill remain the same, but the quantitative values of the data change, compared with Fig. 4. The reason for this is an increase in the coefficient of kinematic viscosity at $T = 7$ °C compared with the corresponding value of this thermodynamic parameter at $T = 21$ °C. The results shown in Fig. 5 confirm Hoult's conclusions [6] that at the initial moments there is the dependence $R \sim V^{1/4}t^{1/2}$ of the spot radius on its volume and time from the beginning of the process.

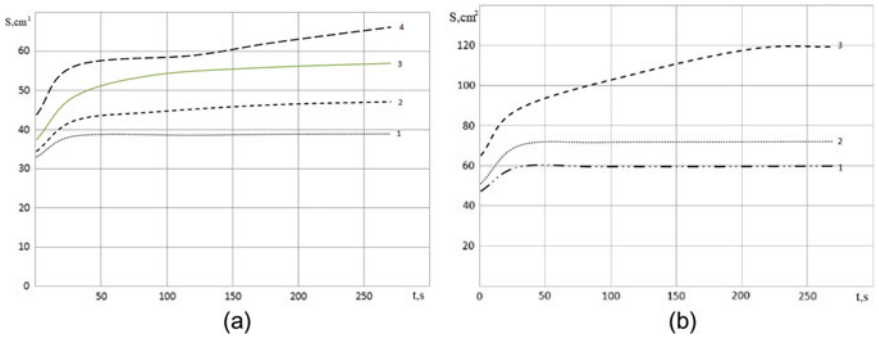

Fig. 4 Temporary realizations of oil spot squares at the volume $V = 10$ ml on fresh ($S = 0\,^{\circ}/_{\circ\circ}$) **a** and salt ($S = 35\,^{\circ}/_{\circ\circ}$), **b** water for different temperatures (1—$T = 15$ °C, 2—$T = 21$ °C, 3—$T = 28$ °C, 4—$T = 37$ °C)

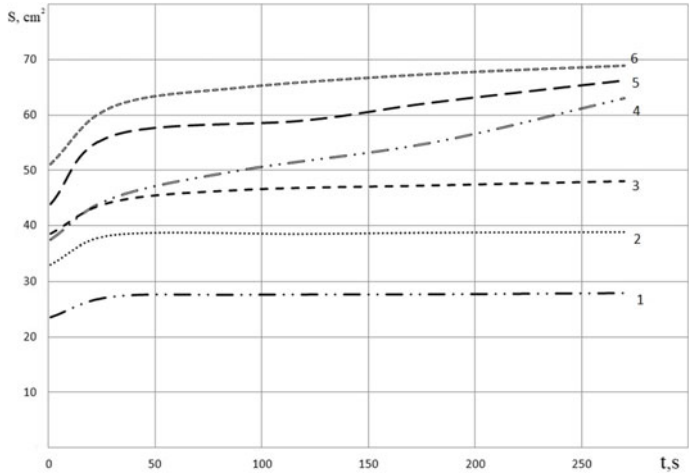

Fig. 5 Temporary realizations of oil spot squares at a fixed temperature $T = 7\,^{\circ}C$ on fresh ($S = 0\,^{\circ}/_{\circ\circ}$) (1—$V = 10$ ml, 2—$V = 20$ ml, 3—$V = 30$ ml) and salt ($S = 35\,^{\circ}/_{\circ\circ}$) water (4—$V = 10$ ml, 5—$V = 20$ ml, 6—$V = 30$ ml) at different volumes Kistovich and Chaplina [5]

The characteristic features of oil spillage with changing salinity of water are shown in Fig. 6. The experiments were carried out at constant water temperature and oil volume. An increase in temperature compared to the previous conditions of laboratory experiments led to a decrease in the surface tension coefficient not only

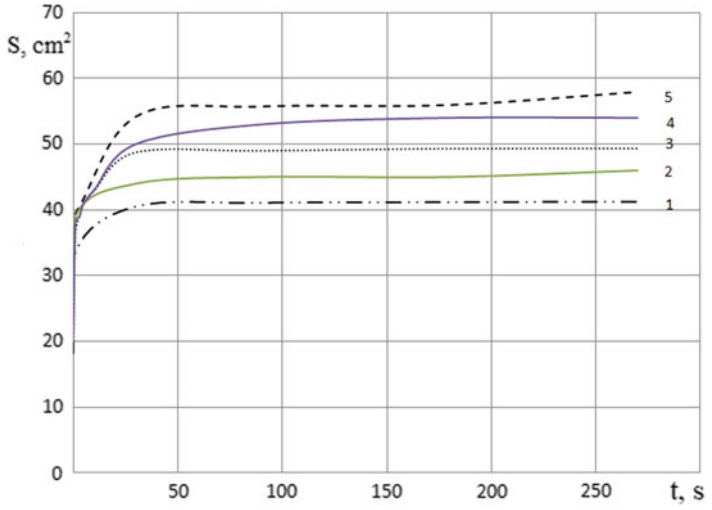

Fig. 6 Temporary realizations of oil spot squares at fixed temperatures $T = 21$ °C of water and oil volume $V = 15$ ml, at different salinities of water (1—$S = 0\,^{\circ}/_{\circ\circ}$, 2—$S = 7\,^{\circ}/_{\circ\circ}$, 3—$S = 15\,^{\circ}/_{\circ\circ}$, 4—$S = 25\,^{\circ}/_{\circ\circ}$, 5—$S = 35\,^{\circ}/_{\circ\circ}$)

at the water–air boundary, but also at the water–oil boundary due to heating of the oil due to thermal contact with water. As a result, there is an increase in the spill area with a constant volume of oil. But at the initial moments of time, the growth rate of the spot area depends on the salinity.

The dynamics of the process predicted in Hoult [6] does not always coincide with the values obtained in modern experiments. Similarly, in the cases presented, the graphs in Figs. 3 and 4b and 4–6 in Fig. 7 coincide qualitatively.

Similarly to the remark made above, there are differences in the values of the maximum spill areas obtained in experiments (Graph 1 of Fig. 4a, Graphs 2 and 3. in Fig. 7), and predicted in the works of Pujado and Scriven [7], Buckmaster [8].

The characteristics of the oil involved in the experiments, which are not presented in Table 1 (these parameters did not vary and kept a constant value), can be found in [9, 10].

4 Conclusions

A set of equations describing the energy and mass characteristics of the spreading olein spot, and supplementary materials of the review [11], is obtained. An experimental study of the process of increasing the area of a compact spot of engine oil on the water surface under various physical conditions (temperature and salinity of water) was carried out. On a saltier or warmer water surface, a drop of oil spreads faster than on the surface of fresh or colder water. The dependence of the spreading rate of the hydrocarbon spot on the initial volume and surface tension of oil is revealed.

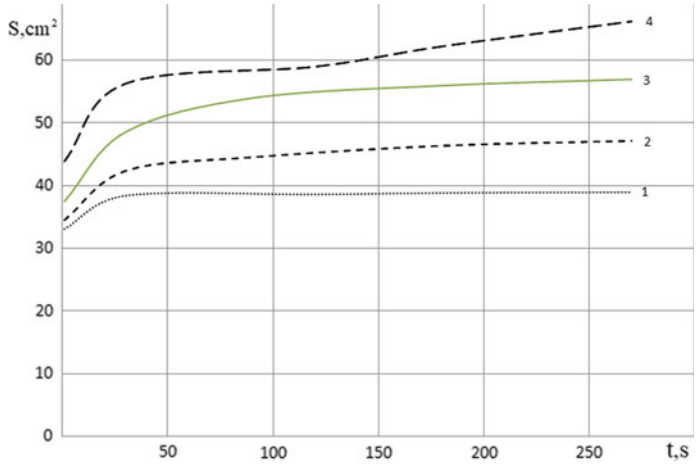

Fig. 7 Temporary realizations of oil spot squares at fixed temperatures $T = 7$ °C of water and oil volume $V = 20$ ml, at different salinities of water (1—$S = 0\,°/_{\circ\circ}$, 2—$S = 7\,°/_{\circ\circ}$, 3—$S = 15\,°/_{\circ\circ}$, 4—$S = 25\,°/_{\circ\circ}$)

The independence of the spot propagation velocity from the salinity of the water at the initial moments of time is shown.

The thickness of the spill spot in the center increases with an increase in the surface tension at the water-olein boundary, but changes slightly with an increase in the radius of the spill and, consequently, with an increase in the volume of the spilled olein. It has been shown that away from the edge of the olein spill, the thickness of the spot changes very little. The assessment of the spill area based on the results of aerial photography and calculations of the thickness of the spot in the center based on the above formulas allow us to give an independent assessment of the spilled volume with a high degree of reliability.

Acknowledgements The work was carried out with the financial support of the project of the Russian Federation represented by the Ministry of Education and Science of Russia AAAA-A17-117021310371-9.

References

1. Sørheim K.R. Physical and Chemical Analyses of Crude and Refined Oils: Laboratory and Mesoscale Oil Weathering Final Report. US Department of the Interior Bureau of Ocean Energy Management Alaska OCS Region. 2016.
2. Stiver W., Mackay D. Evaporation Rate of Spills of Hydrocarbons and Petroleum Mixtures. Environmental Science & Technology, 1984, Vol. 18, No. 11, pp. 834–840.
3. Fingas V.F. Water-in-Oil Emulsions: Formation and Prediction. Journal of Petroleum Science Research, 2014, Vol. 3, pp. 38–49. DOI: https://doi.org/10.14355/jpsr.2014.0301.04.
4. CRC Handbook of Chemistry and Physics. 2019. 102nd Edition, Editor-in-Chief John R. Rumble.
5. Kistovich A.V., Chaplina T.O. Analytical and experimental modelling of the hydrocarbon slick form and its spreading on the water surface//Physics of Fluids. 2021. V. 33. 076605. https://doi.org/10.1063/5.0054709.
6. Hoult D.P. Oil Spreading on the Sea//Annual Review of Fluid Mechanics. 1972. V. 4. Pp. 341–368.
7. Pujado P.R., Scriven L.E. Sessile Lenticular Configurations: Translationally and Rotationally Symmetric Lenses//Journal of Colloid and Interface Sciences. 1972. V. 40. pp. 82–98.
8. Buckmaster J. Viscous-gravity spreading of an oil slick//JFM. 1973. V. 59. Pt. 3. pp. 481–491.
9. https://www.engineeringtoolbox.com/fluid-mechanics-t_21.html.
10. https://volga-oil.ru/oils/motornye-masla_7.html.
11. Lehr W.J. Review of Modelling Procedures for Oil Spill Weathering Behavior. Advances in Ecological Sciences, 2001, No. 9, pp. 51–90.

Experimental Studies of the Transport of a Soluble Admixture on the Surface of a Vortex Flow

T. O. Chaplina and V. P. Pachnenko

Abstract The paper presents the results of experimental studies of the transport of a soluble impurity from a compact spot on a free surface and in the vortex flow. Soluble dyes form spiral arms, the directions of the main flow and growth of the spiral arms are opposite. The experiments carried out on the placement of a solid-state marker with an applied soluble dye on the free surface of a composite vortex clearly demonstrate the presence of dye arms leading and lagging relative to the solid-state marker. The results obtained make it possible to describe in more detail the flow in the thickness of a composite vortex flow.

Keywords Vortex flows · Waves · Vortices · Software processing · Experimental data · Tinting impurity · Uranyl · Spiral

1 Introduction

The need to solve ecological problems, improve the reliability and accuracy of weather forecasts, and assess climate variability requires significant improvements in the accuracy of both velocity and force calculations, as well as in substance transport processes. Existing calculation programs use averaged models (turbulence theories, large vortex methods), in which small-scale processes are taken into account with sub-center parameterization.

Real media are not homogeneous due to variations in the fundamental parameters of density, temperature, concentration of dissolved substances and suspended solids. Although density variations are relatively small, density gradients reach large values and significantly affect the structure, dynamics and energy of the processes taking place. In ocean mechanics, the study of modeling the interaction of microstructural singular and macrostructural regular components of currents, the dynamics of their formation, propagation and decay over a wide range of spatial and temporal scales and energy properties of processes plays a fundamental role.

T. O. Chaplina (✉) · V. P. Pachnenko
Institute for Problems in Mechanics of the RAS, Moscow, Russia
e-mail: tanya75.06@mail.ru

© The Author(s), under exclusive license to Springer Nature Switzerland AG 2022

V. I. Karev (ed.), *Physical and Mathematical Modeling of Earth and Environment Processes*,
Springer Proceedings in Earth and Environmental Sciences,
https://doi.org/10.1007/978-3-030-99504-1_25

It is of particular practical interest to study atmospheric and oceanic transport processes. As the economy grows and production develops, more and more chemicals and compounds, including environmentally hazardous compounds, enter the natural environment and enter the air basin and the hydrosphere as well. To control the level of pollution and ensure environmental safety or even to plan evacuation of people it is necessary to assess the transport of a substance from a compact source under the prevailing hydrometeorological conditions. The transport of matter is influenced by currents in the hydrosphere, analogous to wind in the atmosphere, eddies and waves (Stokes drift).

This chapter presents the results of experimental studies of soluble impurity transport from a compact spot on the free surface of the liquid and inside the resting or involved in the composite vortex motion of the liquid, as well as a visualisation and qualitative analysis of the flow near the disc edge.

2 Experimental Studies of Solute Transport in a Vortex Flow

Only a few works have been devoted to problems of experimental study of transfer of marking impurity from a drop falling on the surface of rotating liquid. In the first of them [1] formation of a "wall of paint" from a droplet falling on the surface of a rotating liquid in a cylindrical or rectangular container, the uniformity of rotation of which was specially perturbed, was first described. The next work, in which the transfer of an impurity from a droplet falling on the surface of a rotating liquid and the analogy between the effects of rotation and stratification was visualized again, appeared more than thirty years later [2]. The annular and spiral structure of vortex currents is visualised in the laboratory using soluble dyes [3], smoke [4] and fine particles in electrolytic precipitation [5] (Fig. 1).

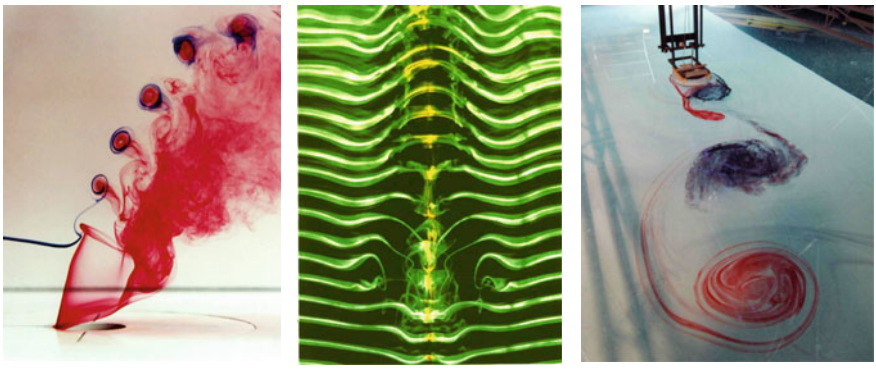

a b c

Fig. 1 Visualisation of vortex structures: **a** [6]; **b** [7]; **c** [8]

A number of works are devoted to experimental study of propagation of different impurities from a spot placed on free surface of composite vortex in cylindrical container [9–11]. Specially designed experiments have shown that important elements of the substance transfer pattern are not predicted by existing models. For example, the transformation of a dye spot in the core of a compound vortex [10], as well as the behaviour of a small amount of immiscible impurity on the rotating free surface of a liquid [11].

It is of practical interest to study the stability of the structure of spiral arms into which a compact spot placed on the surface of a composite vortex is transformed [12], which can be tested by successive application of the marker to the same or different flow regions.

A surface spiral structure develops from a dye droplet deposited on the rotating free surface, which elongates in two directions—towards the centre of rotation of the free surface and towards its periphery. A short arm gradually extends from the solid droplet in the anticyclonic direction and a longer arm in the cyclonic direction. The sleeves are split into individual strands and filamentation of the dye structure occurs (Fig. 2).

The length of the spiral arm growing in the anticyclonic direction (paint rises along the surface) and its distance from the centre of rotation grow monotonically with time. A hose growing in the cyclonic direction (the dye sinks to the centre of the cavern) grows more rapidly. Spiral arms on the surface of a rotating liquid exist for a long time. Long observations of a spiral structure formed by a single droplet dropping allow the formation of a return flow at the periphery of the spiral structure to be traced.

To demonstrate the structural stability of the flow pattern, Fig. 2 shows photographs of the flow pattern with two consecutive drops of ink falling from a fixed pipette with a $t = 0.1$ c delay (dye is black aniline ink, drop height and drop

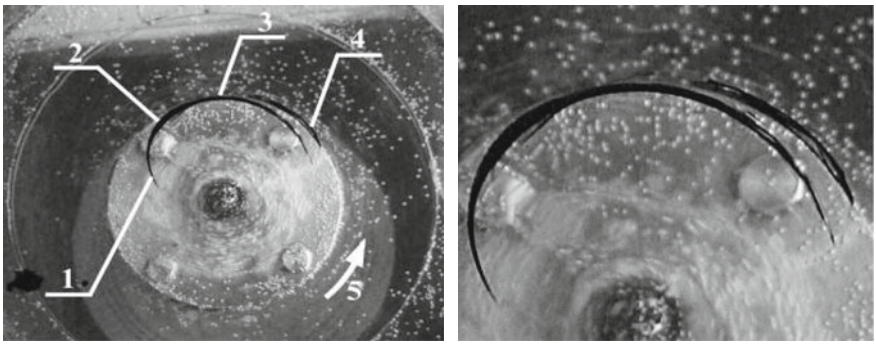

Fig. 2 Drawing of spiral arms from dye spots on a rotating liquid surface ($H = 10$ cm, $\Omega = 100$ rpm, $R = 7.5$ cm): **a** Distribution of the dye after 1 s after the drop comes into contact with the surface; **b** part of the enlarged image [12]

volume are 4 cm, 0.1 ml). The scale of the image is indicated at the bottom of the figure.

Both droplets transformed into elongated spiral arms (*1*—cyclonic part of the inner spiral, *2*—droplet drop location, *3*—anticyclonic part of the inner spiral, *4*—anticyclonic part of the outer arm, *5*—disc rotation direction). The remains of the spot formed a thickening (3.5 mm) on the inner arm of spiral *2* (Fig. 2a), which corresponds to the displaced initial position of the dye spot on the free surface. The cyclonic arm of the first drop developing in the direction of the basic rotation of the liquid surface is longer; its edge is shifted to the instantaneous rotation centre (Fig. 2a, curve *1*) and its thickness smoothly decreases from 1.5 to 1.3 mm. The thinning anticyclonic arm is 2.2 cm long and 3 mm to 1.5 mm thick. The outer (anticyclonic) arm is shorter and thicker. The detailed structure of the split arms is shown in Fig. 2b. At the stage of active structure formation, the width of the clear water band separating the arms decreases.

The noted features of the initial evolution of the dye transfer process from the spot arising when the ink drop falls on the surface of the composite vortex are retained at longer times.

The structural stability of the dye transfer process in the composite vortex is illustrated by a series of photographs in Fig. 3. Here one marker (a drop of violet ink) was applied to the free surface of the vortex cavern at a distance of 2.98 cm from the centre (a 0.1 ml drop was falling freely from 2 cm height). The second drop (blue ink) was introduced 2 s later at a distance of 1.67 from the centre of the cavern. By the time it was introduced, the first marker had formed a spiral sleeve of angular size 166°, with a distance of 4.23–4.63 cm from the centre of the free surface rotation (Fig. 3a).

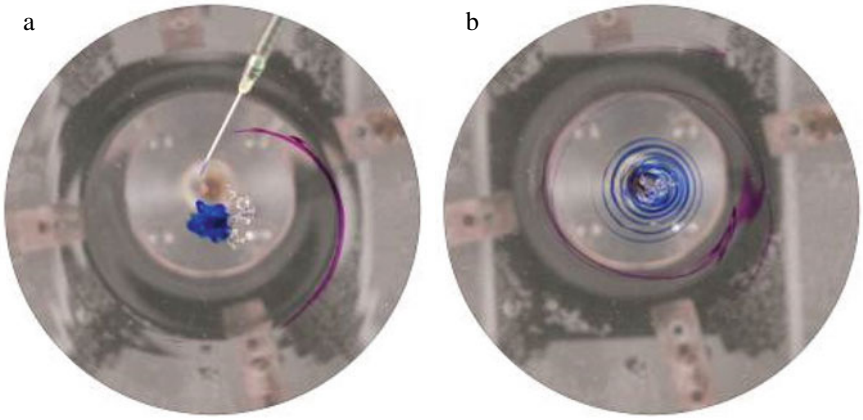

Fig. 3 Change of area occupied by spiral arms on the surface of the composite vortex ($H = 40$ cm, $\Omega = 180$ rpm, $R = 5$ cm): **a**–**d** 2, $t = 4, 7, 23$ s [12]

3 Experimental Study of the Transfer of a Soluble Admixture from a Solid-State Marker on the Surface of a Vortex Flow

To clarify the flow pattern and measure the rotation speed of the free surface of a liquid in a compound vortex, a series of experiments was carried out, where solid and soluble markers were used simultaneously as indicators. A solid marker was placed on the free surface of a steady vortex flow with the selected parameters, on which a layer of a soluble admixture of a contrasting color was additionally applied. In Fig. 4a shows a photograph from an experiment using a tinting impurity (uranyl). The parameters of this experiment: depth $H = 40$ cm, radius of the disk $R = 7,5$ cm, disk rotation frequency $\Omega = 200$ rpm.

In Fig. 4b schematically depicts the propagation of the leading and lagging arms from the marker, where R_m—is the radial coordinate of the marker relative to the center of the free surface, the radial positions R_{fi}—the end of the advancing and R_{bi}—the end of the retarded colored arms relative to the center of the rotating free surface, φ_m—is the angle of rotation of the marker relative to the center of the rotating free surface free surface, φ_{fi} and φ_{bi}—angular positions of the ends of the leading and trailing painted sleeves.

After placing a solid floating marker with an applied dye on the free surface of the composite vortex, the dye is removed (washed off) from it in portions, each portion of the dye forms a colored area—a sleeve.

The data obtained made it possible to find the time dependences of the change in the angular positions of the leading and lagging ink sleeves and to approximate them by functions of the form $\varphi_{fi} = at + b$ and $\varphi_{bi} = at + b$, where, t—is the time elapsed from the moment the marker was placed on the free flow surface, is the angle of the leading ink sleeve, and is the angle of the retarded ink sleeve. The uranyl sleeves are rinsed off the solid-state marker in batches. In Fig. 5. shows the dependence of the angular positions of the leading arms, in Fig. 6—delayed sleeves. A linear approximation was built and the standard deviation was calculated for each leading arm as a function: $\varphi_{fi} = at + b$ (Table 1).

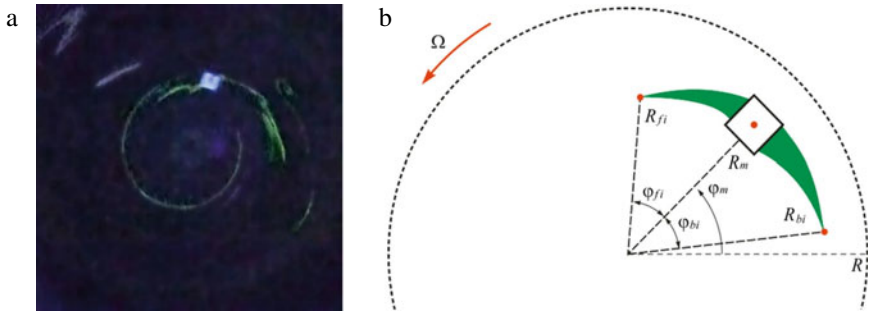

Fig. 4 The spread of the tinting admixture is relatively solid-state marker: **a** photo, **b** scheme

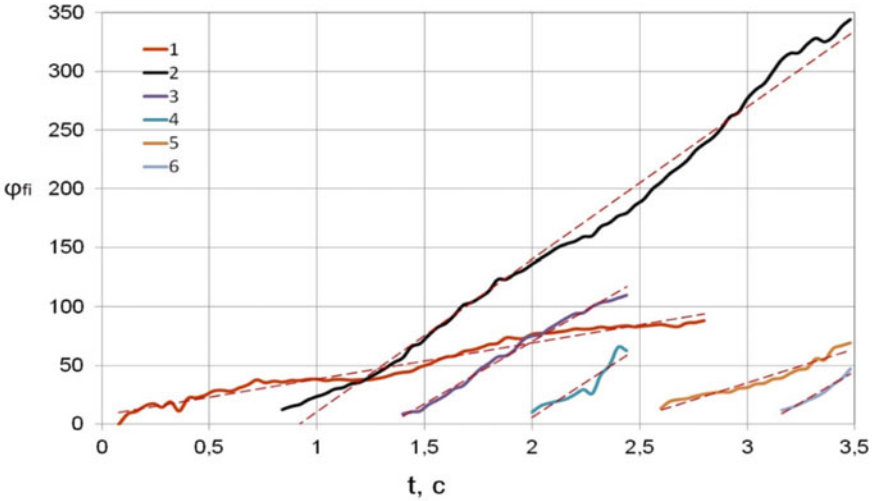

Fig. 5 Dependence of the angular positions of the leading colored sleeves on time, the sleeve departs from the marker at the moment of time: *1*—$t = 0{,}12$ s, *2*—$t = 0{,}84$ s, *3*—$t = 1{,}4$ s, *4*—$t = 2$ s, *5*—$t = 2{,}6$ s, *6*—$t = 3{,}16$ s

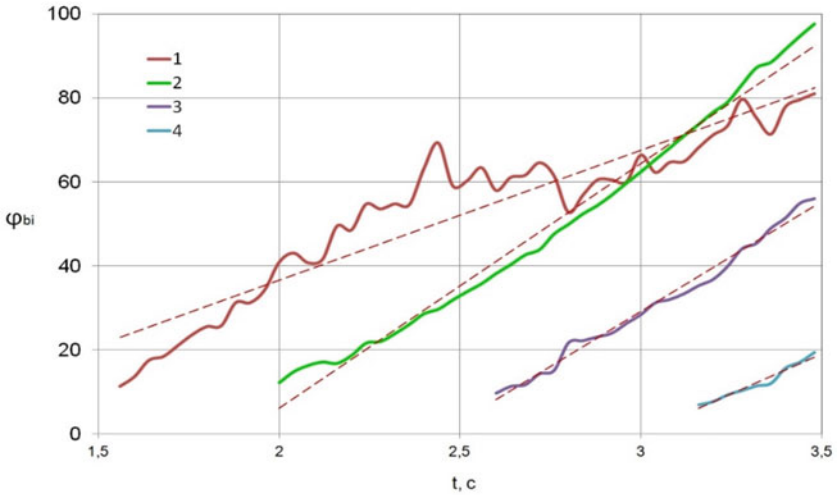

Fig. 6 Dependence of the angular positions of the retarded ink sleeves on time, the sleeve moves away from the marker at the moment of time: *1*—$t = 1{,}56$ s, *2*—$t = 2$ s, *3*—$t = 2{,}6$ s, *4*—$t = 3{,}16$ s

A linear approximation was built and the error was calculated for each lagging arm as a function: $\varphi_{bi} = at + b$ (Table 2).

Table 1 A linear approximation and the standard deviation for each leading arm

	a	Δa	b	Δb	S	$\overline{S}$
φ_{f1}	30,50	0,72	8,28	1,19	4,61	5,15
φ_{f2}	129,76	1,68	−119,26	3,86	10,57	
φ_{f3}	106,30	2,06	−142,23	4,00	3,26	
φ_{f4}	119,83	13,90	−233,79	30,91	6,34	
φ_{f5}	57,62	3,11	−137,51	9,49	3,86	
φ_{f6}	105,96	7,78	−325,85	25,85	2,25	

Table 2 A linear approximation and the standard deviation for each lagging arms

	a	Δa	b	Δb	S	$\overline{S}$
φ_{b1}	30,95	1,73	−25,23	4,47	6,788	3,07
φ_{b2}	58,27	1,16	−110,35	3,21	3,082	
φ_{b3}	52,41	1,27	−128,05	3,87	1,575	
φ_{b4}	38,25	2,88	−114,72	9,58	0,835	

The behavior of the first portions of paint on the free surface differs from the subsequent ones. The interval between sequences of dye portions is 0,6 s for leading arms and 0,5 s for lagging arms.

4 Conclusions

Soluble admixture form spiral arms that form a transport pattern on the rotating surface of the liquid. The directions of the main flow and growth of the spiral arms are opposite. The spiral arms grow over the entire range of the studied flow parameters.

The experiments carried out on the placement of a solid-state marker with an applied soluble dye on the free surface of a composite vortex clearly demonstrate the presence of dye arms leading and lagging relative to the solid-state marker. The Soluble admixture spreads along the free surface of the composite vortex flow in portions, moving away from the marker both forward and backward at approximately the same time, and the time intervals between the formation of new portions are approximately equal.

The studies carried out are important for understanding the mechanisms of admixture spread in complex vortex structures. The results obtained make it possible to describe in more detail the flow in the thickness of a composite vortex flow. The technique used made it possible to obtain results suitable for further study of vortex structures.

Acknowledgements The work was carried out with the financial support of the grant of the Russian Federation represented by the Ministry of Science and Higher Education of the Russian Federation No. 13.1902.21.0018 (agreement 075-15-2020-802).

References

1. Taylor G.I. Experiments with rotating fluids // Roy. Soc. Proc. A. 1921. V. 100. Pl. 2. P. 114–121.
2. Long R. R. Note on Taylor's "ink walls" in a rotating fluid // Journal of the Atmospheric Sciences. 1954. V. 11. № 3. P. 247–249.
3. Stepanova E.V., Chashechkin Yu.D. Anisotropic transport of admixture in a compound vortex// Reports AN. 2008. V. 423, № 4. P. 474–478 (in Russian).
4. Van Dyke M. Album of flows of liquid and gas. Moscow: Mir. 1986. 184 p.
5. Honji H. Vortex motions in a stratified wake flows // Fluid Dyn. Res. 1988. V. 3. № 1–4. P. 425–430.
6. Kelso R.M., Lim T.T., Perry A.E. An experimental study of a round jet in a cross-flow // J. FLUID MECH. 1996. Vol. 306.
7. http://www.efluids.com/efluids/gallery/gallery_pages/vortex_dislocate.jsp.
8. Stegner A. Nonlinear Dynamics of Rotating Shallow Water: Methods and Advances // Edited Series on Advances in Nonlinear Science and Complexity. V. 2. 2007. P. 323–379.
9. Stepanova E.V., Chashechkin Yu.D. Anisotropic transport of admixture in a compound vortex // Reports AN. 2008. V. 423, № 4. P. 474–478 (in Russian).
10. Chaplina T.O., Stepanova E.V., Chashechkin Yu.D., Features of the transfer of admixture in a stationary vortex flow // Moscow University Bulletin, Series 3: Physics and Astronomy. 2012. № 4. P. 69–75 (in Russian).
11. Chaplina T.O., Stepanova E.V., Chashechkin Yu.D., Deformation of a compact oil slick in the cavity of a compound vortex // Reports AN. 2010. V. 432. № 2. P. 185–189 (in Russian).
12. Stepanova E.V., Trofimova M.V., Chaplina T.O., Chashechkin Yu.D., Structural stability of the process of transfer of matter in a compound vortex // Izvestia RAN: Physics of the Atmosphere and Ocean, 2012, V 48, № 5, P. 1–13 (in Russian).

The System of Storage and Access to the Black Sea Oceanographic Data

E. V. Zhuk

Abstract The paper describes the oceanographic data access system developed at MHI RAS. The data access system is based on a Client–Server Architecture using the Model-View-Controller (MVC), which was realised using the free and open source Django framework. The PostgreSQL object-relational DBMS was implemented for archiving the oceanographic data. The part of the database responsible for accessing the oceanographic metadata is interactive, using the OLTP access template. The in-situ data archiving module was developed in accordance with the "star" architecture, which is typical for the OLAP access template. The user interface (UI) is developed using Django templates, jQuery and mapBox GL for visualization of maps. The data exchange between UI and the Server is provided in JSON format. The user's access to the oceanographic database is provided through web-sessions. The UI allows the selection of oceanographic data using several criteria/filters, such as: cruises (cruise name, ship name, cruises year), region, time period, season, parameters. The authorized users of the online oceanographic data access system of the MHI RAS can download the requested data, after receiving individual permission.

Keywords Oceanographic database · Online data access · Black sea · Mapbox GL · Django · JQuery

1 Introduction

The importance of developing oceanographic data access systems is defined from the use of oceanographic data and information products in many spheres of human activity and particular for scientific research. Due to the rapid developments of the information technology and of the communication resources, geo-spatial information is becoming closer in our life and data access software using GIS technology is one of the important tool forthe marine scientific community. The development of online

E. V. Zhuk (✉)
Marine Hydrophysical Institute of RAS, Sevastopol, Russia
e-mail: alenixx@gmail.com

© The Author(s), under exclusive license to Springer Nature Switzerland AG 2022

V. I. Karev (ed.), *Physical and Mathematical Modeling of Earth and Environment Processes*,
Springer Proceedings in Earth and Environmental Sciences,
https://doi.org/10.1007/978-3-030-99504-1_26

data access systems and GIS for the Black Sea is one of the main areas for MHI RAS [1–4].

The main feature of this new online data access software is to provide data access to the Oceanographic Data Base of MHI using authorize module allowing the use of special data permissions.

2 Structure of the System

The Data access system is based on a Client–Server Architecture using the MVC pattern. To realize this approach the free and open source Django framework was selected. It is a high level Python web framework that enables rapid development of secure and maintainable web applications.

The structure system schema is shown at Fig. 1. The Server part includes different type of data, such as relational data, vector file data, raster file data and software modules, which provide data processing, accessing and visualization of each data type.

2.1 Database Structure

The PostgreSQL object-relational DBMS was implemented for archiving the oceanographic data. To provide the faster data access the new database structure was developed. The dual nature of the processed database queries was taken into account. On

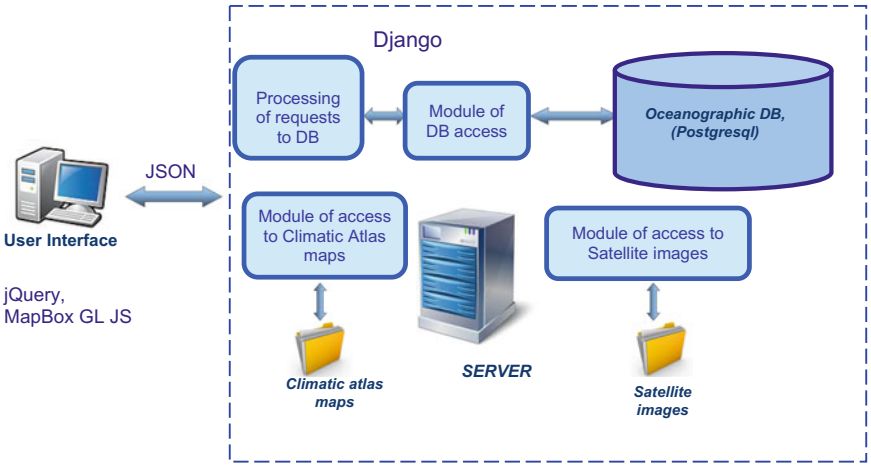

Fig. 1 Schematic of the data access system structure

one side, the interactive work of the users with metadata was considered through a function which is necessary to generate requests for data. On the other side, it was considered and provided the capability to select large data sets in accordance with the criteria specified by metadata selection. Taking these two features into account, the part of the database responsible for accessing the metadata, was designed for interactive transaction processing (OLTP access template), while the other part, responsible for the in-situ data archiving was developed in accordance with the "star" architecture, which is typical for the OLAP access template [5].

After analyzing the oceanographic in-situ observations, the following main entities were identified: Metadate—Cruise, Ship, Station, as well as Measured parameters and Data—Measurements. Therefore, the BSOD includes the following.

2.2 Metadata Tables

Cruises—information about cruises (id, cruise name, dates, ship name, cruise owner organization, number of obtained stations),

Ships—information about ship (id, ship name, code, owner),

Stations—information about obtained stations (name, id of the cruise in which the station was carried out, cruise code, date, coordinates, depth of the place, number of measurements, organization code and quality flags),

Stations_parameters—information about the parameters that were measured at the station (station number, flight number, parameter name, parameter code in dictionaries P01 and P02, device code that was used to measure from the L05 dictionary, unit code from the P06 dictionary).

2.3 Data Tables

Measurements—information about the measured values (station id, cruise id, cruise number, coordinates, date and time, depth of place, organization code, depth of measurement, parameter name, measured value, quality flag, units of measurement).

Reference data tables:

gebco—table of the depth, includes coordinates and depth at the point [6],

edmo—includes EDMO codes for each organization [7],

p01_vocabuary—includes codes of the P01 parameters [8],

p02_vocabuary—includes codes of the P02 parameters [9],

id	session_key	User_name	User_info	Time_creation	queryset_json	info

Fig. 2 Sessions table structure

p06_vocabuary—includes codes of the P06 units [10],

l05_vocabuary—includes codes of the L05 equipments [11],

Sessions table which keeps all information about connected users, users' requests, selected data sets, approved data sets (Fig. 2).

The data access is provided based on the following rules:

- Open data (data_access_flag = 0). It is not necessary to get permission request. It will be downloaded automaticaly.
- Not open data (data_access_flag = 1). It is necessary to get permission request from MHI director.
- Not open data (data_access_flag = 2). It is necessary to get permission request from the department head.
- Not open data (data_access_flag = 3). It is necessary to get permission request from MHI director and from the department head.

The download data requests are created automatically after filling the relevant downloading request form and sent it to the MHI director or/and the head of the department by e-mail. After the request will be approved, the user receives an e-mail notification and a download link.

The data access flags (data_access_flag) is kept in metadata table Stations.

2.4 Climatic Atlas Maps

Climatic atlas maps are kept as a file set with special file name rules and directory structure. It includes oceanographic parameters for main oceanographic levels and are kept as shape files.

2.5 Satellite Images

Satellite images which were obtained from MODIS-AQUA by department of remote sensing are presented for the following three parameters: sea surface temperature, water leaving radiation and chlorophyll-a concentration and stored as raster geotiff format also using special file naming rules and directory structure.

To provide data access, visualisation, data processing and interaction between UI and Server, dedicated software modules were developed. The exchange between

User Interface and server is created in the frame of the web sessions in JSON format. All the user set selections and downloads are kept in Session table of DB.

3 Data Access User Interface

The user interface is developed using Django templates [12], jQuery [13] and mapBox GL [14], for visualization of maps. It allows the selection of oceanographic data using several criteria/filters, such as [15]:

- Cruises (cruise name, ship name, cruises year). It is possible to select one or many cruises (Fig. 3).
- Region (draw rectangle area by mouse on the map (Fig. 4).
- Time period and/or months (Set date start and date and of the data set and/or months (Fig. 5).
- Parameters. User can select one or several oceanographic parameters from the parameter selection list, such as temperature, salinity, oxygen saturation, PH, Nitrates, Nitrites, Phosphates, Ammonium, Silicates, TSM and so on (more than 20 parameters at all). After that the list of corresponding cruises will be loaded (Fig. 6).

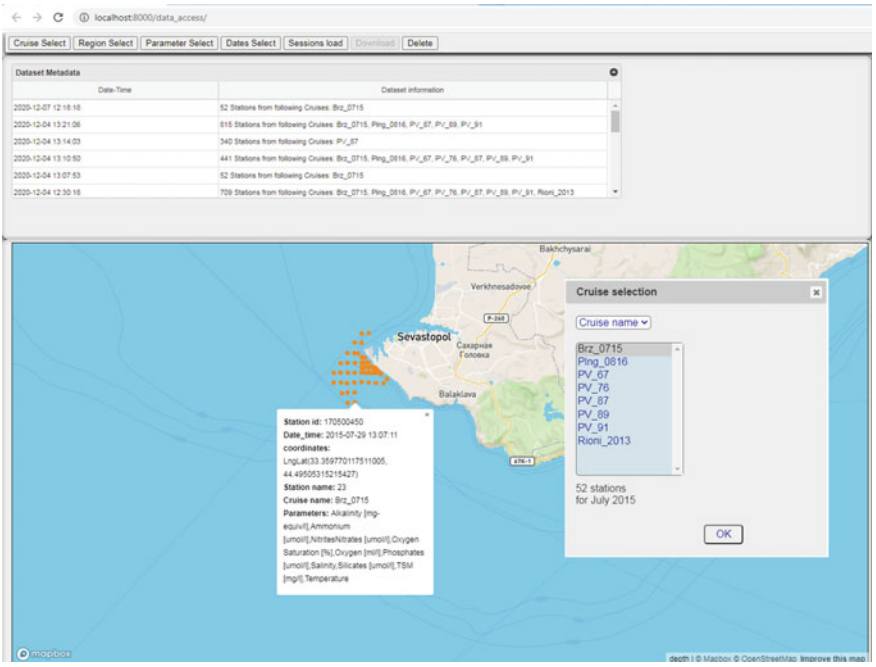

Fig. 3 Selection by cruise (cruise Brz_0715)

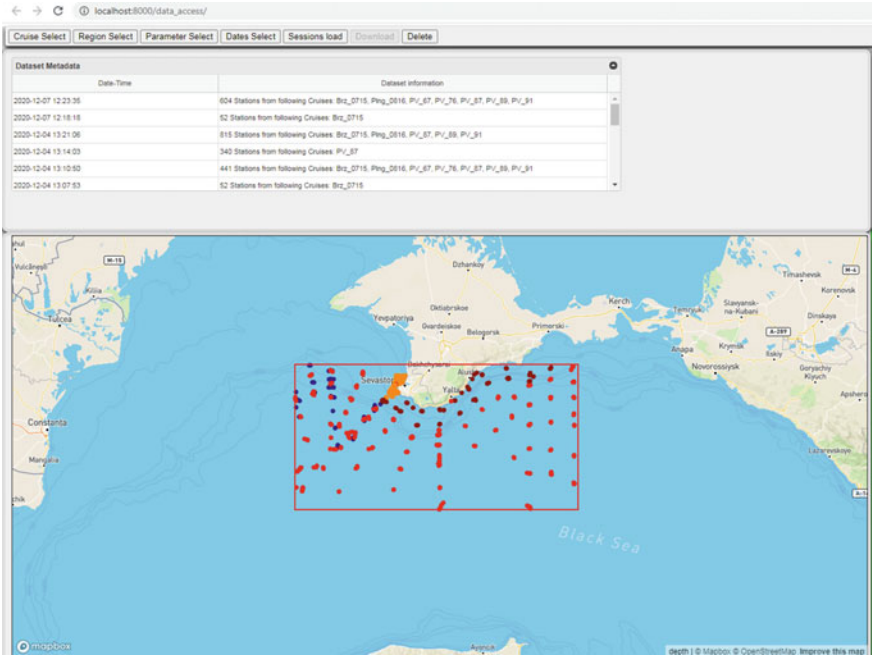

Fig. 4 Selection by region

- Atlas map selection is shown at the Fig. 7. It provides the possibility to select atlas map parameters, level and corresponding period.
- Satellite images selection is presented at Fig. 8. User can select one of the three parameters and select the required date from the date list.
- Profile data selection and plot. It allows the selection of the oceanographic station on the map and viewing the station's parameter list. After the selection of the interested parameter the correspondent plot will be created.

To overlay different types of data, such as for example the cruise data and Satellite images, the overlay module was developed. It allows the visualization of the different data at the same interactive map (Fig. 9).

In addition to data selection interface, the authorize user module was developed. It has two different parts—one for oceanography users, which select and download data, the other for administer users which set approvements for selected data sets.

Oceanography user authorize module is an important part of the system, which provides maintaining the information for each user, such as date and time connection, selected data sets, the obtained permits, downloaded data sets and so on. All these data are kept in Session table. User Interface allows viewing user's data sets, to check data set permissions, delete data sets from the list, downloaded selected data sets.

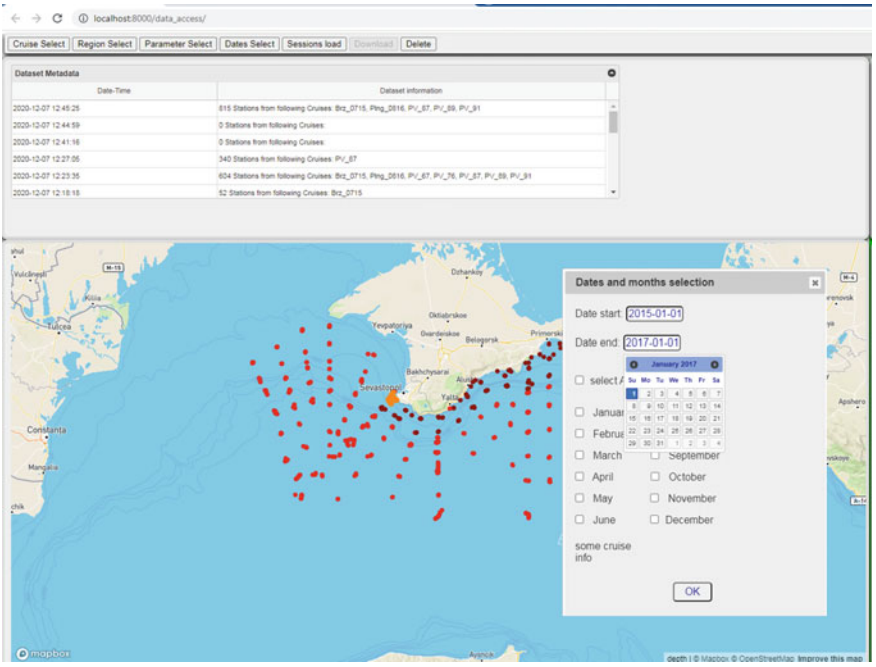

Fig. 5 Selection by time period (Jan 01, 2015–Jan 01, 2017)

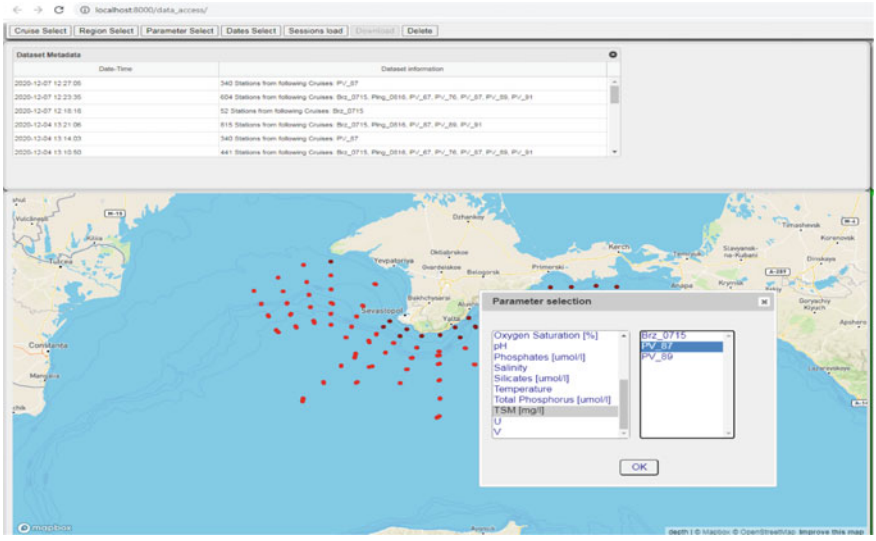

Fig. 6 Selection by parameters

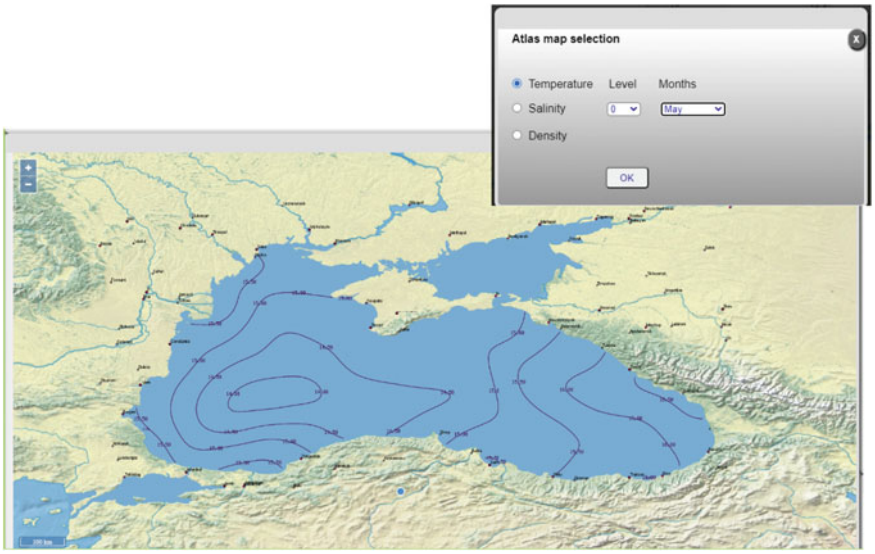

Fig. 7 Climatic atlas map selection

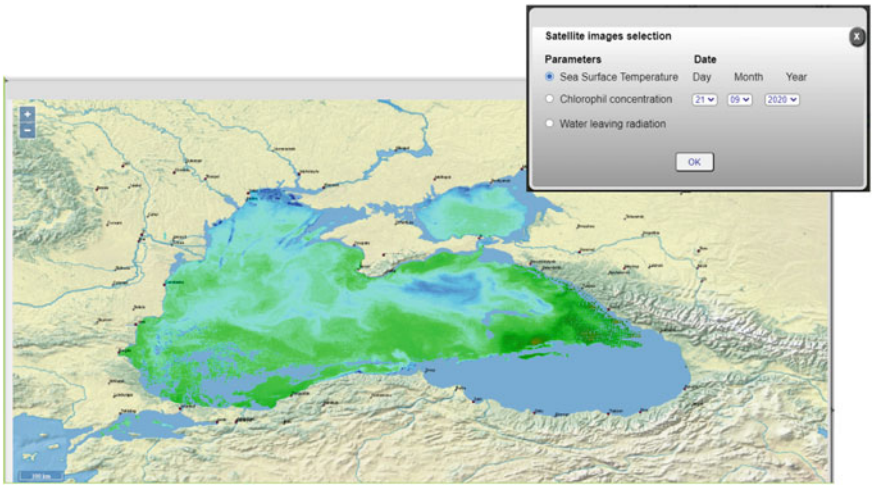

Fig. 8 Selection of the satellite images

Administrative user module provides access to oceanographic user's data sets selections and requests, gives the possibility to set permissions to requested data sets.

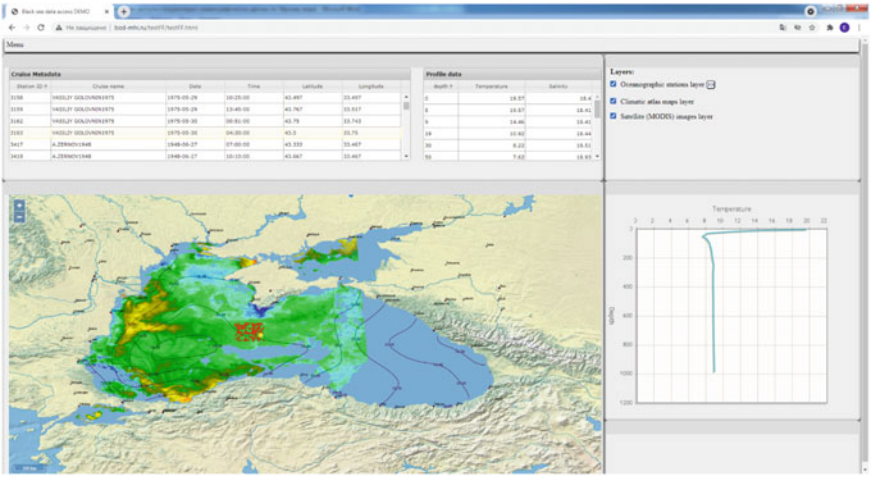

Fig. 9 Overlay of the cruise data, climatic atlas map and satellite image

4 Conclusions

The development of online data access system is a user-friendly software which provides convenient tools for data access, visualization, receiving the approval for selecting data sets and downloading oceanographic data. It allows the selection of different types of oceanographic parameters, presenting them in user-friendly form and overlying different data types at the same map.

This new online system is in progress to be embedded in MHI for automatic data access for authorize users.

Acknowledgements This work is carried out within the framework of the state assignment: 0555-2021-0003 "Development of methods of operational oceanology based on interdisciplinary research of the formation and evolution of the marine environment and mathematical modeling using data from remote and contact measurements" (code "Operational Oceanology").

References

1. Eremeev V., Khaliulin A., Godin E., Ingerov A., Belokopytov V., Zhuk E., Galkovskaya L., Isaeva E., Problemno-orientirovannaya geoinformacionnaya systema Chernogo morya // Ustoichyvost i evoluciya okenologicheskyh harakteristik ekosystemy Chernogo morya. – SEvastopol: EKOCY – Gydrophysica, 2012. – C. 8 – 31.
2. Eremeev V., Khaliulin A., Ingerov A., Zhuk E., Godin E., Plastun T. Sovremennoe sostoyanye banka okeanographicheskyh dannyh MHI NAN Ukrainy: programno-matematicheskoe obespechenye // Morskoy gydrophysicheskyi jurnal, 2014, № 2, C. 54-66, ISSN 0233-7584.
3. Zhuk, E., A. Khaliulin, G. Zodiatis, A. Nikolaidis, E. Isaeva/ Black Sea GIS developed in MHI Proc. SPIE 9688, Fourth International Conference on Remote Sensing and Geoinformation

of the Environment (RSCy2016), 96881C (August 12, 2016); doi: https://doi.org/10.1117/12.2241631 Volume 9688 http://proceedings.spiedigitallibrary.org/proceeding.aspx?articleid=2545474.
4. A.Yu. Basykina*, E.V. Zhuk, A.Kh. Khaliulin " The Geo-Information System Application for Display of the Tsunami Type Long Wave Propagation Modeling Results in the Black Sea Coastal Area" / Physical Oceanography, 2017, №3, c. 74–81; DOI: https://doi.org/10.22449/0233-7584-2017-3-74-81.
5. Zhuk, E., Vecalo, M., and Ingerov, A.: The new online Black Sea Oceanographic Database, EGU General Assembly 2020, Online, 4–8 May 2020, EGU2020–873, https://doi.org/10.5194/egusphere-egu2020–873, 2019.
6. GEBCO https://www.gebco.net/data_and_products/gridded_bathymetry_data/.
7. EDMO https://www.seadatanet.org/Metadata/EDMO-Organisations.
8. P01 http://seadatanet.maris2.nl/v_bodc_vocab_v2/search.asp?lib=P01.
9. P02 http://seadatanet.maris2.nl/v_bodc_vocab_v2/search.asp?lib=P02.
10. P06 http://seadatanet.maris2.nl/v_bodc_vocab_v2/search.asp?lib=P06.
11. L05 http://seadatanet.maris2.nl/v_bodc_vocab_v2/search.asp?lib=L05.
12. Django https://www.djangoproject.com/.
13. jQuery https://jquery.com/.
14. Mapbox GL JS https://www.mapbox.com/mapbox-gljs.
15. Elena Zhuk, "The Black Sea oceanographic web GIS interface new developments," Proc. SPIE 11524, Eighth International Conference on Remote Sensing and Geoinformation of the Environment (RSCy2020), 1152413 (26 August 2020); https://doi.org/10.1117/12.2570979.

Ice Research in the Gulf of Finland

N. A. Podrezova and K. V. Kravtsova

Abstract The article presents and analyses the results of ice cover research in the Gulf of Finland, which were obtained in the course of the training ice practice by oceanology students of the 2nd year of the Russian State Hydrometeorological University in February 2021. During the practice about 100 measurements of snow cover thickness and density as well as ice thickness were made; more than 20 ice samples were taken for analysis of ice structure through polarizer. Two thermal oblique experiments were performed to determine the vertical temperature profile in a multilayer medium. Heat fluxes in the multilayer medium have also been calculated.

Keywords Baltic sea · Gulf of Finland · Ice cover · Snow cover · Multilayer environment · Heat fluxes

Ice forms in the Gulf of Finland every year, but the timing of its formation and disappearance, as well as the extent of its spreading, depends on the severity of the winter. Ice formation occurs in an east–west direction. The first ice usually appears in bays and inlets that are deep inland. In the Gulf of Finland, the ice period starts in mid-November. The maximum development of the ice cover is recorded in late February–March. The average ice thickness in the area described is not great (0.1–0.3 m) but during severe and very severe winters, it can increase to 0.8 m and sometimes to 1 m. Ice cover break-up in the eastern part of the sea occurs in a west-to-east direction. In the Gulf of Finland, landfast ice break-up begins in the third decade of March and early April. The inter-annual variability in the timing of ice break-up in the Gulf of Finland reaches between 60 and 70 days. During harsh winters the Gulf of Finland is finally cleared of ice in the second half of May, during mild winters in early May and during mild winters in the first or second decade of April [1].

In the period from 8/02/2021 to 20/02/2021 there was an ice practicum for second-year oceanology students of Russian Hydrometeorological University in the eastern part of Gulf of Finland near Oranienbaum (Fig. 1). During the practical training, the

N. A. Podrezova (✉) · K. V. Kravtsova
Russian State Hydrometeorological University, St Petersburg, Russian Federation
e-mail: Nadinapod@mail.ru

© The Author(s), under exclusive license to Springer Nature Switzerland AG 2022

V. I. Karev (ed.), *Physical and Mathematical Modeling of Earth and Environment Processes*,
Springer Proceedings in Earth and Environmental Sciences,
https://doi.org/10.1007/978-3-030-99504-1_27

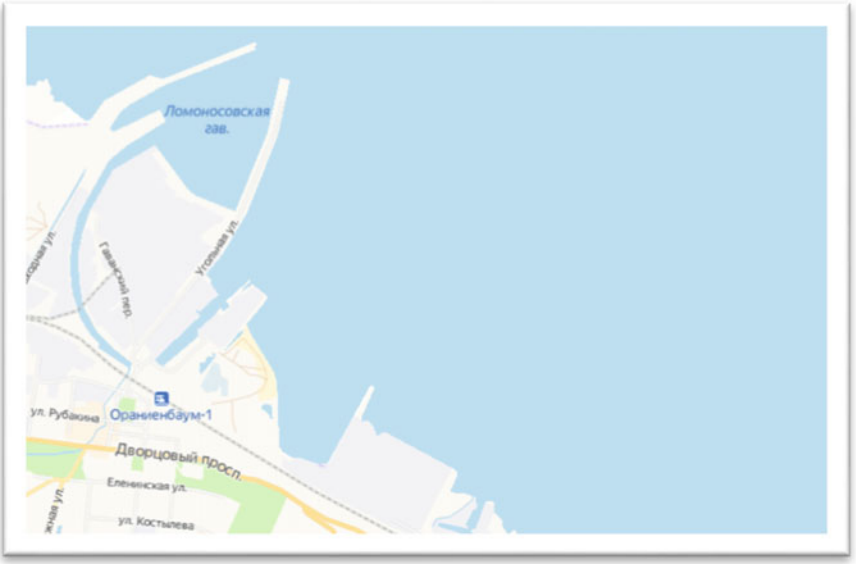

Fig. 1 Coast of the Gulf of Finland near Oranienbaum

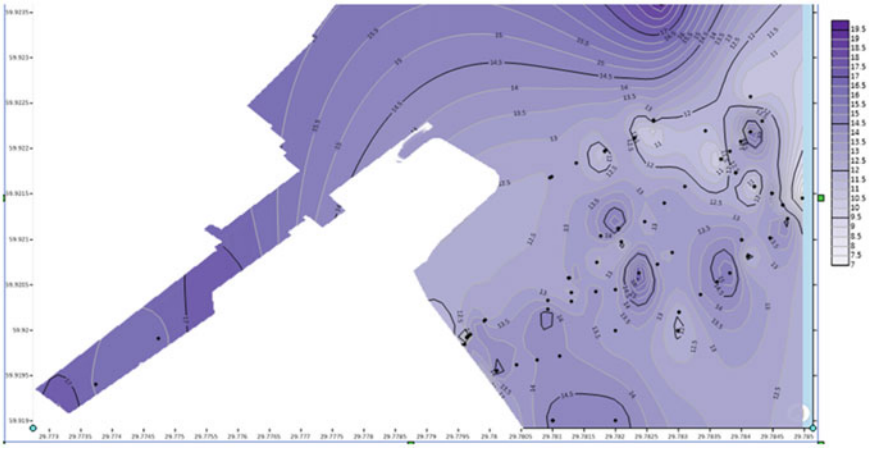

Fig. 2 Height of snow cover

oceanology students carried out the following measurements: determination of snow cover thickness and density, ice thickness, as well as depth in the investigated point. About 100 measurements were made and more than 20 ice samples were taken.

On average, the height of the snow cover in the studied area ranged from 11 to 15 cm (Fig. 2). As can be seen from the figure, the thickness of the snow cover is not uniform. The maximum snow height was 20 cm and was observed in the Sidorovsky

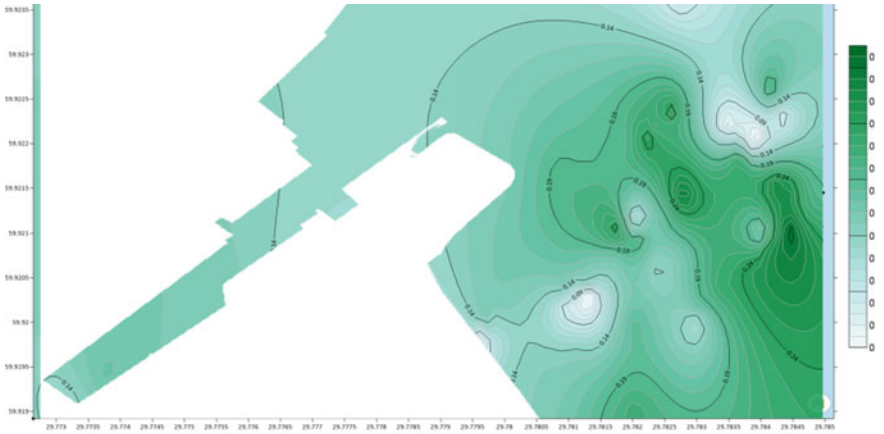

Fig. 3 Snow density

channel, where it is more difficult for the wind to blow away snow that has not yet compacted, and in a place quite distant from the shore and the main study field. The minimum value of snow cover was about 5–7 cm and was observed in different places in the study area.

The snow density was found using a snow gauge [2]. Snow density is defined as the ratio of the sample weight to its volume, according to (1):

$$\rho = G / (S \cdot H) \quad (1)$$

where: ρ is the snow sample density, g/cm^3; G is the sample mass, in grams; S is the reception area of the cylinder, cm^2; H is the snow sample height, cm.

Figure 3 shows the density of snow in the study area. The average density of snow was—0.164 g/cm^3. The minimum density value was—0.023 g/cm^3, the maximum density value—0.304 g/cm^3. It can be noted that snow density is not uniform in the studied area. However, the lowest density was observed in the areas with the highest snow height, while the highest density, on the contrary, was observed in the areas with the lowest snow height. This suggests that the snow initially fell evenly, but subsequently, due to various factors, uneven snow melting and compaction occurred.

On average, ice thickness ranged from 32 to 36 cm, just above the long-term average (Fig. 4) [1, 3]. The ice cover thickness, as well as in the case of snow cover, was distributed unevenly over the whole study area, but in general, its increase from shore to bay was traceable. The maximum value of ice thickness was 54 cm. The minimum values were mostly observed near the shore, and amounted to about 26 cm. The depth of the study area did not exceed 3 m.

During the practice, 20 ice samples were taken. In most cases, 2 layers can be distinguished in the studied samples (Fig. 5a). The upper layer, frozen snow of about

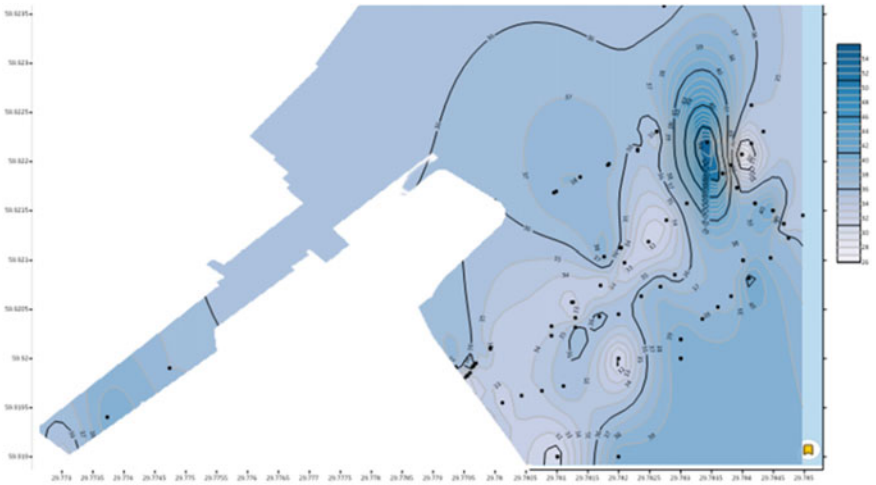

Fig. 4 Ice thickness

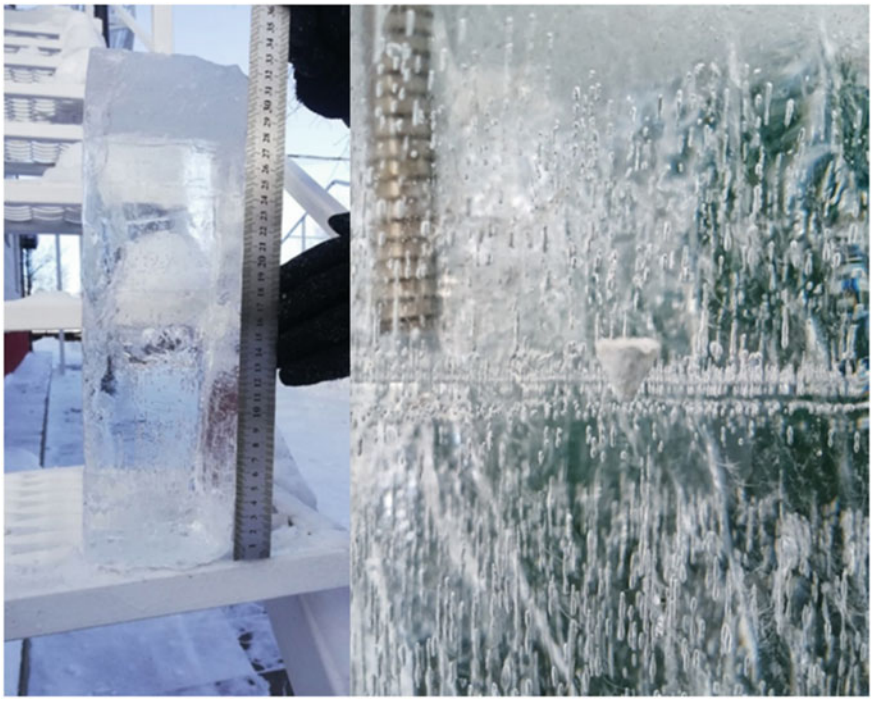

Fig. 5 Study of ice sample thickness (**a**), inclusions in ice sample (**b**)

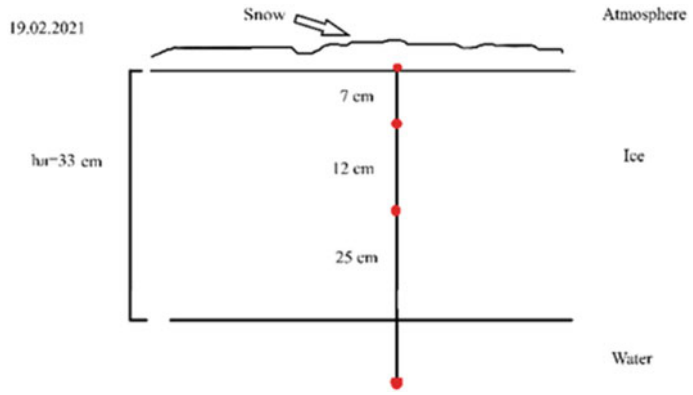

Fig. 6 Location of the sensors

5 cm and the lower layer, transparent dense ice formed from water, with air bubbles inclusions, 25–30 cm thick (Fig. 5b).

To determine the ice structure, some of the samples were examined with a polarizer. Ice crystals are irregularly grained, approximately 2 cm long. The air bubbles are oblong, up to 3 cm in size. Due to changing ice formation conditions, the studied samples have a layered structure.

The multilayer atmosphere-snow-ice-water environment, characteristic of ice-covered waters, is very challenging as a measurement object. The solution of various thermodynamic problems requires information on the vertical temperature distribution in all media and at their interfaces. At the same time the media are fundamentally different in characteristics important in measurement tasks—density, thermophysical (heat capacity, thermal conductivity) and electrophysical (conductivity, dielectric permeability) properties [4].

In order to obtain information about vertical temperature distribution in the multilayer atmosphere-snow-ice-water medium, a thermal braid containing 4 sensors was frozen in. Moreover, the sensors were installed so that 1 sensor was in the snow, 2 and 3 sensors were frozen into the ice and 4 sensor was in the sub-ice water. A schematic of the location of the sensors on February 19 is shown in Fig. 6. Temperature values were measured on February 18 and 19, thus 2 experiments were conducted.

Experiment 1. On February 18, the average atmospheric temperature, at the time of the experiment, was—18 °C [5]. Cloudiness—0 points. Wind—doldrums. Closed terrain—Sidorovsky channel. Time of the experiment was 3 h 10 min. The resulting temperature profile is shown in Fig. 7. It can be noted that the largest temperature changes are recorded at sensor 1, which is located in the snow. Where one can note an increase in temperature from −4 °C to −1 °C within an hour. Sensors 2 and 3 record small temperature variations from 0 °C to 1 °C throughout the experiment.

Experiment 2. On February 19, the average atmospheric temperature, during the experiment, was—10 °C. Cloudiness—8–9. Wind—2 m/s. Terrain—open, on a bay. Time of the experiment was—3 h. Obtained temperature profile is presented in Fig. 8.

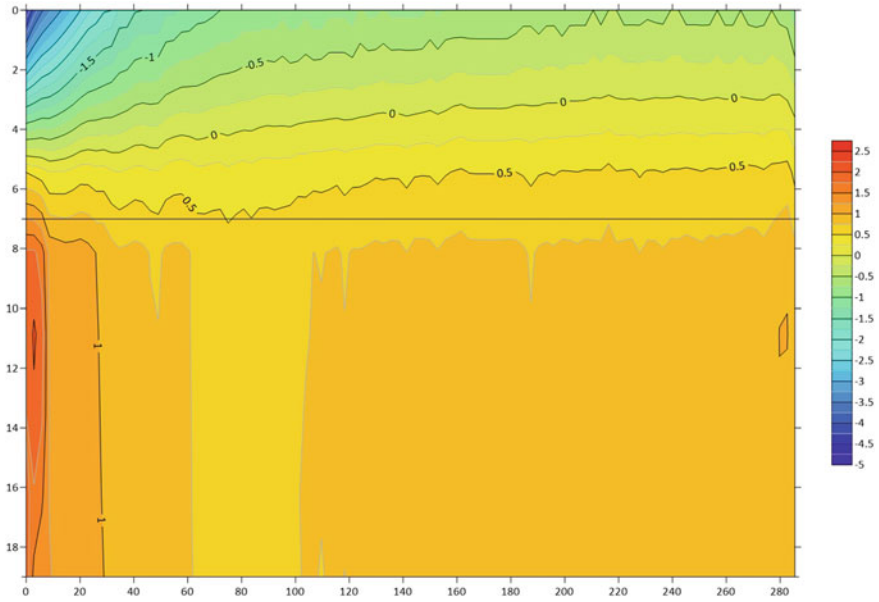

Fig. 7 Temperature profile 18.02.2021

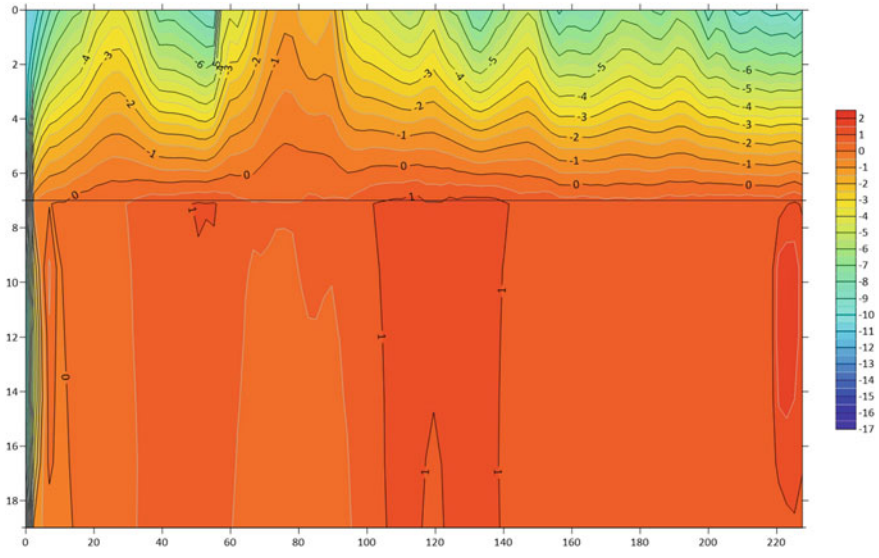

Fig. 8 Temperature profile 19.02.2021

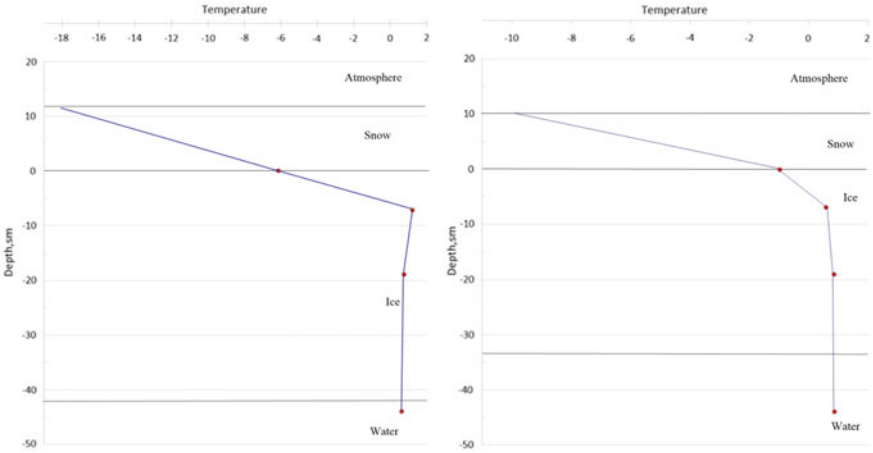

Fig. 9 Vertical temperature distribution in atmosphere-snow-ice-water for 18.02.21 (**a**) and 19.02.21 (**b**) -snow-ice-water for 18.02.21 (**a**) and 19.02.21 (**b**)

It can be noted that throughout the experiment, the greatest temperature changes are observed on sensor 1, in the snow, which are from −6° C to −3° C. On sensors 2 and 3 the temperature stabilises within a few minutes and records a temperature of −0.5 °C. It can be seen that there is a small interval on the graph with temperatures above the presented values, as a kind of an anomaly. This relatively warm interval can be explained by the fact that the thermo sensors are very sensitive even to slight interference, maybe someone walked by it, or the device itself was checked. In further experiments we tried to exclude any outside influences.

It may be noted that the temperature profiles obtained in the two experiments differ significantly only on 1 sensor, which captures the temperature in the snow. What can be explained by different conditions of the experiment, namely by the fact that the thermocouple was frozen in different parts of the bay (closed and open parts), exposure to different values of atmospheric temperature, as well as different wind speeds.

A vertical temperature profile of the atmosphere-snow-ice-water environments was then plotted (Fig. 9a and b). As can be seen from both plots, the sub-ice water and lower ice boundary has a temperature just above 0 °C. While the upper ice-lower snow boundary temperature is significantly different in both cases. On February 18, the temperature of the upper ice-lower snow limit is −6 °C, while on February 19, it is about −1 °C. The difference in the snow cover temperature values is explained by different meteorological conditions during the experiments. On 18 February the atmospheric temperature was −18 °C, while on 19 February the weather was warmer and the atmospheric temperature was −10 °C. However, the thermal dynamics of the sea ice cover is determined not only by meteorological conditions and the hydrological regime of the water area but also depends to a great extent on the properties of

Table 1 Calculated values of heat fluxes

F_{water},W/m^2	F_{ice}(lower boundary),W/m^2	F_{ice}(upper boundary), W/m^2	F_{snow},W/m^2
540.94	783.11	40,945.62	19,383.71

snow on its surface. Snow cover serves as a protective shell of the upper ice boundary in areas with negative air temperatures [6, 7].

Heat flux through the snow cover in the quasi-stationary regime is directly proportional to the temperature gradient and inversely proportional to the thermal resistance of the snow cover. Therefore, the contribution of air temperature and the thermal resistance of the snow cover, largely depending on the thermal conductivity coefficient of the snow.

The known dependencies of the snow thermal conductivity coefficient show a large scatter of values for the same snow density. One of the reasons for this is the structural features of the snow cover. Thus, the thermal conductivity coefficient of deep frost is several times lower than that of granular snow with equal density. Therefore, the layering of snow cover, due to both meteorological conditions and metamorphism processes, affects its thermal resistance and the temperature regime of underlying bases [8].

To calculate the heat fluxes in each of the studied media, (2) was used [7, 9]:

$$F = \left(\frac{T - \mathrm{T}}{h}\right) kC\rho, \ [\mathrm{W/m}] \tag{2}$$

where, h is distance between sensors, k is turbulent exchange coefficient equal to 10^{-3}, C is heat capacity of medium, ρ is density of medium.

The calculated values of heat fluxes are presented in Table 1. From calculations, it is visible, that the heat flow gradually increases, from water to atmosphere. In natural conditions, heat flux from water to ice usually occurs. It decreases the value of frost days summation the more the ice is thicker. Also, under the influence of this heat flow, melting of ice from its lower surface can occur in spite of the negative air temperature.

It is known that the thickness of snow-covered ice is less than that of non-snow-covered ice. This reduction depends on the thickness of the snow layer and the thermal conductivity. This results from the fact that snow is a good thermal insulating material, i.e. the temperature of ice under snow is higher than under snowless ice. Further experiments with snow-covered ice, as well as with ice without snow cover, are planned.

As a result of the study, we obtained data on the thickness and density of the snow cover, the thickness of the ice cover in February 2021 near Oranienbaum. A polarizer was used to study the structure of the ice samples taken. The thermometric slant measurements showed vertical temperature profiles and made it possible to calculate heat fluxes in the multilayer environment.

References

1. Baltic Sea – ice conditions. Available at: http://esimo.oceanography.ru/esp1/index.php?sea_code=1&section=9 (Accessed 17.12.2021).
2. Zakharov V.F. Sea Ice in Climate System. Problems of Arctic and Antarctic. Issue 69. SPb: Gidrometeoizdat, 1995. - pp. 15–26.
3. A snow gauge is a meteorological instrument for measuring snow density and height. Available at:https://ru.wikipedia.org/wiki//%D0%A1%D0%BD%D0%B5%D0%B3%D0%BE%D0%BC%D0%B5%D1%80 (Accessed 17.12.2021).
4. Kovchin I.S., Stepanyuk I.A. Methods of special oceanological measurements. Textbook - SPb.izd., RGGMU,2002–271p.
5. Podrezova N.A., Angudovich J.I. Study of ice cover in the eastern part of the Gulf of Finland in February 2019. In the book: Contemporary problems of hydrometeorology and sustainable development of the Russian Federation. Collection of abstracts of All-Russian scientific and practical conference. 2019. C. 827.
6. Zavyalov D.D., Solomakha T.A. Influence of freshly fallen snow on sea ice build-up and melting. Marine Hydrophysical Institute of RAS, Sevastopol, Russia, 2019.
7. Doronin Y.P. Ocean physics. Textbook - St. Petersburg: ed. RGGMU, 2002.-340 p.
8. Kotlyakov V.M., Sosnovsky A.V., Osokin N.I. Estimation of snow thermal conductivity coefficient by its density and hardness on West Spitsbergen. Institute of Geography, Russian Academy of Sciences, Moscow, Russia, 2018.
9. Doronin Y.P., Lukyanov S.V. Laboratory manual on ocean physics,-SPb,eds.RGMI,1993–87 p.
10. Weather in 243 countries of the world. Available at: https://rp5.ru/ (Accessed 17.12.2021).

Density Stratification in the White Sea

N. A. Podrezova and P. V. Pogorelova

Abstract This paper analyzes the White Sea data obtained during the expedition in June 2020. The calculation is performed and the type of density stratification in the selected points is determined. The frequency of recurrence of stability types in percentage was also obtained. One of the secular sections of the White Sea was constructed.

Keywords White-sea · Density stratification of water · Temperature and salinity stability

The White Sea is the most isolated inland sea of the Arctic Ocean. It is entirely inland waters of Russia. It is connected to the Barents Sea in the north through a narrow strait—the Gorlo. The White Sea water area is divided into several parts: Basin of the White Sea, Gorlo Strait, Voronka, Onega Bay, Dvina Bay, Mezen' Bay and Kandalaksha Bay.

The study of density stratification is an important step in solving a number of applicable problems. If the stratification is stable, it can exist for a long time, preventing the development of turbulence. Unstable stratification, on the contrary, provokes turbulence development. The White Sea under study is characterized by tidal phenomena, which influence water stratification, causing pockets of instability. It is also known that acoustic traces are less noticeable in unstable stratification than in stable stratification. The specifics of the development of hydrophysical processes in the ocean are related to water stratification [1–3].

The work analyzed the fine structure of the White Sea. The initial data were the values of temperature and salinity obtained in the course of industrial practice by the students of the Russian State Hydrometeorological University in the expeditionary works of the Federal State Budgetary Administration (FSBI) Northern Hydrometeorology and Environmental Monitoring Administration in June 2020. To compare the density stratification of the White Sea, 7 stations were selected (Fig. 1). Point №

N. A. Podrezova (✉) · P. V. Pogorelova
Russian State Hudrometeorological University, St Petersburg, Russian Federation
e-mail: Nadinapod@mail.ru

© The Author(s), under exclusive license to Springer Nature Switzerland AG 2022

V. I. Karev (ed.), *Physical and Mathematical Modeling of Earth and Environment Processes*,
Springer Proceedings in Earth and Environmental Sciences,
https://doi.org/10.1007/978-3-030-99504-1_28

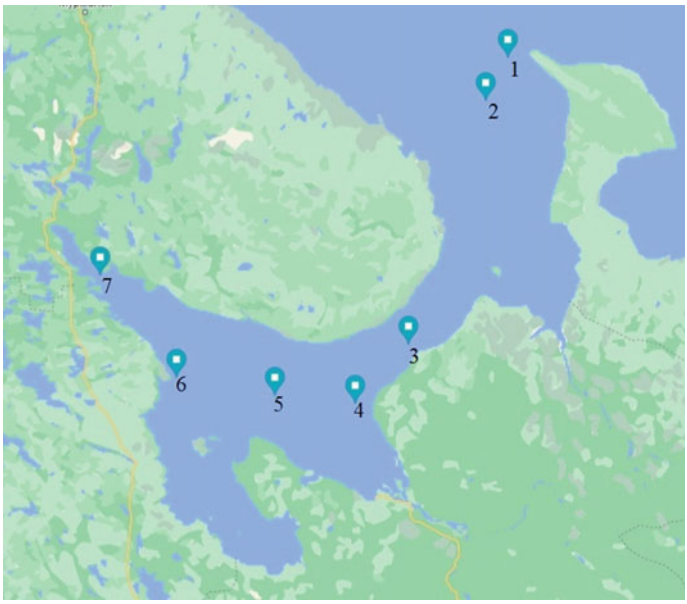

Fig. 1 Station location map

1 and № 2 are on the border with the Barents Sea, point № 3 is in the Gorlo Strait, points № 4, № 5, № 6 are in the basin of the White Sea, point № 7 refers to the Kandalaksha Bay.

The Hesselberg-Sverdrup criterion, oscillation period, and stratification type by strata were calculated from the field data on temperature and salinity. The frequency of occurrence of the stability types in percentages was then obtained. For each station, the number of occurrences and percentage content were summarized in a table.

The first station is on the border with the Barents Sea, the depth of the station is—57 m. Water temperature changes from the surface to the bottom—from 6.3 to 2 °C respectively. From a depth of 45 m to the bottom the temperature remains unchanged. The highest values of water salinity are observed at this station. Water salinity increases from the surface to the bottom—from 30.4 to 34 ‰ respectively, and from 42 m depth does not change. The definition was determined in layers equal to 1 m. The predominant stratification type is complete stable, the number of cases is 33, which is 60%. The stratification type of salt fingers occurs in 12 cases, which is 21.8%. The type of stratified convection and absolute instability occur in 5 cases, which is 9.1% each (Table 1).

The second station is also on the border with the Barents Sea, the depth of the station is—57 m. Intrusive type is observed from the surface to the bottom. There is little variation in temperature. Water temperature at the surface is a little more than 6 °C. Near the bottom the water temperature is about 5.6 °C. Water salinity at the surface is 33.1 ‰. While at the bottom the salinity has a value of 33.4 ‰. The definition was determined in layers equal to 1 m. The predominant stratification type

Table 1 Stratification type at station 1

Stratification type	Full stability	Layered convection	Salt fingers	Absolute instability
Number of cases	33	5	12	5
Percentage	60	9.1	21.8	9.1

Table 2 Stratification type at station 2

Stratification type	Full stability	Layered convection	Salt fingers	Absolute instability
Number of cases	28	14	9	4
Percentage	50.9	25.4	16.4	7.3

Table 3 Stratification type at station 3

Stratification type	Full stability	Layered convection	Salt fingers	Absolute instability
Number of cases	18	1	6	6
Percentage	58.1	3.2	19.35	19.35

is full stability, the number of cases is 28, which is 50.9%. Stratification type layered convection occurs in 14 cases, which is 25.4%. Salt fingers type occurs in 9 cases, it is 16,4%, whereas, absolute instability only in 4 cases, it is 7,3% (Table 2).

The third station is 34 m deep. The station is located in the Gorlo Strait, temperature and salinity values are almost uniform along the depth, due to tidal phenomena in the sea. Water temperature at the surface is 5 °C. The upper boundary of the thermocline is at the surface. At the bottom, the water temperature is 4.5 °C. From a depth of 10 m and up to the bottom, an intrusive type is observed. Slight changes in depth are also observed in salinity, with values at the surface and near the bottom of 26 and 26.05 ‰, respectively. Definition was determined in layers equal to 1 m. The predominant type of stratification—complete stability, is found in 18 cases, which is 58.1%. Stratification type—layered convection occurred in only 1 case and accounted for 3.2%. Stratification type—salt fingers and absolute instability occurs in 6 cases and amounts to 19.35% each (Table 3).

The fourth station is the shallowest, with a depth of 15 m. The water temperature at the surface is 14.5 °C. The upper boundary of the thermocline is at a depth of 5 m. Further the water temperature decreases and at the bottom is 5.4 °C. Water salinity from the surface to 5 m depth decreases from 22.2 to 22.0 ‰. Further, from the depth of 5 m salinity increases up to 26 ‰, and only near the bottom there is slight. The definition was determined in layers equal to 1 m. The predominant stratification type is full stability, the number of cases is 12, which is 85.7%. Stratification type layered convection and salt fingers did not occur. Stratification type - absolute instability accounts for only 2 cases, which is 14.3% (Table 4).

The fifth station is located in the Basin, its depth is 135 m. The water temperature at the surface is 13.5 °C. The upper boundary of the thermocline at the surface. The lower boundary of the thermocline is at a depth of 24 m. At the lower boundary

Table 4 Stratification type at station 4

Stratification type	Full stability	Layered convection	Salt fingers	Absolute instability
Number of cases	12	0	0	2
Percentage	85.7	0	0	14.3

Table 5 Stratification type at station 5

Stratification type	Full stability	Layered convection	Salt fingers	Absolute instability
Number of cases	26	0	0	0
Percentage	100	0	0	0

Table 6 Stratification type at station 6

Stratification type	Full stability	Layered convection	Salt fingers	Absolute instability
Number of cases	43	13	4	2
Percentage	69.35	21	6.45	3.2

of the thermocline the temperature is 1 °C. Water temperature below 55 m to the bottom does not change and is—1 °C, this is the lowest values of water temperature. Water salinity increases from the surface to the bottom—from 21 to 28.5 ‰. The upper boundary of the halocline is observed near the surface, the lower boundary at a depth of 10 m. The definition was determined in layers equal to 5 m. In all cases, the stratification type is full stability, which is 100%. Stratification types—layered convection, salt fingers as well as absolute instability were not detected (Table 5).

The sixth station is 64 m deep. Water temperature at the surface is 10 °C. The upper boundary of the thermocline is at the surface. From 25 to 37 m small temperature increases from - 0.8 to 1 °C are observed. Below 42 m the temperature is unchanged and is 0 °C. Water salinity at the surface is 21.5 ‰. The upper boundary of the halocline is also at the surface. At the depths from 19 to 40 m the intrusive type is observed. As in the case of water temperature, the salinity from 42 m and below does not change and is 27.2 ‰. The definition was determined in layers equal to 1 m. The predominant stratification type is full stability, 43 cases, which is 69.35%. Stratification type layered convection occurs in 13 cases, which is 21%. Stratification type of salt fingers and absolute instability occurs in 4 and 2 cases, respectively, which is 6.45 and 3.2% (Table 6).

The seventh station is the deepest, with a depth of 140 m, located in Kandalaksha Bay. The water temperature at the surface is 16 °C. The upper boundary of the thermocline is at a depth of 10 m. The lower boundary of the thermocline is at a depth of 20 m. Water temperature below the horizon of 40 m practically does not change and is about 0 °C. Water salinity at the surface is 15 ‰. The upper and lower boundaries of the halocline are 10 and 15 m, respectively. From the depth of 15 m and to the bottom the salinity is about 28 ‰. The definition was determined in layers equal to 5 m. The predominant stratification type is complete stability, 25 cases, which is

Table 7 Stratification type at station 7

Stratification type	Full stability	Layered convection	Salt fingers	Absolute instability
Number of cases	25	0	3	0
Percentage	89.3	0	10.7	0

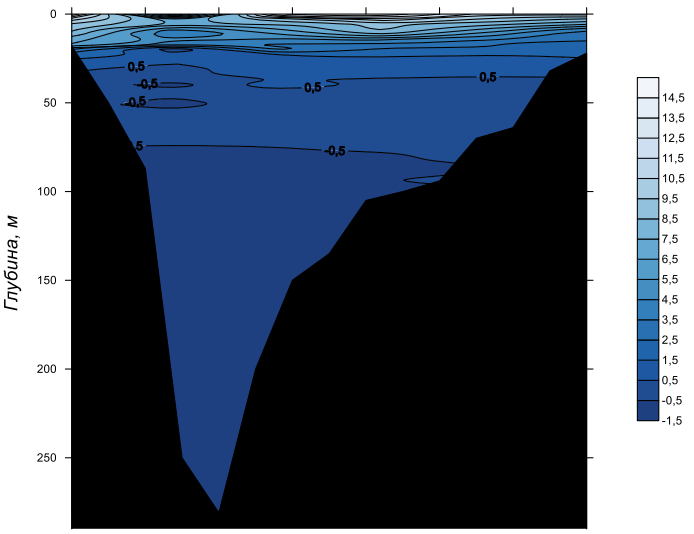

Fig. 2 Section on the temperature, through points 6, 5 and 4

89.3%. Stratification type—salt fingers is only 3 cases, which is 10.7%. Stratification type is layered convection and absolute instability does not occur (Table 7).

The surface layer has a pronounced full stability. However, near the surface, absolute instability can be observed, which is related to wind action. In the near-bottom layer full stability prevails. But, some inclusions and layered convection as well as salt fingers can be noted [2].

For further analysis, temperature-based (Fig. 2.) and salinity-based (Fig. 3.) transects were constructed from the expedition data. The transects are located in the White Sea Basin and include previously analyzed stations 6, 5 and 4. The transects show a basin with a depth of up to 290 m.

The average temperature in the transect is 2.1 °C. The upper warmed layer is well traced in the section. The maximum values—14.5 °C, are observed on the surface. Values also agree with the works of Tolstikov A.V. and Serykh I.V. [4, 5]. As can be noted, the lower boundary of thermocline is observed at a depth of 15–20 m throughout the section. Below the depth of 25 m the temperature values do not rise above 0.5 °C. It may be noted that the basin is filled with waters with negative temperature values [6]. The minimum temperature value of 1.6 °C is observed at a depth of 281 m. In general, the temperature distribution is rather even, without sharp rises and falls [7–10].

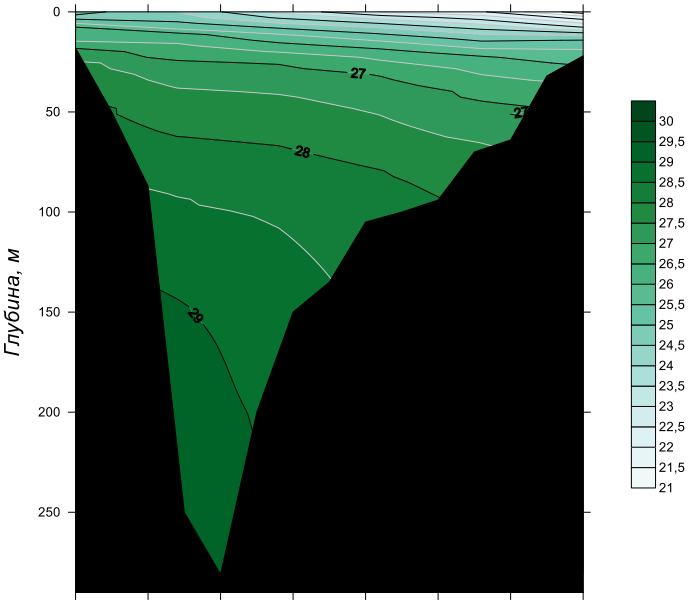

Fig. 3 Transect by salinity, through points 6, 5 and 4

The average value of salinity in the section is 26.9 ‰. The surface desalinization at the boundary of the Dvina Bay and the White Sea Gorlo Strait, which correlates with station 4, is well traced in the transect. The minimum salinity is observed at the surface and is equal to 21 ‰. Desalinated water is observed up to 10 m depth. Below 10 m salinity values exceeding 26 ‰ are observed. Trough fills with salinity of 28–29 ‰. Maximum salinity value of 29.2 ‰ is observed at the depth of 281 m. In general, the distribution of salinity, as well as in the case of temperature, is rather uniform [7, 8, 10].

As a result of this work, we can conclude that the summer temperature distribution of the White Sea is typical for this time of the year [7]. The warmest water at the surface (16 °C) was observed in the Kandalaksha Bay, with salinity equal to 15 ‰. The coldest area was Gorlo Strait, where the surface temperature was about 5 °C, with salinity equal to 26 ‰. Stratification in the Basin is pronounced. The thermocline in the Basin corresponded to the position of the halocline and was located at horizons of 10 to 20 m.

References

1. Oskotskaya S.A., Podrezova N.A., 2021. Ice regime of the White Sea in 2017–2020. Integrated research of the World Ocean. Proceedings of the VI All-Russian Scientific Conference of Young Scientists. Moscow, 2021. P. 155. (In Russian).
2. Arsentieva E.K., Podrezova N.A. , 2018. Formation of density stratification of the White Sea waters in 2014. Processes in geospheres. № 3 (17). P. 190. (In Russian).
3. Terentyeva K.S., Podrezova N.A., 2019. Peculiarities of water exchange in the White Sea throat. In the collection: Marine research and education (MARESEDU-2018). Proceedings of the VII International scientific and practical conference. Collection. 2019. P. 180–187. (In Russian).
4. Tolstikov A.V. Variability of the surface layer temperature of the White Sea, 2016. (In Russian).
5. Serykh I.V., Tolstikov A.V. On the climatic changes of the surface air temperature in the White sea region. Collection: IOP Conference Series: Earth and Environmental Science. Causes, Risks, Consequences, Problems of Adaptation and Management. Cep. "Climate Change: Causes, Risks, Consequences, Problems of Adaptation and Management" 2020. C. 012054.
6. 7. Podrezova N.A., Tsarev V.A., 2016. Main features of distribution of near-bottom saline waters in the White Sea. In the collection: Young Science - 2015. Proceedings of the VI Open International Youth Scientific and Practical Conference. 2016. P. 243–245. (In Russian).
7. Tolstikov A.V., Filatov N.N., Bogdanova M.S., Litvinenko A.V., Karpechko V.A., Derusova O.V., Balagansky A.F. Electronic Atlas of the White Sea and its Watershed, 2017. (In Russian).
8. Kirilova A.A., Frolova N.S. Study of biogenic elements distribution in Kandalaksha Bay of the White Sea in summer according to field data. In the book: Modern problems of hydrometeorology and environmental monitoring in the CIS. Collection of theses of International scientific-practical conference devoted to 90th anniversary of Russian State Hydrometeorological University. 2020. P. 371–374. (In Russian).
9. Baklagin V.N. Results of analysis of satellite data on water surface temperature of the White Sea. Engineering Bulletin of the Don. 2017. № 2 (45). P. 32. (In Russian).
10. Lebedev S.A., Kostyanoy A.G., Kostyanaya E.A., Serykh I.V. Interannual and seasonal variability of basic hydrometeorological parameters of the White Sea state according to satellite altimetry. In the collection: Fundamental and applied aspects of geology, geophysics and geoecology using modern information technologies. Proceedings of the VI International Scientific and Practical Conference. 2021. P. 189–200. (In Russian).

Features of Geological and Commercial Characteristics of the Kumak Ore Field (Southern Urals)

P. V. Pankratjev, V. A. Repkin, A. V. Kolomoets, A. V. Snachev, R. S. Kisil, and V. S. Panteleev

Abstract This article discusses the promising gold ore region of the Orenburg Urals, where the gold-quartz and gold-sulfide-quartz formations are developed. The main industrial value of the ore field is represented by two gold deposits: Kumakskoye and Vasin, within which two geological and industrial types of objects are distinguished: weathering crusts and bedrock deposits. The use of underground and heap leaching methods will allow more efficient industrial mining of gold ore objects, replenish the balance of mineral reserves of the Orenburg region.

Keywords East Ural Uplift · Kumak Ore field · Geological and industrial type · Underground leaching · Gold · Orenburg region

The Kumak ore field is located in the eastern part of the Anikhovsky graben and is confined to the Kumak-Kotansi crumple zone, composed mainly of black shale formations of the Breda formation (C1bd) [1]. Its section is dominated by carbonaceous terrigenous-sedimentary formations: siltstones, carbonaceous-clay shales and sandstones, as well as rare interlayers of limestone and coal. Of subordinate importance are effusions such as dacite and andesite porphyrites and their tuffs. The age of the formation deposits was determined by the definitions of foraminifera in limestone interlayers and the remains of micro fauna and spores of ancient ferns, calamites and other plants [2, 3]. The capacity is 350–700 m. The Bredinskaya formation lies with erosion on the Bereznyakovskaya thickness (D3—C1bz) and is overlain with erosion by the Birgilda thickness (C1br). The carbonate rocks of the latter (C1br) are

P. V. Pankratjev · A. V. Kolomoets (✉) · V. S. Panteleev
Orenburg State University, Orenburg, Russian Federation
e-mail: kolomoyets56@mail.ru

V. A. Repkin
LLC “Magma”, Mariupol, Ukraine

A. V. Snachev
Ufa Federal Research Centre RAS, Ufa, Russian Federation

R. S. Kisil
LLC “Udinsk-Gold”, Khorinsky, Russian Federation

© The Author(s), under exclusive license to Springer Nature Switzerland AG 2022

V. I. Karev (ed.), *Physical and Mathematical Modeling of Earth and Environment Processes*,
Springer Proceedings in Earth and Environmental Sciences,
https://doi.org/10.1007/978-3-030-99504-1_29

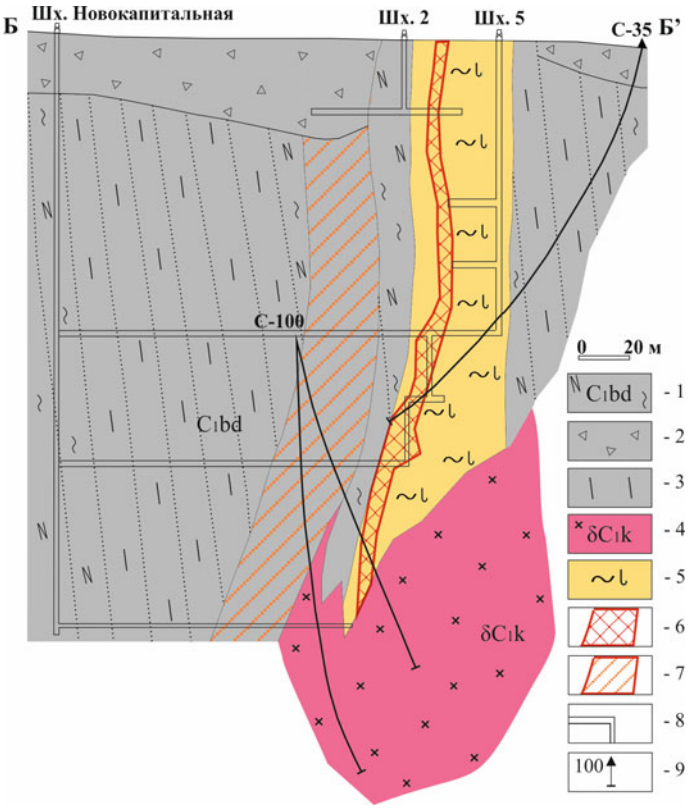

Fig. 1 Geological section of the Kumak deposit. Symbols: 1–carbonaceous shales of the Breda formation, 2–gravel-crushed weathering crust, 3–quartz-chlorite shales, 4–diorites of the Kumak complex, 5–quartz-mica-tourmaline metasomatically altered carbonaceous shales, 6–ore body composed of quartz-sericite metasomatites with poor pyrite inclusions and native gold, 7–contact inclusions of sulfides, 8–mine workings, 9–wells on sections and their number)

developed in the eastern and southern parts of the ore region and are mainly represented by limestones, marbles, with a subordinate amount of dolomites, calcareous mudstones. In the lower part of the section of the strata, dark gray carbonaceous-clay organogenic and organogenic-detrital limestones predominate. Above them lie gray, light gray limestones with a weakly pronounced layering, usually recrystallized, marbled to varying degrees, less often dolomitized.

Industrial concentrations of gold in the ore field are associated both with a series of quartz veins and veins, and with zones of veined-interspersed mineralization in rocks enriched with carbonaceous matter. Ore bodies are represented by quartz-chlorite-sericite and quartz-tourmaline composition in the form of veins, lenses and formation-like deposits and apophysis, confined to the thickness of carbonaceous shales, with the layers of which they mainly lie in accordance, having a meridional strike (Fig. 1).

Ore bodies are timed to the zones of manifestation of intense metasomatosis and mineralization [4]. The areas of mineralization development correspond to the places of intensively crushed, shale rocks, in which a large number of quartz, quartz-carbonate veins, quartz-carbonate-sulfide veins are recorded. The total length of the zones of metasomatites containing mineralization reaches the first tens of kilometers, with a width of up to 400–600 m and are characterized by a backstage-intermittent placement.

The prospects for the gold content of the Kumak ore mine are associated with incomplete development of the deep horizons of the mine, the operation of which was discontinued for technical reasons in 1954. Within its limits, more than 20 gold-ore manifestations were revealed, many of which were subjected to various degrees of prospecting [5, 6]. The total reserves (C2) of gold ore objects of the ore field according to Lyadsky et al. [2] amount to 77.75 tons. Of these, at the Kumakskoye field – 15.1 tons (average content of 5–15 g/t), at Vasin—44.3 tons (average content of 9.4 g/t).

The Vasin field is located 9 km northwest of the Kumakskoye field. It is composed of Middle-Upper Devonian tuff-sedimentary rocks and is controlled by a sub meridional tectonic zone, and is also accompanied by a wide development of ore-bearing metasomatites. At the deposit, gold-bearing mineralization is confined to steeply falling metasomatic zones of sub meridional strike, with a capacity of up to 60 m and a length of up to 2.0–2.5 km. Metasomatites are saturated with veins of quartz, quartz-feldspar-ankerite-chlorite, quartz-tourmaline composition with fine inclusions of pyrite, chalcopyrite, magnetite. Among the main ore minerals at the Vasin deposit are sulfides (pyrite, chalcopyrite), the amount of which usually does not exceed 2%, magnetite, titanomagnetite, hematite and native gold.

As a result of the industrial development of the gold deposits of the Kumak ore field, technogenic accumulations (dumps) and several landfills were formed (Figs. 2, 3). The largest of them is the landfill of the Novokapitalnaya mine located in the village of Kumak. It has a height of about 25 m and an area of 1.5 hectares. In 30 ore samples, uniformly selected from mining dumps over 600 m, in half of the cases the gold content ranged from 1 to 20 g/t, in the rest 0.1–0.8 g/t.

Fig. 2 Dumps of the Kumak deposit. Conducting fieldwork, 2019. Photo by the authors

Fig. 3 The landfill of the Novocapitalnaya mine (Kumakskoye field). Conducting fieldwork, 2020. Photo by the authors

Currently, the deposits of the Kumak ore field may represent a promising gold ore object suitable for industrial development by underground and heap leaching methods, which are among the most important geotechnologies in the gold mining industry and require early implementation into development practice. From these positions, the features of the geological and commercial characteristics of the ore field are considered.

The main aquifer determining the hydrogeological conditions of development is the weathering crust of volcanogenic sedimentary deposits of the Lower Paleozoic age. Groundwater is of the type of fractured and fractured-vein with a predominantly non-pressure filtration mode. The water is typically acidic; there is a high chlorine content, which is favorable for dissolving the finest dispersed gold in the oxidation zone and moving it by mine waters to the secondary gold enrichment zone. The high content of CaO and SO3 in mine waters is the reason for the appearance of large gypsum crystals installed in mines at a horizon of 200 m. The capacity of the active groundwater circulation zone at the field is about 70 m [7]. Underground drainage is difficult below. The chemical composition of the waters is mixed with a predominance of chlorides, sulfates and sodium. Water mineralization 0.9–1.5 g/l. The content of micro-components corresponds to the normal hydrochemical background of the territory. Water supply occurs due to atmospheric precipitation, unloading is carried out in the lower parts of the relief by springs with a flow rate of no more than 1 l/s.

According to its filtration properties, the Kumak ore field is divided into two different geotechnological types of section [6]. The first type is the upper part of the rock mass to a depth of 35–50 m (on average 45 m), represented by a zone of disintegration in the form of strongly fractured ores and rocks overlain by sandy-clay and clay-gravel-gravelly weathering crust. The second type is the lower part of the massif, composed of rocks with separated fracture zones.

Filtration properties of the first type are characterized by a filtration coefficient of 0.3–0.4 m/day, which should be assessed as favourable for underground leaching. Based on the existing methods of controlling the movement of solutions in the aquifer during underground leaching, the most rational for the first type of sections is injection by free filling into wells or trenches, and pumping from wells with a single-filter

column. For the second type of incisions, more complex technical solutions will be required.

The concept of industrial development of gold deposits of the Kumak ore field involves the adaptation of the technology of borehole underground leaching to the specific geological and commercial characteristics of two types of ore bodies (weathering crust and bedrock deposits) and the involvement in the use of old dumps, which may be potential mineral deposits [8–11]. The stages of development should include:

1. In-depth study of the world and Russian experience of underground leaching.
2. Laboratory studies and modeling of this process.
3. Pilot testing of the recommended technology.
4. Recalculation of residual gold reserves.
5. Industrial development of residual reserves.

Preliminary conclusions on experimental and technological studies of underground leaching are as follows:

1. Host rocks of the Deposit are characterized by high cyclotouriste associated with carbonates (60–100 kg/t), causing the need for the planning process of leaching in acidic media (pH = 2–5).
2. Recovery of gold was investigated in weakly acidic environments (pH = 4.1–5.1) remains low, at the level of 34.5–40.5%.
3. The lower limit of the content of recoverable gold is 0.1 g/t, therefore in determining the contours of leachable ores can consider the content of gold received assay analysis and 0.1 g/t and "traces" (equating them to 0.1 g/t).
4. When engaging in the process of underground leaching of ore deposits, the usual filtration and infiltration system of opening is effective, when irrigation is carried out through ditches (trenches) and pumping of productive solutions through wells.
5. It is proposed to introduce specific conditions of environmental control and environmental protection measures into the list of recommended conditions.

References

1. V.N. Sazonov, V.A. Koroteev, V.N. Ogorodnikov, Yu.A. Polenov, A. Ya . Velikanov. Gold in the "black shales" of the Urals. Lithosphere. 2011. No. 4. pp. 70-92. (In Russian)
2. P. V. Lyadsky. State Geological Map of the Russian Federation. Scale 1:200000. Second edition. The South Ural series. Sheet M-41-I (Anikhovka). Explanatory note / comp.: P. V. Lyadsky, B. I. Chen-Len-Son, G. A. Alekseeva, T. V. Olenitsa, L. N. Kvasnyuk, N. V. Manuilov; scientific ed. A. P. Kazak. M.: Moscow branch of FSBI "VSEGEI", 2018. 100 p. (In Russian).
3. B. I. Chen-Len-Son. Searches and GDP200 in the Orenburg Trans-Urals. Ural. geologist. journal. Yekaterinburg, 2008. No. 1(61). pp. 56–58. (In Russian).
4. M.I. Novgorodova, E.I. Jacobs, Yu.G. Shinkarenko. Gold mineralization and metasomatites of one of the districts of the Southern Urals. Questions of petrology and metallogeny of the Urals. Sverdlovsk: UNC of the USSR Academy of Sciences, 1981. pp. 115–116. (In Russian).

5. 6. P. V. Pankratiev, V. P. Loshchinin. Technogenic objects of the Orenburg region and prospects for their development. Izv. Vuzov. Mining magazine. 1999. No. 5–6. pp. 84–87. (In Russian).
6. 7. P. V. Pankratiev, A.V. Kolomoets, A. S. Stepanov, E. V. Teplyakova. Kumak ore field as a promising gold ore object in the Orenburg region. Mining magazine. 2019. No. 1. pp. 8–12. (In Russian).
7. K. A. Harkevich. Exploration of the Vasin gold deposit in the eastern Orenburg region. Orenburg: Federal State University "TFI po PrFO", Orenburg Phil., 2007. (In Russian).
8. A. A. Vercheba, S. V. Markelov. Technogenic deposits, methods of their formation and processing: studies. Manual. M.: Moscow State Geological Development University 2003. 66 p. (In Russian).
9. A.V. Kolomoets. On the issue of the development of residual reserves and dumps of gold in the areas of old gold mining enterprises (on the example of the Kumak ore field) [Electronic resource]. New in the knowledge of ore formation: materials of the Fourth Russian Youth School with International Participation. Moscow: IGEM RAS, 2014. pp. 160–163. (In Russian).
10. 11. S. K. Mustafin, G. S. Anisimova, A. N. Trifonov, K. K. Struchkov. Technogenic mineral raw materials of subsurface use regions: nature, composition and prospects of rational use. Science and Education, 2017. No. 4. pp. 7–16. (In Russian).
11. 12. V. A. Naumov, B. S. Lunev, O. B. Naumova. Technogenic deposits - reserve of the mineral base of Russia. Bulletin of Perm University. Geology. 2011. No. 1. pp. 50–56. (In Russian).

Anisotropy of Strength and Filtration Properties of Rocks in Geomechanical Modeling

V. I. Karev and A. Yu. Zobnina

Abstract The purpose of the work is studying an mutual effect of the anisotropy of rock reservoir strength and filtration properties. The paper focuses on experiments carried out on samples from core of the deposit using by the unique true triaxial loading system created at the IPMech RAS TILTS. Scientific novelty lies in the identification of patterns of mechanical behavior of various rocks with anisotropic properties. The results obtained allow identifying stress states that need to be created in the bottom hole formation zone to increase the permeability of such anisotropic rocks and increase the productivity of wells, which is especially relevant for horizontal wells.

Keywords Rock · Strength anisotropy · Fracture criterion · True triaxial tests

1 Introduction

Practice of hydrocarbon production has shown the importance taking into account of geomechanical processes for efficient and trouble-free field development [1–3]. Recently, this issue has become especially acute, when the technology of drilling directional and horizontal wells, including underbalanced drilling [4], has become the main tool for the development of oil and gas fields. During its implementation, several completely new problems arose that did not occur during the drilling and operation of vertical wells. The issues of wellbore stability during drilling and its dependence on the geometry of the well and issues of determining the permissible drawdowns during the operation of horizontal wells, etc. came to the fore [5–7].

Considering the anisotropy of deformation and especially the strength properties of rocks can have a decisive influence on the result and prediction of deformations and destruction of the borehole walls. This work demonstrate the example of testing core material from a reservoir of one offshore oil field.

V. I. Karev (✉) · A. Yu. Zobnina
Ishlinsky Institute for Problems in Mechanics RAS, Moscow, Russia
e-mail: wikarev@ipmnet.ru

© The Author(s), under exclusive license to Springer Nature Switzerland AG 2022

V. I. Karev (ed.), *Physical and Mathematical Modeling of Earth and Environment Processes*,
Springer Proceedings in Earth and Environmental Sciences,
https://doi.org/10.1007/978-3-030-99504-1_30

2 Details Experimental

The field is planned operated using long-distance horizontal wells. So the issues of determining the limiting (critical) flow rates and pressure drawdowns the excess of which leads to a loss of wellbore stability, as well as the influence of pressure drawdowns created at the bottom of the wells on filtration properties of reservoir rocks become especially important.

2.1 Setup

For this purpose, a cycle of tests of rock samples from the reservoir was carried out on the Triaxial Independent Loading Test System of the Institute for Problems in Mechanics of the Russian Academy of Sciences (TILTS) [8].

The TILTS setup is equipped with an automatic permeability measurement system, which makes it possible to study the dependence of the permeability of rocks on the magnitude and type of acting stresses. It is known that the permeability of rocks can both decrease and increase depending on the stresses arising in them. The type and level of these stresses are determined by the bottomhole design (the presence or absence of casing, the type of perforation, and so on) and the pressure drawdowns created at the bottom of the well. The TILTS allows simulating these conditions on rock samples and continuously registering the change in their permeability.

2.2 Subject and Research Methodology

Core material of five lithotypes from exploration wells Nos. 2, 4, 5 of the field was used for testing at the TILTS—clean sandstone, aleurite sandstone, clayey sandstone, and interbedding. The cubic samples with an edge of 40 mm were cut from the core under study, in such a way that one of the faces was perpendicular to the vertical axis of the core.

The velocities of the longitudinal elastic waves were measured along each of the three axes of the samples on a special setup. They turned out to be close for the samples of all lithotypes, which indicates the isotropy of the elastic properties of the rocks under study.

The TILTS setup, as noted above, makes it possible to load cubic samples independently along each of the three axes. This gives the opportunity to recreate during experiments any stress states that arise in rock mass during various technological operations and to study the deformation processes and filtration properties changing of rocks caused by them.

The results of testing samples of reservoir rocks of the field according to the program corresponding to the change in stresses on the contour of a horizontal well

with a decrease in pressure at its bottom are presented below. Figure 1 shows the hoop and radial stresses σ_θ, σ_r acting in the vicinity of a horizontal well at two points M and N. The stress acting along the well axis is σ_z.

The main difference when testing samples for points M and N is that at the point M the maximum compressive stresses σ_θ act perpendicular to the core axis, at point N parallel to it. The rock samples should be properly positioned in the loading assembly of the test rig during testing.

Sounding of the samples showed that the rocks of all four lithotypes of the reservoir are isotropic in elastic properties, therefore, the stresses in the bottomhole zone of an open hole, assuming that the initial stress field is isotropic, are determined by the well-known solution of the Lamé problem [9] for an isotropic medium.

The sample loading program corresponding to the change in stresses in the bottom hole formation zone with decreasing pressure in the well p_w is shown in Fig. 2.

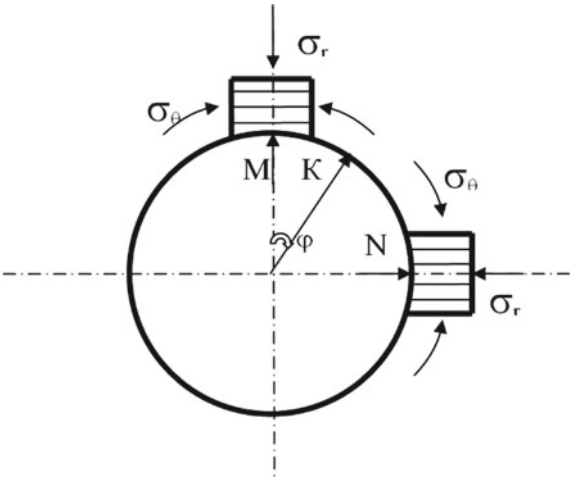

Fig. 1 Stresses acting in the vicinity of a horizontal well

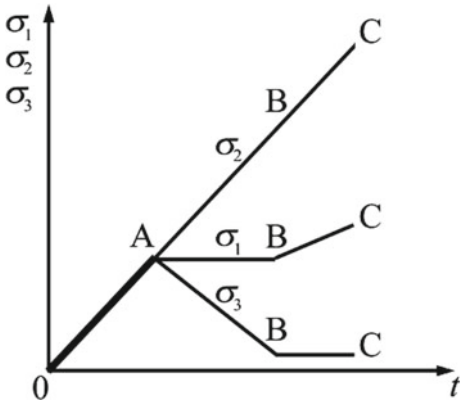

Fig. 2 Sample loading program

The stresses $\sigma_1, \sigma_2, \sigma_3$ acting on the sample along the machine axes correspond to the effective stresses $\sigma_z, \sigma_\theta, \sigma_r$ acting in the vicinity of an uncased horizontal well in the horizontal, circumferential, and radial directions, Fig. 1.

The sample loading program includes three stages.

Stage 1. The sample is evenly compressed from all sides to a stress equal to the difference between the rock pressure q and the formation pressure p_0 (OA segment in Fig. 2). Point A corresponds to the stresses acting in the soil skeleton before drilling the well.

Stage 2. The stress component σ_2 continues to grow, σ_1 remains constant, σ_3 decreases (segments AB), the load changes in such a way that the average stress remaines constant.

The end point of the stage B corresponds to the state when the well is drilled and the bottomhole pressure is equal to the reservoir pressure.

Stage 3. At the third stage, the process of creating and increasing a pressure drawdown is simulated, that is, a decrease in pressure at the bottom of the well (sections of the BC). In this case, the radial stress in the soil skeleton remains practically equals to zero as the pressure drawdown grows, and the hoop and axial stresses increase, but the axial stress increases approximately twice as slow. The stress components $\sigma_1, \sigma_2, \sigma_3$ acting along the axes of the setup in the experiment change accordingly. The third stage is the last and continues until the sample breaks.

On some of the samples, the stress state was modeled at the point M on the contour of the horizontal well M (top), and on some ones—at point N (side), Fig. 1 [10]. This was achieved by the appropriate positioning of the sample in the loading assembly of TILTS. When modeling point N, the sample was positioned in such a way that the axis 2 of the setup, along which the load increased monotonically during the experiment (Fig. 2), coincided with the axis of the core. When modeling point M, the sample was positioned in such a way that the axis 2 of the installation was perpendicular to the axis of the core. The permeability of the sample at the points N and M was measured along different axes of the sample: at the point M—along the axis of the core, and at the point N—perpendicular to it, that is, in both cases in the direction of the well axis.

3 Results and Discussion

The tests revealed several interesting facts. It turned out that σ_2^*—the maximum compressive stress at which the fracture of the samples occurred depends significantly on the location of the sample on the contour of the horizontal well. The destruction of the samples located at the upper point M on the borehole contour occurred at much lower values x σ_2^*, than of the samples located at the lateral point N. For example, Fig. 3 shows tests of two samples cut from one piece of core.

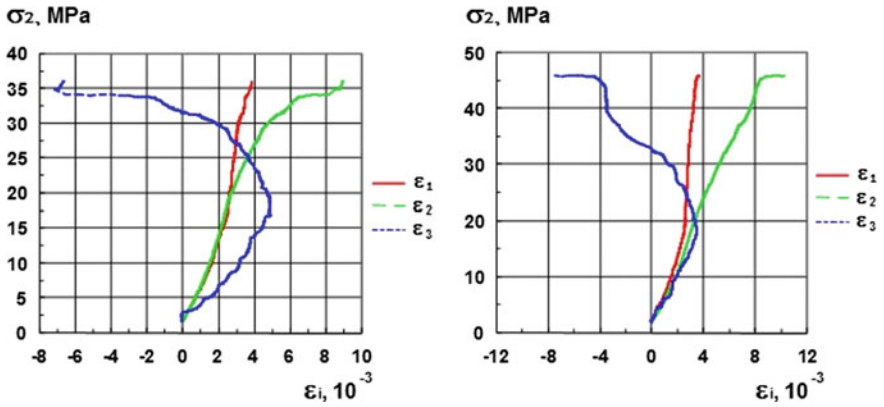

Fig. 3 Test results for samples F2-PsG-5–1 and F2-PsG-5–2

It follows from Fig. 3 that the sample F2-PsG-5–1, on which stresses were been modeled corresponding to the top point of the horizontal borehole contour (point M), collapsed under stresses corresponding to the pressure drawdown 2.4 MPa, and the sample F2-PsG-5–2, corresponding to side point of the contour of the well (point N), under a significantly greater drawdown of 6.1 MPa.

Rock samples of other lithotypes behaved in the same way. The samples tested under conditions at the top point of horizontal borehole contour had been collapsed under stresses corresponding to lower values of pressure drawdown then the samples tested under conditions at the side point of the horizontal borehole contour. Table 1 shows the results of sample testing with an indication which point of horizontal borehole contour was modeled, the values of stress σ_2^*, at which the samples were collapsed, as well as the values of the drawdowns at the bottom of the well Δp corresponding to these stresses.

Tests of all rock samples under study showed that they have anisotropy properties on strength which greatly impacts on the stability of the horizontal wellbore. Testing

Table 1 The results of modeling on rocks samples of reservoir of a decrease in pressure in a well

Sample №	Litotype	Depth, м	Position	σ_2^*, MPa	Δp, MPa
F2-P4	Sandstone	1358.2	top	39	3.5
F4-P-9–2	Sandstone	1412.7	side	63	15
F2-PsA-1	Aleurite Sandstone	1352.1	top	36	1.5
F4-PsA-7–2	Aleurite Sandstone	1405.7	side	66	15
F2-PsG-5–1	Clayey Sandstone	1367.3	top	36	2.5
F2-PsG-5–2	Clayey Sandstone	1367.3	side	46	6.2
F8-PR-2	Interbedding	1444.8	top	38	1.8
F8-PR-1	Interbedding	1443.2	side	64	13.2

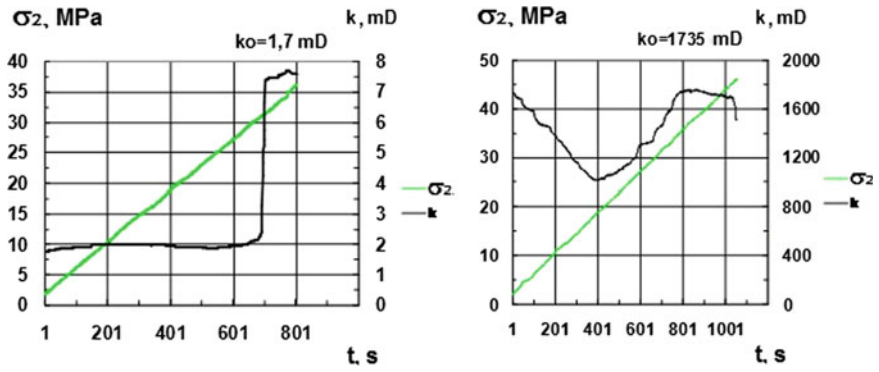

Fig. 5 Permeability curves of the samples F2-PsG-5–1 and F2-PsG-5–2

revealed that fracture of the samples when modeling the stress state at the upper point of the borehole contour was much earlier than the samples when modeling the stress state at the side point of the borehole contour. The tests also showed considerable anisotropy of rock permeability. Rocks permeability in the horizontal plane turned out to be much more than in the direction perpendicular to bedding. Modeling lowering the pressure in a horizontal borehole by using TILTS showed that the occurrence of an uneven stresses in the bottomhole zone can lead to a considerable change in permeability of rocks. It is possible both its decrease and an increase in dependence on rock properties. Moreover, a growth in rock permeability was mainly when modeling stresses at the top point of horizontal borehole contour. Figure 5. shows the permeability curves of samples F2-PsG-5–1 and F2-PsG-5–2 at the experiment. The permeability of the sample F2-PsG-5–1 was not being changed during loading and had been increased sharply before fracture, while the permeability of the sample F2-PsG-5–2 was being decreased during loading first, then increased, and ultimately remained practically unchanged.

4 Conclusions

Such studies make it possible to identify those stresses which need to be created in the bottom hole formation zone to enhance its permeability and increase well efficiency, which is especially relevant for horizontal boreholes. Findings and guidances for providing stability of wellbores, creating maximum allowable pressure drawdowns that do not take into account the anisotropy of the strain and strength properties of rocks [10], as well as the dependence of their filtration properties on the acting stresses, can be quite far from reality and not to solve the main task to reduce risks of borehole destruction and increase efficiency in the operation of wells.

Acknowledgements The present work was supported by the Ministry of Science and Higher Education within the framework of the Russian State Assignment under contract No. AAAA-A20-120011690133-1.

References

1. Blohin V.S., Terentyev V.D. (1984) Method for assessing the stabiliry of the borehole walls. Oil industry 7:12–15 (in Russian).
2. Vasilyev Y.N., Dubinina N.I. (2000) Model of the stress state of the bottom hole zone. Oil and Gas 4:44–47 (in Russian).
3. Spivak A.I. Popov A.N. (1994) Destruction of rocks while drilling wells. Nedra. Moscow. 261 p (in Russian).
4. Tagirov KM, Nifontov VI (2003) Well drilling and opening of oil and gas reservoirs under underbalanced conditions. Nedra. Moscow. 160 p (in Russian).
5. Klimov DM, Karev VI, Kovalenko YuF, Ustinov KB (2013) Mechanical-mathematical and experimental modeling of well stability in anisotropic geomedia. Sol Mech 4:4–12.
6. Karev VI, Klimov DM, Kovalenko YuF, Ustinov KB (2018) Modeling of Deformation and Filtration Processes Near Wells with Emphasis of their Coupling and Effects Caused by Anisotropy. In: V.Karev (ed) Physical and Mathematical Modeling of Earth and Environment Processes (2018). 3rd International Scientific School of Young Scientists, Ishlinsky Institute for Problems in Mechanics of Russian Academy of Science. Springer Gelogy:350–359.
7. Karev VI, Klimov DM, Kovalenko YuF, Ustinov KB (2018) Fracture Model of Anisotropic rocks under Complex Loading. Phys Mesomech 21(3):216–222.
8. Karev VI, Klimov DM, Kovalenko YuF (2018) Modeling Geomechanical Processes in Oil and Gas Reservoirs at the True Triaxial Loading Apparatus. In: V.Karev (ed) Physical and Mathematical Modeling of Earth and Environment Processes (2018). 3rd International Scientific School of Young Scientists, Ishlinsky Institute for Problems in Mechanics of Russian Academy of Science. Springer Gelogy: 336–349.
9. Lyav A. (1935) Mathematical theory of elasticity. ONTI NKGiP USSR. Moscow-Leningrad. 676 p (in Russian).
10. Shadchnev RA, Zorina AP, Sharapov DN, Ponomareva EV, Kulagin RA Preparation of initial data for the formation of a geomechanical model of the Yu.Korchagin field (2014) Oil industry 9:80–83 (in Russian).

Physico-Chemical Conditions of Metamorphism of Carbonaceous Deposits of the Sait and Igish Formations (Southern urals, russia)

A. V. Snachev

Abstract The paper briefly considers the geological structure of the eastern side of the Ilmenogorsk-Sysert zone. Within its limits, carbon-bearing quartzites of the Saitovskaya and Igishskaya formations are widely developed, composing extended members up to 500 m thick. The petrochemical features of the considered rocks point to their formation within the deepest area of the open reservoir with a slight addition of volcanic material. Thermal analysis of black shale deposits showed low TOC values in them from 0.5 to 3.6%, which makes it possible to attribute quartzites to low-carbon and carbonaceous types. The temperatures of the onset of the exothermic effect of carbon in black shales and quartzites were 580–590 and 580–600 °C, and the temperatures obtained from the maxima on thermograms were 700–770 and 720–770 °C. Similar temperature values indicate epidote–amphibolite and greenschist facies of regional rock metamorphism. In the contact zone of large granite massifs, volcanogenic-sedimentary complexes underwent metamorphism of a higher stage. The study of the compositions of minerals of the amphibole-garnet paragenesis in several samples of the Saitovskaya suite, taken just a few meters from the contact of the Argazinsky massif, showed a temperature of 750–770 °C and a pressure of 8.8–9.0 kbar, which corresponds to the conditions of the facies of almandine amphibolites.

Keywords Southern Urals · Ilmenogorsk-Sysert Zone · Igish formation · Black shale · Quartzite · Granite · TOC · Temperature · Metamorphism

1 Introduction

In recent decades, great importance has been attached to the black shale strata in the world, due to the production of shale gas and oil from them. At the same time, one of the main parameters characterizing the oil and gas content of carbon deposits is the content of organic carbon in them. Carbonaceous rocks are quite widely represented among the deposits of the Ilmenogorsko-Sysertsky anticlinorium and they

A. V. Snachev (✉)
Ufa Federal Research Centre of the Russian Academy of Sciences, Ufa, Russian Federation
e-mail: savant@rambler.ru

© The Author(s), under exclusive license to Springer Nature Switzerland AG 2022

V. I. Karev (ed.), *Physical and Mathematical Modeling of Earth and Environment Processes*,
Springer Proceedings in Earth and Environmental Sciences,
https://doi.org/10.1007/978-3-030-99504-1_31

can provide very important information about the paleogeographic and physico-chemical conditions of precipitation accumulation, about the sources of demolition of terrigenous material, about the degree of transformation of rocks as a result of regional and zonal contact metamorphism. In this article, the author attempts to make a certain contribution to clarifying the history of the formation of black shale strata, the study of organic carbon, and the clarification of the physico-chemical conditions of metamorphism.

2 Research Methodology

Thermogravimetric analysis of carbonaceous rocks was carried out on a Q-1500 derivatograph (analyst T. I. Chernikova, IG UFSC RAS). Heating was carried out in air from 20 to 1000 °C at a speed of 10° C/min. Samples of the least quartic and sulfidized rocks outside the zones of intrusive exocontacts and intensive tectonic processing were selected for analysis, which made it possible to exclude their influence and reconstruct the degree of regional metamorphism.

The compositions of amphiboles and garnets harvested from the rocks of the Sait formation were analyzed by I. A. Blinov (IMin UrO RAS, Miass) on a Tescan Vega 3sbu scanning electron microscope with an Oxford Instruments X-act energy-dispersion spectrometer (accelerating voltage 20 kV, standards for amphibole—amphibole, for garnet—pyrope, andradite and grossular).

3 Geological Structure of the Sait and Igish Formations

In the eastern part of the Ilmenogorsko-Sysertsky block, carbonaceous deposits are widely represented in the Sait and Igish formations, therefore, we will focus only on them below, using the report of Petrov et al. [5], as well as the author's own data obtained during geological survey and thematic work within sheet N–41–VII (Miass) [8, 9] (Fig. 1).

Sait formation (RF2vs + ns) is common in the western and eastern wings of the Ilmenogorsky structure and is composed of amphibole apobasalt plagioslants, rarely biotite and garnet-biotite schists and quartzites often graphite. The thickness of the formation is 560 m. Graphite quartzites contain biotite, garnet and inclusions of carbonaceous phosphorites, sometimes overgrown with apatite. The rocks were metamorphosed in the conditions of the epidote–amphibolite and green shale facies. Graphite mineralization and potential prospects for platinoids are associated with the rocks of the strata.

Igish formation (RF2ig) is marking, as it is represented by monotonous graphite dark gray to black quartzites. A characteristic feature of Igish quartzites is the presence of lenticular and fragment-shaped inclusions of black fine-grained phosphorites with a thickness from 2.0 to 15.0 m. The contact between Igish quartzites and Upper

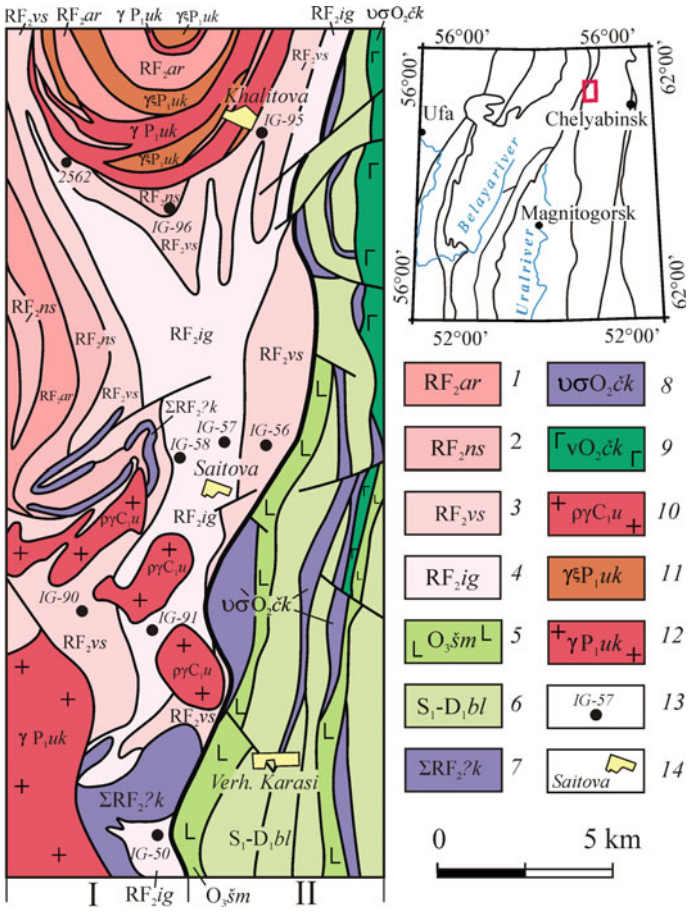

Symbols: 1 - Arakul formation; 2 - Nizhnesait sub-formation; 3 - Verkhnesait sub-formation; 4 - Igish formation; 5 - Shemetovskaya strata; 6 - Bulatovskaya strata; 7 - Kagan complex of metamorphosed ultramafites and gabbroids; 8, 9 - Chebarkul-Kazbaevsky complex of ultramafites and gabbroids; 10 - Urazbaevsky tonalite-plagiogranite complex; 11-12 - Uvilda granite-granosienite complex; 13 - testing points; 14 - settlements. I - Ilmenogorsko-Sysertsky anticlinorium, II - Aramilsko-Sukhtelinsky zone.

Fig. 1 Geological structure of the work site (compiled from the materials of Petrov et al. [5], with the author's simplifications)

Sait shales has been drilled by a number of wells and in most cases has a consonant character, but in places it is undermined and low-power bodies of metamorphosed ultramafites (antigorite serpentinites and talc-carbonate rocks) are wedged between the rocks of the formations. The capacity of the formation according to drilling and adjustment of sections is estimated at 400–500 m.

The Middle-Riphean age of the described formations was adopted in accordance with the Stratigraphic Schemes of the Urals, 1993 [5]. However, there are grounds for attributing them to Paleozoic formations, in particular the Bulatov strata [6], characterized by the fauna of graptolites and conodonts.

4 Discussion of Research Results

The chemical composition of the black shale rocks of the Sait and Igish formations practically does not differ from each other, they have fairly stable values and in the diagram A-S-C of [4] compactly fit into the field of the siliceous-carbon formation. Taking into account the inversely proportional dependence of the coefficient S with the proportion of terrigenous admixture in sediments, which in turn is related to the depth of the sedimentation basin, it is possible to draw an unambiguous conclusion about the deposition of the rocks in question within the deepest area of the reservoir.

When dealing with carbonaceous deposits, it is first necessary to specify the content of Sorg in them. The determination of this parameter in the rocks of the Sait and Igish formations was carried out by the thermal method (the positions of the sampling points are indicated in Fig. 1). For the first of them, the values of TOC were 0.5–1.9%, for the second—1.4–3.6% (Table 1), which, according to the classification of [12], corresponds to low-carbon and carbonaceous types.

In addition to TOC, thermal analysis also allowed us to assess the degree of regional metamorphism of the sediments of the Sait and Igish formations (Table 1) [3]. The temperature of the beginning of the exothermic effect in them was 580–590 and 580–600° C, and the temperature obtained from the maximum of the thermogram graphs was 700–770 and 720–770° C. Similar temperature values, according to [1], indicate the epidote–amphibolite and green shale facies of rock metamorphism. It is noteworthy that all these samples are shown on the diagram of thermal stability of carbonaceous substances by [7] (Fig. 2) fall into field IV (higher kerites, anthraxolites, shungites) located in the central part of the trend.

Table 1 Results of thermal analysis of carbonaceous rocks

No	No. sample	The onset of thermal oxidation, T °C	The maximum of thermal oxidation, T °C	TOC
1	IG-56	590	700	1.4
2	IG-96	590	740	1.9
3	IG-90	580	770	0.5
4	IG-57	580	720	3.6
5	IG-58	600	770	1.4
6	IG-91	580	760	1.5

Note 1—3—Sait formation, 4—6—Igish formation

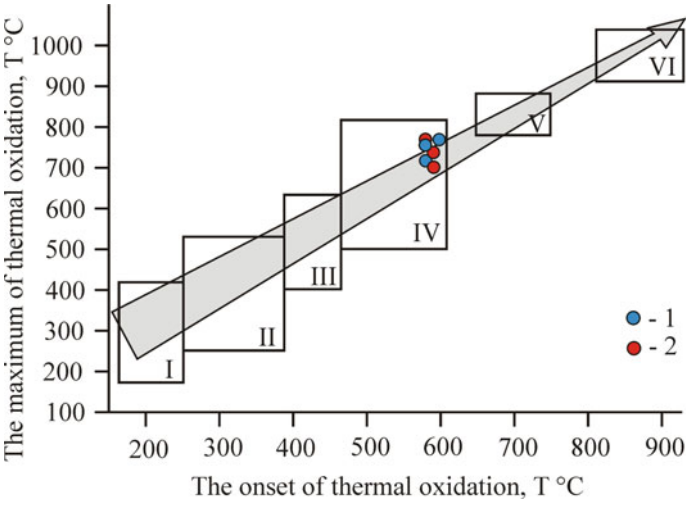

Note: 1 - Sait formation, 2 - Igish formation; burnout stages according to V.I. Silaev et al. [2012]: I - modern plants, organic matter in unmetamorphosed sedimentary rocks, coprolites; II - asphalts, lower kerites; III - asphaltites, kerites; IV - higher kerites, anthraxolites, shungites; V - graphite, carbonado; VI - diamonds.

Fig. 2 The position of the points of carbonaceous rocks of the Sait and Igish formations on the diagram of thermal stability of carbonaceous substances

The territory under consideration, located in the eastern part of the Ilmenogorsko-Sysertsky block, is saturated with granitoid bodies of various sizes and formation affiliation: from the north, black shale deposits break through the large Argazinsky massif (Fig. 1), small intrusions of the Urazbaevsky tonalite-plagiogranite and Uveldinsky granite-granosienite complexes, from the east—Kisegachsky, from the south—Elanchikov and Chashkovsky gneiss-migmatite massifs, which led to intensive contact metamorphism of the rocks of the Sait and Igish formations. Earlier [10] it was shown that before the introduction of granitoids, these carbonaceous deposits experienced regional metamorphism in the conditions of the epidote–amphibolite facies (T = 550–580 °C, P = 6.8–7.2 kbar, abyssal depth zone), which is confirmed by the above thermal analysis data.

To assess the parameters of contact metamorphism, the compositions of amphibole-garnet paragenesis were studied in several samples of the Sait formation taken just a few meters from the contact of the Argazinsky massif (sample 2562) (Table 2). Microprobe study of three pairs of garnet and amphibole made it possible to calculate mineral formulas according to the method of [2], and then using phase correspondence diagrams [11] to obtain temperatures and pressure of contact metamorphism.

It is important to note that the compositions of amphiboles and almandine garnets are very stable, the variations of the components in them are insignificant. According

Table 2 Composition of amphibole (Amf) and garnet (Gr) from the rocks of the Sait formation (wt. %).

Mineral	SiO_2	TiO_2	Al_2O_3	FeO	MnO	CaO	MgO	Na_2O	K_2O	Sum	$X_{Mg}^{Bi,Gr}$
Amf -1	43.65	0.79	14.61	18.33	–	10.66	8.69	1.32	0.33	98.37	0.46
Amf -2	43.45	0.92	15.60	17.60	–	10.49	8.56	1.37	0.42	98.41	0.46
Amf -3	43.55	0.75	15.18	17.12	–	10.74	9.10	1.39	0.41	98.26	0.49
Gr-1	37.95	0.30	21.38	30.94	0.67	4.30	4.68	–	–	100.22	0.21
Gr-2	37.71	0.28	21.43	30.57	0.91	4.52	4.32	–	–	99.74	0.20
Gr-3	37.65	0.18	21.24	30.70	0.73	4.21	4.70	–	–	99.41	0.21

Amf -1 – $(Ca_{1.66}Na_{0.37}K_{0.06})_{2.09}(Fe_{2.22}Mg_{1.88}Ti_{0.09}Al_{0.82})_5(Si_{6.33}Al_{1.67})_8O_{22}[O_{0.10}(OH)_{1.90}]_2$
Amf -2 – $(Ca_{1.62}Na_{0.38}K_{0.08})_{2.08}(Fe_{2.12}Mg_{1.84}Ti_{0.10}Al_{0.93})_5(Si_{6.28}Al_{1.72})_8O_{22}[O_{0.09}(OH)_{1.91}]_2$
Amf -3 – $(Ca_{1.67}Na_{0.39}K_{0.08})_{2.14}(Fe_{2.07}Mg_{1.96}Ti_{0.08}Al_{0.88})_5(Si_{6.30}Al_{1.70})_8O_{22}[O_{0.13}(OH)_{1.87}]_2$
Gr-1 – $(Ca_{0.36}Fe_{2.03}Mg_{0.55}Mn_{0.04}Ti_{0.02})_3(Al_{1.99}Fe_{0.01})_2Si_3O_{12}$
Gr-2 – $(Ca_{0.38}Fe_{2.03}Mg_{0.51}Mn_{0.06}Ti_{0.02})_3Al_2Si_3O_{12}$
Gr-3 – $(Ca_{0.36}Fe_{2.03}Mg_{0.56}Mn_{0.05}Ti_{0.01})_3(Al_{1.99}Fe_{0.01})_2Si_3O_{12}$

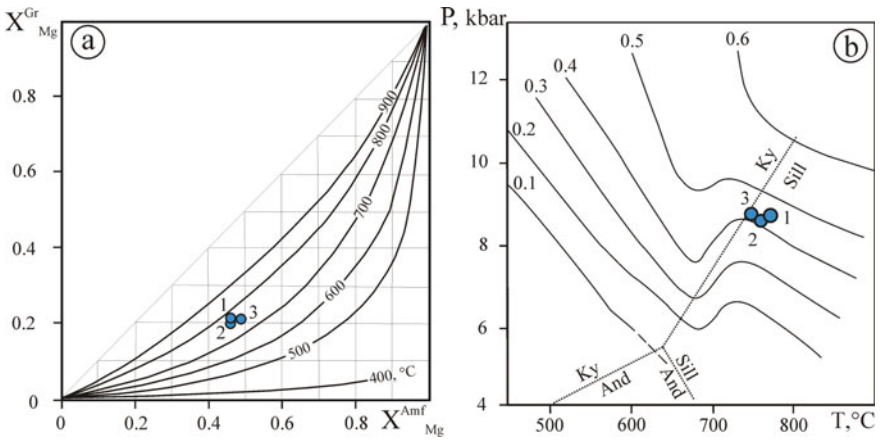

Fig. 3 Phase correspondence diagram for a pair of amphibious grenades (**a**) and the position of the lines of equal values of $K_{Mg\ Gr-Amf}$ In the diagram T-P [11] (points 1–3, see Table 2)

to Fig. 3, and all mineral vapors form a compact field corresponding to T = 750–770 °C and a pressure of 8.8–9.0 kbar (Fig. 3, b).

In the scheme of facies of regional metamorphism, these points clearly fit into the field of almandine amphibolites [11]. It is clear that such a high degree of contact metamorphism of carbonaceous deposits of the Sait and Igish formations led to the burnout of Sorg, which sharply reduces their potential oil and gas potential throughout the frame of the Argazinsky, Kisegachsky, Elanchikov and Chashkovsky massifs.

5 Conclusions

Thus, taking into account the above data, it can be assumed that the carbon-containing sediments of the Sait and Igish formations were formed in the distal deep-water and remote from the coastline area of the sedimentary basin. They belong to the low-carbon and carbonaceous types, as well as the siliceous-carbon formation, which has a minimum amount of terrigenous admixture in its composition. At the turn of the Riphean and Vendian, when a major structural restructuring took place in the Southern Urals, the black shale strata experienced regional metamorphism in the conditions of the epidote–amphibolite facies (T = 550–580° C, P = 6.8–7.2 kbar). Later, during the formation of the large Argazinsky, Kisegachsky, Elanchikov and Chashkovsky granitoid massifs, the deposits under consideration underwent contact metamorphism under the conditions of the almandine amphibolite facies (T = 750–770° C, P = 8.8–9.0 kbar), which led to the burning out of Sorg in them, as well as a sharp decrease in the potential oil and gas content of the rocks framing intrusions.

Acknowledgements The work was carried out within the framework of the State Order on the topic No. № FMRS-2022-0011.

References

1. Bluman B.A., Dyakonov Y.S., Krasavina T.N., Pavlov M.G.. The use of thermal and radiographic characteristics of graphite to determine the level and type of metamorphism. Notes of the All-Union Mineralogical Society. 1974. Vol. 103. No. 1. pp. 95–103.
2. Borneman-Starynkevich I.D. Guide to the calculation of mineral formulas / M.: Nauka, 1964. 224 p.
3. Busek P.R., Beissak O. From organic matter to graphite: graphitization. Elements, 2014. Volume 10. No. 6. pp. 421–426. DOI: https://doi.org/10.2113/gselements.10.6.421
4. Gorbachev O.V., Sozinov N.A. Some petrochemical and geochemical aspects of typification of Precambrian carbonaceous deposits. Problems of sedimentary geology of the Precambrian. M.: Nauka. 1985. pp. 55–62.
5. Petrov V.I., Shalaginov A.E., Punegov B.N. State Geological Map of the Russian Federation. Scale 1: 200 000. 2nd ed. South Ural Series. Sheet N-41-VII (Miass). Explanatory note. Moscow: Moscow branch of FSUE "VSEGEI", 2003. 167 P.
6. Savelyev D.E., Snachev A.V., Puchkov V.N., Snachev V.I. Petrogeochemical and geodynamic features of the formation of Ordovician-Early Silurian basalts of the eastern slope of the Southern Urals. Geological Collection No. 5. IG UNC RAS. Ufa: LLC "Designpoligrafservice". 2006. pp. 86–104.
7. Silaev V.I., Smoleva I.V., Antoshkina A.I., Tchaikovsky I.I. Experience of conjugate analysis of isotopic composition of carbon and nitrogen in carbonaceous substances of different origin. Problems of mineralogy, petrography and metallogeny: Materials of scientific readings in memory of P.N. Chirvinsky. Perm: Publishing House of PSU. 2012. No. 15. pp. 342–366.
8. Snachev A.V., Snachev V.I., Romanovskaya M.A. Geology, petrogeochemistry and ore bearing of carbonaceous deposits of the Larinsky dome (Southern Urals). Geological Bulletin of Moscow University. 2015. Vol. 70. Part 2. pp. 131–140. DOI: https://doi.org/10.3103/S014587521502009X
9. Snachev A.V., Snachev V.I., Rykus M.V., Savelyev D.E., Bazhin E.A., Ardislamov F.R. Geology, petrogeochemistry and ore bearing of carbonaceous deposits of the Southern Urals. - Ufa: Designpoligrafservice, 2012. - 208 p.
10. Snachev V.I. Conditions of metamorphism of rocks of the Sait formation (Ilmenogorsko-Sysertsky anticlinorium). Geology. Proceedings of the Department of Earth Sciences and Natural Resources of the Academy of Sciences of the Republic of Bashkortostan. 2020. No. 27. pp. 16–23.
11. Thermo- and barometry of metamorphic rocks / edited by V.A. Glebovitsky. L.: Nauka. 1977. 207 p.
12. Yudovich Ya.E., Ketris M.P. Geochemistry of black shales. M.-Berlin: Direct-Media, 2015. 272 p. DOI: https://doi.org/10.23681/428042.

User Interface to Access the Russian Black Sea Coastal Zone Data

E. V. Zhuk

Abstract The paper describes the development, functions, and main features of the online user interface (UI) providing access and visualization of the Russian Black Sea coastal zone data. The UI is part of the Black Sea coastal zone geoinformation system which has been developed at the MHI RAS. This dedicated GIS is an open system with a modular structure, providing the potential to integrate new data. The user friendly interface of the GIS allows the visualization of relevant information concerning the coastal zone of the Russian Black Sea in a comprehensive way.

Keywords Black sea · Coastal zone oceanographic database · Online data access · User Interface · Black sea · Mapbox GL · JQuery

1 Introduction

The last decades the importance of the oceanographic data and marine information have considerably increased due to the fact that are essential for carrying out a variety of near coastal area projects related to the exporation and exploitation of the marine resources, maritime transport, recreational facilities, marine pollution, marine construction, scientific research, etc.

Therefore, the assessment of the state of the marine coastal areas are of particular importance and require reliable information support. Developing, implementing and using modern methods and Information Technologies, as well as ensuring the automatic processing and representation of oceanographic data and marine information, are nowadays the most appropriate and efficient tools for the users.

E. V. Zhuk (✉)
Marine Hydrophysical Institute of RAS, Sevastopol, Russia
e-mail: alenixx@gmail.com

© The Author(s), under exclusive license to Springer Nature Switzerland AG 2022

V. I. Karev (ed.), *Physical and Mathematical Modeling of Earth and Environment Processes*,
Springer Proceedings in Earth and Environmental Sciences,
https://doi.org/10.1007/978-3-030-99504-1_32

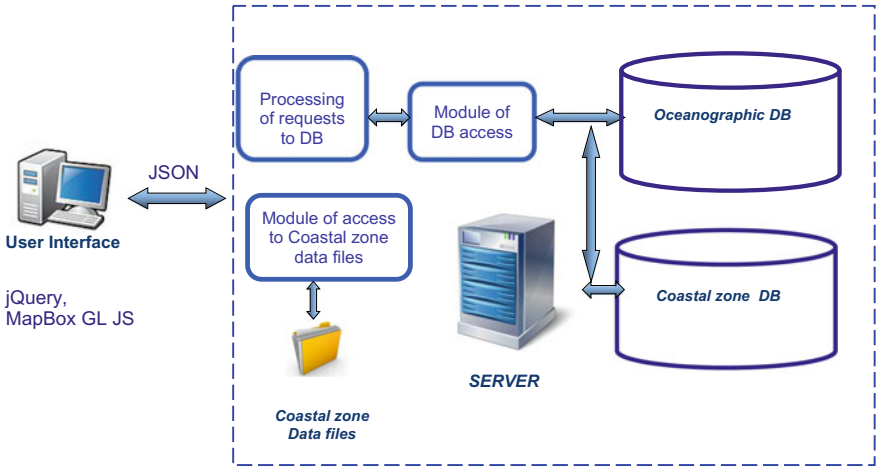

Fig. 1 Schematic of the data with the system structure

2 Data and System Structure

The system is based on a Client–Server Architecture. The Server part includes data and software modules, which provide data processing, accessing and visualization.

The general structure of the database for information support of coastal research consists of two main blocks: "Oceanographic data" and "Coastal zone data". The first block includes oceanographic data up to the 200 m isobath, the second one contains data obtained during coastal research. The structure and composition of the database of the Russian coastal zone in the Black Sea were presented in [3–5]. The Schematic of the data with the system structure are shown at Fig. 1. The exchange between the UI and the server is provided in JSON format.

3 User Interface

The User Interface was developed using jQuery [6] and mapBox GL [7], for visualization of maps. It is providing better performance and functionality than the previously used library. To provide access and visualization for different types of data the modular structure of the UI was implemented. It allows creating requests and displaying results as information layers formaps, tables, graphs, descriptions, and photos in interactive mode.

3.1 Timeseries Data Access and Visualization

This modular approach was developed to process with the time series data obtained at Kacively platform.

This data is represented as two data arrays:

- data obtained using temperature profiler (17 sensors located at depths from 2.5 to 25 m) at the period from June 2013 to January 2014.
- data of hydrological and hydrochemical parameters measured on the Katsiveli platform from 2009 to 2014 at depths of 0, 0.5 and 5 m.

Data sets are stored in relational database tables.

To access the data, the user can set the time interval, i.e. the start and end date of sampling using the calendar tool, select a parameter from the drop-down list (temperature, salinity, oxygen concentration, dissolved oxygen, nitrite, nitrate, phosphate, ammonium concentrations) and the depth of measurement, specifying one sensor or all available. Data exchange between client and server is carried out in JSON format. The obtained data is displayed in the form of an interactive graph, where user can view the parameter values at each point and build a profile at a given time. Plotting is implemented using the jQuery and jqplot libraries.

Figure 2 shows the user interface with the example of sampling data from temperature profiles for all sampling depths from 20 to 24 July 2013.

Figure 3 shows the time series of the temperature measured by the 1st sensor (depth 2.6 m) over the same period.

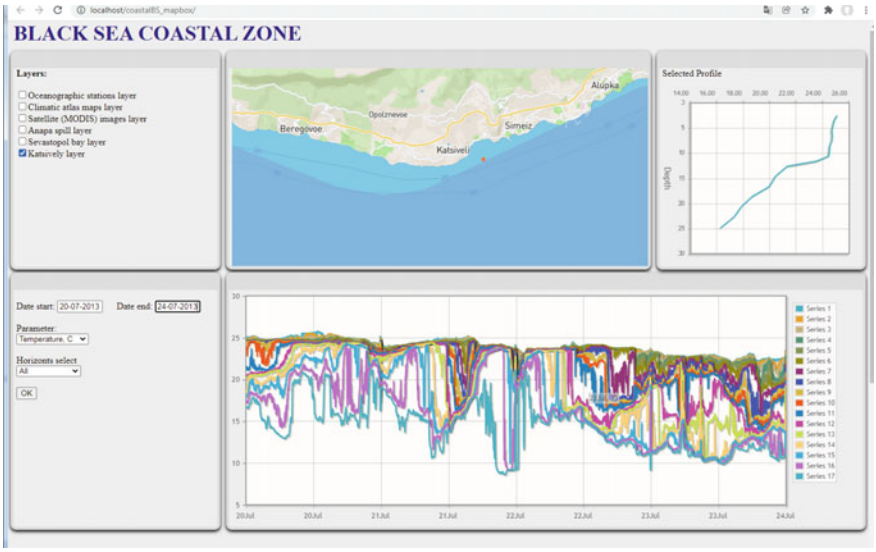

Fig. 2 UI, data from temperature profiles for all sampling depths

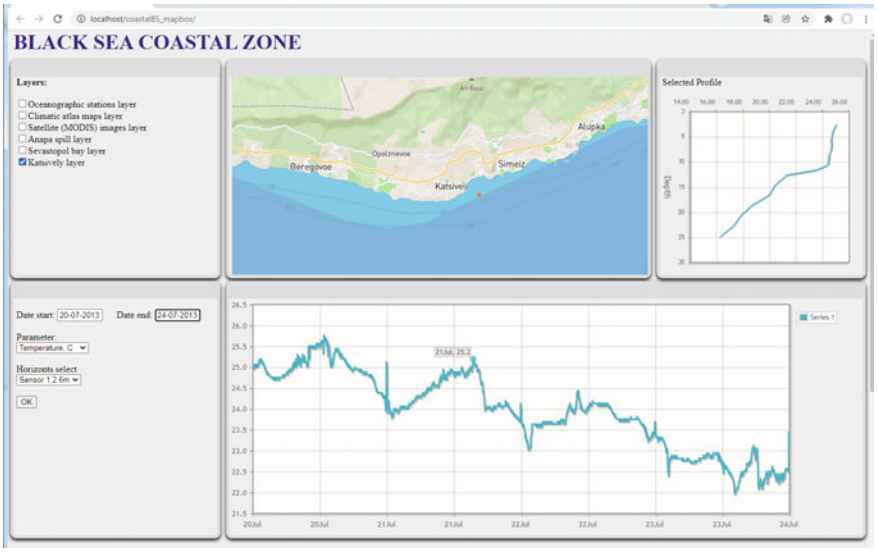

Fig. 3 UI, data from temperature profiles for 1st sampling depthof 2.6 m

Figure 4 shows example of sampling and displaying time series data and profiles of salinity from 3 to 21 July 2009.

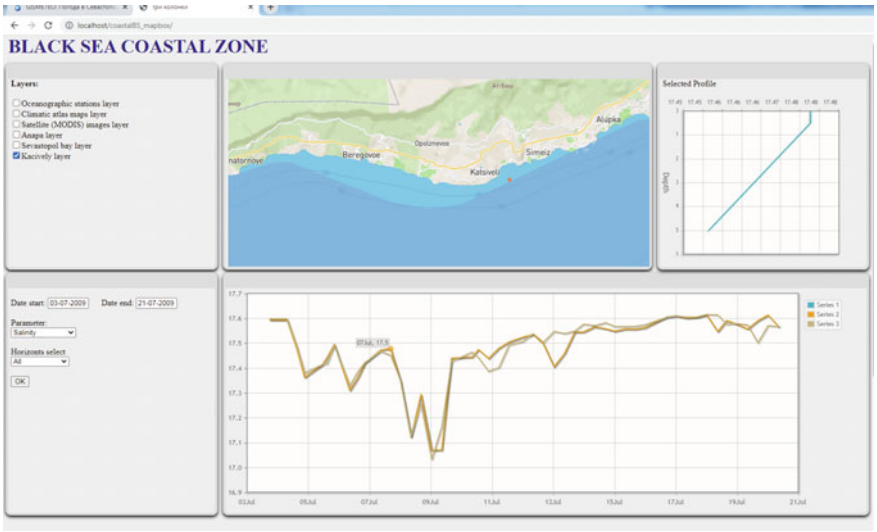

Fig. 4 UI, data from salinity profiles from 3 to 21 July 2009

3.2 *Data of Granulometric Composition of the Anapa Bay-Bar, Data Access and Visualization*

These data represent the coordinates of measurements and the granulometric composition of the samples at points for 45 profiles sampled at the Anapa bay and are archived as relational database tables. Previously, a shapefile was used to display the position of these profiles. Currently, in order to visualize the points of the profiles on the map, data *from* a file in the geojson format is used, and the jQuery and jqplot libraries are used to plot the distribution of the particle size over the profiles. An example of an interface with visualization of granulometric composition data of the Anapa bay-bar is shown in Fig. 5.

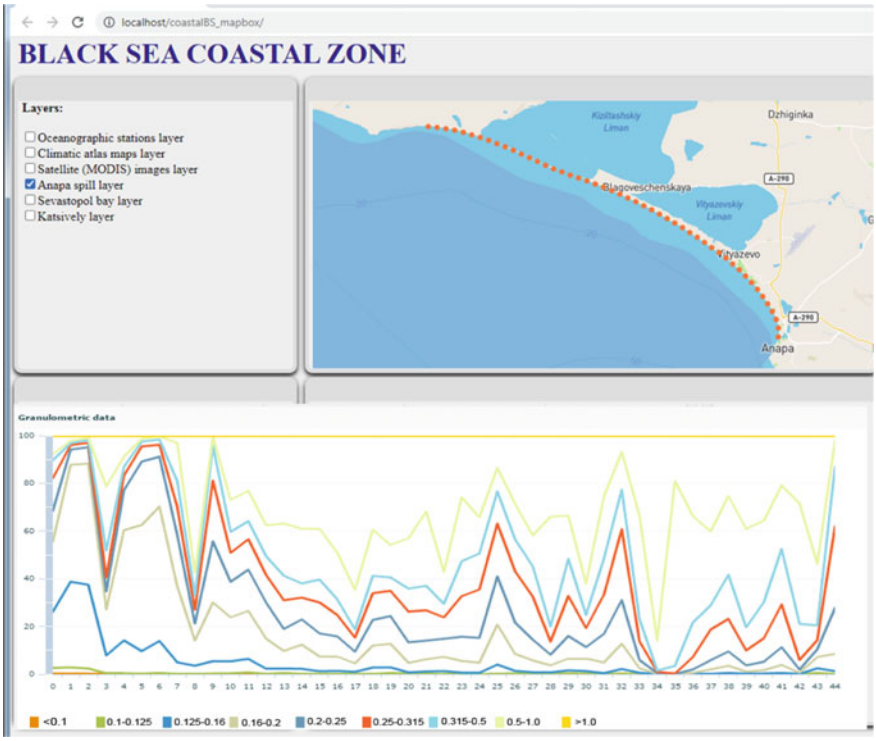

Fig. 5 Granulometric composition of the Anapa bay-bar

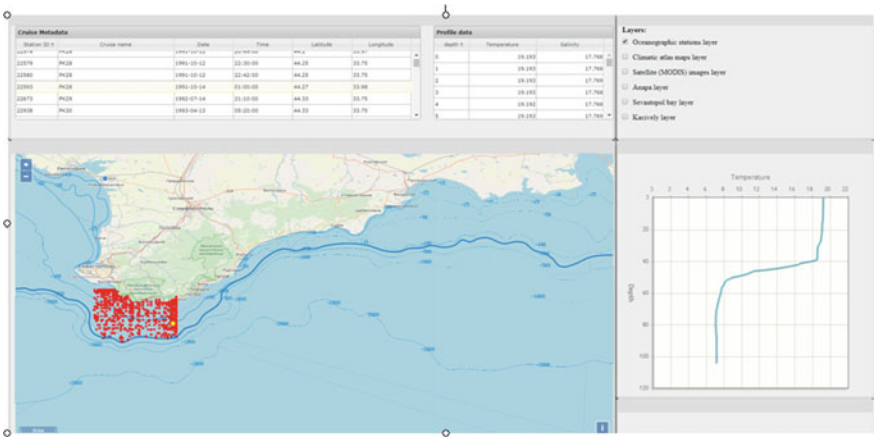

Fig. 6 Example of oceanographic data selection

3.3 Oceanographic Data up to 200 m Isobath, Data Access and Visualization

This data is part of the MHI's Black Sea Oceanographic database and contains more than 55,000 oceanographic and more than 10,500 hydrochemical stations. The data can be selected by region (Sevastopol Bay, for example), by interactive mouse selection or by metadata selection, such as time period, cruises, months and etc. Example of oceanographic data selection and visualization is presented at Fig. 6.

3.4 File Data Selection

Climatic atlas maps are kept as a file set with special file name rules and directory structure. It includes oceanographic parameters for main oceanographic levels and are kept as shape files. It provides the possibility to select atlas map parameters, level and corresponding period.

Satellite images are presented for the following three parameters: sea surface temperature, water leaving radiation and chlorophyll-a concentration and stored as raster geotiff format also using special file naming rules and directory structure. User can select one of the three parameters and select the required date from the date list.

4 Conclusion

The developed at MHI RAS User Intrface for the Black Sea can be used to provide oceanographic data access for coastal areas combining and overlaying different types of information to obtain complex characteristics of the local marine environment. The UI provides to the user the possibilities to selectand visualizing data for each of the Russian Black Sea coastal regions. Particularly, for each region the UI provides the display of graphical files (photos of the coastal zone and coast-protecting structures); the highlighting of the region of interest; displaying descriptions; plotting distribution of the granulometric composition; overlaying coastal data upon other information layers such as the Climatic atlas maps and satellite images. The openness and modular structure of the GIS gives a wide potential for further improvement of the system to include new data and functionality.

Acknowledgements This work is carried out within the framework of the state assignment: 0555-2021-0005 “Complex interdisciplinary studies of oceanologic processes which determine functioning and evolution of ecosystems in the coastal zones of the Black Sea and the Sea of Azov” (“Coastal Research” code).

References

1. Zhuk E, E. Godin, A. Ingerov and E. Isaeva Geoinformation system of the Russian Black Sea coastal zone. Bollettino di Geofisica teorica ed applicata An International Journal of Earth Sciences Istituto Nazionale di Oceanografia ISSN 0006–6729 e di Geofisica Sperimentale IMDIS 2018 International Conference on Marine Data and Information Systems, 2018, Vol 59.(1). p. 233–235.
2. Krylenko M., Zhuk E., Khaliulin A. Using of GIS technology for access to coastal data. The XIII International MEDCOAST Congress on Coastal and Marine Sciences, Engineering, Management and Conservation. Mugla: MEDCOAST Foundation, 2017. V.2. P. 757–764.
3. Zhuk E., Godin E., Ingerov A., Vetsalo M., Isaeva E. Razvitie GIS “Pribrejnaya zona Rossiy v Chernom more. Morya Rossyy: issledovaniya beregovoy I shelfovoy zon / Tezisy dokladov vserossyiskoy konferencyy – g. Sevastopol, 21–25 sentyabrya 2020. S 283–285.
4. Godin E., Zhuk E., Plastun T., Galkovskaya L., Ingerov A., Isaeva E., Kasyanenko T, Vetsalo M. Bank okeanographicheskyh dannyh MHI: informacionnaya podderjka issledovanyi pribrejnoy i shelfovoi zon Chernogo moray. Morya Rossyy: issledovaniya beregovoy I shelfovoy zon / Tezisy dokladov vserossyiskoy konferencyy – g. Sevastopol, 21–25 sentyabrya 2020. S65–66.
5. Zhuk E., E. Godin, A. Ingerov and E. Isaeva Geoinformation system of the Russian Black Sea coastal zone. Bollettino di Geofisica teorica ed applicata An International Journal of Earth Sciences Istituto Nazionale di Oceanografia ISSN 0006–6729 e di Geofisica Sperimentale IMDIS 2018 International Conference on Marine Data and Information Systems, 2018, Vol 59.(1). p. 233–235.
6. jQuery https://jquery.com/.
7. Mapbox GL JS https://www.mapbox.com/mapbox-gljs.

Modeling of Transfer of Soluble Impurity into the Vortex Flow

T. O. Chaplina

Abstract The results of experimental studies of the transfer of a soluble impurity from a compact spot on the free surface of a liquid and into a liquid at rest or involved in a composite vortex motion are presented in the article, visualization and qualitative analysis of the flow near the edge of the disk are carried out. The rate of change in the sinking of the dye into the thickness of the liquid is calculated depending on the frequency of rotation of the inductor. It has been found that the characteristic features of the vortex flow are set in the region of the boundary layer on the disk and then are transferred with the preservation of the shape of the flow structure to the entire region occupied by the liquid. This is confirmed by the coincidence of the types of spiral motion of liquid particles on the surface and near the disk.

Keywords Vortices · Waves · Matter transfer · Laboratory modeling

1 Introduction

The study of vortex and wave currents is one of the traditional tasks of fluid mechanics, the practical importance of which has increased significantly in recent years. Structural features of vortex currents—closed or spiral geometries (and the same trajectories of separated particles), allow to identify individual vortices in the background of complex processes and to develop their theory. Vortex currents are observed in natural air currents (tornadoes and typhoons) and are widely used in various technical applications such as aeronautics, heat transfer, spray drying, separation, enrichment, combustion, etc. [1].

There is a great variety of the vortices in the world's oceans. A common distinction is made between frontal vortices, open ocean vortices arising from baroclinic instability; topographic vortices associated with the flow of water masses around underwater obstacles, and synoptic vortices generated by atmospheric processes

T. O. Chaplina (✉)
Ishlinsky Institute for Problems in Mechanics of the Russian Academy of Sciences, Moscow, Russian Federation
e-mail: tanya75.06@mail.ru

© The Author(s), under exclusive license to Springer Nature Switzerland AG 2022

V. I. Karev (ed.), *Physical and Mathematical Modeling of Earth and Environment Processes*,
Springer Proceedings in Earth and Environmental Sciences,
https://doi.org/10.1007/978-3-030-99504-1_33

Fig. 1 Intense vortices: **a** water tornado off the coast of Florida [2]; **b** aircraft engine generated vortex [3] **c** marine structure off the island of Gotland in the Baltic Sea [3]

(e.g. typhoons). A distinction is made between cyclonic and anticyclonic vortices (by rotation type), large-scale, intermediate-scale and mesoscale (by spatial scale), and quasipermanent, long-lived and short-lived (by time of existence) (Fig. 1).

Satellite information provides a unique opportunity to see the pattern of vortex motion in the ocean. Images from space made in the visible, thermal infrared and radio bands have shown that in addition to large-scale, long-lived quasi-stationary vortices in the ocean (discovered, incidentally, by contact measurements) there are a variety of different-scale vortex formations with lifetimes ranging from several days to several weeks. It has been possible to gain insight into the spatial and temporal scales, formation, evolution and dissipation mechanisms of vortex structures. One of the problems of using vortex devices is related to the loss of stability of axisymmetric swirling flows and emergence of various kinds of complex three-dimensional non-stationary structures in them, affecting all processes in vortex apparatuses.

Despite the centuries-long history of hydrodynamics, dating back to the works of Torricelli and Newton in the seventeenth century [4, 5], many of its problems still remain unsolved. First of all, this applies to eddy currents. Navier–Stokes equation describing the Newtonian fluid motion, written in the first half of XIX century, contains problems which at the turn of XX and XXI centuries was declared by Clay Institute of Mathematics as one of the seven problems of the millennium. The problem of computational prediction of flow characteristics of real practical interest is often far from being solved and is extremely urgent.

The study of vortex motion of fluids, initiated in the seminal work of Helmholtz [6] and continued by outstanding scientists of the century before last and the beginning of the last century Kelvin [7, 8], Prandtl [9], Poincaré [10], Zhukovsky [11] and others, remains actual, until now, as evidenced by a large number of monographs and articles.

Vortex currents have a different structure in the fluid column and at the free surface, where they coexist and interact with waves of different nature. Although the existence of different types of vortices in contact with the free surface (such as the vertical Rankine vortex or the Helmholtz semi-ring) has been known for quite some

time, important questions about their dynamics and impact on the transport of matter require more in-depth analysis.

The study of atmospheric and oceanic transport processes is of particular practical interest. As economic activity and production intensify, more and more chemicals and compounds, including environmentally hazardous ones, enter the natural environment and enter both the air basin and the hydrosphere.

Consideration of substance transfer processes in such complex systems as natural water bodies is associated with many difficulties of methodological and principle nature: extreme complexity of conducting a full-scale experiment, complexity and variability of hydrophysical fields of the ocean and hydrometeorological conditions during studies and, in some cases, complexity and variability of properties of the substance being transferred. In this regard, it is of particular interest to study the transport of matter in stationary vortices and wave currents, which can be formed in laboratory installations with unchanged external conditions. In this case it is possible to avoid problems related to spatial and temporal variability of natural sources of vortex formations and directly trace dependencies of characteristic parameters of flow or characteristics of movement of solid or other objects placed in the flow.

The experimental set-up allows experimental conditions to be reproduced and the stable components of the complex transfer pattern of marker impurities in a composite vortex flow to be investigated.

This chapter presents the results of experimental studies of soluble impurity transport from a compact spot on the free surface of the liquid and inside the resting or involved in the composite vortex motion of the liquid, as well as a visualisation and qualitative analysis of the flow near the disc edge. The rate of change of dye lowering into the liquid column depending on the inductor rotation speed was calculated. It is found that the characteristic features of vortex flow are determined in the region of boundary layer on the disk and then transferred with preservation of the flow pattern shape to the whole area occupied by the liquid. This is confirmed by coincidence of types of spiral motion of liquid particles on the surface and near the disk.

2 Experimental Modeling Vortex Flows: Equipment, Methodology of Laboratory Experiments and Parameters of the Flows Under Study

Several centres for modelling geophysical currents are currently active around the world. In Russia, centres for laboratory modelling of geophysical currents are located in Moscow (Lomonosov Moscow State University, P.P. Shirshov Institute of Oceanology, Russian Academy of Sciences, Obukhov Institute of Atmospheric Physics, Russian Academy of Sciences, Institute for Problems of Mechanics, Russian Academy of Sciences), St. Petersburg, Novosibirsk (Kutateladze Institute of Thermophysics, Russian Academy of Sciences) and Novosibirsk. In St. Petersburg and Novosibirsk (S.S. Kutateladze Institute of Thermophysics SB RAS, M.A. Lavrent'ev

Institute of Hydrodynamics, RAS). The results of the study were published in the Russian Academy of Sciences (Institute of Applied Physics, Russian Academy of Sciences).

Of particular interest are vortex flows, allowing direct comparison with calculations based on fundamental equations, among which the main one is the current generated by a rotating disk in free space, in a narrow fixed shell or in a cylindrical chamber of limited volume completely filled with liquid [12]. The measured parameters here are the velocity and pressure components.

Experiments done in a cylindrical vessel of limited volume, where flow was created by rotation of both upper and lower lids [13–15], gave the results, the structure and main features of which are similar to those obtained in papers, where the source of pulsing is only one of the cylindrical container ends [16].

Realization of steady-state vortex flows under laboratory conditions is alsodescribed in [17] (container with rotating inductors in a closed fluid volume) and in [18], where free surface currents are investigated in a container with various rotating inductors. The vortex flow, created by fluid expulsion from a rotating cylinder, is studied in [19].

Experiments using a mixing impurity as a marker were carried out by the group of T. Leveque (Marseille, France) and published in [20]. A study on the behaviour of immiscible slurry in a rotating-bottom cylinder and the comparison with numerical simulations [21] have shown the possibility of using a composite vortex flow as a separator for petroleum products. Lack of data about properties of vortex currents with free surface and properties of surface of such kind of currents itself makes the theme of research actual.

The rotating end cylinder is the elementary model of various vortex devices in which intensive heat and mass exchange takes place, in particular chemical and biological reactors. In the study of flows in vortex chambers the existence of stagnation or recirculation zones, slowing down exchange processes, therefore, their appearance significantly affects the efficiency of vortex reactors [22, 23].

3 Transfer of Miscible Impurities into the Vortex Flow

The independent transfer of the dye into the vortex flow is illustrated in Fig. 2. In the pictures shown, the experiment carried out with water dyeing using a water-soluble fluorescent dye (uranyl), which emits green light in ultraviolet light. The penetration depth of the coloured central column increases with time. As soon as the main part of the dye descending in the central near-axial flow area to the activator disk reaches the bottom, intensive staining of the entire volume under investigation occurs (Fig. 2b). Intensely stained with uranium, the central part of the flow is green despite the general staining of the volume due to the UV illumination.

An algorithm has been developed to estimate the image brightness over the entire thickness of the volume under study, which is used to calculate the spatial distribution of the dye in the flow. In Fig. 2c, the blue broken line *4* reflects the image

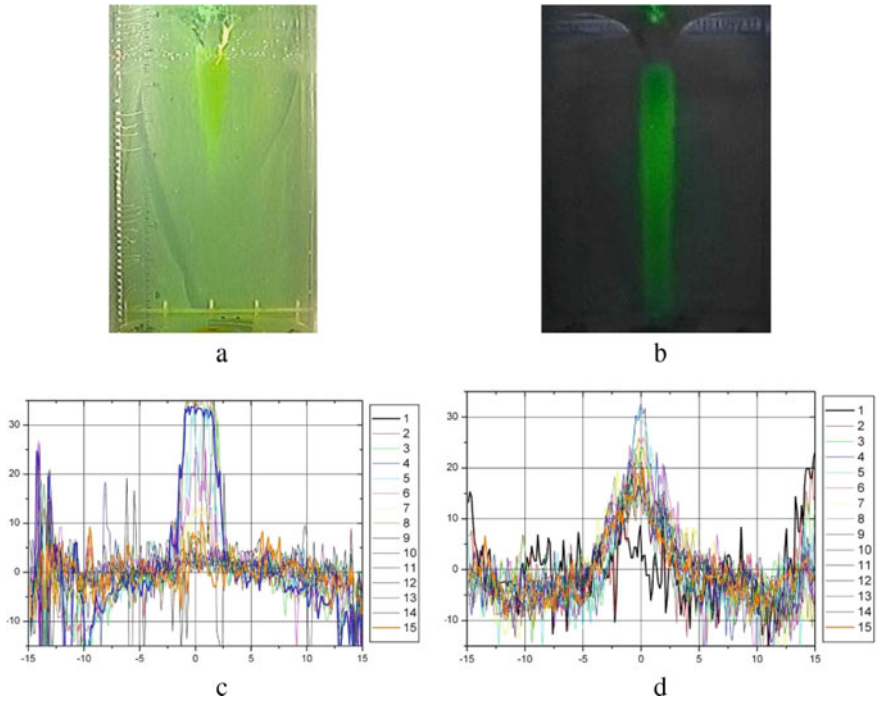

Fig. 2 Impurity transport into the liquid column ($H = 50$ cm, $\Omega = 820$ rpm, $R = 7.5$ cm): **a**—28; **b**—78 s. Change of illuminance in the working area of the container: **c**—22 s; **d**—128 s

brightness distribution along the horizontal at the level of 31 cm above the rotating activator disk; the broken line shows well the area in the middle of the pool where brightness is maximal and, accordingly, there is a dye-filled area (Fig. 2d). The transverse dimension of the central stained column at this level is 3.8 cm. The intensely stained part has clear contours. The broken line *15* runs everywhere near the zero mark, this indicates that at the level of 3 cm above the rotating activator the total background brightness is uniform and, therefore, no more or less intensely coloured areas, compared to the total part of the flux, are observed.

Dependence of the dye penetration depth into the thickness of the compound vortex is shown in Fig. 3. The initial depth of the surface cavern is 4.5 cm, i.e. the initial level of impurity entry is 35.5 cm above the level of the rotating activator. From this mark the plots of dependence of complete filling (staining) of the column for the whole width (symbols *2*) and penetration of "tail of impurity" (symbols *1*) on time began to be plotted.

The evolution of dye propagation into the thickness of the composite vortex is illustrated in Fig. 4 using the example of the development of structures formed by two dye droplets of different colours simultaneously placed on the free surface of the composite vortex.

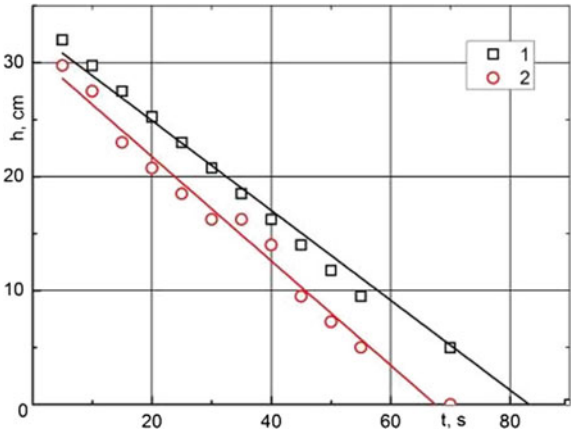

Fig. 3 Change of dye penetration depth with time ($H = 40$ cm, $\Omega = 480$ rpm, $R_d = 7.5$ cm): *1*—lower level of change compared to background brightness, *2*—lower level of full width dyed column

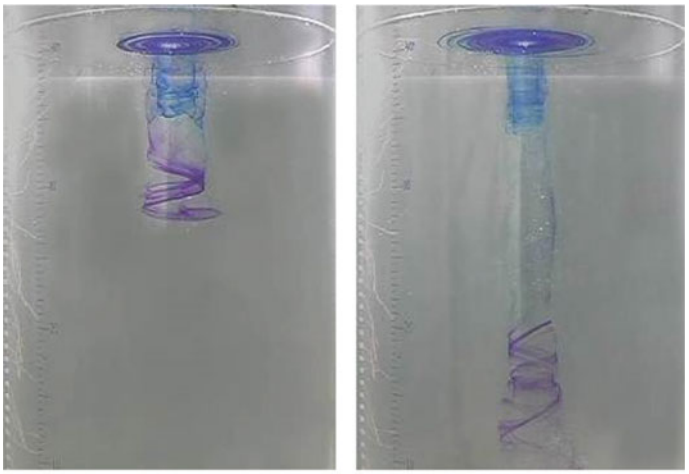

Fig. 4 Evolution of the vertical distribution of the dye of the two colours ($H = 40$ cm, $\Omega = 195$ rpm, $R = 5.0$ cm): **a**, **b**—$t = 1$, 12 s

Both when droplets are placed smaller and farther apart, a separate system of spiral arms on the free surface and a separate helical stained structure in the liquid column are drawn from each dye droplet.

Each helical structure in the fluid column is stretched in the direction of gravity and the current created by the rotating disc. The dyes from the different helical structures do not mix; each one grows independently. The dyed structure closer to the axis of the flow elongates more slowly.

Similar behavior is exhibited by helical structures formed from droplets of soluble dye of different composition. In all cases, helical structures form on the surface of the liquid, the degree of cohesion of which is determined by the duration of the process (Fig. 4). At the periphery of the flow, thin filaments are formed, separated by bands of clear water.

In order to obtain data about the flow pattern as a whole, aluminium powder markers were injected into the investigated liquid volume. In order to highlight a part of the working volume of the installation, the flow pattern data was obtained, illumination was performed by a laser beam unfolded in a plane. Using this technique it was possible to obtain flat "slices" of the flow pattern at different parameters of the experiment.

As a result of capturing the flow pattern on digital still and video cameras, images were obtained, the analysis of which provided information on the nature of impurity particle movement in different areas of the flow studied.

All the experiments carried out can be divided into two groups. The first group includes experiments in which the particles were in the liquid volume before the vortex flow was created. The main purpose of these experiments was to visualise the structure of the vortex flow as a whole. The second group includes experiments where an impurity was introduced into individual regions of the steady flow, aimed at visualising the individual components of the flow.

The primary objective of this type of experiment was to confirm the results obtained with a miscible impurity. For this purpose, experiments were carried out in which markers were injected in the centre of the free surface of the liquid. The comparison of obtained results (Fig. 5a) with the results of similar experiment in which miscible admixture was used (Fig. 5b) has shown the geometrical similarity and similar dynamics of size change of the structures formed at the initial moment. The marker accumulation in the central part of the unit at steady-state flow (Fig. 5c) coincided in shape and size (with 95% accuracy) with the similar structure in the experiment with soluble impurity. The dynamics of marker and impurity propagation also coincided within the margin of error.

The structure of the central part of the composite vortex recorded in the experiment suggested the presence of a solidly rotating core in the flow, the outer part of which had the shape of a cylinder (this was repeatedly confirmed by experiments with mixing admixture, in which the shape of the vortex core was well visualised), while the inner part consisted of so-called secondary vortices, which had a non-stationary character of motion.

Also in all experiments a weak particle transfer from the core to the outer part of the liquid and vice versa was observed. Markers introduced through the centre of the free surface filled the vortex core, after which the transfer of particles almost completely stopped. Subsequently, particles gradually began to fill the outer region of the flow until an equilibrium concentration of markers in the core and outer part was established, after which the transfer of particles between these two regions ceased to be visualised (this was determined by a gradual decrease in brightness of the central part of the frame and appearance of particles in lateral regions outside the core).

The calculated marker penetration rate characteristics are shown in Table 1.

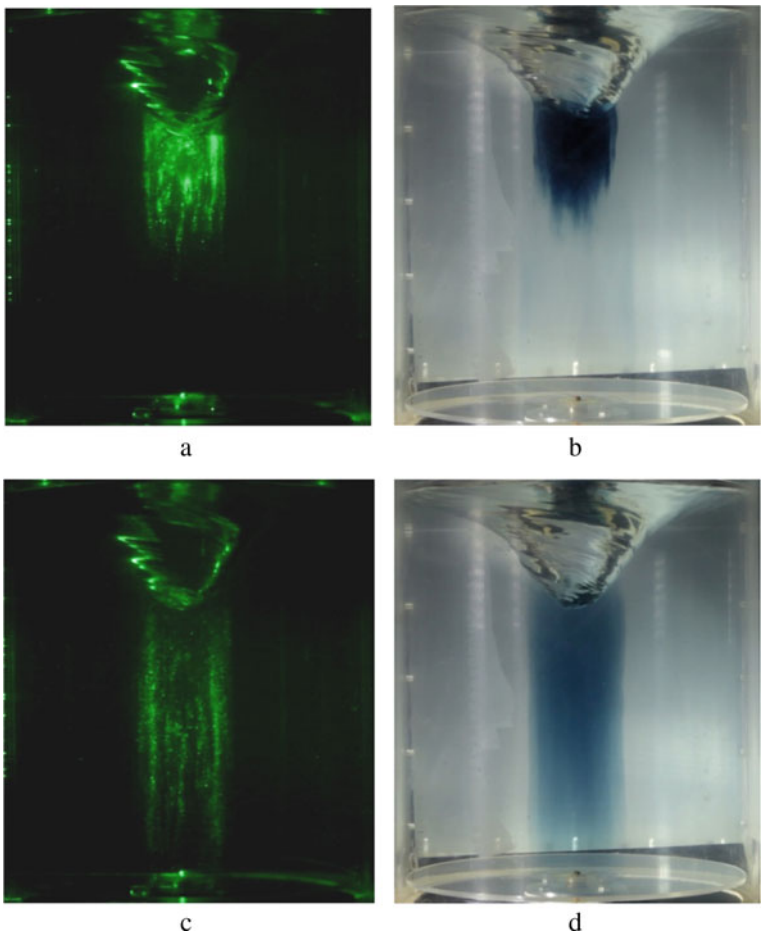

Fig. 5 Comparison of the results of marker (**a**, **c**) and miscible admixture (**b**, **d**) injection experiments through the free surface at cm, $H = 30$ cm, $R = 14$ $\Omega = 220$ rpm. Time elapsed from introduction of the impurity: **a**—13 s, **b**—15 s, **c**—24 s, **d**—16 s

The experiments carried out to determine the main characteristics of suspended solids transport into the liquid column in the composite vortex flow confirmed the linear dependence of the penetration depth of impurity near the vertical axis of the flow on time. Based on the results of these experiments, the shape and size of the area occupied by the particles were traced over time.

An analytical solution of the flow near the disk generating the composite vortex is presented in [24]. This problem is considered under the assumption that the rotating inductor is in contact with liquid only. From the solution of such a problem [24] it follows that, with respect to the disk surface, the liquid elements move in logarithmic spirals.

Table 1 Velocity of impurity penetration into the vortex flow

H, cm	R, cm	Ω = rpm	Approximation Coefficients	
			V, mm/s	ΔV, mm/s
25	5	300	2.24	0.07
25	5	650	3.02	0.05
25	5	1000	5.32	0.09
25	5	1480	7.12	0.06
20	7.5	150	1.98	0.07
20	7.5	300	0.83	0.01
30	7.5	140	2.21	0.05
30	7.5	340	1.22	0.02
20	5	1600	5.58	0.04

4 Conclusions

The experiments carried out to determine the main characteristics of the solute-impurity propagation process in the liquid column in the composite vortex flow confirmed the linear character of the time dependence of the impurity penetration depth near the vertical axis of the flow. Based on the results of these experiments, the change in the shape and size of the dyed region was traced. The rate of change in the dye penetration into the liquid column was calculated as a function of the inductor rotation frequency.

The findings suggest that there is a difference in the size of the areas where the change in fluid velocity should occur according to a linear law (depending on the distance from the vertical axis of rotation) and the central coloured area.

It is found that the characteristic features of the vortex flow are set in the boundary layer region on the disk and then transferred with preservation of the flow structure form to the whole region occupied by the liquid. This is confirmed by coincidence of types of spiral motion of liquid particles on the surface and near the disk.

The results obtained allow a more detailed description of the flow in the thickness of a composite vortex current. The methodology used has yielded results suitable for further studies of vortex structures.

Acknowledgements The work was carried out with the financial support of the grant of the Russian Federation represented by the Ministry of Science and Higher Education of the Russian Federation No. 13.1902.21.0018 (agreement 075-15-2020-802).

References

1. Gupta A., Lilly D., Cyred N. Swirling flows. M .: Mir, 1987. 590 p.
2. Nalivkin D.V., Hurricanes, storms and tornadoes. L .: Science, 1969. 487 p.
3. http://www.nasa.gov/multimedia/imagegallery/image_feature_735.html
4. Newton I. Mathematical principles of natural philosophy / Philosophiæ Naturalis Principia Mathematica. Moscow: Nauka, 1989. 688 p.
5. Faber T. E. Fluid Dynamics for Physicists. Cambridge University Press, 1995. 440 p.
6. Helmholtz H. Uber Integrale der hydrodynamischen Gleichungen, welche den Wirbelbewegungen entsprechen. Journal fur die reine und angewandte Mathematik. 1858. V. 55. P. 25–55.
7. Kelvin Lord. On vortex motion. Royal Soc. Edinburgh. 1868. V. 25. P. 217–260.
8. Kelvin Lord. Vortex statics. Collected works. 1875. V.4. P. 115–128.
9. Prandtl L., Tragflügeltheorie. I Mitteilung. Nachrichten von der Gesellschaft der Wissenschaften Zu Göttingen. Mathematisch-Physikalische Klasse. 1918. P. 151–177.
10. Poincaré A. Theory of vortices. M .: Izhevsk: RKhD, 2000. 160 p.
11. Zhukovsky H. Ye. About attached vortices. Full collection cit., vol. 5, M.-L .: State publishing house of technical and theoretical literature, 1937.
12. Escudier M.P. Observations of the flow produced in a cylindrical container by a rotating endwall. Experiments in fluids, 1984. P. 189–196.
13. Okulov V.L., Sorensen J.N., Voigt L.K. Alternation of right- and left-handed vortex structures at increasing intensity of swirling flow. Letters to Journal of Technical Physics. 2002. T. 28. Vol. 2. P. 37–44.
14. Naumov I. V., Okulov V. L., Sorensen J. N. Two scenarios of instability development in an intensely swirling flow. Letters to Journal of Technical Physics. 2007. T. 33. Vol. 18. P. 32–39.
15. Okulov, V.L.; Naumov, I.V.; Sorensen, J.N. Peculiarities of the optical diagnostics of the pulsating currents (in Russian). Zhurnal tekhnicheskikh fiziki, 2007. T. 77, Vol. 5. P. 47–57.
16. Hoerner S.F., Borst H.V. Fluid-dynamic lift. Practical information on aerodynamic hydrodynamic lift. Bakersfield: Hoerner fluid dynamics. 1985.
17. Gushchin V.A., Konshin V.N. Computational aspects of the splitting method for incompressible flow with a free surface. Journal of Computers and Fluids. 1992. V. 21. № 3. P. 345–353.
18. Kremenetskiy V.V., Stroganov O.Yu., Zatsepin A.G., et al. Frontal currants in the rotating fluid over sloping bottom: influence of canyons. Selected papers of international conference “Fluxes and structures in fluids - 2003”. Moscow: IPMech RAS. 2004. P. 111–114.
19. Andersen A., Bohr T., Stenum B., et al. The bathtub vortex in a rotating container. Journal of Fluid Mechanics. 2006. V. 556. P. 121–146.
20. Beguier C., Bousgarbies J.-L., Leweke T. Tourbillion, Instabilite et Decollement 2001. ISBN 2–85428–551–4. CEPAD 2001. 126 p.
21. Popescu N., Robescu D. Separation of Petroleum Residues Using the Vortex Separation Technique. U. P. B. Sci. Bull., Series D, 2011. Vol. 73, Iss. 1.
22. Naumov I.V., Mikkelsen R.F., Okulov V.L. Formation of stagnation zone on the axis of closed swirling flow. Thermal Physics and Aeromechanics. 2014. T. 21, № 6. P. 799–802.
23. Herrada M.A., Shtern V.N., Torregrosa M.M. The instability nature of Vogel-Escudier flow. J. Fluid Mech. 2015. Vol. 766. P. 590–610.
24. Kistovich A.V., Chaplina T.O., Stepanova E.V. Spiral structure of trajectories of liquid particles near the vortex surface. Computational technologies. 2019. T. 24. № 2. P. 67–77.

Mass Transfer in Underground Mining-Containers in Rock Salt

V. P. Malyukov

Abstract The paper considers a complex mass transfer, consisting of local mass transfers, during the construction and operation of a tank-work under the hydrodynamic effect of a solution on rock salt with various separation of the boundary layer (Malyukov in Online 16:25–40, November 2021; Malyukov V.P. Physical processes and technologies for the construction of underground workings-tanks under the hydrodynamic effect of solution on rock salt: monograph / V.P. Malyukov - Moscow: RUDN, 2021. - 299 p.;): diffusion mass transfer (mass transfer) with a concentration separation of the boundary layer, mass transfer of insoluble inclusions (different in composition, scattered and from interlayers), vortex mass transfer, separation mass transfer (when salt plates are separated from crystals), gas mass transfer (when gas is released from salt). Local mass transfer processes include fluid infiltration into rock salt and convergence (a change in the volume of production when the rock salt of the production zone is displaced into the tank space), cyclic infiltration and convergence. Similar processes occur in the chambers (caverns) of brine mills.

Keywords Rock salt · Solution · Underground mining · Mass transfer · Concentration · Insoluble inclusions · Vortices · Separation of particles · Gas

It was established for the first time that in the process of mass transfer, when a solution is exposed to rock salt, a complex mechanism of various separation of the boundary layer is formed: concentration separation, surface separation due to surface irregularities (protrusions of the depression), separation when insoluble inclusions fall out of the salt—mechanical separation, vortex separation during the formation of vortices at the surface, mechanodynamic separation when the salt plate is detached from the crystal, gas separation when gas is released from rock salt (gas-mechanical separation when the salt plate is detached and gas is ejected from the crystal, gas-microcrystalline when gas is ejected from the intercrystalline space) [1, 2].

V. P. Malyukov (✉)
Peoples' Friendship, University of Russia, Moscow, Russia
e-mail: v.malyukov@mail.ru

© The Author(s), under exclusive license to Springer Nature Switzerland AG 2022

V. I. Karev (ed.), *Physical and Mathematical Modeling of Earth and Environment Processes*,
Springer Proceedings in Earth and Environmental Sciences,
https://doi.org/10.1007/978-3-030-99504-1_34

Based on the hydrodynamic analogy, it is possible to determine the ratio of the mass transfer coefficient K to the average flow velocity V, which is a dimensionless quantity and is called the Stanton diffusion criterion Std = K/V.

By analogy with the Stanton diffusion criterion, it is possible to represent the ratio of the mass transfer coefficient K to the average velocity of the liquid being torn off V_1 as a criterion of the flow being torn off during the hydrodynamic action of the solution on rock salt Mo = K/ V_1.

In the process of exposure of the solution to rock salt, when the boundary layer is separated, a concentration diffusion-turbulent boundary layer (DT) is formed.

The ratio of the mass transfer coefficient K to the average flow velocity V_2 of the concentration diffusion-turbulent boundary layer during separation of the boundary layer during hydrodynamic action on rock salt, which is a dimensionless value, can be called the diffusion-turbulent criterion Mdt = K/ V_2.

Taking into account the above results of experimental studies of rock salt mass transfer at various separation of the boundary layer under the hydrodynamic action of the solution [1, 2], the article considers a complex mass transfer—M, consisting of local mass transfers, during the construction and operation of workings of reservoirs for reserving hydrocarbons: diffusion mass transfer (mass transfer) with concentration separation—Md, mass transfer of insoluble inclusions (various in composition, scattered and from interlayers)—Mi, vortex mass transfer—Mv, separation mass transfer (when salt plates are separated from crystals)—Me, gas mass transfer (when gas is released from salt crystals)—Mgc, gas mass transfer when gas is released from the intercrystalline space—Mgs. Local mass transfers include fluid infiltration into rock salt: liquid infiltration into rock salt—Mil, gas infiltration into rock salt—Mig. Local mass transfers include convergence (displacement of rock salt of the near-circuit zone of production into the space of the tank)—Mc. Mass transfer of the solution supplied to the production (usually water) in a mineralized (stratified) solution in a container (the process of surfacing a light solution in a denser one) is Mls. Mass transfer of a denser solution located above a less dense one in the gravity field, with the development of concentration convection (concentration-convective motion, the process of lowering a denser solution into a less dense one)—Mhs.

Complex mass transfer is equal to the sum of local mass transfers:

$$\begin{aligned} M = {} & Md + Mi + Mv + Me + Mgc + Mgs + Mail + Mig \\ & + Mc + Mls + Mss \end{aligned} \tag{1}$$

In real conditions, the number of local transfers and their combination may be different.

Laboratory experiments made it possible to see and analyze the separation of rock salt particles from crystals under the hydrodynamic action of the solution—mass transfer with tear-off destruction.

A laboratory installation for determining the mass transfer coefficient of rock salt is shown in Fig. 1.

The mass transfer coefficient of rock salt (K) is determined by the formula

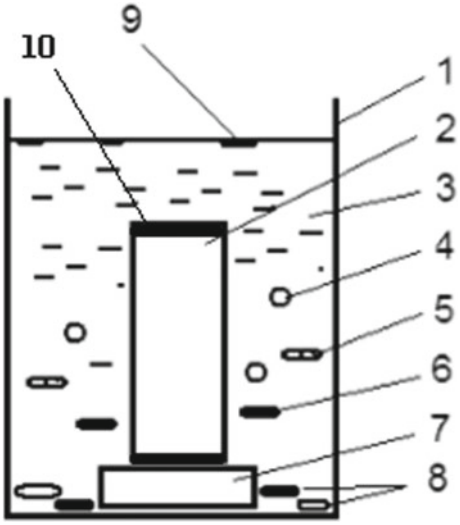

Fig. 1 Diagram of a laboratory installation for determining the mass transfer coefficient of rock salt under the hydrodynamic action of a solution: 1—container; 2—core; 3—solution; 4—gas bubbles; 5—salt plates; 6—particles of insoluble inclusions; 7—stand; 8—insoluble particles and salt plates that have fallen out; 9—light particles of impurities that have surfaced; 10—insulating coating of the ends of the core

$$K = \frac{\Delta G}{S_{av} \cdot t \cdot (C_l - C_o)} \tag{2}$$

where K is the mass transfer coefficient of rock salt, m/s——weight loss of the sample, g; s_{av} is the average value of the dissolution surface, cm^2; t is the duration of dissolution, s; C_l is the maximum concentration of NaCl in an aqueous solution; C_o is the concentration of the solvent, g/cm^3.

The singularity of the tear-off destruction (mass transfer) lies in the fact that a part of the rock salt (small fragments, plates) is torn off—destruction occurs under the hydrodynamic action of the solution with the formation of cavities on the surface of the rock salt with a flat base with a thickness equal to the thickness of the torn plate, in contrast to the formation of hemispherical cavities under the influence of vortex structures [1, 2].

The breakaway destruction of rocks during the development of deposits is noted in various types of rocks and mining and geological conditions, including in salts (mines of the Russian Federation, USA, Germany) [3].

Experimental studies on the separation of rock salt plates from crystals under the hydrodynamic action of the solution were carried out for two variants. The first variant of rock salt plate separation was considered for core samples taken from the Botuobinskoye deposit, Sakha Republic. The second variant of rock salt plate separation is considered for core samples with gas inclusions in crystals from the Tuz-Gelu deposit, Turkey.

Under the destruction of some part of the near-contour zone of production during the separation of rock salt plates, under the hydrodynamic action of an aqueous solution, the transition of rock salt in a solid state into a solution with an increase in

the interaction surface of rock salt and solution (mass transfer of rock salt in a solid state under the hydrodynamic action of the solution) is considered.

This mass transfer of rock salt is defined as the separation of plates from salt crystals perpendicular to the surface.

The separation of rock salt plates is characterized by an increase in the intensity of the mass transfer process, which is characterized by the amount of destroyed material per unit of time, the size of the plates, and sound accompaniment. The separation of the plates is accompanied by a sound like a pencil hitting wood.

For rock, pores in the form of ellipsoids are more typical than balls [3]. Rock salt plates, when detached during hydrodynamic action, have the shape of ellipsoids. The size of the ellipsoidal plates: the large axis is about 3 mm, the small ~2 mm, the thickness is ~1 mm.

The size of salt crystals from the Tyuz-Gelu and Botuobinsky deposits are approximately the same. The shapes and sizes of the torn plates are also approximately the same. The torn plates bounce approximately the same distance from the samples.

The effect of "zonal disintegration of rocks" [4] is that around deep underground workings there is an alternation of zones of induced fracturing and zones of weakly intact rocks. The effect was discovered by employees of IGD SB RAS and NMMC during experimental studies at the Oktyabrsky mine.

Similarly, the effect of "zonal disintegration of rock salt" for the case under consideration of the separation of plates from rock salt crystals under the hydrodynamic action of the solution can be characterized by zonal disintegration of the stressed state of rock salt along the thickness of the formation—alternating zones (intervals) of various stressed states of rock salt formed during the genesis process or under the influence of: natural (earthquake), man-made (nuclear explosions, for example, in the region of the Botuobinsky deposit).

The tear-off destruction of rock salt under the hydrodynamic action of the solution occurs when the salt crystals contain compressed free gas, which causes the formation of microcracks near the pores and the separation of plates when the crystal wall is thinned on contact with the solution. In this case, the action of the expanding gas is characterized by the dynamic separation of the plates from the crystals and the movement of the detached plates to a certain distance from the rock. The released gas also moves some distance away from the rock. The process of separation of plates from salt crystals and the release of gas is characterized by the micro-release of rock salt and gas during the hydrodynamic effect of the solution on rock salt.

Infiltration is the advance of a fluid (liquid, gas) into a solid layer (rock salt in the near-circuit zone of production) when the pressure exceeds a critical value [5, 6].

Studies on the filtration of fluids into rock salt during underground dissolution during the construction of underground tank workings were carried out using research by French specialists with implementation at the Astrakhan Gas Condensate field (AGCM) [5–9].

Studies on the infiltration of fluids into rock salt during underground dissolution were first conducted by French scientists Desgree P., Durup J.-G. During the experiment at the well of the Etrez field (France), the parameters of infiltration (penetration into rock salt) of saturated solution and gas (nitrogen) at the corresponding pressure

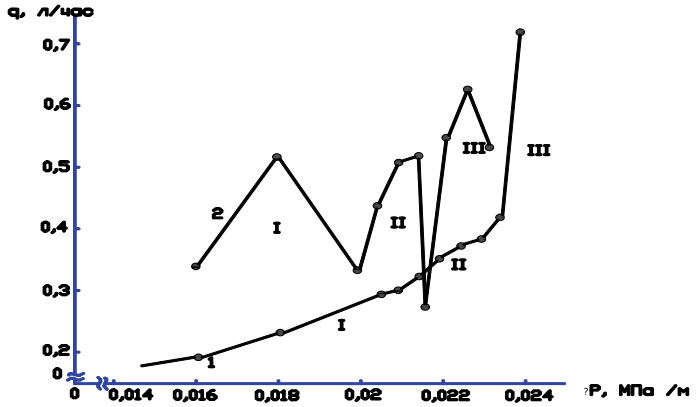

Fig. 2 Change in the flow rate of fluid infiltration into rock salt depending on the pressure gradient: 1—saturated brine; 2—gas; I, II, III—stages of the process

gradients of the current medium (back pressure) were obtained. Using these data, we obtained the magnitude of the change in the flow rate of fluid filtration into rock salt depending on the pressure gradient (Fig. 2).

Three stages of the process can be distinguished on the graph, which characterize the development of the process of fluid penetration into rock salt at appropriate pressure gradients.

From the dependence shown in Fig. 2. it follows that during infiltration, various mechanisms of fluid penetration into rock salt for liquid and gas are possible (curves 1 and 2).

When the solution is infiltrated into the near-contour zone of production, the process of cracking of rock salt occurs at stages 1, 2—hydraulic cracking of the rock—HRC—1, at the third stage, hydraulic fracturing of the rock—HRF—2 occurs.

There is a critical back pressure value (critical pressure) when filtering the fluid into the rock salt of the contact zone, at which an effective tensile stress occurs, which exceeds the strength of the rock salt and leads to cracking.

Similar to the manifestation of the infiltration mechanism, Russian scientists, in order to increase the productivity of oil and gas wells, proposed a method of drilling for the development of multiple cracking in the rock [10].

Similarly to the presented dependence of the mass transfer coefficient during the hydrodynamic effect of the solution on rock salt, it is possible to present a dependence for determining the mass transfer coefficient during fluid (solution, gas) infiltration at each stage $K = V/St$, where K is the mass transfer during fluid infiltration, V is the volume of the fluid, S is the contact area of the fluid and the salt surface, t is time.

As a result of the manifestation of the plastic properties of rock salt in the underground mine-tank, there is a shift (sliding) of the production contour towards the axis of production—mass transfer of solid salt.

Full-scale studies of mass transfer processes during convergence in an underground mine-tank in rock salt were carried out at the Astrakhan gas condensate field.

The numerical values of the parameters characterizing the rheological properties are determined by the phenomenological relations that evaluate the experimental results of the study of the deformation of salt rocks over time. When using structural rheological models, the "full-scale" creep parameter acts as a rheological parameter determining the temporal nature of geomechanical processes [11–16].

Under the action of a load not exceeding the limit of long-term strength, rheological processes in salt rocks are satisfactorily evaluated by linear viscoelasticity equations with a power-law Abel core.

The processes of mass transfer in the underground mine-tank at various technological stages are characterized by: the movement of the contour during the dissolution of rock salt (with an increase in the volume of the mine-tank in the process of its creation); displacement of the contour of the mine due to the creep of rock salt (the ability of salt to deform plastically and flow in the direction of lower pressure)—convergence (decrease in the volume of the mine-tank); it is possible by simultaneous flow of convergence and infiltration of fluid into the contiguous rock salt massif or alternation of convergence and infiltration, depending on physicochemical, thermobaric and hydrodynamic conditions.

In the process of field studies in an underground mine, a tank constructed with the hydrodynamic effect of the solution on rock salt, at the initial stage, the flow rate of the pouring solution is recorded on the open head of the well at a constant pressure of the saturated solution column. Then, the pressure change over time is recorded on the closed head with varying pressure at the wellhead. The observations were carried out during the period when there was a saturated solution in the underground mining tank at the temperature of the surrounding massif.

As a result of the field studies carried out, the dependence of the pressure growth rate on the back pressure was obtained. With increasing pressure at the wellhead, the rate of pressure growth decreases, approaching the minimum value at a certain stage (Fig. 3).

Based on the results of measurements of the free outflow of saturated solution from the underground reservoir and the increase in pressure at the wellhead with the valve closed, the displacements of the contour rocks around the workings at the Astrakhan gas condensate field were calculated and the deformation and rheological characteristics of rock salt were evaluated (Table 1).

To quantify the parameters of the creep of rock salt in the contour zone of underground mining in full-scale conditions, a model is used to recalculate the measured values characterizing the deformability of rocks containing underground mining in time to creep parameters. In this case, the rock mass in the vicinity of the mine is considered as homogeneous, and its viscoelastic deformations are described by an integral equation with an Abelian creep kernel.

The creep rate of a sodium chloride sample when impregnated with an aqueous NaCl solution in laboratory conditions is 6.3 microns/h. At a higher temperature

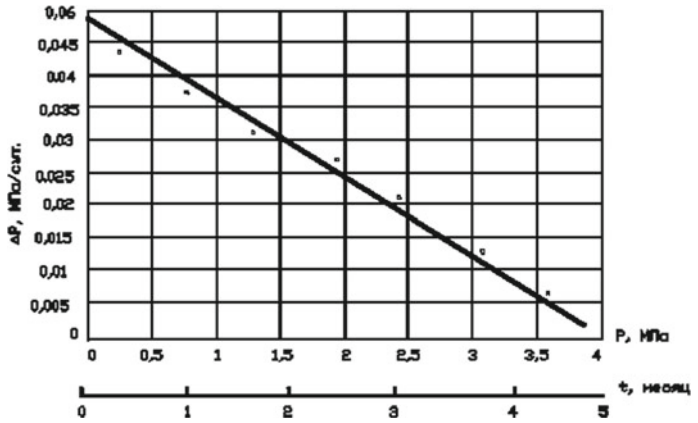

Fig. 3 Dependence of the pressure change (ΔP) on the pressure (P) at the mouth of the underground mine

Table 1 Parameters of rock salt creep in the vicinity of an underground mine-tank

Overpressure, P_o, MPa	Contour offset, m/month	Indicator $\delta_1 P_o/E$, C − 0.3	Parameter δ_1, C − 0.3
7.8	3.65	$1.0559 \cdot 10^{-6}$	0.00.206
6.30	2.8	$0.8 \cdot 10^{-6}$	0.00.197
5.35	2.26	$0.6538 \cdot 10^{-6}$	0.00.187

(~40 °C) and under the influence of back pressure, the rate of displacement of the contour of the underground reservoir is 3.65 mm/month (5.1 microns/h).

For an underground mine filled with saturated solution, the deformation-rheological index of the contiguous rocks is represented in the form, where $\delta_1(\gamma_n - \gamma_p)H/E$ is the average volume weight of the overlying rocks, γ_p is the volume weight of the saturated brine, H is the depth of the mine, E is the Young's modulus.

It is assumed that the natural stress state of the salt dome in the vicinity of the workings under consideration is close to geostatic. Underground production of cylindrical shape (radius R = 8.2 m, height h = 91 m, N = 722.5 m, E = 1.53 · 104 MPa, a dimensionless parameter of the creep of rock salt α = 0.7).

The change of deformation rheological index of rock salt rock underground circuit output capacitance into the array with free spout of the solution (2) shows that removal into the array deformability decreases the marginal rocks

$$\delta_1 P_u/E_{r=R+1} = 0.94 \cdot 10^{-6} C^{-0.3};$$
$$\delta_1 P_u/E_{r=R+2} = 0.85 \cdot 10^{-6} C^{-0.3}; \delta_1 P_u/E_{r=R+3} = 0.77 \cdot 10^{-6} C^{-0.3} \quad (3)$$

where r is the distance from the contour to the depth of the array.

The "full-scale" creep parameter δ_1 characterizes a certain "aggregate" creep of the material and takes into account the type of stress state of the contiguous rocks in the vicinity of the reservoir, as well as the ratio between the operating stresses and the strength characteristics of the rock in the array. The above values of the "full-scale" parameter characterize the deformability in time of the rock salt of the rock contour of the underground mine at varying values of overpressure.

Full-scale studies were carried out on the change in the deformed state of the rock mass in the vicinity of the production-capacity.

The determination of the back pressure in the underground mine-a tank created by a special method in rock salt was carried out at the AGCM.

In the previous period of time, there was a tendency in the leading countries to use nuclear charges for peaceful purposes, and for this purpose, explosions of nuclear charges (special method) were carried out at a certain depth at the AGCM in salt domes to create underground workings-tanks for hydrocarbon reserves.

The explosions of nuclear charges in rock salt in order to create underground workings for the reservation of hydrocarbons had a significant thermodynamic effect on the surrounding rock mass. In the future, there was a problem of possible negative manifestations of radioactivity from underground workings-tanks and the impact on the environment. In some cases, the distance between underground workings-tanks created by a special method and underground workings-tanks created by the traditional method (with the hydrodynamic effect of the solution on rock salt) was ~300 m.

In [17], a recommendation is given to reduce convergence: when the tank is operated according to a "dry" scheme: convergence is prevented by back pressure of natural gas or other gases under high pressure. This recommendation was used to reduce convergence at underground workings created by a special method (explosion of nuclear charges) at the AGCM. At that time there was no information on the infiltration of fluids in rock salt. I happened to get acquainted with the work [5] on fluid infiltration and the corresponding parameters of the production created by a special method at the facility.

Convergence took place in the underground mining tank—the displacement of the rock salt of the contour zone and the extrusion of components from the underground mining tank. To reduce convergence, natural gas was pumped into the underground production tank under high pressure, which was periodically released from the production to the surface. But at the same time, the manifestation of infiltration in the contiguous zone of production was not taken into account. Due to infiltration after gas delivery and pressure reduction, the sliding (sliding) of rock salt from the near-circuit zone of production into the tank space increased. At that time, for specific conditions, I performed a calculation to determine the pressure at which infiltration did not occur. The design pressure was set at the wells. Perhaps for the first time, the cyclic mechanism of infiltration—convergence was considered—a complex mechanism of mass transfer during infiltration and convergence in an underground mine created by a special method.

References

1. Malyukov V. P. . Detached Flows at Rock Salt Exposition to Aqueous Solution, «Processes in GeoMedia — Volume IV», First Online: 16 November 2021, P. 25–40.
2. Malyukov V.P. Physical processes and technologies for the construction of underground workings-tanks under the hydrodynamic effect of solution on rock salt: monograph / V.P. Malyukov - Moscow: RUDN, 2021. - 299 p.
3. Odintsev V.N. Separated destruction of a rock mass. - M .: IPKON RAN, 1996, 166 p.
4. . Shemyakin E.I., Fisenko G.D., Kurlenya M.V., Oparin V.N. et al. Effect of zonal disintegration of rocks around underground workings // Dokl. Academy of Sciences of the USSR. - T. - 289. - N 5. - P. 1088–1094.
5. Desgree P., Durup J.-G. Behaviour of in situ satl at extremely high pressure levels. International Gas Research conference Cannes, France, 1995, pp.240–252.
6. Malyukov V.P. Infiltration of fluid into rock salt of the near-contour zone of an underground mine. Mining information and analytical bulletin.-M .: MGGU, 2004, No. 9, P. 110–114.
7. Malyukov V.P. Investigation of fluid infiltration into rock salt in the near-contour zone of an underground mine. Bulletin of the Peoples' Friendship University of Russia. Series: engineering research, 2006, No. 1 (12), P. 87–92.
8. Maljukov V.P. Mass exchange in an underground reservoir at they manifestation of salt flow and brine infiltration. SMRI. Fall Meeting, El Paso, 1997, P. 117–129.
9. Malyukov V.P. Deformability of rock salt in the near-contour area of an underground mine-tank during fluid infiltration. International Conference. Moscow - Navoi, 2005, P. 328–330.
10. Khristianovich S.A., Kovalenko Yu.F., Kulinich Yu.V., Karev V.I. Increasing the productivity of oil wells using the georexing method // Oil and Gas Eurasia. 2000. No. 2. P. 90–94.
11. Baklashov I.V. Deformation and destruction of rock massifs. M., Nedra, 1988. - p. 271.
12. Viktorov S.D., Iofis M.A., Goncharov S.A. Displacement and destruction of rocks [Otv. ed. K.N. Trubetskoy]. - M.: Nauka, 2005 - 277 p.
13. Nadai A. Plasticity and destruction of solids. Volume 2.M., 1969. 863 p.
14. Nikolaevsky V.N. Geomechanics and fluid mechanics. M., Nedra, 1996. 447 p.
15. Malyukov V.P. Fedorov B.N., Shafarenko E.M. Field studies of the stability of the rock salt massif in the vicinity of the underground reservoir. International Conference on Underground Gas Storage. M, Section S.P. 1, 1995, P. 93–95.
16. Malyukov V.P. Field studies of mass transfer processes in the near-contour zone of underground reservoirs in rock salt. Mining information and analytical bulletin. Miner's Week - 2002, M., No. 11, 2002, P. 220–224.
17. Mazurov V.A. Underground gas and oil storage facilities in rock salt deposits. Moscow, Nedra, 1982.212 p.